frontiers | Research Topics

Permian-triassic tethyan orogeny along the southern eurasian margin

Edited by
Mingcai Hou, Fuhao Xiong, Changqian Ma, Gillian Foulger and Shengyao Yu

Published in
Frontiers in Earth Science

ISSN 1664-8714
ISBN 978-2-83251-382-8
DOI 10.3389/978-2-83251-382-8

About Frontiers

Frontiers is more than just an open access publisher of scholarly articles: it is a pioneering approach to the world of academia, radically improving the way scholarly research is managed. The grand vision of Frontiers is a world where all people have an equal opportunity to seek, share and generate knowledge. Frontiers provides immediate and permanent online open access to all its publications, but this alone is not enough to realize our grand goals.

Frontiers journal series

The Frontiers journal series is a multi-tier and interdisciplinary set of open-access, online journals, promising a paradigm shift from the current review, selection and dissemination processes in academic publishing. All Frontiers journals are driven by researchers for researchers; therefore, they constitute a service to the scholarly community. At the same time, the *Frontiers journal series* operates on a revolutionary invention, the tiered publishing system, initially addressing specific communities of scholars, and gradually climbing up to broader public understanding, thus serving the interests of the lay society, too.

Dedication to quality

Each Frontiers article is a landmark of the highest quality, thanks to genuinely collaborative interactions between authors and review editors, who include some of the world's best academicians. Research must be certified by peers before entering a stream of knowledge that may eventually reach the public - and shape society; therefore, Frontiers only applies the most rigorous and unbiased reviews. Frontiers revolutionizes research publishing by freely delivering the most outstanding research, evaluated with no bias from both the academic and social point of view. By applying the most advanced information technologies, Frontiers is catapulting scholarly publishing into a new generation.

What are Frontiers Research Topics?

Frontiers Research Topics are very popular trademarks of the *Frontiers journals series*: they are collections of at least ten articles, all centered on a particular subject. With their unique mix of varied contributions from Original Research to Review Articles, Frontiers Research Topics unify the most influential researchers, the latest key findings and historical advances in a hot research area.

Find out more on how to host your own Frontiers Research Topic or contribute to one as an author by contacting the Frontiers editorial office: frontiersin.org/about/contact

Permian-triassic tethyan orogeny along the southern eurasian margin

Topic editors

Mingcai Hou — Chengdu University of Technology, China
Fuhao Xiong — Chengdu University of Technology, China
Changqian Ma — China University of Geosciences Wuhan, China
Gillian Foulger — Durham University, United Kingdom
Shengyao Yu — Ocean University of China, China

Citation

Hou, M., Xiong, F., Ma, C., Foulger, G., Yu, S., eds. (2023). *Permian-triassic tethyan orogeny along the southern eurasian margin*. Lausanne: Frontiers Media SA.
doi: 10.3389/978-2-83251-382-8

Table of contents

frontiers | Frontiers in Earth Science

TYPE Editorial
PUBLISHED 06 January 2023
DOI 10.3389/feart.2022.1049535

OPEN ACCESS

EDITED AND REVIEWED BY
Derek Keir,
University of Southampton,
United Kingdom

*CORRESPONDENCE
Fuhao Xiong,
fhxiong@cdut.edu.cn

SPECIALTY SECTION
This article was submitted to Structural Geology and Tectonics, a section of the journal Frontiers in Earth Science

RECEIVED 20 September 2022
ACCEPTED 23 September 2022
PUBLISHED 06 January 2023

CITATION
Hou M, Xiong F, Ma C, Foulger GR and Yu S (2023), Editorial: Permian-Triassic Tethyan orogeny along the southern Eurasian margin.
Front. Earth Sci. 10:1049535.
doi: 10.3389/feart.2022.1049535

Editorial: Permian-Triassic Tethyan orogeny along the southern Eurasian margin

Mingcai Hou[1], Fuhao Xiong[2]*, Changqian Ma[3], Gillian R. Foulger[4] and Shengyao Yu[5]

[1]State Key Laboratory of Oil and Gas Reservoir Geology and Exploitation, Chengdu University of Technology, Chengdu, China, [2]College of Earth Science, Chengdu University of Technology, Chengdu, China, [3]School of Earth Sciences, China University of Geosciences, Wuhan, China, [4]Department of Earth Sciences, Durham University, Durham, United Kingdom, [5]College of Marine Geosciences, Ocean University of China, Qingdao, China

KEYWORDS

Tethyan, magmatism, metamorphism, sediment provenance, tectonic, geodynamic

Editorial on the Research Topic
Permian-Triassic Tethyan orogeny along the southern Eurasian margin

As one of the major Phanerozoic orogenic belts on Earth, the Palaeo–Tethyan orogenic system along the southern Eurasian margin is characterized by multiple magmatic, sedimentary, metamorphic and mineralization events, recording the oceanic basin closure and terrane accretion during the convergence of Cimmerian microplates. A systematic study of these petrological and metallogenic records is beneficial to understand the assembling processes of the Cimmerian terranes, and thus helps to reconstruct the pre–Cenozoic evolution history of the Tethyan orogenic system. Although important advances have been made over the last decades, many parts of this orogenic system are poorly studied, and some key scientific problems need to be further studied by multidisciplinary integrated approaches. Therefore, we launched a Research Topic in Frontiers in Earth Science to discuss 1) Tethyan tectonic evolution and dynamic processes; 2) sediment provenance and paleogeographic reconstructions within the Tethyan realm; 3) geodynamic similarities and differences in other tectonic realms.

This Research Topic collects 10 papers from different disciplines, which helps to understand the tectonic evolution and geodynamic processes in the Tethyan realm. Among them, three articles focus on sedimentary provenance, sedimentary structure and tectonic implications. For example, Han et al. studied the provenance of the Lower Triassic Qingtianbao Formation in the southwestern margin of the South China Craton. Their results suggest that the Palaeo–Tethyan Ocean may undergo unidirectional subduction westward beneath the Indochina Block during the Late Permian–Early Triassic, providing an important constraint to the subduction polarity of the Eastern Tethyan ocean. Lv et al. studied the sandstone petrography and detrital U-Pb age of the Lower Jurassic Baitianba Formation from the Sichuan Basin, which helps to understand the pre-collisional tectonic evolution of the basin–mountain system at the margin of the

Tibetan plateau in the Cenozoic. Liang et al. focused on the age and tectonic nature of the late Paleozoic to early Mesozoic sedimentary succession in the Sanjiang Tethyan orogenic belt, SE Tibetan Plateau, and revealed that the studied succession deposited within a retro-foreland basin along the rear part of the Permian-Triassic magmatic arc in response to flat subduction of the Palaeo–Tethyan Ocean.

Three papers within this Research Topic provide insights into tectono-magmatism and mineralization. Gan et al. studied one Triassic adakitic pluton in East Kunlun orogen, Northern Tibetan Plateau, to constrain its petrogenesis and tectonic setting. Their study results suggest that the Late Triassic adakitic magmatism in East Kunlun orogen may be the response to the tectonic transition from oceanic subduction to post–subduction extension, and the reworking of ancient continental crust is the major mechanism of continental crust evolution in the Palaeo–Tethyan orogenic belt. Li et al. studied the Peridotite xenoliths to constrain the nature and evolution of the mantle beneath SE China. Their study reveals the precise timing of the mantle evolution from enriched to depleted, providing ideas and references for exploring the evolution process of the Tethyan mantle. Liu et al. studied the geochronology and geochemistry of high-Mg monzodiorite in the Lhasa terrane, Southern Tibetan Plateau. Their study results suggest that the delamination of the thickened crust may have occurred after the collision between the Lhasa block and the Qiangtang block.

Two articles published on this Research Topic focus on metamorphism and Tethyan tectonic evolution. Lu et al. presented EPMA major and LA-ICP-MS trace element studies on the garnets in the ultrahigh-pressure eclogites from the Changning-Menglian Tethyan suture. Their results reveal the rapid exhumation, cooling and decompression processes after short-term peak metamorphism during the closure of the Palaeo-Tethyan ocean. Fu et al. studied petrology, geochemistry, geochronology and Sr-Nd-Hf isotopes of the Bangbing eclogites in the SE Tibetan Plateau. Their study suggests that the Changning-Menglian Tethyan suture zone is a typical oceanic subduction-accretionary belt, and the Palaeo-Tethyan oceanic subduction lasted during the Early-Middle Triassic followed by the rapid exhumation in the Late Triassic.

Big Data and Machine Learning are becoming more and more important tools for geoscience research, and their combination may create unexpected solutions to conventional geoscience problems. This Research Topic collects two representative studies to show the powerful role of this new research tool. Li et al. used big data and geostatistical models of geochemical elements to study the viscosity variation of basalts, aiming to discover more potential new hydrothermal or massive sulfide fields. Their studies provide a possible rule for the hydrothermal vents' exploration. Hu et al. used computer image recognition technology to calculate fault multifractality and applied this method to fault study of the Permian Maokou Formation in Sichuan Basin, western Yangtze Block. Their study results suggest that the Sichuan basin was affected by Tethyan collisional orogeny in Triassic, which controlled the NW–SE compressional environment and the NE-trending faults.

In conclusion, the articles collected in this topic are the results of multidisciplinary research including petrology, sedimentary geology, structural geology, marine geology and geochemistry. We hope that the articles within this Research Topic would provide further insights into the tectonic evolution and geodynamics of the Tethyan orogenic system.

Author contributions

MH and FX wrote the original text. CM, GF, and SY conducted the revisions. All authors reviewed the final manuscript and approved it for publication.

Funding

The work was supported by NSFC Program (No. 41602049) and the Research Project of Chengdu University of Technology (No. 2021ZF11412).

Acknowledgments

We gratefully acknowledge the efforts of the reviewers for their helpful comments. We would like to thank the authors for their valuable contributions to this Research Topic.

Conflict of interest

The authors declare that the research was conducted in the absence of any commercial or financial relationships that could be construed as a potential conflict of interest.

Publisher's note

frontiers in Earth Science

ORIGINAL RESEARCH
published: 29 March 2022
doi: 10.3389/feart.2022.845763

Petrogenesis and Geodynamic Implications of Late Triassic Mogetong Adakitic Pluton in East Kunlun Orogen, Northern Tibet: Constraints from Zircon U–Pb–Hf Isotopes and Whole-Rock Geochemistry

Jie Gan[1,2], *Fuhao Xiong*[1,2,3]*, *Qianru Xiao*[1,4]*, *Wei Wang*[2] *and Dongdong Yan*[2]

[1]*Key Laboratory of Tectonic Controls on Mineralization and Hydrocarbon Accumulation, Chengdu University of Technology, Chengdu, China,* [2]*College of Earth Science, Chengdu University of Technology, Chengdu, China,* [3]*State Key Laboratory of Oil and Gas Reservoir Geology and Exploitation, Chengdu University of Technology, Chengdu, China,* [4]*College of Tourism and Urban-Rural Planning, Chengdu University of Technology, Chengdu, China*

OPEN ACCESS

Edited by:
Guillermo Booth-Rea,
University of Granada, Spain

Reviewed by:
Liang Liu,
Institute of Geochemistry (CAS), China
Bin Liu,
Yangtze University, China

***Correspondence:**
Fuhao Xiong
xiongfuhao2014@cdut.edu.cn
Qianru Xiao
xiaoqianru@cdut.edu.cn

Specialty section:
This article was submitted to "Structural Geology and Tectonics", a section of the journal Frontiers in Earth Science

Received: *30 December 2021*
Accepted: *31 January 2022*
Published: *29 March 2022*

Citation:
Gan J, Xiong F, Xiao Q, Wang W and Yan D (2022) Petrogenesis and Geodynamic Implications of Late Triassic Mogetong Adakitic Pluton in East Kunlun Orogen, Northern Tibet: Constraints from Zircon U–Pb–Hf Isotopes and Whole-Rock Geochemistry. Front. Earth Sci. 10:845763. doi: 10.3389/feart.2022.845763

Adakites or adakitic rocks usually show special geochemical signatures and are petrological probes to reveal the tectono–magmatic evolutionary history of paleo–orogenic belts. Here, we present a comprehensive study on the zircon U–Pb geochronology, whole-rock geochemistry, and zircon Lu-Hf isotopes of Mogetong adakitic pluton in East Kunlun orogen, Northern Tibetan Plateau, to constrain its petrogenesis and tectonic setting, and thus to reveal its implications for the Paleo–Tethyan orogeny. The studied pluton comprises of quartz monzonite porphyry with zircon U–Pb crystallization age of ca. 215 Ma, which is coeval to their diorite enclaves (ca. 212 Ma). The quartz monzonite porphyries have intermediate SiO_2 (63.31–65.74 wt %), relatively high Al_2O_3 (15.52–16.02 wt%), K_2O (2.83–3.34 wt%), and Sr (462–729 ppm), but low Y (9.14–15.7 ppm) and Yb (0.73–1.39 ppm) with high $Mg^{\#}$ (47–55), Sr/Y (30–57) and La/Yb ratios resembling typical high–K calc-alkaline and high $Mg^{\#}$ adakitic rocks. Zircon Lu–Hf isotopes show that the studied samples have weakly juvenile zircon Lu-Hf isotopes ($\varepsilon Hf(t)$ = 1.80–4.03) with older model age (1.00–1.14 Ga). The relative low content of Cr (14–59 ppm) and Ni (8–30 ppm), as well as the petrological, geochemical, and Lu-Hf isotopic data, indicates that the Mogetong adakitic rocks were generated by partial melting of thickened lower crust with a certain contribution of the underplated mantle-derived magma in slab break-off setting. This study shows that the Late Triassic adakitic magmatism in East Kunlun orogen may be the response of tectonic transition from oceanic subduction to post–subduction extension, and the reworking of ancient continental crust with subsequent variable crust-mantle magma mixing is the major mechanism of continental crust evolution in the Paleo–Tethyan orogenic belt.

Keywords: East Kunlun, magmatism, adakitic rocks, paleo-tethyan, tectonic evolution

INTRODUCTION

The East Kunlun orogen, one composite Tethyan tectonic belt in the Northern Tibet Plateau, contains large–scale Permian–Triassic granitoid batholiths and coeval volcanic rocks and thus constitutes a giant magmatic arc (Xiong et al., 2014; Zhang et al., 2021; Zhong et al., 2021). The East Kunlun magmatic arc records the subduction of the Paleo–Tethyan oceanic lithosphere and the subsequent syn–collision and post–collisional extension, which is the ideal window to understand the tectonic evolution, magma–related mineralization, and crustal growth of Paleo–Tethyan orogenic belt and to understand the crustal growth mechanism and orogeny of Tibetan Plateau (Xiong et al., 2012, 2014, 2019; Huang et al., 2014; Li et al., 2015, 2018). However, the petrogenesis and tectonic settings of these Paleo–Tethyan

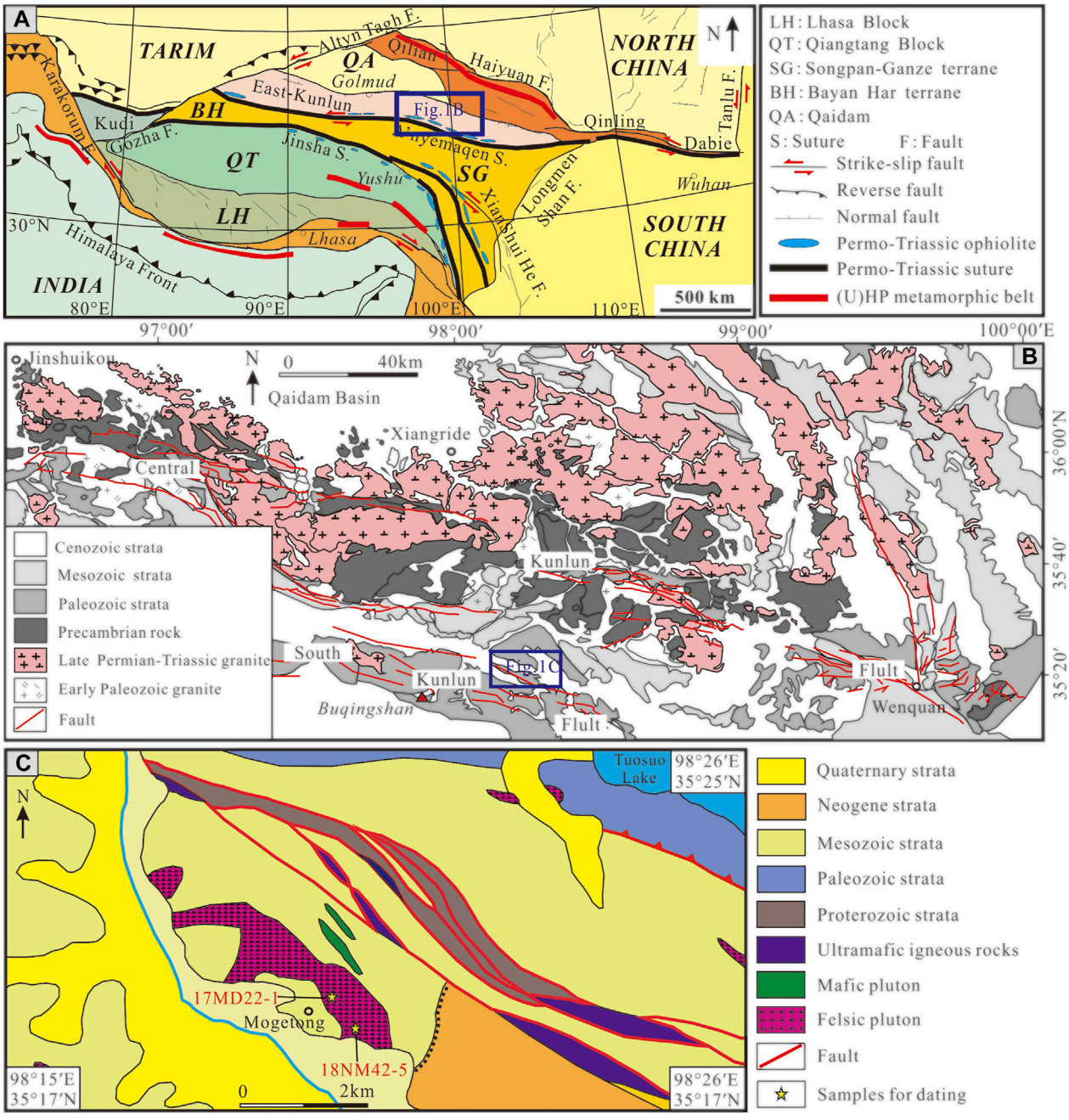

FIGURE 1 | (A) Tectonic outline of the Tibetan Plateau showing the location of East Kunlun orogen (after Roger et al., 2004); **(B)** Simplified geological map of the eastern section of East Kunlun showing the distribution of Permian-Triassic granites (after Xiong et al., 2014); **(C)** Simplified geological map of the studied Mogetong pluton.

TABLE 1 | Compilation of geochronological age data for Triassic magmatic rocks associated mineralization in East Kunlun.

Region/Mining area	Deposit type	Dating sample	Dating method	Age (Ma)	Reference
Tawenchahan	Skarn-type Fe-Cu-Zn deposit	Muscovite	39Ar-^{40}Ar	229.9 ± 3.5	Tian et al. (2013)
Yazigou	Skarn-type Fe-Mo deposit	Molybdenite	Re-Os isochron	210.1 ± 4.8	Feng et al. (2010)
Hutouya	Skarn-type Fe-Cu-Zn deposit	Molybdenite	Re-Os isochron	225.0 ± 4.0	Feng et al. (2011)
Suolajier	Skarn-type Cu-Mo deposit	Molybdenite	Re-Os isochron	239 ± 1.1	Feng et al. (2009)
Yazigou	Porphyry-type Cu-Mo deposit	Molybdenite	Re-Os isochron	224.7 ± 3.4	He et al. (2009)
Changshan	Porphyry-type Mo deposit	Molybdenite	Re-Os isochron	218 ± 228	Feng et al. (2010)
Yemaquan	Skarn-type Fe-Zn deposit	Phlogopite	39Ar-^{40}Ar	222.0 ± 1.3	Liu et al. (2017)
Shuangqing	Skarn-type Fe deposit	Molybdenite	Re-Os isochron	226.5 ± 5.1	Xia et al. (2015)
Lalingzaohuo	Skarn-type Mo-Fe deposit	Molybdenite	Re-Os isochron	214.5 ± 4.9	Wang et al. (2013)
Saishentang	Skarn-type Cu deposit	Molybdenite	Re-Os isochron	223.4 ± 1.5	Wang et al. (2015)
Naomuhun	Skarn-type Au deposit	Sericite	39Ar-^{40}Ar	227.8 ± 1.3	Li et al. (2017)
Shiduolong	Skarn-type Mo-Pb-Zn deposit	Molybdenite	Re-Os isochron	233.4 ± 9.6	Xia et al. (2015)

orogeny–related granitoids and volcanic equivalents are still hotly debated and several controversial models have been proposed For example, some studies propose that most Permian to Middle Triassic granitoids are formed in a subduction setting and the Kunlun Paleo–Tethyan ocean was finally closed in Late Triassic, while other studies emphasize that the Kunlun Paleo–Tethyan ocean was closed in Late Permian, and the Late Permian–Triassic granitoids all are generated in post–collisional setting, while some scholars even propose that the Paleo–Tethyan oceanic subduction lasted until the Late Triassic or Jurassic (Huang et al., 2014; Xiong et al., 2014; Chen et al., 2015, 2017; Ding et al., 2015; Li et al., 2015, 2018; Liu et al., 2017; Dong et al., 2018; Yu et al., 2020).

Recently, some studies reveal that Triassic adakites or adakitic rocks were developed in East Kunlun orogen (Yuan et al., 2009; Xiong et al., 2014; Chen et al., 2017; Zhang et al., 2017; Liang et al., 2021; Zhong et al., 2021), providing a special probe to unravel the tectonic–magmatic evolution of East Kunlun Paleo–Tethyan orogeny, since the adakites or adakitic rocks are unique with distinct geochemical signatures (e.g., high Sr/Y ratios and low Y and Yb) and can be formed in certain tectonic settings (Defant and Drummond, 1990; Martin et al., 2005; Castillo, 2012). Early studies show that adakites can be formed by partial melting of the subducted oceanic slab (Defant and Drummond, 1990; Castillo, 2012), melting of the thickened lower crust (Petford and Gallagher, 2001; Chung et al., 2003; Hou et al., 2011; Yu et al., 2018, 2019), melting of delaminated lower crust with mixing with mantle material (Xu et al., 2002; Wang et al., 2007a), magma mixing between mafic and felsic magma and differentiation of mantle–derived magma by fractional crystallization of hornblende and/or garnet (Qin et al., 2010; Foley et al., 2013). Thus, identifying the petrogenetic types of adakitic rocks and constraining their magmatic ages and tectonic settings is the key to revealing the tectonic–magmatic evolutionary history and crustal growth mechanism of Paleo–orogenic belt.

In this study, new petrological, geochronological, and geochemical data for a Late Triassic adakitic pluton in East Kunlun orogen are presented. Since previous case studies focus on the Middle Triassic adakitic rocks in East Kunlun orogen, the petrogenesis and tectonic setting of Late Triassic adakitic rocks remain unknown. Thus, the aim of this study is to: 1) comprehensively characterize the geochemical affinities of the Late Triassic adakitic rocks in East Kunlun orogen, and 2) reveal their petrogenesis and geodynamic implications for the Triassic tectonic–magmatic evolution of East Kunlun orogen. Collectively, this dataset aims to advance the understanding of the Paleo–Tethyan orogeny, magmatism–related metallization and crustal growth in Northern Tibet Plateau.

GEOLOGICAL SETTING

The East Kunlun Orogenic Belt (EKOB), located in northwestern China, extends east–west for up to 1,500 km, is bounded by the Qaidam Basin to the north, the Bayan Har–Songpan–Ganzi block to the south, the Qinling–Dabie orogenic belt to the east and the NE–trending Altyn Tagh fault to the west (**Figure 1A**; Xiong et al., 2015; Yu et al., 2018; Liu et al., 2021; Peng et al., 2021). Based on the central and south Kunlun faults, the EKOB can be divided into the North East Kunlun terrane and the South East Kunlun terrane (**Figure 1B**). The EKOB is part of the Paleo–Tethyan tectonic domain, and the Kunlun A'nyemaqen ophiolite belt represents the missing Paleo–Tethys ocean (Yang et al., 1996; Bian et al., 2004). Previous studies indicate that the Kunlun A'nyemaqen Paleo–Tethys oceanic slab began to subduct beneath the Kunlun terrane in the late Permian, but when and how did the ocean close remains a great debate. Due to the Paleo–Tethys oceanic subduction and subsequent collision, large–scale late Permian to Triassic magmatism occurred in the EKOB (**Figure 1B**; Xiong et al., 2014; Yu et al., 2017; Dong et al., 2018). Furthermore, numerous late Triassic porphyry and skarn–type mineral deposits occurred during the Paleo–Tethys orogeny (**Table 1**; Xia et al., 2017; Zhang et al., 2017; Qu et al., 2019; Zhong et al., 2021), making the EKOB one of the most important polymetallic belts in China. Thus, studying the petrogenesis of late Triassic igneous rocks is not only conducive to revealing the magmatic–tectonic evolution of EKOB, but also conducive to understanding the metallogeny background of late Triassic porphyry or skarn–type deposits.

SAMPLING AND PETROGRAPHY

The studied Mogetong pluton is located in the south Kunlun terrane and exposes it as a small stock of about 8 km southwest to

FIGURE 2 | Field and microscope graphics of the Mogetong pluton in the East Kunlun. **(A–B)** Host quartz monzonite porphyry; **(C–D)** Mafic enclave hosted in quartz monzonite porphyry; **(E–F)** Microphotographs of the quartz monzonite porphyry and enclave, respectively. Abbreviations: Amp, amphibole; Bi, biotite; Kfs, K-feldspar; Pl, plagioclase; Q, quartz.

the Tuosuo Lake (**Figures 1B,C**). The studied pluton consists of quartz monzonite porphyry and it intrudes into the early Triassic sandstone (**Figures 2A,B**). Mafic microgranular enclaves (MMEs) occur sporadically in the Mogetong pluton, and the MMEs are mainly composed of diorite and usually show sharp contact with the host quartz monzonite or quartz monzonite porphyry (**Figures 2C,D**).

The host quartz monzonite porphyry shows porphyritic texture with phenocryst minerals of plagioclase (5–7 vol%), K-feldspar (3–5 vol%), quartz (5–8 vol%), and biotite (2–3 vol. %). The matrix of the quartz monzonite porphyry comprises fine-grained plagioclase (40–45 vol. %), K-feldspar (25–30 vol%), quartz (8–10 vol%) and biotite (2 vol%) as well as minor accessory minerals of zircon, titanite, apatite, and opaque minerals (**Figure 2E**). While the MMEs are texturally and mineralogically different to their host rocks, showing fine-grained granitic texture with major minerals of euhedral plagioclase (45–50 vol%), hornblende (20–25 vol%), biotite (5

TABLE 2 | LA-ICP-MS zircon U-Pb data for the Mogetong quartz monzonite porphyry and enclave in the East Kunlun orogen, northern Tibetan Plateau.

Analysis	Contents		Ratios	Isotopic ratios						Isotopic ages (Ma)					
	Th	U	Th/U	207Pb/^{206}Pb	1σ	207Pb/^{235}U	1σ	206Pb/238U	1σ	207Pb/^{206}Pb	1σ	207Pb/235U	1σ	206Pb/^{238}U	1σ
17MD11-2 (quartz monzonite porphyry)															
1	537	1,430	0.38	0.0503	0.0022	0.2404	0.0107	0.03448	0.00049	209	102	219	9	219	3
2	436	852	0.51	0.0507	0.0029	0.2382	0.0132	0.03440	0.00056	228	133	217	11	218	3
3	738	1,213	0.61	0.0507	0.0034	0.2391	0.0155	0.03375	0.00049	228	156	218	13	214	3
4	298	576	0.52	0.0549	0.0056	0.2497	0.0235	0.03406	0.00097	409	236	226	19	216	6
5	552	1,133	0.49	0.0528	0.0065	0.2442	0.0279	0.03374	0.00077	320	288	222	23	214	5
6	317	609	0.52	0.0482	0.0056	0.2242	0.0256	0.0335	0.0008	109	252	205	21	212	5
7	395	746	0.53	0.0497	0.0031	0.2335	0.0147	0.0337	0.0005	189	144	213	12	213	3
8	354	709	0.50	0.0609	0.0044	0.2848	0.0195	0.0345	0.0009	639	157	254	15	219	5
9	463	992	0.47	0.0504	0.0035	0.2404	0.0163	0.0342	0.0007	217	156	219	13	217	4
10	403	837	0.48	0.0512	0.0042	0.2382	0.0181	0.0344	0.0007	250	189	217	15	218	4
11	464	896	0.52	0.0517	0.0067	0.2435	0.0283	0.0341	0.0010	272	274	221	23	216	6
12	558	1,057	0.53	0.0499	0.0032	0.2300	0.0146	0.0334	0.0005	187	150	210	12	212	3
13	332	639	0.52	0.0517	0.0056	0.2433	0.0275	0.0342	0.0010	272	51	221	22	217	6
14	423	763	0.55	0.0517	0.0049	0.2387	0.0210	0.0342	0.0007	272	218	217	17	217	4
15	547	733	0.75	0.0505	0.0044	0.2353	0.0206	0.0336	0.0006	217	5	215	17	213	4
16	626	784	0.80	0.0512	0.0030	0.2336	0.0133	0.0338	0.0005	256	140	213	11	214	3
17	444	900	0.49	0.0531	0.0044	0.2404	0.0205	0.0332	0.0010	345	195	219	17	211	6
18	652	1,610	0.40	0.0527	0.0044	0.2509	0.0198	0.0345	0.0006	322	186	227	16	218	4
19	480	1,077	0.45	0.0519	0.0034	0.2402	0.0147	0.0339	0.0006	280	155	219	12	215	4
20	321	710	0.45	0.0534	0.0057	0.2439	0.0206	0.0345	0.0011	346	241	222	17	219	7
21	250	493	0.51	0.0535	0.0095	0.2445	0.0407	0.0337	0.0012	354	357	222	33	214	8
22	648	1,151	0.56	0.0498	0.0026	0.2307	0.0117	0.0336	0.0004	187	120	211	10	213	3
23	314	658	0.48	0.0529	0.0068	0.2404	0.0291	0.0336	0.0012	328	97	219	24	213	8
18NM42-4 (enclave)															
1	510	791	1.02	0.0506	0.0027	0.2316	0.0123	0.0330	0.0004	233	121	211	10	209	3
2	315	568	1.11	0.0537	0.0056	0.2472	0.0250	0.0336	0.0007	367	237	224	20	213	4
3	458	876	0.41	0.0512	0.0036	0.2384	0.0167	0.0337	0.0007	250	165	217	14	214	4
4	527	1,016	0.74	0.0510	0.0030	0.2339	0.0137	0.0332	0.0006	243	137	213	11	210	4
5	601	1,032	0.41	0.0494	0.0031	0.2297	0.0136	0.0339	0.0005	169	148	210	11	215	3
6	448	837	0.10	0.0502	0.0032	0.2356	0.0147	0.0335	0.0006	211	146	215	12	213	4
7	603	1,068	0.68	0.0498	0.0035	0.2301	0.0159	0.0329	0.0006	187	165	210	13	208	4
8	608	1,112	0.03	0.0499	0.0030	0.2300	0.0142	0.0329	0.0006	191	134	210	12	208	4
9	425	773	0.54	0.0504	0.0029	0.2264	0.0118	0.0331	0.0005	217	133	207	10	210	3
10	564	931	0.72	0.0504	0.0039	0.2330	0.0171	0.0334	0.0006	213	178	213	14	212	4
11	673	935	0.43	0.0520	0.0022	0.2380	0.0099	0.0332	0.0004	287	98	217	8	211	3
12	491	816	0.63	0.0510	0.0031	0.2448	0.0157	0.0342	0.0006	239	136	222	13	217	3
13	311	580	0.40	0.0541	0.0035	0.2557	0.0147	0.0352	0.0006	372	151	231	12	223	4
14	498	922	1.24	0.0548	0.0039	0.2555	0.0170	0.0341	0.0006	467	159	231	14	216	4
15	622	1,241	1.03	0.0553	0.0040	0.2463	0.0160	0.0329	0.0007	433	168	224	13	209	4

vol%) as well as subhedral K-feldspar (10–15 vol%) and anhedral quartz (5 vol%) (**Figure 2F**). Nine representative samples were sampled for the geochemical study, and two samples, i.e., the quartz monzonite porphyry (sample 17MD22–1) and the MMEs (sample 18NM42–4) were collected for zircon U–Pb dating at N35°18.8′, E98°18.9'.

ANALYTICAL METHODS

The studied samples were collected from fresh outcrops and zircons were separated by heavy liquid and magnetic methods. Zircon grains were photographed with an optical microscope and the internal structures were analyzed by cathodoluminescence (CL). Zircon U–Pb dating was finished by laser ablation–inductively coupled plasma–mass spectrometry (LA–ICP–MS) at the Stake Key Laboratory of Geological Processes and Mineral Resources (GPMR), China University of Geosciences, Wuhan. Laser sampling was performed using a GeoLas 2005 system with a spot size of 32 μm. An Agilent 7500a ICP–MS instrument was used to acquire ion signal intensities. Helium was applied as a carrier gas, and Ar was used as the make–up gas and mixed with the carrier gas via a T–connector before entering the ICP source. Nitrogen was added to the central gas flow (Ar + He) of the Ar plasma to lower the detection limits and improve precision. Concordia diagrams and weighted–mean ages were made by Isoplot/Ex_ver3 (Ludwig, 2003). Data were processed using *ICPMSDataCal* (Liu et al., 2010). The detailed operating conditions for the laser system and ICP–MS instrument are as described by Liu et al. (2013).

Whole–rock samples were crushed in a corundum jaw crusher (to 60 mesh). About 60 g of this material was powdered in an

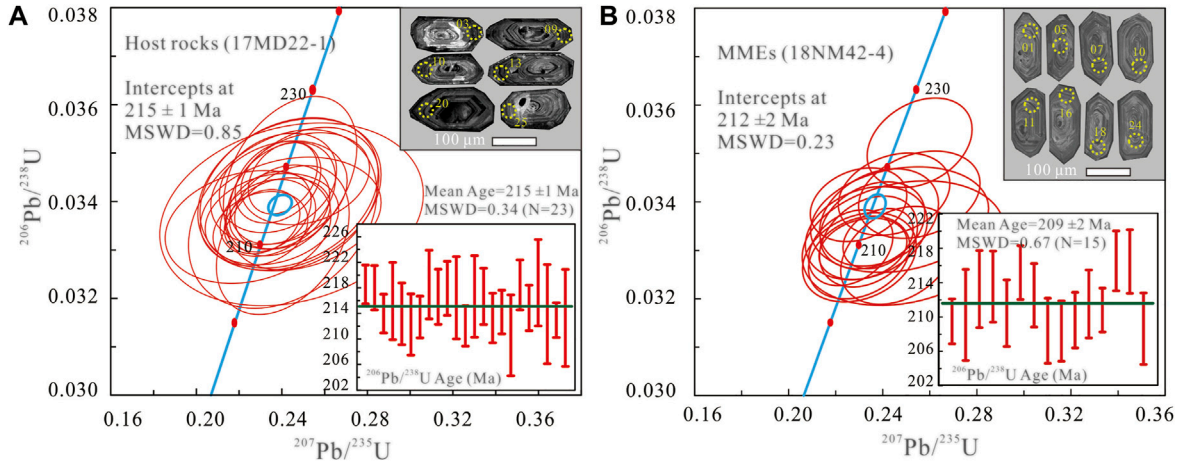

FIGURE 3 | Zircon U-Pb concordia diagrams and reprehensive zircon CL images for the Mogetong quartz monzonite porphyry and MMEs.

agate ring mill to<200 mesh for whole–rock geochemical analysis. The major element analysis was conducted by standard X–ray fluorescence (XRF) methods, using a Shimadzu Sequential 1800 spectrometer at the GPMR. Precision is <4% and accuracy is <3% for the major element. The detailed techniques for the major element analysis were described by Ma et al. (2012). Trace elements were analyzed using an Agilent 7500a ICP–MS at GPMR. The samples were digested by HF + HNO_3 acid in Teflon bombs. Analyses of USGS standards (AGV–2, BHVO–2, BCR–2, and RGM2) indicate an accuracy of <5–10% for most trace elements. The sample digestion procedures and ICP–MS methods are as described by Liu et al. (2008).

In situ zircon Hf isotopic analysis was performed on the dated zircon domains using an excimer (193 nm wavelength) laser ablation inductively coupled plasma mass spectrometer (LA–MC–ICP–MS) at the State Key Laboratory of Continental Dynamics, Northwest University, Xi'an, China. The GeoLas 200 M laser–ablation system (MicroLas, Göttingen, Germany) was used for the laser ablation experiments. Helium was used as carrier gas transporting the ablated sample from the ablation cell to the ICP–MS torch. A 44 μm beam size was adopted in this study with a laser pulse frequency of 10 Hz. Zircon standards 91,500, GJ–1 and Monastery were used as references. The detailed analytical technique for this method was described by Yuan et al. (2008).

RESULTS

Zircon U–Pb Geochronology

All the studied zircons are euhedral, elongate, inclusion–free, and transparent. LA–ICP–MS zircon U–Pb data are given in **Table 2**, and representative zircon CL images and analyzed spots are shown in **Figure 3**. The zircons have euhedral crystal shapes and exhibit oscillatory or broad zoning. The zircons from the quartz monzonite porphyry (sample 17MD22–1) and MMEs (18NM42–4) all have high concentrations of Th and U and high Th/U ratios (0.38–0.80 and 0.49–0.85, respectively; **Table 2**), indicating their magmatic origin (Corfu et al., 2003).

Twenty-three analyses from sample 17MD22–1 yield concordant $206Pb/^{238}U$ ages of 211–219 Ma (**Table 2**) and a weighted mean age of 215 ± 1 Ma (MSWD = 0.34; **Figure 3A**), which is identical to their Tera-Wasserburg U–Pb lower intercept age of 215 ± 1 Ma (MSWD = 0.85), were within the acceptable error. Thus, the 215 ± 1 Ma is interpreted as the crystallization age of the Mogetong quartz monzonite porphyry. Fifteen analyses from sample 18NM42–4 exhibit $206Pb/^{238}U$ show ages ranging from 208 Ma to 223 Ma and yield a concordant age of 212 ± 2 Ma with a weighted mean age of 209 ± 2 Ma (MSWD = 0.67; **Figure 3B** and **Table 2**). These two ages were consistent with the acceptable error, so the concordant age of 212 ± 2 Ma represented the crystallization age of MMEs. Thus, the above results indicate the zircons of MMEs have nearly identical crystallization age to that of the zircons in host rocks.

Whole–Rock Geochemistry

Geochemical analyses of representative samples are listed in **Table 3**. The Mongetong quartz monzonite porphyries have a narrow range of SiO_2 contents (63.31–65.74 wt%), moderate contents of TiO_2 (0.47–0.68 wt%), Al_2O_3 (15.19–16.02 wt%), FeO^T (2.54–3.83 wt%), MgO (1.33–2.67 wt%), and high contents of total alkaline (Na_2O + K_2O = 7.03–8.19 wt%). The quartz monzonite porphyries define a sub–alkaline trend in the total alkalis–silica (TAS) diagram (**Figure 4A**) and a high-K calc–alkaline trend with high K_2O contents (2.83–3.34 wt%; **Table 3** and **Figure 4B**). These samples are metaluminous with A/CNK values of 0.94–1.02 (**Table 3**), and it is worth noting that the Mongetong quartz monzonite porphyries exhibit high $Mg^{\#}$ values (47–55). The MMEs show mafic-intermediate composition with SiO_2 of 49.73–56.94 wt%, TiO_2 of 1.14–1.20 wt%, FeO^T of 6.00–7.93 wt%, MgO of 3.88–3.91 wt %, and exhibit much higher Na_2O/K_2O values (2.18–3.23) and similar $Mg^{\#}$ (47–54).

TABLE 3 | Whole-rock major and trace element compositions of the studied pluton in the EKOB, northern Tibetan Plateau.

Samples	17MD18-4	17MD19-1	17MD20-1	18NM42-5	18NM42-6	18NM42-7	18NM42-8	18NM42-4	18NM42-9
Rock types	quartz monzonite porphyry							enclave	
Major element (wt%)									
SiO_2	64.32	65.74	63.55	63.35	63.43	63.69	63.31	56.94	49.73
TiO_2	0.53	0.47	0.64	0.67	0.68	0.65	0.64	1.20	1.14
Al_2O_3	15.19	15.74	15.40	15.88	16.02	15.66	15.52	16.17	19.59
FeO^T	3.02	2.54	3.83	3.54	3.63	3.31	3.32	6.00	7.93
MnO	0.05	0.04	0.07	0.05	0.05	0.06	0.05	0.12	0.16
MgO	1.98	1.33	2.67	1.78	1.79	2.15	2.25	3.88	3.91
CaO	2.45	2.57	2.26	2.52	2.60	3.41	3.19	3.67	10.29
Na_2O	5.11	5.00	4.52	4.48	4.51	3.89	4.12	4.66	2.23
K_2O	3.08	2.83	3.30	3.28	3.34	3.14	3.19	2.14	0.69
P_2O_5	0.21	0.20	0.25	0.30	0.31	0.25	0.24	0.46	0.25
LOI	3.65	3.10	2.84	2.97	2.95	2.86	3.43	3.07	2.27
Total	98.85	98.88	98.85	98.68	98.78	98.96	98.76	98.98	99.05
K_2O/Na_2O	0.60	0.57	0.73	0.73	0.74	0.81	0.77	0.46	0.31
$Mg^{\#}$	54	48	55	47	47	54	55	54	47
Trace element (ppm)									
Li	36.9	26.1	60.8	42.4	43.6	64.6	72.0	55.5	34.0
Be	2.35	2.08	2.06	2.51	2.70	2.38	2.19	2.25	1.10
Sc	6.92	4.22	8.48	6.03	6.17	7.75	7.67	14.6	20.8
V	46.1	27.3	60.6	32.9	34.0	52.2	49.9	116	200
Cr	47.7	13.6	59.1	14.1	17.0	37.9	37.7	60	14.5
Co	10.0	6.42	12.7	9.38	9.64	11.3	11.0	22.1	19.7
Ni	25.4	8.22	30.1	10.3	10.6	22.5	21.9	38.0	8.06
Cu	6.94	5.74	10.73	5.00	4.83	10.7	9.4	96.5	8.3
Zn	44.4	56.3	51.1	63.5	62.4	52.2	50.9	77.6	97.0
Ga	17.8	18.4	18.2	18.8	18.4	18.7	18.0	19.6	19.4
Rb	104	92.4	118	135	131	100	113	89.7	29.1
Sr	557	524	599	515	462	729	660	770	668
Y	12.9	9.14	15.2	15.4	15.7	14.1	13.8	24.1	21.7
Zr	166	174	173	196	193	172	163	194	105
Nb	19.7	17.9	25.6	26.1	26.4	18.8	18.5	29.7	5.47
Mo	0.33	0.22	0.92	0.18	0.18	0.38	0.25	0.42	0.13
Sn	1.82	1.50	2.49	1.94	2.27	1.65	1.80	2.48	0.92
Cs	4.45	7.07	5.59	5.66	5.21	5.46	7.12	5.46	11.2
Ba	811	881	1,019	800	812	877	752	582	213
La	39.1	35.6	47.0	49.0	39.2	34.0	33.2	44.6	13.1
Ce	70.4	62.4	86.3	91.0	73.3	62.9	61.5	84.5	31.0
Pr	7.64	6.66	8.96	9.35	7.84	6.71	6.46	9.25	4.20
Nd	26.0	22.7	30.9	32.5	28.7	24.5	24.3	35.0	19.0
Sm	4.33	3.63	5.19	5.10	4.94	4.41	4.36	6.36	4.38
Eu	1.06	1.02	1.32	1.29	1.32	1.17	1.14	1.71	1.40
Gd	3.34	2.79	3.99	3.77	3.62	3.37	3.26	5.33	4.34
Tb	0.46	0.35	0.54	0.51	0.50	0.46	0.45	0.77	0.65
Dy	2.37	1.74	2.90	2.78	2.86	2.60	2.58	4.54	3.92
Ho	0.42	0.31	0.56	0.51	0.53	0.50	0.48	0.82	0.76
Er	1.19	0.80	1.52	1.40	1.40	1.36	1.31	2.35	2.17
Tm	0.18	0.12	0.21	0.21	0.20	0.19	0.18	0.32	0.31
Yb	1.13	0.73	1.39	1.24	1.37	1.25	1.18	2.04	1.99
Lu	0.17	0.12	0.22	0.20	0.19	0.18	0.18	0.32	0.31
Hf	4.05	4.06	4.30	4.58	4.49	4.12	3.93	4.51	2.67
Ta	1.43	1.23	1.71	1.80	1.77	1.23	1.16	1.79	0.27
Tl	0.48	0.47	0.66	0.66	0.53	0.48	0.48	0.38	0.17
Pb	21.5	20.6	20.1	22.8	19.4	18.5	16.7	17.0	17.2
Th	12.5	9.82	14.6	14.0	12.1	9.23	8.99	9.76	1.50
∑REE	171	148	206	214	182	158	154	222	109
(La/Yb)N	23.3	32.9	22.9	26.7	19.3	18.4	19.0	14.7	4.5
δEu	0.85	0.98	0.89	0.90	0.95	0.93	0.93	0.90	0.98

*Note: Total Fe as FeO^T; $Mg^{\#}$ = 100*molar MgO/(MgO + FeO); δEu = $Eu_N/(Sm_N*Gd_N)^{1/2}$.*

The Mongetong quartz monzonite porphyries are characterized by enrichment in light rare earth elements (LREEs) and depletion in heavy rare earth elements (HREEs) [$(La/Yb)_N$ = 14.73–32.87; **Figure 5A**]. The host rocks and MMEs all display high total REEs (RREE = 148–222 ppm) and slightly negative Eu anomalies (Eu/Eu* = 0.8–0.9). To sum up, the host rocks and MMEs exhibit

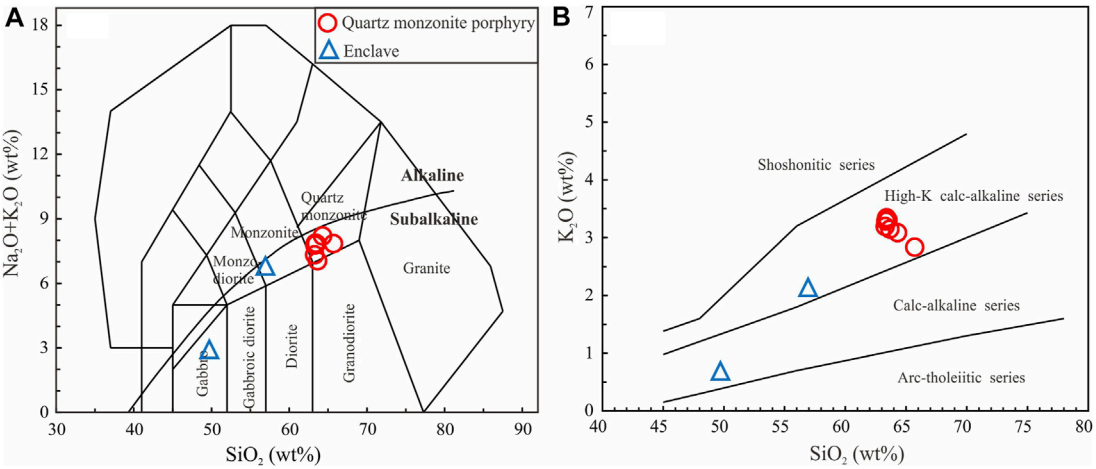

FIGURE 4 | (A) TAS classification and nomenclature diagram (Middlemost, 1994); **(B)** SiO_2 versus K_2O diagram for the studied rocks (Peccerillo and Taylor, 1976).

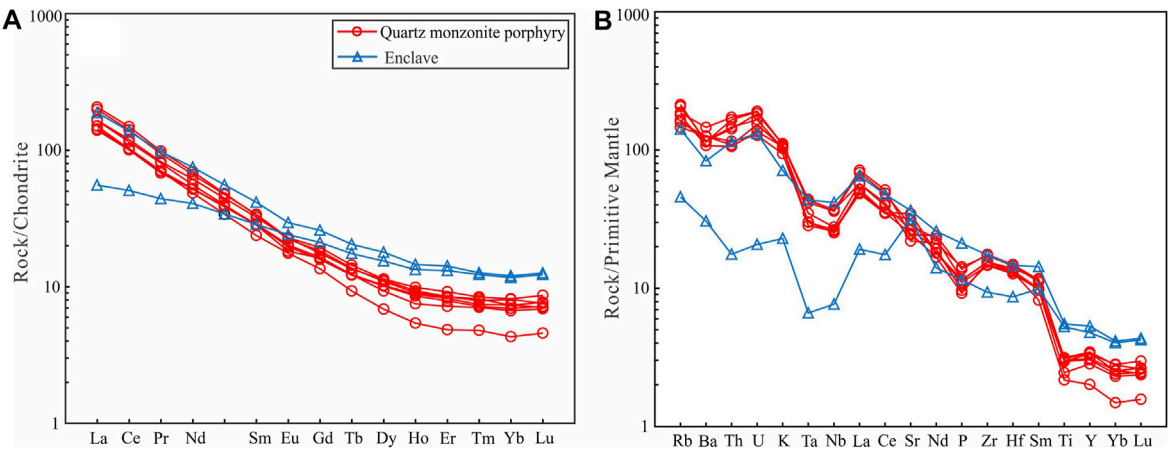

FIGURE 5 | (A) Chondrite-normalized REE patterns [normalization values after Taylor and Mclennan (1985)] and **(B)** Primitive mantle-normalized trace element spider diagrams [normalization values after Sun and McDonough (1989)] for the studied Mogetong pluton.

TABLE 4 | Zircon Lu-Hf isotopic compositions for the Mogetong quartz monzonite porphyry in EKOB, northern Tibetan Plateau.

Spots	$^{176}Yb/^{177}Hf$	2σ	$^{176}Lu/^{177}Hf$	2σ	176Hf/177Hf	2σ	$(^{176}Hf/^{177}Hf)_i$	$\varepsilon_{Hf(t)}$	2σ	T_{DM1}(Ga)	T_{DM2} (Ga)
17MD22-1 (quartz monzonite porphyry, t = 215 Ma)											
1	0.037963	0.000498	0.001003	0.000018	0.282744	0.000027	0.282740	3.57	0.94	0.72	1.03
2	0.039701	0.000682	0.000992	0.000024	0.282694	0.000028	0.282690	1.80	0.97	0.79	1.14
3	0.037362	0.000340	0.001033	0.000015	0.282738	0.000024	0.282734	3.37	0.84	0.73	1.04
4	0.030288	0.000296	0.000760	0.000007	0.282731	0.000031	0.282728	3.16	1.09	0.73	1.05
5	0.031988	0.000344	0.000808	0.000011	0.282725	0.000029	0.282722	2.95	1.00	0.74	1.07
6	0.025587	0.000049	0.000641	0.000002	0.282703	0.000033	0.282700	2.19	1.14	0.77	1.12
7	0.033537	0.000051	0.000839	0.000003	0.282716	0.000027	0.282712	2.61	0.96	0.76	1.09
8	0.046984	0.000145	0.001152	0.000005	0.282734	0.000029	0.282729	3.20	1.00	0.74	1.05
9	0.026424	0.000038	0.000649	0.000001	0.282733	0.000030	0.282730	3.23	1.05	0.73	1.05
10	0.026513	0.000050	0.000646	0.000002	0.282695	0.000030	0.282693	1.92	1.05	0.78	1.13
11	0.039158	0.000119	0.000987	0.000005	0.282740	0.000028	0.282736	3.43	0.99	0.73	1.04
12	0.032284	0.000085	0.000802	0.000003	0.282698	0.000029	0.282695	1.99	1.02	0.78	1.13
13	0.028618	0.000043	0.000704	0.000002	0.282724	0.000029	0.282722	2.94	1.03	0.74	1.07
14	0.042915	0.000034	0.001048	0.000001	0.282715	0.000029	0.282711	2.57	1.01	0.76	1.09
15	0.048916	0.000041	0.001180	0.000002	0.282757	0.000024	0.282753	4.03	0.83	0.71	1.00

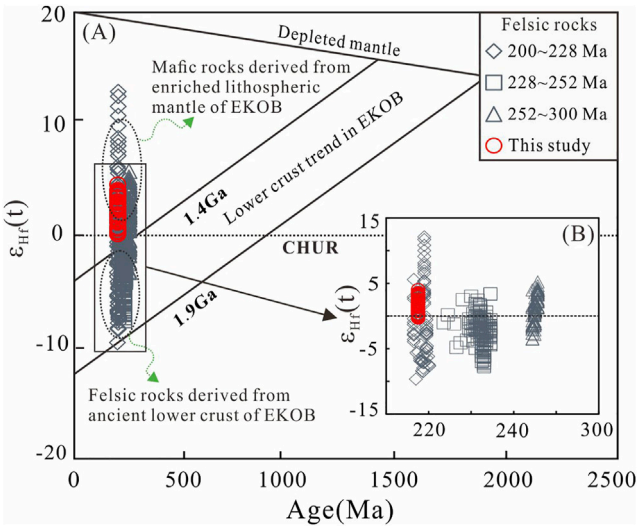

FIGURE 6 | Zircon εHf(t) versus age diagram. Data sources for the Triassic felsic igneous rocks in East Kunlun are as follows: Xiong et al. (2012, 2014, 2019), Huang et al. (2014), Li et al. (2015, 2018).

similar trace elements patterns, exhibiting overall enrichment in large ion lithophile elements (LILE; e.g., Th, U, K) and LREE, and depleted in high field strength elements (HFSE; e.g., Nb, Ta, Ti and *p*; **Figure 5B**). Importantly, the quartz monzonite porphyries have high contents of Sr (462–729 ppm) and Ba (752–1,019 ppm), but low contents of Y (9.14–15.7 ppm) and Yb (0.73–1.39 ppm) and low values of Sr/Y (30–57) and La/Yb (27–49), resembling typical adakites or adakitic rocks.

Zircon Lu–Hf Isotope

Zircon Lu–Hf isotopic data are shown in **Table 4**. Fifteen spots were analyzed for the sample 17MD22–1 and all the analyses have similar initial $^{176}Hf/^{177}Hf$ values of between 0.282690 and 0.282753. The zircons exhibit weakly juvenile Hf isotopes (εHf(t) = 1.80–4.03), with Hf isotopic model ages ranging from 1.00 Ga to 1.14 Ga (**Table 4**; **Figure 6**).

DISCUSSION

Magma Source and Petrogenesis

Several Triassic adakitic rocks have been reported in the East Kunlun orogenic belt, and most of them exhibit crystallization age of Middle–Late Triassic (Yuan et al., 2009; Xiong et al., 2014; Chen et al., 2017; Zhang et al., 2017; Liang et al., 2021; Zhong et al., 2021), thus providing a window to constrain the magma-tectonic evolution of East Kunlun Paleo-Tethyan orogen. The studied Mongetong quartz monzonite porphyries have adakitic affinities, e.g., intermediate SiO_2, high Sr, low Y and Yb contents, and high Sr/Y and La/Yb ratios (**Table 3**; **Figure 7**). Their high SiO_2 contents and moderate ($CaO + Na_2O$) values show that the studied pluton is a high–silicon adakite like the other Triassic adakitic rocks in East Kunlun (**Table 3**; Martin et al., 2005; Castillo, 2012).

Adakites or adakitic rocks were originally recognized in Cenozoic Aleutian island arcs where their generation is associated with the subduction of relatively young (≤25 Ma) oceanic slabs (Defant and Drummond, 1990). Slab melting of subducted oceanic slabs has been proposed to account for the genesis of adakitic rocks (Defant and Drummond, 1990; Drummond et al., 1996; Ma et al., 2014; Zheng et al., 2021). However, several other mechanisms have also been proposed to account for the origin of adakitic rocks, such as partial melting of the thickened basaltic lower crust (Atherton and Petford, 1993; Chung et al., 2003; Wang et al., 2007a; Yu et al., 2018, Yu et al., 2019), partial melting of mantle peridotite metasomatized by slab melt under water–bearing condition (Martin et al., 2005; Castillo, 2008), magma mixing between felsic and basaltic magmas (Qin et al., 2010; Foley et al., 2013), low–pressure fractional

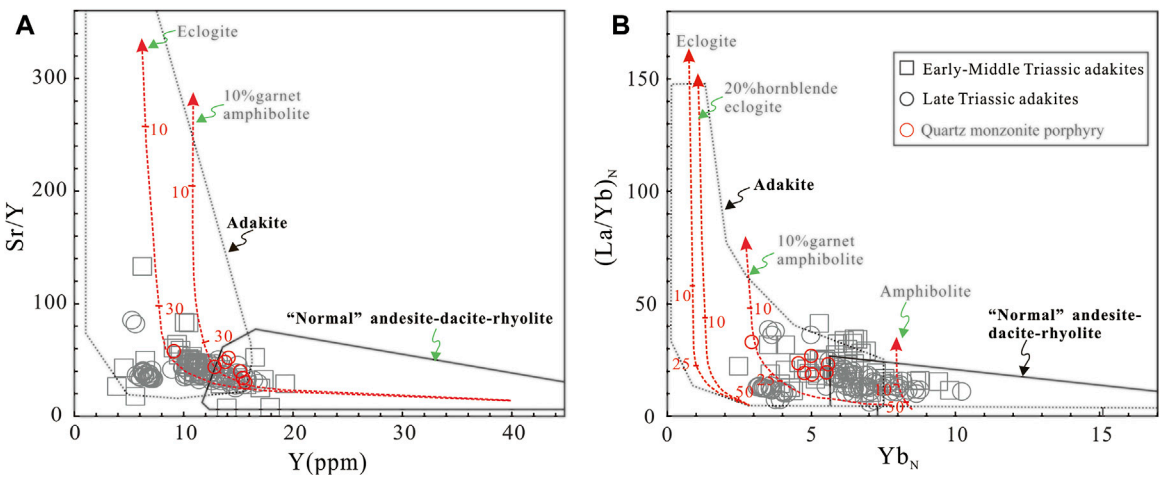

FIGURE 7 | (A) Sr/Y versus Y and **(B)** $(La/Yb)_N$ versus $(Yb)_N$ diagrams for the studied adakitic rocks (Defant and Drummond, 1990; Martin et al., 2005). Data sources for the adakites are from Yuan et al. (2009), Ding et al. (2014), Xia et al. (2014), Xiong et al. (2014), Chen et al. (2017), Shao et al. (2017), Zhang et al. (2017), Yin et al. (2020), Li et al. (2021), Liang et al. (2021), Zhong et al. (2021) and this study.

crystallization of parental basaltic magmas (Castillo, 2012; Chen et al., 2016), and high–pressure fractional crystallization (involving garnet) of mafic magmas (Martin et al., 2005; Macpherson et al., 2006; Chiaradia, 2009). Adakitic magmas derived from melting of subducted oceanic slabs usually have the following geochemical characteristics: depleted or relative juvenile radiogenic isotopes with young model ages, and sodic series with relatively low K_2O content and K_2O/Na_2O values (Defant and Drummond, 1990; Martin et al., 2005; Wang et al., 2007b). The Mogetong adakitic quartz monzonite porphyries have old zircon Hf isotopic model ages (1.00–1.14 Ga; **Figure 6**) and they exhibit high K_2O/Na_2O values (0.57–0.81) with high-K calc-alkaline affinities (**Figure 4**, **8A**), which is identical to the felsic rocks derived from partial melting of the ancient lower continental crust in East Kunlun (Xiong et al., 2014; Ding et al., 2015; Li et al., 2021). Moreover, the studied adakitic rocks have weak juvenile zircon Hf isotopes (εHf(t) = 1.80–4.03), which is much lower than the East Kunlun Paleo-Tethyan MORB (εHf(t) = 15–20; Huang et al., 2014; Hu et al., 2016), and it is unlikely that the Mogetong adakitic quartz monzonite porphyries were derived from basaltic slab melting. Besides, phase equilibrium modeling and experimental studies reveal that melting of either pristine or altered oceanic basaltic slab usually leads to the generation of high-SiO_2 and strongly sodic adakitic melts (Hernández-Uribe et al., 2019; Li et al., 2022), and the melts are usually rich in SiO_2 (>68 wt%) and Al_2O_3 (>18 wt%), but poor in FeO and MgO (<0.2 wt%), which is not the case of the studied Mogetong adakitic rocks (e.g., potassium, low contents of Al_2O_3 (15.19–16.02 wt%) and moderate contents of SiO_2 (63.31–65.74 wt%) and MgO (1.33–2.67 wt%); **Figures 4**, **8** and **Table 3**). Besides, the partial melts from fresh or hydrothermally altered MORB usually have $(La/Yb)_N$ >194 and $(La/Yb)_N$ >15, respectively, and those from altered MORB are characterized by strong negative Th anomalies (Hernández-Uribe et al., 2019), which are not the case of the studied Mogetong adakitic rocks (e.g., $(La/Yb)_N$ = 18–33; enrichment in Th; **Figure 5B** and **Table 3**).

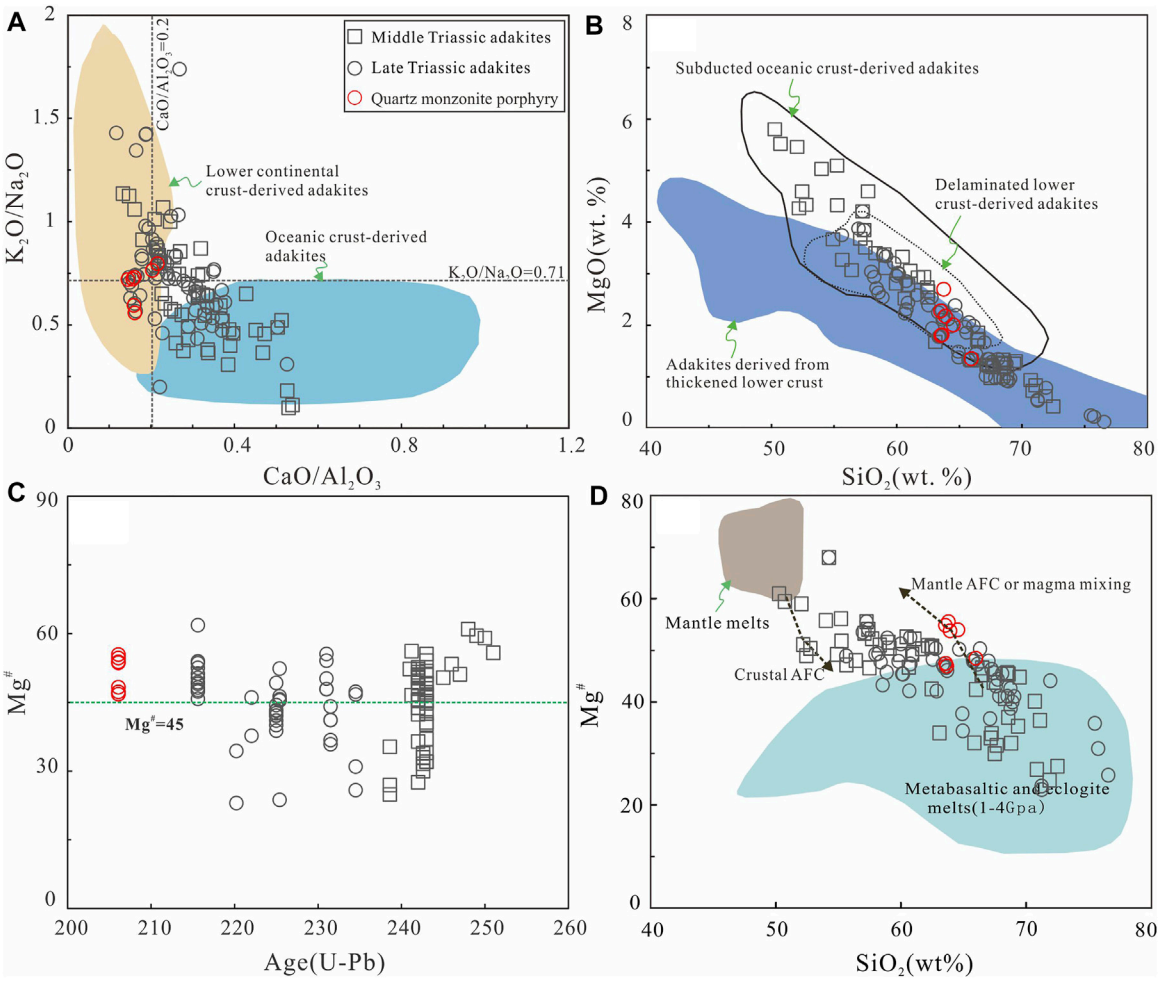

FIGURE 8 | Geochemical characteristics of major elements for the studied adakitic rocks and published data for other Triassic adakites in EKOB. Mantle melts, mantle AFC curves, and crust AFC curves are from Stern and Kilian (1996). Data for metabasaltic and eclogite experimental melts (1–4.0 GPa) are from Rapp et al. (1999) and references therein. K_2O/Na_2O versus CaO/Al_2O_3 and MgO versus SiO_2 diagrams are from Wang et al. (2006), Chen et al. (2018) and references therein. Data sources are same to **Figure 7**.

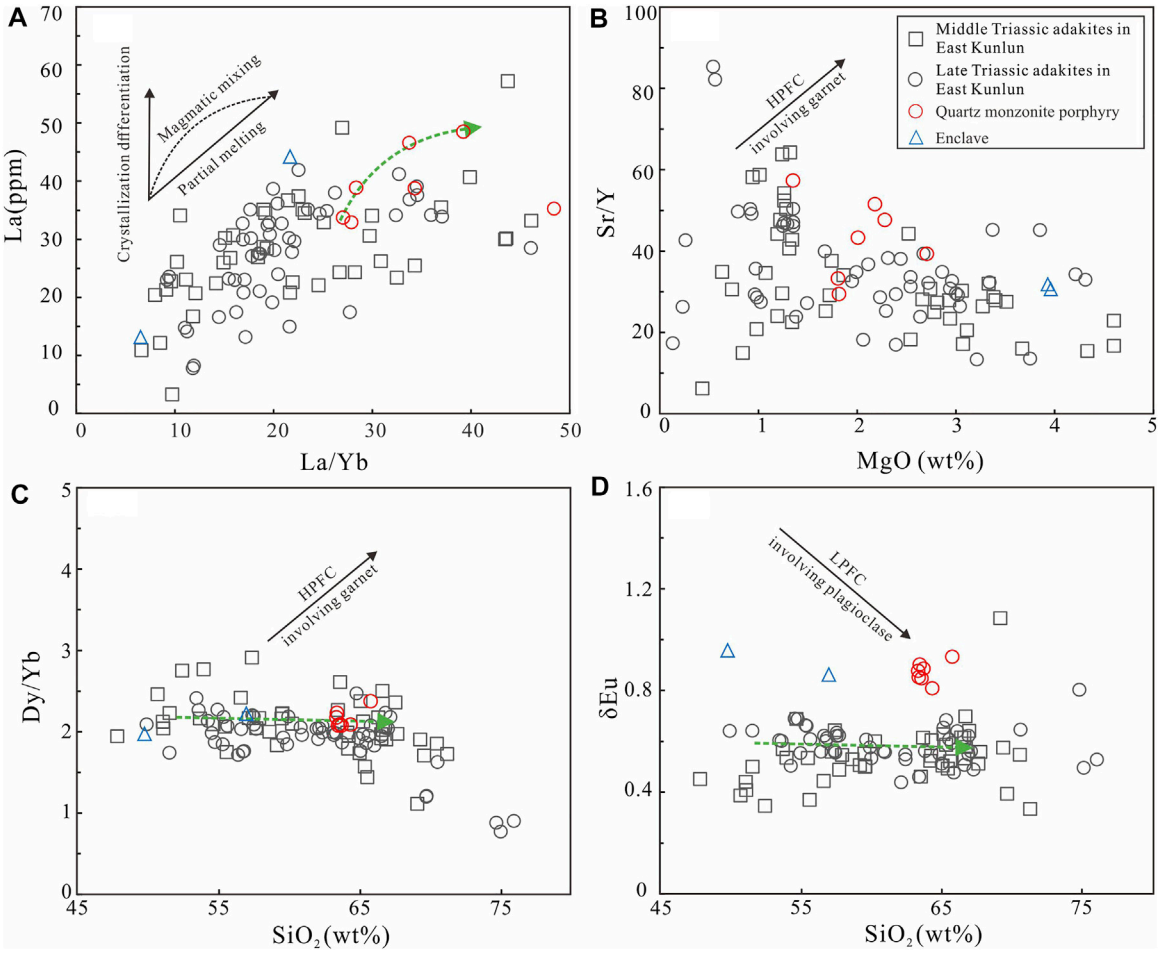

FIGURE 9 | (A) La versus La/Yb, **(B)** Sr/Y versus MgO, **(C)** Dy/Yb versus SiO_2, and **(D)** δEu versus SiO_2 (Drummond et al., 1996) diagrams showing the compositional evolution of the studied Mogetong adakitic quartz monzonite porphyries and enclaves. Abbreviations: HPFC = high-pressure fractional crystallization; LPFC = low-pressure fractional crystallization. Data sources are same to **Figure 7**.

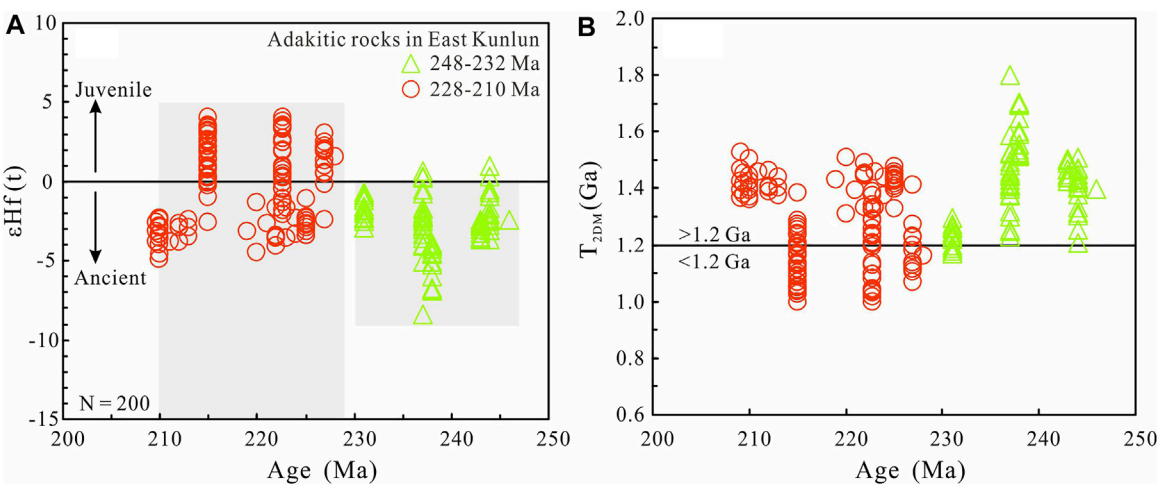

FIGURE 10 | Temporal evolution of zircon εHf(t) and Hf isotope model age for the Triassic adakites in East Kunlun orogenic belt. Data sources are same to **Figure 7**.

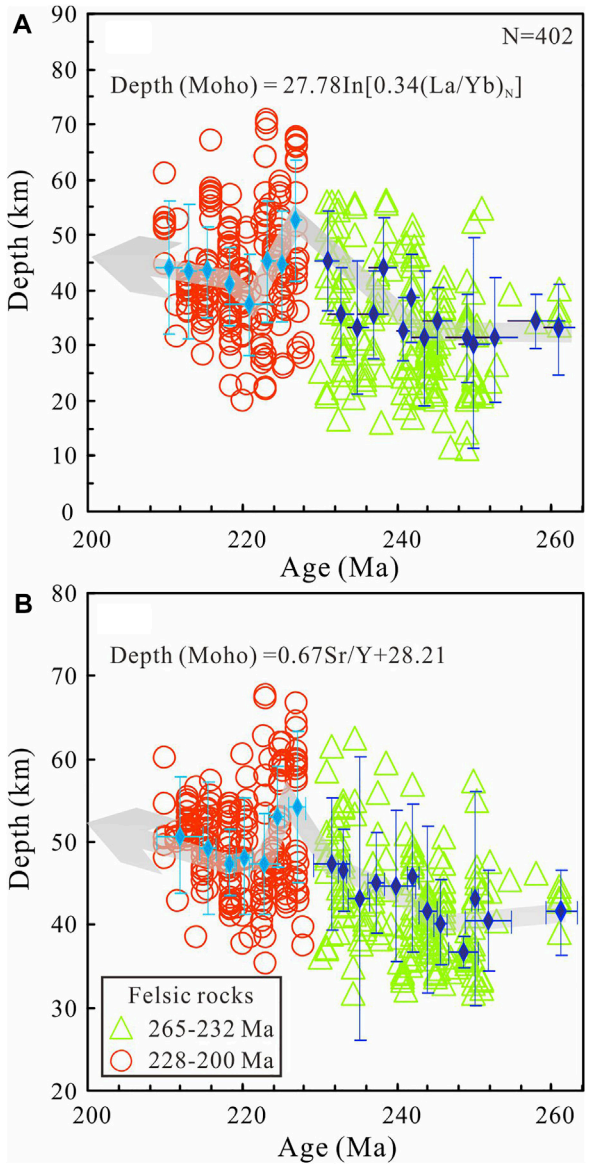

FIGURE 11 | Temporal changes of calculated crustal thickness from $(La/Yb)_N$ **(A)** and Sr/Y **(B)** for the East Kunlun during the Triassic. Crustal thickness with uncertainty is calculated by using the correlation equations in Chapman et al. (2015). Data sources are from Xiong et al. (2012), Huang et al. (2014), Xiong et al. (2014), Chen et al. (2015), Ding et al. (2015), Li et al. (2015), Xiong et al. (2016), Chen et al. (2017), Liu et al. (2017), Dong et al. (2018), Li et al. (2018), Xiong et al. (2019), Yu et al. (2020).

Besides, adakitic magmas derived from partial melting of thickened basaltic lower crust without crust-mantle interaction would have relatively low MgO contents and $Mg^{\#}$ values, and these melts are usually characterized by low $Mg^{\#}$ values (<40) regardless of the melting degree (Atherton and Petford, 1993; Castillo, 2012). The Mogetong adakitic quartz monzonite porphyries have high $Mg^{\#}$ values ($Mg^{\#}$ = 47–55; **Figures 8B–D**), which is distinct from the thickened basaltic lower crust–derived adakitic rocks. Conversely, adakitic rocks formed by high-pressure partial melting of continental crust would have relatively high $(Gd/Yb)_N$ ratios (>5.8) (Huang and He, 2010), however, this is not the case of the Mogetong adakitic rocks ($(Gd/Yb)_N$ = 2.14–3.09). The Mogetong adakitic quartz monzonite porphyries show partial melting trends rather than fractional crystallization trends (**Figure 9A**), indicating fractional crystallization of parental basaltic magmas may not be the most critical factor accounting for the genesis of the studied rocks. Typical adakitic rocks derived by fractional crystallization of basaltic magmas usually have low SiO_2 content (Martin et al., 2005; Chiaradia, 2009; Castillo, 2012), which is different from the Mogetong adakitic rocks as well as other Triassic adakitic rocks in East Kunlun (**Figures 8B,D**). In addition, given that high–pressure fractional crystallization involving garnet usually causes a decrease in HREEs and Y contents, the Sr/Y and Dy/Yb ratios in the residual magmas should increase with increasing SiO_2 and MgO content (Macpherson et al., 2006; Laurent et al., 2013). However, the Mogetong adakitic quartz monzonite porphyries do not show such a trend in the Sr/Y versus MgO and Dy/Yb versus SiO_2 diagrams (**Figures 9B,C**). During low–pressure fractional crystallization involving hornblende and plagioclase, the net effect of hornblende and plagioclase fractionation is a decrease in δEu with increasing SiO_2 content, which is observed in most typical arc adakites (Martin et al., 2005; Moyen, 2009), but is not present in the Mogetong adakitic rocks (**Figure 9D**).

Here, we propose that magma mixing between felsic and basaltic magmas is the most possible mechanism accounting for the generation of the studied Mogetong quartz monzonite porphyries. Their moderate SiO_2 contents (63.31–65.74 wt%) but high $Mg^{\#}$ values (47–55), as well as weak juvenile Hf isotopes, support the model of crust-mantle interaction (**Figures 6**, **8D**). The studied rocks exhibit much more depleted zircon Hf isotope than those derived from the ancient continent crust (**Figure 6**), indicating the significant contribution of mantle-derived magma. Furthermore, the high field strength element ratios of these samples also support the crust–mantle mixing model, such as their Nb/Ta values (average 14.87) ranging between the average continental crust (Nb/Ta = 11; Sun and McDonough, 1989) and the average primary mantle (Nb/Ta = 17.7; Taylor and McLennan, 1985). The correlation trend between La and La/Yb also confirms the major role of magma mixing (**Figure 9A**). Besides, the presence of the MMEs further indicate the occurring of magma mixing, although several petrogenetic models have been proposed for the origin of MMEs (Qin et al., 2010; Xiong et al., 2012, 2014), including 1) restites, 2) cognate fragments of cumulates, 3) quenched mafic melts derived from the mantle, and 4) mixing of mafic and felsic magmas. The MMEs in the Late Triassic Mogetong pluton have granitic textures with euhedral plagioclase, biotite and amphibole, subhedral K-feldspar, and anhedral quartz (**Figure 2F**), which does not support the cumulates and quenched mafic melts model but indicates that the MMEs crystallized from a melt. The MMEs have mafic-intermediate compositions with slightly silica contents of 49.73–56.94 wt%, which also contradicts the idea of the MMEs being cognate fragments of mafic cumulates and quenched mafic melts. Moreover, the euhedral magmatic

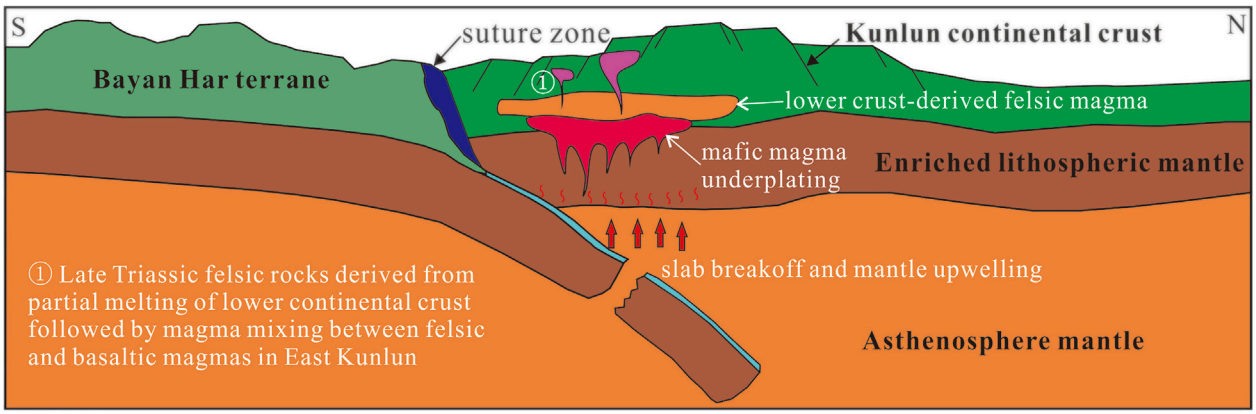

FIGURE 12 | Schematic cartoon showing the possible Paleo-Tethyan tectono-magma dynamic model for the generation of the studied Late Triassic adakitic pluton in the East Kunlun.

zircons with clear igneous oscillatory and identical U-Pb ages to their host rocks also preclude the restite model, but support the magma mixing model (**Figure 3**). These features, as well as the fact of different trace elemental patterns between the MMEs and their host rocks, support the magma mixing model for the origin of the studied Mogetong pluton and MMEs, and the contemporary most mafic enclave (sample 18NM42–9) could represent the basaltic end-member. The Mogetong adakitic rocks have variable and positive values of εHf(t) (1.80–4.03) with moderate $Mg^{\#}$ (47–54), which also indicate a mantle component in their source. However, petrological and geochemical evidence indicates that the contribution of mantle material is not significant. For example, the MMEs are sporadically developed in the Mogetong adakitic pluton and the host rocks have low contents of Cr (14–59 ppm) and Ni (8–30 ppm). More importantly, the Hf isotopes of the studied rocks are much lower than those of the underplating primitive basaltic magma (εHf(t) = 8–15; Hu et al., 2018) or the Paleo-Tethyan MORB in the East Kunlun (εHf(t) = 15–20; Huang et al., 2014; Hu et al., 2016). The continental crust-like Nb/Ta values of the Mogetong adakitic rocks (14–16) are much lower than the MORB-like Nb/Ta values of the MMEs (17–20), which also support this suggestion (Taylor and McLennan, 1985; Sun and McDonough, 1989).

Implications for Tectonic Setting and Continent Crustal Evolution

The tectonic evolution of East Kunlun Paleo-Tethyan orogen during the late Paleozoic to early Mesozoic is still controversial and the key problem is the timing of the tectonic transition from oceanic slab subduction to continental collision (Li et al., 2013a, Li et al., 2018; Liu et al., 2017; Dong et al., 2018; Xiong et al., 2019; Yu et al., 2020; Zhang et al., 2021). Since there is an obvious genetic link between the magma source and tectonic setting of adakitic rocks, the detailed petrogenesis study could contribute to our understanding of the evolution of Triassic East Kunlun Paleo–Tethyan orogen. The above discussion on the petrogenesis shows that the Mogetong adakitic magma was originated from crust-mantle mixing, indicating that there was a significant contribution of mantle material in the Late Triassic. This is further supported by the zircon Hf isotopes of Triassic adakites (**Figure 10**). A comprehensive comparison of the Hf isotopic composition of Triassic adakites in East Kunlun orogen shows that there is a significant juvenile trend in the Late Triassic (**Figure 10**). Besides, the published data shows that there were two episodic adakitic magmatisms in the East Kunlun orogen, i.e. the Middle Triassic and Late Triassic, however, the latter is the main metallogeny stage for the porphyry–and/or skarn–type deposits (Yuan et al., 2009; Xiong et al., 2014; Chen et al., 2017; Zhang et al., 2017; Liang et al., 2021; Zhong et al., 2021). The above characteristics all indicate that the East Kunlun was in a special tectonic setting during the Late Triassic.

Through an integrated geochemical comparison among the Triassic adakites in East Kunlun orogen, we propose a revised tectonic evolution model for the East Kunlun Paleo-Tethyan orogen. As mentioned above, the crust-mantle magma mixing is the main genetic mechanism for the Late Triassic adakites in the East Kunlun, thus, revealing the properties of the late Triassic mantle-derived magma is the key to understanding the tectonic setting of Late Triassic adakitic magmatism. Previous studies have shown that mid-ocean ridge subduction, slab break–off, and slab roll–back and lithospheric delamination could trigger the underplating of mantle-derived magma and subsequent crustal melting and magma mixing (Martin et al., 2005; Wang et al., 2007b; Tang et al., 2010; Keller and Schoene, 2018). At present, however, Triassic mafic magmatic rocks with N–MORB affinities, back-arc basalts, back-arc basin, and the temporal–spatial migration trend of Triassic magmatism have not been found or reported in the East Kunlun orogen, precluding the model of mid-ocean ridge subduction and slab rollback (Hu et al., 2016; Xiong et al., 2019). Besides, lithospheric delamination-related magma will interact with mantle peridotite, forming adakitic magmas with high contents of Ni and Cr (Huang et al., 2008; Qin et al., 2010), but the Mogetong adakitic quartz monzonite porphyries do not exhibit high Cr and Ni contents.

Meanwhile, recent studies have shown that whole-rock Sr/Y and La/Yb ratios of felsic rocks can effectively reveal continent crustal thickness (Chapman et al., 2015). To eliminate mafic rocks generated in the mantle and to avoid the influence of magma mixing and/or highly fractional crystallization on the calculation results, the data set was filtered to include rocks with moderate SiO_2 content (55–68 wt%) and MgO content (one to four wt%). Data with Rb/Sr > 0.2 or Rb/Sr < 0.05 were further discarded, providing a trace elemental filter for mantle-derived rocks or rocks formed by melting of pre-existing metasedimentary framework rocks (Chapman et al., 2015). Using these empirical correlations, we investigate temporal variations of crustal thickness in the East Kunlun orogen, and our results suggest that crustal thickness increased during the Early-Middle Triassic and remained constant during the Late Triassic (**Figure 11**). The calculated results also indicate that the continent crustal thinning of East Kunlun did not occur during the Late Triassic, precluding the model of lithospheric delamination in the Late Triassic. Here, we propose that slab break-off may occur in the Late Triassic, which induced the underplating of mantle-derive mafic magma and promoted the melting of thickened crust and subsequent magma mixing (**Figure 12**). The Late Triassic OIB-like mafic igneous rocks and mafic dyke swarms in East Kunlun may be the response of slab break-off (Hu et al., 2016; Xiong et al., 2019). The slab break–off model also matches the linear distribution of Late Triassic adakites along the Eastern Kunlun Paleo-Tethyan suture zone (Dong et al., 2018). Besides, mantle-derived mafic magma underplating in the break–off model not only provides heat, but also provides ore-forming metals, which may be the key to the Late Triassic mineralization flare-up in the Eastern Kunlun orogen (Zhang et al., 2017; Zhong et al., 2021). Several pieces of evidence support the idea that late Triassic Mogetong adakites were formed in a post–subduction extensional setting, such as mantle–derived high Nb–Ta rhyolite (213 Ma; Ding et al., 2011), crustal–derived shoshonitic volcanic rocks (228–215 Ma; Hu et al., 2016), and coeval mafic dyke (226–210 Ma; Xiong et al., 2011, 2019; Hu et al., 2016; Liu et al., 2017). The angular unconformity between Late Triassic land facies volcanic-sedimentary rocks, e.g., Babaoshan Formation red clastic sedimentary rocks and E'lashan Formation volcanic rocks, and underlying sea-land facies strata is the records of tectonic transition from oceanic subduction to post-subduction collision or extension (Li et al., 2013a).

This study also suggests that the reworking of the ancient lithosphere and subsequent magma mixing are the important mechanisms for the generation of granitoids and continental crust growth. It is previously well accepted that the growth and evolution of the continental crust in orogen is mostly dominated by felsic magmatism, such as the Central Asian Orogenic Belt (Li et al., 2013b; Kröner et al., 2014), and the late Paleozoic to early Mesozoic felsic igneous rocks in the Central Asian Orogenic Belt are characterized by much depleted Sr–Nd–Hf isotopic compositions, indicating juvenile materials played a key role in crustal growth in Central Asia (Jahn et al., 2000; Li et al., 2013b; Xiao and Santosh, 2014). However, our study shows that the isotopic compositions of the Triassic adakites in East Kunlun are different from those of the Central Asian Orogenic Belt but identical to those derived from the melting of Precambrian continental crust with a contribution of mantle-derived magma, implying a different crustal evolution mechanism in East Kunlun (Xiong et al., 2012, 2014; Yu et al., 2017; Li et al., 2018). We propose that the reworking of a dominantly ancient continental crust with certain addition of lithospheric mantle materials is another major mechanism for the generation of felsic igneous rocks and the evolution of the continental crust.

CONCLUSION

(1) LA–ICP–MS zircon U–Pb geochronology studies show that the Mogetong quartz monzonite porphyries and enclaves in East Kunlun have identical crystallization ages of ca. 215–212 Ma. The Mogetong quartz monzonite porphyries are characterized by high SiO_2, K_2O and Sr, but low Y and Yb with high $Mg^{\#}$ values, Sr/Y and La/Yb ratios, resembling typical high–K calc–alkaline and high $Mg^{\#}$ adakitic rocks.
(2) Petrology, geochemistry and zircon Lu–Hf isotope reveals that the Mogetong adakitic quartz monzonite porphyries were generated by partial melting of thickened lower crust with a certain contribution of magma mixing in slab break-off setting.
(3) This study shows that the Late Triassic adakitic magmatism in East Kunlun orogen may be the response of tectonic transition from oceanic subduction to post–subduction extension and the reworking of ancient continental crust with subsequent crust-mantle magma mixing is the major mechanism of continental crust evolution in Paleo–Tethyan orogenic belt.

DATA AVAILABILITY STATEMENT

The original contributions presented in the study are included in the article/Supplementary Material, further inquiries can be directed to the corresponding authors.

AUTHOR CONTRIBUTIONS

JG, QX, and FX contributed to conception and design of the study and wrote the first draft of the manuscript. WW and DY helped writing the manuscript, provided comments and suggestions, and revised the manuscript.

FUNDING

This study was financially supported by National Natural Science Foundation of China (No. 41602049) and Research Project of Chengdu University of Technology (No. 2021ZF11412).

ACKNOWLEDGMENTS

We thank Wen Zhang and Keqing Zong for their contribution to the laboratory work.

REFERENCES

Atherton, M. P., and Petford, N. (1993). Generation of Sodium-Rich Magmas from Newly Underplated Basaltic Crust. *Nature* 362, 144–146. doi:10.1038/362144a0

Bian, Q.-T., Li, D.-H., Pospelov, I., Yin, L.-M., Li, H.-S., Zhao, D.-S., et al. (2004). Age, Geochemistry and Tectonic Setting of Buqingshan Ophiolites, North Qinghai-Tibet Plateau, China. *J. Asian Earth Sci.* 23 (4), 577–596. doi:10.1016/j.jseaes.2003.09.003

Castillo, P. R. (2012). Adakite Petrogenesis. *Lithos* 134-135, 304–316. doi:10.1016/j.lithos.2011.09.013

Castillo, P. R. (2008). Origin of the Adakite-High-Nb basalt Association and its Implications for Postsubduction Magmatism in Baja California, Mexico. *Geol. Soc. America Bull.* 120 (3-4), 451–462. doi:10.1130/B26166.1

Chapman, J. B., Ducea, M. N., DeCelles, P. G., and Profeta, L. (2015). Tracking Changes in Crustal Thickness during Orogenic Evolution with Sr/Y: An Example from the North American Cordillera. *Geology* 43 (10), 919–922. doi:10.1130/G36996.1

Chen, J., Wei, J., Fu, L., Li, H., Zhou, H., Zhao, X., et al. (2017). Multiple Sources of the Early Mesozoic Gouli Batholith, Eastern Kunlun Orogenic Belt, Northern Tibetan Plateau: Linking Continental Crustal Growth with Oceanic Subduction. *Lithos* 292-293, 161–178. doi:10.1016/j.lithos.2017.09.006

Chen, S., Niu, Y., Li, J., Sun, W., Zhang, Y., Hu, Y., et al. (2016). Syn-Collisional Adakitic Granodiorites Formed by Fractional Crystallization: Insights from Their Enclosed Mafic Magmatic Enclaves (Mmes) in the Qumushan Pluton, North Qilian Orogen at the Northern Margin of the Tibetan Plateau. *Lithos* 248-251, 455–468. doi:10.1016/j.lithos.2016.01.033

Chen, S., Niu, Y., and Xue, Q. (2018). Syn-Collisional Felsic Magmatism and Continental Crust Growth: A Case Study from the North Qilian Orogenic Belt at the Northern Margin of the Tibetan Plateau. *Lithos* 308-309, 53–64. doi:10.1016/j.lithos.2018.03.001

Chen, X., Gehrels, G., Yin, A., Zhou, Q., and Huang, P. (2015). Geochemical and Nd-Sr-Pb-O Isotopic Constrains on Permo-Triassic Magmatism in Eastern Qaidam Basin, Northern Qinghai-Tibetan Plateau: Implications for the Evolution of the Paleo-Tethys. *J. Asian Earth Sci.* 114 (4), 674–692. doi:10.1016/j.jseaes.2014.11.013

Chiaradia, M. (2009). Adakite-Like Magmas from Fractional Crystallization and Melting-Assimilation of Mafic Lower Crust (Eocene Macuchi Arc, Western Cordillera, Ecuador). *Chem. Geology.* 265 (3-4), 468–487. doi:10.1016/j.chemgeo.2009.05.014

Chung, S.-L., Liu, D., Ji, J., Chu, M.-F., Lee, H.-Y., Wen, D.-J., et al. (2003). Adakites from Continental Collision Zones: Melting of Thickened Lower Crust beneath Southern Tibet. *Geol* 31 (11), 1021–1024. doi:10.1130/g19796.1

Corfu, F., Hanchar, J. M., Hoskin, P. W. O., and Kinny, P. (2003). 16. Atlas of Zircon Textures. *Rev. Mineralogy Geochem.* 53, 469–502. doi:10.1515/9781501509322-019

Defant, M. J., and Drummond, M. S. (1990). Derivation of Some Modern Arc Magmas by Melting of Young Subducted Lithosphere. *Nature* 347 (6294), 662–665. doi:10.1038/347662a0

Ding, Q.-F., Jiang, S.-Y., and Sun, F.-Y. (2014). Zircon U-Pb Geochronology, Geochemical and Sr-Nd-Hf Isotopic Compositions of the Triassic Granite and Diorite Dikes from the Wulonggou Mining Area in the Eastern Kunlun Orogen, NW China: Petrogenesis and Tectonic Implications. *Lithos* 205, 266–283. doi:10.1016/j.lithos.2014.07.015

Ding, Q., Liu, F., and Yan, W. (2015). Zircon U–Pb Geochronology and Hf Isotopic Constraints on the Petrogenesis of Early Triassic Granites in the Wulonggou Area of the Eastern Kunlun Orogen, Northwest China. *Int. Geol. Rev.* 57, 1–20. doi:10.1080/00206814.2015.1029541

Ding, S., Huang, H., Niu, Y. L., Zhao, Z. D., Yu, X. H., and Mo, X. X. (2011). Geochemistry, Geochronology and Petrogenesis of East Kunlun High Nb-Ta Rhyolites. *Acta Petrol. Sin.* 27, 3603–3614.

Dong, Y., He, D., Sun, S., Liu, X., Zhou, X., Zhang, F., et al. (2018). Subduction and Accretionary Tectonics of the East Kunlun Orogen, Western Segment of the Central China Orogenic System. *Earth-Science Rev.* 186, 231–261. doi:10.1016/j.earscirev.2017.12.006

Drummond, M. S., Defant, M. J., and Kepezhinskas, P. K. (1996). Petrogenesis of Slab-Derived Trondhjemite-Tonalite-Dacite/adakite Magmas. *Earth Environ. Sci. Trans. R. Soc. Edinb.* 87, 205–215. doi:10.1130/0-8137-2315-9.20510.1017/s0263593300006611

Feng, C. Y., Li, D. S., Wu, Z. S., Li, J. H., Zhang, Z. Y., Zhang, A. K., et al. (2010). Major Types, Time-Apace Distribution and Metallogeneses of Polymetallic Deposits in the Qimantage Metallogenic belt , Eastern Kunlun Area. *Northwest. Geology.* 43 (4), 10–17. (in Chinese with English abstract).

Feng, C. Y., Wang, X. P., Shu, X. F., Zhang, A. K., Xiao, Y., Liu, J. N., et al. (2011). Isotopic Chronology for Hutouya Skarn-type lead–zinc Polymetallic Metallogenic District in the Qimantage Area, Qinghai Province, and its Geological Significance. *J. Jilin Univ. (Earth Sci. Ed.* 41 (6), 1806–1817. (in Chinese with English abstract).

Feng, C. Y., Li, D. S., Qu, W. J., Du, A. D., Wang, S., Su, S. S., et al. (2009). Re-Os Isotopic Dating of Molybdenite from the Suolajier Skarn-type Copper-Molybdenum Deposit of Qimantage Mountain in Qinghai Province and its Geological Significance. *Rock Mineral. Anal.* 8 (3), 223–227. (in Chinese with English abstract).

Foley, F. V., Pearson, N. J., Rushmer, T., Turner, S., and Adam, J. (2013). Magmatic Evolution and Magma Mixing of Quaternary Adakites at Solander and Little Solander Islands, New Zealand. *J. Petrol.* 54 (4), 703–744. doi:10.1093/petrology/egs082

He, S. Y., Li, D. S., Li, L. L., Qi, L. Y., and He, S. F. (2009). Re-Os Age of Molybdenite from the Yazigou Copper (Molybdenum) Mineralized Area in Eastern Kunlun of Qinghai Province, and its Geological Significance. *Geotecton. Metallog.* 33 (2), 236–242. (in Chinese with English abstract).

Hernández-Uribe, D., Hernández-Montenegro, J. D., Cone, K. A., and Palin, R. M. (2019). Oceanic Slab-Top Melting during Subduction: Implications for Trace-Element Recycling and Adakite Petrogenesis. *Geology* 48, 216–220. doi:10.1130/G46835.1

Hou, Z., Zhang, H., Pan, X., and Yang, Z. (2011). Porphyry Cu (–Mo–Au) Deposits Related to Melting of Thickened Mafic Lower Crust: Examples from the Eastern Tethyan Metallogenic Domain. *Ore Geol. Rev.* 39 (1), 21–45. doi:10.1016/j.oregeorev.2010.09.002

Hu, C. B., Li, M., Zha, X. F., Gao, X. F., and Li, T. (2018). Genesis and Geological Significance of Late Paleozoic Mantle-Derived Magmatism in Qimantag, East Kunlun: A Case Study of Intrusion in Yingzhuagou. *Earth Sci.* 43 (12), 4334–4349. (in Chinese with English abstract). doi:10.3799/dqkx.2018.120

Hu, Y., Niu, Y., Li, J., Ye, L., Kong, J., Chen, S., et al. (2016). Petrogenesis and Tectonic Significance of the Late Triassic Mafic Dikes and Felsic Volcanic Rocks in the East Kunlun Orogenic Belt, Northern Tibet Plateau. *Lithos* 245, 205–222. doi:10.1016/j.lithos.2015.05.004

Huang, F., and He, Y. (2010). Partial Melting of the Dry Mafic Continental Crust: Implications for Petrogenesis of C-type Adakites. *Chin. Sci. Bull.* 55 (22), 2428–2439. doi:10.1007/s11434-010-3224-2

Huang, F., Li, S., Dong, F., He, Y., and Chen, F. (2008). High-Mg Adakitic Rocks in the Dabie Orogen, Central China: Implications for Foundering Mechanism of Lower Continental Crust. *Chem. Geol.* 255 (1), 1–13. doi:10.1016/j.chemgeo.2008.02.014

Huang, H., Niu, Y., Nowell, G., Zhao, Z., Yu, X., Zhu, D.-C., et al. (2014). Geochemical Constraints on the Petrogenesis of Granitoids in the East Kunlun Orogenic Belt, Northern Tibetan Plateau: Implications for Continental Crust Growth through Syn-Collisional Felsic Magmatism. *Chem. Geology.* 370, 1–18. doi:10.1016/j.chemgeo.2014.01.010

Jahn, B.-m., Wu, F., and Chen, B. (2000). Granitoids of the Central Asian Orogenic Belt and Continental Growth in the Phanerozoic. *Trans. R. Soc. Edinb. Earth Sci.* 91 (1-2), 181–193. doi:10.1130/0-8137-2350-7.181

Keller, B., and Schoene, B. (2018). Plate Tectonics and Continental Basaltic Geochemistry throughout Earth History. *Earth Planet. Sci. Lett.* 481, 290–304. doi:10.1016/j.epsl.2017.10.031

Kröner, A., Kovach, V., Belousova, E., Hegner, E., Armstrong, R., Dolgopolova, A., et al. (2014). Reassessment of Continental Growth during the Accretionary History of the Central Asian Orogenic Belt. *Gondwana Res.* 25 (1), 103–125. doi:10.1016/j.gr.2012.12.023

Laurent, O., Doucelance, R., Martin, H., and Moyen, J.-F. (2013). Differentiation of the Late-Archaean Sanukitoid Series and Some Implications for Crustal Growth: Insights from Geochemical Modelling on the Bulai Pluton, Central Limpopo Belt, South Africa. *Precambrian Res.* 227, 186–203. doi:10.1016/j.precamres.2012.07.004

Li, H., Hermann, J., and Zhang, L. (2022). Melting of Subducted Slab Dictates Trace Element Recycling in Global arcs. *Sci. Adv.* 8 (25), h2166. (in Chinese with English abstract). doi:10.1126/sciadv.abh2166

Li, J. C., Kon, H. L., Li, Y. Z., Namkha, N., Jia, Q. Z., and Guo, X. Z. (2017). Ar-Ar Age of Altered Sericite, Zircon U-Pb Age of Quartz Diorite and Geochemistry of the Naomuhun Gold deposit, East Kunlun. *Acta Geologica Sinica* 91, 979–991.

Li, R. B., Pei, X. Z., Li, Z. C., Sun, Y., Pei, L., Chen, G. C., et al. (2013a). Regional Tectonic Transformation in East Kunlun Orogenic Belt in Early Paleozoic: Constraints from the Geochronology and Geochemistry of Helegangnaren Alkali-Feldspar Granite. *Acta Geologica Sinica-English Edition* 87 (2), 333–345.

Li, R., Pei, X., Pei, L., Li, Z., Chen, G., Chen, Y., et al. (2018). The Early Triassic Andean-type Halagatu Granitoids Pluton in the East Kunlun Orogen, Northern Tibet Plateau: Response to the Northward Subduction of the Paleo-Tethys Ocean. *Gondwana Res.* 62, 212–226. doi:10.1016/j.gr.2018.03.005

Li, S., Wang, T., Wilde, S. A., and Tong, Y. (2013b). Evolution, Source and Tectonic Significance of Early Mesozoic Granitoid Magmatism in the Central Asian Orogenic Belt (Central Segment). *Earth-Science Rev.* 126, 206–234. doi:10.1016/j.earscirev.2013.06.001

Li, X., Huang, X., Luo, M., Dong, G., and Mo, X. (2015). Petrogenesis and Geodynamic Implications of the Mid-triassic Lavas from East Kunlun, Northern Tibetan Plateau. *J. Asian Earth Sci.* 105, 32–47. doi:10.1016/j.jseaes.2015.03.009

Li, Z.-C., Pei, X.-Z., Bons, P. D., Li, R.-B., Pei, L., Chen, G.-C., et al. (2021). Petrogenesis and Tectonic Setting of the Early-Middle Triassic Subduction-Related Granite in the Eastern Segment of East Kunlun: Evidences from Petrology, Geochemistry, and Zircon U-Pb-Hf Isotopes. *Int. Geology. Rev.* 64 (5), 698–721. doi:10.1080/00206814.2021.1875268

Liang, Y., Xia, R., Ma, Y., Zhao, E., and Guo, W. (2021). Petrogenesis and Tectonic Significance of Late Triassic Baishiya Granodiorite Porphyries in the Dulan Area, Eastern Segment of the East Kunlun Orogenic Belt, China. *Geol. J.* 56 (1), 284–297. doi:10.1002/gj.3961

Liu, B., Ma, C.-Q., Huang, J., Wang, L.-X., Zhao, S.-Q., Yan, R., et al. (2017). Petrogenesis and Tectonic Implications of Upper Triassic Appinite Dykes in the East Kunlun Orogenic Belt, Northern Tibetan Plateau. *Lithos* 284-285, 766–778. doi:10.1016/j.lithos.2017.05.016

Liu, D., Li, H., Ge, C., Bai, M., Wang, Y., Pan, J., et al. (2021). Northward Growth of the West Kunlun Mountains: Insight from the Age-Elevation Relationship of New Apatite Fission Track Data. *Front. Earth Sci.* 9. doi:10.3389/feart.2021.784812

Liu, J. N., Feng, C. Y., Zhao, Y. M., Li, D. X., Xiao, Y., Zhou, J. H., et al. (2013). Characteristics of Intrusive Rock, Metasomatites, Mineralization, and Alteration in Yemaquan Skarn Fe–Zn Polymetallic deposit, Qinghai Province. *Mineral. Deposit* 32 (1), 77–93. (in Chinese with English abstract).

Liu, Y., Gao, S., Hu, Z., Gao, C., Zong, K., and Wang, D. (2010). Continental and Oceanic Crust Recycling-Induced Melt–Peridotite Interactions in the Trans-North China Orogen: U–Pb Dating, Hf Isotopes and Trace Elements in Zircons from Mantle Xenoliths. *J. Petrol.* 51 (1-2), 537–571. doi:10.1093/petrology/egp082

Liu, Y., Hu, Z., Gao, S., Günther, D., Xu, J., Gao, C., et al. (2008). *In Situ* Analysis of Major and Trace Elements of Anhydrous Minerals by La-Icp-Ms without Applying an Internal Standard. *Chem. Geology.* 257 (1-2), 34–43. doi:10.1016/j.chemgeo.2008.08.004

Ludwig, K. R. (2003). *User's Manual for Isoplot/Ex Version 3.00: A Geochronological Toolkit for Microsoft Excel (No. 4ed.)*. Berkeley: Berkeley Geochronology Center, Special Publication.

Ma, L., Wang, B.-D., Jiang, Z.-Q., Wang, Q., Li, Z.-X., Wyman, D. A., et al. (2014). Petrogenesis of the Early Eocene Adakitic Rocks in the Napuri Area, Southern Lhasa: Partial Melting of Thickened Lower Crust during Slab Break-Off and Implications for Crustal Thickening in Southern Tibet. *Lithos* 196-197, 321–338. doi:10.1016/j.lithos.2014.02.011

Ma, Q., Zheng, J., Griffin, W. L., Zhang, M., Tang, H., Su, Y., et al. (2012). Triassic "Adakitic" Rocks in an Extensional Setting (North China): Melts from the Cratonic Lower Crust. *Lithos* 149, 159–173. doi:10.1016/j.lithos.2012.04.017

Macpherson, C. G., Dreher, S. T., and Thirlwall, M. F. (2006). Adakites without Slab Melting: High Pressure Differentiation of Island Arc Magma, Mindanao, the Philippines. *Earth Planet. Sci. Lett.* 243 (3-4), 581–593. doi:10.1016/j.epsl.2005.12.034

Martin, H., Smithies, R. H., Rapp, R., Moyen, J. F., and Champion, D. (2005). An Overview of Adakite, Tonalite-Trondhjemite-Granodiorite (Ttg), and Sanukitoid: Relationships and Some Implications for Crustal Evolution. *Lithos* 79 (1-2), 1–24. doi:10.1016/j.lithos.2004.04.048

Middlemost, E. A. K. (1994). Naming Materials in the Magma/Igneous Rock System. *Earth-sci. Rev.* 37 (3), 215–224. doi:10.1016/0012-8252(94)90029-9

Moyen, J. (2009). High Sr/Y and La/Yb Ratios: The Meaning of the "Adakitic Signature". *Lithos* 112 (3), 556–574. doi:10.1016/j.lithos.2009.04.001

Peccerillo, A., and Taylor, S. R. (1976). Geochemistry of Eocene Calc-Alkaline Volcanic Rocks from the Kastamonu Area, Northern Turkey. *Contr. Mineral. Petrol.* 58 (1), 63–81. doi:10.1007/bf00384745

Peng, Y., Yu, S., Zhang, J., Li, Y., Li, S., and Lv, P. (2021). Building a continental Arc Section: Constraints from Paleozoic Granulite-Facies Metamorphism, Anatexis, and Magmatism in the Northern Margin of the Qilian Block, Northern Tibet Plateau. *Geol. Soc. Am. Bull.* doi:10.1130/B36100.1

Petford, N., and Gallagher, K. (2001). Partial Melting of Mafic (Amphibolitic) Lower Crust by Periodic Influx of Basaltic Magma. *Earth Planet. Sc. Lett.* 193 (3-4), 483–499. doi:10.1016/s0012-821x(01)00481-2

Qin, J.-F., Lai, S.-C., Diwu, C.-R., Ju, Y.-J., and Li, Y.-F. (2010a). Magma Mixing Origin for the post-collisional Adakitic Monzogranite of the Triassic Yangba Pluton, Northwestern Margin of the South China Block: Geochemistry, Sr-Nd Isotopic, Zircon U-Pb Dating and Hf Isotopic Evidences.

Qin, J. F., Lai, S. C., Grapes, R., Diwu, C., Ju, Y. J., and Li, Y. F. (2010b). Origin of Late Triassic High-Mg Adakitic Granitoid Rocks from the Dongjiangkou Area, Qinling Orogen, Central China: Implications for Subduction of continental Crust. *Lithos* 120 (3-4), 347–367. doi:10.1016/j.lithos.2010.08.022

Qu, H., Friehauf, K., Santosh, M., Pei, R., Li, D., Liu, J., et al. (2019). Middle-Late Triassic Magmatism in the Hutouya Fe-Cu-Pb-Zn deposit, East Kunlun Orogenic Belt, NW China: Implications for Geodynamic Setting and Polymetallic Mineralization. *Ore Geology. Rev.* 113, 103088. doi:10.1016/j.oregeorev.2019.103088

Rapp, R. P., Shimizu, N., Norman, M. D., and Applegate, G. S. (1999). Reaction between Slab-Derived Melts and Peridotite in the Mantle Wedge: Experimental Constraints at 3.8 Gpa. *Chem. Geology.* 160 (4), 335–356. doi:10.1016/s0009-2541(99)00106-0

Roger, F., Malavieille, J., Leloup, P. H., Calassou, S., and Xu, Z. (2004). Timing of Granite Emplacement and Cooling in the Songpan-Garzê Fold Belt (Eastern Tibetan Plateau) with Tectonic Implications. *J. Asian Earth Sci.* 22 (5), 465–481. doi:10.1016/s1367-9120(03)00089-0

Shao, F., Niu, Y., Liu, Y., Chen, S., Kong, J., and Duan, M. (2017). Petrogenesis of Triassic Granitoids in the East Kunlun Orogenic Belt, Northern Tibetan Plateau and Their Tectonic Implications. *Lithos* 282-283, 33–44. doi:10.1016/j.lithos.2017.03.002

Stern, C. R., and Kilian, R. (1996). Role of the Subducted Slab, Mantle Wedge and Continental Crust in the Generation of Adakites from the Andean Austral Volcanic Zone. *Contrib. Mineralogy Pet.* 123 (3), 263–281. doi:10.1007/s004100050155

Sun, S.-s., and McDonough, W. F. (1989). Chemical and Isotopic Systematics of Oceanic Basalts: Implications for Mantle Composition and Processes. *Geol. Soc. Lond. Spec. Publications* 42, 313–345. doi:10.1144/gsl.sp.1989.042.01.19

Tang, G., Wang, Q., Wyman, D. A., Li, Z. X., Zhao, Z. H., Jia, X. H., et al. (2010). Ridge Subduction and Crustal Growth in the Central Asian Orogenic Belt: Evidence from Late Carboniferous Adakites and High-Mg Diorites in the Western Junggar Region, Northern Xinjiang (West China). *Chem. Geol.* 277 (3-4), 281–300. doi:10.1016/j.chemgeo.2010.08.012

Taylor, S. R., and McLennan, S. M. (1985). *The Continental Crust: Its Composition and Evolution*. Oxford: Blackwell Scientific Publications.

Tian, C. S., Feng, C. Y., Li, J. H., and Cao, D. Z. (2013). 40Ar–39Ar Geochronology of Tawenchahan Fe-Polymetallic deposit in Qimantag Mountain of Qinghai Province and its Geological Implications. *Mineral. Deposits* 3 (1), 169–176. (in Chinese with English abstract).

Wang, F. C., Chen, J., Xie, Z. Y., Li, S. P., Tan, S. X., Wang, Y. B., et al. (2013). Geological Features and Re-os Isotopic Dating of the Lalingzaohuo Molybdenum Polymetallic deposit in East Kunlun. *Geol. China.* 40 (4), 1209–1217. (in Chinese with English abstract).

Wang, H., Feng, C. Y., Li, D. X., Li, C., Ding, T. Z., and Zhou, J. H. (2015). Molybdenite Re-os Geochronology and Sulfur Isotope Geochemistry of the

Saishitang Copper Deposit,Qinghai Province. *Acta Geologica Sinica* 89 (3), 487–497. (in Chinese with English abstract).

Wang, Q., Wyman, D. A., Xu, J. F., Zhao, Z. H., Jian, P., and Zi, F. (2007a). Partial Melting of Thickened or Delaminated Lower Crust in the Middle of Eastern China: Implications for Cu-Au Mineralization. *J. Geology.* 115 (2), 149–161. doi:10.1086/510643

Wang, Q., Wyman, D. A., Xu, J., Jian, P., Zhao, Z., Li, C., et al. (2007b). Early Cretaceous Adakitic Granites in the Northern Dabie Complex, Central China: Implications for Partial Melting and Delamination of Thickened Lower Crust. *Geochimica et Cosmochimica Acta* 71 (10), 2609–2636. doi:10.1016/j.gca.2007.03.008

Wang, Q., Xu, J.-F., Jian, P., Bao, Z.-W., Zhao, Z.-H., Li, C.-F., et al. (2006). Petrogenesis of Adakitic Porphyries in an Extensional Tectonic Setting, Dexing, South China: Implications for the Genesis of Porphyry Copper Mineralization. *J. Petrol.* 47, 119–144. doi:10.1093/petrology/egi070

Xia, R., Deng, J., Qing, M., Li, W., Guo, X., and Zeng, G. (2017). Petrogenesis of Ca. 240 Ma Intermediate and Felsic Intrusions in the Nan'getan: Implications for Crust-Mantle Interaction and Geodynamic Process of the East Kunlun Orogen. *Ore Geology. Rev.* 90, 1099–1117. doi:10.1016/j.oregeorev.2017.04.002

Xia, R., Wang, C., Qing, M., Deng, J., Carranza, E. J. M., Li, W., et al. (2015). Molybdenite Re-os, Zircon U-Pb Dating and Hf Isotopic Analysis of the Shuangqing Fe-Pb-Zn-Cu Skarn deposit, East Kunlun Mountains, Qinghai Province, China. *Ore Geology. Rev.* 66, 114–131. doi:10.1016/j.oregeorev.2014.10.024

Xia, R., Wang, C., Deng, J., Carranza, E. J. M., Li, W., and Qing, M. (2014). Crustal Thickening Prior to 220Ma in the East Kunlun Orogenic Belt: Insights from the Late Triassic Granitoids in the Xiao-Nuomuhong Pluton. *J. Asian Earth Sci.* 93, 193–210. doi:10.1016/j.jseaes.2014.07.013

Xiao, W., and Santosh, M. (2014). The Western Central Asian Orogenic Belt: A Window to Accretionary Orogenesis and Continental Growth. *Gondwana Res.* 25 (4), 1429–1444. doi:10.1016/j.gr.2014.01.008

Xiong, F., Ma, C., Jiang, H. A., and Zhang, H. (2016). Geochronology and Petrogenesis of Triassic High-K calc-alkaline Granodiorites in the East Kunlun Orogen, West China: Juvenile Lower Crustal Melting During Post-Collisional Extension. *J. Earth Sci.* 27 (3), 474–490. doi:10.1007/s12583-016-0674-6

Xiong, F., Ma, C., Chen, B., Ducea, M. N., Hou, M., and Ni, S. (2019). Intermediate-Mafic Dikes in the East Kunlun Orogen, Northern Tibetan Plateau: A Window into Paleo-Arc Magma Feeding System. *Lithos* 340-341, 152–165. doi:10.1016/j.lithos.2019.05.012

Xiong, F., Ma, C., Wu, L., Jiang, H. A., and Liu, B. (2015). Geochemistry, Zircon U-Pb Ages and Sr-Nd-Hf Isotopes of an Ordovician Appinitic Pluton in the East Kunlun Orogen: New Evidence for Proto-Tethyan Subduction. *J. Asian Earth Sci.* 111, 681–697. doi:10.1016/j.jseaes.2015.05.025

Xiong, F., Ma, C., Zhang, J., Liu, B., and Jiang, H. A. (2014). Reworking of Old Continental Lithosphere: An Important Crustal Evolution Mechanism in Orogenic Belts, as Evidenced by Triassic I-type Granitoids in the East Kunlun Orogen, Northern Tibetan Plateau. *J. Geol. Soc.* 171 (6), 847–863. doi:10.1144/jgs2013-038

Xiong, F.-H., Ma, C.-Q., Zhang, J.-Y., and Liu, B. (2012). The Origin of Mafic Microgranular Enclaves and Their Host Granodiorites from East Kunlun, Northern Qinghai-Tibet Plateau: Implications for Magma Mixing during Subduction of Paleo-Tethyan Lithosphere. *Miner. Petrol.* 104, 211–224. doi:10.1007/s00710-011-0187-1

Xiong, F. H., Ma, C. Q., Zhang, J. Y., and Liu, B. (2011). LA-ICP-MS Zircon U-Pb Dating, Elements and Sr-Nd-Hf Isotope Geochemistry of the Early Mesozoic Mafic Dyke Swarms in Eastern Kunlun Orogenic Belt. *Acta Petrol. Sin.* 27, 3350–3364.

Xu, J.-F., Shinjo, R., Defant, M. J., Wang, Q., and Rapp, R. P. (2002). Origin of Mesozoic Adakitic Intrusive Rocks in the Ningzhen Area of East China: Partial Melting of Delaminated Lower Continental Crust. *Geol* 30 (12), 1111–1114. doi:10.1130/0091-7613(2002)030<1111:oomair>2.0.co;2

Yang, J. S., Robinson, P. T., Jiang, C. F., and Xu, Z. Q. (1996). Ophiolites of the Kunlun Mountains, China and Their Tectonic Implications. *Tectonophysics* 258 (1-4), 215–231. doi:10.1016/0040-1951(95)00199-9

Yin, S., Ma, C., and Xu, J. (2021). Recycling of K-Feldspar Antecrysts in the Baishiya Porphyritic Granodiorite, East Kunlun Orogenic Belt, Northern Tibet Plateau: Implications for Magma Differentiation in a Crystal Mush Reservoir. *Lithos* 402-403, 105622. doi:10.1016/j.lithos.2020.105622

Yu, M., Dick, J. M., Feng, C., Li, B., and Wang, H. (2020). The Tectonic Evolution of the East Kunlun Orogen, Northern Tibetan Plateau: A Critical Review with an Integrated Geodynamic Model. *J. Asian Earth Sci.* 191, 104168. doi:10.1016/j.jseaes.2019.104168

Yu, M., Feng, C. Y., Santosh, M., Mao, J. W., Zhu, Y. F., Zhao, Y. M., et al. (2017). The Qiman Tagh Orogen as a Window to the Crustal Evolution in Northern Qinghai-Tibet Plateau. *Earth-Science Rev.* 167, 103–123. doi:10.1016/j.earscirev.2017.02.008

Yu, S., Li, S., Zhang, J., Sun, D., Peng, Y., and Li, Y. (2018). Linking High-Pressure Mafic Granulite, TTG-like (Tonalitic-trondhjemitic) Leucosome and Pluton, and Crustal Growth during continental Collision. *GSA Bull.* 131 (3-4), 572–586. doi:10.1130/B31822.1

Yu, S., Zhang, J., Li, S., Santosh, M., Li, Y., Liu, Y., et al. (2019). TTG-Adakitic-Like (Tonalitic-Trondhjemitic) Magmas Resulting from Partial Melting of Metagabbro under High-Pressure Condition during Continental Collision in the North Qaidam UHP Terrane, Western China. *Tectonics* 38 (3), 791–822. doi:10.1029/2018TC005259

Yuan, C., Sun, M., Xiao, W., Wilde, S., Li, X., Liu, X., et al. (2009). Garnet-Bearing Tonalitic Porphyry from East Kunlun, Northeast Tibetan Plateau: Implications for Adakite and Magmas from the Mash Zone. *Int. J. Earth Sci. (Geol Rundsch)* 98 (6), 1489–1510. doi:10.1007/s00531-008-0335-y

Yuan, H. L., Gao, S., Dai, M. N., Zong, C. L., Günther, D., Fontaine, G. H., et al. (2008). Simultaneous Determinations of U-Pb Age, Hf Isotopes and Trace Element Compositions of Zircon by Excimer Laser-Ablation Quadrupole and Multiple-Collector Icp-Ms. *Chem. Geol.* 247 (1-2), 100–118. doi:10.1016/j.chemgeo.2007.10.003

Zhang, J., Ma, C., Li, J., and Pan, Y. (2017). A Possible Genetic Relationship between Orogenic Gold Mineralization and Post-Collisional Magmatism in the Eastern Kunlun Orogen, Western China. *Ore Geology. Rev.* 81, 342–357. doi:10.1016/j.oregeorev.2016.11.003

Zhang, J., Yu, M., Wang, H., Li, B., Feng, C., Dick, J. M., et al. (2021). Geodynamic Setting and Cu-Ni Potential of Late Permian Xiwanggou Mafic-Ultramafic Rocks, East Kunlun Orogenic Belt, Nw China. *Front. Earth Sci.* 9. doi:10.3389/feart.2021.666967

Zheng, S., An, Y., Lai, C., Wang, H., and Li, Y. (2021). Genesis of High-Mg Adakites in the Southeastern Margin of North China Craton: Geochemical and U-Pb Geochronological Perspectives. *Front. Earth Sci.* 9. doi:10.3389/feart.2021.731233

Zhong, S., Li, S., Feng, C., Liu, Y., Santosh, M., He, S., et al. (2021). Porphyry Copper and Skarn Fertility of the Northern Qinghai-Tibet Plateau Collisional Granitoids. *Earth-Science Rev.* 214, 103524. doi:10.1016/j.earscirev.2021.103524

Conflict of Interest: The authors declare that the research was conducted in the absence of any commercial or financial relationships that could be construed as a potential conflict of interest.

Publisher's Note: All claims expressed in this article are solely those of the authors and do not necessarily represent those of their affiliated organizations, or those of the publisher, the editors and the reviewers. Any product that may be evaluated in this article, or claim that may be made by its manufacturer, is not guaranteed or endorsed by the publisher.

frontiers | Frontiers in Earth Science

ORIGINAL RESEARCH
published: 17 May 2022
doi: 10.3389/feart.2022.909166

Image Recognition–Based Identification of Multifractal Features of Faults

Xiuquan Hu[1,2], Hong Liu[1], Xiucheng Tan[1], Chi Yi[2], Zhipeng Niu[2], Jianghan Li[2] and Jieyi Li[2]*

[1]School of Earth Science and Techology, Southwest Petroleum University, Chengdu, China, [2]College of Energy, Chengdu University of Technology, Chengdu, China

Geologists have made several advances in applying multifractal theory in geology; however, some questions such as a large statistical workload and low efficiency remain unanswered. Thus, this study proposes an image recognition–based method for calculating fault multifractality. First, grayscale processing and binarization of the fault distribution map were performed. The image was then gridded, and the grids were numbered. Subsequently, computer image recognition technology was used to count the number of faults in each grid as a replacement for manual counting. Finally, the fractal dimensions of the faults were calculated using a multifractal box-counting algorithm. This method was successfully applied to fracture studies of the Maokou Formation in southeast Sichuan. Compared to the conventional approach, the proposed method demonstrated considerably improved work efficiency and accuracy. The results showed that the faults in the study area exhibited good statistical self-similarity in the scale range, indicating fractal characteristics. The fractal dimensions of faults with different orientations and the planar distribution of the fractal dimension contours indicate tectonic stages and stress magnitude in the study area. The results indicate that the tectonic setting of southeast Sichuan was formed primarily during the Indosinian, Yanshanian, and Himalayan periods. From the Indosinian to the early Yanshanian periods, NE-trending faults with relatively large fractal dimensions developed under NW–SE compressional tectonic stress. From the Late Yanshanian to Early Himalayan, EW-trending faults were formed by relatively weak N–S compressional stress and had the lowest fractal dimensions. The NW-trending faults formed by intense NE–SW compressional tectonic stress in the Late Himalayan region had the highest fractal dimensions. To promote oil and gas migration and ensure that faults do not destroy the caprock, oil and gas reservoirs must be in a relatively mild tectonic environment. Thus, the fractal dimensions of faults in favorable areas should be neither too high nor too low. The relationship between the fractal dimensions of faults and well test results in southeast Sichuan indicates that the region along the wells “ls1–xia14–guan3” (with fractal dimensions of 1.49–1.57) in the study area is a relatively favorable region for oil and gas preservation.

Keywords: image recognition, multifractal, faults, tectonic stages, fractal dimensions of faults

OPEN ACCESS

Edited by:
Gillian Foulger,
Durham University, United Kingdom

Reviewed by:
Fei Ning,
SINOPEC Petroleum Exploration and Production Research Institute, China
Lei Gong,
Northeast Petroleum University, China

***Correspondence:**
Hong Liu
nd123@163.com

Specialty section:
This article was submitted to Structural Geology and Tectonics, a section of the journal Frontiers in Earth Science

Received: *31 March 2022*
Accepted: *29 April 2022*
Published: *17 May 2022*

Citation:
Hu X, Liu H, Tan X, Yi C, Niu Z, Li J and Li J (2022) Image Recognition–Based Identification of Multifractal Features of Faults. Front. Earth Sci. 10:909166. doi: 10.3389/feart.2022.909166

INTRODUCTION

Faults play a vital role in the formation of hydrocarbon reservoirs by providing pathways for oil and gas migration (Woods, 1992; Nagy et al., 2012; Kasyanova, 2018; Gong et al., 2019; Gong et al., 2021; Zeng et al., 2022a). Multiple studies on geological structures (particularly fault systems) have revealed that the distribution and geometry of geological structures exhibit fractal characteristics. Fractal theory is a highly effective tool for quantitatively describing irregular and complex natural structures (Mandelbrot, 1983). It has been widely and successfully employed to describe geological features and reveal inherent formation patterns. For example, Boulassel et al. proposed a multifractal analysis–based method for identifying reservoir fluids that can be used to delineate oil and gas layers and detect fluid properties (Boulassel et al., 2021). Flores-Márquez et al. applied multifractal theory to study the earthquake magnitude series of the Mexican South Pacific region, and Agterberg constructed multifractal and geostatistical models of geochemical element concentrations in rocks and deposits (Agterberg, 2012; Flores-Márquez et al., 2015). Tan et al. analyzed the multifractality of ore-controlling faults in Altay, Xinjiang, China (Tan et al., 2010). Xu et al. performed a multifractal analysis of the fault system in the Nanpu Sag, Jidong Oilfield, China, and identified hydrocarbon accumulation areas (Xu et al., 2019). However, in conventional multifractal studies, the faults in each grid are typically counted manually, and a constantly changing grid length results in a very large workload and low efficiency. If the faults in a certain grid are incorrectly counted, the final calculation result is inaccurate. Thus, this approach has become infeasible with the rapid development of the information era, as it cannot be used to process the vast amount of data required for multiple fault analyses.

In recent years, with the rapid development of image recognition methods, computer image processing and analysis have been extensively applied in oil exploration, and a comprehensive system of methods that yields good results has been achieved (Thompson et al., 2001; Izadi et al., 2015; Ashok et al., 2016; Patel et al., 2016; Yathunanthan et al., 2017; Ma et al., 2018; Kuang et al., 2021). For instance, Budennyy et al. proposed an intelligent lithological method for the description of thin-section images of rocks under polarized light (Budennyy et al., 2017). For oil reservoir descriptions, Tyurin et al. applied Ridge filtering to preprocess borehole image logs for more accurate identification of the bedding interface (Tyurin et al., 2016). Additionally, Semukhin et al. used the SUSAN edge detector to binarize images and introduced an algorithm to calculate the geometric parameters of the fractures and thus describe their features (Semukhin et al., 2019). Shape features, which are among the critical features of images, are stable and do not vary with image color. Fault distribution maps are often used in structural geological research as they consist of a collection of lines, image recognition tools can be applied to them. Therefore, fault counting in multifractal analyses of fault structures can be transformed into pattern recognition tasks. The cross-platform computer vision library OpenCV is one of the most widely used image recognition tools (Bradski, 2008; Hongbo et al., 2020). It has overcome the shortcomings of conventional software, namely, large size and slow running speed, and provides high-efficiency, lightweight graphics, and image processing. The OpenCV recognition process primarily consists of image preprocessing, color extraction, filtering, segmentation, grayscaling, binarization, and fitting and can recognize the contours and colors of images that include different shapes (Zhou et al., 2016a; Wei, 2019). In multifractal analysis of fault structures using computer image recognition, the faults in each grid can be counted automatically, replacing manual counting. The fractal dimensions of all faults in the region and faults with different orientations were then calculated by solving the equations of the multifractal box-counting algorithm. Finally, contour maps of the fractal dimensions were plotted. This method improves the efficiency and reliability of research and reduces production and labor costs. In this study, the fractal dimensions of faults in the entire region of the Maokou Formation in southeast Sichuan and the differences in fractal dimensions between faults with different orientations were analyzed. The results were used to explore the relationship between the fractal dimensions and tectonic stages, geodynamics, and hydrocarbon accumulation. We also searched for favorable oil and gas development areas related to faults and associated fractures. This study introduces a concept and method with broad application prospects for oil and gas exploration.

GEOLOGICAL BACKGROUND

Southeast Sichuan is in the southeastern part of the Sichuan Basin, spanning Guizhou Province, Chongqing Municipality, and parts of Sichuan Province, including the cities and counties of Shuijiang, Qijiang, Fengdu, Xingwen, Gulin, Tongzi, Chishui, and Renhuai. The main tectonic structure in the Sichuan Basin is part of the East Sichuan arc-shaped high-steep fold belt and the southern low-steep fold belt of the South Sichuan broom-shaped fold belt. These regions have the strongest tectonic movements in the basin (**Figure 1**). This area is a tertiary geotectonic unit of the Yangtze quasi-platform with widely distributed mountains, hills, and complex geological structures. The terrain is high in the south and low in the north, and karst landforms are common (Xu et al., 2019; Wang et al., 2021; Zhong et al., 2021). The Maokou Formation in southeastern Sichuan is in the interior of the craton basin, where marine carbonate rocks have been deposited. The tectonic uplift of the Dongwu Movement resulted in the exposure of the Maokou Formation limestone to the surface for a long time (8–7 Ma). The Maokou Formation experienced an epigenetic weathering stage that was affected by atmospheric water, and its top surface was exposed to corrosion and weak erosion.

CONCEPTS AND PROCESSES

OpenCV image recognition technology is used in the image recognition–based multifractal analysis of fault structures to automatically count the number of faults in each grid. Multifractal algorithms include box-counting, fixed-radius, and

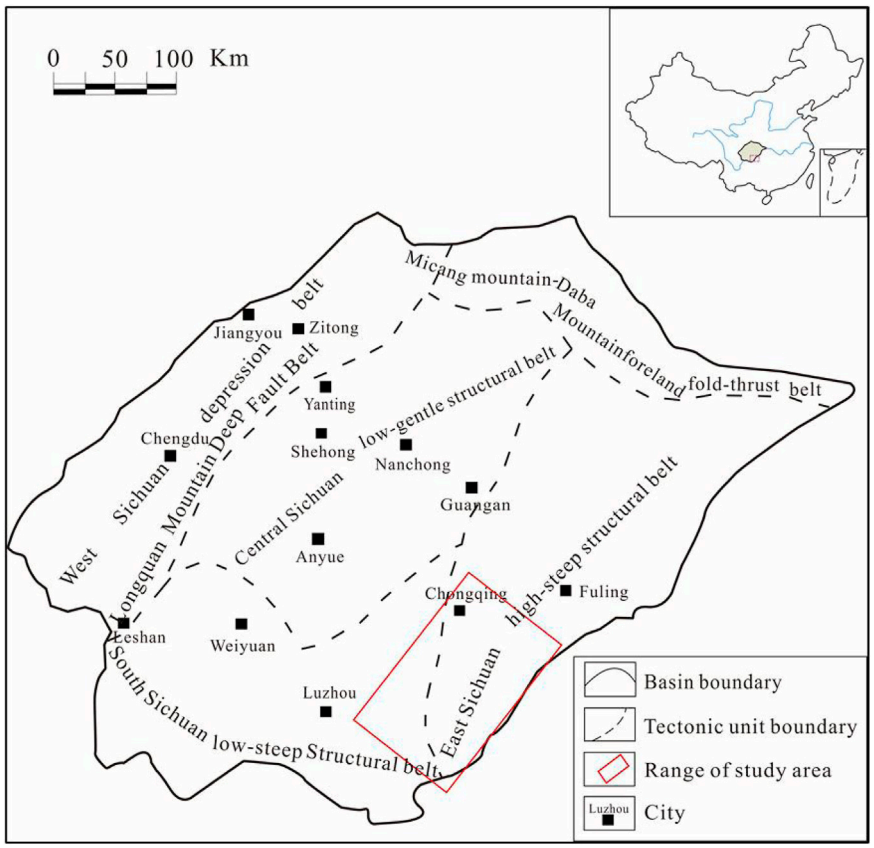

FIGURE 1 | Schematic map of geology of southeast Sichuan (modified from Liu et al., 2019)

fixed-mass methods (Gao, 2004; Sun et al., 2003; Xie et al., 2002; Xiong et al., 2016; Salat et al., 2017). Because the box-counting method can be applied to images of arbitrary shapes in practical applications with outstanding results, most scholars have used this algorithm to study the fracture fractal dimension value. Therefore, we employed this algorithm in this study. The main steps in the image recognition–based multifractal analysis of fault structures are as follows:

Step 1: The fault distribution map was obtained by a detailed interpretation of seismic cross-sections and seismic attributes.

Step 2: The color fault distribution map is converted into a grayscale image using a color transfer function. The grayscale image was then binarized using the image thresholding function to distinguish the colors representing faults from the background color.

Step 3: The height and width of the fault distribution map were determined, and the initial grid-side length r was set to cover as much of the study area as possible by a mesh using the fewest grids possible. The entire image was divided into N grids numbered 1, 2, 3, . . . i.

Step 4: The outlines of faults in the grids of the binarized image are detected using the cv2.findContours function in OpenCV, and the number of faults in each grid n_i is counted, thus completing the fault detection.

Step 5: The number of faults in all grids is summed to obtain the number of faults in the entire region M, and the frequency of fault occurrence in each grid Pi(r) is calculated. The value of parameter q in the multifractal analysis formula was set, and Iq(r) was calculated using this formula (Hu et al., 2014).

M is calculated as follows:

$$M = \sum_{i=1}^{N} n_i$$

where n_i is the number of faults in the i-th grid, when the scale is set to r.$P_i(r)$ is calculated as follows:

$$P_i(r) = \frac{n_i}{M}$$

$I_q(r)$ is calculated as follows:

$$I_q(r) = \begin{cases} \frac{1}{1-q} ln \sum P_i(r)^q \; q \neq 1 \\ \sum P_i(r) ln\left(\frac{1}{P_i(r)}\right) \; q = 1 \end{cases}$$

where q is the order, which can be any real number in the interval $(-\infty, +\infty)$.

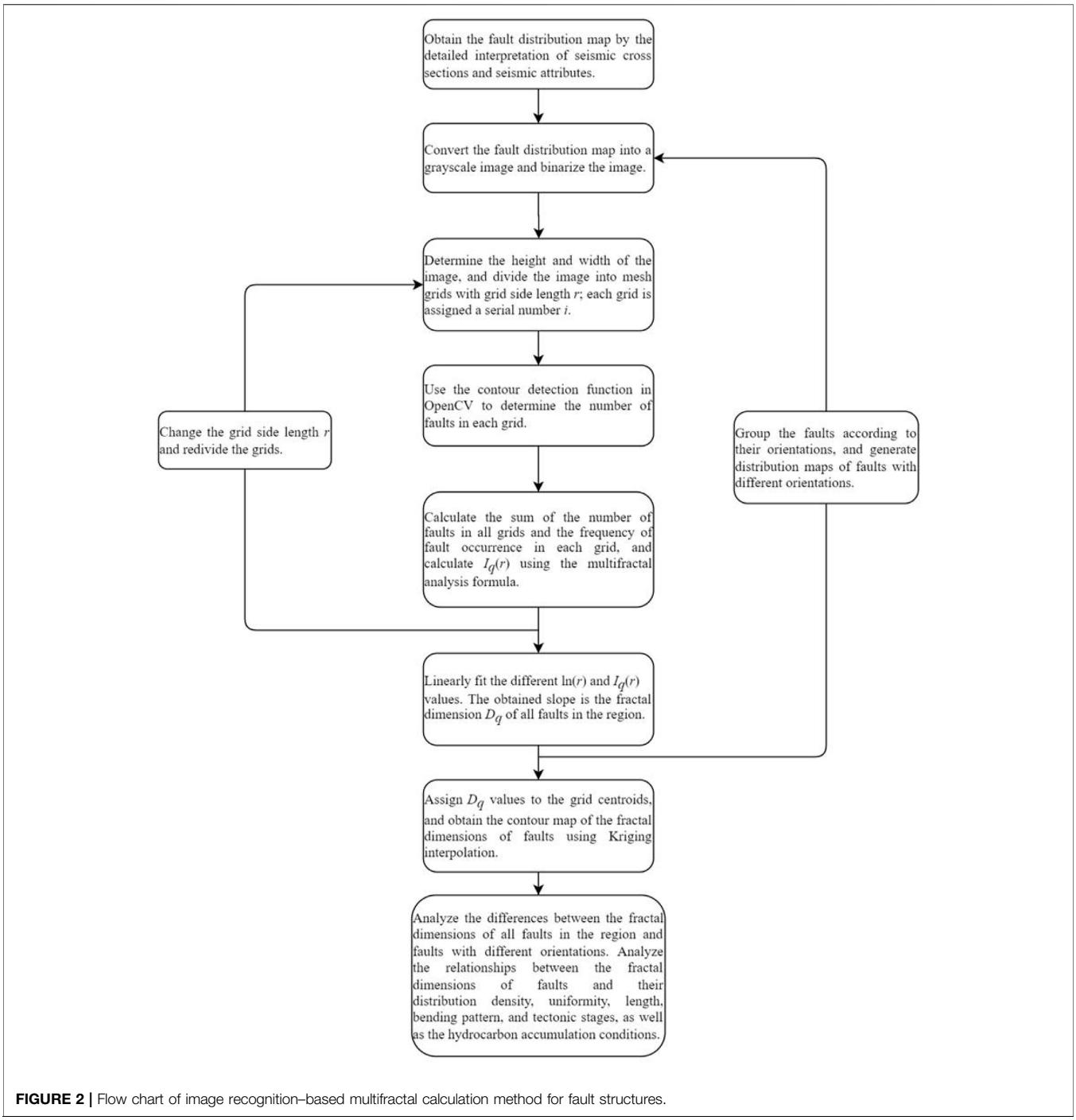

FIGURE 2 | Flow chart of image recognition–based multifractal calculation method for fault structures.

Step 6: The grid-side length r is gradually reduced to redivide the fault distribution map with continuously finer grids. Steps 2–4 are repeated k times ($k \geq 2$) to obtain $I_q(r)$ for different values of r.

Step 7: The $I_q(r)$ values obtained in Steps 1–5 were linearly fitted with different ln(r) values (data for linear fitting should be no less than three groups, five groups, and above best), and the slope of the obtained function was the fractal dimension D_q of the faults in the entire region (Cheng et al., 2020). The regression equation is as follows:

$$I_q(r) = -D_q \ln(r) + I_0$$

When the correlation coefficient is greater than 0.9, the obtained slope is the fractal dimension D_q of all faults in the region. When q = 0, 1, and 2, D_q corresponds to D_0 (the capacity dimension), D_1 (the

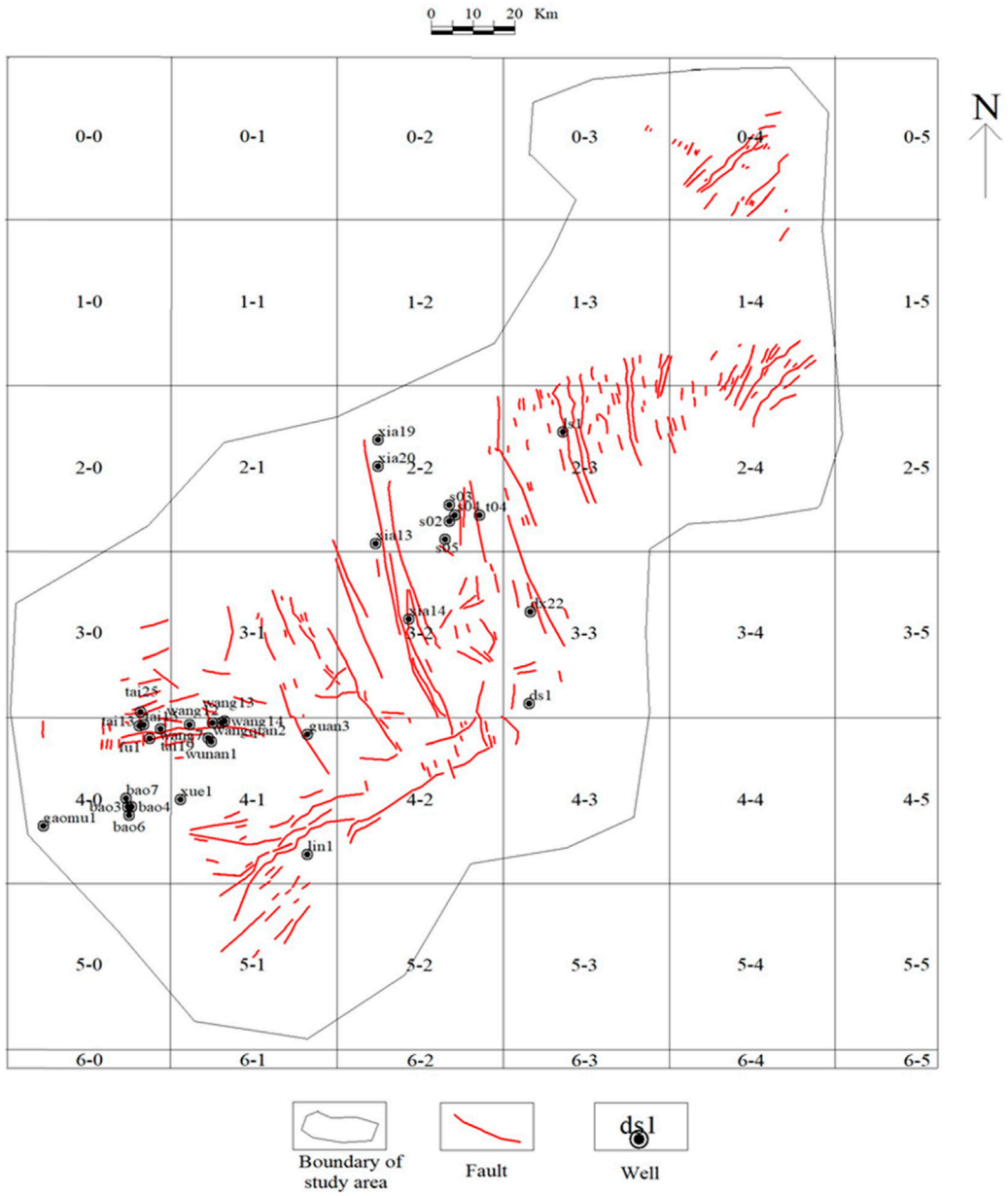

FIGURE 3 | Fault distribution map of Maokou Formation in southeast Sichuan (modified from Hu et al., 2014).

information dimension), and D_2 (the correlation dimension), respectively.

Step 8: The values of the fractal dimensions of the faults, D_q, were assigned to the grid center point, and contour maps of D_q were obtained by interpolation.

Step 9: Distribution maps of faults with different orientations are generated, and Steps 2–8 are repeated to obtain the fractal dimensions D_q of faults with different orientations.

Step 10: The differences between the fractal dimensions of all faults in the region and faults with different orientations were obtained from the fractal dimensions of faults with different orientations and a map of fractal dimensions. The relationships between the fractal dimensions of the faults and their distribution density, uniformity, length, bending pattern, tectonic stage, and hydrocarbon accumulation conditions were analyzed.

Specific method flow chart as shown in **Figure 2**:

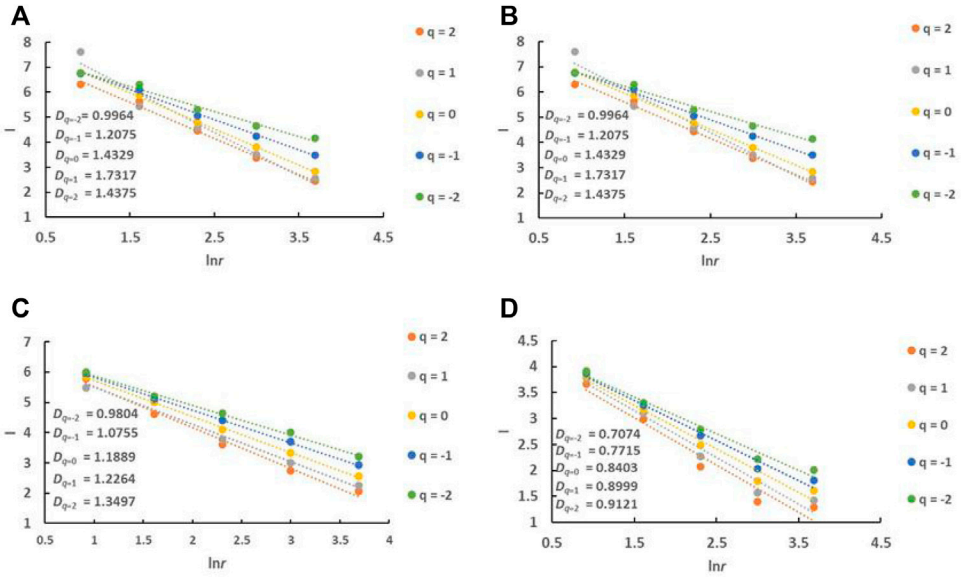

FIGURE 4 | ln(r)-I_q(r) curves of fault distribution in Maokou Formation in southeast Sichuan **(A)** all faults in study area; **(B)** NW-trending faults; **(C)** NE-trending faults; **(D)** EW-trending faults.

PRACTICAL APPLICATION

Data Processing

Through the collection of two-dimensional seismic line data, we performed detailed horizon tracing and fault interpretation using seismic cross-sections based on synthetic record calibration and then analyzed the planar fault combination patterns and seismic coherence attributes. Next, a fault distribution map of the Maokou Formation in southeast Sichuan was plotted at a scale of 1:250,000 to serve as the base map (**Figure 3**). This map was converted into a grayscale image using the color transfer function cv2.cvtColor and the grayscale image was binarized using the image thresholding function cv2.threshold. The comparison threshold X was set to 127, that is, pixel points with a grayscale value greater than or equal to 127 were set to 255 (white), and the other pixel points were set to 0 (black). The height and width of the fault distribution map of the Maokou Formation in southeastern Sichuan were determined. To ensure that the initial mesh covered the entire study area with as few grids as possible, we first divided the fault distribution map into 42 square grids with a side length r of 40 km, and the grids were numbered accordingly. The cv2. findContours function in OpenCV was applied to search for fault outlines in the binarized image grids and return the number of faults within each grid, n_i, thus completing the fault detection. The number of faults in the entire region M was obtained by summing the number of faults in all grids, and the frequency of fault occurrence in each grid $P_i(r)$ was calculated using n_i and M. Parameter q in the multifractal analysis formula was set to −2, −1, 0, 1, and 2, and the corresponding $I_q(r)$ values were calculated by substituting the data into the multifractal analysis formula. The regression curves of ln(r) and $I_q(r)$ were drawn by the linear fitting of five different groups of ln(r) and $I_q(r)$ (**Figure 4**), and the slope of the regression line was the fractal dimension of the faults, D_q, for each q value. We divided the faults in the study area into three sets according to their orientation: NW-trending-, NE-trending-, and near-EW-trending. When distinguishing NE and NW, we grouped the NNE-trending and ENE-trending faults into NE-trending faults and the NNW-trending and WNW-trending faults into NW-trending faults. In addition, because there were only a few near-NS-trending faults, they were also grouped with NW-trending faults for convenience of analysis. Distribution maps of faults with different orientations were then generated, and the above steps were repeated to obtain the fractal dimensions D_q of these sets of faults.

Characteristics and Distribution of Fractal Dimensions

The ln(r)–$I_q(r)$ regression curves (**Figure 4**) display linearity between the $I_q(r)$ and ln(r) values of the faults with different orientations in the Maokou Formation. The absolute values of the regression slopes are the fractal dimensions D_q of the fault structures. The correlation coefficient R^2 is > 0.9, indicating that, at a scale of 40–2.5 km, the spatial pattern of fault distribution shows a good statistical match and apparent fractal features. The fractal dimensions of all faults in the region and faults with different orientations both increase as q increases. The fractal dimension of all faults in the Maokou Formation ranges between 0.9964 and 1.7317, with the NW-trending faults ranging between 0.8848 and 1.4196, the NE-trending faults ranging between 0.9804 and 1.3497, and the EW-trending faults ranging between 0.7074 and 0.9121.

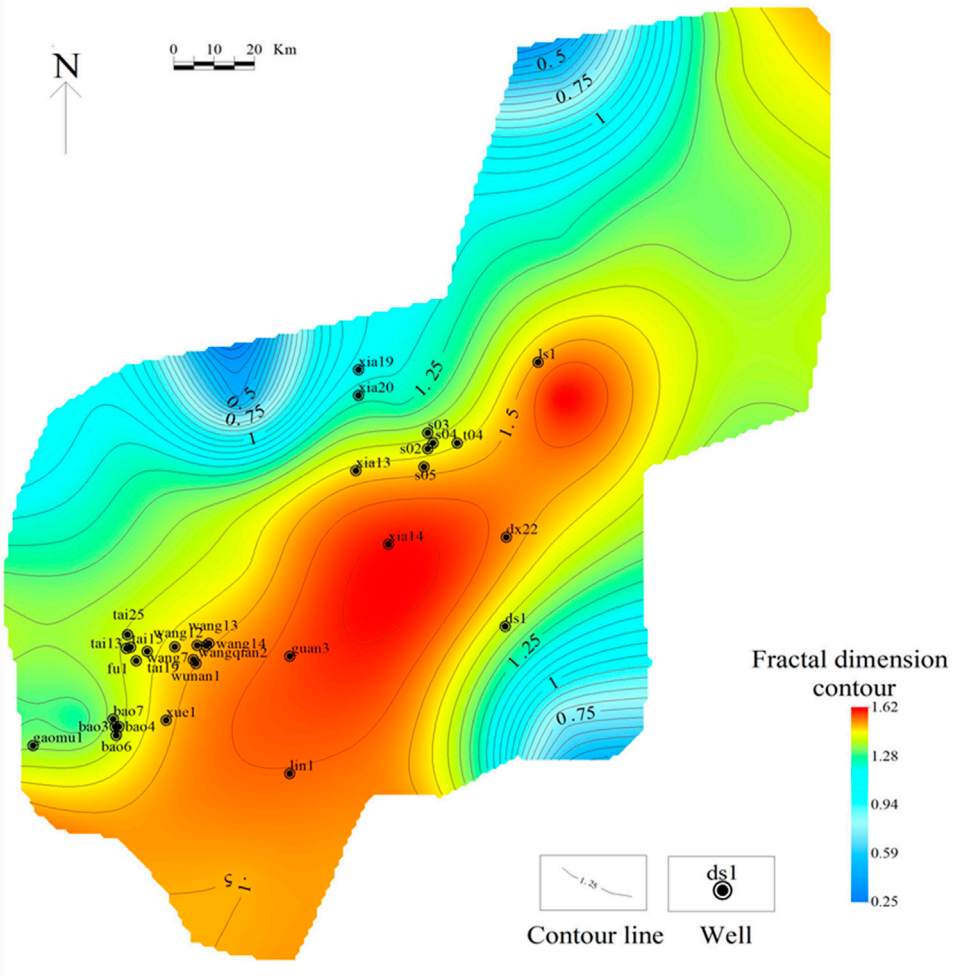

FIGURE 5 | Contour map of fractal dimensions of faults in Maokou Formation in southeast Sichuan (q = 0)

The calculated fractal dimensions corresponding to different q values were assigned to the center point of each grid, and contour maps of the fractal dimensions of faults in the Maokou Formation in southeast Sichuan were obtained by planar interpolation (**Figures 5–7**). Contour maps have the following characteristics. 1) The contour lines of the fractal dimensions generally trend NE–SW. 2) The planar distribution of the fractal dimensions of the faults in the study area shows zonal characteristics, and three regions can be identified. The high-value region lies along with wells, "ls1–xia14–guan3," whereas the low-value regions are distributed to the northwest and southeast of the high-value region. 3) Overall, the fractal dimension increased gradually with increasing q; however, the distribution range of the high- and low-value regions varied slightly.

DISCUSSION

Comparison With a Conventional Method

In conventional multifractal studies of fault structures, faults are typically counted manually, which is time-consuming, labor-intensive, and inefficient. As the grid-side length decreases, the number of grids increases, and the counting workload increases exponentially. If the faults in a grid are incorrectly counted, the final calculation result will be inaccurate, thereby reducing the reliability of the research. For oil and gas exploration in the big data era, manual counting is not suitable for processing the vast amounts of data used in the multifractal analysis of faults. In this study, we applied image recognition–based multifractal analysis to identify fault structures. We divided the grayscale and binarized fault distribution maps into numbered grids. Next, the faults in each grid were automatically counted using computer image recognition. A comparison of the conventional and image recognition–based methods showed that for a single researcher working 10 h per day, counting would take five days, whereas the proposed method shortened the entire counting time to 5 h and increased the efficiency by a factor of 10, thus solving the problems of low efficiency of manual counting. Moreover, automatic counting increases the accuracy of fault identification; therefore, the results are more

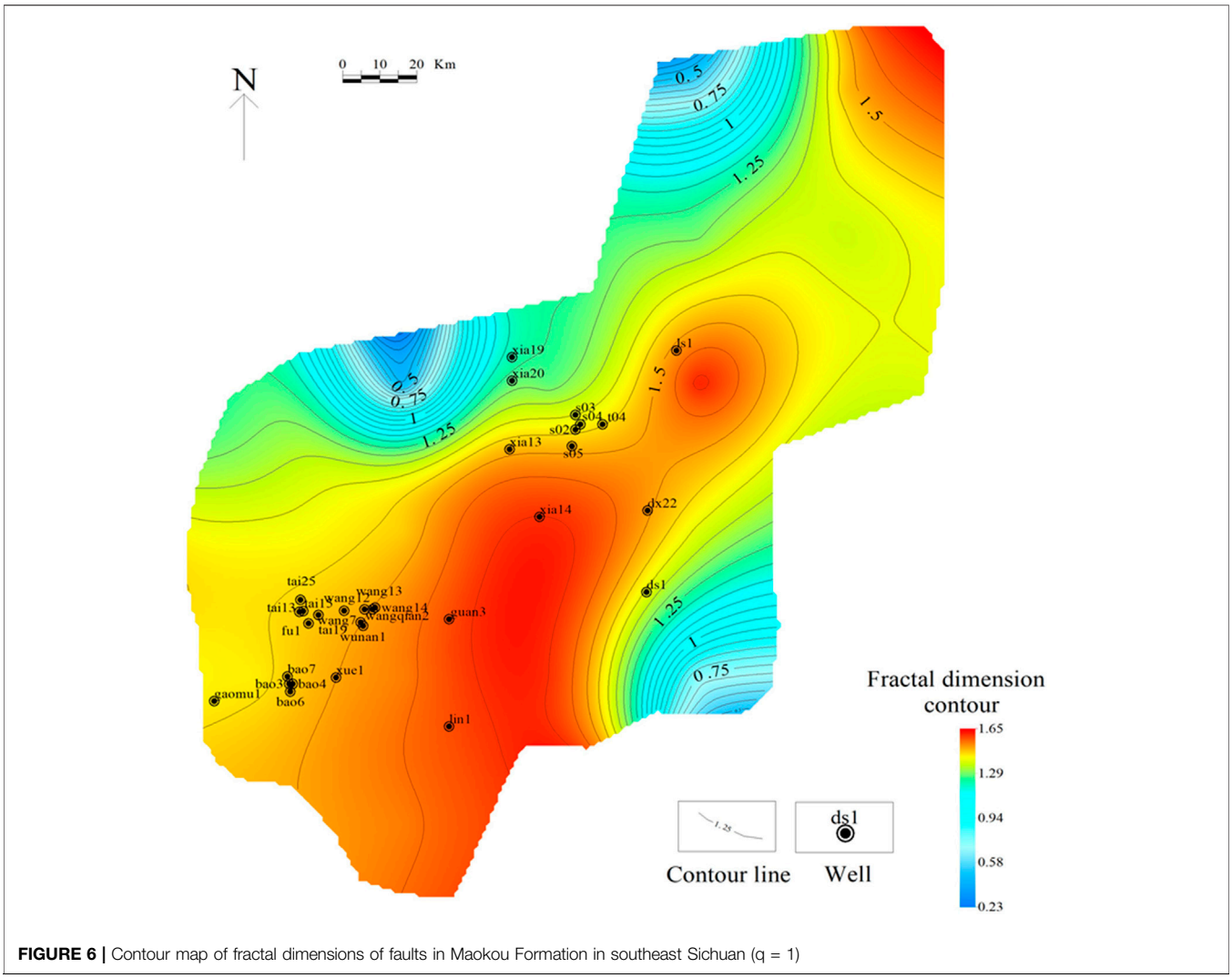

FIGURE 6 | Contour map of fractal dimensions of faults in Maokou Formation in southeast Sichuan (q = 1)

reliable. In some cases, the two faults were completely adjacent to each other on the plane map. This method, based on image recognition, cannot effectively distinguish between these two faults, and it is judged as the same fault. To reduce the influence of this situation on the recognition accuracy, the relative positions of the two faults can be manually adjusted to separate them when drawing the fault distribution map in the early stage, which lays a solid foundation for subsequent image recognition. Although it takes a certain amount of time to manually adjust the relative positions of the two faults, the number of faults adjacent to the plane is generally not too large. Therefore, compared with that of the traditional manual counting method, the efficiency of multifractal research based on image recognition faults was significantly improved.

Diversity of Fractal Dimensions of Faults With Different Orientations

We analyzed the relationship between q and the fractal dimensions D_q of all faults in the Maokou Formation in southeast Sichuan and faults with different orientations (**Figure 8**). Overall, the fractal dimension increased gradually with increasing q. The variation trend of the fractal dimension of the NW-trending faults was almost the same as that of all faults in the region. The fractal dimension of all faults in the region ranged between 0.9964 and 1.7317, with an extreme difference of 0.7353 and a mean value of 1.3612. The NW-trending faults range between 0.8848 and 1.4196, with an extreme difference of 0.869 and a mean value of 1.28974. The NE-trending faults range between 0.9804 and 1.3497, with an extreme difference of 0.3693 and a mean value of 1.16418. The EW-trending faults range between 0.7074 and 0.9121, with an extreme difference of 0.2047 and a mean value of 0.82624. The NW-trending faults have the highest fractal dimensions, and the extreme difference and mean values are closest to those of the fractal dimension of all faults in the region. These results indicate that the NW-trending faults are more complex and active than the NE- and EW-trending faults, with the NW-trending faults being the dominant faults in southeast

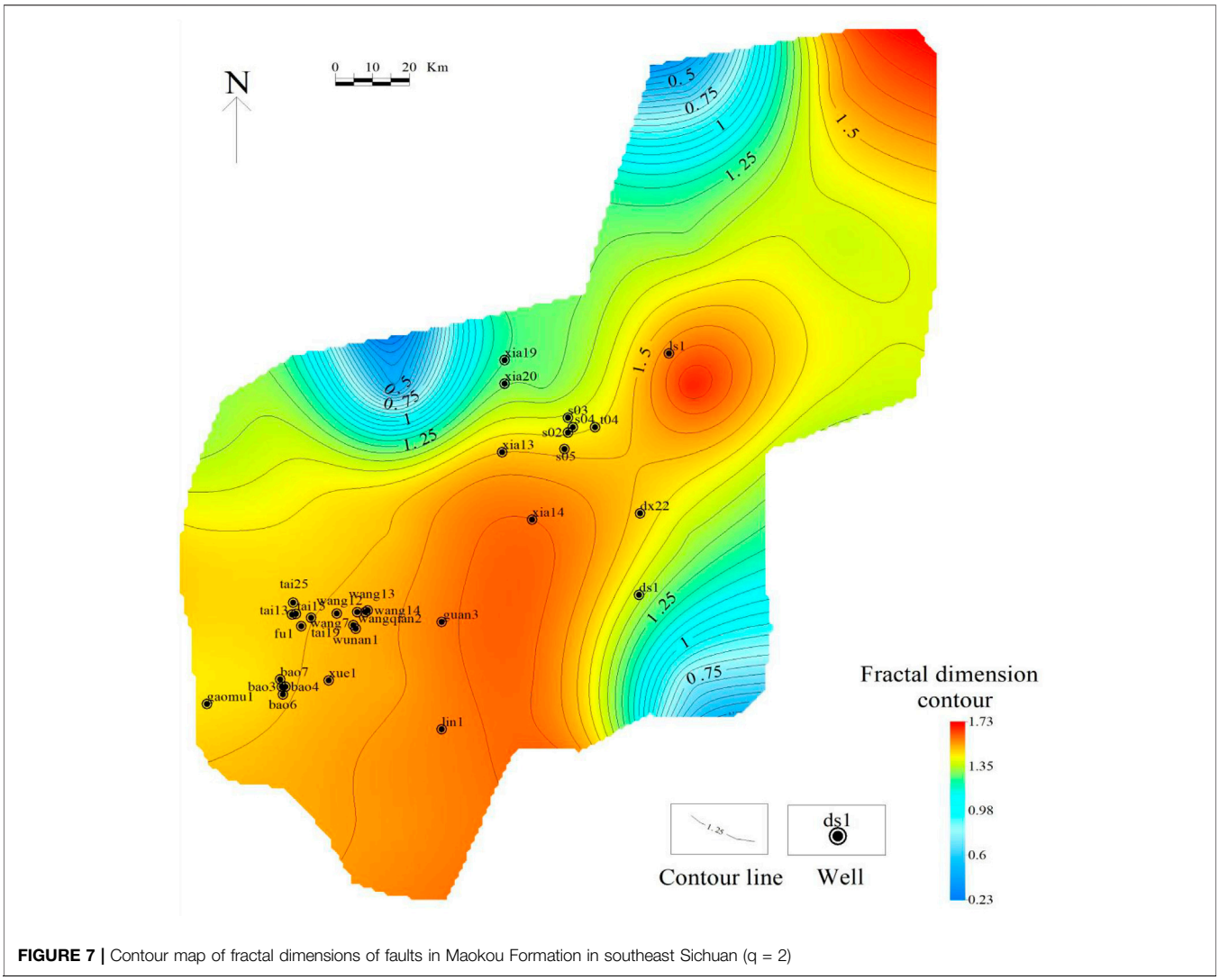

FIGURE 7 | Contour map of fractal dimensions of faults in Maokou Formation in southeast Sichuan (q = 2)

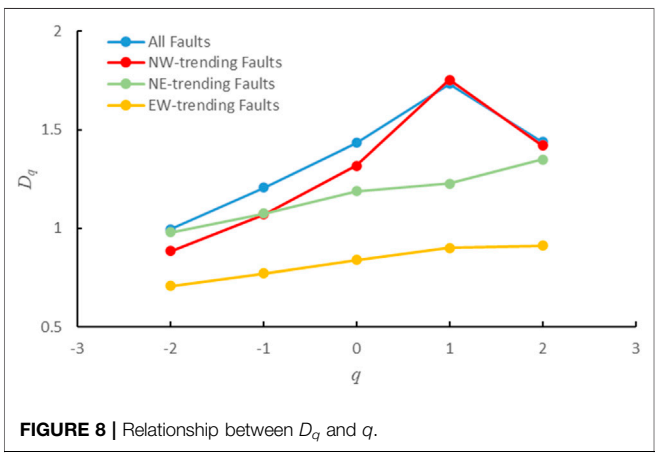

FIGURE 8 | Relationship between D_q and q.

Sichuan. The differences in the variation trends of the fractal dimensions of faults with different orientations reflect the different mechanisms of fault genesis in the study area.

Relationships Between Fractal Dimensions and Tectonic Stages and Geodynamics

Southeast Sichuan is in the Tethys-Himalayan and marginal-Pacific tectonic domains. Its tectonic framework is controlled by both the Xuefeng intracontinental tectonic system to the east and the Tibetan Plateau to the southwest and exhibits the characteristics of multistage tectonic superposition (Lv, 2005; Zhao, 2005; Deng et al., 2013; Tang et al., 2021). The geodynamics of the tectonic stages in southeast Sichuan have been extensively analyzed, and the accepted view has shifted from one-stage to multistage tectonic superposition. However, there is still disagreement regarding whether the tectonic setting was shaped in two, three, or four stages (Guo et al., 2016; Jia, 2016; Zeng et al., 2022b; Wang et al., 2022). In addition, there are three main types of *in-situ* stresses in southeast Sichuan, each with different magnitudes in different geological periods. Based on previous studies of tectonic stages in southeast Sichuan, we investigated the relationship between the fractal dimensions of faults and tectonic stages. We suggest that the magnitude of the fractal dimensions of faults with different orientations and the planar distribution of fractal

TABLE 1 | Fractal dimensions of faults and well test results.

Well	Fractal dimension of faults	Test production (gas 10^4 m^3/d)	Test production (water m^3/d)
xia14	1.606	Micro-gas layer	
guan3	1.5657	0.176	
dx22	1.5258	16.4	
ls1	1.5061	20.6	
wunan1	1.4993	0.03	
wang14	1.4949	100	
wang13	1.4943	0.005	
wangqian2	1.4941	1	
wang7	1.4863	Water layer	133
xue1	1.4854	Water layer	No data were collected
s05	1.4791	Gas layer (log interpretation)	
wang12	1.466	0.05	
tai19	1.4358	0.005	
fu1	1.4233	Dry layer	
tai15	1.4129	Water layer	2.66
tai13	1.4078	0.008	
tai25	1.4046	0.1	
bao4	1.3882	0.015	
bao3	1.3789	0.1	
bao7	1.3687	Trace amount of gas	
gaomu1	1.3416	2.95	
xia19	1.1734	Dry layer	

dimension contours reflect the tectonic stages and *in-situ* stress magnitudes in the study area. We believe that the tectonic setting of southeast Sichuan formed primarily during the Indosinian, Yanshanian, and Himalayan periods.

Tectonic movements in southeast Sichuan were not complex during the Caledonian-Hercynian primarily tensile environment, which is characterized by lifting movement. Since the Indosinian period, the extensional regime of the Caledonian-Hercynian has gradually transitioned to a NW–SE compressional environment. This regime affected the formation of the tectonic setting of southeast Sichuan (Tan et al., 2013; Tang et al., 2021; Zeng et al., 2022a) and caused NE-trending faults to appear. Since the Early Yanshanian, compressional stress from SE to NW within the Xuefeng tectonic system has been transmitted to southeast Sichuan. However, the thrust faulting effect gradually weakened with increasing distance, and the SE–NW compression was blocked and deflected to some extent (Tang et al., 2021), resulting in a compression–torsion effect in the study area. NE-trending faults continued to develop, and their fractal dimensions are generally large. In addition, the tectonic settings of the central and southern parts of southeast Sichuan differ because the kinematic mechanisms differ. The central part of southeast Sichuan experienced primarily progressive compressional stress, and the high-steep structural belt showed a NW-trending en-echelon pattern. The southern part was dominated by compressional–torsional stress, which resulted in a broom-shaped rotational structure. Therefore, the fault system in the southern Sichuan region became highly developed under compressional–torsional stress. There were more faults, and the southern part of the contour map showed a wider region with high fractal dimensions (**Figure 5**).

From the Late Yanshanian to the Early Himalayan, the southward thrust of the Qinling orogenic belt was transmitted to southeast Sichuan and blocked by the inherited Luzhou paleo-uplift. In addition, the EW-trending Lushan fault zone was compressed northward, forming near-EW-trending structures in southeast Sichuan (Zhou et al., 2016b; Hu, 2018). During this period, the impact of the tectonic activity was relatively weak. The scale of the EW-trending structural faults is small; thus, their fractal dimensions are low.

From the Late Himalayan period to the present, the East Sichuan arc- and broom-shaped structural belts acquired their current shapes. Under the continuous effect of the collision between the Indian and Eurasian plates, the deformation of the Daliangshan structural belt gradually became more intense and expanded into the basin, forming a NE–SW compressional regime that resulted in the development of NW-trending faults in the study area. This stress regime has persisted to date (Li et al., 2014; Tang et al., 2018). During this period, intense NE–SW-trending forces were superimposed on pre-existing tectonic features, forming NW-trending faults. This set of faults has the highest fractal dimensions, indicating that they were under the greatest tectonic stress. This indicates that the Himalayan period had the strongest influence on the current tectonic setting of southeast Sichuan. After the tectonic stresses in the Indosinian, Yanshanian, and Himalayan periods, a composite pattern consisting of NE-trending, NW-trending, and near-EW-trending structures was formed.

Relationship Between Fractal Dimensions and Hydrocarbon Accumulation

Fractal dimensions of the faults indicate the strength of tectonic movements and the patterns of superposition and neogenesis during fault development in the hydrocarbon basin during

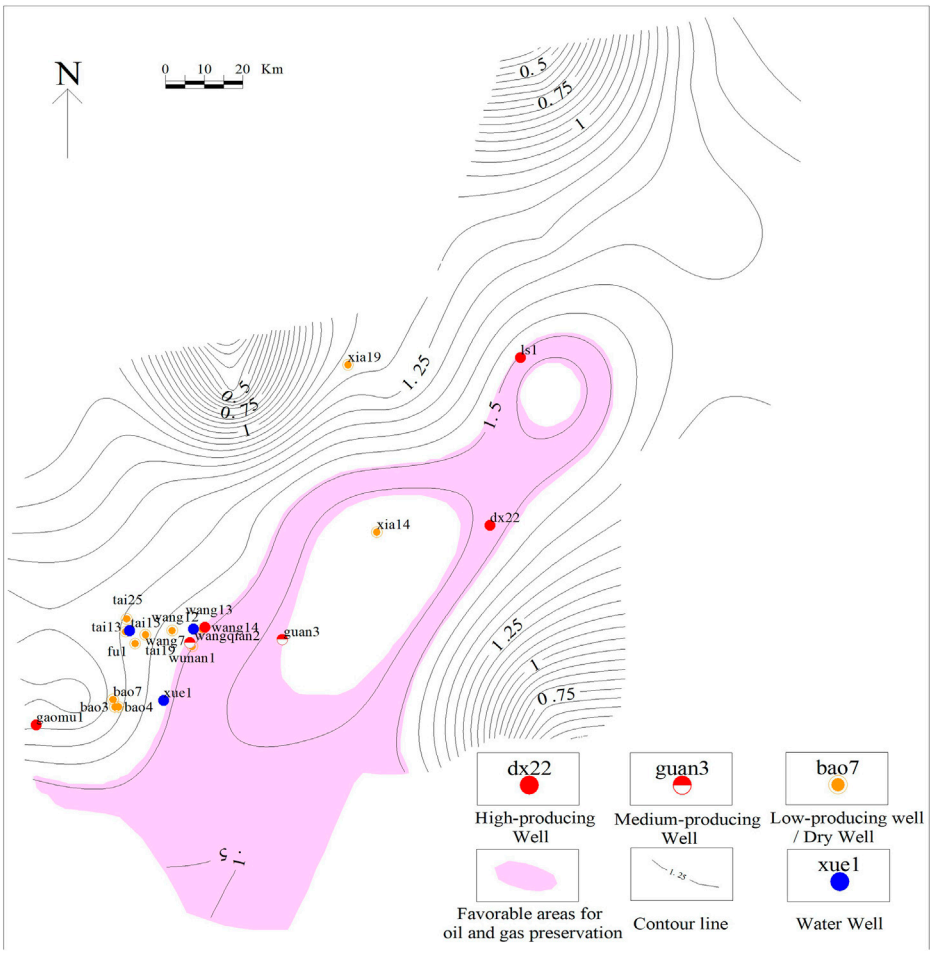

FIGURE 9 | Relatively favorable areas for oil and gas preservation in southeast Sichuan (labeled with fractal dimensions of faults).

different periods. In addition, faults significantly affect hydrocarbon accumulation. Therefore, the fractal dimensions of faults may be related to oil and gas distributions, and thus can serve as an essential parameter for predicting and evaluating hydrocarbon distribution and accumulation patterns. The lateral variation in the fractal dimensions of faults in the study area reflects the spatiotemporal heterogeneity of fault development processes, as well as differences in the geometry of the fault systems. These differences in tectonic evolution directly affect the area of the hydrocarbon-bearing zones and the production of fluid (Zhou et al., 1997). It is generally believed that the fractal dimension comprehensively reflects the scale, distribution density, spatial pattern, and formation mechanism of faults. We defined the wells with test gas production of more than 1×10^4 m^3/d in the Maokou Formation in southeast Sichuan as high-producing wells, those with test gas production of $(0.1–1) \times 10^4$ m^3/d as medium-producing wells, and those with production less than or equal to 0.1×10^4 m^3/d as low-producing wells. The relationship between the fractal dimensions and oil and gas production during well testing in southeast Sichuan was explored using the capacity dimension ($q = 0$) as an example (**Table 1**). Generally, faults are densely distributed in areas containing faults with high fractal dimensions, and their tectonic structures are complex. These faults serve as favorable channels for upward fluid migration. Most of the wells in the relatively high-value region (with fractal dimensions of 1.49–1.57) were medium- to high-producing wells. For example, the test gas production of wells "ls1" and "dx22" are 20.6×10^4 and 16.4×10^4 m^3/d, respectively; the test production of well "wang14" is as high as 100×10^4 m^3/d, with a good showing of oil and gas. However, faults generated by excessively intense tectonic movements can destroy the hydrocarbon preservation environment and cause the escape or migration of oil and gas. For instance, the fractal dimension of well "xia14" in the core of the high-value area is 1.606, but the presence of oil and gas is poor, appearing as a micro-gas layer in gas testing. The level of fault development is generally low in fault regions with low fractal dimensions. There are too few channels for fluid movement, which is not conducive to the migration and accumulation of oil and gas. For example, the well

test results of wells "bao3" and "tai15" in the low-value area reveal gas production of 0.1×10^4 m^3/d and a water layer, respectively. In summary, oil and gas reservoirs are expected to appear in relatively mild tectonic environments with low structural relief, facilitating oil and gas migration and ensuring that the faults do not destroy the caprock. Thus, the fractal dimensions of faults in a favorable area should be neither too high nor too low. Considering these factors, we selected two contours with fractal dimensions of 1.49 and 1.57 as boundary lines to divide the study area into three zones. The zone lying roughly along the wells "ls1–xia14–guan3" (with fractal dimensions of 1.49–1.57) is considered relatively favorable for oil and gas perservation in the Maokou Formation in southeast Sichuan (**Figure 9**).

CONCLUSION

We analyzed the multifractal characteristics of faults in the Maokou Formation in southeast Sichuan by applying an image recognition–based multifractal calculation method to identify fault structures. The conclusions and insights obtained are as follows:

1. In contrast to the conventional approach, the proposed method uses automatic fault counting with image recognition technology. Consequently, the data processing time and research and labor costs are greatly reduced, and the efficiency is as much as 10 times higher. Moreover, the accuracy of fault counting can be significantly improved, making the results more reliable.
2. The fractal dimensions of faults with different orientations and the planar distribution pattern of fractal dimension contours indicate tectonic stages and stress magnitudes in the study area. The tectonic setting of southeast Sichuan was formed primarily during the Indosinian, Yanshanian, and Himalayan periods. From the Indosinian to the early Yanshanian, NE-trending faults with relatively large fractal dimensions developed under NW–SE compressional tectonic stress. From the Late Yanshanian to the Early Himalayan, EW-trending faults with low fractal dimensions were formed by relatively weak N–S compressional stress. The NW-trending faults formed by intense NE–SW compressional tectonic stress in the Late Himalayan are the dominant faults of the Maokou Formation in southeast Sichuan and have the largest fractal dimensions.
3. Oil and gas reservoirs are expected to appear in relatively mild tectonic environments with low structural relief, which facilitates oil and gas migration and ensures that the faults do not destroy the caprock. Thus, the fractal dimensions of faults in favorable areas should be neither too high nor too low. According to the relationship between the fractal dimensions of faults and the well test results in southeast Sichuan, the region along the wells "ls1–xia14–guan3" (with fractal dimensions of 1.49–1.57) in the study area is recognized as relatively favorable for oil and gas preservation in the Maokou Formation.

DATA AVAILABILITY STATEMENT

The raw data supporting the conclusion of this article will be made available by the authors, without undue reservation.

AUTHOR CONTRIBUTIONS

XH and HL contributed to the conception and design of the study. XH and XT wrote the first draft of this manuscript. ZN and CY conducted the investigations and data collation. JeL and JiL reviewed and edited the manuscript. All authors contributed to the revision of the manuscript and read and approved the version submitted.

FUNDING

This study was supported financially by the National Natural Science Foundation of China (Grant No. 42172175).

ACKNOWLEDGMENTS

We would like to thank the Sinopec Exploration Company for providing the data and allowing the publication of this article.

REFERENCES

Agterberg, F. P. (2012). Multifractals and Geostatistics. *J. Geochem. Explor.* 122, 113–122. doi:10.1016/j.gexplo.2012.04.001

Boulassel, A., Zaourar, N., Gaci, S., and Boudella, A. (2021). A New Multifractal Analysis-Based for Identifying the Reservoir Fluid Nature. *J. Appl. Geophys.* 185. doi:10.1016/j.jappgeo.2020.104185

Bradski, G., and Kaehler, A. (2008). *Learning OpenCV: Computer Vision with the OpenCV Library*. M.Sebastopol:" O'Reilly Media, Inc.

Budennyy, S., Pachezhertsev, A., Bukharev, A., Erofeev, A., Mitrushkin, D., and Belozerov, B. (2017). *Image Processing and Machine Learning Approaches for Petrographic Thin Section analysisSPE Russian Petroleum Technology Conference Richardson*. Society of Petroleum Engineers. doi:10.2118/187885-MS

Deng, B., Liu, S. G., Wang, G. Z., Li, Z. W., Liu, S., and Cao, J. X. (2013). Cenozoic Uplift and Exhumation in Southern Sichuan Basin - Evidence from Low-Temperature Thermochronology. *Chin. J. Geophys.* 56, 1958–1973.doi:10.6038/cjg20130618

Flores-Márquez, E. L., Ramírez-Rojas, A., and Telesca, L. (2015). Multifractal Detrended Fluctuation Analysis of Earthquake Magnitude Series of Mexican South Pacific Region. *Appl. Math. Comput.* 265, 1106–1114.

Gao, H. X. (2004). *Research and Application of Multifractal Algorithm D*. Chengdu: Chengdu University of Technology.

Gong, L., Fu, X., Wang, Z., Gao, S., Jabbari, H., Yue, W., et al. (2019). A New Approach for Characterization and Prediction of Natural Fracture Occurrence in Tight Oil Sandstones with Intense Anisotropy. *Bulletin* 103 (6), 1383–1400. doi:10.1306/12131818054

Gong, L., Gao, S., Liu, B., Yang, J. G., Fu, X. F., Xiao, F., et al. (2021). Quantitative Prediction of Natural Fractures in Shale Oil Reservoirs. *Geofluids* 2021. Article ID 5571855, 15 pages. doi:10.1155/2021/5571855

Guo, W. X., Liang, X., and Wei, L. M. (2016). Structure Deformation of Southeast Sichuan and its Influences on Preservation of Shale Gas. *Coal Geol. Explor.* 44, 21–26. doi:10.3969/j.issn.1001-1986.2016.06.004

Cheng, G. X., Jiang, B., Li, M., Li, F. L., and Xu, S. C. (2020). Quantitative Characterization of Fracture Structure in Coal Based on Image Processing and Multifractal Theory. *International Journal of Coal Geology* 228.

Hu, J. M. (2018). *Research of Structural Characteristics and Genetic Mechanism of the Changyuanba Structural Belt in Southern Sichuan D*. Chengdu: Chengdu University of Technology 38, 538–551. Available at: https://kns.cnki.net/kcms/detail/detail.aspx?FileName=1018264988.nhandDbName=CMFD2019.

Hu, X. Q., Shi, Z. J., Tian, Y. M., Wang, C. C., and Cao, J. F. (2014). Multifractal Feature and Significance of Maokou Formation Faults in the Southeast of Sichuan. *J. Chengdu Univ. Technol. Sci. Technol. Ed.* 41, 476–482. doi:10.3969/j.issn.1671-9727.2015.04.10

Izadi, H., Sadri, J., and Mehran, N.-A. (2015). A New Intelligent Method for Minerals Segmentation in Thin Sections Based on a Novel Incremental Color Clustering. *Comput. Geosciences* 81, 38–52. doi:10.1016/j.cageo.2015.04.008

Jia, X. L. (2016). *Structural Geometry and Kinematics of Southeast Sichuan Basin: Insights into Tectonic Relationship with the Western Segment of Xue Feng Mountain Orogenic Belt D*. (Beijing: China University of Geosciences.

Kasyanova, N. A. (2018). The Role of Young Fracturing in the Formation and Spatial Distribution of Hydrocarbon Deposits in the North-Western Caspian Sea. *Oij* 5, 36–39. doi:10.24887/0028-2448-2018-5-36-39

Kuang, L., Liu, H., Ren, Y., Luo, K., Shi, M., Su, J., et al. (2021). Application and Development Trend of Artificial Intelligence in Petroleum Exploration and Development. *Petroleum Explor. Dev.* 48, 1–14. doi:10.1016/s1876-3804(21)60001-0

Li, J. Y., Zhang, J., and Liu, J. F. (2014). Major Deformation Systems in the Mainland of China. *Earth Sci. Front.* 21, 226–245.doi:10.13745/j.esf.2014.03.025

Lv, B. F. (2005). The Tectonization and Petroleum Accumulation in Southeast Sichuan Basin D. *Guangzhou Institute of Geoehemistry Chinese Aeademy of Sciences* 41, 338–415. Available at: https://kns.cnki.net/kcms/detail/detail.aspx?FileName=2005128952.nhandDbName=CDFD2005.

Ma, W. L., Li, Z. P., and Lu, T. (2018). Application of Machine Vision in Oil & Gas Exploration and Exploitation: A Review. *Sci. Technol. Eng.* 18, 112–119. Available at: https://kns.cnki.net/kcms/detail/detail.aspx?FileName=TZCZ201902003andDbName=CJFQ2019.

Mandelbrot, B. B., and Wheeler, J. A. (1983). The Fractal Geometry of Nature. *Am. J. Phys.* 51, 286–287. doi:10.1119/1.13295

Nagy, A., and Tóth, M. T. (2012). Petrology and Tectonic Evolution of the Kiskunhalas-NE Fractured Hydrocarbon Reservoir, South Hungary. *Cent. Eur. Geol.* 55. doi:10.1556/ceugeol.55.2012.1.1

Patel, A. K., and Chatterjee, S. (2016). Computer Vision-Based Limestone Rock-type Classification Using Probabilistic Neural Network. *Geosci. Front.* 7, 53–60. doi:10.1016/j.gsf.2014.10.005

Salat, H., Murcio, R., and Arcaute, E. (2017). Multifractal Methodology. *Phys. A Stat. Mech. its Appl.* 473, 467–487. doi:10.1016/j.physa.2017.01.041

Semukhin, M. V., Yadryshnikova, O. A., Yadryshnikova, O. A., Serkin, M. F., and Chertina, K. N. (2017). Development of a Fracture Recognition System to Read off Experimental Data from Petrographic Thin Section Images. *OIJ* 05, 27–31. doi:10.24887/0028-2448-2017-5-27-31

Tan, Z. P., Liu, S. G., Deng, B., Li, Z. W., and Sun, W. (2013). Multiphase Structural Features and Evolution of the Southeast Sichuan Tectonic Belt in China [J]. *Chengdu Univ. Technol. (Sci. Technol. Ed.)* 40 (6), 703–711.doi:10.3969/j.issn.1671-9727.2013.06.10

Tan, K. X., and Xie, Y. S. (2010). Multifractal Mechanism of Faults Control Hydrothermal Deposits in Altay, Xinjiang, China [J]. *Geotectonica et Metallogenia* 34 (1), 32–39.doi:10.16539/j.ddgzyckx.2010.01.013

Tang, J. G., Wang, K. M., and Qin, D. C. (2021). Tectonic Deformation and its Constraints to Shale Gas Accumulation in Nanchuan Area, Southeastern Sichuan Basin. *Bull. Geol. Sci. Technol.* 40, 11–21.doi:10.19509/j.cnki.dzkq.2021.0502

Tang, Y., Zhou, L. F., Chen, K. Q., Dong, X. X., and Tang, W. J. (2018). Analysis of Tectonic Stress Field of Southeastern Sichuan and Formation Mechanism of Tectonic Deformation, *Scholarly J* 64, 15–28. doi:10.16509/j.georeview.2018.01.002

Thompson, S., Fueten, F., and Bockus, D. (2001). Mineral Identification Using Artificial Neural Networks and the Rotating Polarizer Stage. *Comput. Geosciences* 27, 1081–1089. doi:10.1016/s0098-3004(00)00153-9

Tyurin, E., and Kusov, A. (2016). *Quantitative Characterization of River Depositional System Employing Detailed Automated Dip Picking Based on Optimized Ridge filteringSPE Russian Petroleum Technology Conference*. Richardson: Society of Petroleum Engineers.

Wang, P. W., Zhang, D. W., Liu, Z. B., Chen, X., Li, P., and Cai, B. (2022). Shale Gas Enrichment Conditions and Primary Controllers of Upper Permian Longtan Transitional Shale in Southeast Sichuan to Northwest Guizhou. *Nat. Gas. Geosci.* 33, 431–440. doi:10.11764/j.issn.1672-1926.2021.10.005

Wang, Z. F. (2021). Understandings of Maokou Formation-Qixia Formation Gas Reservoirs in Nanchuan Area. *Coal Technol.*, 43–45. doi:10.13301/j.cnki.ct.2021.01.012

Wei, J. (2019). Design of Graphics Recognition System Based on OpenCV. *J.Electronic Technol. Softw. Eng.* (21), 60–62. Available at: https://kns.cnki.net/kcms/detail/detail.aspx?FileName=DZRU201921037andDbName=CJFQ2019.

Woods, E. P. (1992). Vulcan Sub-basin Fault Styles - Implications for Hydrocarbon Migration and Entrapment. *APPEA J.* 32 (Papers). doi:10.1071/aj91012

Xie, Y. S., and Tan, K. X. (2002). Fractal Research on Fracture Structures and Application in Geology. *Geol. Geochem.*, 71–77. Available at: https://kns.cnki.net/kcms/detail/detail.aspx?FileName=DZDQ200201011andDbName=CJFQ2002.

Xiong, G., Yu, W., Xia, W., and Zhang, S. (2016). Multifractal Signal Reconstruction Based on Singularity Power Spectrum. *Chaos, Solit. Fractals* 91, 25–32. doi:10.1016/j.chaos.2016.04.021

Xu, Z. X. (2019). Genesis and Source of Gas in Middle Permian Maokou Formation of Eastern Sichuan Basin. *Spec. Oil Gas. Reserv.* 16–22. doi:10.3969/j.issn.1006-6535.2019.02.003

Zeng, L. B., Gong, L., Guan, C., Zhang, B. J., Wang, Q. Q., Zeng, Q., et al. (2022). Natural Fractures and Their Contribution to Tight Gas Conglomerate Reservoirs: A Case Study in the Northwestern Sichuan Basin, China [J]. *J. Petroleum Sci. Eng.* 210. 110028. doi:10.1016/j.petrol.2021.110028

Zeng, Y., Hou, Y. G., Hu, D. F., Hu, S., Liu, R. B., Dong, T., et al. (2022). Characteristics of Shale Fracture Veins and Paleopressure Evolution in Normal Pressure Shale Gas Zone, Southeast Margin of Sichuan Basin. *Earth Sci.*, 1–16. doi:10.3799/dqkx.2022.011

Zhao, Z. W. (2005). *The Regional Tectonic Characteristic of Southeast Sichuan Basin and its Control to Oil and Gas Reservoir*. Beijing: China University of Geosciences.

Zhong, Y., Yang, Y. M., Wen, L., Luo, B., Xiao, D., Li, M. L., et al. (2021). Reconstruction and Petroleum Geological Significance of Lithofacies Paleogeography and Paleokarst Geomorphology of the Middle Permian Maokou Formation in Northwestern Sichuan Basin, SW China. *Pet. explor. Dev.* 48, 95–109. doi:10.1016/s1876-3804(21)60007-1

Zhou, L. F., Chen, K. Q., Tang, Y., and Tang, J. G. (2016a). Tectonic Deformation in Qijiang-Chishui Area of South Sichuan since Late Yanshanian. *J. Geol.*, 66–73. Available at: https://kns.cnki.net/kcms/detail/detail.aspx?FileName=DZKQ201604011andDbName=CJFQ2016

Zhou, Q., Wang, J., and Wang, L. L. (2016b). Android Simple Graphics Recognition Based on OpenCV Contour Approximation. *Fujian Comput.* 32, 122–123.doi:10.16707/j.cnki.fjpc.2016.02.064

Zhou, X. G., Sun, B. S., and Liu, J. H. (1997). Fractal Characteristics of Fault Systems and its Relation to Oil-Gas Traps in Kerkang Oil Field of Liaohe Basin. *J. Geomech.*, 83–89. Available at: https://kns.cnki.net/kcms/detail/detail.aspx?FileName=DZLX701.010andDbName=CJFQ1997

Conflict of Interest: The authors declare that the research was conducted in the absence of any commercial or financial relationships that could be construed as a potential conflict of interest.

Publisher's Note: All claims expressed in this article are solely those of the authors and do not necessarily represent those of their affiliated organizations, or those of the publisher, the editors and the reviewers. Any product that may be evaluated in this article, or claim that may be made by its manufacturer, is not guaranteed or endorsed by the publisher.

frontiers | Frontiers in Earth Science

ORIGINAL RESEARCH
published: 17 June 2022
doi: 10.3389/feart.2022.950626

The Discovery and Geochemical Characteristics of an Eocene Peridotite Xenolith-Bearing Mafic Volcanic Neck in Coastal Southeast China

Chuanshun Li[1], Xilin Zhao[2,3,4], Yang Jiang[2], Guangfu Xing[2], Minggang Yu[2] and Zheng Duan[2]*

[1]First Institute of Oceanography, Ministry of Natural and Resources, Qingdao, China, [2]Nanjing Center, China Geological Survey, Nanjing, China, [3]Research Center for Petrogenesis and Mineralization of Granitoid Rocks, China Geological Survey, Wuhan, China, [4]School of Resources and Environmental Engineering, Hefei University of Technology, Hefei, China

The mantle beneath coastal SE China evolved from enriched to depleted between the Cretaceous and the Neogene, although the precise timing of this change remains unclear. Here, we focus on a newly discovered Eocene mafic volcanic neck that contains peridotite xenoliths in the Fuding area of Fujian Province, and present new whole-rock Ar–Ar data which indicate that flood basalts formed during the Eocene (ages of 38.5 ± 1.2 and 42.3 ± 2 Ma). The basalt, gabbro, and diabase in the Fuding area are geochemically similar to ocean island basalt (OIB) and have Sr_I values that range from 0.703794 to 0.703911 (average of 0.703865) and εNd(t) values from 3.05 to 4.56 (average of 3.90). These samples yield two-stage Nd model (T_{DM2}) ages of 0.61–0.73 Ga (average of 0.67 Ga). These data indicate that all of these units formed from magmas derived from an OIB-type mantle source, with both the gabbro and diabase units recording minor amounts of crustal contamination. Its OIB type geochemical characteristics may be inherited from crustal materials with similar characteristics. Peridotite xenoliths within the Fuding basalts provide evidence of the nature of the Eocene mantle in this area, especially the post late-Mesozoic evolution of the mantle beneath coastal SE China. The mantle beneath coastal SE China evolved from enriched in the Cretaceous to depleted in the Neogene, with this change occurring during the Eocene.

Keywords: coastal SE China, eocene, mafic volcanic neck, peridotite xenolith, whole-rock Ar-Ar

OPEN ACCESS

Edited by:
Fuhao Xiong,
Chengdu University of Technology, China

Reviewed by:
Chenyue Liang,
Jilin University, China
Weimin Li,
Jilin University, China

****Correspondence:***
Xilin Zhao
zxl24@126.com

Specialty section:
This article was submitted to Petrology, a section of the journal Frontiers in Earth Science

Received: *23 May 2022*
Accepted: *31 May 2022*
Published: *17 June 2022*

Citation:
Li C, Zhao X, Jiang Y, Xing G, Yu M and Duan Z (2022) The Discovery and Geochemical Characteristics of an Eocene Peridotite Xenolith-Bearing Mafic Volcanic Neck in Coastal Southeast China. Front. Earth Sci. 10:950626. doi: 10.3389/feart.2022.950626

1 INTRODUCTION

Continental lithosphere is an important component of the Earth, and peridotite xenoliths captured by rapidly ascending basaltic magmas produced in some tectonic environments can provide direct samples of the upper mantle or lower crust of continental lithosphere. Such xenoliths also provide evidence of the nature and evolution of the mantle, the composition of the mantle, and the tectonic setting of the basaltic magmatism that captured the xenoliths. There are two main models for the petrogenesis of peridotite xenoliths: 1) they represent the refractory residue of the upper mantle after partial melting that generated basaltic magmas (Wang and Yang, 1987a; Wang and Yang., 1987b; Deng et al., 1988; Cong et al., 1996; Yan et al., 2007), or 2) they represent rock fragments of the upper mantle that were captured by ascending basaltic magma as accidental enclaves, meaning they played no direct role in the formation of the basaltic magmas (Tatsumoto et al., 1992; C. ; Liu et al., 1995; T. ; Li and Ma, 2002).

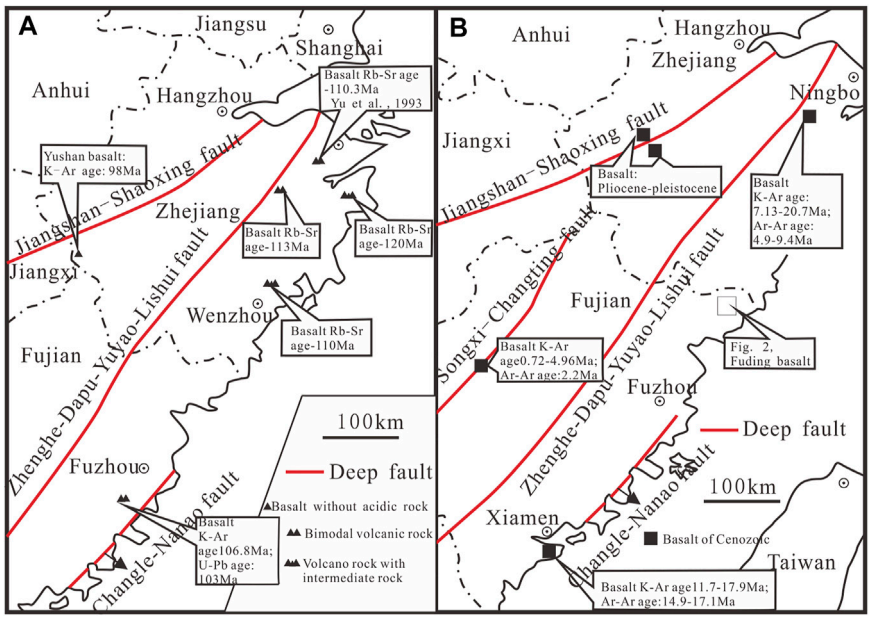

FIGURE 1 | Temporal and spatial distribution of late Mesozoic–Cenozoic basalts in SE China (revised after Xu and Xie, 2005). **(A)** Temporal and spatial distribution of late Mesozoic basalts in SE China; **(B)** Temporal and spatial distribution of Cenozoic basalts in SE China.

Southeastern China has a complex geological history that includes late Mesozoic to Cenozoic lithospheric thinning and extensive basaltic magmatism. This magmatism peaked in coastal SE China after the late Mesozoic and has been the focus of many studies (Cui et al., 2011; C. ; Liu et al., 1995; Tang et al., 2010; G. ; Xie et al., 2005; Xing et al., 1999; J. ; Yan et al., 2005a; Zhou et al., 2006), including a large body of research devoted to the nature of the mantle during this magmatism (D. Chen et al., 1997; C. Chen et al., 2008; C. Dong C. W. et al., 2006; C. Dong Y. X. et al., 2006; He and Xu, 2011; Li, 2000; Z. Li and Li, 2007; X. Li et al., 2007; J. Liu and Yan, 2007; Shen et al., 1999; D. Y. Wang et al., 2002; D.Z. Wang and Shen, 2003; Xiao et al., 2006; X. Xu et al., 2008; W. Zhang and Fang, 2014; Zhi and Qin, 2004; Zhi et al., 1994). This previous research focused on the Late Cretaceous and Miocene mantle in this area and was based on mantle xenoliths obtained mainly from late Neogene basaltic rocks. Peridotite xenoliths also occur within post-Neogene alkaline basalts that have been used to characterize the Cenozoic evolution of the mantle beneath SE China (Bodinier and Garrido, 2008; C. ; Dong et al., 1997; Z. ; Dong et al., 1999; X. ; Wang et al., 2012).

However, the Paleogene (and especially the Eocene) evolution of the mantle in this area is poorly known, primarily due to the rarity of basic rocks hosting mantle xenoliths that formed at this time, meaning that the characteristics and the evolution of the Cretaceous to Neogene mantle beneath coastal SE China are uncertain.

Rare peridotite xenoliths are present within Mesozoic and Paleogene basalts in coastal SE in China (**Figure 1**), including peridotite xenoliths within Mesozoic basalts of the Fuxin area of Liaoning Province, the Daoxian area in Hunan Province, and the Daxizhuang area of eastern Shandong Province (Guo et al., 2013a; Guo et al., 2013b; Pei et al., 2004; D. Y. ; Wang et al., 2002; Xia et al., 2010; W. ; Xu et al., 2013; J. ; Yan et al., 2005a; G. ; Yang et al., 2012; J. ; Ying et al., 2010; J. ; Ying et al., 2013; X. ; Yang et al., 2008; Zheng et al., 1999; Q.J. ; Zhou et al., 2013). Previous research on this Mesozoic mantle has been based on inference, meaning the characteristics of this mantle source region are poorly constrained.

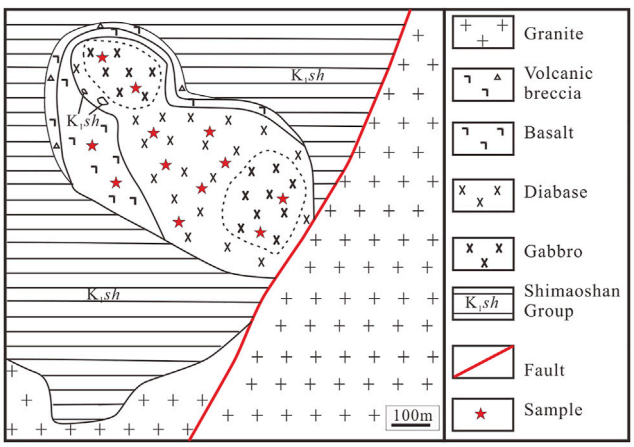

FIGURE 2 | Tectonic and geological maps of the Fuding area, Fujian province (adapted from Dai and Chen, 2008).

A mafic volcanic neck located in the Fuding area of coastal SE China, within the southern section of the Cretaceous Fuding volcanic basin, is associated with a Mesozoic tectono-magmatic belt that is controlled by the NE–SW striking Fuding–Fuqing

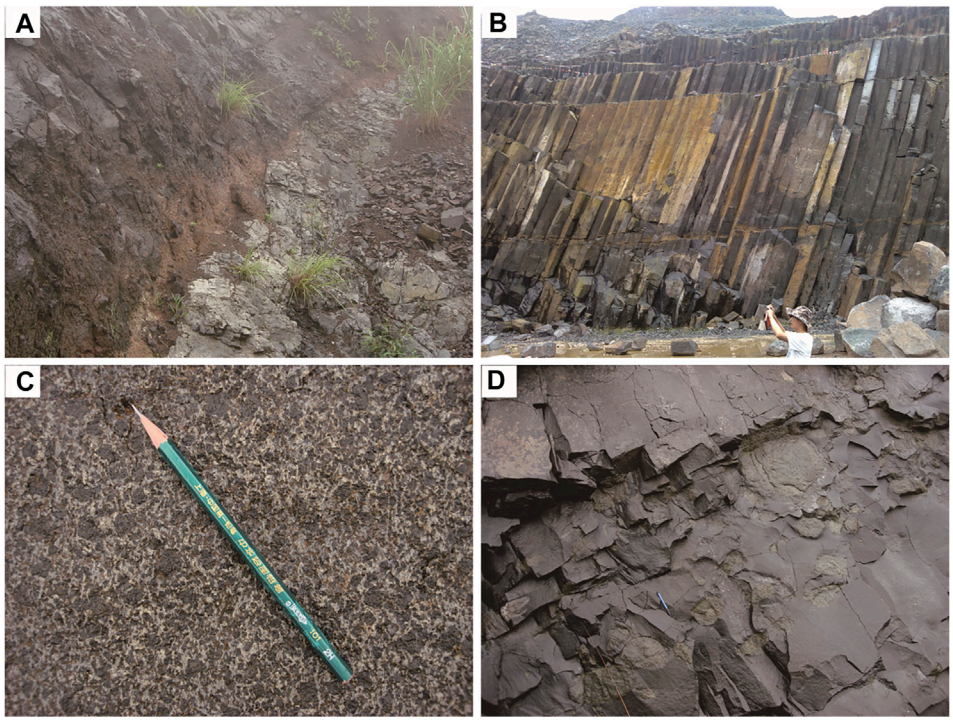

FIGURE 3 | Photographs showing typical characteristics of the Fuding mafic volcanic neck. **(A)** Contact between basalts and units of the Shimaoshan Group, showing a maroon baked margin, **(B)** columnar-jointed gabbro and diabase, **(C)** general characteristics of the cumulate-textured Fuding gabbro, **(D)** rounded peridotite xenoliths within the layered basalt.

Fault. The Fuding basalts were erupted onto volcanic rocks of the lower Shimaoshan Formation (**Figure 2**), contain peridotite xenoliths, and were assigned by L. Li et al. (2011) to the late Oligocene to middle Pleistocene Fotan Group.

Here, we present new whole-rock Ar–Ar ages and geochemical data for mafic rocks from the Fuding mafic volcanic neck. These data constrain the formation age and tectonic setting of the Fuding mafic rocks, which contain peridotite xenoliths that provide clues to the characteristics of the Eocene mantle and to the post late-Mesozoic evolution of the mantle in coastal SE China.

2 GEOLOGICAL BACKGROUND AND PETROLOGICAL CHARACTERISTICS

The Fuding mafic volcanic neck is oval shaped and has a long axis that trends NW–SW, with a length of 790 m, a width of 420 m (**Figure 2**), and with clearly developed columnar joints. The neck is divided into three facies: an outermost eruption facies basaltic breccia volcano, an intermediate effusive facies basalt, and an innermost central neck facies volcano containing olivine-bearing gabbro–diabase rocks (**Figure 3A**). The neck contains basaltic volcanic breccias, basalts, gabbros, and diabasic rocks. The lithofacies within the neck are heterogeneously distributed, with a columnar jointed cumulate gabbro section located above the diabase (**Figures 3B,C**). The geological characteristics of the neck are as follows.

2.1 Volcanic Breccia

The volcanic breccias are gray–black, are brecciated and massive, and are dominated by breccias and crystals in a basaltic matrix. The rocks comprise angular–subangular breccia (60%–70% of the rock mass), and crystals (10%) of olivine, clinopyroxene, spinel, and others (**Figure 4A**) in a basaltic matrix (20%) containing skeletal crystals.

2.2 Basalt

The basalt is gray–black, porphyritic, and has an almond-shaped structure. These rocks contain olivine (0.3–3 mm in size), clinopyroxene, and plagioclase phenocrysts that form 10%–20% of the rock. The amygdales in the basalt are filled with zeolite (**Figures 4B,C**), and both amygdales and phenocrysts are hosted by an intergranular matrix that contains clinopyroxene (50%–55%), olivine (5%), feldspar (12%–15%), basaltic glass (15%), and minor ilmenite. The presence of basaltic glass indicates that the basaltic magma underwent rapid cooling to form a rock with minor amounts of iddingsite and chlorite alteration.

These basalts contain many rounded peridotite xenoliths (**Figure 3D**) that are generally 3–15 cm across (largest, 20 cm). The xenoliths are spinel lherzolites with a subhedral granular

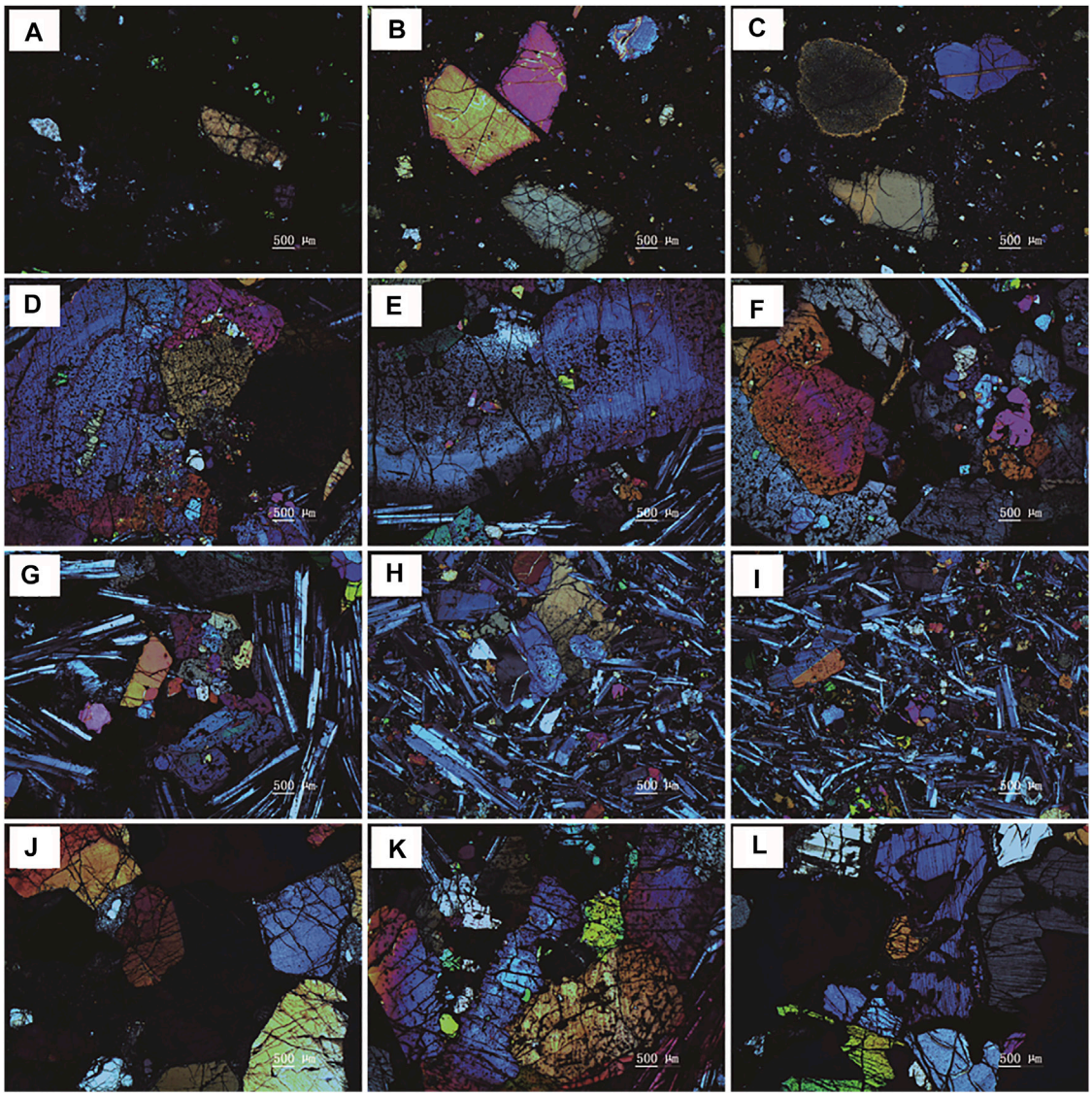

FIGURE 4 | Representative photomicrographs showing typical petrographic features of the Fuding mafic volcanic neck. **(A)** Typical basaltic breccia, **(B)** olivine and clinopyroxene phenocrysts within basalt, **(C)** olivine phenocrysts within vesicular basalt, **(D)** clinopyroxene phenocrysts overprinting olivine within cumulate-textured gabbro, **(E)** zoned clinopyroxene phenocrysts within cumulate-textured gabbro, **(F)** diabasic textured diabase, **(G)** diabasic and intersertal textured diabase, **(H)** diabasic textured diabase, **(I)** diabasic textured diabase containing twinned clinopyroxene, **(J)** granular mosaic textured and zoned clinopyroxene phenocrysts, **(K)** peridotite xenoliths with small olivines enclosed by clinopyroxene, **(L)**: peridotite xenoliths and olivines containing visible kink banding.

texture (**Figures 4J–L**) and they contain olivine (95%) with minor amounts of spinel, clinopyroxene, and orthopyroxene (<5%).

2.3 Gabbro

The gabbro is dark–gray, medium-grained, and has a cumulate gabbroic texture. The largest phenocrysts are ~15 mm in diameter and the rock contains 60%–80% phenocrysts, mainly plagioclase, clinopyroxene, and olivine with minor and localized alkali feldspar. The clinopyroxenes are subhedral, columnar (**Figures 4D,E**), zoned, and make up 15%–20% of the rock, whereas the plagioclase (25%–30%) is euhedral–subhedral and columnar, 0.2–6 mm in size, has clear polysynthetic twinning. The olivine gabbro is subhedral–subhedral, granular, and overprinted by the development of clinopyroxene megacrysts, with some of the olivine being visibly corroded. The olivines have diameters of 0.2–2 mm and make up 10%–20% of the rock. The alkali feldspars are platy and make up 5%–10% of the rock. These minerals occur in a fine-grained matrix of clinopyroxene, olivine, and plagioclase that forms 20%–35% of the rock. The gabbros also contain minor amounts of magnetite, ilmenite, zircon, apatite, and other accessory minerals, and the overall phenocryst abundance within the gabbro unit decreases from top to bottom.

TABLE 1 | Results of $^{40}Ar/^{39}Ar$ dating of Fuding basalt sample TMS2-2.

Power (%)	$^{40}Ar/^{39}Ar$	$^{37}Ar/^{39}Ar$	$^{36}Ar/^{39}Ar$	$^{40}Ar^*/^{39}Ar_k$	$^{40}Ar^*$(%)	^{39}Ark(%)	Age (Ma)	± 2s
Sample name	TMS2-2	groundmass			J = 0.004 650 0 ± 0.000 011 6			
1.5	112.501 99	4.746 41	0.364 51	5.186 578	4.59	3.96	43.09	±23.90
2.0	28.230 86	2.355 78	0.081 00	4.490 241	15.87	21.39	37.37	± 5.00
2.3	11.321 80	1.778 28	0.023 78	4.443 908	39.19	30.21	36.99	± 1.62
2.5	9.599 40	2.068 70	0.017 75	4.527 275	47.08	19.13	37.67	± 1.96
2.8	11.670 14	3.489 24	0.024 22	4.804 107	41.04	7.71	39.95	± 2.54
3.0	11.031 14	2.787 49	0.021 91	4.789 155	43.31	9.74	39.83	± 1.48
3.3	10.380 98	4.863 20	0.019 16	5.127 514	49.19	3.34	42.61	± 2.17
3.8	9.747 77	7.679 70	0.020 28	4.392 694	44.77	1.59	36.56	± 1.75
6.0	11.558 83	28.221 70	0.028 52	5.508 695	46.51	2.20	45.74	± 2.96
9.0	11.050 45	51.606 10	0.027 33	7.402 019	64.04	0.73	61.19	± 4.41

TABLE 2 | Results of $^{40}Ar/^{39}Ar$ dating of Fuding basalt sample TMS2-1.

Power (%)	$^{40}Ar/^{39}Ar$	$^{37}Ar/^{39}Ar$	$^{36}Ar/^{39}Ar$	$^{40}Ar^*/^{39}Ar_k$	$^{40}Ar^*$(%)	^{39}Ark(%)	Age (Ma)	± 2s
Sample name	TMS2-1	groundmass			J = 0.004 650 0 ± 0.000 011 6 (%)			
12	9.918 20	15.160 35	0.023 59	4.205 163	41.85	11.14	35.02	± 8.41
18	10.320 55	24.103 48	0.024 70	5.041 588	47.85	23.27	41.90	± 4.80
23	8.210 10	26.809 99	0.017 64	5.249 289	62.48	65.59	43.61	± 2.13

2.4 Diabase

Diabase occurs beneath the gabbro and has a diabasic texture and a partly visible intersertal texture (**Figures 4F,G**). Some of the clinopyroxenes within the diabase are twinned (**Figures 4H,I**), and this unit has a similar mineralogy to the gabbros described above.

3 ANALYTICAL METHODS

3.1 Whole-Rock Ar–Ar Analytical Procedures

The basalts dated during this study contain peridotite xenoliths and phenocrysts that were removed before analysis. Two basalt samples were dated by whole-rock Ar–Ar methods. The samples were crushed into small chips (≤5 mm) that were hand-picked under a binocular microscope to remove phenocrysts. The $^{40}Ar/^{39}Ar$ dating was carried out using a GV5400 mass spectrometer at the State Key Laboratory of Lithospheric Evolution, Institute of Geology and Geophysics, Chinese Academy of Sciences, Beijing, China, using the analytical procedures described by H. Qiu and Jiang (2007). All errors are reported at 2σ values and argon gas was extracted from the sample by step-heating using a MIR10 CO_2 laser. The released gases were purified using two Zr/Al getter pumps operated for 5–8 min at room temperature and ~450°C, respectively. The background signal prior to analysis was <2 mV and the signal derived from the sample generally fluctuated between 40 and 200 mV. The dating results were calculated and plotted using ArArCALC software (Koppers, 2002), with a J-value of 0.00955 as determined using ZBH-2506 biotite (132 Ma) flux monitors. The results of these Ar–Ar analyses are given in **Tables 1** and **2**.

3.2 Whole-Rock Geochemical Analyses

Bulk-rock major, trace, and rare earth element (REE) concentrations were determined using X-ray fluorescence (XRF) and inductively coupled plasma–mass spectrometry (IC–MS) at the National Research Center for Geoanalysis, Chinese Academy of Geological Sciences (CAGS), Beijing, China. Major element concentrations were determined by XRF and yielded analytical uncertainties better than 5%. Trace and REE concentrations were determined by ICP–MS, with the REE separated using cation exchange techniques. Analytical uncertainties during ICP–MS analysis were 10% for elements with concentrations of <10 ppm and ~5% for those with concentrations of >10 ppm (Zeng et al., 2012). The results of these analyses are listed in **Table 3**.

3.3 Whole-Rock Sr–Nd Isotopic Analyses

Whole-rock Sr and Nd isotope ratios were determined by thermal ionization mass spectrometry (TIMS) using a Finnigan MAT-262 instrument at the CAS Key Laboratory of Crust–Mantle Materials and Environments, University of Science and Technology of China (USTC), Hefei, China. Analytical precision for these isotope ratio measurements is given as ± 2σ (standard error). Sr isotopic ratios were corrected for mass fractionation relative to a $^{86}Sr/^{88}Sr$ value of 0.1194, and analysis of the NBS987 standard yielded a measured $^{87}Sr/^{86}Sr$ ratio of 0.710298 ± 20 with a

TABLE 3 | Major (wt.%) and trace (ppm) compositions of mafic volcanic samples from the northeast of Fujian Province.

Sample	TMS-1-1	TMS-1-2	TMS-1-3	TMS-1-4	TMS-1-5	TMS-2-5	TMS-2-6	TMS-3-1	TMS-3-2	TMS-3-3	TMS-2-1	TMS-2-2
	Gabbro/Diabase										Basalt	
SiO_2	46.54	47.03	46.63	46.73	46.78	46.63	46.60	46.91	46.95	46.86	43.36	44.20
Al_2O_3	12.12	14.23	12.29	13.13	12.86	12.69	12.33	13.01	12.50	13.15	12.01	12.19
Fe_2O_3	2.10	1.75	2.66	2.01	1.77	2.13	1.94	1.70	1.85	2.21	3.26	3.72
FeO	9.01	8.62	8.12	8.85	9.05	9.13	9.33	9.07	9.26	8.65	8.69	7.70
CaO	10.07	8.92	9.95	9.41	9.66	9.28	9.73	9.57	9.60	9.50	8.91	8.51
MgO	10.16	8.64	10.00	9.51	9.60	9.65	10.17	9.36	9.87	9.16	11.12	10.75
Na_2O	2.67	3.30	2.68	2.85	3.01	3.27	2.86	3.17	3.13	3.25	4.46	4.16
K_2O	2.18	2.35	1.99	2.29	2.24	2.26	2.16	2.33	2.04	2.24	2.32	1.90
TiO_2	2.00	1.95	1.97	1.99	1.99	2.05	2.01	2.01	2.00	2.13	2.21	2.09
MnO	0.15	0.14	0.15	0.15	0.15	0.15	0.15	0.15	0.15	0.15	0.17	0.16
P_2O_5	0.65	0.70	0.63	0.67	0.66	0.72	0.66	0.69	0.69	0.73	1.13	1.08
L.O.I	1.78	1.83	2.34	1.84	1.69	1.59	1.62	1.50	1.48	1.52	1.70	2.85
SO_3	0.20	0.22	0.23	0.22	0.20	0.14	0.16	0.17	0.17	0.17	0.23	0.28
Fe_2O_3T	12.13	11.34	11.70	11.86	11.84	12.29	12.32	11.79	12.16	11.84	12.93	12.29
Na_2O+K_2O	4.85	5.65	4.67	5.14	5.25	5.53	5.02	5.50	5.17	5.49	6.78	6.06
FeOT	10.90	10.19	10.51	10.66	10.64	11.05	11.08	10.60	10.92	10.64	11.62	11.05
Mg#	66.13	63.96	66.58	65.14	65.39	64.66	65.79	64.90	65.42	64.33	66.71	67.09
K	18097	19509	16520	19010	18595	18761	17931	19342	16935	18595	19259	15773
Ti	11988	11688	11808	11928	11928	12288	12048	12048	11988	12767	13247	12527
P	2836	3055	2749	2924	2880	3142	2880	3011	3011	3186	4931	4713
AR	1.56	1.65	1.53	1.59	1.61	1.67	1.59	1.64	1.61	1.64	1.96	1.83
Li	5.92	5.55	6.01	5.91	5.51	5.49	5.43	5.75	5.68	6.48	8.60	9.01
Be	1.36	1.53	1.37	1.47	1.44	1.47	1.36	1.48	1.50	1.49	2.24	2.36
Sc	28.30	21.20	27.00	24.00	25.30	22.90	25.60	24.70	26.40	23.20	16.30	17.20
V	217	168	198	184	183	178	193	190	198	183	167	167
Cr	358	206	364	252	292	242	299	282	308	247	526	525

Sample	TMS-1-1	TMS-1-2	TMS-1-3	TMS-1-4	TMS-1-5	TMS-2-5	TMS-2-6	TMS-3-1	TMS-3-2	TMS-3-3	TMS-2-1	TMS-2-2
	Gabbro/Diabase										Basalt	
Co	55	50	52	54	54	51	54	52	54	49	52	53
Ni	164	141	159	154	158	144	158	149	155	136	275	291
Cu	73	75	72	76	75	73	72	76	78	78	63	66
Zn	167	162	160	168	170	161	164	167	171	168	191	192
Ga	20	21	19	20	19	18	18	20	19	20	20	21
Rb	59	60	55	62	65	58	56	66	60	59	68	107
Sr	691	833	627	790	735	652	672	739	692	694	978	991
Y	21.90	21.70	21.30	21.80	21.90	21.50	21.30	22.40	22.90	22.40	23.20	25.10
Nb	55.20	61.20	53.40	58.80	56.00	57.60	54.60	59.10	59.50	60.90	88.90	89.20
Mo	2.02	2.73	2.48	1.96	2.05	2.52	2.02	2.88	2.40	2.93	2.73	2.17
Cd	0.07	0.06	0.07	0.06	0.07	0.06	0.06	0.07	0.08	0.06	0.15	0.18
In	0.07	0.07	0.07	0.07	0.07	0.07	0.07	0.07	0.07	0.07	0.08	0.10
Sb	0.07	0.07	0.06	0.07	0.07	0.06	0.06	0.07	0.07	0.07	0.07	0.11
Cs	0.70	1.21	1.37	0.95	1.15	1.21	1.02	1.06	1.24	1.26	1.37	1.94
Ba	587	680	586	650	624	615	593	659	633	639	758	857
La	47.6	51.9	46.3	50.5	48.8	49.2	46.8	50.9	51.1	50.6	75.9	79.9
Ce	83.5	89.2	80.1	87.2	83.8	84.9	81.0	87.8	88.8	87.6	129.0	136.0
Pr	10.0	10.4	9.4	10.2	9.8	10.0	9.6	10.3	10.5	10.3	15.1	16.0
Nd	40.4	40.9	38.0	40.8	38.8	39.5	38.5	41.1	41.6	40.8	59.3	62.9
Sm	7.83	7.65	7.34	7.72	7.21	7.53	7.37	7.79	7.86	7.72	10.70	11.40
Eu	2.44	2.43	2.28	2.39	2.20	2.29	2.25	2.43	2.44	2.38	3.17	3.30
Gd	6.82	6.55	6.50	6.75	5.96	6.45	6.31	6.75	6.89	6.73	8.60	9.06
Tb	1.16	1.11	1.09	1.14	1.02	1.11	1.08	1.15	1.18	1.14	1.41	1.48
Dy	5.41	5.17	5.07	5.26	4.82	5.11	5.08	5.34	5.48	5.28	5.85	6.35
Ho	0.86	0.82	0.81	0.83	0.79	0.81	0.80	0.85	0.86	0.83	0.85	0.94

Sample	TMS-1-1	TMS-1-2	TMS-1-3	TMS-1-4	TMS-1-5	TMS-2-5	TMS-2-6	TMS-3-1	TMS-3-2	TMS-3-3	TMS-2-1	TMS-2-2
	Gabbro/Diabase										Basalt	
Er	2.24	2.15	2.10	2.19	2.07	2.12	2.08	2.21	2.24	2.16	2.21	2.44
Tm	0.30	0.29	0.28	0.29	0.28	0.28	0.28	0.30	0.30	0.29	0.26	0.30
Yb	1.76	1.71	1.67	1.74	1.67	1.69	1.65	1.75	1.79	1.72	1.54	1.77

(Continued on following page)

TABLE 3 | (*Continued*) Major (wt.%) and trace (ppm) compositions of mafic volcanic samples from the northeast of Fujian Province.

Sample	TMS-1-1	TMS-1-2	TMS-1-3	TMS-1-4	TMS-1-5	TMS-2-5	TMS-2-6	TMS-3-1	TMS-3-2	TMS-3-3	TMS-2-1	TMS-2-2
	Gabbro/Diabase										Basalt	
Lu	0.24	0.24	0.23	0.24	0.23	0.23	0.23	0.24	0.25	0.24	0.21	0.24
Ta	2.64	2.85	2.49	2.74	2.49	2.65	2.52	2.75	2.78	2.76	4.07	4.13
W	0.70	1.38	0.64	0.76	0.85	1.05	0.90	1.42	1.06	1.04	0.49	0.71
Re	0.00	0.00	0.00	0.00	0.00	0.00	0.00	0.00	0.00	0.00	0.00	0.00
Tl	0.04	0.04	0.04	0.04	0.04	0.04	0.04	0.04	0.04	0.04	0.07	0.09
Pb	3.08	3.12	2.69	2.98	2.83	2.88	2.74	3.07	3.70	2.98	5.45	5.70
Bi	0.01	0.00	0.00	0.00	0.00	0.00	0.00	0.00	0.00	0.00	0.02	0.01
Th	7.02	7.42	6.54	7.14	6.75	6.98	6.56	7.18	7.22	7.24	10.90	12.50
U	1.33	1.40	1.23	1.35	1.26	1.32	1.22	1.35	1.38	1.36	2.10	2.56
Zr	296	315	288	308	301	304	290	312	317	317	406	422
Hf	6.32	6.27	5.94	6.29	5.84	6.08	5.94	6.31	6.51	6.26	7.76	8.25
Eu*	1.02	1.05	1.01	1.01	1.03	1.00	1.01	1.02	1.01	1.01	1.01	0.99
$(La/Yb)_N$	18.23	20.46	18.69	19.57	19.70	19.63	19.12	19.61	19.25	19.83	33.23	30.43
∑REE	210.56	220.51	201.20	217.26	207.41	211.20	203.02	218.91	221.29	217.79	314.10	332.08
∑HREE	18.79	18.03	17.75	18.45	16.83	17.80	17.51	18.59	18.99	18.39	20.93	22.58
∑LREE	191.77	202.48	183.45	198.81	190.58	193.40	185.51	200.32	202.30	199.40	293.17	309.50
∑LREE/∑HREE	10.21	11.23	10.34	10.78	11.32	10.87	10.60	10.78	10.65	10.85	14.01	13.71
$(La/Sm)_N$	3.82	4.27	3.97	4.11	4.26	4.11	3.99	4.11	4.09	4.12	4.46	4.41
$(Gd/Yb)_N$	3.13	3.09	3.14	3.13	2.88	3.08	3.09	3.11	3.11	3.16	4.51	4.13

*Fe_2O_{3T} = FeO*1.1113 + Fe_2O_{3T} in wt.%; ∑REE = total REE concentration; ∑LREE = total LREE concentration; ∑HREE = total HREE concentration; subscript N denotes normalization to the chondrite value of Sun and McDonough (1989); Eu* = $Eu_N/(Sm_N + Gd_N)^{1/2}$.*

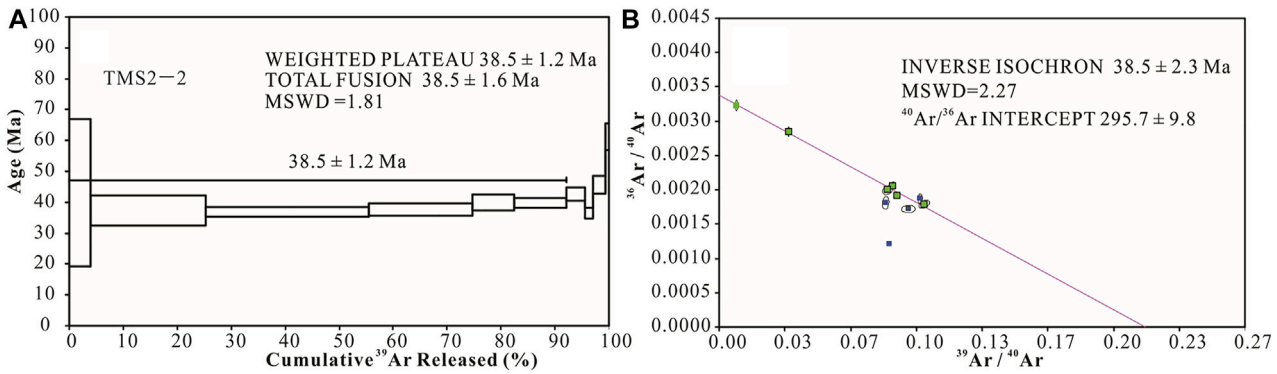

FIGURE 5 | Plateau and isochron Ar–Ar ages for sample TMS2-2. **(A)** and isochron Ar-Ar age **(B)** for sample TMS2-2.

precision of ~0.002%. Measured $^{143}Nd/^{144}Nd$ ratios were normalized to a $^{146}Nd/^{144}Nd$ value of 0.7219, and analysis of the La Jolla Nd standard yielded a measured $^{143}Nd/^{144}Nd$ ratio of 0.511851 ± 45. Single-stage Nd model ages (T_{DM1}) are calculated relative to the depleted mantle reservoir (Depaolo, 1988), and two-stage Nd model ages (T_{DM2}) are calculated for different ages of magmatism relative to average continental crustal values with a $^{147}Sm/^{144}Nd$ ratio of 0.118 (Jahn and Condie, 1995).

4 ANALYTICAL RESULTS

4.1 Ar–Ar Geochronology

The Funding basalt samples (TMS2-2 and TMS2-1) from the Fotan volcanic succession dated by the $^{40}Ar/^{39}Ar$ method yielded apparent ages that were determined using age spectra and isotope correlation ($^{36}Ar/^{40}Ar$ vs. $^{39}Ar/^{40}Ar$) diagrams (**Figures 5**, **6**; **Tables 1**,**2**). The latter provides a quantitative measure of the initial argon composition and allows the identification of excess argon that has $^{40}Ar/^{36}Ar$ ratios greater than the present day atmospheric value of 295.5. The data in **Table 1** and **Figure 2** indicate that little excess argon was present in the basalt samples.

The plateau age for sample TMS2-2 is 38.5 ± 1.2 Ma (**Figure 5A**), a date that is within error of the isochron age for this sample (38.5 ± 2.3 Ma; **Figure 5B**). The second sample (TMS2-1) was collected from the basal section of the Fuding area and yielded an older plateau age (42.3 ± 2 Ma; **Figure 6**). As such, we interpret the plateau ages for these samples to represent the volcanism that formed the Fuding basalts, indicating that the final eruption of the Fotan Formation occurred at 42.3–38.5 Ma. Hence, the eruption of the Fuding basalt occurred at 42.3–38.5 Ma, during the Eocene.

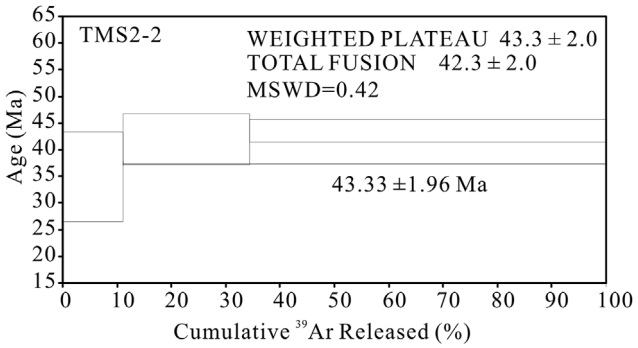

FIGURE 6 | Plateau Ar–Ar age for sample TMS2-1.

4.2 Whole-Rock Geochemical Characteristics

4.2.1 Gabbro and Diabase

The gabbro and diabase samples from the Fuding area have restricted ranges of SiO_2 (46.54–47.03 wt.%), total Fe expressed as FeO (FeO_T; 11.34–12.32 wt.%), CaO (8.92–10.07 wt.%), and Al_2O_3 (12.12–14.23 wt.%) concentrations, but a wide range of MgO concentrations (8.64–10.17 wt.%). Plotting these samples on a total alkali versus silica (TAS; SiO_2 versus $Na_2O + K_2O$) classification diagram indicates the majority are trachybasalts with a few basalts, although all of the samples plot above the alkaline curve in this diagram (**Figure 7A**). These samples have K_2O and $K_2O + Na_2O$ concentrations of 1.99–2.35 and 4.67–5.65 wt.%, respectively, yielding high K_2O/Na_2O ratios (0.65–0.82) that indicate these samples are alkaline basaltic rocks (**Figures 7B,C,D**).

Plotting data of the gabbro and diabase samples on Harker diagrams yields negative correlations between SiO_2 and CaO, FeOT, and MgO concentrations, and positive correlations between SiO_2 and Na_2O, K_2O, and Al_2O_3 concentrations (**Figure 8**).

All of the gabbro and diabase samples have high total REE (ΣREE) values (201.2–221.29 ppm; average of 212.91 ppm) and they are light REE (LREE) enriched, with total LREE to total heavy REE (HREE; ΣLREE/ΣHREE) ratios of 10.21–11.32 (average of 10.76). These samples have $(La/Yb)_N$ (where $_N$ denotes normalization to the chondrite ratio of Sun and McDonough, 1989) ratios of 18.26–20.46 (average of 19.41), reflecting the degree of fractionation of the LREE from the

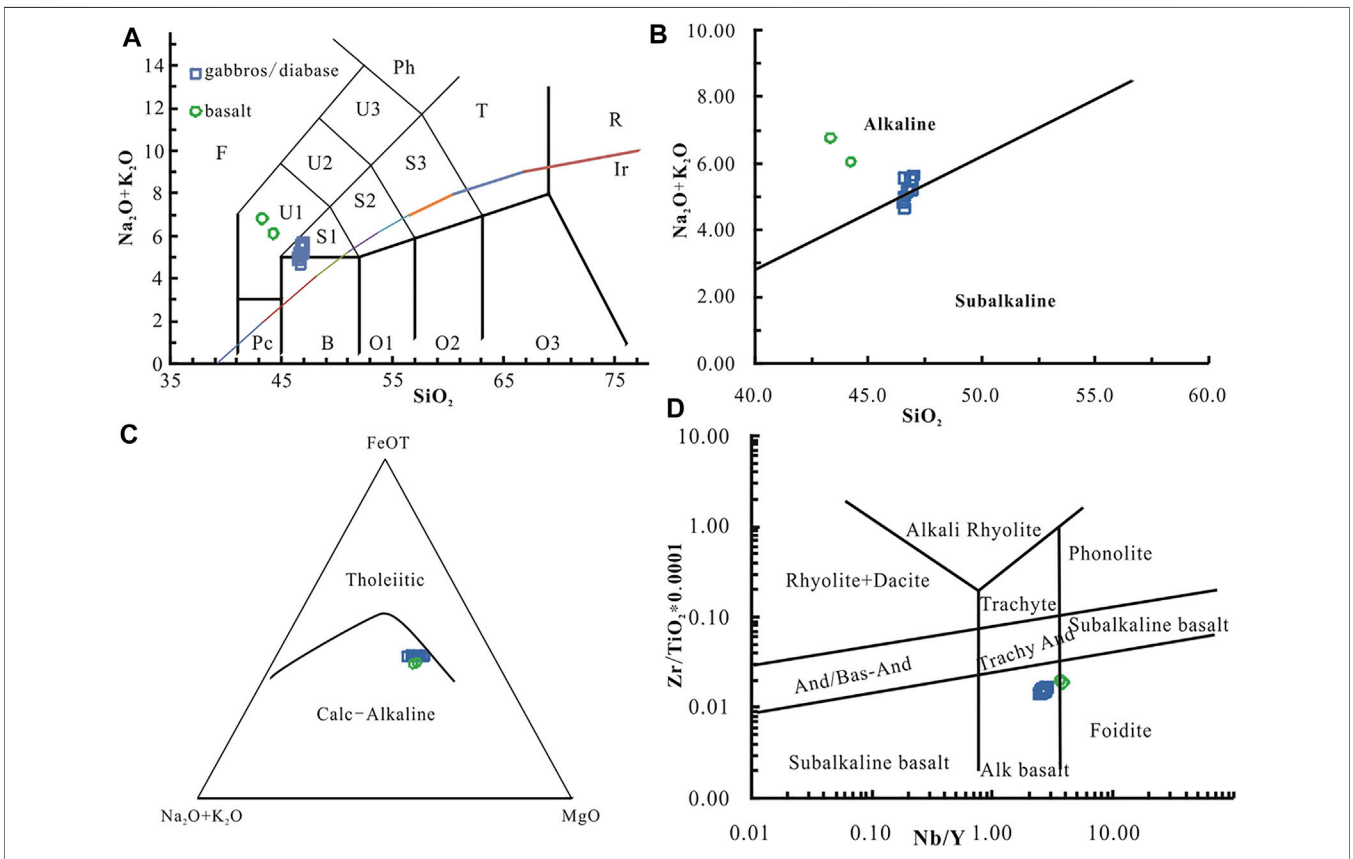

FIGURE 7 | Geochemical classification diagrams showing variations in the compositions of samples from the Fuding mafic volcanic neck. **(A)** Total alkali versus silica (TAS) diagram (after Middlemost, 1994); **(B)** SiO_2 vs. $K_2O + Na_2O$ diagram (after LeMaitre et al., 1989); **(C)** AFM diagram; and **(D)** Zr/TiO_2 versus Nb/Y diagram (after Pearce, 1996).

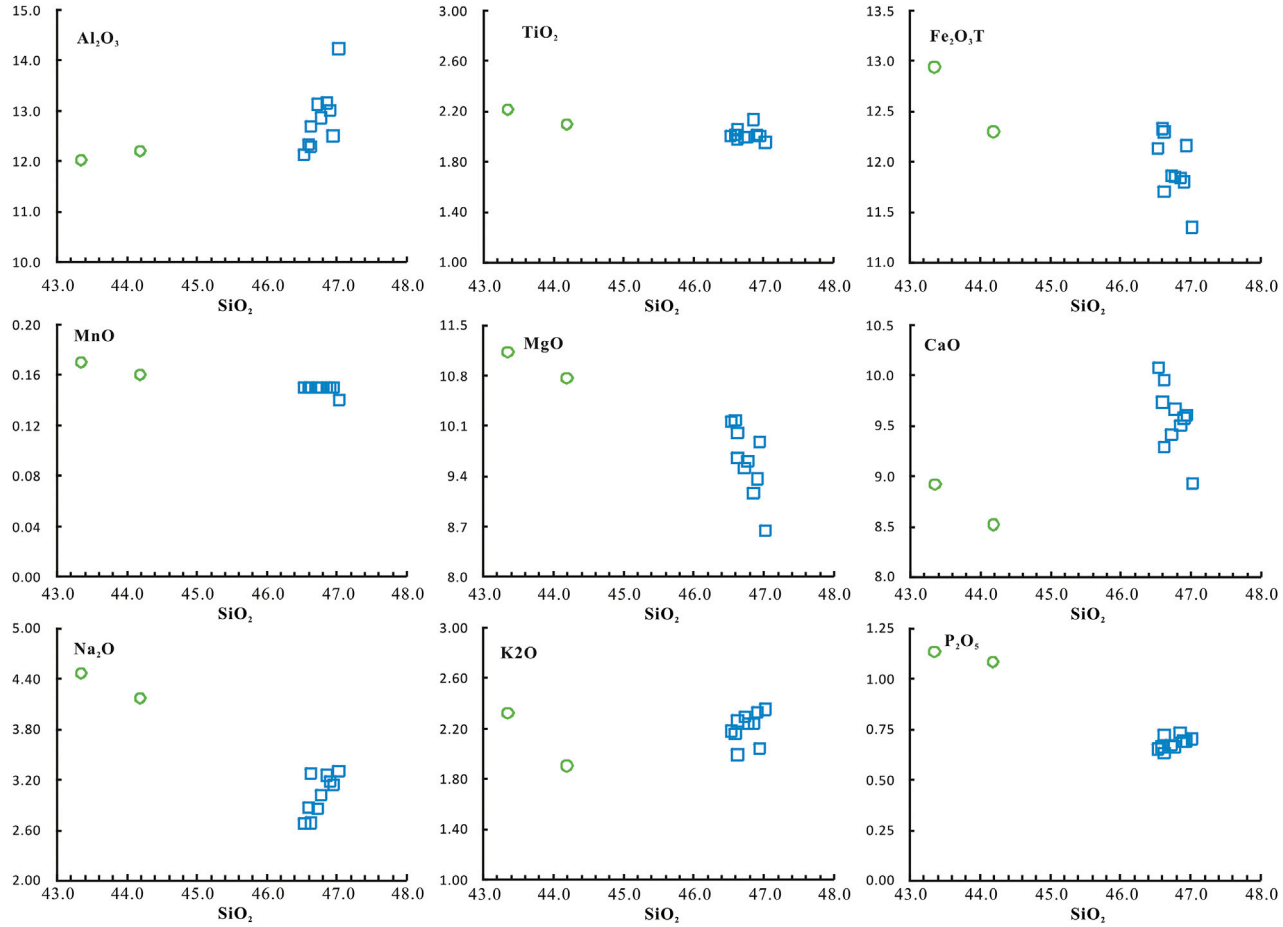

FIGURE 8 | Harker-type diagrams showing variations in the geochemical compositions of mafic rocks from the Fuding volcanic neck.

HREE. These samples show $(La/Sm)_N$ values from 3.82 to 4.27 (average of 4.09) and $(Gd/Yb)_N$ values from 2.88 to 3.16 (average of 3.09). They are free of significant Eu anomalies ($Eu/Eu^* = 1.00–1.05$, average of 1.02) and have smooth chondrite-normalized REE patterns (**Figure 9A**). All of the samples are enriched in the large ion lithophile elements (LILE), have differentiated high field strength element (HFSE) concentrations, and are slightly depleted in Ti and Y (**Figure 9C**). They have chondrite-normalized REE and primitive-mantle-normalized multi-element variation patterns that are similar to those of typical OIB compositions but differ from typical N- or E-type mid-ocean-ridge basalt (MORB) compositions.

4.2.2 Basalts

The basalts analyzed during this study contain higher concentrations of MgO (10.75–11.12 wt.%) than the gabbro and diabase samples, with both basalt samples classified as tephrites or basanites and both plotting above the alkaline curve (**Figure 7A**), indicating that both of these basalts are alkaline basaltic rocks (**Figures 7B,D**).

Both of the basalt samples contain higher ΣREE concentrations (314.10–332.08 ppm; average of 323.09 ppm) than the gabbro and diabase samples, although the basalts are similar to these other samples in that they have OIB-type REE and multi-element variation diagram characteristics that contrast with typical N- or E-type MORB compositions (**Figures 9B,D**).

4.3 Whole-Rock Sr–Nd Characteristics

The isotopic Rb–Sr and Sm–Nd ratios of the whole-rock samples are given in **Table 4**. The gabbro, diabase, and basalt samples have uniform initial εNd(t) (3.05–4.56, average of 3.90) and initial $^{87}Sr/^{86}Sr$ (0.703794–0.703911, average of 0.703865) values. They have two-stage Nd model (T_{DM2}) ages than range from 0.61 to 0.73 Ga (average of 0.67 Ga).

5 DISCUSSION

5.1 Petrogenetic Evolution

5.1.1 Basalts

The basalts from the Fuding mafic volcanic neck are enriched in the REE and have highly differentiated HFSE compositions that are apparent in their OIB-type primitive-mantle-normalized multi-element diagrams (**Figures 9B,D**; Edwards et al., 1994;

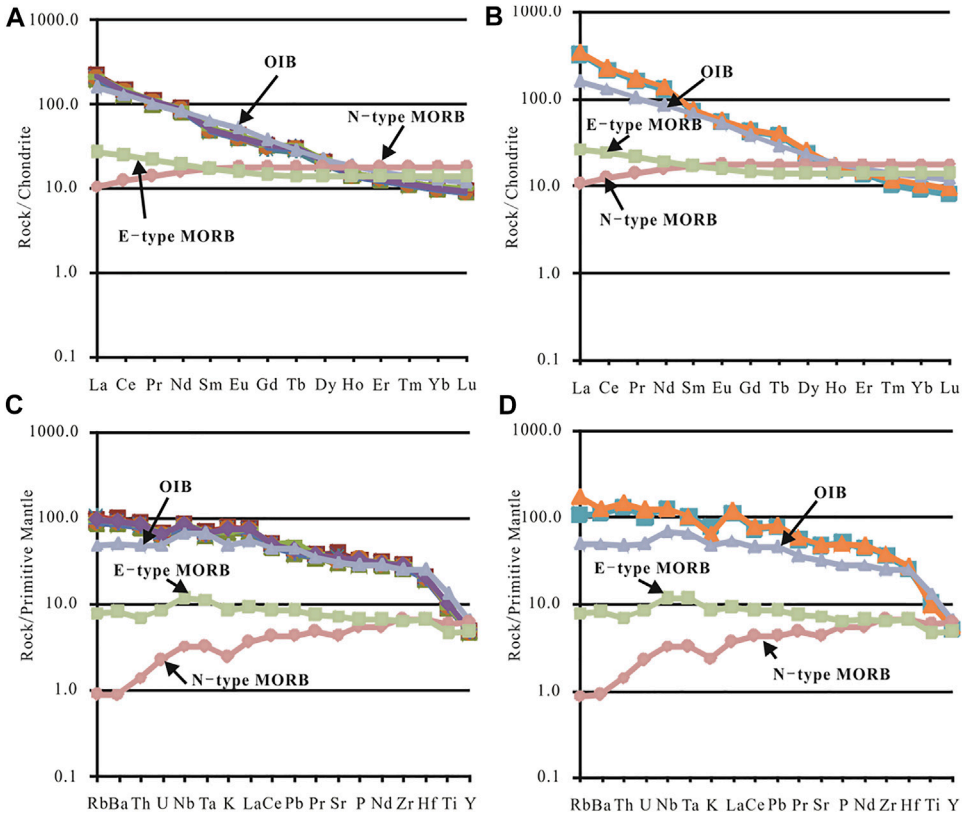

FIGURE 9 | Chondrite-normalized REE and primitive-mantle-normalized multi-element diagrams for samples from the Fuding mafic volcanic neck. Diagrams are normalized to the chondrite and primitive mantle compositions of Sun and McDonough (1989). **(A)** and **(C)** for gabbro and diabase samples; **(B)** and **(D)** for basalt samples.

TABLE 4 | Rb–Sr and Sm–Nd isotopic compositions of mafic volcanics from the northeast of Northeast Fujian Province.

Sample	Rock types	Age (Ma)	Rb (ppm)	Sr (ppm)	$^{87}Rb/^{86}Sr$	$^{87}Sr/^{86}Sr$	I_{Sr}	Sm (ppm)	Nd (ppm)	$^{147}Sm/^{144}Nd$	$^{143}Nd/^{144}Nd$	εNd	t_{Nd} (Ga)
TMS-1-1	Gabbro/ Diabase	38.5	59.0	691	0.247	0.704 016 ± 7	0.703 881	7.83	40.4	0.117 2	0.512 808 ± 11	3.71	0.68
TMS-1-2		38.5	60.0	833	0.208	0.704 025 ± 6	0.703 911	7.65	40.9	0.113 1	0.512 817 ± 12	3.90	0.67
TMS-1-4		38.5	55.0	627	0.254	0.704 016 ± 5	0.703 878	7.34	38	0.116 8	0.512 774 ± 9	3.05	0.73
TMS-2-5		38.5	66.0	739	0.258	0.704 018 ± 5	0.703 877	7.79	41.1	0.114 6	0.512 783 ± 9	3.23	0.72
TMS-2-6		38.5	60.0	692	0.251	0.704 006 ± 6	0.703 868	7.86	41.6	0.114 2	0.512 851 ± 8	4.56	0.61
TMS-3-1		38.5	59.0	694	0.246	0.703 997 ± 6	0.703 862	7.72	40.8	0.114 4	0.512 849 ± 9	4.52	0.62
TMS-2-1	Basalt	42.3	107	991	0.312	0.703 982 ± 5	0.703,794	11.4	62.9	0.109 6	0.512 843 ± 8	4.47	0.62
TMS-2-2		42.3	58.0	652	0.257	0.704 006 ± 7	0.703 851	7.53	39.5	0.115 3	0.512 808 ± 10	3.76	0.68

Sun and McDonough, 1989; Zhao and Zhou, 2007). Both of these samples are classified as within-plate alkali basalts in the Nb–Zr–Y diagram of Meschede ,1986; **Figure 10A**). These basalts have Ti/V ratios between 75 and 80 that are much higher than those of arc basalts, and they plot in the OIB field on a modified Ti versus V diagram (**Figure 10B**; Shervais, 1982). Both samples plot in the OIB field on a Nb/Yb versus Th/Yb diagram (**Figure 10C**; J. Pearce and Peate, 1995). They yield high Mg# values (= 100*MgO/(MgO + 0.85*Fe_2O_3T) and contain low concentrations of SiO_2, suggesting that they originated from a

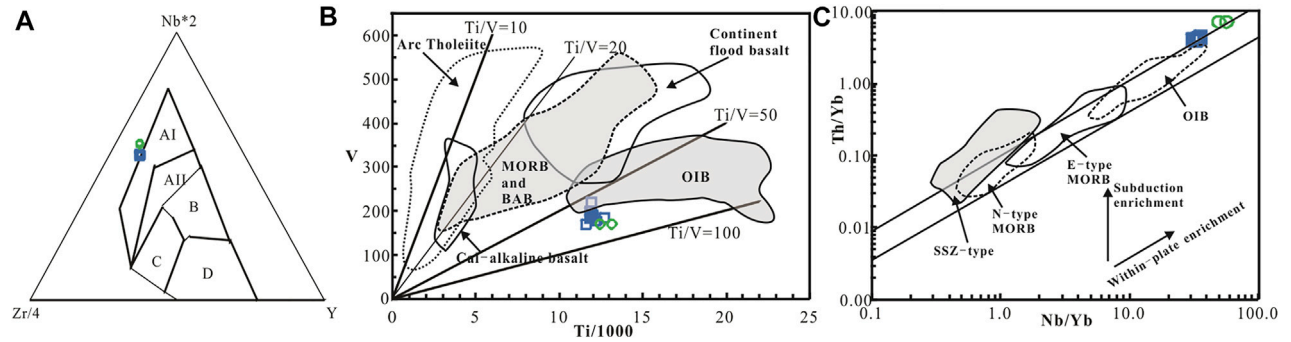

FIGURE 10 | (A) Nb-Zr-Y, **(B)** Ti versus V (after Shervais, 1982) and **(C)** Th/Yb–Nb/Yb (after Pearce & Peate, 1995) diagrams for samples from the study area. Average N-MORB, E-MORB, and OIB compositions are from Sun and McDonough (1989), and SSZ-, N-MORB-, E-MORB-, and OIB-type fields are from Mahe et al., 2004, Saccani and Photiades (2005), and Aldanmaz et al., 2008.

parental magma that was derived from an OIB-like mantle source in a continental rift environment, without any crustal input.

5.1.2 Gabbro and Diabase

The gabbro and diabase samples from the Fuding area have similar REE and HFSE characteristics as the basalt samples, again indicating that these units have an OIB-type affinity (**Figures 9A,C**, **Figures 10A–C**; Edwards et al., 1994; Sun and McDonough, 1989; Zhao and Zhou, 2007). However, the gabbro and diabase units have Mg# values of 63.96–66.58, suggesting that they record the minor differentiation of olivine and pyroxene. This fractionation is also evidenced by a negative

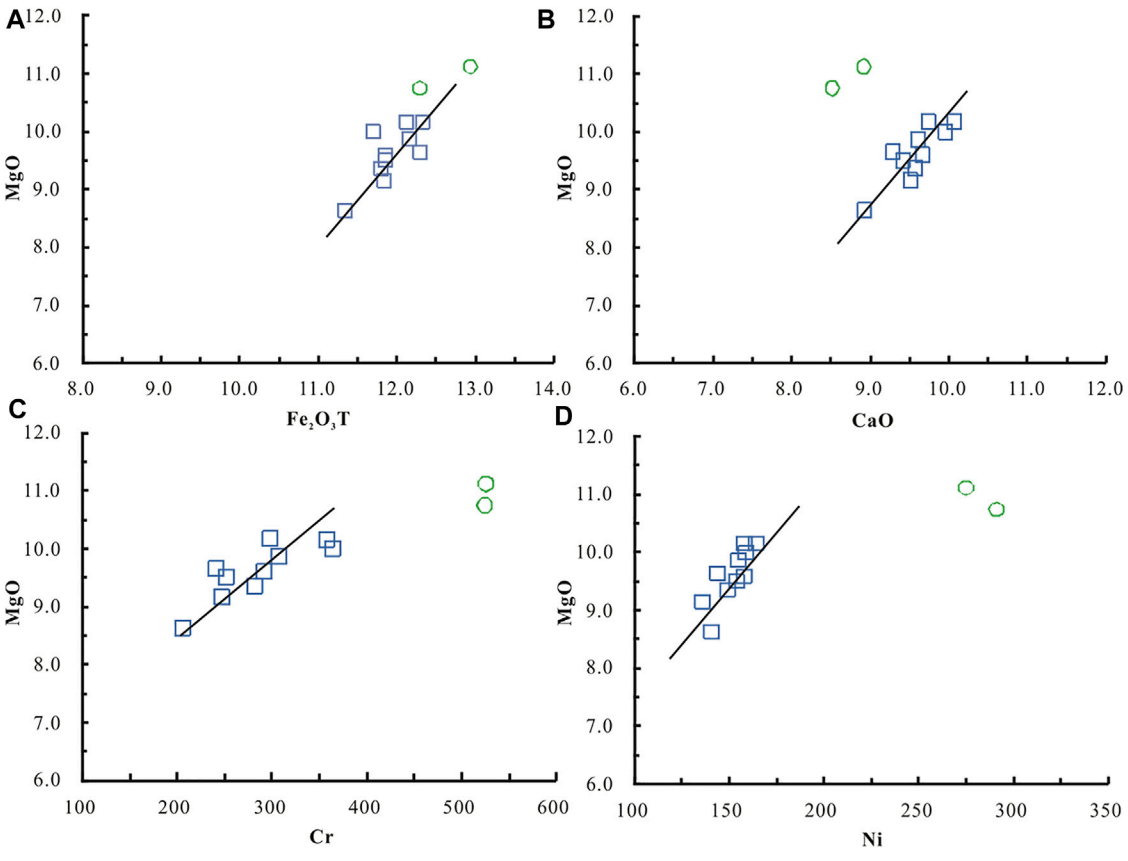

FIGURE 11 | Harker-type diagrams showing variations in the Fe_2O_3T, CaO, Cr, and Ni concentrations of samples from the Fuding area relative to MgO. **(A)**, CaO **(B)**, Cr **(C)**, and Ni **(D)** concentrations of samples from the Fuding area relative to MgO.

correlation between SiO_2 and MgO concentrations (**Figure 8**). In addition, the positive correlation between Fe_2O_3T and MgO concentrations shown by the gabbro samples is indicative of the fractionation of olivine (**Figure 11A**), whereas the positive correlation between CaO and MgO concentrations in these samples is evidence of the fractionation of clinopyroxene (**Figure 11B**). This conclusion is also supported by the presence of positive correlations between Cr, Ni, and MgO concentrations (**Figures 11C,D**).

The lack of any significant Eu anomalies (Eu/Eu^* = 1.00–1.05; **Figure 9A**) indicates that the gabbro and diabase units do not record any plagioclase fractionation. However, crustal contamination can modify the composition of mantle-derived magmatic rocks. Crustal materials are enriched in the LILE, K_2O, and Na_2O, and are depleted in P_2O_5 and TiO_2. The gabbro and diabase units within the Fuding area contain low and invariant concentrations of K_2O and Na_2O, suggesting that they record minimal amounts of crustal contamination. Crustal contamination can also produce negative Nb and Ta, and positive Zr and Hf anomalies relative to the LILE and LREE (Sun and McDonough, 1989; Zhao and Zhou, 2007); however, these anomalies are absent in the primitive-mantle-normalized multi-element diagrams for the gabbro and diabase samples from the study area (**Figure 9C**), again suggesting that these units record minimal crustal contamination. All of the samples show low initial $^{87}Sr/^{86}Sr$ values (average of 0.703865) and high εNd(t) values (3.05–4.56, average of 3.90). These data indicate that the basalt, gabbro, and diabase units in the Fuding area were derived from an OIB-type mantle source, with the gabbro and diabase units recording minor amounts of crustal contamination.

5.2 Implications of Ar–Ar Dating

The basalts from the Fuding mafic volcanic neck in coastal SE China are generally alkaline (average $Na_2O + K_2O$ = 5.77 wt.%) and are enriched in TiO_2 (average TiO_2 = 2.15 wt.%), whereas Neogene basalts in this area are largely subalkaline (average $Na_2O + K_2O$ = 2.79 wt.%) and contain lower concentrations of TiO_2 (average $TiO_{2=}$<1.5 wt.%; Lu et al., 2000), indicating significant geochemical differences between these basalts.

The trace and REE compositions of the Fuding mafic volcanic neck are different from those of the Neogene basalts of coastal SE China. The basalts from the former contain higher Rb (average of 87 ppm), Sr (average of 984 ppm), Ba (average of 807 ppm), and total REE (average of 243 ppm) concentrations and have higher light REE/heavy REE (LREE/HREE) ratios (average of 11.93) than the Neogene basalts of coastal SE China (average Rb, Sr, Ba, and total REE concentrations of 17.5, 339, 201, and 112 ppm, respectively, with an average LREE/HREE ratio of 4.22; Lu et al., 2000; J. Qiu et al., 1999; S. Wang, 1998; X. Wang et al., 2012; J. Zhang and Lu, 1997; Zouet al, 2000).

L. Li et al. (2011) reported that the Taimushan granite formed at 96.16 ± 1.6 Ma and suggested that the Fuding basalts formed part of the late Oligocene to middle Pleistocene Fotan Group. Our unpublished zircon U–Pb laser ablation (LA)–ICP–MS analyses yielded a Late Cretaceous age of 88.2 ± 1.0 Ma for these basalts, although these ages may be unreliable. The two basalt samples from the Fuding mafic volcanic neck yield similar Ar–Ar ages of 38.5 ± 1.2 and 42.3 ± 2 Ma, indicating that the basalts within both the neck and within the Fotan Group were emplaced during the Eocene.

5.3 Implications of the Presence of Peridotite Xenoliths

Cretaceous basalts in coastal SE China are usually associated with other contemporaneous bimodal volcanic rocks. The basalts in this area crop out over a much smaller area than associated acidic volcanic rocks and are thought to have been derived from either an enriched region of mantle, from a depleted region of the mantle and then either assimilated crustal material or underwent magma mixing, or were derived from the crust–mantle transition zone (C. Chen et al., 2008; Cui et al., 2011; He and Xu, 2011; Z. Li and Li, 2007; X. Li et al., 2007; H. Li et al., 1995; Tang et al., 2010; Xing et al., 1999; G. Xie et al., 2005; X. Xu et al., 2008; J. Yan et al., 2005b; Yu et al., 1993).

As mentioned above, both the petrogenesis of the basalts in coastal SE China and the nature of the mantle beneath this region remain uncertain. The main cause of this uncertainty is the lack of mantle rocks in this area; however, peridotite xenoliths within the Fuding basalts can be used to determine the characteristics of the Eocene mantle in this area, including the post late-Mesozoic evolution of the mantle beneath coastal SE China.

The nature of the late Mesozoic mantle in coastal SE China remains debated. Several different models have been proposed, including 1) enriched lithospheric mantle beneath Fujian and Zhenjiang provinces (Cui et al., 2011; Tang et al., 2010; G. ; Xie et al., 2005; J. ; Yan et al., 2003; J. ; Yan et al., 2005a; Yan et al., 2005b; Z. ; Yang et al., 1999; B. ; Zhang et al., 2004), 2) enriched mantle that mixed with both depleted and EMII type enriched mantle material (X. Xie et al., 2001), 3) local areas of weakly enriched mantle that is compositionally similar to EMII-type enriched mantle (H. Zhang et al., 2005), and 4) depleted asthenospheric mantle (Q. Zhou et al., 2010).

Both the late Mesozoic basalts and acidic volcanic rocks in coastal SE China have isotopic characteristics similar to those of enriched mantle (C. Dong C. W. et al., 2006; Y. Dong Y. X. et al., 2006; C. Dong et al., 2007; Z. Yang et al., 1999; Xing et al., 1999; Xue et al., 1996; J. Zhou and Chen, 2001), suggesting that the Cretaceous upper mantle in this region was relatively stable but also weakly enriched.

The Paleocene basalts in coastal SE China generally crop out in the northern parts of the Jiangsu and Hefei basins, as well as in the Mingguang and Fushan areas (Qian and Li, 1996; Z. ; Yang et al., 1999). These basalts contain abundant peridotite xenoliths, were emplaced at 64–56 Ma, have the characteristics of typical continental basalts, and were derived from weakly enriched mantle (D. Chen, 1992; Cong et al., 1996; Z. Yang et al., 1999; X. Zhou, 1992).

Eocene basalts are sporadically exposed within coastal SE China and have been reported from the Sanshui Basin in Guangdong Province (Y. Dong Y. X. et al., 2006; Hu et al., 2013; Xiao et al., 2006; X. Zhang et al., 1993; W. Zhang and Fang, 2014; Zhu et al., 1991). X. Zhang et al. (1993) reported

K–Ar ages of 45–55 Ma for these basalts, and Y. Dong Y. X. et al. (2006) obtained a zircon U–Pb age of 46–45 Ma for basaltic rocks in the Sanshui Basin. The latter basalts are thought to have been generated by partial melting of a depleted region of the mantle that generated continental rift-type magmatic rocks (Y. Dong Y. X. et al., 2006; W. Zhang and Fang, 2014), or partial melting of an enriched region of the mantle within a continental rift setting (Hu et al., 2013). The Sanshui basalts yield recalculated εNd(t) values of −0.77 to +1.23 (mean age 50 Ma) (Zhu et al., 1991) that reflect the weakly depleted nature of the Eocene mantle in coastal SE China. The basalt, gabbro, and diabase units within the Fuding area have OIB-type geochemical affinities with low initial $^{87}Sr/^{86}Sr$ ratios (average of 0.703865) and high εNd(t) values (average of 3.90) which similar with the depleted mantle. Its OIB type geochemical characteristics may be inherited from crustal materials with similar characteristics. Meanwhile, the widespread Neogene basalts in coastal SE China are exposed in the Xinchang area of Zhejiang Province, the Jiashan area of Anhui province, the Fangshan area of Jiangsu province, and the Sanshui Basin in Guangdong Province, and all of these Neogene basalts were derived from a depleted region of the mantle (R. Wang and Yang, 1987a, Wang and Yang, 1987b; Zhi et al., 1994). Thus, the mantle beneath coastal SE China evolved between the Cretaceous and the Neogene from enriched to depleted, and this change occurred during the Eocene.

6 CONCLUSION

Whole-rock Ar–Ar analyses of two basalt samples from the Fuding mafic volcanic neck yield ages of 38.5 ± 1.2 and 42.3 ± 2 Ma, indicating that the basalts were erupted at 42.3–38.5 Ma.

The basalt, gabbro, and diabase units within the Fuding area have OIB-type geochemical affinities with low initial $^{87}Sr/^{86}Sr$ ratios (average of 0.703865) and high εNd(t) values (average of 3.90). Both gabbro and diabase units record minor amounts of crustal contamination.

Peridotite xenoliths within the Fuding basalt provide evidence of the nature of the Eocene mantle in this area, especially the post late-Mesozoic evolution of the mantle beneath coastal SE China. The mantle beneath coastal SE China evolved from enriched to depleted between the Cretaceous and the Neogene, with this change occurring during the Eocene.

DATA AVAILABILITY STATEMENT

The original contributions presented in the study are included in the article/supplementary material, further inquiries can be directed to the corresponding author.

AUTHOR CONTRIBUTIONS

XZ designed the study. CL wrote the first draft. YJ analyzed the geochemical data. GX drew some of the figures. MY and ZD completed the geochemical experimental analysis. All authors discussed the results and contributed to the preparation of the manuscript.

FUNDING

This work was supported by Geological Survey projects (DD20221633) of the China Geological Survey, National key research and development program (No 2016YFC0600205) and Geological Survey projects (Nos 121201008000150002, 1212011121098, 121201008000150002, and 12120113070800) of the China Geological Survey.

REFERENCES

Aldanmaz, E., Yaliniz, M. K., Güctekin, A., and Göncüoğlu, M. C. (2008). Geochemical Characteristics of Mafic Lavas from the Neotethyan Ophiolites in Western Turkey: Implications for Heterogeneous Source Contribution during Variable Stages of Ocean Crust Generation. *Geol. Mag.* 145, 37–54. doi:10.1017/s0016756807003986

Bodinier, J.-L., Garrido, C. J., Chanefo, I., Bruguier, O., and Gervilla, F. (2008). Origin of Pyroxenite-Peridotite Veined Mantle by Refertilization Reactions: Evidence from the Ronda Peridotite (Southern Spain). *J. Petrology* 49, 999–1025. doi:10.1093/petrology/egn014

Chen, C.-H., Lee, C.-Y., Lu, H.-Y., and Hsieh, P.-S. (2008). Generation of Late Cretaceous Silicic Rocks in SE China: Age, Major Element and Numerical Simulation Constraints. *J. Asian earth Sci.* 31, 479–498. doi:10.1016/j.jseaes.2007.08.002

Chen, D. G. (1992). "Geochemistry of Cenozoic Basalts in the Southern Section of Tanlu Fault," in *Geochemistry of Cenozoic Volcanic Rocks of China*. Editor R. X. LIU (Beijing: Earthquake press), 171–209. (in Chinese).

Chen, D. G., Xia, Q. K., and Zhi, X. C. (1997). Geochemistry of Megacrysts in Cenozoic Basalts of Eastern China. *Acta Geosci. Sin.* 18, 299–306. (in Chinese with English abstract).

Cong, B. L., Wang, Q. C., Zhang, H. Z., Yan, X., and Jiang, L. L. (1996). Petrogenesis of Cenozoic Volcanic Rocks in Hefei Basin, China. *Acta Petrol. Sin.* 3, 370–381. (in Chinese with English abstract).

Cui, Y. R., Xie, Z., Wang, B., Chen, J. F., Yu, Y. W., and He, J. F. (2011). Geochemical Characteristics of the Late Mesozoic Basalts in Southeastern Zhejiang Province and Constraints on Magma Source Materials. *Geol. J. China Univ.* 17, 492–512. (in Chinese with English abstract). doi:10.1007/s11769-011-0446-4

Dai, Q. Z., and Chen, R. K. (2008). On the Geologic Characteristics and Formation Mechanisms of the Basalt Pillars in Shanhoujian, Fuding City. *Geol. Fujian* 4, 369–377. (in Chinese with English abstract).

Deng, J. F., E, M. L., and Lu, F. X. (1988). The Chemistry of Hannuoba Basalts and Their Trends of Magmatic Revolution. *Acta Petrol. Sin.* 4, 22–33. (in Chinese with English abstract).

Depaolo, D. J. (1988). *Neodymium Isotope Geochemistry: An Introduction*. New York: Springer-Verlag, 181.

Dong, C. W., Xu, X. S., Chen, X. M., and Zhou, X. M. (1997). Mineralogical Record of Crystallization Processes of Pingtan Hornblende Gabbro, Fujian. *Acta Mineral. Sin.* 17, 285–290. (in Chinese with English abstract).

Dong, C. W., Xu, X. S., Yan, Q., Lin, X. B., and Zhu, G. Q. (2007). A New Case of Late Mesozoic Crust-Mantle Interaction in Eastern Zhejiang: Geochronology and Geochemistry of the Ru'ao Diabase-Granite Composite Intrusions. *Acta Petrol. Sin.* 23, 1303–1312. (in Chinese with English abstract). doi:10.3969/j.issn.1000-0569.2007.06.007

Dong, C. W., Zhang, D. R., Xu, X. S., Yan, Q., and Zhu, G. Q. (2006a). SHRIMP U-Pb Dating and Litho Geochemistry of Basic-Intermediate Dike Swarms

from Jinjiang, Fujian Province. *Acta Petrol. Sin.* 22, 1696–1702. (in Chinese with English abstract). doi:10.1016/j.sedgeo.2006.03.014

Dong, Y. X., Xiao, L., Zhou, H. M., Zeng, G. C., Wang, X. D., Xiang, H., et al. (2006b). Spatial Distribution and Petrological Characteristics of the Bimodal Volcanic Rocks from Sanshui Basin, Guangdong Province: Implication for Basin Dynamics. *Geotect. Metallogenia* 30, 82–92. (in Chinese with English abstract). doi:10.3969/j.issn.1001-1552.2006.01.010

Dong, Z. X., Chen, L. H., Yang, J. M., and Ma, H. W. (1999). The Characteristics of Spinel Compositions in Mantle-Derived Xenoliths from Alkali Basalts and Their Petrogenetic Significance. *Acta Petrol. Sin.* 15, 607–615. (in Chinese with English abstract).

Edwards, C. M. H., Menzies, M. A., Thirlwall, M. F., Morris, J. D., Leeman, W. P., and Harmon, R. S. (1994). The Transition to Potassic Alkaline Volcanism in Island Arcs: The Ringgit--Beser Complex, East Java, Indonesia. *J. Petrology* 35, 1557–1595. doi:10.1093/petrology/35.6.1557

Guo, F., Guo, J. T., Wang, Y., Fan, W. M., Li, C. W., Li, H. X., et al. (2013b). The Genesis of Lower $\delta^{18}O$ Olivine Basalts in Junan and Qingdao Area, Jiangsu-Shangdong Provinces. *Sci. China* 58, 1289–1299. doi:10.1007/s11434-012-5607-z

Guo, F., Guo, J., Wang, Y., Fan, W., Li, C., Li, H., et al. (2013a). A Metasomatized Mantle Wedge Origin for Low-δ 18O Olivine in Late Cretaceous Junan and Qingdao Basalts in the Sulu Orogen. *Chin. Sci. Bull.* 58, 3903–3913. doi:10.1007/s11434-012-5607-z

He, Z. Y., and Xu, X. S. (2011). Petrogenesis of the Late Yanshanian Mantle-Derived Intrusions in Southeastern China: Response to the Geodynamics of Paleo-Pacific Plate Subduction. *Chem. Geol.* 328, 208–221.

Hu, J. J., Li, Q., Zhai, Y. J., Zhang, W., Zhang, Y. F., and Bai, X. Y. (2013). Distribution and Geodynamics of Volcanic Rock of the Huayong Group, Sanshui Basin, Guangdong Province. *J. East China Inst. Technol. Sci.* 36, 175–181. (in Chinese with English abstract). doi:10.3969/j.issn.1674-3504.2013.02.011

Jahn, B.-M., and Condie, K. C. (1995). Evolution of the Kaapvaal Craton as Viewed from Geochemical and SmōNd Isotopic Analyses of Intracratonic Pelites. *Geochimica Cosmochimica Acta* 59, 2239–2258. doi:10.1016/0016-7037(95)00103-7

Koppers, A. A. P. (2002). ArArCALC-software for 40Ar/39Ar Age Calculations. *Comput. Geosciences* 28, 605–619. doi:10.1016/s0098-3004(01)00095-4

LeMaitre, R. W., Bateman, P., Dudek, A., Keller, J., Lebas, M. J. L., Sabine, P. A., et al. (1989). *A Classication of Igneous Rocks and Glossary of Terms*. Oxford: Blackwell.

Li, H. M., Dong, C. W., Xu, X. S., and Zhou, X. M. (1995). Single Grain Zircon U-Pb Dating of Quanzhou Gabbro: Origin of the Mafic Magmativte in the Southeast Fujian Province. *Chin. Sci. Bull.* 40, 158–160. (in Chinese with English abstract).

Li, L. L., Zhou, H. W., Chen, Z. H., Wang, J. R., and Xiao, Y. (2011). Geochemical Characteristics of Granites in Taimushan Area, Fujian Province, and Their Geological Significance. *Acta Petrologica Mineralogica* 30, 593–609. (in Chinese with English abstract). doi:10.1007/s11589-011-0776-4

Li, T. F., and Ma, H. W. (2002). Clinopyroxene-melt Equilibrium Temperature and Pressure of Cenozoic Basalts with Special Reference to the Genesis of Mantle Xenoliths in Some Areas of Eastern China. *Acta Petrologica Mineralogica* 21, 11–23. (in Chinese with English abstract).

Li, X.-h. (2000). Cretaceous Magmatism and Lithospheric Extension in Southeast China. *J. Asian Earth Sci.* 18, 293–305. doi:10.1016/s1367-9120(99)00060-7

Li, X.-H., Li, Z.-X., Li, W.-X., Liu, Y., Yuan, C., Wei, G., et al. (2007). U-pb Zircon, Geochemical and Sr-Nd-Hf Isotopic Constraints on Age and Origin of Jurassic I- and A-type Granites from Central Guangdong, SE China: A Major Igneous Event in Response to Foundering of a Subducted Flat-Slab? *Lithos* 96, 186–204. doi:10.1016/j.lithos.2006.09.018

Li, Z.-X., and Li, X.-H. (2007). Formation of the 1300-km-wide Intracontinental Orogen and Postorogenic Magmatic Province in Mesozoic South China: A Flat-Slab Subduction Model. *Geol* 35, 179–182. doi:10.1130/g23193a.1

Liu, C. Q., Xie, G. H., and Akimasa, M. (1995). Geochemistry of Cenozoic Basalts from Eastern China--I. Major Element and Trace Element Compositions: Petrogenesis and Characteristics of Mantle Source. *Geochimica* 24, 1–19. (in Chinese with English abstract). doi:10.1016/S1872-5813(08)60001-8

Liu, J. H., and Yan, J. (2007). Peridotitic Xenoliths in the Cenozoic Basalts from the Subei Basin. *Mineral. Pet.* 27, 39–46. (in Chinese with English abstract).

Lu, Q. D., Zhu, G. L., and Qing, Z. J. (2000). Geochemical Feature and Genesis of the Mesozoic and Cenozoic Basalt in Fujian Province. *Regional Geol. China* 19, 85–91. (in Chinese with English abstract).

Mahéo, G., Bertrand, H., Guillot, S., Villa, I. M., Keller, F., and Capiez, P. (2004). The South Ladakh Ophiolites (NW Himalaya, India): an Intra-oceanic Tholeiitic Arc Origin with Implication for the Closure of the Neo-Tethys. *Chem. Geol.* 203, 273–303. doi:10.1016/j.chemgeo.2003.10.007

Meschede, M. (1986). A Method of Discriminating between Different Types of Mid-ocean Ridge Basalts and Continental Tholeiites with the Nbō1bZrō1bY Diagram. *Chem. Geol.* 56, 207–218. doi:10.1016/0009-2541(86)90004-5

Middlemost, E. A. K. (1994). Naming Materials in the Magma/igneous Rock System. *Earth-Science Rev.* 37, 215–224. doi:10.1016/0012-8252(94)90029-9

Pearce, J. A. (1996). "A User's Guide to Basalt Discrimination Diagrams," in *Trace Element Geochemistry of Volcanic Rocks: Applications for Massive Sulfide Exploration*. Editor D. A. Wyman (St. John's,Canada: Geological Association of Canada), 12, 79–113.

Pearce, J. A., and Peate, D. W. (1995). Tectonic Implications of the Composition of Volcanic Arc Magmas. *Annu. Rev. Earth Planet. Sci.* 23, 251–285. doi:10.1146/annurev.ea.23.050195.001343

Pei, F. P., Xu, W. L., Wang, Q. H., Wang, D. Y., and Lin, J. Q. (2004). Mesozoic Basalt and Mineral Chemistry of the Mantle-Derived Xenocrysts in Feixian, Western Shandong, China: Constraints on Nature of Mesozoic Lithospheric Mantle. *Geol. J. China Univ.* 10, 88–97. (in Chinese with English abstract). doi:10.1007/BF02873097

Qian, Q., and Li, K. Y. (1996). The Geological Time of Basalt and Strata in North Jiangsu Basin. *Volcanol. Mineral. Resour.* 17, 86–93. (in Chinese with English abstract).

Qiu, H., and Jiang, Y. (2007). Sphalerite 40Ar/39Ar Progressive Crushing and Stepwise Heating Techniques. *Earth Planet. Sci. Lett.* 256, 224–232. doi:10.1016/j.epsl.2007.01.028

Qiu, J. S., Wang, D. Z., and Zhou, J. C. (1999). Geochemistry and Petrogenesis of the Late Mesozoic Bimodal Volcanic Rocks at Yunshan Caldera, Yongtai Country, Fujian Province. *Acta petrologica Mineralogica* 18, 97–107. (in Chinese with English abstract.

Saccani, E., and Photiades, A. (2005). Petrogenesis and Tectonomagmatic Significance of Volcanic and Subvolcanic Rocks in the Albanide-Hellenide Ophiolitic Melanges. *Isl. Arc* 14, 494–516. doi:10.1111/j.1440-1738.2005.00480.x

Shen, W. Z., Hong, L. F., and Li, W. X. (1999). Study on the Sr-Nd Isotopic Compositions of Granitoids in SE China. *Geol. J. China Univ.* 5, 22–32. (in Chinese with English abstract). doi:10.1007/BF02885998

Shervais, J. W. (1982). Ti-V Plots and the Petrogenesis of Modern and Ophiolitic Lavas. *Earth Planet. Sci. Lett.* 59, 101–118. doi:10.1016/0012-821x(82)90120-0

Sun, S.-s., and Mcdonough, W. F. (1989). Chemical and Isotopic Systematics of Oceanic Basalts: Implications for Mantle Composition and Processes. *Geol. Soc. Lond. Spec. Publ.* 42, 313–345. doi:10.1144/gsl.sp.1989.042.01.19

Tang, L. M., Chen, H. L., Dong, C. W., Shen, Z. Y., Cheng, X. G., and Fu, L. L. (2010). Late Mesozoic Tectonic Extension in SE China: Evidence from the Basic Dike Swarms in Hainan Island, China. *Acta Petrol. Sin.* 26, 1204–1216. (in Chinese with English abstract). doi:10.1016/j.sedgeo.2010.03.004

Tatsumoto, M., Basu, A. R., Wankang, H., Junwen, W., and Guanghong, X. (1992). Sr, Nd, and Pb Isotopes of Ultramafic Xenoliths in Volcanic Rocks of Eastern China: Enriched Components EMI and EMII in Subcontinental Lithosphere. *Earth Planet. Sci. Lett.* 113, 107–128. doi:10.1016/0012-821x(92)90214-g

Wang, D. Y., Xu, W. L., Feng, H., Lin, J. Q., and Zheng, C. Q. (2002). Nature of Mesozoic Lithospheric Mantle in Western Liaoning Province: Evidences from Basalt and the Mantle-Derived Xenoliths. *J. Jilin Univ. (Earth Sci. Ed.* 32, 319–324. (in Chinese with English abstract). doi:10.13278/j.cnki.jjuese.2002.04.002

Wang, D. Z., and Shen, W. Z. (2003). Genesis of Granitoids and Crustal Evolution in Southeast China. *Earth Sci. Front.* 10, 209–220. (in Chinese with English abstract).

Wang, R. J., and Yang, S. R. (1987b). On the Evolution and Mineral Chemistry of Olivine, Pyroxene, Plagioclase in Cenozoic Basalts from the Chenxian-Xinchang Basin in Zhejiang Province. *Acta Petrol. Sin.* 2, 27–39. (in Chinese with English abstract).

Wang, R. J., and Yang, S. R. (1987a). The Study of Cenozoic Basalts and its Xenolithos in Shengxian Area, Zhejiang Province. *Earth Sci. J. Wuhan Geol. Coll.* 12, 241–248. (in Chinese).

Wang, S. X. (1998). Discussion of the Chemical Composition of Different-Time Basalt Series and its Formation Environment in Fujian Province. *Geol. Fujian* 18, 68–80. (in Chinese with English abstract).

Wang, X.-C., Li, Z.-X., Li, X.-H., Li, J., Liu, Y., Long, W.-G., et al. (2012). Temperature, Pressure, and Composition of the Mantle Source Region of Late Cenozoic Basalts in Hainan Island, SE Asia: a Consequence of a Young Thermal Mantle Plume Close to Subduction Zones? *J. petrology* 53, 177–233. doi:10.1093/petrology/egr061

Xia, Q. K., Xing, L. B., Feng, M., Liu, S. C., Yang, X. Z., and Hao, Y. T. (2010). Water Content and Element Geochemistry of Peridotite Xenoliths Hosted by Early-Jurassic Basalt in Ningyuan, Hunan Province. *Acta Petrologica Mineralogical* 29, 113–124. (in Chinese with English abstract). doi:10.3724/SP.J.1084.2010.00199

Xiao, L., Zhou, H. M., Dong, Y. X., Zeng, G. C., and Wang, F. Z. (2006). Geochemistry and Petrogenesis of Cenozoic Volcanic Rocks from Sanshui Basin: Implications for Spatial and Temporal Variation of Rock Types and Constraints on the Formation of South china Sea. *Geotect. Metallogenia* 30, 72–81. (in Chinese with English abstract). doi:10.1007/s11442-006-0415-5

Xie, G. Q., Mao, J. W., Hu, R. Z., Li, R. L., and Cao, J. (2005). Discussion on Some Problems of Mesozoic and Cenozoic Geodynamics of Southeast China. *Geol. Rev.* 51, 613–620. (in Chinese with English abstract).

Xie, X., Xu, X. S., Zou, H. B., and Xing, G. F. (2001). Trace Element and Nd-Sr-Pb Isotope Studies of Mesozoic and Cenozoic Basalts in Coastal Area of SE China. *Acta Petrol. Sin.* 17, 617–628. (in Chinese with English abstract).

Xing, G. F., Yang, Z. L., and Tao, K. Y. (1999). Sources of Cretaceous Bimodal Volcanic Rocks in the Coastal Region of Southeastern China-Constraints of the Sr Conten and its Isotopes. *Acta Geol. Sin.* 73, 84–92.

Xu, W. L., Zhou, Q. J., and YangYang, D. B. J. H. (2013). Timing, Style and Process of Modifying Adjacent Lithospheric Mantle by Melts Derived from Deeply Subducted Continental Crust: Evidence from Peridotite and Pyroxenite Xenoliths in Western Shandong. Chinese. *Sci. Bull.* 58, 2300–2305. (in Chinese with English abstract).

Xu, X., Griffin, W. L., O'Reilly, S. Y., Pearson, N. J., Geng, H., and Zheng, J. (2008). Re-Os Isotopes of Sulfides in Mantle Xenoliths from Eastern China: Progressive Modification of Lithospheric Mantle. *Lithos* 102, 43–64. doi:10.1016/j.lithos.2007.06.010

Xu, X. S., and Xie, X. (2005). Late Mesozoic-Cenozoic Basaltic Rocks and Crust-Mantle Interaction, SE China. *Geol. J. China Univ.* 11, 318–334. (in Chinese with English abstract).

Xue, H. M., Tao, K, Y., and Shen, J. L. (1996). Sr and Nd Isotopic Characteristics and Magma Genesis of Mesozoic Volcanic Rocks along the Coastal Region of Southeastern china. *Acta Geol. Sin.* 70, 35–47. (in Chinese with English abstract). doi:10.1111/j.1755-6724.1996.mp9003004.x

Yan, J., Chen, J. F., Xie, Z., Gao, T. S., Foland, K. A., Zhang, X. D., et al. (2005a). Studies on Petrology and Geochemistry of the Later Cretaceous Basalts and Mantle-Derived Xenoliths from Eastern Shandong. *Acta Petrol. Sin.* 219, 99–112. (in Chinese with English abstract).

Yan, J., Chen, J. F., Xie, Z., Yang, G., Yu, G., and Qian, H. (2005b). Geochemistry of Late Mesozoic Basalt from Kedoushan in Middle and Lower Yangtze Regions: Constraints on Characteristics and Evolution of the Lithospheric Mantle. *Geochemica* 34, 455–469. (in Chinese with English abstract).

Yan, J., Chen, J. F., Yu, G., Qian, H., and Zhou, X. (2003). Pb Isotopic Characteristics of Late Mesozoic Mafic Rocks from the Lower Yangtze Region: Evidence for Enriched Mantle. *Geol. J. China Univ.* 9, 195–206. (in Chinese with English abstract).

Yan, Q. S., Shi, X. F., Wang, K. S., and Bu, W. R. (2007). Mineral Chemistry and its Genetic Significance of Olivine in Cenozoic Basalts from the South China Sea. *Acta Petrol. Sin.* 23, 2981–2989. (in Chinese with English abstract). doi:10.1631/jzus.2007.B0900

Yang, G. C., Yang, X. Z., Hao, Y. T., and Xia, Q. K. (2012). Water Content Difference between Continental Lower Crust and Lithospheric Mantle: Granulite and Peridotite Xenoliths Hosted in Basalts from Junan, Shandong Province. *Acta Petrologica Mineralogica* 31, 691–700. (in Chinese with English abstract). doi:10.1007/s11783-011-0280-z

Yang, X.-Z., Xia, Q.-K., Deloule, E., Dallai, L., Fan, Q.-C., and Feng, M. (2008). Water in Minerals of the Continental Lithospheric Mantle and Overlying Lower Crust: A Comparative Study of Peridotite and Granulite Xenoliths from the North China Craton. *Chem. Geol.* 256, 33–45. doi:10.1016/j.chemgeo.2008.07.020

Yang, Z. L., Shen, W. Z., Tao, K. Y., and Shen, J. L. (1999). Sr, Nd and Pb Isotopic Characteristics of Early Cretaceous Basaltic Rocks from the Coast of Zhejiang and Fujian: Evidences for Ancient Enrichied Mantle Source. *Sci. Geol. Sin.* 34, 59–67. (in Chinese with English abstract).

Ying, J.-F., Zhang, H.-F., and Tang, Y.-J. (2010). Lower Crustal Xenoliths from Junan, Shandong Province and Their Bearing on the Nature of the Lower Crust beneath the North China Craton. *Lithos* 119, 363–376. doi:10.1016/j.lithos.2010.07.015

Ying, J. F., Zhang, H. F., Zhou, X. H., and Tang, Y. J. (2013). Tectonic Affinity of the Sub-continental Lithosphere of the Sulu Orogenic Belts: Constraints from Granulite and Peridotites Xenoliths. *Bull. Mineralogy, Petrology Geochem.* 32, 328–334. (in Chinese with English abstract).

Yu, Y. W., Zhou, T. X., and Chen, J. F. (1993). The Characteristics and Genesis of Early Cretaceous Bimodal Volcanic Rocks in Xuantandi Area, Zhejiang Province. *J. Nanjing Univ. Nat. Sci.* 5, 420–429. (in Chinese with English abstract).

Zeng, L., Gao, L.-E., Dong, C., and Tang, S. (2012). High-pressure Melting of Metapelite and the Formation of Ca-Rich Granitic Melts in the Namche Barwa Massif, Southern Tibet. *Gondwana Res.* 21, 138–151. doi:10.1016/j.gr.2011.07.023

Zhang, B. T., Chen, P. R., Ling, H. F., and Kong, X. G. (2004). Pb-Nd-Sr Isotopic Study of the Middle Jurassic Basalts in Southern Jiangxi Province: Characteristic of Mantle Source and Tectonic Implication. *Geol. J. China Univ.* 10, 145–156. (in Chinese with English abstract). doi:10.1142/9789812565839_0011

Zhang, H. F., Zhou, X. H., Fan, W. M., Sun, M., Guo, F., Ying, J. F., et al. (2005). Nature, Composition, Enrichment Processes and its Mechanism of the Mesozoic Lithospheric Mantle beneath the Southeastern North China Craton. *Acta Petrol. Sin.* 21, 1271–1280. (in Chinese with English abstract). doi:10.1016/j.sedgeo.2005.05.009

Zhang, J. C., and Lu, Q. D. (1997). On the Characteristics and Origin of the Cenozoic Basalts in Fujian Province. *Geol. Fujian* 1, 1–9. (in Chinese with English abstract).

Zhang, W., and Fang, N. Q. (2014). Geochemistry Characteristics of Eocene Volcanic Rocks in Sanshui Basin, Guangdong. *Earth Science-Journal China Univ. Geosciences* 39, 37–44. (in Chinese with English abstract). doi:10.4028/www.scientific.net/AMM.275-277.322

Zhang, X. Q., Zhou, X. P., and Chen, X. Y. (1993). *The Atlas of Cretaceous-Paleogene Drilling Stratigraphic in Sanshui Basin*. Beijing: China ocean Press, 183. (in Chinese).

Zhao, J.-H., and Zhou, M.-F. (2007). Geochemistry of Neoproterozoic Mafic Intrusions in the Panzhihua District (Sichuan Province, SW China): Implications for Subduction-Related Metasomatism in the Upper Mantle. *Precambrian Res.* 152, 27–47. doi:10.1016/j.precamres.2006.09.002

Zheng, C. Q., Xu, W. L., and Wang, D. Y. (1999). The Petrology and Mineral Chemistry of the Deep-Seated Xenoliths in Mesozoic Basalt in Fuxin District from Western Liaoning. *Acta Petrol. Sin.* 15, 616–622. (in Chinese with English abstract).

Zhi, X. C., Chen, D. G., Zhang, Z. Q., and Wang, J. H. (1994). Neodymium and Strontium Isotopic Compositions for Later Tertiary Alkalic Basalts from Liuhe-Yizheng, Jiangsu Province, China. *Acta Petrol. Sin.* 10, 383–390. (in Chinese with English abstract).

Zhi, X. C., and Qin, X. (2004). Re-Os Isotope Geochemistry of Mantle-Derived Peridotite Xenoliths from Eastern China: Constraints on the Age and Thinning of Lithosphere Mantle. *Acta Petrol. Sin.* 20, 989–998. (in Chinese with English abstract). doi:10.2116/analsci.20.717

Zhou, J. C., and Chen, R. (2001). Late Mesozoic Interaction between Crust and Mantle in Coastal Area of Zhejiang-Fujian. *Prog. Nat. Sci.* 10, 714–717. doi:10.2183/pjab.76.97

Zhou, Q. J., Xu, W. L., Yang, D. B., Pei, F. P., Wang, W., Yuan, H. L., et al. (2013). Modification of the Lithospheric Mantle by Melt Derived from Recycled Continental Crust Evidenced by Wehrlite Xenoliths in Early Cretaceous High-Mg Diorites from Western Shandong. *Sci. China (Earth Sci.* 43, 1179–1194. (in Chinese with English abstract). doi:10.1007/s11430-012-4533-x

Zhou, Q., Wu, F. Y., Chu, Z. Y., and Ge, W. C. (2010). Isotopic Compositions of Mantle Xenoliths and Age of the Lithospheric Mantle in Yitong, Jilin Province. *Acta Petrol. Sin.* 26, 1241–1264. (in Chinese with English abstract).

Zhou, X. H. (1992). "The Discovery of Cenozoic Transition Series Basalts: the Study of its Geochemical Characteristics and Genesis," in *The Chronology and Geochemistry of Cenozoic Volcanic Rocks in China*. Editor U. R. X. Li (Beijing: Earthquake Press), 285–297. (in Chinese).

Zhou, X., Sun, T., Shen, W., Shu, L., and Niu, Y. (2006). Petrogenesis of Mesozoic Granitoids and Volcanic Rocks in South China: a Response to Tectonic Evolution. *Episodes* 29, 26–33. doi:10.18814/epiiugs/2006/v29i1/004

Zhu, B. Q., Wang, H. F., Mao, C. X., Zhu, N. J., Huang, R. S., Peng, J. H., et al. (1991). Geochonology and Nd-Sr-Pb Isotopic Evidence for Mantle Source in the Ancient Subduction Zone beneath Sanshui Basin, Guangdong Province, China. *Geochemica* 1, 27–32. (in Chinese with English abstract). doi:10.1007/bf02842215

Zou, H., Zindler, A., Xu, X., and Qi, Q. (2000). Major, Trace Element, and Nd, Sr and Pb Isotope Studies of Cenozoic Basalts in SE China: Mantle Sources, Regional Variations, and Tectonic Significance. *Chem. Geol.* 171, 33–47. doi:10.1016/s0009-2541(00)00243-6

Conflict of Interest: The authors declare that the research was conducted in the absence of any commercial or financial relationships that could be construed as a potential conflict of interest.

frontiers | Frontiers in Earth Science

ORIGINAL RESEARCH
published: 24 June 2022
doi: 10.3389/feart.2022.951553

Geochemical Analogy Viscosity of Mid-Ocean Ridge Basalt as an Indicator for Determining the Location of Seafloor Hydrothermal Fields?

Chuanshun Li[1,2], *Guohuai Wang*[3]*, *Shijuan Yan*[1,2] *and Dewen Du*[1,2]

[1]First Institute of Oceanography, Ministry of Natural and Resources, Qingdao, China, [2]Laboratory for Marine Mineral Resources, Pilot National Laboratory for Marine Science and Technology, Qingdao, China, [3]Tianjin Geology Research and Marine Geological Center, Tianjin, China

Many achievements have been made in the exploration of seafloor polymetallic hydrothermal vents, however, it needs to further study how to discovery more potential new hydrothermal or massive sulfide fields. In this study, we collected 9818 major-element geochemical data sets of basalt samples from the Mid-Atlantic Ridge (MAR, 78°N–53°S) and the seafloor topographic data for eleven known hydrothermal vents (e.g., TAG, Snake Pit, MAR 22°30′N, Lilliput). Based on the different spatial distances between basalts and hydrothermal vents, we classified all the basalts into three categories: 1) basalt near known vent (focal objects of the research, 29 samples), 2) basalt around known vent (observed objects, 155 samples), and 3) other basalt of the MAR (as background basalt). Meanwhile, we used major element components of basalts to calculate the analogy viscosity and analyzed the possible correlation between analogy viscosity and the spatial distribution of seafloor hydrothermal vents. We found that the analogy viscosity of basalt near known vent fall into a narrow medium value range (~46.8–68.5 Pa s) contrasted with the range of background basalt values range (~4.0–356.0 Pa·s). It infers that these basalts on the Mid-Atlantic Ridge with the medium values of analogy viscosity favor the formation of hydrothermal vents. However, due to the complexities of magmatic activity and fault structure, as well as the multi-stage water-rock reaction, whether the analogy viscosity of basalts can be used as an indicator for determining the location of seafloor hydrothermal field or not needs further verification. Hence, this paper provides a possible rule (the variation of analogy viscosity estimated by major element components in the basalts) for exploration the location of hydrothermal vents rather than a fully developed method.

Keywords: basalt, geochemical characteristics, hydrothermal vents, Mid-Atlantic Ridge, viscosity

OPEN ACCESS

Edited by:
Shengyao Yu,
Ocean University of China, China

Reviewed by:
Qian Wang,
Shandong University of Science and Technology, China
Liming Dai,
OUC, China

***Correspondence:**
Guohuai Wang
18306485567@sina

Specialty section:
This article was submitted to Petrology, a section of the journal Frontiers in Earth Science

Received: *24 May 2022*
Accepted: *31 May 2022*
Published: *24 June 2022*

Citation:
Li C, Wang G, Yan S and Du D (2022) Geochemical Analogy Viscosity of Mid-Ocean Ridge Basalt as an Indicator for Determining the Location of Seafloor Hydrothermal Fields? Front. Earth Sci. 10:951553. doi: 10.3389/feart.2022.951553

INTRODUCTION

Hydrothermal fields are rich in biological and mineral resources and provide a window to the Earth's depth. Finding and studying hydrothermal vents is one of the most interesting scientific aims worldwide. However, finding hydrothermal vents, especially those inactive hydrothermal zones on the vast, and dark seafloor, which is covered by several kilometers of water, is an extremely

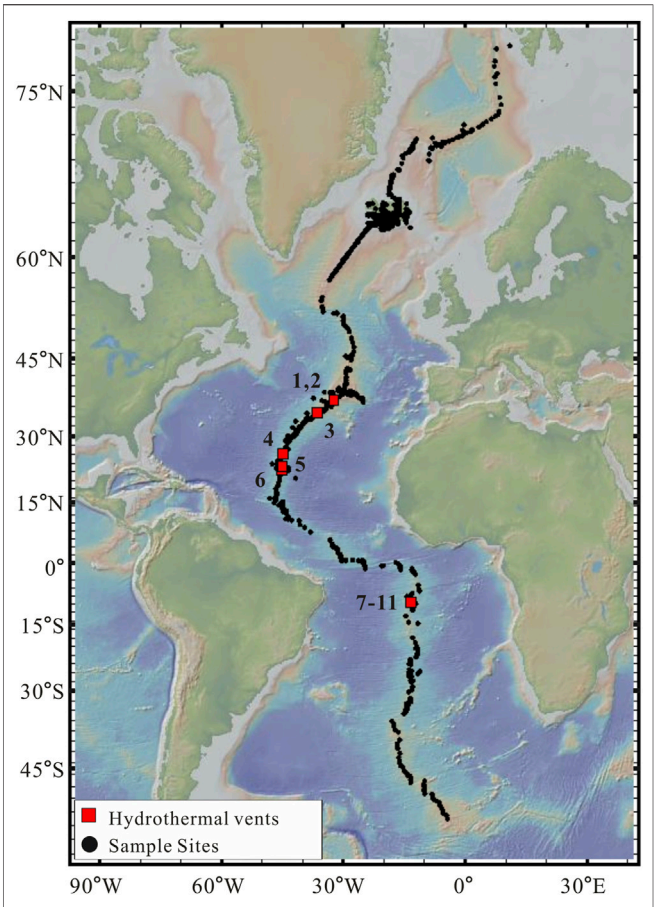

FIGURE 1 | Basalt sampling sites and locations of the 11 known seabed hydrothermal vents (for information, see **Table 1**). Shaded relief bathymetric map from GeoMapApp, 2021.

challenging task. The vicinities of seafloor hydrothermal fields exhibit special characteristics: higher anomalies of heat flow on the seafloor (e.g., Chiba et al., 2001; Dias et al., 2010; Schmidt et al., 2011), frequent seismic activity (e.g., Johnson et al., 2000; Seewald et al., 2003; Crone et al., 2010), oceanic core complex outcrop and detachments around some of the vents (e.g., Morris et al., 2009; Cheadle and Grimes, 2010; Macleod et al., 2011), increased turbidity on the seafloor (e.g., Baker et al., 2006), and high magnetic anomalies (e.g., Miranda et al., 2005; Rona et al., 2013). According to Baker and German (2004), hydrothermal activity is positively correlated with the full spreading rate of the mid-ocean ridge. The search for new indicators of hydrothermal vents will therefore assist both the study and exploration of these fascinating appearances.

The geochemical characteristics of basalt near hydrothermal vents differ from those of normal mid-ocean ridge basalt (N-MORB) in the Mid-Atlantic Ridge (MAR). Wang et al. (2014) reported that the basalt of the 49.6°E hydrothermal field on the southwest Indian Ridge is richer in K_2O, Na_2O, Fe_2O_3, and MnO, and poorer in SiO_2 and Al_2O_3, than N-MORB. Gale et al. (2013b) compared the compositions of basaltic glass in the French American Mid-Ocean Undersea Study (FAMOUS) data and North FAMOUS segment. Basaltic glass on the North FAMOUS segment, which is near a hydrothermal vent, is rich in SiO_2, FeO, TiO_2, and K_2O and poor in Al_2O_3, CaO, and MgO. The viscosity of basalt might reflect its geochemical characteristics (Zhu et al., 1997). It is an important physical property that affects the rising, crystallization differentiation, degassing, ejection, and other behaviors of magma (e.g., Papale, 1999; Sparks, 2003; Dingwell, 2006) and restricts the occurrence, topography, and other features of basalt. By analyzing the viscosity difference between the basalt around known vents (BNV) and the background basalt of MAR, we might obtain a new identifying indicator of hydrothermal vents.

Seafloor hydrothermal activity was first discovered in 1948 (Bruneau et al., 1953). In 1985, the first active hydrothermal field, the trans-Atlantic geotraverse (TAG) field, was discovered in the MAR (Rona et al., 1986). Since then, 721 hydrothermal seabed vents have been discovered worldwide. Among these, 304 have been confirmed as active, 362 have been inferred as active, and more than 50% are located in the mid-ocean ridge (The InterRidge Database, 2020, Accessed date is 2021. 03. 21). By studying the known hydrothermal vents, we might reveal their

TABLE 1 | Hydrothermal vents of MAR.

Name id	Number	Activity	Latitude/°	Longitude/°	Maximum depth/m	Full spreading rate/mm·a^{-1}	References
Lucky strike	1	active, confirmed	37.29422	−32.29217	1740	20.2	InterRidge vent database, 2000
Evan	2	active, confirmed	37.2667	−32.2833	1775	20.2	InterRidge vent database, 2000
S oceanographer	3	active, inferred	34.867	−36.433	3,460	21.1	InterRidge vent database, 2000
TAG	4	active, confirmed	26.1369	−44.8259	3,670	23.6	InterRidge vent database, 2000
Snake pit	5	active, confirmed	23.3683	−44.95	3,500	24.1	InterRidge vent database, 2000
MAR, 22°30′N	6	inactive	22.4994	−44.9999	2,800	24.3	InterRidge vent database, 2000
Lustrog-1	7	active, confirmed	−9.54433	−13.20883	1,501	33.2	Haase et al. (2009)
Lustrog-2	8	active, confirmed	−9.54417	−13.20867	1,505	33.2	Haase et al. (2009)
Main lilliput	9	active, confirmed	−9.54733	−13.2085	1,495	33.2	Haase et al. (2009)
Limtoc	10	active, confirmed	−9.5495	−13.20833	1,494	33.2	Haase et al. (2009)
Roman ruins	11	active, confirmed	−9.55183	−13.20667	1,495	33.2	Haase et al. (2009)

The position in bathymetric map of MAR 22°30′N, lucky strike and Evan vents is corrected by the depth. Positive latitude represents north latitude; negative value represents south latitude. And positive longitude represents east longitude, negative value represents west longitude. Data from interridge global database of active submarine hydrothermal vent Fields (the interridge vent database) (http://vents-data.interridge.org).

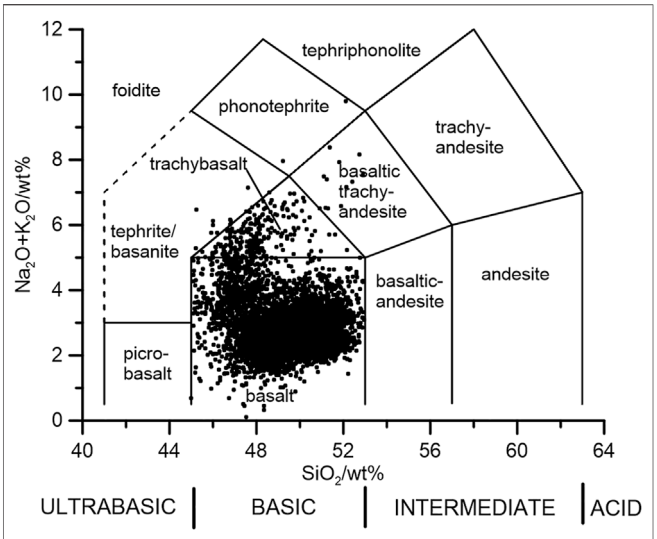

FIGURE 2 | TAS classification of samples collected from the MAR.

spatial distribution rules and control factors. To determine the differences in the major elements and viscosities of the BNV and background basalt on the MAR, we collected and analyzed thousands of basalt datasets sampled from the MAR. This paper reports the findings of the study.

DATA AND METHODS

Petro-Geochemistry Data

More than 35,000 datasets of rock/glass samples from the MAR were collected and preliminarily analyzed. Some of these samples were located near 11 known hydrothermal vents. The locations and basic information of the samples near the 11 vents, on which this research focuses, are presented in **Figure 1** and **Table 1**, respectively. The data were mainly collected from the Petrological Database of the Ocean Floor (PetDB, http://www.earthchem.org/petdb/search), a database of global seabed rock (Lehnert et al., 2000) was downloaded on 26 September 2017. In addtition, we also collected some data from Haase et al. (2009). Gale et al. (2013a) used datasets from PetDB to study the mean composition

TABLE 2 | Coefficients for calculation of VFT parameters B and C [A = −4.55 (± 0.21)[a]] from melt compositions expressed as mol% oxides (Giordano et al., 2008).

	Oxides	Values		C-terms	Values
b_1	$SiO_2 + TiO_2$	159.6 (7)	c_1	SiO_2	2.75 (0.4)
b_2	Al_2O_3	−173.3 (22)	c_2	TA[b]	15.7 (1.6)
b_3	$FeO_T + MnO + P_2O_5$	72.1 (14)	c_3	FM[d]	8.3 (0.5)
b_4	MgO	75.7 (13)	c_4	CaO	10.2 (0.7)
b_5	CaO	−39.0 (9)	c_5	NK[e]	−12.3 (1.3)
b_6	$Na_2O + V^b$	84.1 (13)	c_6	ln (1+V)	−99.5 (4)
b_7	$V + \ln(1 + H_2O)$	141.5 (19)	c_{11}	$(Al_2O_3+FM+CaO-P_2O_5)^*(NK+V)$	0.3 (0.04)
b_{11}	$(SiO_2 + TiO_2)^*(FM)$	−2.43 (0.3)			
b_{12}	$(SiO_2 + TA + P_2O_5)^*(NK + H_2O)$	−0.91 (0.3)			
b_{13}	$(Al_2O_3)^*(NK)$	17.6 (1.8)			

[a]*Numbers in brackets indicate 95% confidence limits on values of model coefficients.*
[b]*Sum of H_2O+FeO_T.*
[c]*Sum of $TiO_2+Al_2O_3$.*
[d]*Sum of $FeO_T+MnO+MgO$.*
[e]*Sum of Na_2O+K_2O.*

TABLE 3 | Sample calculation of viscosity (Pa·s) using model coefficients in **Table 2**.

Sample	wt%	$wt\%_N$	mol%	B-terms	Values	C-terms	Values
SiO_2	50.57	50.72	52.44	b_1	8,563.43	c_1	144.20
TiO_2	1.57	1.57	1.22	b_2	−1,607.11	c_2	164.71
Al_2O_3	15.20	15.25	9.27	b_3	634.68	c_3	178.94
FeOT[a]	9.89	9.92	8.54	b_4	970.61	c_4	124.00
MnO	0.22	0.22	0.19	b_5	−474.11	c_5	−33.49
MgO	8.24	8.27	12.82	b_6	−270.56	c_6	−44.68
CaO	10.94	10.98	12.16	b_7	143.74	c_{11}	42.36
Na_2O	2.64	2.65	2.65	b_{11}	−2,810.98		
K_2O	0.11	0.11	0.07	b_{12}	−188.57	A (constant)[c]	−4.55
P_2O_5	0.15	0.15	0.07	b_{13}	444.39	B (computed)[c]	5405.50
H_2O[b]	0.16	0.16	0.57			C (computed)[c]	576.05

[a]*We treat all iron as FeO (Giordano et al., 2008). FeOT, $FeO+0.9^*Fe_2O_3$.*
[b]*Our database doesn't include the H_2O wt%, which can be estimated by the empirical formula $H_2O_{est} = 1.5 \times K_2O$ (Gale et al., 2013a).*
[c]*$\log\eta = A+B/(T-C)$; predicted values for this melt at 1423 K is 67.97.*

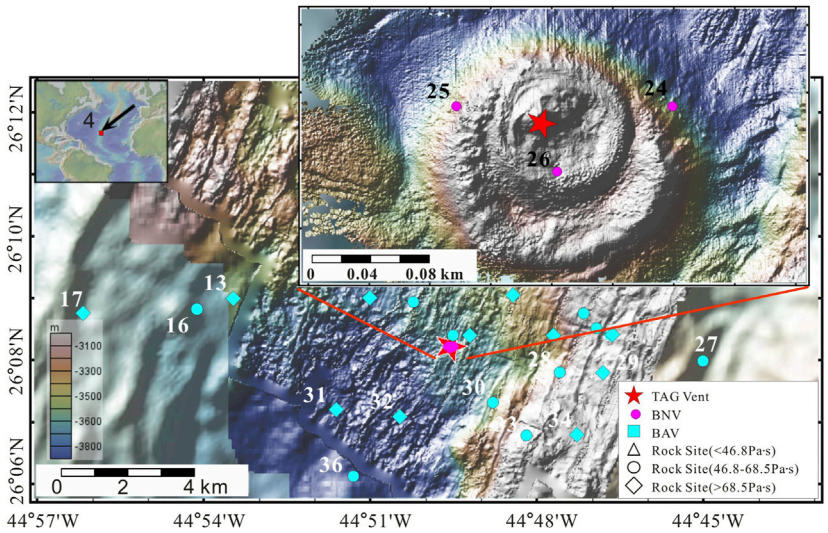

FIGURE 3 | Bathymetric map from GeoMapApp, showing the locations of the TAG vent and the sample sites. The inset (upper left) shows the MAR location of the TW vent. The color bar on the left indicates the depths of the contours (where red represents shallow and blue represents deep). The red star indicates the hydrothermal vent. The pink circle and cyan triangles denote the BNV and BAV sites, respectively. At the sites marked by open triangles, circles, and rhombuses, the basalt viscosity is <46.8, 46.8–68.7, and >68.7 Pa·s, respectively. The vicinities of the vents are delineated by the red boxes.

of mid-ocean ridge basalts and found some geochemical problems associated with Earth composition and evolution.

According to Gale et al. (2013a), the sequence of steps that are required to eliminate questionable or inapplicable analyses and retain only the highest-quality data can be given as follows: 1) Sample location: To assign each sample to the appropriate MAR, only the samples that were located on MAR and its flanks were retained. 2) Altered samples: According to the descriptions that were obtained from PetDB regarding the samples, we eliminated the altered or mineralized rock samples, including those that were altered by seawater. Further, only fresh basalt/basalt glass remained. 3) Complete set of oxides: For the major element data, each sample was required to contain Fe (as FeO and/or Fe_2O_3), SiO_2, TiO_2, Al_2O_3, MgO, CaO, Na_2O, and K_2O. Duplicate samples, which possess identical location and major element compositions, were eliminated. Fe required special attention to determine the total amount of Fe (FeO_T) due to the diverse forms in which it has been reported in PetDB, which is given by Gale et al. (2013a) as $FeO_T = FeO + 0.9 \times Fe_2O_3$. 4) Igneous compositions and major-element sums: Data were further filtered to eliminate the samples outside the basic-rock range because the vast majority of known hydrothermal vents are observed to develop on a basalt basement (only eight known hydrothermal vents are located in the ultramafic basement worldwide). We retained the samples having 45– 53 wt% composition of SiO_2. The final filter to ensure data quality involved a check of the major elemental sum ($SiO_2 + Al_2O_3 + MgO + TiO_2 + FeO_T + CaO + K_2O + Na_2O + MnO + P_2O_5$). Since MnO and P_2O_5 are not analyzed by all the laboratories, we calculated the placeholder values strictly for the sum calculations (MnO = FeOT/54; P_2O_5 was estimated using the polynomial best-fit equation that is based on the K_2O–contents). Further, the sum was estimated as mentioned previously, and any analyses depicting a sum that was either less than 98 wt% or greater than 101 wt% were eliminated. 5) Estimating H_2O: H_2O was estimated using $H_2O_{est} = 1.5 \times K_2O$ (Langmuir et al., 2006) that was applicable for open-ocean ridge basalts. Finally, 9818 datasets were retained to be the study materials. Their locations are illustrated in **Figure 1**. The basalt/basalt glass datasets were classified by their total alkali silica (TAS) (Maitre, 1984). The classification results are shown in **Figure 2**. Most of the samples are basalt; the remaining minority are trachybasalt, basaltic trachyandesite, tephrite/basanite, or phonotephrite. Herein, all samples are referred to as basalt.

Bathymetry Data

Bathymetric maps were taken from the GeoMapApp of the Marine Geoscience Data System on 21 Jan 2022 (GeoMapApp, 2021). Bathymetric data were extracted from the Global Multi-Resolution Topography database with a 100 m grid (for MAR 22°30′N, Snake Pit, the Lilliput field (vents 7–11), and S oceanographer) (Ryan et al., 2009), the Woods Hole Oceanographic Institute (WHOI) with a 20 m grid (Tivey et al., 2003) and a 0.25 m grid (Roman and Singh, 2005; Roman and Singh, 2007) (for TAG), and the WHOI with a 10 m grid (for Lucky Strike and Evan) (Scheirer et al., 2000).

Analogy Viscosity

The earliest models that were used for estimating the viscosity of geologically relevant silicate melts adopted a strict Arrhenius temperature dependence such as the most commonly used Arrhenius model of Fulcher (1925) and Shaw (1972). Giordano et al. (2008) compared their non-Arrhenius model with the model of Shaw (1972) and demonstrated that the former is better. Hence, viscosity was estimated using the model of Giordano et al. (2008) in the following manner:

TABLE 4 | Major elements (wt%) and viscosity of basalt (Pa·s) on TAG vent (data from PetDB).

Type	No.	Lat./°	Lon./°	SiO_2	TiO_2	Al_2O_3	TFeO	MnO	MgO	CaO	Na_2O	K_2O	P_2O_5	H_2O	Visc.
BNV	24	26.137	−44.825	50.57	1.57	15.20	9.89	0.22	8.24	10.94	2.64	0.11	0.15	***0.16***	***67.97***
	25	26.137	−44.8265	49.71	1.60	15.12	9.88	0.17	8.36	10.48	2.73	0.13	0.16	***0.20***	***57.23***
	26	26.1366	−44.8258	49.97	1.61	15.05	10.14	0.17	9.34	11.03	2.29	0.08	0.16	***0.12***	***54.74***
BAV	1	26.2	−44.79	50.97	1.86	15.12	10.44	***0.19***	7.00	10.76	3.00	0.10	0.20	***0.15***	***108.44***
	2	26.19	−44.81	50.18	1.03	16.15	8.28	0.17	9.10	12.32	2.24	0.08	0.08	***0.13***	***48.30***
	3	26.182	−44.84	50.60	1.64	15.07	10.33	0.19	7.90	10.73	2.79	0.10	0.13	***0.15***	***76.95***
	4	26.174	−44.813	50.71	1.56	15.43	9.66	0.18	7.94	11.20	2.83	0.07	0.13	***0.10***	***88.62***
	5	26.174	−44.81	50.57	1.54	15.55	9.68	0.17	8.02	11.25	2.82	0.07	0.12	***0.10***	***82.68***
	6	26.168	−44.839	50.83	1.32	15.72	8.96	0.15	8.75	11.30	2.53	0.08	0.09	***0.11***	***70.44***
	7	26.166	−44.813	50.55	1.47	15.55	9.49	0.15	7.84	11.05	2.82	0.07	0.13	***0.11***	***86.33***
	8	26.162	−44.823	50.52	1.51	15.54	9.61	0.19	8.00	11.23	2.84	0.07	0.13	***0.10***	***80.52***
	9	26.161	−44.79	49.90	1.44	16.05	9.18	0.17	8.70	10.90	2.80	0.10	0.14	***0.15***	***53.50***
	10	26.16	−44.842	51.11	1.90	14.65	10.73	0.19	7.23	10.44	2.95	0.08	0.16	***0.13***	***116.18***
	11	26.158	−44.805	50.81	1.53	15.52	9.50	0.16	7.93	11.00	2.82	0.07	0.14	***0.10***	***92.16***
	12	26.151	−44.807	50.56	1.67	14.99	10.25	0.18	7.95	10.81	2.91	0.07	0.15	***0.10***	***88.33***
	13	26.15	−44.891	50.48	1.39	15.86	9.26	0.16	8.44	11.17	2.59	0.07	0.15	***0.11***	***69.82***
	14	26.15	−44.85	50.22	1.54	15.30	9.48	0.18	7.99	11.00	2.95	0.07	0.15	***0.11***	***82.70***
	15	26.149	−44.837	50.71	1.48	15.50	9.39	0.19	8.60	10.89	2.70	0.12	0.17	***0.17***	***62.46***
	16	26.147	−44.902	50.56	1.23	15.87	9.19	0.19	8.48	11.55	2.50	0.08	0.10	***0.12***	***63.71***
	17	26.146	−44.936	50.37	1.31	15.73	9.01	0.20	8.43	11.44	2.63	0.07	0.13	***0.10***	***71.61***
	18	26.146	−44.786	50.26	1.47	15.26	9.70	0.17	8.72	10.96	2.75	0.11	0.15	***0.16***	***56.59***
	19	26.142	−44.782	50.56	1.47	15.73	9.55	0.18	8.10	11.35	2.68	0.12	0.13	***0.18***	***61.48***
	20	26.14	−44.795	50.82	1.55	14.87	9.94	0.19	7.75	11.41	2.72	0.06	0.14	***0.08***	***102.56***
	21	26.14	−44.82	50.84	1.64	15.62	9.52	***0.18***	7.70	11.22	2.82	0.12	0.13	***0.18***	***78.97***
	22	26.14	−44.778	50.52	1.42	15.58	9.14	0.16	8.37	11.04	2.71	0.07	0.12	***0.10***	***80.29***
	23	26.14	−44.825	49.90	1.63	14.90	9.90	0.18	8.77	11.10	2.82	0.08	0.16	***0.12***	***62.60***
	27	26.133	−44.75	50.67	1.32	16.08	8.69	0.12	8.36	11.37	2.80	0.14	0.15	***0.21***	***55.35***
	28	26.13	−44.793	50.33	0.86	16.05	8.33	0.16	9.64	12.86	1.82	0.03	0.07	***0.04***	***52.80***
	29	26.13	−44.78	51.30	1.55	15.72	9.38	***0.17***	7.78	11.23	2.90	0.08	0.16	***0.12***	***96.20***
	30	26.122	−44.813	49.68	1.54	16.50	9.69	0.19	7.30	11.40	2.94	0.09	0.14	***0.14***	***65.54***
	31	26.12	−44.86	50.80	1.45	15.80	9.22	***0.17***	8.03	11.40	2.65	0.12	0.12	***0.18***	***69.19***
	32	26.118	−44.841	50.71	1.48	15.37	9.76	0.21	8.08	11.24	2.69	0.10	0.14	***0.15***	***71.03***
	32	26.118	−44.841	51.03	1.51	15.29	9.85	0.18	8.06	11.25	2.70	0.10	0.14	***0.15***	***76.52***
	33	26.113	−44.803	49.86	1.23	16.15	9.35	0.22	8.35	11.53	2.77	0.06	0.14	***0.09***	***58.40***
	34	26.113	−44.788	50.65	1.58	15.43	9.28	0.15	8.17	11.03	2.88	0.12	0.18	***0.18***	***69.76***
	35	26.11	−44.73	50.94	1.20	16.42	8.32	***0.15***	8.42	12.00	2.65	0.06	0.10	***0.09***	***76.22***
	35	26.11	−44.73	50.48	1.20	16.57	8.33	***0.15***	8.35	12.00	2.62	0.05	0.11	***0.08***	***74.53***
	35	26.11	−44.73	50.62	1.59	15.42	9.48	***0.18***	7.83	11.33	2.72	0.14	0.15	***0.21***	***69.51***
	36	26.102	−44.855	50.32	1.15	16.26	8.93	0.14	8.74	11.75	2.42	0.06	0.09	***0.08***	***60.61***

*"No." is the number of basalt sampling site, and a plurality of samples can be found around a site. "Lat." is latitude, and "Lon." is longitude. "Visc." is viscosity. "***value***" refers to compute value. Bold values are compute values.*

$$\log \eta = A + B/(T - C) \tag{1}$$

$$B = \sum_{i=1}^{7} (b_i M_i) + \sum_{j=1}^{3} \left[b_{1j} \left(M1_{1j} \times M2_{1j} \right) \right] \tag{2}$$

$$C = \sum_{i=1}^{6} (c_i N_i) + [c_{11} (N1_{11} \times N2_{11})] \tag{3}$$

Here, η is the viscosity of magmatic silicate melt (Pa·s), T is the thermodynamic temperature (K), and A, B, and C are adjustable parameters, including the pre-exponential factor, pseudo-activation energy, and VFT[1]–temperature, respectively.

The optimal values for the 18 model parameters and their corresponding confidence limits are reported in **Table 2**; and a demonstration calculation is provided in **Table 3**. The minimum temperature of tholeiite erupting from the Kilauea volcano (Hawaii) is 1,423 K (Wright et al., 1968), and 1,433 K at a vapor pressure of 1,000 × 10^5 kPa (Xu & Qiu, 2010). Therefore, in the viscosity estimates of **Eq. 1**, we set the melting temperature of oceanic basalt to the middle temperature (1428 K) of the Kilauea tholeiite in 1,000–4,000 m depth range (100 × 10^5–400 × 10^5 kPa) in which vents may appear. Due to constraints such as the water content in the melting basalts was given indirectly with an empirical formula, the analogy viscosity more like a comprehensive geochemical characteristics of basalt than the viscosity value in the physical sense.

THREE CLASSIFICATIONS OF BASALTS

To compare the characteristics of the BNVs and the background basalt on MAR, we classified the basalt samples into three categories based on the spatial distance and topography coherence of their sampling sites to known hydrothermal vents. 1) Basalt near known vent (BNV): The

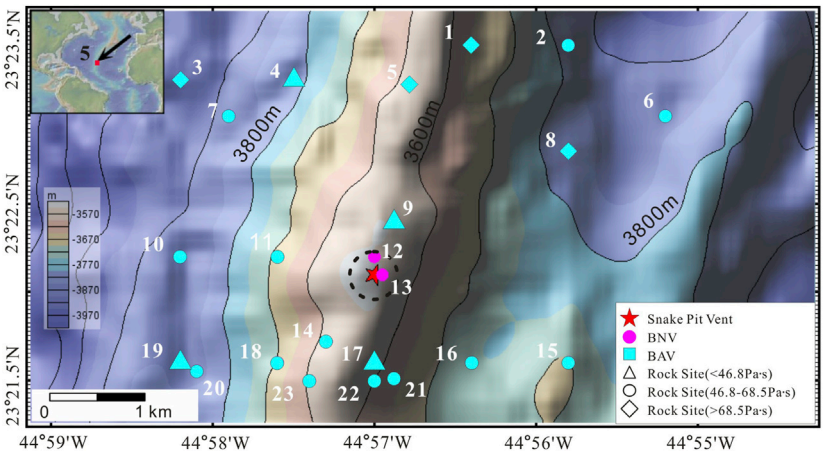

FIGURE 4 | Bathymetric map from GeoMapApp, showing the location of the Snake Pit vent and the sample sites. The dashed circle encloses the range of BNV. Black solid lines are the 10 m isobaths. The symbols and color bar are described in the caption of **Figure 3**.

TABLE 5 | Major elements (wt%) and viscosity of basalt (Pa·s) on snake pit vent (data from PetDB).

Type	No.	Lat./°	Lon./°	SiO_2	TiO_2	Al_2O_3	TFeO	MnO	MgO	CaO	Na_2O	K_2O	P_2O_5	H_2O	Visc
BNV	12	23.37	−44.95	50.25	1.36	16.42	8.84	***0.16***	8.44	11.47	2.66	0.12	0.12	***0.18***	***51.70***
	12	23.37	−44.95	50.12	1.38	16.25	8.96	***0.17***	8.08	11.35	2.80	0.12	0.14	***0.18***	***56.63***
	12	23.37	−44.95	50.15	1.40	16.21	9.04	***0.17***	8.27	11.40	2.85	0.13	0.14	***0.20***	***51.41***
	12	23.37	−44.95	50.62	1.40	16.10	8.90	***0.16***	8.20	11.38	2.78	0.16	0.14	***0.24***	***52.93***
	12	23.37	−44.95	50.78	1.41	16.37	8.92	***0.17***	8.15	11.55	2.80	0.12	0.15	***0.18***	***59.93***
	12	23.37	−44.95	50.27	1.40	16.20	8.90	***0.16***	8.11	11.64	2.81	0.11	0.15	***0.17***	***59.20***
	13	23.3683	−44.9492	49.53	1.40	15.72	8.91	0.16	8.41	11.25	2.83	0.15	0.13	***0.23***	***46.86***
BAV	1	23.39	−44.94	50.63	1.73	15.06	10.31	0.18	7.35	11.13	3.12	0.13	0.19	***0.19***	***75.68***
	2	23.39	−44.93	49.99	1.73	15.52	10.46	0.19	7.55	10.82	3.12	0.15	0.20	***0.22***	***56.94***
	3	23.3867	−44.97	50.92	1.78	14.89	10.19	0.18	7.16	11.21	3.25	0.13	0.21	***0.20***	***83.46***
	4	23.3867	−44.9583	50.12	1.35	16.17	8.80	0.16	8.66	11.44	2.90	0.13	0.18	***0.20***	***46.71***
	5	23.3863	−44.9464	50.66	1.64	15.12	10.03	0.18	7.45	11.15	3.21	0.12	0.20	***0.17***	***77.24***
	6	23.3833	−44.92	50.14	1.60	15.64	9.65	0.18	7.92	11.02	3.08	0.12	0.19	***0.18***	***61.67***
	7	23.3833	−44.965	50.20	1.62	15.69	9.49	0.17	7.89	11.10	3.10	0.14	0.20	***0.21***	***59.88***
	8	23.38	−44.93	50.65	1.34	16.26	8.89	***0.16***	8.33	11.47	2.75	0.10	0.14	***0.15***	***61.66***
	9	23.3733	−44.948	49.46	1.40	15.60	9.01	0.16	8.46	11.17	2.80	0.16	0.14	***0.24***	***44.84***
	10	23.37	−44.97	50.41	1.39	16.22	8.79	***0.16***	8.39	11.40	2.88	0.12	0.13	***10.18***	***55.65***
	10	23.37	−44.97	50.24	1.55	15.78	9.45	***0.18***	7.56	11.52	2.86	0.13	0.14	***0.20***	***64.81***
	10	23.37	−44.97	50.59	1.35	16.50	8.95	***0.17***	8.15	11.53	2.81	0.14	0.14	***0.21***	***51.84***
	10	23.37	−44.97	50.29	1.36	16.41	8.66	***0.16***	8.01	11.68	2.81	0.11	0.13	***0.17***	***60.56***
	11	23.37	−44.96	50.26	1.36	16.34	8.77	***0.16***	8.53	11.49	2.78	0.13	0.13	***0.20***	***49.20***
	14	23.362	−44.955	49.56	1.42	15.91	9.14	0.17	8.23	11.19	2.89	0.14	0.15	***0.22***	***47.52***
	15	23.36	−44.93	50.21	1.69	15.36	10.41	0.19	8.05	10.91	3.00	0.13	0.20	***0.19***	***56.62***
	16	23.36	−44.94	50.47	1.42	16.13	8.84	***0.16***	7.96	11.44	2.82	0.14	0.13	***0.21***	***59.32***
	16	23.36	−44.94	50.44	1.70	15.29	10.07	0.18	7.48	11.15	3.11	0.22	0.22	***0.34***	***51.17***
	17	23.36	−44.95	50.26	1.31	16.54	8.95	***0.17***	8.49	11.32	2.81	0.14	0.16	***0.21***	***45.32***
	18	23.36	−44.96	50.29	1.43	15.92	9.34	0.16	8.27	11.42	2.94	0.15	0.20	***0.22***	***49.04***
	19	23.36	−44.97	50.24	1.74	15.59	9.95	0.18	7.50	10.79	3.19	0.25	0.23	***0.38***	***46.36***
	20	23.3592	−44.9683	50.22	1.65	15.64	9.85	0.17	7.75	11.22	3.13	0.14	0.22	***0.21***	***58.36***
	21	23.3585	−44.948	49.78	1.62	15.67	9.55	0.17	7.36	11.18	2.98	0.23	0.17	***0.35***	***48.09***
	22	23.3583	−44.95	50.59	1.69	15.43	9.98	0.18	7.69	11.21	3.09	0.22	0.22	***0.33***	***49.33***
	23	23.3583	−44.9567	50.16	1.71	15.48	10.14	0.18	7.87	10.96	3.08	0.13	0.21	***0.20***	***59.71***

Bold values are compute values.

BNV samples are located near known hydrothermal vents and are assumed to represent the basement basalt of the hydrothermal vents. The sampling sites and the known hydrothermal vents coexist in the same topographic unit and are adjacent to each other (i.e., separated by 10–10^3 m). 2) Basalt around known vent (BAV): These basalt sampling

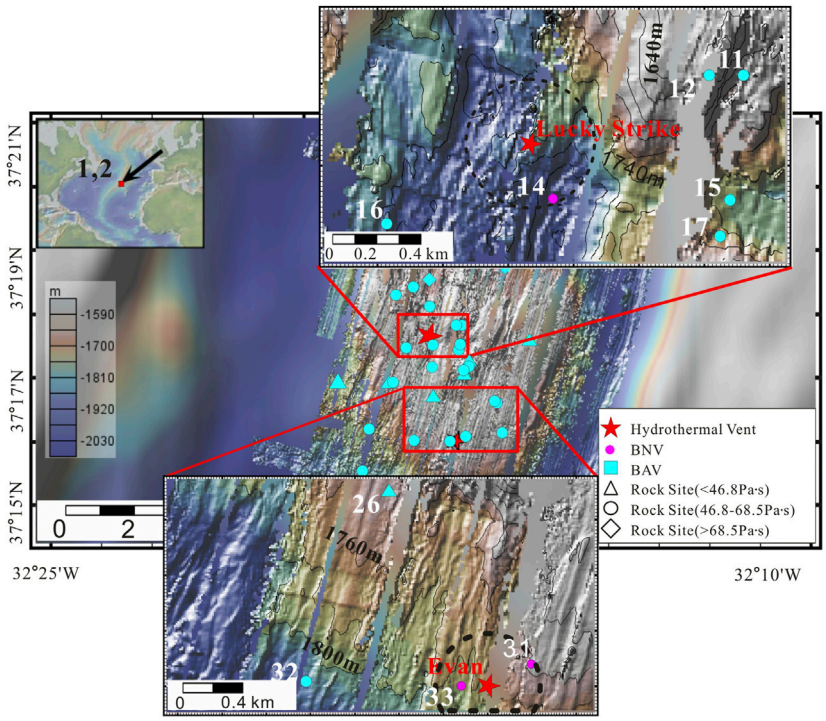

FIGURE 5 | Bathymetric map from GeoMapApp, showing the locations of the Lucky Strike vent, the Evan vent, and the sample sites. The color bar is not applicable to the two local maps. Black solid lines are the 20 m isobaths. The symbols and color bar are explained in the caption of **Figure 3**.

sites are located farther from the known hydrothermal vents than BNVs, but may be associated with hydrothermal vents. They are separated by 10^3–10^4 m from the known hydrothermal vents and all in the same topographic unit. Or, they are separated by 10^2–10^3 m from the known hydrothermal vents in different topographic units. 3) Basalt of the MAR: The basalt samples in the MAR are far (>10^4 m) from the known hydrothermal vents or no hydrothermal vents were found in the range. The basalt of the MAR is treated as the background basalt of the first two categories (especially of BNV). According to the above BNV classification standard, BNV samples from only 11 hydrothermal vents were collected over the whole MAR. These vents are the focal objects of this paper. The classifications of the sampling sites near each vent are described below.

Trans-Atlantic Geotraverse Vent

The TAG vent was discovered by Rona et al. (1986) in 1985. It is located on the north side of a large hydrothermal sulfide mound at the bottom of the axial valley, which has a maximum depth of 3,670 m. Thirty-nine basalt geochemical datasets have been collected from 36 sampling sites around the TAG vent (**Figure 3**). The major-element concentrations and viscosities at each site are listed in **Table 4**. Sites 24, 25, and 26 occupy the basement basalt under the large hydrothermal sulfide mound containing the TAG vent. Basalt samples from sites 24 and 26 were collected by drilling, and the sample from site 25 was collected by submersible equipment. These basalt samples were classified as BNV. The remaining sites are not beneath the hydrothermal sulfide mound and are approximately 1–15 km from the TAG vent; hence, their basalt samples were classified as BAV.

Snake Pit Vent

The Snake Pit vent was discovered by Kong et al. (1985). It is situated on an intensely fissured neovolcanic ridge along the axial valley, which occupies the south side of the 3500-m-deep Kane transform fault. Thirty-two basalt geochemical datasets from 23 basalt sampling sites have been collected around the Snake Pit vent (**Figure 4**). **Table 5** to continue lists the major-element concentrations and viscosities of the basalt at these sites. The Snake Pit vent and sites 12, 13 are located at the top of the same neovolcanic ridge, belong to the same topography unit, and are less than 300 m apart. Therefore, the basalt samples from these sites were classified as BNV. The remaining sites are located 1–5 km from the vent even in different topographic units. Therefore, samples from these sites were classified as BAV.

Lucky Strike Vent and Evan Vent

The Lucky Strike vent was discovered by Alvin in 1993 (Langmuir et al., 1993), and the Evan vent was discovered by Nautile in 2006 (Escartin, 2009). Both vents are located on the seamount in the central part of the Lucky Strike segment (**Figure 5**). Water depths at the Lucky Strike and Evan vents are 1740 and 1775 m, respectively, and the vents are approximately 3.5 km apart. 42 basalt geochemical datasets were collected from the 40 sampling sites around the two

TABLE 6 | Major elements (wt%) and viscosity of basalt (Pa·s) on lucky strike and evan vents (data from PetDB).

Type	No.	Lat./°	Lon./°	SiO_2	TiO_2	Al_2O_3	TFeO	MnO	MgO	CaO	Na_2O	K_2O	P_2O_5	H_2O	Visc
BNV	14	37.292	−32.291	51.70	1.19	14.66	9.61	0.17	7.79	12.16	2.29	0.25	0.14	***0.38***	***53.94***
	31	37.268	−32.28	50.94	1.18	15.35	9.87	0.18	7.14	12.11	2.36	0.20	0.12	***0.30***	***56.40***
	33	37.2667	−32.2853	50.98	1.07	14.83	10.08	0.17	8.24	11.85	2.29	0.18	0.12	***0.27***	***48.37***
BAV	1	37.341	−32.2695	52.10	1.35	14.49	10.65	0.16	6.90	11.26	2.46	0.22	0.14	***0.33***	***77.22***
	1	37.341	−32.2695	50.78	0.99	14.97	9.31	0.17	8.50	12.59	2.11	0.22	0.14	***0.32***	***39.64***
	2	37.335	−32.3	51.62	1.15	14.85	8.93	0.15	7.78	12.53	2.20	0.42	0.18	***0.63***	***38.61***
	3	37.332	−32.294	51.66	1.05	14.84	9.04	0.16	8.19	12.62	2.15	0.22	0.12	***0.33***	***52.01***
	4	37.316	−32.279	50.86	0.93	14.91	8.99	0.18	8.77	12.85	2.07	0.15	0.12	***0.22***	***46.68***
	5	37.316	−32.302	51.75	0.97	14.78	8.89	0.15	8.23	12.88	2.09	0.15	0.09	***0.23***	***64.54***
	6	37.312	−32.267	51.53	1.28	14.65	10.29	0.18	7.36	11.62	2.40	0.24	0.17	***0.36***	***58.06***
	7	37.309	−32.292	51.55	1.28	14.62	10.18	0.18	7.31	11.53	2.36	0.20	0.14	***0.30***	***68.93***
	8	37.307	−32.297	50.71	0.98	15.46	9.35	0.16	7.69	12.71	2.23	0.13	0.09	***0.20***	***57.02***
	9	37.305	−32.303	51.07	0.93	15.12	8.04	0.15	8.85	13.77	1.90	0.23	0.11	***0.35***	***38.31***
	10	37.302	−32.2918	51.35	1.28	14.64	10.18	0.18	7.55	11.74	2.42	0.21	0.16	***0.31***	***58.99***
	11	37.297	−32.2813	51.06	1.05	14.81	9.88	0.22	8.10	12.04	2.23	0.20	0.14	***0.30***	***47.99***
	12	37.297	−32.283	50.95	1.08	14.75	9.85	0.17	7.92	12.01	2.17	0.18	0.11	***0.27***	***54.23***
	13	37.293	−32.259	49.76	1.52	15.66	8.42	0.15	7.40	12.50	2.74	0.86	0.31	***1.29***	***18.60***
	15	37.292	−32.282	51.23	1.07	14.76	9.89	0.19	7.82	12.23	2.24	0.19	0.12	***0.29***	***53.78***
	16	37.291	−32.2995	51.19	1.07	14.81	9.53	0.18	8.13	12.31	2.23	0.20	0.14	***0.30***	***50.35***
	17	37.2905	−32.2825	51.44	1.05	14.74	9.74	0.18	8.08	12.03	2.20	0.19	0.14	***0.29***	***53.69***
	17	37.2905	−32.2825	51.38	1.07	14.69	9.80	0.18	8.14	12.08	2.17	0.20	0.14	***0.30***	***51.69***
	18	37.287	−32.279	50.55	1.28	15.60	7.72	0.13	8.32	13.33	2.27	0.49	0.20	***0.74***	***26.10***
	19	37.286	−32.279	51.74	1.10	14.59	10.15	0.18	7.93	11.69	2.30	0.19	0.11	***0.29***	***59.05***
	20	37.286	−32.291	51.37	1.08	14.63	9.72	0.17	8.03	11.97	2.19	0.18	0.12	***0.27***	***58.50***
	21	37.285	−32.281	51.27	1.08	14.65	9.84	0.17	8.00	12.02	2.19	0.18	0.11	***0.27***	***56.54***
	22	37.284	−32.2805	50.75	1.26	15.46	8.24	0.17	8.37	12.95	2.29	0.49	0.22	***0.74***	***25.82***
	23	37.282	−32.322	50.61	0.77	15.19	8.93	0.16	8.88	13.34	2.05	0.12	0.07	***0.18***	***42.53***
	24	37.282	−32.305	50.65	1.27	15.40	7.98	0.14	8.33	13.09	2.23	0.46	0.20	***0.69***	***28.18***
	25	37.282	−32.304	51.44	1.13	14.67	9.60	0.16	7.56	12.22	2.24	0.18	0.11	***0.27***	***66.67***
	26	37.2783	−32.2907	50.00	1.27	15.91	7.18	0.14	8.63	13.85	2.23	0.58	0.24	***0.87***	***19.37***
	27	37.277	−32.27	51.38	1.00	14.88	8.86	0.16	8.18	12.55	2.10	0.16	0.10	***0.24***	***61.49***
	28	37.2767	−32.2698	51.06	1.05	14.77	10.17	0.20	8.09	11.70	2.34	0.20	0.14	***0.30***	***47.39***
	29	37.27	−32.312	51.50	1.23	14.51	10.34	0.18	7.60	11.56	2.31	0.21	0.14	***0.32***	***60.32***
	30	37.269	−32.268	51.44	1.13	14.60	9.95	0.18	7.59	11.97	2.44	0.19	0.13	***0.29***	***61.07***
	32	37.267	−32.297	51.34	1.06	14.74	10.10	0.18	7.87	11.74	2.35	0.20	0.12	***0.30***	***52.77***
	34	37.259	−32.314	51.74	1.10	14.80	10.08	0.17	7.76	11.69	2.30	0.18	0.11	***0.27***	***62.47***
	35	37.2562	−32.2878	51.71	1.13	15.03	9.78	0.16	7.42	11.93	2.37	0.21	0.15	***0.31***	***61.32***
	36	37.2557	−32.2997	51.40	0.98	15.03	9.07	0.17	8.28	13.02	2.14	0.17	0.13	***0.26***	***51.37***
	37	37.255	−32.317	51.42	1.08	14.79	10.08	0.18	7.49	11.80	2.30	0.21	0.13	***0.32***	***57.31***
	38	37.2525	−32.2933	51.58	1.09	15.03	10.28	0.16	7.73	11.82	2.21	0.18	0.10	***0.27***	***57.25***
	39	37.246	−32.28	51.89	1.20	14.57	9.91	0.16	7.78	11.80	2.25	0.21	0.13	***0.32***	***63.13***
	40	37.245	−32.317	51.70	0.94	14.84	8.79	0.15	8.45	12.96	2.04	0.13	0.09	***0.20***	***64.65***

Bold values are compute values.

vents (**Figure 5**). The major-element concentrations and viscosities at the sampling sites are listed in **Table 6**. The Lucky Strike vent and site 14 occupy the depression between the two high topographies and are observed to be not more than 200 m apart. The Evan vent and sites 31 and 33 are also separated by only 400 m and occupy the same slope of the seamount having a similar water depth. Therefore, the basalt samples at sites 14, 31, and 33 were classified as BNVs. The remaining 37 sites and two hydrothermal vents are located in different topographic units or are separated by more than 1 km; hence, the samples that were collected from these sites were classified as BAVs.

S Oceanographer Vent

The S Oceanographer vent, located on a smaller seamount at the bottom of the axial valley, was discovered by Chin et al. (1998). Its depth is 3,460 m. There are 32 basalt sampling sites around the vent, from which 37 geochemical datasets of basalt were collected (**Figure 6**). Their major-element concentrations and viscosities are listed in **Table 7**. The S Oceanographer vent and site 20 are separated by approximately 500 m at the bottom of the axial valley; hence, the basalt sample at site 20 was classified as BNV. The other sites are 1–20 km from the vent; hence, their basalt samples were classified as BAV.

Mid-Atlantic Ridge 22°30′N Vent

The MAR 22°30′N vent was discovered by Rona et al. (1986). It is located on the east of the axial valley scarp, which is 2,800 m deep. Twelve basalt geochemical datasets were collected from four basalt sampling sites around the vent (**Figure 7**). The major-element concentrations and viscosities of the basalt at each site are listed in **Table 8**. Site 2 is only 10 m from the MAR 22°30′N vent; hence, its four basalt samples were classified as BNV. The

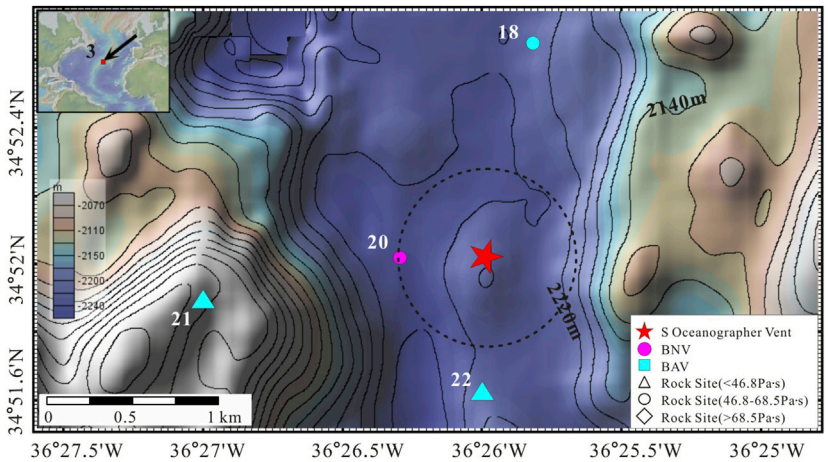

FIGURE 6 | Bathymetric map from GeoMapApp, showing the locations of the S Oceanographer vent and the sample sites. Black solid lines are the 20 m isobaths. The symbols and color bar are described in the caption of **Figure 3**.

TABLE 7 | Major elements (wt%) and viscosity of basalt (Pa·s) on S oceanographer vent (data from PetDB).

Type	No.	Lat./°	Lon./°	SiO_2	TiO_2	Al_2O_3	TFeO	MnO	MgO	CaO	Na_2O	K_2O	P_2O_5	H_2O	Visc
BNV	20	34.867	−36.4382	49.67	1.16	14.54	9.84	0.20	8.38	12.06	2.44	0.10	0.03	***0.15***	***53.62***
	20	34.867	−36.4382	49.51	1.2	14.57	10.38	0.22	7.82	12.27	2.55	0.09	0.12	***0.14***	***56.31***
	20	34.867	−36.4382	50.00	1.12	14.70	10.10	0.19	7.85	12.1	2.47	0.12	0.12	***0.18***	***55.02***
BAV	1	34.98	−36.3933	50.67	1.30	15.11	9.13	0.16	7.86	12.53	2.66	0.25	0.15	***0.37***	***43.92***
	2	34.9795	−36.4185	49.90	1.21	15.00	9.80	0.19	7.75	11.98	2.48	0.25	0.15	***0.38***	***38.39***
	3	34.9773	−36.4203	49.90	1.42	15.10	9.45	0.18	7.30	11.72	2.80	0.34	0.21	***0.51***	***38.14***
	4	34.9615	−36.4248	50.80	1.28	14.78	9.77	0.20	7.61	12.27	2.55	0.26	0.16	***0.39***	***45.05***
	5	34.95	−36.42	49.97	1.36	14.79	9.45	0.17	7.49	12.52	2.68	0.39	0.17	***0.59***	***32.05***
	6	34.94	−36.61	49.40	1.93	15.14	10.11	***0.19***	7.24	11.38	2.82	0.80	0.24	***1.20***	***20.33***
	7	34.9373	−36.4122	50.80	1.30	14.82	10.16	0.19	7.52	11.96	2.60	0.22	0.15	***0.33***	***50.05***
	8	34.904	−36.4245	50.33	1.43	15.36	9.09	0.17	8.11	12.42	2.60	0.29	0.19	***0.43***	***36.29***
	9	34.8955	−36.4183	50.08	1.42	15.12	9.29	0.10	7.83	12.13	2.55	0.30	0.18	***0.45***	***38.08***
	9	34.8955	−36.4183	49.49	1.34	14.99	10.01	0.23	7.90	11.99	2.57	0.26	0.17	***0.39***	***33.58***
	10	34.8947	−36.419	49.75	1.18	15.75	8.91	0.23	8.32	12.73	2.35	0.26	0.16	***0.39***	***29.77***
	10	34.8947	−36.419	48.53	1.17	16.27	8.46	0.14	8.69	12.62	2.47	0.28	0.17	***0.42***	***21.48***
	11	34.8947	−36.527	48.26	0.66	17.35	9.49	0.22	9.10	12.02	2.45	0.04	0.04	***0.06***	***26.97***
	11	34.8947	−36.527	49.52	1.68	14.82	11.26	0.25	7.04	10.95	2.69	0.35	0.20	***0.53***	***35.09***
	12	34.8945	−36.4355	49.40	1.14	14.85	10.10	0.18	7.84	12.04	2.56	0.12	0.12	***0.18***	***49.26***
	13	34.8937	−36.428	49.76	1.18	14.60	10.08	0.19	8.11	11.96	2.62	0.10	0.12	***0.15***	***55.50***
	14	34.89	−36.4143	49.80	1.23	15.10	9.62	0.18	7.72	12.12	2.60	0.23	0.16	***0.35***	***39.76***
	15	34.8887	−36.4105	49.18	1.42	15.60	8.91	0.14	8.02	12.70	2.68	0.35	0.17	***0.53***	***26.09***
	16	34.8878	−36.3997	48.39	1.31	16.18	8.60	0.26	8.26	12.36	2.57	0.39	0.25	***0.59***	***19.53***
	17	34.8783	−36.3763	49.50	1.48	16.80	7.30	0.14	7.37	12.95	2.72	0.74	0.27	***1.11***	***19.17***
	18	34.8775	−36.4303	50.43	1.20	14.90	9.77	0.17	7.87	12.29	2.31	0.12	0.14	***0.18***	***61.19***
	19	34.8718	−36.5305	50.30	1.20	16.00	8.60	0.17	7.38	12.52	2.54	0.26	0.13	***0.39***	***42.30***
	21	34.8648	−36.45	48.75	1.66	15.55	8.57	0.19	7.50	12.99	2.82	0.70	0.28	***1.05***	***17.98***
	22	34.8603	−36.4333	49.10	1.85	15.88	8.76	0.13	7.31	12.61	2.72	0.72	0.30	***1.08***	***19.92***
	23	34.838	−36.43	49.50	1.57	16.36	8.98	0.14	7.92	12.14	2.64	0.59	0.27	***0.89***	***19.07***
	24	34.8378	−36.3888	50.49	1.25	14.38	10.00	0.17	7.66	12.16	2.43	0.10	0.14	***0.15***	***75.46***
	25	34.786	−36.4628	48.65	0.75	16.20	9.01	0.17	9.81	13.38	1.89	0.07	0.05	***0.10***	***25.02***
	26	34.781	−36.463	50.93	1.28	15.46	9.04	0.16	7.96	12.10	2.13	0.27	0.16	***0.40***	***44.69***
	27	34.7552	−36.4768	50.71	1.26	15.17	9.10	0.16	7.90	12.44	2.68	0.25	0.16	***0.38***	***42.71***
	28	34.7463	−36.4793	49.73	1.00	15.39	9.19	0.22	9.01	11.59	2.49	0.07	0.09	***0.11***	***50.51***
	29	34.74	−36.49	49.75	0.88	14.98	8.75	0.17	8.92	13.13	2.13	0.09	0.09	***0.14***	***46.10***
	30	34.7378	−36.4923	48.50	0.75	17.80	8.64	0.15	9.30	11.95	2.38	0.05	0.07	***0.08***	***27.98***
	31	34.726	−36.4623	51.43	1.56	14.99	10.23	0.19	6.64	10.89	2.87	0.70	0.27	***1.04***	***32.13***
	32	34.7082	−36.4857	50.08	0.81	16.26	8.51	0.15	9.43	12.31	2.24	0.04	0.07	***0.06***	***48.05***

Bold values are compute values.

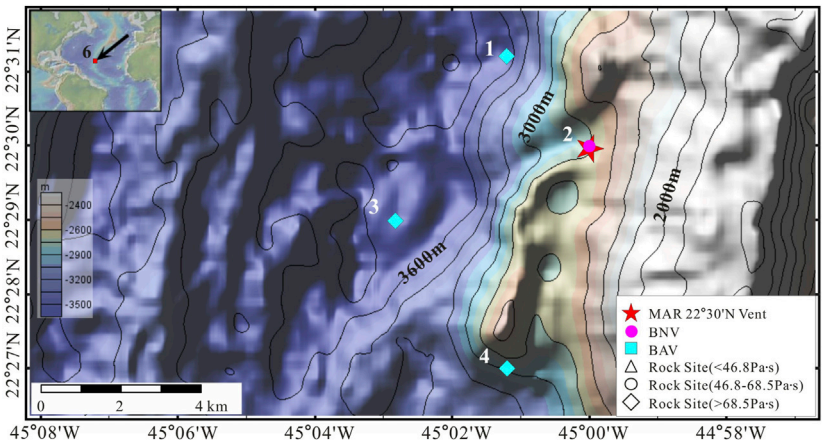

FIGURE 7 | Bathymetric map from GeoMapApp, showing the locations of the MAR 22°30′N vent and the sample sites. Black solid lines are the 20 m isobaths. The symbols and color bar are described in the caption of **Figure 3**.

TABLE 8 | Major elements (wt%) and viscosity of basalt (Pa·s) on MAR 22°30′N vent (data from PetDB).

Type	No.	Lat./°	Lon./°	SiO_2	TiO_2	Al_2O_3	TFeO	MnO	MgO	CaO	Na_2O	K_2O	P_2O_5	H_2O	Visc
BNV	2	22.5	−45	49.89	1.76	15.49	10.26	***0.19***	7.47	10.98	2.88	0.13	0.17	***0.195***	***64.80***
	2	22.5	−45	49.52	1.66	15.52	9.52	***0.18***	7.78	11.28	2.8	0.14	0.17	***0.21***	***57.68***
	2	22.5	−45	49.83	1.62	15.58	9.68	***0.18***	7.7	11.39	2.87	0.13	0.17	***0.195***	***60.08***
	2	22.5	−45	50.34	1.64	15.33	9.87	***0.18***	7.52	11.32	2.9	0.14	0.15	***0.21***	***66.63***
BAV	1	22.52	−45.02	50.76	1.65	15.22	9.97	***0.18***	7.24	11.57	2.92	0.12	0.16	***0.18***	***80.62***
	1	22.52	−45.02	50.13	1.77	15.49	10.34	***0.19***	7.60	11.31	2.70	0.12	0.17	***0.18***	***65.67***
	3	22.483	−45.047	50.80	1.65	15.36	9.82	***0.18***	7.24	11.27	2.88	0.13	0.13	***0.20***	***81.44***
	3	22.483	−45.047	51.36	1.66	15.18	9.93	***0.18***	7.28	11.72	2.77	0.15	0.13	***0.23***	***78.99***
	3	22.483	−45.047	50.40	1.78	14.97	9.96	***0.18***	6.87	11.41	2.90	0.16	0.15	***0.24***	***79.95***
	4	22.45	−45.02	51.12	1.58	15.63	9.99	***0.19***	7.81	11.28	2.80	0.11	0.13	***0.17***	***73.10***
	4	22.45	−45.02	50.42	1.51	15.57	9.84	***0.18***	7.74	11.27	2.85	0.10	0.13	***0.15***	***70.62***
	4	22.45	−45.02	50.34	1.51	15.16	9.86	***0.18***	7.70	11.25	2.82	0.11	0.13	***0.17***	***71.93***

Bold values are compute values.

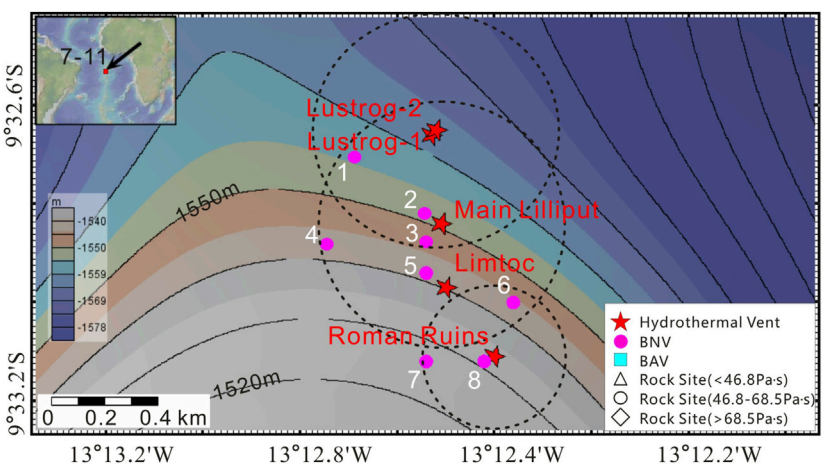

FIGURE 8 | Bathymetric map from GeoMapApp, showing the locations of vents in the Lilliput hydrothermal field and the sample sites. Black solid lines are the 10 m isobaths. The symbols and color bar are described in the caption of **Figure 3**.

TABLE 9 | Major elements (wt%) and viscosity of basalt (Pa·s) on lilliput field (data from PetDB; Haase et al., 2009).

Type	No.	Lat./°	Lon./°	SiO_2	TiO_2	Al_2O_3	TFeO	MnO	MgO	CaO	Na_2O	K_2O	P_2O_5	H_2O	Visc
BNV	1	−9.545	−13.211	49.89	2.67	13.57	12.66	0.24	5.16	9.45	3.50	0.45	0.43	***0.68***	***61.91***
	2	−9.547	−13.209	50.42	2.39	13.92	11.87	0.23	5.74	10.20	3.32	0.44	0.40	***0.66***	***56.28***
	3	−9.548	−13.209	50.13	2.47	13.87	11.99	0.21	5.61	10.12	3.29	0.44	0.40	***0.66***	***57.38***
	4	−9.548	−13.212	49.79	2.55	13.81	12.47	0.24	5.42	9.81	3.19	0.44	0.41	***0.66***	***57.52***
	5	−9.549	−13.209	50.70	2.57	14.38	12.13	0.21	5.72	10.18	3.14	0.44	0.26	***0.66***	***58.09***
	5	−9.549	−13.209	51.09	2.74	14.31	12.00	0.21	5.76	10.11	3.19	0.43	0.24	***0.65***	***66.27***
	6	−9.550	−13.206	50.35	2.45	13.80	11.94	0.22	5.64	10.15	3.31	0.44	0.40	***0.66***	***58.79***
	7	−9.552	−13.209	50.95	2.83	14.09	12.78	0.22	5.16	9.38	3.26	0.48	0.32	***0.72***	***68.51***
	8	−9.552	−13.207	50.51	2.46	14.37	11.95	0.21	5.88	10.15	3.16	0.41	0.25	***0.62***	***57.53***
BAV	9	−9.532	−13.213	50.90	2.67	14.09	12.24	***0.23***	5.47	9.89	3.14	0.47	***0.28***	***0.71***	***64.63***
	10	−9.558	−13.209	50.13	2.41	13.76	12.03	0.22	5.62	10.01	3.38	0.44	0.40	***0.66***	***56.42***
	11	−9.56	−13.21	50.90	2.41	14.21	11.70	0.21	5.75	10.22	3.20	0.46	0.43	***0.69***	***58.64***
	11	−9.56	−13.21	50.46	2.63	13.42	12.08	0.25	5.22	9.93	3.31	0.52	0.46	***0.78***	***62.78***
	12	−9.562	−13.207	50.08	2.48	14.39	11.50	0.21	5.94	10.12	3.03	0.44	0.26	***0.66***	***55.46***
	13	−9.564	−13.208	50.22	2.45	13.88	11.90	0.21	5.63	10.19	3.31	0.43	0.40	***0.65***	***58.69***
	14	−9.565	−13.205	50.98	2.62	14.15	12.22	0.22	5.55	9.96	3.14	0.44	0.27	***0.66***	***66.08***
	15	−9.569	−13.209	49.86	2.33	13.95	11.64	0.22	5.91	10.15	3.29	0.42	0.38	***0.63***	***53.36***
	16	−9.57	−13.21	50.00	1.31	15.20	8.58	0.18	8.17	12.20	2.42	0.21	0.23	***0.32***	***45.99***
	17	−9.573	−13.208	50.06	2.29	13.87	11.62	0.20	5.93	10.15	3.31	0.43	0.38	***0.65***	***53.61***
	18	−9.573	−13.206	50.32	2.34	13.93	11.76	0.19	5.75	10.22	3.29	0.43	0.39	***0.65***	***57.11***
	18	−9.573	−13.206	49.24	1.98	14.10	11.75	0.21	6.35	10.81	3.16	0.31	0.31	***0.47***	***46.34***
	19	−9.576	−13.207	50.10	2.40	13.76	11.79	0.23	5.70	10.16	3.29	0.42	0.40	***0.63***	***59.06***

Bold values are compute values.

other sites are more than 5 km from the vent; hence, their basalt samples were classified as BAV.

Lilliput Field

The Lilliput field was preliminarily discovered by German et al. (2002) in 2002 and confirmed by ROV investigation in 2002 (Haase and Scientific Party, 2009). It occupies the segment between the Ascension and the Bode Verde fracture zones, which are 1,500 m deep. The areal coverage of the Lilliput hydrothermal field is approximately (1,000 × 250) m^2. Five relatively small hydrothermal vents are found on a large (~5,000 m × 600 m) young (estimated as <100 years old) lava flow. From observations of the Lilliput vent fauna over four consecutive years, researchers have inferred a pulsed hydrothermal activity (Haase et al., 2009). Twenty-two basalt geochemical datasets have been collected from 19 sampling sites around the Lilliput vent (**Figure 8**). The major-element concentrations and viscosities at these sites are listed in **Table 9**. The vents of the Lilliput field and sites 1–8 are separated by <500 m on the same slope (possibly created by the same lava flow); hence, their basalt samples were classified as BNV. The remaining sites were distant (<1 km) from the hydrothermal vents; hence, their basalt samples were classified as BAV.

The above classification grouped the 9818 sampled basalt datasets into 29 BNV datasets and 155 BAV datasets. The differences between both types of basalt samples and the background basalts on the MAR are compared in the following section.

RESULTS

The latitudes and the analogy viscosity provided in the 9818 datasets were plotted in a scatter diagram, with latitude as the ordinate and viscosity as the abscissa (**Figure 9**). The viscosities of the basalts from the MAR, BAV, and BNV groups were 4–356, 17–117, and 46.8–68.5 Pa·s, respectively. As shown in **Figure 9**, the viscosity range narrows near the vents (e.g., 46.8–68.5 Pa·s), but many of the BAV samples are likely to be background basalt on the MAR. Among the whole 9818 basalt samples collected from the MAR, 31.1% have viscosities ranging from 46.8 to 68.5 Pa·s. In other words, less than one-third of the basalt samples from the MAR fall within the viscosity range of BNV.

Meanwhile, the viscosities of the BNV, BAV, and MAR basalt samples were statistically analyzed, and the results were plotted as histograms (**Figure 10**). The modes and means of the viscosities are 54–56 Pa·s and 50.49 Pa·s for the MAR basalt, 58–60 Pa·s and 56.07 Pa·s for BAV, 56–58 Pa·s and 57.71 Pa·s for BNV respectively. The mean viscosities of the BNV and BAV samples are similar but clearly differ from those of the MAR basalt. The viscosity standard deviations of the MAR basalt, BAV, and BNV are 24.30, 18.44, and 5.30, respectively. Note that the standard deviation is much smaller in BNV than in the other basalt groups, indicating a stronger aggregation effect of the viscosity in BNV.

In addition, all basalt samples are classified by the maximum and minimum concentrations of BNV major elements and the proportion of the Mid- Ridge basalt samples belonging to BNV category is listed in **Table 10**. These results show that the concentration range of major elements in most basalts as the same as that of BNV, while only 31% of basalts had the analogy viscosity similar to BNV which shows that the analogy viscosity may be another suitable indicator for the seafloor hydrothermal vents.

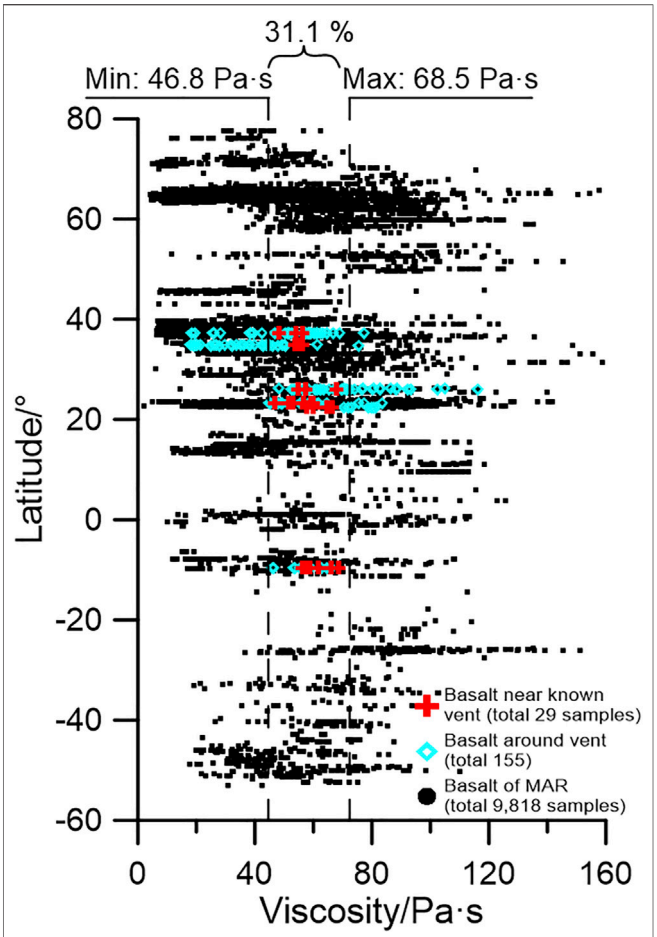

FIGURE 9 | BNV, BAV, and MAR basalt samples (distinguished by pink crosses, cyan diamonds, and black circles, respectively) plotted on a viscosity–latitude scatter diagram. All BNV and BAV, and MAR basalts with viscosities below 160 Pa·s (this excludes 20 samples with viscosities between 160 Pa.s and the maximum viscosity of 574 Pa·s) are shown.

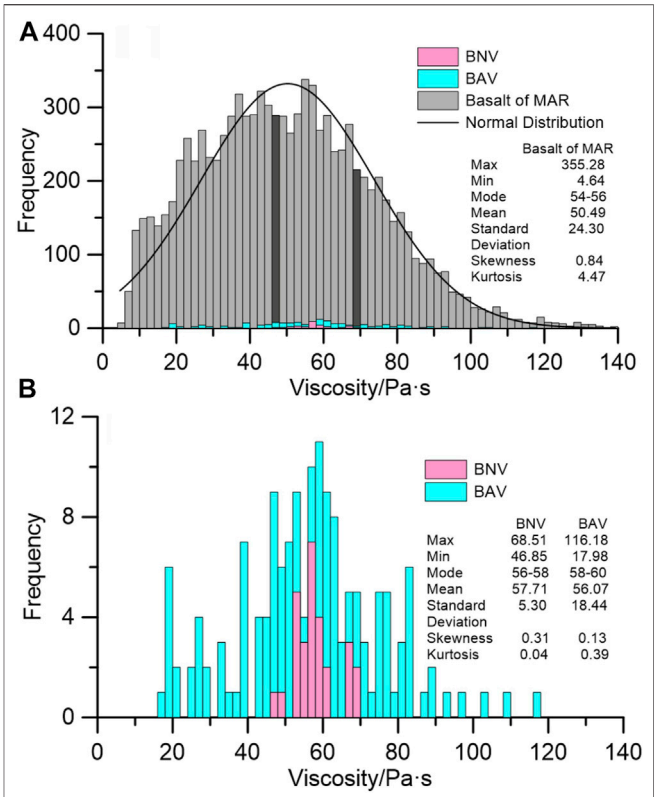

FIGURE 10 | (A) Frequency histograms of BNV, BAV, and MAR basalt samples. The darker grayscale shows the range of BNV. The statistical parameters on the right were computed for MAR basalt. **(B)** Frequency histograms of BNV and BAV.

DISCUSSION

The major-element concentrations of basalt have limited ability to identify hydrothermal vents (**Table 10**). To understand this result, we plotted the analogy viscosity versus oxide content for the three types of basalt (**Figure 11**). BNV is divided into two distinct categories along the horizontal axis: Type 1, located in the north MAR (20–40°N), and Type 2, located in the south MAR (9°S). Because the geochemical compositions of BNV differ among the MAR locations, they are unsuitable as indicators of hydrothermal vents. In contrast, the analogy viscosity of BNV is highly consistent among the locations and better identifies the hydrothermal vents. According to statistical analysis, the range of BNV analogy viscosity differs from that of the MAR (46.8–68.5 Pa·s in the former vs. 4–356 Pa·s in the latter). This suggests that a narrow analogy viscosity range (e.g. 46.8–68.5 Pa.s) favors the formation and development of hydrothermal vents. To date, the role of basalt viscosity in restricting the hydrothermal vents is not clear, which require further research.

Due to the complex formation mechanism, controlling factors and individual differences of the seafloor magmatic system, tectonic fault system and hydrothermal evolution system, it may not be comprehensive to take the basalt viscosity of the

TABLE 10 | Major element (wt%) and viscosity (Pa·s) range of BNV and their recognition rate of basalt on MAR.

	SiO_2	TiO_2	Al_2O_3	FeO_T	MnO	MgO	CaO	Na_2O	K_2O	P_2O_5	Viscosity
Max	51.70	2.83	16.42	12.78	0.24	9.34	12.27	3.50	0.48	0.43	68.5
Min	49.51	1.07	13.57	8.84	0.16	5.16	9.38	2.29	0.08	0.03	46.8
Proportion	61.8%	71.8%	78.9%	73.3%	80.0%	83.7%	72.8%	61.8%	66.7%	90.2%	31.1%

"Max" and "min" means the maximum and minimum of BNV. "Proportion" means the ratio of samples between max and min to the total samples on MAR., The smaller the ratio, the better the recognition rate of the hydrothermal vents. Obviously, the viscosity has the best identification rate for the hydrothermal vents.

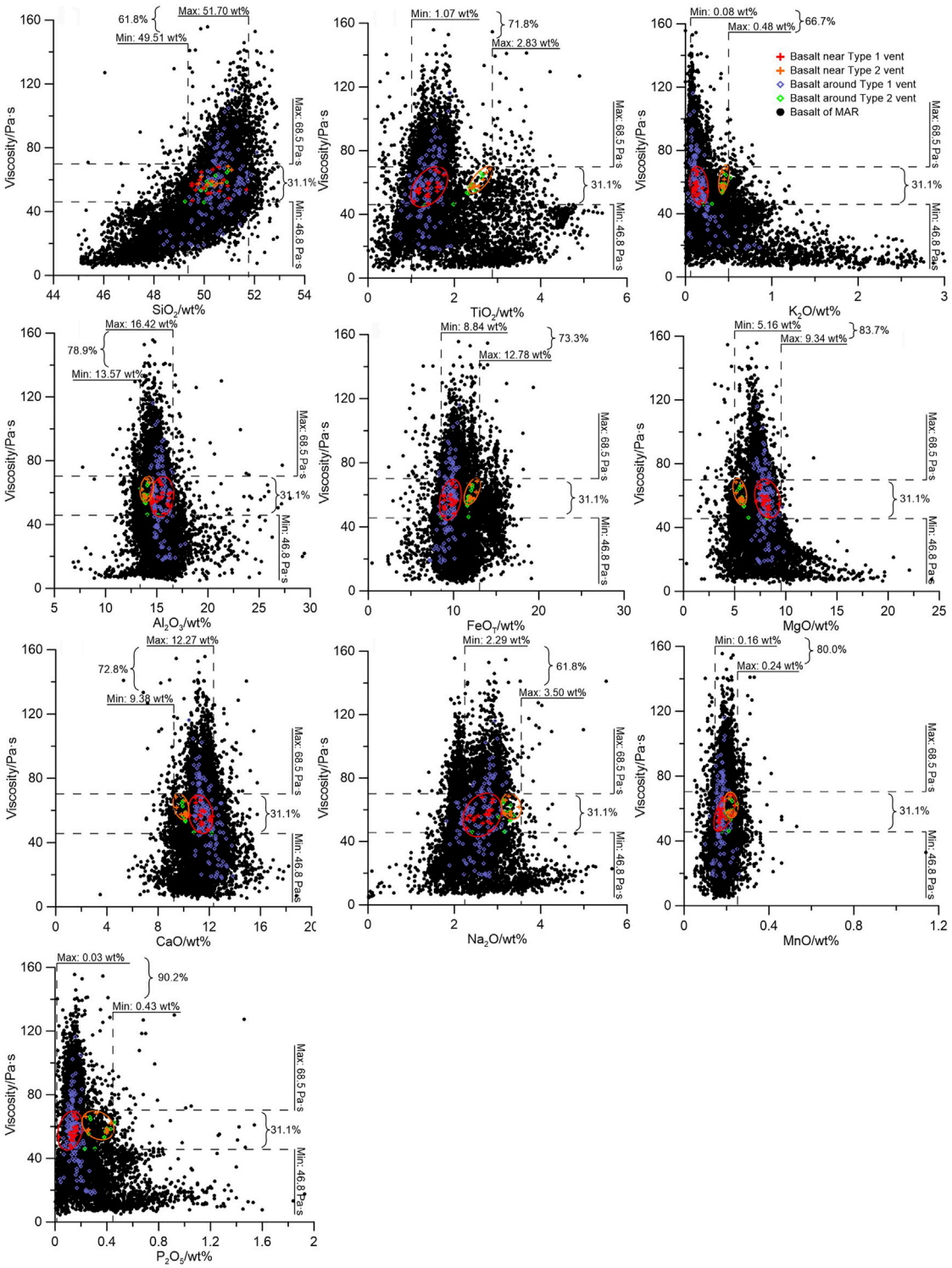

FIGURE 11 | Major-element–viscosity scatter diagrams for BNV and MAR basalt. The BNV vents are divided into Type 1 (vents 1–6, enclosed by red circles) and Type 2 (vents 7–11, enclosed by orange circles). The dashed lines delineate the upper and lower values in BNV, and the annotations report the proportions of MAR samples in each range.

mid-ocean ridge as a characteristic parameter to indicate the formation and existence of hydrothermal zone. However, the calculation results and statistical rules in this paper do find that the simulated viscosity data of basalt is correlated with the distance of the hydrothermal vent, as shown in the **Figures 9**, **10**. It should be noted that, according to the thermal cooling of

deep magma, fractional crystallization of magma chamber, different development degree of fault zone, and the timing of water-rock reaction, the indicator of analogy viscosity may only provide a possibility for the exploration of submarine hydrothermal field.

First, the viscosity or composition of the rock formations hosting such systems may be of little influence in their generation (besides having some influence on the elastic properties and therewith the fracture behavior of the material). The fracture process itself is governed by the local stress field and the elastic, response of the solidified magma to this stress. In fact, all of the zones that selected for analyses of hydrothermal vent regions in this study lie on fault zones. These are the result of tectonic processes that induce the fractures requires for the generation of permeability. How recovering samples from the ocean floor, performing compositional analyses and then calculating viscosity should return better results at identifying hydrothermal vents than the first order observations made during the dives required to recover these samples in the first place. Further, identifying thermal or chemical signatures of active vents in the water column maybe drastically faster, easier than analogy viscosity, though it may be a useful tool for exploration for hydrothermal vents as found here.

Second, crustal magma transport systems, independent of their geometry, remain filled with rock after solidification of the magma and fluid pathways (used by sea water during hydrothermal activity) are subsequently induced by fracturing. It is this fracturing process in combination with the temperature differential between the intrusion and the sea water that drives fluid circulation and hydrothermal activity (Baker and German 2004). Hydrothermal activity is correlated to spreading velocity since higher spreading velocity means higher heat flow and more intense fracturing. On the other hand, since the H_2O content drastically affects melt viscosity, simply assuming H_2O = 1.5* K_2O maybe not a suitable approach for global mid-ocean ridge system. Varying the water content from 0 to 0.3 wt% for the melt of **Table 3** at constant temperature induces a variation in modelled viscosity of > 100 Pas - much larger than the proposed "identifier viscosity range." Especially since water solubility in melts is extremely sensitive to changes in pressure, water depth would likely be a much better indicator for water solubility.

Third, calculated viscosity from compositional data using an empirical model would introduce further uncertainty, and any apparent differences between the samples are composition driven and that information is already present in the compositional data, so whether viscosity is a better parameter for determining the location of hydrothermal vents than composition is not certain. For example, the uncertainty of the GRD model is ~ ± 5% of the measured viscosity value (in this case that translates to ~ ± 2.5 Pa s, i.e. ~ ± 10% of the range suggested relevant to vent formation).

Fourth, the computed viscosities change only with composition and are assumed to have the same temperature (1,423°C). This may be not suitable because lava viscosity is very sensitive to temperature, and lava composition changes with temperature, due to fractional crystallization. The proposed explanation for finding that vents favoring a limited range of intermediate viscosities is based on the assumption that the computed viscosities were those of the lavas when they erupted and eventually formed as crust. But it is not clear the computed viscosities accurately represent the eruption viscosities, given the lack of temperature information. Alternative methods such as the MELTS algorithm are able to compute viscosity from major element compositions of basalts by also calculating the liquidus temperatures. Using such a method would be more meaningful to this study. Assuming one temperature for all the lavas is an important shortcoming.

Therefore, whether the analogy viscosity of basalts can be used as an indicator for determining the location of seafloor hydrothermal field needs more observations to be verified due to the complexities of magmatic activity and fault structure, as well as the multi-stage water-rock reaction. Hence, this paper provides a possible insight for exploration of hydrothermal vents rather than a fully developed method.

CONCLUSION

According to the calculation results of analogy viscosity, the basalts along the MAR system with analogy viscosity values ranged from 46.8 to 68.5 Pa·s are considered to be suitable for exploration the location of hydrothermal vents. However, because of the complex seafloor magmatic system, tectonic fault system and hydrothermal evolution system, the analogy viscosity parameter may only provide a possible insight for the exploration of submarine hydrothermal field rather than a developed method, which needs more observations to be verified.

DATA AVAILABILITY STATEMENT

The original contributions presented in the study are included in the article/supplementary material, further inquiries can be directed to the corresponding author.

AUTHOR CONTRIBUTIONS

CL designed the study and wrote the first draft. GW collected and analyzed the data. All authors discussed the results and contributed to the preparation of the manuscript.

FUNDING

This work was supported by the China Ocean Mineral Resources R&D Association (grant numbers DY135-S2-2) and by the National Nature Science Foundation of China (grant number 42006180).

ACKNOWLEDGMENTS

We gratefully acknowledge the efforts of all parties involved in collecting data.

REFERENCES

Baker, E. T., and German, C. R. (2004). "On the Global Distribution of Hydrothermal Vent Fields," in *Mid-Ocean Ridges* (Washington, DC: American Geophysical Union), 245–266. doi:10.1029/148GM10

Baker, E. T., Resing, J. A., Walker, S. L., Martinez, F., Taylor, B., and Nakamura, K.-i. (2006). Abundant Hydrothermal Venting along Melt-Rich and Melt-free Ridge Segments in the Lau Back-Arc Basin. *Geophys. Res. Lett.* 33, L07308. doi:10.1029/2005GL025283

Bruneau, L., Jerlov, N. G., and Koczy, F. F. (1953). *Physical and Chemical Methods*. Elanders boktr.

Cheadle, M., and Grimes, C. (2010). To Fault or Not to Fault. *Nat. Geosci.* 3, 454–456. doi:10.1038/ngeo910

Chiba, H., Masuda, H., Lee, S.-Y., and Fujioka, K. (2001). Chemistry of Hydrothermal Fluids at the TAG Active Mound, MAR 26°N, in 1998. *Geophys. Res. Lett.* 28, 2919–2922. doi:10.1029/2000GL012645

Chin, C. S., Klinkhammer, G. P., and Wilson, C. (1998). Detection of Hydrothermal Plumes on the Northern Mid-Atlantic Ridge: Results from Optical Measurements. *Earth Planet. Sci. Lett.* 162, 1–13. doi:10.1016/s0012-821x(98)00141-1

Crone, T. J., Wilcock, W. S. D., and Mcduff, R. E. (2010). Flow Rate Perturbations in a Black Smoker Hydrothermal Vent in Response to a Mid-ocean Ridge Earthquake Swarm. *Geochem. Geophys. Geosyst.* 11, a–n. doi:10.1029/2009GC002926

Dias, Á. S., Mills, R. A., Ribeiro da Costa, I., Costa, R., Taylor, R. N., Cooper, M. J., et al. (2010). Tracing Fluid-Rock Reaction and Hydrothermal Circulation at the Saldanha Hydrothermal Field. *Chem. Geol.* 273, 168–179. doi:10.1016/j.chemgeo.2010.02.020

Dingwell, D. B. (2006). Transport Properties of Magmas: Diffusion and Rheology. *Elements* 2, 281–286. doi:10.2113/gselements.2.5.281

Escartin, J. (2009). Graviluck 2006 Cruise Blog. Available at: http://www.insu.cnrs.fr/a1890,decouverte-un-site-hydrothermal-jour-19.html.

Fulcher, G. S. (1925). Analysis of Recent Measurements of the Viscosity of Glasses. *J Am. Ceram. Soc.* 8, 339–355. doi:10.1111/j.1151-2916.1925.tb16731.x

Gale, A., Dalton, C. A., Langmuir, C. H., Su, Y., and Schilling, J.-G. (2013a). The Mean Composition of Ocean Ridge Basalts. *Geochem. Geophys. Geosyst.* 14, 489–518. doi:10.1029/2012GC004334

Gale, A., Laubier, M., Escrig, S., and Langmuir, C. H. (2013b). Constraints on Melting Processes and Plume-Ridge Interaction from Comprehensive Study of the Famous and North Famous Segments, Mid-Atlantic Ridge. *Earth Planet. Sci. Lett.* 365, 209–220. doi:10.1016/j.epsl.2013.01.022

GeoMapApp (2021). Available at: http://www.geomapapp.org/.

German, C. R., Connelly, D. P., Evans, A. J., and Parson, L. M. (2002). *Hydrothermal Activity on the Southern Mid-Atlantic Ridge*. San Francisco: Agu Fall Meeting Abstracts.

Giordano, D., Russell, J. K., and Dingwell, D. B. (2008). Viscosity of Magmatic Liquids: a Model. *Earth Planet. Sci. Lett.* 271, 123–134. doi:10.1016/j.epsl.2008.03.038

Haase, K. M., Koschinsky, A., Petersen, S., Devey, C. W., German, C., Lackschewitz, K. S., et al. (2009). Diking, Young Volcanism and Diffuse Hydrothermal Activity on the Southern Mid-Atlantic Ridge: The Lilliput Field at 9°33′SDiking, Young Volcanism and Diffuse Hydrothermal Activity on the Southern Mid-Atlantic Ridge: the Lilliput Field at 9°33′S. *Mar. Geol.* 266, 52–64. doi:10.1016/j.margeo.2009.07.012

Haase, K. M., and Scientific Party, M. (2005). Hydrothermal Activity and Volcanism on the Southern Mid-Atlantic Ridge. American Geophysical Union, Fall Metting Abstract, San Francisco.

InterRidge Vent Database (2020). InterRidge Global Database of Active Submarine Hydrothermal Vent Fields. Available at: http://vents-data.interridge.org/.

Johnson, H. P., Hutnak, M., Dziak, R. P., Fox, C. G., Urcuyo, I., Cowen, J. P., et al. (2000). Earthquake-induced changes in a hydrothermal system on the Juan de Fuca mid-ocean ridge. *Nature* 407, 174–177. doi:10.1038/35025040

Kong, L., Ryan, W. B. F., Mayer, L., Detrick, R., Fox, P. J., and Manchester, K. (1985). Bare Rock Drill Sites, ODP Legs 106 and 109: Evidence for Hydrothermal Activity at 23'N on the Mid Atlantic Ridge. *Eos Trans. Am. Geophys. Union* 66, 936.

Langmuir, C. H., Bézos, A., Escrig, S., and Parman, S. W. (2006). "Chemical Systematics and Hydrous Melting of the Mantle in Back-Arc Basins," in *Back-Arc Spreading Systems: Geological, Biological, Chemical and Physical Interactions* (Washington, D. C.: American Geophysical Union: Geophysical Monograph Series 166), 87–146. doi:10.1029/166gm07

Langmuir, C. H., Fornari, D., Colodner, D., Charlou, J. L., Costa, I., Desbruyères, D., et al. (1993). Geological Setting and Characteristics of the Lucky Strike Vent Field at 37017'N on the Mid-atlantic Ridge. *Eos Trans. Am. Geophys. Union* 74, 99.

Le Maitre, R. W. (1984). A Proposal by the Iugs Subcommission on the Systematics of Igneous Rocks for a Chemical Classification of Volcanic Rocks Based on the Total Alkali Silica (Tas) Diagram. *Aust. J. Earth Sci.* 31, 243–255. doi:10.1080/08120098408729295

Lehnert, K., Su, Y., Langmuir, C. H., Sarbas, B., and Nohl, U. (2000). A Global Geochemical Database Structure for Rocks. *Geochem. Geophys. Geosyst.* 1, 179–188. doi:10.1029/1999GC000026

Macleod, C. J., Carlut, J., Escartín, J., Horen, H., and Morris, A. (2011). Quantitative Constraint on Footwall Rotations at the 15°45′N Oceanic Core Complex, Mid-Atlantic Ridge: Implications for Oceanic Detachment Fault Processes. *Geochem. Geophys. Geosyst.* 12, a–n. doi:10.1029/2011GC003503

Miranda, J. M., Luis, J. F., Lourenço, N., and Santos, F. M. (2005). Identification of the Magnetization Low of the Lucky Strike Hydrothermal Vent Using Surface Magnetic Data. *J. Geophys. Res.* 110, 387–405. doi:10.1029/2004JB003085

Morris, A., Gee, J. S., Pressling, N., John, B. E., Macleod, C. J., Grimes, C. B., et al. (2009). Footwall Rotation in an Oceanic Core Complex Quantified Using Reoriented Integrated Ocean Drilling Program Core Samples. *Earth Planet. Sci. Lett.* 287, 217–228. doi:10.1016/j.epsl.2009.08.007

Papale, P. (1999). Strain-induced Magma Fragmentation in Explosive Eruptions. *Nature* 397, 425–428. doi:10.1038/17109

PetDB The Petrological Database of the Ocean Floor (PetDB). Available at: http://www.earthchem.org/petdb/search.

Roman, C., and Singh, H. (2007). A Self-Consistent Bathymetric Mapping Algorithm. *J. Field Robot.* 24, 23–50. doi:10.1002/rob.20164

Roman, C., and Singh, H. (2005). Improved Vehicle Based Multibeam Bathymetry Using Sub-maps and SLAM. *Ieee/rsj Int. Conf. Intelligent Robots Syst. IEEE*, 3662–3669. doi:10.1109/IROS.2005.1545340

Rona, P. A., Klinkhammer, G., Nelsen, T. A., Trefry, J. H., and Elderfield, H. (1986). Black Smokers, Massive Sulphides and Vent Biota at the Mid-Atlantic Ridge. *Nature* 321, 33–37. doi:10.1038/321033a0

Ryan, W. B. F., Carbotte, S. M., Coplan, J. O., O'Hara, S., Melkonian, A., Arko, R., et al. (2009). Global Multi-Resolution Topography Synthesis. *Geochem. Geophys. Geosyst.* 10, a–n. doi:10.1029/2008GC002332

Scheirer, D. S., Fornari, D. J., Humphris, S. E., and Lerner, S. (2000). High-resolution Seafloor Mapping Using the Dsl-120 Sonar System: Quantitative Assessment of Sidescan and Phase-Bathymetry Data from the Lucky Strike Segment of the Mid-Atlantic Ridge. *Mar. Geophys. Res.* 21, 121–142. doi:10.1023/A:1004701429848

Schmidt, K., Garbe-Schönberg, D., Koschinsky, A., Strauss, H., Jost, C. L., Klevenz, V., et al. (2011). Fluid Elemental and Stable Isotope Composition of the Nibelungen Hydrothermal Field (8°18′S, Mid-Atlantic Ridge): Constraints on Fluid-Rock Interaction in Heterogeneous Lithosphere. *Chem. Geol.* 280, 1–18. doi:10.1016/j.chemgeo.2010.07.008

Seewald, J., Cruse, A., and Saccocia, P. (2003). Aqueous volatiles in hydrothermal fluids from the main endeavour field, northern Juan de Fuca ridge: temporal variability following earthquake activity. *Earth Planet. Sci. Lett.* 216, 575–590. doi:10.1016/s0012-821x(03)00543-0

Shaw, H. R. (1972). Viscosities of Magmatic Silicate Liquids; an Empirical Method of Prediction. *Am. J. Sci.* 272, 870–893. doi:10.2475/ajs.272.9.870

Sparks, R. S. J. (2003). Dynamics of Magma Degassing. *Geol. Soc. Lond. Spec. Publ.* 213, 5–22. doi:10.1144/GSL.SP.2003.213.01.02

Tivey, M. A., Dyment, J., Dyment, J., and Murton, B. J. (2010). "The Magnetic Signature of Hydrothermal Systems in Slow Spreading Environments," in *Diversity of Hydrothermal Systems on Slow Spreading Ocean Ridges* (American Geophysical Union), 43–66. doi:10.1029/2008GM000773

Tivey, M. A., Schouten, H., and Kleinrock, M. C. (2003). A Near-Bottom Magnetic Survey of the Mid-Atlantic Ridge axis at 26°N: Implications for the Tectonic Evolution of the Tag Segment. *J. Geophys. Res. Atmos.* 108, 2277. doi:10.1029/2002jb001967

Wang, Z. B., Guang-Hai, W. U., and Han, C. H. (2014). Geochemical Characteristics of Hydrothermal Deposits and Basalts at 49.6°E on the

Southwest Indian Ridge. *J. Mar. Sci* 32(1), 64–73. doi:10.3969/j.issn.1001-909X.2014.01.008

Wright, T. L., Kinoshita, W. T., and Peck, D. L. (1968). March 1965 Eruption of Kilauea Volcano and the Formation of Makaopuhi Lava Lake. *J. Geophys. Res.* 73, 3181–3205. doi:10.1029/JB073i010p03181

Xu, X., and Qiu, J. (2010). *Igneous Petrology*. Beijing, China: Science press, 14.

Zhu, Y., Zhao, Y., and Guo, G. (1997). A Theoretical Method to Calculate the Viscosity of $NaAlSi_3O_8$ Melt. *Acta Petrol. Sin.* 13(2), 173–179. (in Chinese with English abstract).

Conflict of Interest: The authors declare that the research was conducted in the absence of any commercial or financial relationships that could be construed as a potential conflict of interest.

Publisher's Note: All claims expressed in this article are solely those of the authors and do not necessarily represent those of their affiliated organizations, or those of the publisher, the editors and the reviewers. Any product that may be evaluated in this article, or claim that may be made by its manufacturer, is not guaranteed or endorsed by the publisher.

frontiers | Frontiers in Earth Science

ORIGINAL RESEARCH
published: 30 June 2022
doi: 10.3389/feart.2022.932486

Provenance of the Lower Triassic Clastic Rocks in the Southwestern Margin of the South China Craton and Its Implications for the Subduction Polarity of the Paleo-Tethyan Ocean

Chao Han[1,2], *Hu Huang*[1,2]*, *Chenchen Yang*[1,2], *Linxi Wang*[1,2] *and Hongwei Luo*[1,2]

[1]State Key Laboratory of Oil and Gas Reservoir Geology and Exploitation, Institute of Sedimentary Geology, Chengdu University of Technology, Chengdu, China, [2]Key Laboratory of Deep-Time Geography and Environment Reconstruction and Applications of Ministry of Natural Resources, Chengdu University of Technology, Chengdu, China

The southwestern margin of the South China Craton preserves a Late Permian to Early Triassic sedimentary succession, the provenance of which helps to constrain the magmatic history and tectonic evolution of the Paleo-Tethyan Orogen. In this study, we present new detrital zircon U-Pb age, trace element, Hf isotope and whole-rock geochemical composition analyses from the Lower Triassic Qingtianbao Formation, to distinguish the provenance of clastic rocks. The results show that the detrital zircons of the Qingtianbao Formation are characterized by an age spectrum of unimodal, with an age peak of ~260 Ma, and have a geochemical affinity to within-plate sources. Most of these zircons have positive $\varepsilon_{Hf}(t)$ values (+1.6 to +5.9), similar to those of the Emeishan rhyolites. The whole-rock geochemistry of most clastic samples shows no Nb–Ta anomalies on primitive mantle-normalized elemental diagrams. These features imply a source related to the Emeishan volcanic rocks. Integration of the geologic and provenance records in the southwestern margin of the South China Craton, we suggest that the Paleo-Tethyan Ocean may undergo a unidirectional subduction westward beneath the Indochina Block during the Late Permian–Early Triassic.

Keywords: provenance, subduction polarity, Lower Triassic, South China Craton, detrital zircon, Paleo-Tethyan

OPEN ACCESS

Edited by:
Shengyao Yu,
Ocean University of China, China

Reviewed by:
Wenchao Yu,
China University of Geosciences Wuhan, China
Bin Liu,
Yangtze University, China

***Correspondence:**
Hu Huang
118huanghu@163.com

Specialty section:
This article was submitted to Geochemistry, a section of the journal Frontiers in Earth Science

Received: *29 April 2022*
Accepted: *23 May 2022*
Published: *30 June 2022*

Citation:
Han C, Huang H, Yang C, Wang L and Luo H (2022) Provenance of the Lower Triassic Clastic Rocks in the Southwestern Margin of the South China Craton and Its Implications for the Subduction Polarity of the Paleo-Tethyan Ocean. Front. Earth Sci. 10:932486. doi: 10.3389/feart.2022.932486

1 INTRODUCTION

During the middle-late Paleozoic, the South China Craton separated from the Gondwana Land and then experienced convergence and collision, as well as accretion (Metcalfe, 2013; Cawood et al., 2018; Wang et al., 2021). It made the Paleo-Tethyan Ocean gradually opened and closed during the Silurian–Triassic (Metcalfe, 2006, 2013; Wang et al., 2021). Meanwhile, there are multiple tectonomagmatic events in the southwestern margin of the South China Craton and Indochina Block, including the Emeishan large igneous province (ELIP) (**Figure 1**) (Chung and Jahn, 1995; Xu et al., 2001, 2004, 2008; Xiao et al., 2004; Zhou et al., 2006; Huang et al., 2018). These magmatic rocks provide significant detritus for adjacent basins, which could reveal the tectonic setting of the basin (Cawood et al., 2012). Moreover, large volumes of magma are produced in the convergent plate margin settings, but rocks from this setting have comparatively poor potential for preservation in the geological record (Scholl and von Huene, 2009; Cawood et al., 2012). Magmatic rocks are poorly

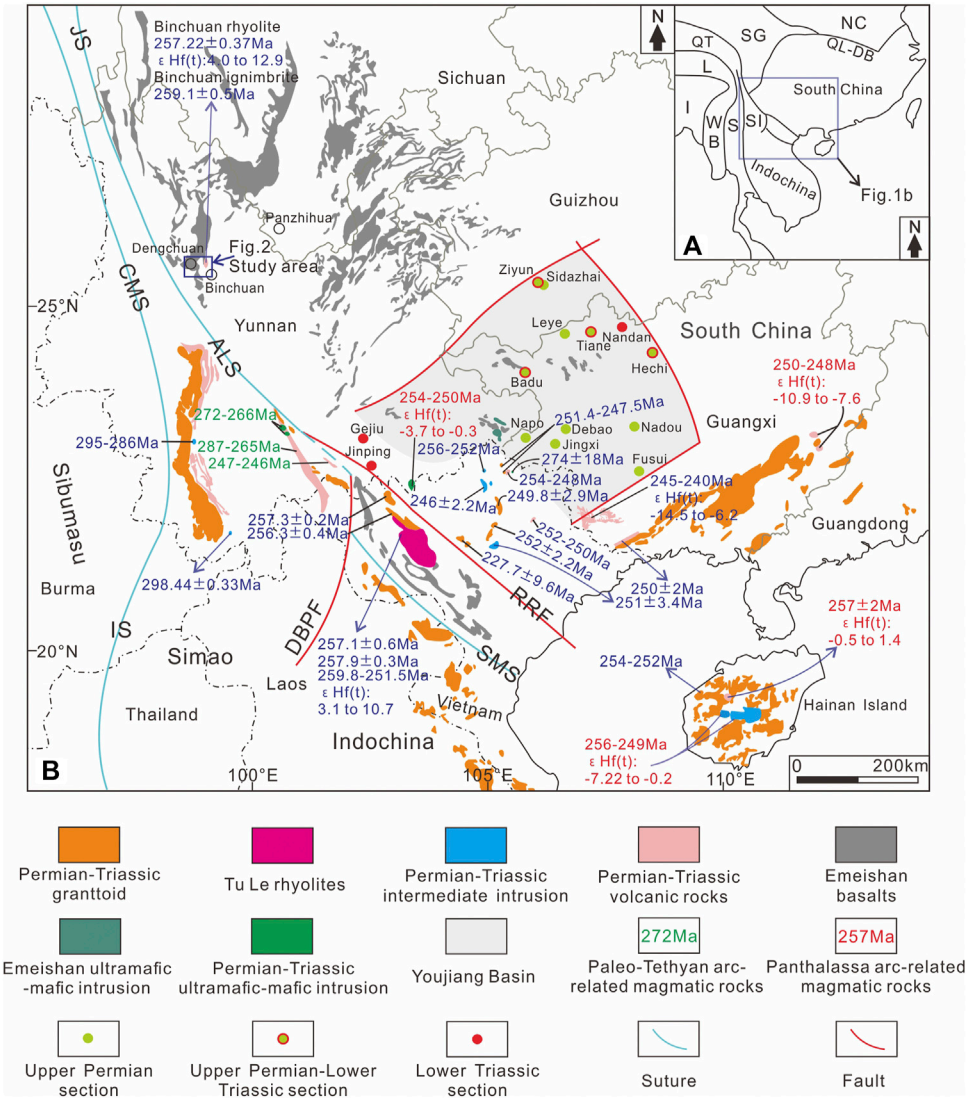

FIGURE 1 | (A) Tectonic outline of SE Asia (modified after Metcalfe, 2013; Wang et al., 2021). **(B)** Simplified geological map of the South China Craton and its adjacent regions showing the distribution of representative magmatic rocks (modified after Fan et al., 2008; Ali et al., 2010; Metcalfe, 2013; Yang et al., 2014; Hu et al., 2017; Shellnutt et al., 2020; Wang et al., 2021; Huang et al., 2022a). Data sources: Zhou et al. (2006); Hoa et al. (2008); Jian et al. (2009); Fan et al. (2010); Liu et al. (2011); Qing et al. (2011); Li et al. (2012); Chen et al. (2014); Lai et al. (2014); Zhong et al. (2014); Usuki et al. (2015); Halpin et al. (2016); Liu et al. (2017); Yan et al. (2017); He et al. (2018, 2020); Shen et al. (2018); Xu et al. (2018); Shellnutt et al. (2020); Tran et al. (2020); Gan et al. (2021); Wang et al. (2021); Huang et al. (2022a; and Huang et al. (2022b). NC: North China Craton, QL-DB: Qinling–Dabie Orogen, SG: Songpan-Ganzi Terrane, QT: Qiangtang, L: Lasha, I: India, WB: West Burma, S: Sibumasu, SI: Simao, JS: Jinshajiang Suture, ALS: Ailaoshan Suture, RRF: Red River Fault, SMS: Song Ma Suture, DBPF: Dien Bien Phu Fault, CMS: Changning–Menglian Suture, IS: Inthanon Suture.

exposed along the Paleo-Tethyan Ocean between the South China Craton and Indochina Block (**Figure 1**), and thus its subduction polarity has been controversial. Some studies suggested that the subduction was bidirectional (e.g., Zhong et al., 2013; Hou et al., 2017; Xia et al., 2019; Xu et al., 2019), whereas other studies argued that the subduction was unidirectional (e.g., Faure et al., 2014; Ngo et al., 2016; Yu et al., 2016; Gan et al., 2021; Li et al., 2021; Wang et al., 2021). The latter suggested that the southwestern margin of the South China Craton was a passive continental margin (Yan et al., 2019), and the Paleo-Tethyan Ocean may only undergo a subduction westward beneath the Indochina Block during the Late Permian–Early Triassic (Jian et al., 2009; Faure et al., 2014; Ngo et al., 2016; Li et al., 2021; Wang et al., 2021).

In this study, we integrate new whole-rock geochemistry compositions, detrital zircon geochronological and geochemical data, as well as zircon Hf isotopic analyses of the Lower Triassic clastic rocks in the southwestern margin of the South China Craton. These data, when combined with data from the Late Permian to Early Triassic sequences in the southwestern South China Craton, allow us to better constrain the subduction polarity of the Paleo-Tethyan Ocean.

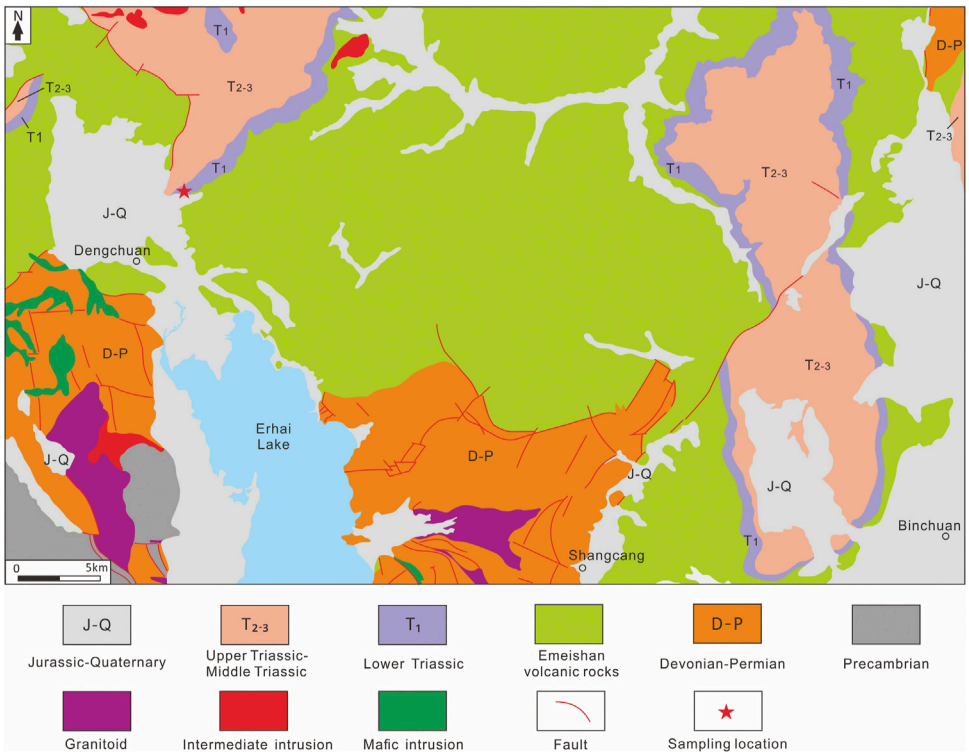

FIGURE 2 | Geological map of the Dengchuan area (modified after Yunnan Geologic Bureau, 1966, Yunnan Geologic Bureau, 1973).

2 GEOLOGICAL SETTING

The South China Craton is bounded to the north by the Qinling–Dabie Orogen belt, to the northwest by the Songpan-Ganzi Terrane, and to the southwest by the Jinshajiang and Ailaoshan–Song Ma Suture (**Figure 1**) (Metcalfe, 2013; Wang et al., 2021). It is adjacent to the Pacific Ocean to the southeast, and the rocks of Hainan Island are also considered to belong to it (Cawood et al., 2018). During the early Neoproterozoic, the South China Craton was formed by collision of the Yangtze and Cathaysia blocks (Li et al., 2009; Cawood et al., 2018). The Ailaoshan–Song Ma Suture between South China and Indochina/Simao is known as the remnants of a branch of the Paleo-Tethyan Ocean (**Figure 1**) (Faure et al., 2014; Wang et al., 2021). This Paleo-Tethyan branch ocean is generally suggested to be opened in the Silurian–Devonian and finally closed no earlier than Middle Triassic (e.g., Jian et al., 2009; Fan et al., 2010; Zi et al., 2012; Xu et al., 2019). Opening and spreading of the Paleo-Tethyan branch ocean, expressed as transgression, led to regional subsidence in the western margin of the South China Craton and the deposition of the carbonate platform before the Middle Permian (Liu and Xu, 1994). During the late Middle Permian, the regional crustal uplift, called the "Dongwu uplift movement," existed in the South China Craton and resulted in a widespread unconformity across most of South China (Hou et al., 2020). The ELIP was recognized as an important magmatic event that occurred in the South China Craton (Xu et al., 2001; Zhou et al., 2002; Xiao et al., 2004; Huang et al., 2014, 2016, 2018; Shellnutt et al., 2020). It mainly comprises voluminous continental flood basalt, ultramafic–mafic intrusive and extrusive rocks, rhyolite, and granitic rock (Xu et al., 2001, 2010; Xiao et al., 2004; Zhou et al., 2006; Liu et al., 2016; Huang et al., 2022a). The ELIP mainly erupted around the Permian Guadalupian–Lopingian boundary (~260–257 Ma) (Zhou et al., 2002; Shellnutt et al., 2012, 2020; Zhong et al., 2014, 2020; Huang et al., 2016, 2018, 2022b). The eruption of the ELIP covers an area of ~2.5×10^5 km^2 in the South China and northern Vietnam (**Figure 1**) (Chung and Jahn, 1995; Xu et al., 2001; Ali et al., 2010), and its volume is ~3.8×10^6 km^3 (He et al., 2007). The total thickness of the volcanic sequence ranges from more than 5 km in the west of the province to several hundred meters in the east (He et al., 2007). The Emeishan volcanic rocks overlie the limestone-dominated Middle Permian Maokou Formation and are, in turn, covered by Upper Permian clastic rocks in the east and Lower Triassic sedimentary rocks in the west (He et al., 2007). The Emeishan basalts were often divided into high-Ti and low-Ti groups according to Ti/Y ratios and TiO_2 values (Xu et al., 2001). In the western parts of the ELIP, such as the Binchuan and Panzhihua areas (**Figures 1**, **2**), the volcanic sequence is usually composed of low-Ti basalts at the bottom, high-Ti basalts in the middle, and felsic volcanic rocks (rhyolite and trachyte) at the top (Xu et al., 2010; Huang et al., 2022a).

3 SAMPLED STRATIGRAPHY AND ANALYTICAL METHODS

The Lower Triassic Qingtianbao Formation at Dengchuan consists of yellowish gray to purplish red sandstone,

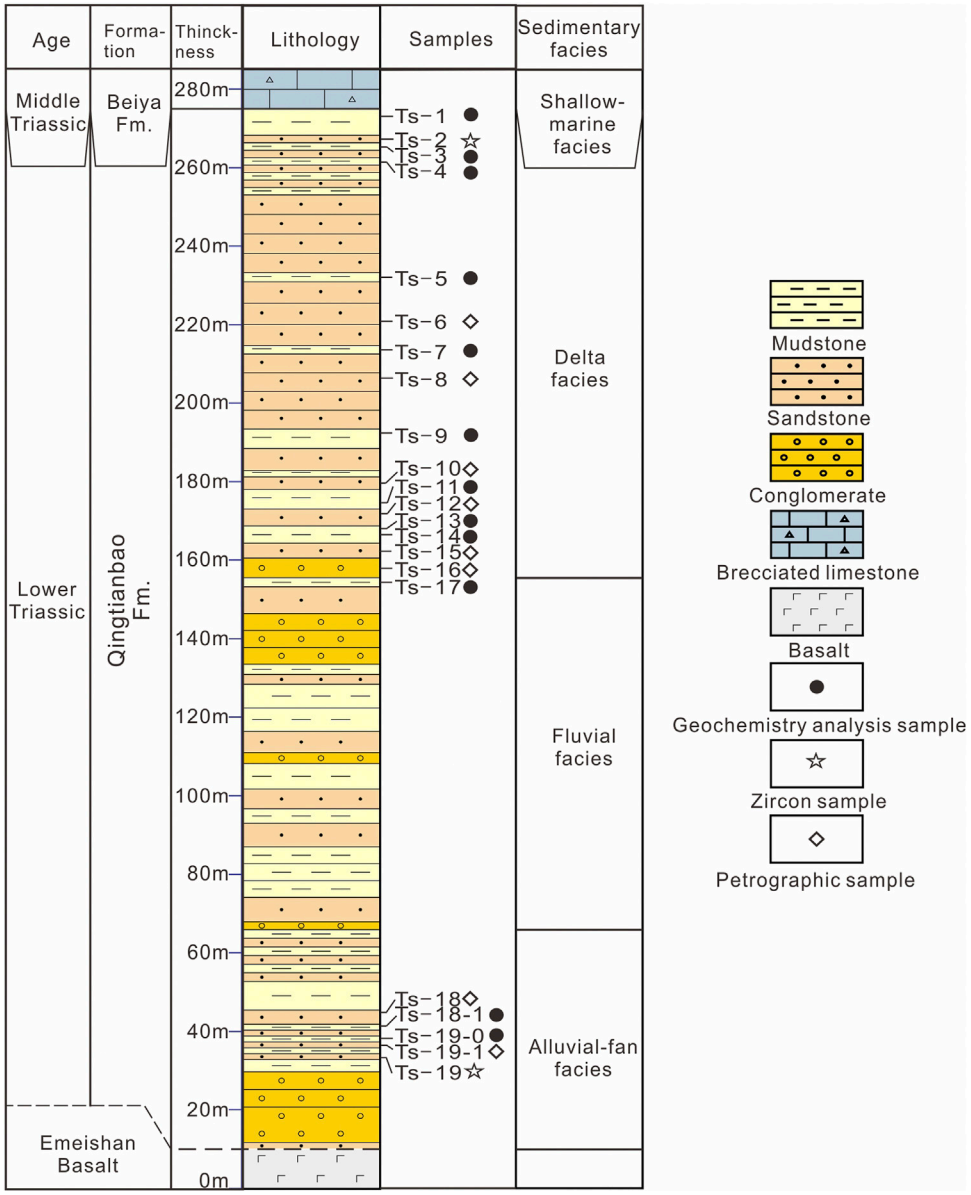

FIGURE 3 | Simplified stratigraphic section and sampling locations at Dengchuan (modified after Zhou et al., 2013).

mudstone, and conglomerate (**Figure 3**; **Figures 4A, B**). It is unconformably underlain by the Emeishan basalts and conformably overlain by breccia limestones of the Middle Triassic Beiya Formation (**Figure 3**) (Yunnan Geologic Bureau, 1973; Zhou et al., 2013). The Qingtianbao Formation can be classified into three sedimentary facies including alluvial-fan facies, fluvial facies, and delta facies (**Figure 3**) (Zhou et al., 2013). The vertical changes of sedimentary facies at Dengchuan indicate that the large-scale transgression occurred in this area, and it has experienced environmental changes from land to shallow sea during the Early Triassic to Middle Triassic (Zhou et al., 2013). Twenty-four samples, including ten petrologic samples, twelve geochemical analysis samples, and two zircon analysis samples, were collected from the Qingtianbao Formation at Dengchuan, Yunnan Province, in the southwestern margin of the South China Craton (**Figures 2**, **3**). The detrital compositions of sandstones from the Lower Triassic Qingtianbao Formation mainly comprise quartz (15–25%), feldspar (45–55%), and lithic fragments (15–45%). The dominant lithic fragments are basalts and felsic volcanic rocks (**Figures 4C, D**). Accessory minerals include zircon and magnetite. Both the roundness and sorting of sandstone samples are moderate (**Figures 4C, D**).

All samples were crushed (to 60 mesh) in a corundum jaw crusher. About 50 g of each sample was ground to a powder of less than 200 mesh in an agate ring mill. Whole-rock major and trace elements were analyzed with XRF (Primus II, Rigaku, Japan) and

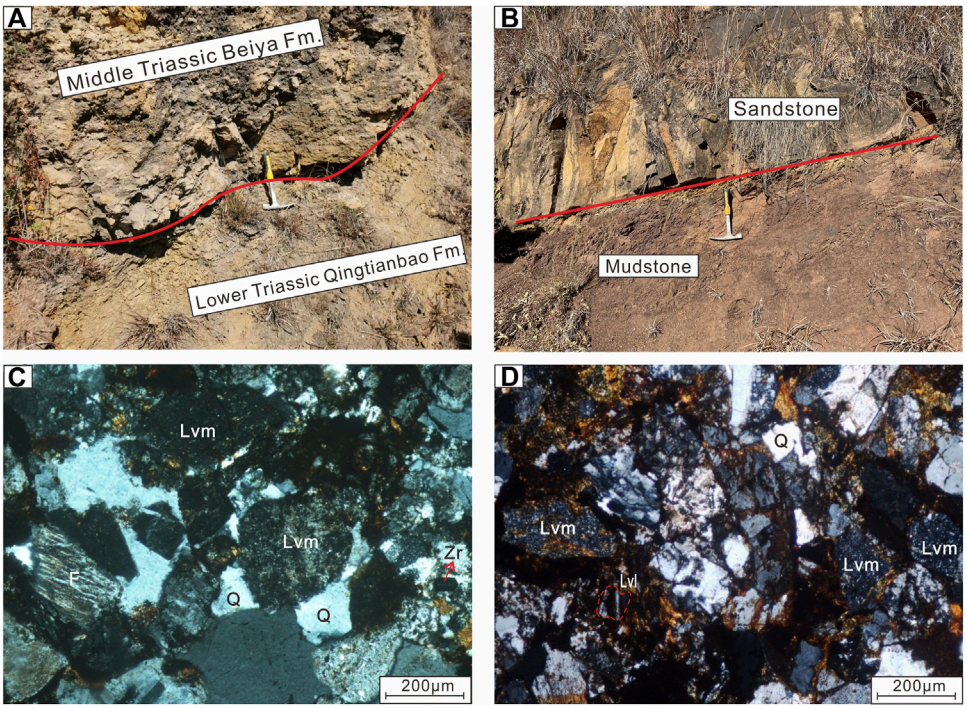

FIGURE 4 | Representative field outcrops and photomicrographs of clastic rocks at Dengchuan. **(A)** Boundary between the Middle Triassic Beiya Formation and Lower Triassic Qingtianbao Formation. **(B)** Sandstone and purple mudstone in the middle part of the Qingtianbao Formation. **(C)** Sandstone sample Ts-10. **(D)** Sandstone sample Ts-19. The photomicrographs of samples are in cross-polarized light. Volcanic rock fragments of lathwork (Lvl) and microlitic (Lvm); quartz (Q); feldspar (F); and zircon (Zr).

ICP–MS (Agilent 7700e) at Wuhan Sample Solution Analytical Technology Co., Ltd., Wuhan, China, respectively. The analytical precision is generally less than 5% and accuracy is better than 5% for most major and trace elements. The detailed analytical techniques of XRF and ICP-MS for element concentrations are the same as described by Ma et al. (2012) and Liu et al. (2008), respectively.

Zircon grains were separated by conventional heavy liquid and magnetic techniques, followed by hand picking under a binocular microscope and mounting in epoxy and polishing for the back-scattered electron (BSE) and cathodoluminescence (CL) imaging. U-Pb dating and trace element analysis of zircons were conducted by LA-ICP-MS at Wuhan Sample Solution Analytical Technology Co., Ltd., Wuhan, China. Detailed equipment configuration and data

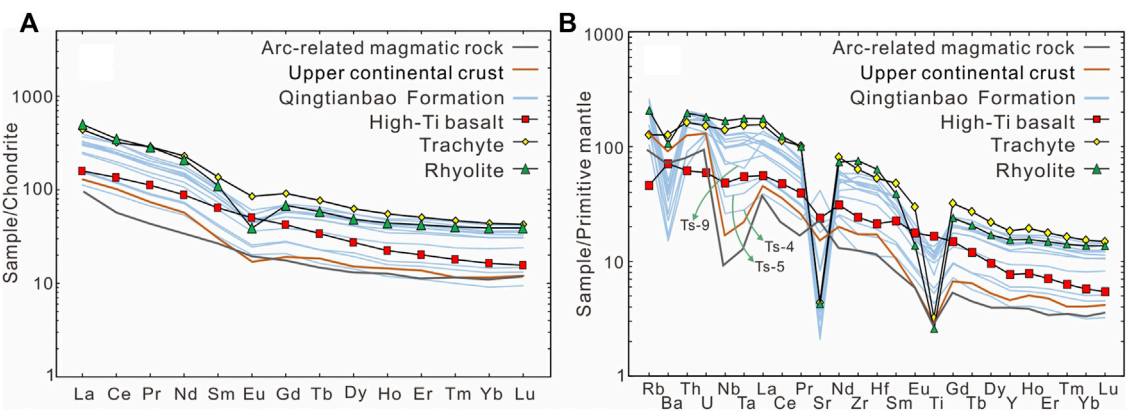

FIGURE 5 | (A) Chondrite-normalized REE diagram. **(B)** Primitive mantle-normalized trace element diagram. Normalized data are from Sun et al. (1989). The average upper continental crust (UCC) (Rudnick and Gao, 2003), arc-related magmatic rocks (Omrani et al., 2008), Emeishan high-Ti basalts (Xiao et al., 2003, 2004; Fan et al., 2008; Song et al., 2008; Anh et al., 2011; Lai et al., 2012; Huang et al., 2014), Emeishan rhyolites (Xu et al., 2010; Cheng et al., 2017; Hei et al., 2018; Huang et al., 2022a), and Emeishan trachytes (Shellnutt and Jahn, 2010; Xu et al., 2010) are displayed for comparison.

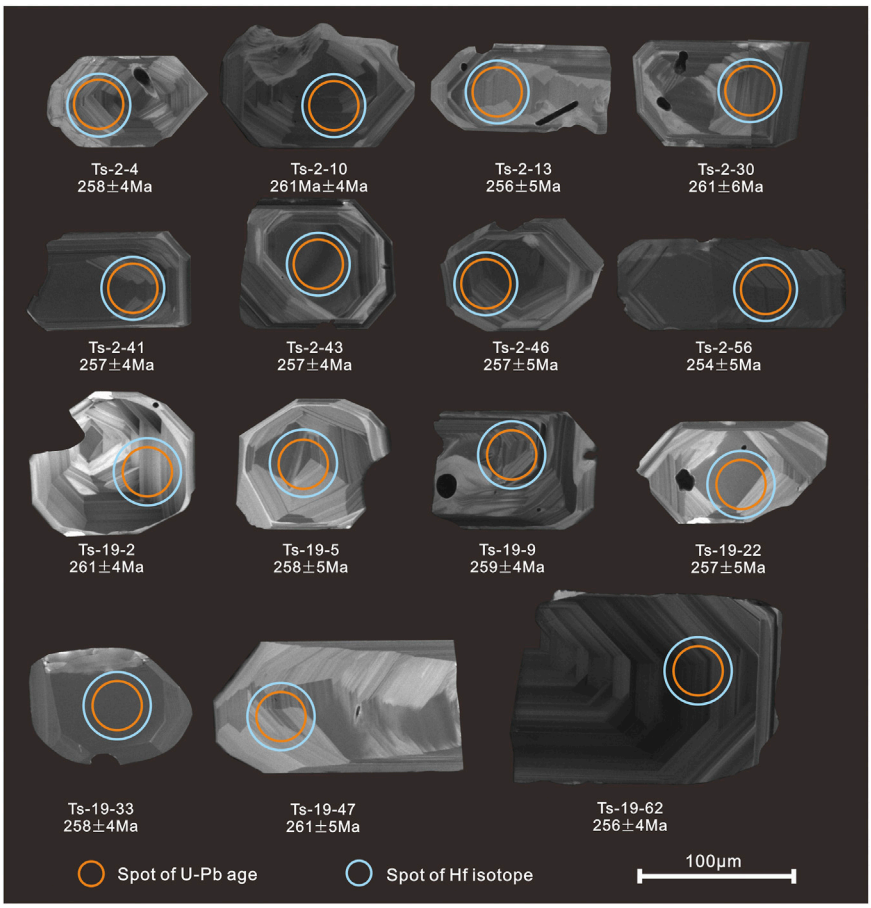

FIGURE 6 | Cathodoluminescence (CL) images of representative zircons from clastic rock samples at Dengchuan.

reduction were given in Zong et al. (2017). The analyses were performed on an Agilent 7700e ICP-MS instrument with a GeoLasPro laser ablation system that consists of a COMPexPro 102 ArF excimer laser (wavelength of 193 nm and maximum energy of 200 mJ) and a MicroLas optical system. In this study, the spot diameter and frequency of the laser were set to 32 μm and 5 Hz, respectively. Zircon 91500 was used as standards for U-Pb dating. Standard silicate glass SRM610 was used to calibrate the contents of elements. Each analysis consisted of approximately 20–30 s blank measurement and 50 s of data acquisition from the sample. Integration of background, off-line selection, analyzed signals, time-drift correction, and quantitative calibration for trace element analysis and U-Pb dating were conducted with Excel-based software ICPMSDataCal (Liu et al., 2008, 2010). All the age calculations and concordia diagrams were made using Isoplot 3.0 (Ludwig, 2003).

In situ zircon Hf isotopic measurements were performed using a Neptune Plus MC-ICP-MS (Thermo Fisher Scientific, Germany) in combination with a GeoLas HD excimer ArF laser ablation system (Coherent, Göttingen, Germany) at Wuhan Sample Solution Analytical Technology Co., Ltd, Wuhan, China. The Hf isotopic analyses were carried out on the same spots that were previously analyzed for U-Pb dating. The analysis parameters mainly include beam diameter of 44 μm, the ablation energy density of ~7.0 J/cm^2, background signal acquisition of 20 s, and ablation signal acquisition of 50 s. Detailed operating conditions and analytical methods were described by Hu et al. (2012). Zircon Plešovice, 91500, GJ-1, and TEM were analyzed as standard samples. The test value is consistent with the recommended value within the error range. Integration of analyte signals and off-line selection, and mass bias calibrations were performed using Excel-based software ICPMSDataCal (Liu et al., 2010). The decay constant of ^{176}Lu is 1.867 × 10^{-11}/year (Söderlund et al., 2004). The values of $\varepsilon_{Hf}(t)$ are calculated relative to chondrites whose ^{176}Hf/^{177}Hf and ^{176}Lu/^{177}Hf ratios are 0.282,772 and 0.0332, respectively (Blichert-Toft and Albarède, 1997). The single-stage model age (T_{DM1}) was calculated relative to the depleted mantle using 0.28325 for the ^{176}Hf/^{177}Hf ratio and 0.0384 for the ^{176}Lu/^{177}Hf ratio (Griffin et al., 2000). The two-stage model age (T_{DM2}) was calculated by assuming that zircon parental magma is derived from an average continental crust with a ^{176}Lu/^{177}Hf ratio of 0.015 (Griffin et al., 2000).

4 RESULTS

4.1 Whole-Rock Geochemistry

The mudstone samples contain variational SiO_2 (21.42–58.18%), Al_2O_3 (7.29–19.74%), TiO_2 (0.93–2.92%), and CaO (0.54–32.8%)

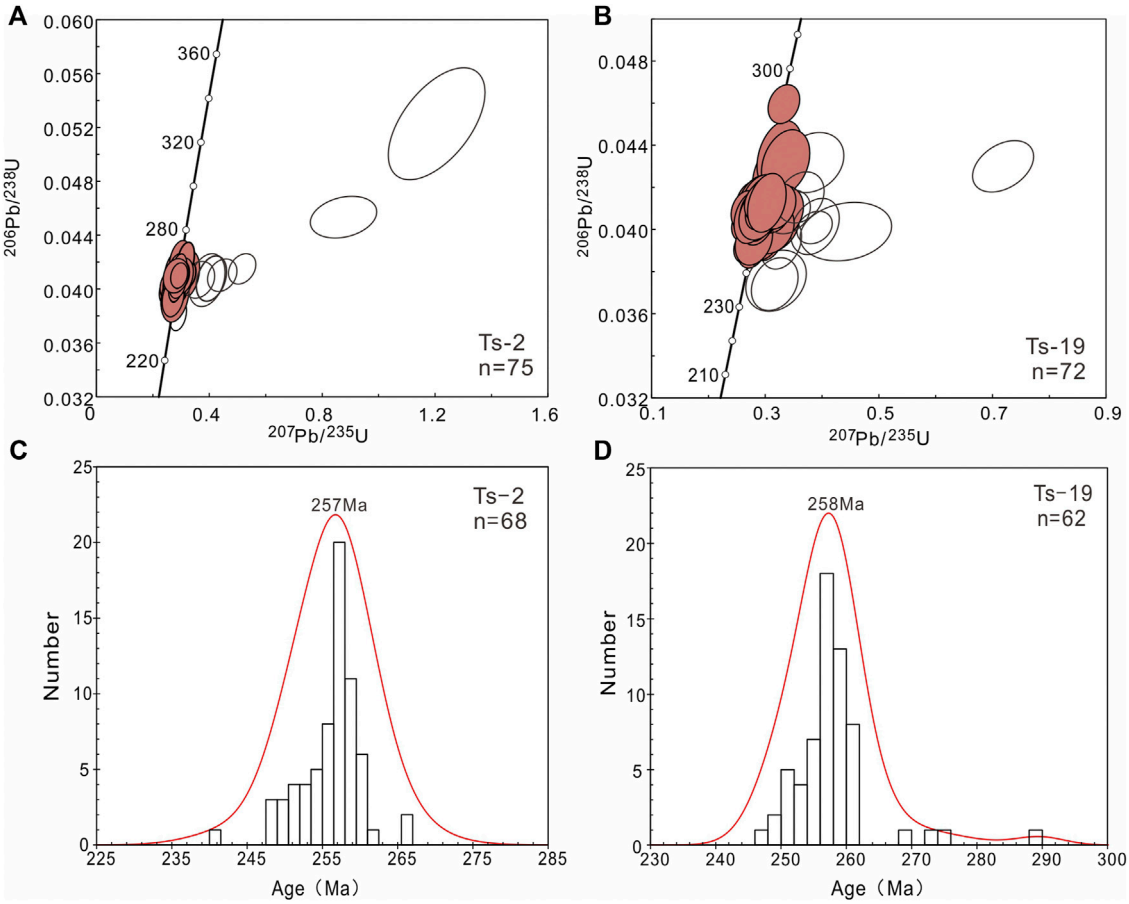

FIGURE 7 | (A,B) U-Pb concordia plots for detrital zircons at Dengchuan. **(C,D)** Histograms and probability curves for detrital zircon ages at Dengchuan.

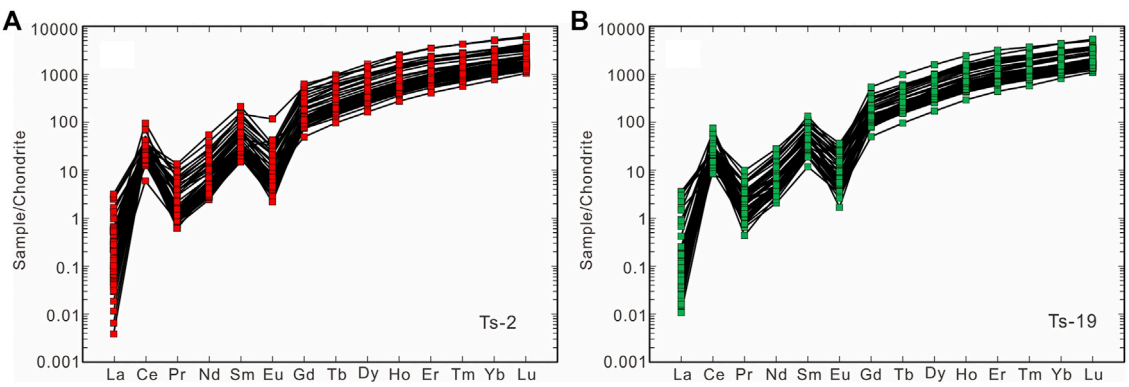

FIGURE 8 | (A,B) Chondrite-normalized REE patterns for zircons from clastic rock samples at Dengchuan. Normalized values for chondrite are from Sun et al. (1989).

values, with low Na_2O values (0.01–0.64%) and high K_2O values (2.2–6.11%) (**Supplementary Table S1**). The TiO_2 values are 0.93–2.92%, which are lower than Emeishan high-Ti basalts (>2.5%) (Xiao et al., 2003, 2004; Zhou et al., 2006; Fan et al., 2008; Song et al., 2008; Xu et al., 2008; Anh et al., 2011; Lai et al., 2012; Huang et al., 2014; He et al., 2018), but higher than Emeishan rhyolites (0.40–0.75%) (Xu et al., 2010; Cheng et al., 2017; Hei et al., 2018; Huang et al., 2022a). High CaO contents in some samples are consistent with the presence of limestone fragments in sandstone samples.

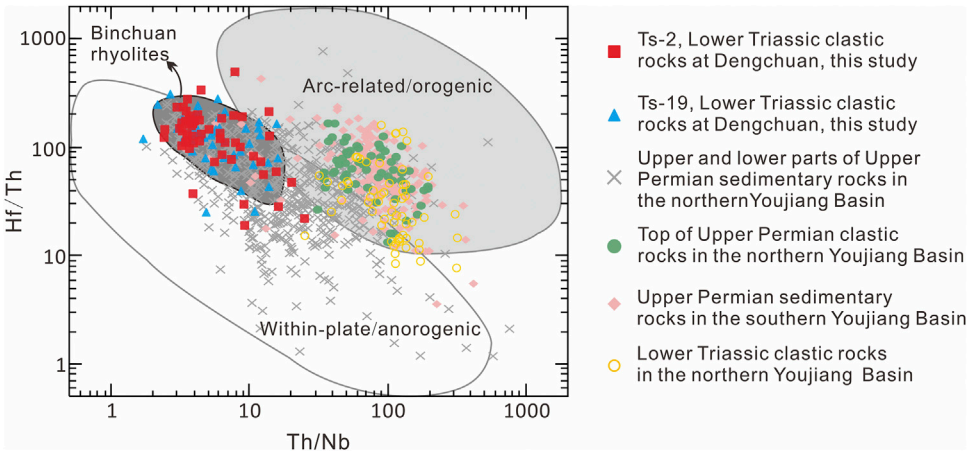

FIGURE 9 | Th/Nb vs. Hf/Th diagram for zircons with ages of ~260 Ma from Lower Triassic clastic samples at Dengchuan (Yang et al., 2012). Zircon trace element data for the upper and lower parts of Upper Permian sedimentary rocks in the northern Youjiang Basin (Yang et al., 2012, 2014, 2015; Huang et al., 2014; Yu et al., 2016), the top of Upper Permian clastic rocks in the northern Youjiang Basin (Yang et al., 2012), Upper Permian sedimentary rocks in the southern Youjiang Basin (Yu et al., 2016), and Lower Triassic clastic rocks in the northern Youjiang Basin are shown for comparison (Yang et al., 2012, 2014).

All samples have similar chondrite-normalized rare Earth element (REE) patterns with LREE enrichment and slightly negative Eu anomalies. In primitive mantle-normalized plots (**Figure 5B**), most of the analyzed samples show negative Sr anomaly and no Nb–Ta anomaly, similar to Emeishan high-Ti basalts and rhyolites (**Figure 5B**). Some samples (Ts-4, Ts-5, and Ts-9) from the upper part of the Qingtianbao Formation show slightly negative Nb–Ta anomalies, similar to the UCC (Rudnick and Gao, 2003) and arc-related magmatic rocks (**Figure 5B**) (Omrani et al., 2008).

4.2 Zircon U-Pb Ages

Zircon grains from sandstone samples are euhedral to subhedral and only a few grains are moderately rounded. They are 80–150 μm in length and have aspect ratios between 1:1 and 2.5:1 (**Figure 6**). Most zircons have oscillatory zoning without inherited core in the cathodoluminescence (CL) images and have high Th/U ratios (0.33–1.43) (**Supplementary Table S2**), indicating a magma origin (Hoskin and Schaltegger, 2003).

Seventy-five analyses were undertaken on 75 detrital zircon grains from the sandstone samples Ts-2, and sixty-eight ages displayed concordance greater than 90% (**Figure 7A**). These concordant ages range from 266 to 241 Ma, with a single peak at 257 Ma (**Figure 7C**).

Of 72 analyses on 72 detrital zircon grains, 62 were concordant for the sandstone sample Ts-19 (**Figure 7B**). The measured ages are between 290 Ma and 241 Ma, with a single peak at 258 Ma (**Figure 7D**).

4.3 Zircon Trace Elements

Trace elements for 103 zircon grains with ages at ~ 260 Ma are listed in **Supplementary Table S3**. Most of the analyzed grains have REE patterns that increase steeply from La to Lu, with positive Ce anomalies and negative Eu anomalies (**Figure 8**). Some trace element data for zircon grains were plotted on the Th/U vs. Nb/Hf diagram (**Figure 9**), which were constructed to distinguish the tectonic setting of the parental magma (Yang et al., 2012). Most zircons from the Qingtianbao Formation are plotted in the within-plate/anorogenic field.

4.4 Zircons Hf Isotope

The Hf isotopic compositions for 76 zircon grains with ages ranging from 290 Ma to 248 Ma are presented in **Supplementary Table S4**. The results show that 73 zircon grains have positive $\varepsilon_{Hf}(t)$ values ranging from +1.6 to +5.9 (**Figure 10A**) and two-stage model ages ranging from 1,063 to 826 Ma, while only three zircon grains have negative $\varepsilon_{Hf}(t)$ values ranging from −7.3 to −6.1 (**Figure 10A**) and two-stage model ages ranging from 1,555 to 1,491 Ma (**Supplementary Table S4**).

5 DISCUSSION

5.1 Provenance of Lower Triassic Succession

The studied sandstone samples from the Lower Triassic Qingtianbao Formation yielded only one predominant peak at ~ 260 Ma. The contemporaneous igneous activity along the southwestern margin of the South China Craton could be related to the ELIP or a convergent plate margin magmatic arc generated by the closure of the Paleo-Tethyan or Panthalassa Ocean (Zhou et al., 2002; Li et al., 2006; Jian et al., 2009; Zhong et al., 2014). The low-Ti basalts of the ELIP are preserved at the bottom of the Emeishan volcanic succession, which were not accessible to surface erosion during the Late Permian and Early Triassic, and thus they would not be the potential source (He et al., 2007). Most studied samples are geochemically similar to Emeishan high-Ti basalts and felsic volcanic rocks (**Figures 5**, **7**, **11**) but different from the arc-related magmatic rocks (**Figure 9**). Some samples show similar geochemical features to the UCC and arc-related magmatic rocks (**Figure 5**), suggestive of a possible genetic link. However, the zircons from the studied sandstone samples mostly fall into the within-plate/anorogenic zone (**Figure 9A**), which is

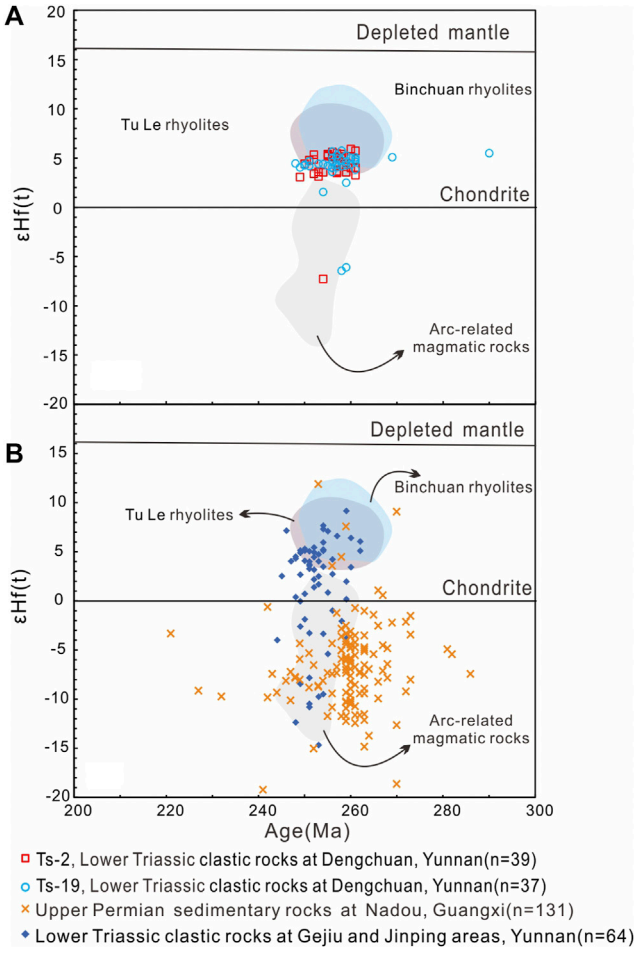

FIGURE 10 | (A,B) Plot of $\varepsilon_{Hf}(t)$ values vs. U-Pb ages for zircons. Date from Upper Permian sedimentary rocks at Nadou (Hou et al., 2017), Lower Triassic clastic rocks at Gejiu and Jinping areas (Xu et al., 2019), Tu Le and Binchuan rhyolites (Usuki et al., 2015; Huang et al., 2022a), and arc-related magmatic rocks from Hainan Island, southern Yunnan and Guangxi provinces (He et al., 2018; Shen et al., 2018; Wang et al., 2021) are shown for comparison. The depleted mantle evolution line data are from Blichert-Toft and Albarède, (1997) and Griffin et al. (2000).

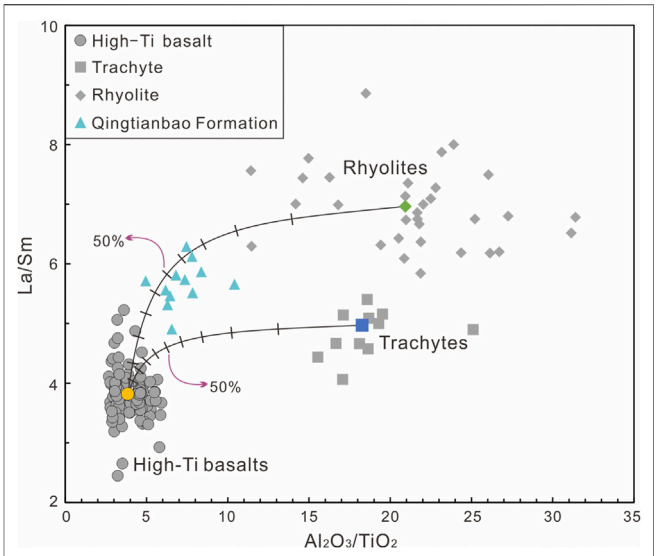

FIGURE 11 | Bivariate plot of Al_2O_3/TiO_2 vs. La/Sm for mudstone samples of the Qingtianbao Formation with two end-member mixing lines (Yang et al., 2015) using average values of Emeishan high-Ti basalts (Xu et al., 2001; Xiao et al., 2003, 2004; Fan et al., 2008; Song et al., 2008; Anh et al., 2011; Lai et al., 2012; Huang et al., 2014), Emeishan rhyolites (Xu et al., 2010; Cheng et al., 2017; Hei et al., 2018; Huang et al., 2022a), and Emeishan trachytes (Shellnutt and Jahn, 2010; Xu et al., 2010) shown for comparison.

consistent with the ELIP being derived from a mantle plume source region (Chung and Jahn, 1995; Xu et al., 2001). The positive $\varepsilon_{Hf}(t)$ values in most zircons from the Lower Triassic sandstones at Dengchuan are similar to those from Emeishan rhyolites in Binchuan and Tu Le (Usuki et al., 2015; Huang et al., 2022a) but different from the arc-related magmatic rocks (most <0) reported in the Hainan Island, southern Yunnan and Guangxi provinces (He et al., 2018; Shen et al., 2018; Xu et al., 2018; Wang et al., 2021). These chemical and isotopic characteristics suggest that the sources of the Lower Triassic clastic rocks at Dengchuan are not related to arc-related magmatism but were derived from the ELIP. The nearby sources related to the ELIP are consistent with the euhedral/prismatic crystal morphology for most analyzed zircons. The presence of basaltic and felsic volcanic lithic fragments in sandstone samples indicates that the sources of clastic rocks in the Qingtianbao Formation are a mixture of mafic and felsic rocks. This is consistent with the unconformity contact of the Lower Triassic clastic rocks with Emeishan rhyolites and high-Ti basalts at the Binchuan and Dengchuan areas. (Huang et al., 2022a; this study). Using average compositions of Emeishan high-Ti basalts (Xu et al., 2001; Xiao et al., 2003, 2004; Fan et al., 2008; Song et al., 2008; Anh et al., 2011; Lai et al., 2012; Huang et al., 2014), rhyolites (Xu et al., 2010; Cheng et al., 2017; Hei et al., 2018; Huang et al., 2022a), and trachytes (Shellnutt and Jahn, 2010; Xu et al., 2010), two end-member mixing calculations based on weathering-insensitive but source-responsive Al_2O_3/TiO_2 and La/Sm ratios (Yang et al., 2014, 2015) indicate that rhyolites and high-Ti basalts may be the most possible sources with similar weight percentages for detritus in the analyzed samples (**Figure 11**).

5.2 Indication of Subduction Polarity by Provenance

The southwestern margin of the South China Craton and Indochina Block have developed abundant magmatic rocks with ages of ~300–200 Ma (**Figure 1**), which are related to opening and closure of the Paleo-Tethyan or Panthalassa Ocean and ELIP (Zhou et al., 2002; Li et al., 2006; Jian et al., 2009; Zi et al., 2012; Zhong et al., 2014; Hu et al., 2017; Huang et al., 2022b). The subduction of the Panthalassa Ocean plate has been demonstrated beneath the eastern–southeastern margin of the South China Craton during the Paleozoic to Mesozoic (Isozaki et al., 2010; Hu et al., 2015a). The Permian arc-related magmatic units in Hainan Island are inferred to represent the southwest extension of this Paleozoic to Mesozoic accretionary belt (Li et al., 2006; Hu et al., 2015b). The arc-related magmatic

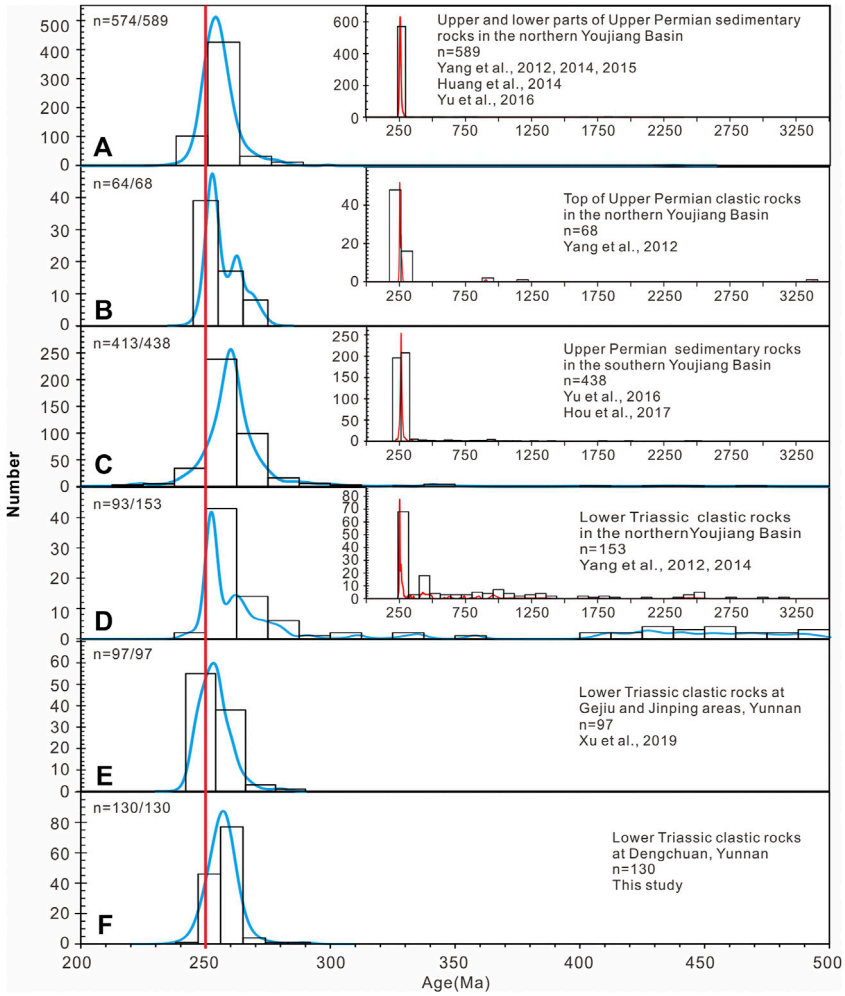

FIGURE 12 | (A–F) Probability density diagram comparing detrital zircon age patterns in the Upper Permian—Lower Triassic succession from the southwestern margin of the South China Craton.

rocks with ages of ~298–246 Ma (Jian et al., 2009; Liu et al., 2011; Li et al., 2012; Lai et al., 2014; Liu et al., 2017; He et al., 2020) were reported in the eastern Indochina Block, indicating the westward subduction of the Paleo-Tethyan Ocean. However, it is still debated whether the Paleo-Tethyan Ocean has undergone a subduction eastward beneath the South China Craton.

Detrital zircons with the main peak at ~ 260–250 Ma were widely reported in the Late Permian to Early Triassic strata from the southwestern margin of the South China Craton (**Figures 1**, **12**) (Yang et al., 2012, 2014, 2015; Huang et al., 2014; Yu et al., 2016; Hou et al., 2017; Xu et al., 2019). Zircons from the upper and lower parts of Upper Permian sedimentary rocks in the northern Youjiang Basin are mostly plotted in the within-plate/anorogenic field (**Figure 9**) and were derived from the Emeishan volcanic rocks (Yang et al., 2012, 2014, 2015; Huang et al., 2014; Yu et al., 2016). However, zircons from the top of Upper Permian and Lower Triassic clastic rocks in the northern Youjiang Basin (Yang et al., 2012, 2014) and Upper Permian sedimentary rocks in the southern Youjiang Basin (Yu et al., 2016) are mostly plotted in the arc-related/orogenic field (**Figure 9**). Most of these zircons have negative $\varepsilon_{Hf}(t)$ values (**Figure 10**) (Hou et al., 2017), similar to those from arc-related magmatic rocks (most <0) in the Hainan Island, southern Yunnan and Guangxi provinces (**Figure 1**) (He et al., 2018; Shen et al., 2018; Xu et al., 2018; Wang et al., 2021). This indicates that the detritus was likely to have been derived from arc-related magmatic rock. Both abundant negative and positive $\varepsilon_{Hf}(t)$ values for detrital zircons with ages of ~260 Ma are present in Lower Triassic clastic rocks at the Gejiu and Jinping areas, southern Yunnan province (Xu et al., 2019), indicating that the detritus was likely derived from a mixture of arc-related and ELIP-related magmatic rocks. The arc-related magmatic rocks have been inferred to generate from the subduction of the Paleo-Tethyan Ocean (Hou et al., 2017; Xu et al., 2019). However, recent studies about arc-related mafic rocks with ages of 254–250 Ma from the Gulinjing–Nanxi area in southern Yunnan province suggested that the subduction was linked to the Panthalassa Ocean to the south and not the Paleo-Tethyan Ocean to the west (**Figure 1**)

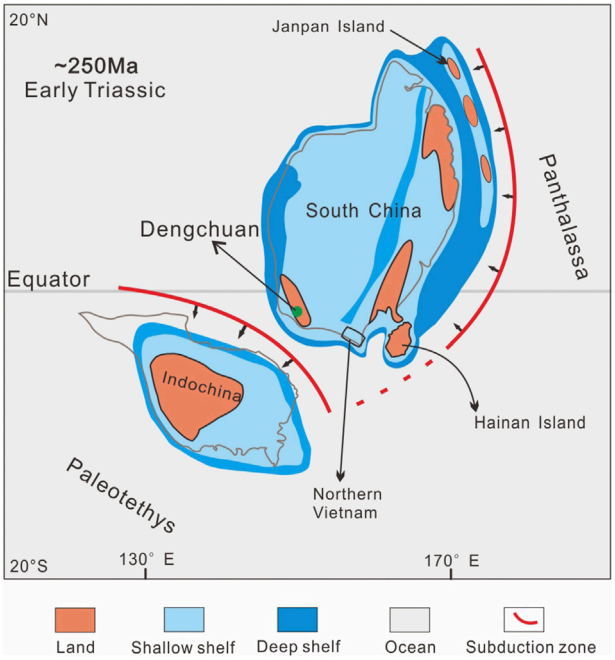

FIGURE 13 | Paleogeography reconstruction diagram of the South China Craton–Indochina Block during ~250 Ma (modified after Li et al., 2006; Ma et al., 2009; Cocks and Torsvik, 2013; Hu et al., 2017).

(Wang et al., 2021). The Lower Triassic clastic rocks at Dengchuan were sourced from the Emeishan volcanic rocks and not from the arc-related magmatic rocks. This is consistent with no Permian–Triassic arc-related magmatic rocks found in the western margin of the South China Craton (Wang et al., 2021). Our results do not support the eastward subduction of the Paleo-Tethyan Ocean, and the southwestern margin of the South China Craton may be a passive continental margin during the Late Permian–Early Triassic (**Figure 13**).

6 CONCLUSION

Provenance studies indicate that the Lower Triassic clastic rocks at Dengchuan were mainly derived from Emeishan volcanic rocks, with a mixture of high-Ti basalts and rhyolites. Integration of our data with those from Late Permian–Early Triassic strata and magmatic rocks along the southwestern margin of the South China Craton suggests that the Paleo-Tethyan Ocean may undergo a unidirectional subduction westward beneath the Indochina Block during the Late Permian–Early Triassic.

DATA AVAILABILITY STATEMENT

The original contributions presented in the study are included in the article/**Supplementary Material**; further inquiries can be directed to the corresponding author.

AUTHOR CONTRIBUTIONS

CH: writing—original draft, investigation, and data curation. HH: conceptualization, writing—review and editing, supervision, investigation, and funding acquisition. CY: writing—review and editing and investigation. LW: writing—review and editing and investigation. HL: writing—review and editing.

FUNDING

This work was supported by the National Natural Science Foundation of China (41972103).

ACKNOWLEDGMENTS

We would like to thank Associate Editor Shengyao Yu and two anonymous reviewers for their constructive comments and suggestions, which substantially improved our manuscript.

SUPPLEMENTARY MATERIAL

The Supplementary Material for this article can be found online at: https://www.frontiersin.org/articles/10.3389/feart.2022.932486/full#supplementary-material

REFERENCES

Ali, J. R., Fitton, J. G., and Herzberg, C. (2010). Emeishan Large Igneous Province (SW China) and the Mantle-Plume Up-Doming Hypothesis. *J. Geol. Soc.* 167 (5), 953–959. doi:10.1144/0016-76492009-129

Anh, T. V., Pang, K.-N., Chung, S.-L., Lin, H.-M., Hoa, T. T., Anh, T. T., et al. (2011). The Song Da Magmatic Suite Revisited: A Petrologic, Geochemical and Sr-Nd Isotopic Study on Picrites, Flood Basalts and Silicic Volcanic Rocks. *J. Asian Earth Sci.* 42 (6), 1341–1355. doi:10.1016/j.jseaes.2011.07.020

Blichert-Toft, J., and Albarède, F. (1997). The Lu-Hf Isotope Geochemistry of Chondrites and the Evolution of the Mantle-Crust System. *Earth Planet. Sci. Lett.* 148 (1), 243–258. doi:10.1016/S0012-821X(97)00040-X

Cawood, P. A., Hawkesworth, C. J., and Dhuime, B. (2012). Detrital Zircon Record and Tectonic Setting. *Geology* 40 (10), 875–878. doi:10.1130/G32945.1

Cawood, P. A., Zhao, G., Yao, J., Wang, W., Xu, Y., and Wang, Y. (2018). Reconstructing South China in Phanerozoic and Precambrian Supercontinents. *Earth-Science Rev.* 186, 173–194. doi:10.1016/j.earscirev.2017.06.001

Chen, Z., Lin, W., Faure, M., Lepvrier, C., Van Vuong, N., and Van Tich, V. (2014). Geochronology and Isotope Analysis of the Late Paleozoic to Mesozoic Granitoids from Northeastern Vietnam and Implications for the Evolution of the South China Block. *J. Asian Earth Sci.* 86, 131–150. doi:10.1016/j.jseaes.2013.07.039

Cheng, L.-L., Wang, Y., Herrin, J. S., Ren, Z.-Y., and Yang, Z.-F. (2017). Origin of K-Feldspar Megacrysts in Rhyolites from the Emeishan Large Igneous Province, Southwest China. *Lithos* 294-295, 397–411. doi:10.1016/j.lithos.2017.10.018

Chung, S.-L., and Jahn, B.-M. (1995). Plume-lithosphere Interaction in Generation of the Emeishan Flood Basalts at the Permian-Triassic Boundary. *Geol* 23 (10), 889–892. doi:10.1130/0091-7613(1995)023<0889:PLIIGO>2.3.CO

Cocks, L. R. M., and Torsvik, T. H. (2013). The Dynamic Evolution of the Palaeozoic Geography of Eastern Asia. *Earth-Science Rev.* 117, 40–79. doi:10.1016/j.earscirev.2012.12.001

Fan, W., Wang, Y., Zhang, A., Zhang, F., and Zhang, Y. (2010). Permian Arc-Back-Arc Basin Development along the Ailaoshan Tectonic Zone: Geochemical, Isotopic and Geochronological Evidence from the Mojiang Volcanic Rocks, Southwest China. *Lithos* 119 (3-4), 553–568. doi:10.1016/j.lithos.2010.08.010

Fan, W., Zhang, C., Wang, Y., Guo, F., and Peng, T. (2008). Geochronology and Geochemistry of Permian Basalts in Western Guangxi Province, Southwest China: Evidence for Plume-Lithosphere Interaction. *Lithos* 102 (1-2), 218–236. doi:10.1016/j.lithos.2007.09.019

Faure, M., Lepvrier, C., Nguyen, V. V., Vu, T. V., Lin, W., and Chen, Z. (2014). The South China Block-Indochina Collision: where, when, and How? *J. Asian Earth Sci.* 79, 260–274. doi:10.1016/j.jseaes.2013.09.022

Gan, C., Wang, Y., Zhang, Y., Qian, X., and Zhang, A. (2021). The Assembly of the South China and Indochina Blocks: Constraints from the Triassic Felsic Volcanics in the Youjiang Basin. *Geol. Soc. Am. Bull.* 133 (9-10), 2097–2112. doi:10.1130/B35816.1

Griffin, W. L., Pearson, N. J., Belousova, E., Jackson, S. E., van Achterbergh, E., O'Reilly, S. Y., et al. (2000). The Hf Isotope Composition of Cratonic Mantle: LAM-MC-ICPMS Analysis of Zircon Megacrysts in Kimberlites. *Geochimica Cosmochimica Acta* 64 (1), 133–147. doi:10.1016/S0016-7037(99)00343-9

Halpin, J. A., Tran, H. T., Lai, C.-K., Meffre, S., Crawford, A. J., and Zaw, K. (2016). U-pb Zircon Geochronology and Geochemistry from NE Vietnam: A 'tectonically Disputed' Territory between the Indochina and South China Blocks. *Gondwana Res.* 34, 254–273. doi:10.1016/j.gr.2015.04.005

He, B., Xu, Y.-G., Huang, X.-L., Luo, Z.-Y., Shi, Y.-R., Yang, Q.-J., et al. (2007). Age and Duration of the Emeishan Flood Volcanism, SW China: Geochemistry and SHRIMP Zircon U-Pb Dating of Silicic Ignimbrites, Post-volcanic Xuanwei Formation and Clay Tuff at the Chaotian Section. *Earth Planet. Sci. Lett.* 255 (3-4), 306–323. doi:10.1016/j.epsl.2006.12.021

He, H., Wang, Y., Cawood, P. A., Qian, X., Zhang, Y., and Zhao, G. (2020). Permo-Triassic Granitoids, Hainan Island, Link to Paleotethyan Not Paleopacific Tectonics. *Geol. Soc. Am. Bull.* 132 (9-10), 2067–2083. doi:10.1130/B35370.1

He, H., Wang, Y., Qian, X., and Zhang, Y. (2018). The Bangxi-Chenxing Tectonic Zone in Hainan Island (South China) as the Eastern Extension of the Song Ma-Ailaoshan Zone: Evidence of Late Paleozoic and Triassic Igneous Rocks. *J. Asian Earth Sci.* 164, 274–291. doi:10.1016/j.jseaes.2018.06.032

Hei, H.-X., Su, S.-G., Wang, Y., Mo, X.-X., Luo, Z.-H., and Liu, W.-G. (2018). Rhyolites in the Emeishan Large Igneous Province (SW China) with Implications for Plume-Related Felsic Magmatism. *J. Asian Earth Sci.* 164, 344–365. doi:10.1016/j.jseaes.2018.05.032

Hoa, T. T., Izokh, A. E., Polyakov, G. V., Borisenko, A. S., Anh, T. T., Balykin, P. A., et al. (2008). Permo-Triassic Magmatism and Metallogeny of Northern Vietnam in Relation to the Emeishan Plume. *Russ. Geol. Geophys.* 49 (7), 480–491. doi:10.1016/j.rgg.2008.06.005

Hoskin, P. W. O., and Schaltegger, U. (2003). 2. The Composition of Zircon and Igneous and Metamorphic Petrogenesis. *Rev. Mineral. Geochem.* 53 (1), 27–62. doi:10.1515/9781501509322-005

Hou, Y.-l., Zhong, Y.-t., Xu, Y.-g., and He, B. (2017). The Provenance of Late Permian Karstic Bauxite Deposits in SW China, Constrained by the Geochemistry of Interbedded Clastic Rocks, and U-Pb-Hf-O Isotopes of Detrital Zircons. *Lithos* 278-281, 240–254. doi:10.1016/j.lithos.2017.01.013

Hou, Z.-s., Fan, J.-x., Henderson, C. M., Yuan, D.-x., Shen, B.-h., Wu, J., et al. (2020). Dynamic Palaeogeographic Reconstructions of the Wuchiapingian Stage (Lopingian, Late Permian) for the South China Block. *Palaeogeogr. Palaeoclimatol. Palaeoecol.* 546, 109667. doi:10.1016/j.palaeo.2020.109667

Hu, L., Cawood, P. A., Du, Y., Xu, Y., Wang, C., Wang, Z., et al. (2017). Permo-Triassic Detrital Records of South China and Implications for the Indosinian Events in East Asia. *Palaeogeogr. Palaeoclimatol. Palaeoecol.* 485, 84–100. doi:10.1016/j.palaeo.2017.06.005

Hu, L., Cawood, P. A., Du, Y., Xu, Y., Xu, W., and Huang, H. (2015b). Detrital Records for Upper Permian-Lower Triassic Succession in the Shiwandashan Basin, South China and Implication for Permo-Triassic (Indosinian) Orogeny. *J. Asian Earth Sci.* 98, 152–166. doi:10.1016/j.jseaes.2014.11.007

Hu, L., Cawood, P. A., Du, Y., Yang, J., and Jiao, L. (2015a). Late Paleozoic to Early Mesozoic Provenance Record of Paleo-Pacific Subduction beneath South China. *Tectonics* 34 (5), 986–1008. doi:10.1002/2014TC003803

Hu, Z., Liu, Y., Gao, S., Liu, W., Zhang, W., Tong, X., et al. (2012). Improved *In Situ* Hf Isotope Ratio Analysis of Zircon Using Newly Designed X Skimmer Cone and Jet Sample Cone in Combination with the Addition of Nitrogen by Laser Ablation Multiple Collector ICP-MS. *J. Anal. At. Spectrom.* 27 (9), 1391–1399. doi:10.1039/c2ja30078h

Huang, H., Cawood, P. A., Hou, M.-C., Ni, S.-J., Yang, J.-H., Du, Y.-S., et al. (2018). Provenance of Late Permian Volcanic Ash Beds in South China: Implications for the Age of Emeishan Volcanism and its Linkage to Climate Cooling. *Lithos* 314-315, 293–306. doi:10.1016/j.lithos.2018.06.009

Huang, H., Cawood, P. A., Hou, M.-C., Xiong, F.-H., Ni, S.-J., Deng, M., et al. (2022a). Zircon U-Pb Age, Trace Element, and Hf Isotopic Constrains on the Origin and Evolution of the Emeishan Large Igneous Province. *Gondwana Res.* 105, 535–550. doi:10.1016/j.gr.2021.09.023

Huang, H., Cawood, P. A., Hou, M.-C., Yang, J.-H., Ni, S.-J., Du, Y.-S., et al. (2016). Silicic Ash Beds Bracket Emeishan Large Igneous Province to < 1 m.Y. At ~ 260 Ma. *Lithos* 264, 17–27. doi:10.1016/j.lithos.2016.08.013

Huang, H., Du, Y.-S., Yang, J.-H., Zhou, L., Hu, L.-S., Huang, H.-W., et al. (2014). Origin of Permian Basalts and Clastic Rocks in Napo, Southwest China: Implications for the Erosion and Eruption of the Emeishan Large Igneous Province. *Lithos* 208-209, 324–338. doi:10.1016/j.lithos.2014.09.022

Huang, H., Huyskens, M., Yin, Q. Z., Cawood, P. A., Hou, M. C., Yang, J. H., et al. (2022b). *Eruptive Tempo of Emeishan Large Igneous Province, Southwestern China and Northern Vietnam: Relations to Biotic Crises and Paleoclimate Changes Around the Guadalupian-Lopingian Boundary*. *Geology*. In Press. doi:10.1130/G50183.1

Isozaki, Y., Aoki, K., Nakama, T., and Yanai, S. (2010). New Insight into a Subduction-Related Orogen: A Reappraisal of the Geotectonic Framework and Evolution of the Japanese Islands. *Gondwana Res.* 18 (1), 82–105. doi:10.1016/j.gr.2010.02.015

Jian, P., Liu, D., Kröner, A., Zhang, Q., Wang, Y., Sun, X., et al. (2009). Devonian to Permian Plate Tectonic Cycle of the Paleo-Tethys Orogen in Southwest China (II): Insights from Zircon Ages of Ophiolites, Arc/back-Arc Assemblages and Within-Plate Igneous Rocks and Generation of the Emeishan CFB Province. *Lithos* 113 (3-4), 767–784. doi:10.1016/j.lithos.2009.04.006

Lai, C.-K., Meffre, S., Crawford, A. J., Zaw, K., Xue, C.-D., and Halpin, J. A. (2014). The Western Ailaoshan Volcanic Belts and Their SE Asia Connection: A New Tectonic Model for the Eastern Indochina Block. *Gondwana Res.* 26 (1), 52–74. doi:10.1016/j.gr.2013.03.003

Lai, S., Qin, J., Li, Y., Li, S., and Santosh, M. (2012). Permian High Ti/Y Basalts from the Eastern Part of the Emeishan Large Igneous Province, Southwestern China: Petrogenesis and Tectonic Implications. *J. Asian Earth Sci.* 47, 216–230. doi:10.1016/j.jseaes.2011.07.010

Li, G., Li, C., Ripley, E. M., Kamo, S., and Su, S. (2012). Geochronology, Petrology and Geochemistry of the Nanlinshan and Banpo Mafic-Ultramafic Intrusions: Implications for Subduction Initiation in the Eastern Paleo-Tethys. *Contrib. Mineral. Pet.* 164 (5), 773–788. doi:10.1007/s00410-012-0770-4

Li, Q., Lin, W., Wang, Y., Faure, M., Meng, L., Wang, H., et al. (2021). Detrital Zircon U Pb Age Distributions and Hf Isotopic Constraints of the Ailaoshan-Song Ma Suture Zone and Their Paleogeographic Implications for the Eastern Paleo-Tethys Evolution. *Earth-Science Rev.* 221, 103789. doi:10.1016/j.earscirev.2021.103789

Li, X.-H., Li, W.-X., Li, Z.-X., Lo, C.-H., Wang, J., Ye, M.-F., et al. (2009). Amalgamation between the Yangtze and Cathaysia Blocks in South China: Constraints from SHRIMP U-Pb Zircon Ages, Geochemistry and Nd-Hf Isotopes of the Shuangxiwu Volcanic Rocks. *Precambrian Res.* 174 (1-2), 117–128. doi:10.1016/j.precamres.2009.07.004

Li, X. H., Li, Z. X., Li, W. X., and Wang, Y. (2006). Initiation of the Indosinian Orogeny in South China: Evidence for a Permian Magmatic Arc on Hainan Island. *J. Geol.* 114 (3), 341–353. doi:10.1086/501222

Liu, B. J., and Xu, X. S. (1994). *Atlas of Lithofacies and Palaeogeography of South China (Sinian to Triassic)*. Beijing: Science Press. (in Chinese).

Liu, B., Ma, C.-Q., Guo, P., Sun, Y., Gao, K., and Guo, Y.-H. (2016). Evaluation of Late Permian Mafic Magmatism in the Central Tibetan Plateau as a Response to Plume-Subduction Interaction. *Lithos* 264, 1–16. doi:10.1016/j.lithos.2016.08.011

Liu, C., Deng, J. F., Liu, J. L., and Shi, Y. L. (2011). Characteristics of Volcanic Rocks from Late Permian to Early Triassic in Ailaoshan Tectono-magmatic Belt and Implications for Tectonic Settings. *Acta Pet. Sin.* 12 (27), 3590. (In Chinese With English Abstract).

Liu, H., Wang, Y., and Zi, J.-W. (2017). Petrogenesis of the Dalongkai Ultramafic-Mafic Intrusion and its Tectonic Implication for the Paleotethyan Evolution along the Ailaoshan Tectonic Zone (SW China). *J. Asian Earth Sci.* 141, 112–124. doi:10.1016/j.jseaes.2016.07.015

Liu, Y., Gao, S., Hu, Z., Gao, C., Zong, K., and Wang, D. (2010). Continental and Oceanic Crust Recycling-Induced Melt-Peridotite Interactions in the Trans-North China Orogen: U-Pb Dating, Hf Isotopes and Trace Elements in Zircons from Mantle Xenoliths. *J. Petrology* 51 (1-2), 537–571. doi:10.1093/petrology/egp082

Liu, Y., Hu, Z., Gao, S., Günther, D., Xu, J., Gao, C., et al. (2008). *In Situ* analysis of Major and Trace Elements of Anhydrous Minerals by LA-ICP-MS without Applying an Internal Standard. *Chem. Geol.* 257 (1-2), 34–43. doi:10.1016/j.chemgeo.2008.08.004

Ludwig, K. R. (2003). *User's Manual for Isoplot 3.00: A Geochronological Toolkit for Microsoft Excel*. California Berkeley: Berkeley Geochronology Center, p39.

Ma, Q., Zheng, J., Griffin, W. L., Zhang, M., Tang, H., Su, Y., et al. (2012). Triassic "Adakitic" Rocks in an Extensional Setting (North China): Melts from the Cratonic Lower Crust. *Lithos* 149, 159–173. doi:10.1016/j.lithos.2012.04.017

Ma, Y. S., Chen, H. D., and Wang, G. L. (2009). *Tectonic-sequence Lithofacies Palaeogeography Atlas of South China: Sinian-Neogene*. Beijing: Science Press. (In Chinese).

Metcalfe, I. (2013). Gondwana Dispersion and Asian Accretion: Tectonic and Palaeogeographic Evolution of Eastern Tethys. *J. Asian Earth Sci.* 66, 1–33. doi:10.1016/j.jseaes.2012.12.020

Metcalfe, I. (2006). Palaeozoic and Mesozoic Tectonic Evolution and Palaeogeography of East Asian Crustal Fragments: The Korean Peninsula in Context. *Gondwana Res.* 9 (1-2), 24–46. doi:10.1016/j.gr.2005.04.002

Ngo, T. X., Santosh, M., Tran, H. T., and Pham, H. T. (2016). Subduction Initiation of Indochina and South China Blocks: Insight from the Forearc Ophiolitic Peridotites of the Song Ma Suture Zone in Vietnam. *Geol. J.* 51 (3), 421–442. doi:10.1002/gj.2640

Omrani, J., Agard, P., Whitechurch, H., Benoit, M., Prouteau, G., and Jolivet, L. (2008). Arc-magmatism and Subduction History beneath the Zagros Mountains, Iran: A New Report of Adakites and Geodynamic Consequences. *Lithos* 106 (3-4), 380–398. doi:10.1016/j.lithos.2008.09.008

Qing, X. F., Wang, Z. Q., Zhang, Y. L., Pan, L. Z., Hu, G. A., and Zhou, F. S. (2011). Geochronology and Geochemistry of Early Mesozoic Acidic Volcanic Rocks in Sw Guangxi: Constraints on Tectonic Evolution of the Sw Qin-Hang Boundary Zone. *Acta Pet. Sin.* 27 (03), 794 (In Chinese With English Abstract).

Rudnick, R. L., and Gao, S. (2003). Composition of the Continental Crust. *Treat. Geochem.* 3, 1–64. doi:10.1016/B0-08-043751-6/03016-4

Scholl, D. W., and von Huene, R. (2009). Implications of Estimated Magmatic Additions and Recycling Losses at the Subduction Zones of Accretionary (Non-collisional) and Collisional (Suturing) Orogens. *Geol. Soc. Lond. Spec. Publ.* 318 (1), 105–125. doi:10.1144/SP318.4

Shellnutt, J. G., Denyszyn, S. W., and Mundil, R. (2012). Precise Age Determination of Mafic and Felsic Intrusive Rocks from the Permian Emeishan Large Igneous Province (SW China). *Gondwana Res.* 22 (1), 118–126. doi:10.1016/j.gr.2011.10.009

Shellnutt, J. G., and Jahn, B.-M. (2010). Formation of the Late Permian Panzhihua Plutonic-Hypabyssal-Volcanic Igneous Complex: Implications for the Genesis of Fe-Ti Oxide Deposits and A-type Granites of SW China. *Earth Planet. Sci. Lett.* 289 (3-4), 509–519. doi:10.1016/j.epsl.2009.11.044

Shellnutt, J. G., Pham, T. T., Denyszyn, S. W., Yeh, M.-W., and Tran, T.-A. (2020). Magmatic Duration of the Emeishan Large Igneous Province: Insight from Northern Vietnam. *Geology* 48 (5), 457–461. doi:10.1130/G47076.1

Shen, L., Yu, J.-H., O'Reilly, S. Y., Griffin, W. L., and Zhou, X. (2018). Subduction-related Middle Permian to Early Triassic Magmatism in Central Hainan Island, South China. *Lithos* 318-319, 158–175. doi:10.1016/j.lithos.2018.08.009

Söderlund, U., Patchett, P. J., Vervoort, J. D., and Isachsen, C. E. (2004). The ^{176}Lu Decay Constant Determined by Lu–Hf and U–Pb Isotope Systematics of Precambrian Mafic Intrusions. *Earth Planet. Sc. Lett.* 219 (3-4), 311–324. doi:10.1016/S0012-821X(04)00012-3

Song, X.-Y., Qi, H.-W., Robinson, P. T., Zhou, M.-F., Cao, Z.-M., and Chen, L.-M. (2008). Melting of the Subcontinental Lithospheric Mantle by the Emeishan Mantle Plume; Evidence from the Basal Alkaline Basalts in Dongchuan, Yunnan, Southwestern China. *Lithos* 100 (1-4), 93–111. doi:10.1016/j.lithos.2007.06.023

Sun, S.-s., Mcdonough, W. F., Saunders, A. D., and Norry, M. J. (1989). Chemical and Isotopic Systematics of Oceanic Basalts: Implications for Mantle Composition and Processes. *Geol. Soc. Lond. Spec. Publ.* 42 (1), 313–345. doi:10.1144/GSL.SP.1989.042.01.19

Tran, T. V., Faure, M., Nguyen, V. V., Bui, H. H., Fyhn, M. B. W., Nguyen, T. Q., et al. (2020). Neoproterozoic to Early Triassic Tectono-Stratigraphic Evolution of Indochina and Adjacent Areas: A Review with New Data. *J. Asian Earth Sci.* 191, 104231. doi:10.1016/j.jseaes.2020.104231

Usuki, T., Lan, C.-Y., Tran, T. H., Pham, T. D., Wang, K.-L., Shellnutt, G. J., et al. (2015). Zircon U-Pb Ages and Hf Isotopic Compositions of Alkaline Silicic Magmatic Rocks in the Phan Si Pan-Tu Le Region, Northern Vietnam: Identification of a Displaced Western Extension of the Emeishan Large Igneous Province. *J. Asian Earth Sci.* 97, 102–124. doi:10.1016/j.jseaes.2014.10.016Wang

Wang, Y., Wang, Q., Deng, J., Xue, S., Li, C., and Ripley, E. M. (2021). Late Permian-Early Triassic Mafic Dikes in the Southwestern Margin of the South China Block: Evidence for Paleo-Pacific Subduction. *Lithos* 384-385, 105994. doi:10.1016/j.lithos.2021.105994

Xia, X.-P., Xu, J., Huang, C., Long, X., and Zhou, M. (2019). Subduction Polarity of the Ailaoshan Ocean (Eastern Paleotethys): Constraints from Detrital Zircon U-Pb and Hf-O Isotopes for the Longtan Formation. *Geol. Soc. Am. Bull.* 132 (5-6), 987–996. doi:10.1130/B35294.1

Xiao, L., Xu, Y.-G., Chung, S.-L., He, B., and Mei, H. (2003). Chemostratigraphic Correlation of Upper Permian Lavas from Yunnan Province, China: Extent of the Emeishan Large Igneous Province. *Int. Geol. Rev.* 45 (8), 753–766. doi:10.2747/0020-6814.45.8.753

Xiao, L., Xu, Y. G., Mei, H. J., Zheng, Y. F., He, B., and Pirajno, F. (2004). Distinct Mantle Sources of Low-Ti and High-Ti Basalts from the Western Emeishan Large Igneous Province, SW China: Implications for Plume-Lithosphere Interaction. *Earth Planet. Sci. Lett.* 228 (3-4), 525–546. doi:10.1016/j.epsl.2004.10.002

Xu, J., Xia, X. P., Lai, C., Long, X., and Huang, C. (2019). When Did the Paleotethys Ailaoshan Ocean Close: New Insights from Detrital Zircon U-Pb Age and Hf Isotopes. *Tectonics* 38 (5), 1798–1823. doi:10.1029/2018TC005291

Xu, W.-C., Luo, B.-J., Xu, Y.-J., Wang, L., and Chen, Q. (2018). Geochronology, Geochemistry, and Petrogenesis of Late Permian to Early Triassic Mafic Rocks from Darongshan, South China: Implications for Ultrahigh-Temperature Metamorphism and S-type Granite Generation. *Lithos* 308-309, 168–180. doi:10.1016/j.lithos.2018.03.004

Xu, Y.-G., Chung, S.-L., Shao, H., and He, B. (2010). Silicic Magmas from the Emeishan Large Igneous Province, Southwest China: Petrogenesis and Their Link with the End-Guadalupian Biological Crisis. *Lithos* 119 (1-2), 47–60. doi:10.1016/j.lithos.2010.04.013

Xu, Y.-G., He, B., Chung, S.-L., Menzies, M. A., and Frey, F. A. (2004). Geologic, Geochemical, and Geophysical Consequences of Plume Involvement in the Emeishan Flood-Basalt Province. *Geology* 32 (10), 917–920. doi:10.1130/G20602.1

Xu, Y.-G., Luo, Z.-Y., Huang, X.-L., He, B., Xiao, L., Xie, L.-W., et al. (2008). Zircon U-Pb and Hf Isotope Constraints on Crustal Melting Associated with the Emeishan Mantle Plume. *Geochimica Cosmochimica Acta* 72 (13), 3084–3104. doi:10.1016/j.gca.2008.04.019

Xu, Y. G., Chung, S. L., Jahn, B. M., and Wu, G. Y. (2001). Petrologic and Geochemical Constraints on the Petrogenesis of Permian–Triassic Emeishan Flood Basalts in Southwestern China. *Lithos* 58 (3), 145–168. doi:10.1016/S0024-4937(01)00055-X

Yan, Q., Metcalfe, I., and Shi, X. (2017). U-pb Isotope Geochronology and Geochemistry of Granites from Hainan Island (Northern South China Sea Margin): Constraints on Late Paleozoic-Mesozoic Tectonic Evolution. *Gondwana Res.* 49, 333–349. doi:10.1016/j.gr.2017.06.007

Yunnan Geologic Bureau. (1973). *Geological Report of the Dali Area at Scale of 1: 200,000*. (in Chinese).

Yunnan Geologic Bureau (1966). *Geological Report of the Heqing Area at Scale of 1: 200,000*. (in Chinese).

Yan, Z., Tian, Y., Li, R., Vermeesch, P., Sun, X., Li, Y., et al. (2019). Late Triassic Tectonic Inversion in the Upper Yangtze Block: Insights from Detrital Zircon U-Pb Geochronology from South-Western Sichuan Basin. *Basin Res.* 31 (1), 92–113. doi:10.1111/bre.12310

Yang, J., Cawood, P. A., Du, Y., Huang, H., and Hu, L. (2014). A Sedimentary Archive of Tectonic Switching from Emeishan Plume to Indosinian Orogenic Sources in SW China. *J. Geol. Soc.* 171 (2), 269–280. doi:10.1144/jgs2012-143

Yang, J., Cawood, P. A., Du, Y., Huang, H., Huang, H., and Tao, P. (2012). Large Igneous Province and Magmatic Arc Sourced Permian-Triassic Volcanogenic Sediments in China. *Sediment. Geol.* 261-262, 120–131. doi:10.1016/j.sedgeo.2012.03.018

Yang, J., Cawood, P. A., and Du, Y. (2015). Voluminous Silicic Eruptions during Late Permian Emeishan Igneous Province and Link to Climate Cooling. *Earth Planet. Sci. Lett.* 432 (1), 166–175. doi:10.1016/j.epsl.2015.09.050

Yu, W., Algeo, T. J., Du, Y., Zhang, Q., and Liang, Y. (2016). Mixed Volcanogenic-Lithogenic Sources for Permian Bauxite Deposits in Southwestern Youjiang Basin, South China, and Their Metallogenic Significance. *Sediment. Geol.* 341, 276–288. doi:10.1016/j.sedgeo.2016.04.016

Zhong, Y.-T., He, B., Mundil, R., and Xu, Y.-G. (2014). CA-TIMS Zircon U-Pb Dating of Felsic Ignimbrite from the Binchuan Section: Implications for the Termination Age of Emeishan Large Igneous Province. *Lithos* 204, 14–19. doi:10.1016/j.lithos.2014.03.005

Zhong, Y.-T., He, B., and Xu, Y.-G. (2013). Mineralogy and Geochemistry of Claystones from the Guadalupian-Lopingian Boundary at Penglaitan, South China: Insights into the Pre-lopingian Geological Events. *J. Asian Earth Sci.* 62, 438–462. doi:10.1016/j.jseaes.2012.10.028

Zhong, Y., Mundil, R., Chen, J., Yuan, D., Denyszyn, S. W., Jost, A. B., et al. (2020). Geochemical, Biostratigraphic, and High-Resolution Geochronological Constraints on the Waning Stage of Emeishan Large Igneous Province. *Geol. Soc. Am. Bull.* 132 (9-10), 1969–1986. doi:10.1130/B35464.1

Zhou, M.-F., Zhao, J.-H., Qi, L., Su, W., and Hu, R. (2006). Zircon U-Pb Geochronology and Elemental and Sr-Nd Isotope Geochemistry of Permian Mafic Rocks in the Funing Area, SW China. *Contrib. Mineral. Pet.* 151 (1), 1–19. doi:10.1007/s00410-005-0030-y

Zhou, M. F., Malpas, J., Song, X. Y., Robinson, P. T., Sun, M., Kennedy, A. K., et al. (2002). A Temporal Link between the Emeishan Large Igneous Province (SW China) and the End-Guadalupian Mass Extinction. *Earth Planet. Sci. Lett.* 196 (3), 113–122. doi:10.1016/S0012-821X(01)00608-2

Zhou, Y. X., Wang, J., Zou, G. F., Wang, P., Ren, F., Dong, L. Y., et al. (2013). Study on Alluvial Fan-Delta Depositional System of Lower Triassic Qingtianbao Formation in Junmachang, Eryuan County, Western Yunnan. *Sediment. Geol. Tethyan Geol.* 33 (04), 6

Zi, J.-W., Cawood, P. A., Fan, W.-M., Wang, Y.-J., Tohver, E., Mccuaig, T. C., et al. (2012). Triassic Collision in the Paleo-Tethys Ocean Constrained by Volcanic Activity in SW China. *Lithos* 144-145, 145–160. doi:10.1016/j.lithos.2012.04.020

Zong, K., Klemd, R., Yuan, Y., He, Z., Guo, J., Shi, X., et al. (2017). The Assembly of Rodinia: The Correlation of Early Neoproterozoic (Ca. 900 Ma) High-Grade Metamorphism and Continental Arc Formation in the Southern Beishan Orogen, Southern Central Asian Orogenic Belt (CAOB). *Precambrian Res.* 290, 32–48. doi:10.1016/j.precamres.2016.12.010

Conflict of Interest: The authors declare that the research was conducted in the absence of any commercial or financial relationships that could be construed as a potential conflict of interest.

frontiers | Frontiers in Earth Science

TYPE Original Research
PUBLISHED 25 August 2022
DOI 10.3389/feart.2022.927695

OPEN ACCESS

EDITED BY
Shengyao Yu,
Ocean University of China, China

REVIEWED BY
Xinlu Hu,
China University of Geosciences Wuhan, China
Qiaoqiao Zhu,
Chinese Academy of Geological Sciences, China

*CORRESPONDENCE
You-Guo Li,
lyguo@cdut.edu.cn
Wen-Chang Li,
lwcyndd@163.com

SPECIALTY SECTION
This article was submitted to Petrology, a section of the journal Frontiers in Earth Science

RECEIVED 24 April 2022
ACCEPTED 12 July 2022
PUBLISHED 25 August 2022

CITATION
Liu H, Li Y-G, Li W-C, Li G-M, Ma D-F, Ouyang Y, Huang H-X, Zhang Z-L, Li T and Wu J-Y (2022), Petrogenesis of the late Cretaceous Budongla Mg-rich monzodiorite pluton in the central Lhasa subterrane, Tibet, China: Whole-rock geochemistry, zircon U-Pb dating, and zircon Lu-Hf isotopes.
Front. Earth Sci. 10:927695.
doi: 10.3389/feart.2022.927695

Petrogenesis of the late Cretaceous Budongla Mg-rich monzodiorite pluton in the central Lhasa subterrane, Tibet, China: Whole-rock geochemistry, zircon U-Pb dating, and zircon Lu-Hf isotopes

Hong Liu[1,2], You-Guo Li[1]*, Wen-Chang Li[2,3]*, Guang-Ming Li[2], Dong-Fang Ma[2], Yuan Ouyang[2], Han-Xiao Huang[2], Zhi-Lin Zhang[4], Tong Li[1] and Jun-Yi Wu[2,5,6]

[1]College of Earth Sciences, Chengdu University of Technology, Chengdu, China, [2]Chengdu Center, China Geological Survey, Chengdu, China, [3]College of Land and Resources Engineering, Kunming University of Science and Technology, Kunming, China, [4]The 5th Geological Team of Tibet Geological Exploration Bureau, Golmud, China, [5]Graduate School, Chinese Academy of Geological Sciences, Beijing, China, [6]Graduate School, China University of Geosciences, Beijing, China

Mg-rich monzodiorite are found in the Budongla gold ore district, Zhongba County, Xizang (Tibet) Autonomous Region, P.R. China. Studying the petrogenesis of this intermediate pluton can provide effective information to explore the geological evolution of the Lhasa terrane. One monzodiorite sample yielded a weighted mean $^{206}Pb/^{238}U$ age of 92.7 ± 1.1 Ma (mean square weighted deviation=0.33) using LA-ICP-MS zircon U-Pb dating, which represents the late phase of Late Cretaceous magmatism. The rock-forming minerals in the Budongla Mg-rich monzodiorite mainly include K-feldspar, plagioclase, quartz, biotite augite, and amphibole, and its accessory minerals mainly include magnetite, titanite, zircon, and apatite. The rocks are rich in K_2O+Na_2O and K_2O with medium contents of SiO_2, CaO, and $A1_2O_3$,, suggesting these rocks belong to the high-K calc-alkaline series. These rocks have high MgO, Fe_2O_3, and FeO, with high Mg# values and low DI, which implies they are Mg-rich intermediate intrusive rocks. The rocks are enriched in LREEs and LILEs and depleted in HREEs and HFSEs. They have negative Eu anomalies, no obvious negative Ce anomalies, and slightly negative $\varepsilon_{Hf}(t)$. We infer that the Budongla pluton is a high-K calc-alkaline metaluminous Mg-rich monzodiorite and intruded during the post-collisional period of the Lhasa and Qiangtang terranes.

KEYWORDS

central Lhasa terrane, Bangong-Nujiang, Budongla, postcollision, Mg-rich intermediate intrusive rocks

Introduction

The Lhasa terrane (LS), which is also known as the Gangdese-Nyainqentanglha terrane, is one of the main massifs of the Qinghai-Xizhang Plateau (Figures 1A,B), located between the Bangong-Nujiang suture zone (BNSZ) in the north and the Indus-Yarlung Zangbo suture zone (YZSZ) in the south (Pan et al., 2001; Yang et al., 2007; Pan et al., 2009; Liu et al., 2016; Liu et al., 2021a; Wang et al., 2022). The Lhasa terrane is critical for understanding the tectonic evolution of this Plateau, particularly with regard to early crustal thickening. Mesozoic to Cenozoic magmatic rocks are widely distributed in this block, which can provide insights into the geodynamic processes related to the growth of the Tibetan Plateau. The Lhasa terrane comprises three roughly parallel subterranes: the South Lhasa subterrane (SL), the Central Lhasa subterrane (CL), and the North Lhasa subterrane (NL) (Pan et al., 2009; Peng et al., 2013; Liu et al., 2020; Geng et al., 2021; Pan et al., 2022). Because of the evolution of the Bangong-Nujiang and Yarlung Zangbo Neo-Tethys during the Mesozoic to Cenozoic (Huang et al., 2017; Wu et al., 2017; Liu et al., 2019a, Liu et al., 2019b; Huang et al., 2020; Huang et al., 2021a), magmatic activity-related polymetallic deposits are widespread in this terrane (Zhao et al., 2013; Cai et al., 2015; Huang et al., 2018a, Huang et al., 2018b). Recent studies suggest that the Lhasa terrane was significantly thickened and elevated prior to the Cenozoic collision between India and Asia plates, probably associated with the Mesozoic collision between the Lhasa and Qiangtang blocks (Zhang et al., 2012; Yan and Zhang, 2020), or owing to the obduction of the fragments of the oceanic plateaus in the Bangong–Nujiang Ocean over the continental margins prior to the closure of the oceanic basin (Zhang et al., 2017).

To date, a large amount of post-collision-related Late Cretaceous (~90 Ma) magmatic activity has been found in the Central Lhasa subterrane (CL) (Figure 1C) (Liu et al., 2015; Gao, 2016; Li et al., 2016; Liu et al., 2018b; Wang et al., 2021a; Liu et al., 2022a), such as Zalongqiongwa (~91 Ma), Ga'erqiong (~88 Ma), Balaza (~90 Ma), Sebuta (~90 Ma), Xiangba (~90 Ma), Adang (~91 Ma), Zhuogapu (~85 Ma), Jingzhushan (~91 Ma), and Jiangla'zangzong (~86 Ma). This episode of magmatic activity is often accompanied by porphyry-epithermal or porphyry-skarn Cu(Au) or Au polymetallic mineralization. Several studies were carried out on the southern Lhasa terrane which suggest an archetype of Andean-style margin related to the northward subduction of the Neo-Tethyan Ocean before the India–Asia

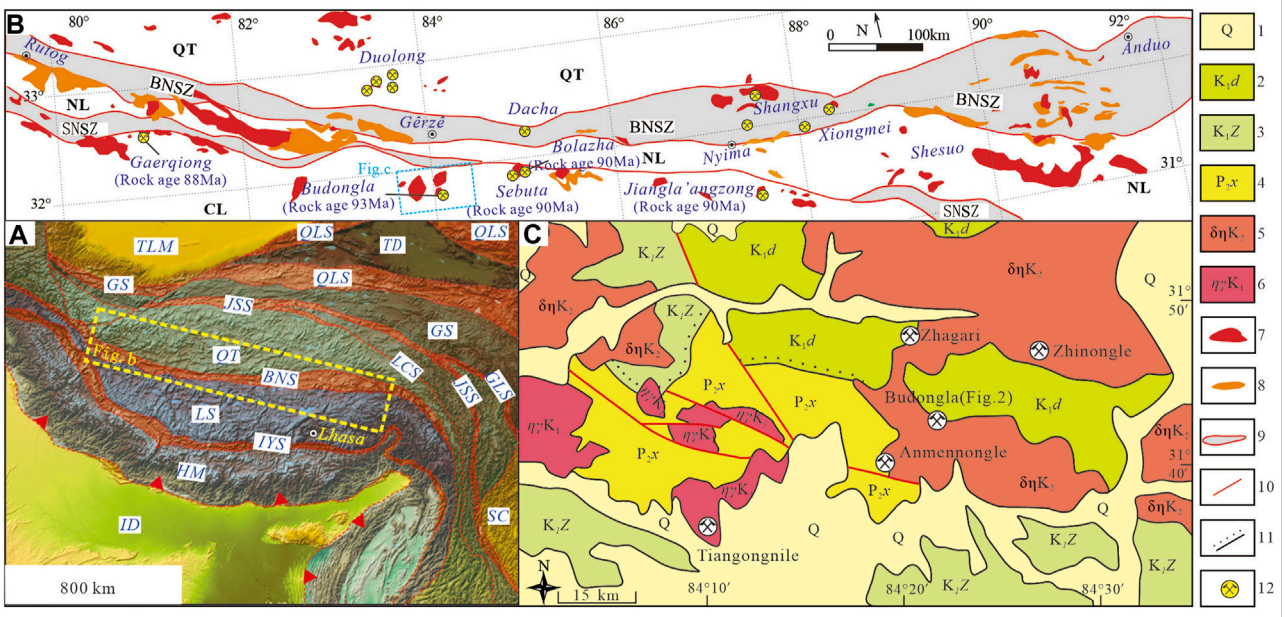

FIGURE 1
Regional geological and mineral maps [**(A)**, after Liu et al., 2015; **(B)**, after Tang et al., 2014; Liu et al., 2017; Liu et al., 2022b; Huang et al., 2021b; **(C)**, after Liu et al., 2021b] 1—Quaternary; 2—Lower Cretaceous Duoni Fm; 3—Lower Cretaceous Zenong Gr; 4—Lower Permian Xiala Gr; 5—Late Cretaceous monzodiorite; 6—Late Cretaceous monzogranite; 7—Ophiolite melange; 8—Cretaceous intrusive rocks; 9—Cretaceous volcanic rocks; 10—Fault; 11—Unconformity boundary; 12—Gold deposit (point); TLM—Tarim block; QLS—Qilian suture zone; WQS—Western Kunlun suture zone; EQS—Eastern Kunlun suture zone; TD—Tsaidam terranes; GS—Ganzi-Songpan terrane; JSS—Jinshajiang suture zone; GLS—Ganzi-Litang suture zone; LCS—Lancangjiang suture zone; QT—Qiangtang terrane; BNSZ—Bangong-Nujiang suture zone; LS—Lhasa terrane; NL—Northern Lhasa subterrane; SNSZ—Shiquanhe-Nam Co fault zone; CL—Central Lhasa subterrane; YZSZ—Yarlung-Tsangpo suture zone; HM—Himalayan terrane; SC—South China block; ID—Indian Plate.

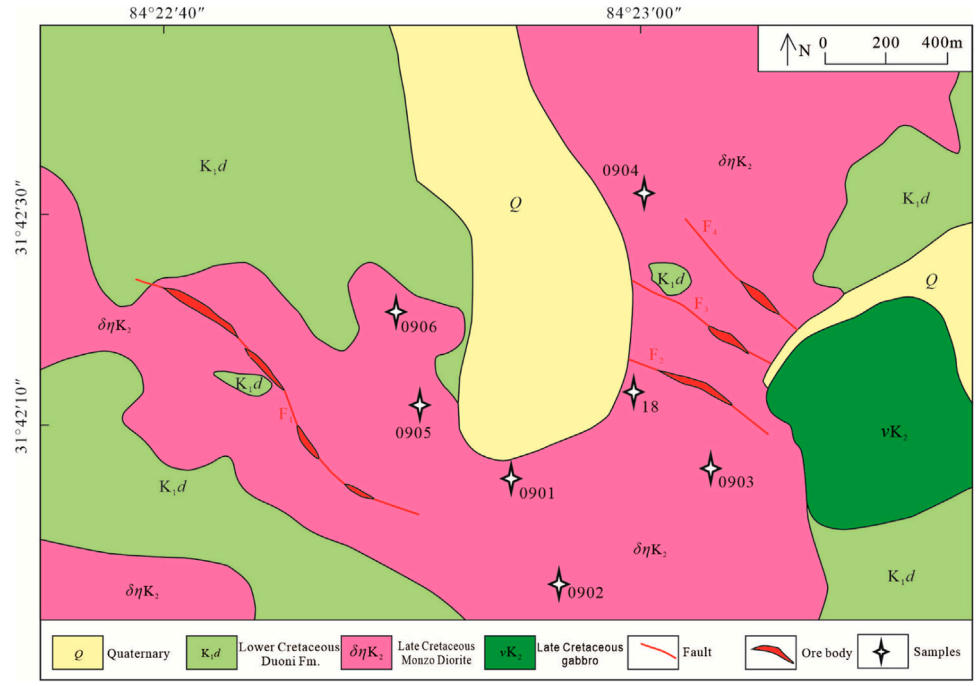

FIGURE 2
Geological map of the Budongla Gold deposit.

collision in the Early Cenozoic. However, the geological background of this Late Cretaceous magmatic activity is still controversial. Some researchers have proposed that the development of these Late Cretaceous magmatic rocks was related to the collision of the Qiangtang-Lhasa terrane (Gao et al., 2011; Wang et al., 2013); other scholars have proposed that these magmatic rocks are related to the northward subduction of the Yarlung Zangbo oceanic crust (Qin et al., 2019).

In this paper, whole-rock geochemistry, zircon U-Pb dating, and zircon Lu-Hf isotopes of the Late Cretaceous monzodiorite pluton (Figure 1C, Figure 2) in the Budongla gold deposit of Zhongba County in the Central Lhasa subterrane are studied. The age of the monzodiorite pluton is precisely determined, and the source area and tectonic setting of its parent magma are discussed.

Geological background

The monzodiorite pluton samples were collected from the Budongla gold district. This gold district is located at the junction of Zhongba County and Gaize County in the Tibet Autonomous Region, P.R. China, which belongs to the western part of the Central Lhasa subterrane (Figure 1). The main stratigraphic units exposed in this region include the Lower Cretaceous Duoni Formation, which consists of limestone and sandstone with some interbedded volcanic rocks; the Lower Cretaceous Zenong Group, which mainly consists of intermediate-felsic volcanic rocks and pyroclastic rocks; and the Middle Permian Xiala Formation, which consists of marble and limestone (Figure 1C). From the perspective of structural deformation characteristics, the structure is mainly compressional deformation, with twists, strike-slip displacements, and extensional structures (Figure 1C). The lithologies of Mesozoic-Cenozoic magmatic rocks is mainly monzodiorite, monzogranite, and biotite granite. They intruded into the Doni Formation and Xiala Formation in the form of composite stocks, batholiths, and dikes and formed skarnization and hornfelsization zones of a certain scale. There is a series of copper-gold hydrothermal deposits related to Late Cretaceous intermediate magmatism (Figure 1C), such as Tiangongnile, Zhagari, Anmennongle, and Zhinongle (Huang et al., 2012a, Huang et al., 2012b; Ouyang et al., 2016; Li et al., 2017).

The stratigraphic units exposed in the Budongla gold ore district mainly include the Lower Cretaceous Doni Formation and the Quaternary system (Figure 2). The Doni Formation is widely distributed on the northern and southern sides of the ore district. It is a set of littoral and

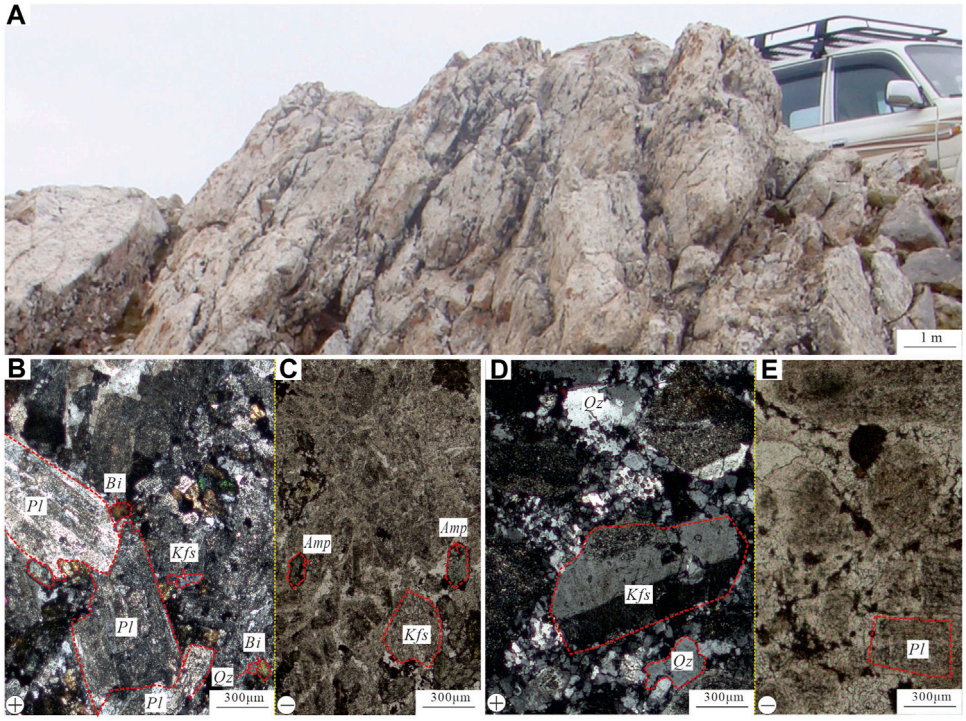

FIGURE 3
Petrographic characteristics of the rocks in Budongla. **(A,B)**: The field outcrops of the mmonzodiorite; **(C–E)**: Microphotographs in plane polarized light (-) and perpendicular polarized light (+) of the monzodiorite. Pl: plagioclase; Kfs: K-feldspar; Qz: Quartz; Bi: Biotite; Amp: Amphibolites.

shallow marine clastic sedimentary formations. The Quaternary is mainly developed in the river valley and consists of alluvial proluvial gravel layers, gravelly sand and clay layers, and residual slope sand gravel layers. The structures in the ore district are mainly NW-trending compressional and torsional faults, which are slightly wave-shaped, and the width of the faults vary from 1 to 5 m (Figure 2). The Late Cretaceous monzodiorite pluton is exposed in a large area in the Budongla mining area and intruded into the sandstone of the Lower Cretaceous Doni Formation. The exposed area of the Late Cretaceous monzodiorite pluton in the mining area is more than 2 km^2, accounting for approximately 1/2 of the total area of the ore district (Figures 2, 3). The monzodiorite is gray with a medium-to coarse-grained porphyritic structure (Figure 3). And the grain size of the main mineral phenocrysts is 2–8 mm. Major minerals are K-feldspar (25%±), plagioclase (45%±), amphibole (15%±), quartz (5%±), augite (3%±), and biotite (3%±). Accessory minerals include magnetite (<1%), titanite (<1%), zircon (<1%), and apatite (<1%). Late Cretaceous gabbro is located in the western part of the ore district, with an exposed area of approximately 0.2 km^2 (Figure 2). At present, several hydrothermal vein-type gold (mineralized) bodies have been found in fracture zones within the pluton (Figure 2). According to the exploration report The fifth Geological Team of Tibet Geological Exploration Bureau, the main ore belt is located in the west of Budongla gold ore district, which is composed of four ore bodies with a grade of 1–11.91 g/t (with the average grade of 7.12 g/t) and a thickness of 1.55–4.51 m (with the average grade of 2.10 m).

Sampling and analytical methods

Seven samples were collected from the Budongla monzodiorite pluton (Figure 1C). All samples were sent for thin section observation and whole-rock major and trace element geochemical analyses, and one of them was used for LA-ICP-MS zircon U-Pb dating and Lu-Hf isotope analyses. Major and trace element analyses were conducted by the XRF (Primus Ⅱ, Rigaku, Japan) and ICP-MS (Agilent 7700e) methods in the Wuhan Sample Solution Analytical Technology Co., Ltd. We performed zircon cathodoluminescence (CL) imaging at Wuhan Sample

TABLE 1 Major element compositions of monzodiorite in the Budongla gold district.

Element	Unit	BDL09-1	BDL09-2	BDL09-3	BDL09-4	BDL09-5	BDL09-6	BDL18
SiO_2	wt%	55.19	55.56	55.75	55.79	54.69	55.28	54.93
TiO_2	wt%	0.93	0.96	1.02	1.06	0.92	0.96	1.00
Al_2O_3	wt%	16.52	16.69	15.54	15.45	16.79	16.59	16.51
Fe_2O_3	wt%	5.04	4.86	5.05	4.14	5.90	5.34	5.18
FeO	wt%	1.66	1.69	1.59	2.55	1.02	1.46	1.72
MnO	wt%	0.11	0.10	0.12	0.12	0.11	0.10	0.12
MgO	wt%	4.92	4.78	5.22	5.54	5.24	4.99	5.20
CaO	wt%	6.75	6.56	7.13	7.48	7.12	6.90	6.94
Na_2O	wt%	3.38	3.47	3.13	3.11	3.31	3.18	3.31
K_2O	wt%	2.67	2.71	2.73	2.64	2.43	2.78	2.68
P_2O_5	wt%	0.52	0.50	0.51	0.52	0.55	0.54	0.53
Loss	wt%	1.94	1.74	1.83	1.38	1.76	1.56	1.54
Total	wt%	99.63	99.62	99.62	99.78	99.84	99.68	99.64
FeOT	wt%	6.19	6.06	6.13	6.28	6.33	6.26	6.32
σ43	mass ratio	2.84	2.90	2.66	2.49	2.68	2.77	2.73
DI	volume ratio	50.52	51.65	49.09	48.44	48.41	49.68	49.76
Mg#	mol ratio	58.60	58.43	60.20	61.15	59.63	58.67	59.01
A/NK	mol ratio	1.96	1.93	2.00	1.94	2.07	2.01	1.98
A/CNK	mol ratio	0.80	0.81	0.78	0.72	0.80	0.80	0.79
La	wt×10^{-6}	67.1	62.0	64.2	61.9	66.1	64.4	64.3
Ce	wt×10^{-6}	130	116	125	121	128	126	124
Pr	wt×10^{-6}	15.0	13.4	13.4	13.9	14.8	14.5	14.7
Nd	wt×10^{-6}	55.6	49.3	53.2	50.7	55.4	53.7	53.0
Sm	wt×10^{-6}	8.61	7.82	8.38	8.18	8.58	8.49	8.44
Eu	wt×10^{-6}	2.03	1.87	1.91	1.79	1.99	1.96	1.96
Gd	wt×10^{-6}	6.84	6.08	6.41	6.27	6.49	6.44	6.45
Tb	wt×10^{-6}	0.869	0.802	0.835	0.828	0.864	0.845	0.826
Dy	wt×10^{-6}	4.36	4.02	4.25	4.15	4.29	4.35	4.22
Ho	wt×10^{-6}	0.741	0.662	0.736	0.711	0.732	0.743	0.720
Er	wt×10^{-6}	2.09	1.96	2.02	1.97	2.07	2.06	2.06
Tm	wt×10–6	0.301	0.270	0.277	0.274	0.282	0.282	0.281
Yb	wt×10^{-6}	1.91	1.65	1.74	1.73	1.75	1.80	1.78
Lu	wt×10^{-6}	0.250	0.242	0.246	0.245	0.244	0.254	0.249
Y	wt×10^{-6}	22.1	20.2	21.5	21.1	21.7	21.6	21.4
Rb	wt×10^{-6}	127	125	122	117	130	121	126
Ba	wt×10^{-6}	612	589	546	540	477	605	562
Th	wt×10^{-6}	21.0	17.1	17.7	18.3	16.9	17.1	18.3
U	wt×10^{-6}	3.25	2.67	3.19	3.86	2.52	3.18	3.08
Nb	wt×10^{-6}	12.0	12.2	12.6	16.1	10.4	11.6	12.5
Ta	wt×10^{-6}	0.784	0.770	0.777	0.981	0.603	0.751	0.779
Pb	wt×10^{-6}	20.7	17.2	18.3	18.0	15.8	20.1	18.0
Sr	wt×10^{-6}	982	941	933	904	901	951	926
Zr	wt×10^{-6}	118	131	125	131	106	126	120
Hf	wt×10^{-6}	3.16	3.23	3.01	3.33	2.72	3.26	3.15
Ga	wt×10^{-6}	20.3	20.4	20.1	19.4	20.8	19.8	20.2
ΣREE	wt×10^{-6}	295	266	282	274	291	286	283
LREE/HREE	mass ratio	16.01	15.95	16.11	15.95	16.42	16.05	16.07
δEu	mass ratio	0.79	0.80	0.77	0.74	0.78	0.78	0.78
δCe	mass ratio	0.95	0.93	0.98	0.96	0.95	0.96	0.94

Notes: A/CNK=Al_2O_3/($CaO+Na_2O+K_2O$) (molar ratio); A/NK= Al_2O_3/(Na_2O+K_2O) (molar ratio); Mg#=Mg/(Mg+Fe) (molar ratio); σ43=(Na_2O+K_2O)2/(SiO_2-43); δEu = 2 × EuN/(SmN+GdN); δCe=2 × CeN/(LaN+PrN); DI= Quartz+Orthoclase+Albite+Nepheline+ Leucite+K-feldspar, from CIPW, calculating values.

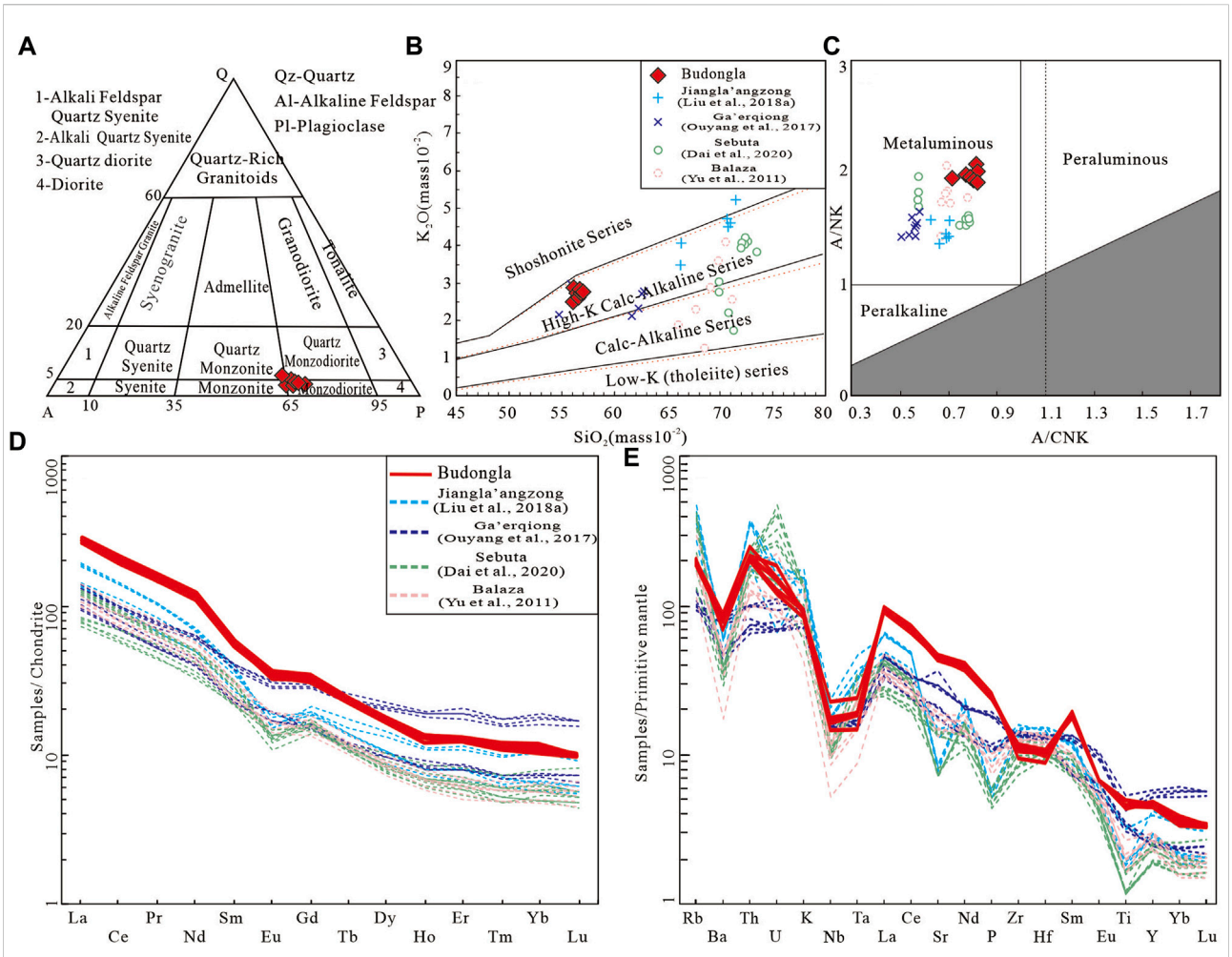

FIGURE 4
Geochemical diagrams of major elements. **(A)**, QAP Plots of rock (base map after LeMaitre, 2002); **(B)**, K_2O vs. SiO_2 Plots (base map after Middlemost, 1994); **(C)**, A/NK vs. A/CNK Plots (base map after Maniar and Piccoli, 1989); **(D)**, Chondrite-normalised REE patterns (The normalizing values for REE are from Sun and McDonough and Sun, 1995); **(E)**, Mantle-normalised multi-element diagrams. (The normalizing values for REE and trace elements are from Sun and McDonough, 1989; McDonough and Sun, 1995).

Solution Analytical Technology Co., Ltd. Wuhan, China, using an analytical scanning electron microscope (JSM-IT100) connected to a GATAN MINICL system. The analytical conditions included a 10.0–13.0 kV electric field voltages and an 80–85 μA current on a tungsten filament. Zircon U-Pb dating, zircon trace element analysis, and zircon Lu-Hf isotope analysis were simultaneously conducted by LA-MC-ICP-MS at the Wuhan Sample Solution Analytical Technology Co., Ltd. The spot size and frequency of the laser were set to 32 μm, and the energy density of laser ablation was ~7.0 J/cm2 in this study. Zircon 91,500. Zircon GJ-1, and glass NIST610 were used as external standards for U-Pb dating and trace element calibration, respectively. Each analysis involved a background acquisition of approximately 20–30 s followed by 50 s of data acquisition for each sample. ICPMSDataCal, an Excel-based software, was used to perform offline data selection, the integration of background and analyzed signals, time-drift corrections, and quantitative calibration for trace element analysis and U-Pb dating. Concordia diagrams and weighted mean calculations were made using Isoplot/Ex_ver 4.15 software.

Results

Major and trace elements

The whole-rock major and trace element geochemical data are listed in Table 1. The rocks are rich in K_2O+Na_2O (5.75 wt% ~6.18 wt%) and K_2O (2.44 wt% ~2.78 wt%), have medium

TABLE 2 LA-ICP-MS zircon U-Pb ages of monzodiorite in the Budongla gold district.

Spots	Pb × 10^{-6}	Th × 10^{-6}	U × 10^{-6}	Th/U	$^{207}Pb/^{206}Pb$	1σ	Isotope ratio		$^{206}Pb/^{238}U$	1σ	$^{207}Pb/^{206}Pb$	1σ	Age (Ma)		$^{206}Pb/^{238}U$	1σ	Con %
							$^{207}Pb/^{235}U$	1σ					$^{207}Pb/^{235}U$	1σ			
91500std	19.18	31.5	88.8	0.36	0.0728	0.0025	1.7989	0.0604	0.1791	0.0023	1,009	69	1,045	22	1,062	13	98
91500std	19.23	31.3	88.7	0.35	0.0770	0.0026	1.9015	0.0625	0.1792	0.0022	1,120	67	1,082	22	1,063	12	98
GJ-1	34.39	9.37	324	0.03	0.0587	0.0016	0.7907	0.0211	0.0973	0.0010	554	59	592	12	599	6	98
GJ-1	34.87	9.39	329	0.03	0.0592	0.0016	0.7988	0.0222	0.0975	0.0010	576	56	596	13	600	6	99
BDL18-1	15.1	177	349	0.51	0.0523	0.0059	0.0973	0.0084	0.0147	0.0004	298.2	224.0	94.3	7.7	93.9	2.5	99
BDL18-2	46.3	712	640	1.11	0.0510	0.0053	0.0988	0.0088	0.0147	0.0003	242.7	207.4	95.6	8.1	94.4	2.1	98
BDL18-3	13.5	155	321	0.48	0.0481	0.0019	0.0970	0.0029	0.0146	0.0001	101.9	87.0	94.0	2.7	93.3	0.8	99
BDL18-4	15.5	146	701	0.21	0.0448	0.0020	0.0886	0.0039	0.0143	0.0002	—	—	86.2	3.7	91.6	1.0	94
BDL18-5	30.7	417	474	0.88	0.0520	0.0034	0.1048	0.0065	0.0147	0.0002	287.1	137.0	101.2	6.0	93.8	1.2	92
BDL18-6	39.0	548	667	0.82	0.0524	0.0038	0.0991	0.0066	0.0144	0.0002	301.9	154.6	96.0	6.1	92.3	1.4	96
BDL18-7	33.3	452	506	0.89	0.0457	0.0021	0.0947	0.0031	0.0146	0.0002	—	—	91.9	2.9	93.6	1.0	98
91500std	18.64	31.0	87.1	0.36	0.0750	0.0027	1.8592	0.0665	0.1800	0.0023	1,133	73	1,067	24	1,067	13	99
91500std	19.03	31.7	88.7	0.36	0.0748	0.0027	1.8412	0.0664	0.1783	0.0022	1,065	79	1,060	24	1,058	12	99
BDL18-8	14.4	183	202	0.91	0.0462	0.0029	0.0927	0.0055	0.0146	0.0002	5.7	137.0	90.0	5.1	93.6	1.0	96
BDL18-9	14.5	184	203	0.91	0.0461	0.0031	0.0998	0.0061	0.0142	0.0002	400.1	49.1	96.6	5.6	90.8	1.1	93
BDL18-10	41.3	584	594	0.98	0.0469	0.0019	0.0955	0.0033	0.0146	0.0001	42.7	95.4	92.7	3.0	93.5	0.8	99
BDL18-11	18.3	237	387	0.61	0.0463	0.0022	0.0938	0.0044	0.0146	0.0001	13.1	110.2	91.1	4.1	93.7	0.8	97
BDL18-12	33.0	462	526	0.88	0.0504	0.0032	0.1002	0.0061	0.0145	0.0002	216.7	135.2	96.9	5.6	92.7	1.1	95
BDL18-13	11.1	151	186	0.81	0.0482	0.0078	0.0935	0.0123	0.0146	0.0006	109.4	317.6	90.7	11.4	93.2	3.5	97
BDL18-14	27.6	356	537	0.66	0.0499	0.0069	0.0980	0.0108	0.0147	0.0006	190.8	276.8	95.0	10.0	94.2	3.7	99
BDL18-15	28.1	373	441	0.85	0.0550	0.0084	0.0978	0.0117	0.0145	0.0004	413.0	287.9	94.7	10.8	92.9	2.7	98
BDL18-16	77.2	846	2,229	0.38	0.0546	0.0055	0.1033	0.0096	0.0145	0.0003	398.2	227.7	99.8	8.8	92.6	1.9	92
91500std	20.41	33.8	94.2	0.36	0.0741	0.0025	1.8286	0.0629	0.1790	0.0025	1,043	67	1,056	23	1,061	14	99
91500std	19.43	32.1	89.7	0.36	0.0757	0.0025	1.8718	0.0624	0.1794	0.0024	1,087	66	1,071	22	1,064	13	99
BDL18-17	30.6	410	658	0.62	0.0545	0.0055	0.1019	0.0095	0.0139	0.0002	390.8	229.6	98.5	8.8	89.0	1.6	89

(Continued on following page)

10.3389/feart.2022.927695

TABLE 2 (*Continued*) LA-ICP-MS zircon U-Pb ages of monzodiorite in the Budongla gold district.

Spots	Pb × 10^{-6}	Th × 10^{-6}	U × 10^{-6}	Th/U	$^{207}Pb/^{206}Pb$	1σ	Isotope ratio		$^{206}Pb/^{238}U$	1σ	$^{207}Pb/^{206}Pb$	1σ	Age (Ma)		$^{206}Pb/^{238}U$	1σ	Con %
							$^{207}Pb/^{235}U$	1σ					$^{207}Pb/^{235}U$	1σ			
BDL18-18	16.1	219	303	0.72	0.0565	0.0043	0.1037	0.0074	0.0138	0.0003	472.3	165.7	100.2	6.8	88.5	1.7	87
BDL18-19	24.6	339	581	0.58	0.0547	0.0041	0.1102	0.0088	0.0146	0.0003	398.2	170.4	106.2	8.0	93.7	1.9	87
BDL18-20	24.4	334	576	0.58	0.0491	0.0035	0.0924	0.0065	0.0141	0.0003	153.8	168.5	89.8	6.1	90.0	1.7	99
BDL18-21	23.2	305	439	0.69	0.0552	0.0037	0.1062	0.0070	0.0141	0.0003	420.4	151.8	102.5	6.5	90.3	1.8	87
BDL18-22	23.3	305	440	0.69	0.0527	0.0037	0.1041	0.0071	0.0147	0.0003	316.7	162.9	100.5	6.6	94.0	1.8	93
GJ-1	35.80	9.61	336	0.03	0.0595	0.0017	0.8029	0.0226	0.0976	0.0012	587	66	598	13	600	7	99
GJ-1	35.68	9.63	333	0.03	0.0593	0.0018	0.8015	0.0246	0.0974	0.0011	589	60	598	14	599	6	99
91500std	20.28	33.9	93.2	0.36	0.0736	0.0027	1.8150	0.0660	0.1792	0.0024	1,031	76	1,051	24	1,062	13	98
91500std	19.82	32.9	91.3	0.36	0.0761	0.0025	1.8854	0.0653	0.1792	0.0028	1,098	67	1,076	23	1,062	15	98

10.3389/feart.2022.927695

TABLE 3 LA-ICP-MS zircon Lu-Hf isotopes compositions of monzodiorite in the Budongla gold district.

Spots	t (Ma)	$^{176}Yb/^{177}Hf$	$^{176}Lu/^{177}Hf$	$^{176}Hf/^{177}Hf$	2σ	$^{176}Hf/^{177}Hf(t)$	$\varepsilon_{Hf}(0)$	$\varepsilon_{Hf}(t)$	T_{DM}(Ma)	TDM2 (Ma)	f_{Lu-Hf}
BDL18-1	93.9	0.050478	0.001219	0.282,706	0.000026	0.282,704	−2.3	−0.4	778	1,176	−0.96
BDL18-2	94.4	0.055745	0.001406	0.282,617	0.000031	0.282,614	−5.5	−3.5	909	1,377	−0.96
BDL18-3	93.3	0.170,006	0.003642	0.282,678	0.000096	0.282,671	−3.3	−1.5	875	1,249	−0.89
BDL18-4	91.6	0.019052	0.000432	0.282,669	0.000716	0.282,668	−3.6	−1.7	813	1,257	−0.99
BDL18-5	93.8	0.027366	0.000582	0.282,628	0.000317	0.282,627	−5.1	−3.1	873	1,348	−0.98
BDL18-6	92.3	0.029551	0.000620	0.282,562	0.000253	0.282,561	−7.4	−5.4	966	1,497	−0.98
BDL18-7	93.6	0.032434	0.000696	0.282,645	0.000708	0.282,644	−4.5	−2.5	852	1,311	−0.98
BDL18-8	93.6	0.024269	0.000537	0.282,640	0.000370	0.282,639	−4.7	−2.7	856	1,322	−0.98
BDL18-9	90.8	0.029035	0.000620	0.282,663	0.000222	0.282,662	−3.9	−1.9	826	1,272	−0.98
BDL18-10	93.5	0.026351	0.000564	0.282,619	0.000033	0.282,618	−5.4	−3.4	887	1,370	−0.98
BDL18-11	93.7	0.038390	0.000786	0.282,602	0.000165	0.282,601	−6.0	−4.0	915	1,408	−0.98
BDL18-12	92.7	0.022271	0.000467	0.282,654	0.000156	0.282,654	−4.2	−2.2	834	1,290	−0.99
BDL18-13	93.2	0.020905	0.000467	0.282,617	0.000332	0.282,617	−5.5	−3.5	886	1,372	−0.99
BDL18-14	94.2	0.016626	0.000345	0.282,662	0.000192	0.282,661	−3.9	−1.9	822	1,272	−0.99
BDL18-15	92.9	0.028649	0.000576	0.282,656	0.000311	0.282,655	−4.1	−2.1	834	1,286	-0.98
BDL18-16	92.6	0.028953	0.000588	0.282,685	0.000367	0.282,684	−3.1	−1.1	794	1,221	−0.98
BDL18-17	89.0	0.040672	0.000796	0.282,617	0.000120	0.282,615	−5.5	−3.6	895	1,378	−0.98
BDL18-18	88.5	0.030673	0.000633	0.282,606	0.000632	0.282,605	−5.9	−4.0	906	1,402	−0.98
BDL18-19	93.7	0.044316	0.000868	0.282,644	0.001298	0.282,642	−4.5	−2.5	858	1,315	−0.97

Notes: $\varepsilon_{Hf}(0)=(^{176}Hf/^{177}Hf/(^{176}Hf/^{177}Hf)_{CHUR}, 0^{-1}) \times 10{,}000$; $\varepsilon_{Hf}(t)=[^{176}Hf/^{177}Hf\text{-}(^{176}Lu/^{177}Hf)_S \times (e^{\lambda t}\text{-}1)]/[(^{176}Hf/^{177}Hf)_{CHUR}, 0\text{-}(^{176}Lu/^{177}Hf)_{CHUR}\times (e^{\lambda t}\text{-}1)]\text{-}1) \times 10{,}000$; $[(^{176}Hf/^{177}Hf)i=^{176}Hf/^{177}Hf\text{-}(^{176}Lu/^{177}Hf)_S\times(e^{\lambda t}\text{-}1)]\text{-}1$; $T_{DM2}=T_{DM1}\text{-}(T_{DM1}\text{-}t)$ $(f_{CC}\text{-}f_{Lu/Hf})/(f_{CC}\text{-}f_{DM})$; $f_{Lu}/Hf=^{176}Lu/^{177}Hf/(^{176}Lu/^{177}Hf)_{CHUR}\text{-}1$; $(^{176}Lu/^{177}Hf)_{CHUR}$, 0.0332, $(^{176}Hf/^{177}Hf)_{CHUR}$, 0=0.282,772 (Blichert-Toft and Albaréde, 1997); (176Lu/177Hf)DM, 0.0384, $(^{176}Hf/^{177}Hf)_{DM}$, 0.28325(Griffin et al., 2000); f_{CC}=−0.55, f_{DM}, 0.16, λ=1.867 × 10^{-11} years-1(Griffin et al., 2002).

contents of SiO_2 (54.85 wt% ~55.79 wt%), CaO (6.56 wt% ~7.48 wt%), and $A1_2O_3$ (15.45 wt% ~16.79 wt%), and have Rittmann indices (σ43) ranging from 2.49 to 2.90. The A/CNK values and A/NK range from 0.72 to 0.81 and 1.93 to 2.07, respectively, and the samples thus belong to the high-K calc-alkaline series (Table 1; Figure 4). The rocks have high MgO (4.92 wt%~5.54 wt%), Fe_2O_3 (4.14 wt%~5.90 wt%), FeO (1.02 wt%~2.55 wt%), the Mg# values of 58.43–61.15, and DI values of 48.41–51.65, implying they are Mg-rich intrusive rocks.

Figures 4D,E show that the Budongla monzodiorite pluton is enriched in light REEs (LREEs) (L_{REE}/H_{REE}: 15.95–16.42) and large ion lithophile elements (LILEs), while relatively depleted in heavy REEs (HREEs) and high field strength elements (HFSEs), and has negative Eu anomalies (δEu=0.74–0.80), no obvious negative Ce anomalies (δCe=0.93–0.98) (Table 1; Figure 4D).

Zircon U–Pb ages and Lu-Hf isotope compositions

The zircon U-Pb and Lu-Hf isotope data are listed in Tables 2, 3. Representative cathodoluminescence images of the zircons are shown in Figure 4A. All zircon Th/U ratios are higher than 0.30 (Th/U=0.5–0.9) (Table 2), and most of the zircon particles display relatively idiomorphic crystal morphology and clear oscillatory growth zoning in cathodoluminescence images (Figure 5A), which indicates that the zircons in this study are of magmatic origin (Figure 5C; Hoskin and Black, 2000; Grimes etal et al., 2007). The zircon data yield a concordia age of 92.7 ±1.1 Ma (n=22, MSWD=0.33) (Figures 5A,B), which suggests that the Budongla monzodiorite pluton was emplaced in the Late Cretaceous. We analyzed 19 zircon grains for Lu-Hf isotopes, as shownedin Table 3.

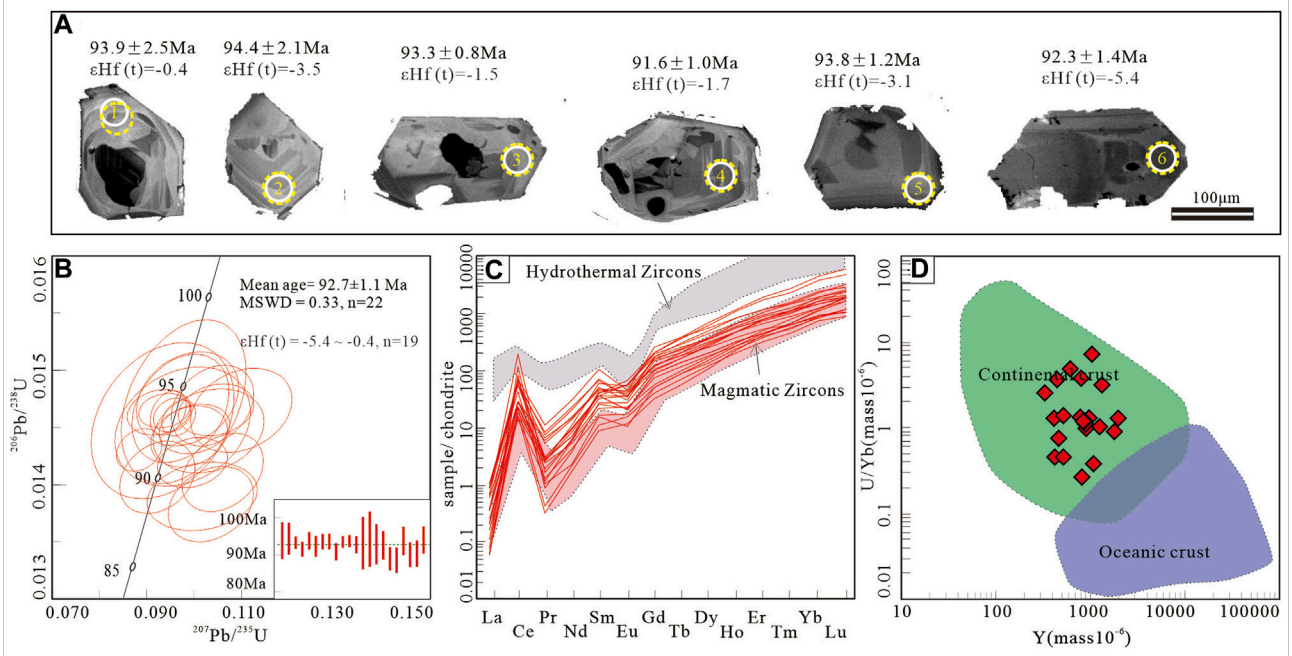

FIGURE 5
Diagrams of Zircon U-Pb geochronology. **(A)** Cathodoluminescence (CL) images of representative zircon grains; **(B)** zircon U-Pb concordia diagrams and weighted mean ages; **(C)** chondrite-normalized REE patterns of zircons (based on Hoskin, 2005); and **(D)** discriminant diagrams with differentcry stallization setting zircon fields (base on Grimes etal et al., 2007) for the Xiabie Co granite.

The zircons have low $^{176}Lu/^{177}Hf$ ratios of 0.000345–0.0036421 and $^{176}Hf/^{177}Hf$ ratios of 0.282,562–0.282,706. We calculated the initial $^{176}Hf/^{177}Hf$ ratio and $_{\varepsilon Hf}(t)$ values based on the zircon U-Pb ages, as showned in Table 3 and Figure 6. The T_{DM2} (two-stage Hf model ages) range from 1,176 to 1,497 Ma, and the $_{\varepsilon Hf}(t)$ values of the zircons in the Budongla monzodiorite pluton range from −5.4 to −0.4.

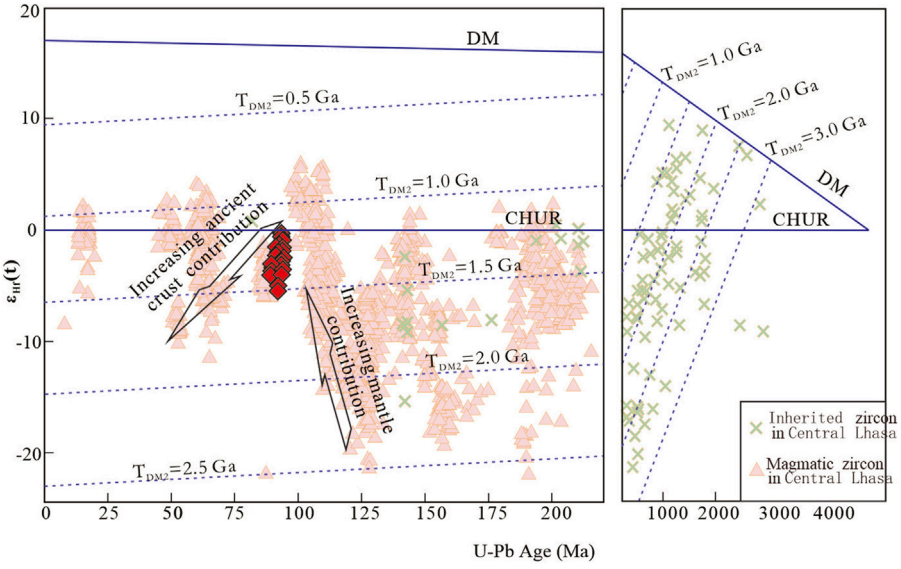

FIGURE 6
$_{\varepsilon Hf}(t)$ vs. U-Pb ages Plots of zircons. (The Central Lhasa values from Yu et al., 2011; Wang et al., 2012; Meng et al., 2014; Hou et al., 2015; Zhao et al., 2011; Liu et al., 2018a; Cao et al., 2019; DM: Depleted Mantle; CHUR: Chondrite uniform reservoir).

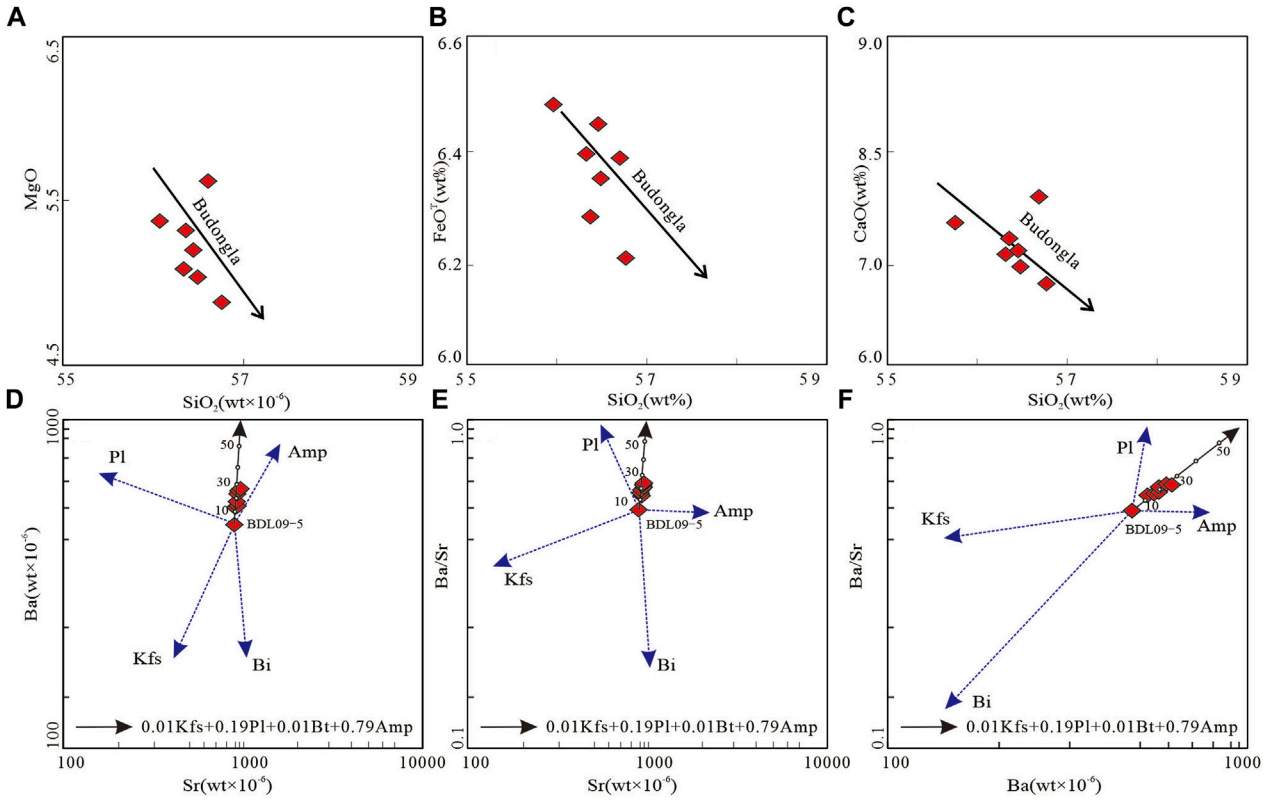

FIGURE 7
Huck diagram. **(A-C)** Element scatter diagrams; and **(D-F)** Quantitative simulation diagrams of crystallization differentiation.

Discussion

Magmatic source

As mentioned above, the Budongla monzodiorite pluton belongs to the metaluminous and high-K calc-alkaline Mg-rich magmatic rock series (Figures 4B,C). Different from other Late Cretaceous intermediate-felsic intrusive rocks in the Central Lhasa subterrane, the Budongla monzodiorite pluton has no obvious depletion in Sr, P, and Ti (Figure 4D). Therefore, there may have been no obvious fractional crystallization of phosphorus-containing minerals (such as apatite) and titanium-containing minerals (such as rutile) in the Budongla monzodiorite pluton. However, the negative Eu anomalies (Table 1; Figure 4D), the negative correlations between FeO^T, Cao, MgO, and SiO_2 (Figures 7A–C), and the obvious depletions in Ba and Ta (Figure 4E), indicate that there was a certain amount of fractional crystallization of plagioclase and iron magnesium minerals (such as amphibole) during magmatic evolution. This interpretation is supported by quantitative modeling of fractional crystallization (Figures 7D–F), which shows that the Budongla monzodiorite can be interpreted as forming through 0%–30% fractional crystallization of 0.01% K-feldspar +0.19% plagioclase +0.01% biotite +0.79% amphibole, and the degree of crystal differentiation is very low. The differentiation coefficient (DI=48.41–51.65) and FeO^T/MgO contents of the Budongla monzodiorite pluton are relatively low (Table 1; Figure 7), which indicates that the magma haven't experience a strong crystallization differentiation process, so it is unlikely to have been the product of crystallization of coeval basaltic magma.

The zircon trace elements have the characteristics of crustal sources (Figure 5D), and the Rb/Y-Nb diagram shows that the rocks have a trend of crustal contamination and obvious depletion in Nb (Figure 4B, Nb_N=14.6–24.6), which shows that the Budongla monzodiorite has crustal components. The Rb/Sr ratio of mongzodiorite in budongla (0.129–0.144) is much higher than the average value of primitive mantle (0.029, Sun and MchDonough, 1989), but close to the average value of continental crust (0.123, Taylor and McLennan, 1985). The rocks are characterized by enrichment of LILEs such as Rb, K, Th, and U, and relative loss of HFSEs such as Nb, Ta, P, and Ti, suggesting that the crust source material makes a great contribution to the source area (McKenzie and Bickle, 1988). The negative εHf(t) (−5.4~−0.4) (Figure 6) and old zircon Lu-Hf isotope two-stage model ages (T_{DM2}=1,176–1,497 Ma) suggest a

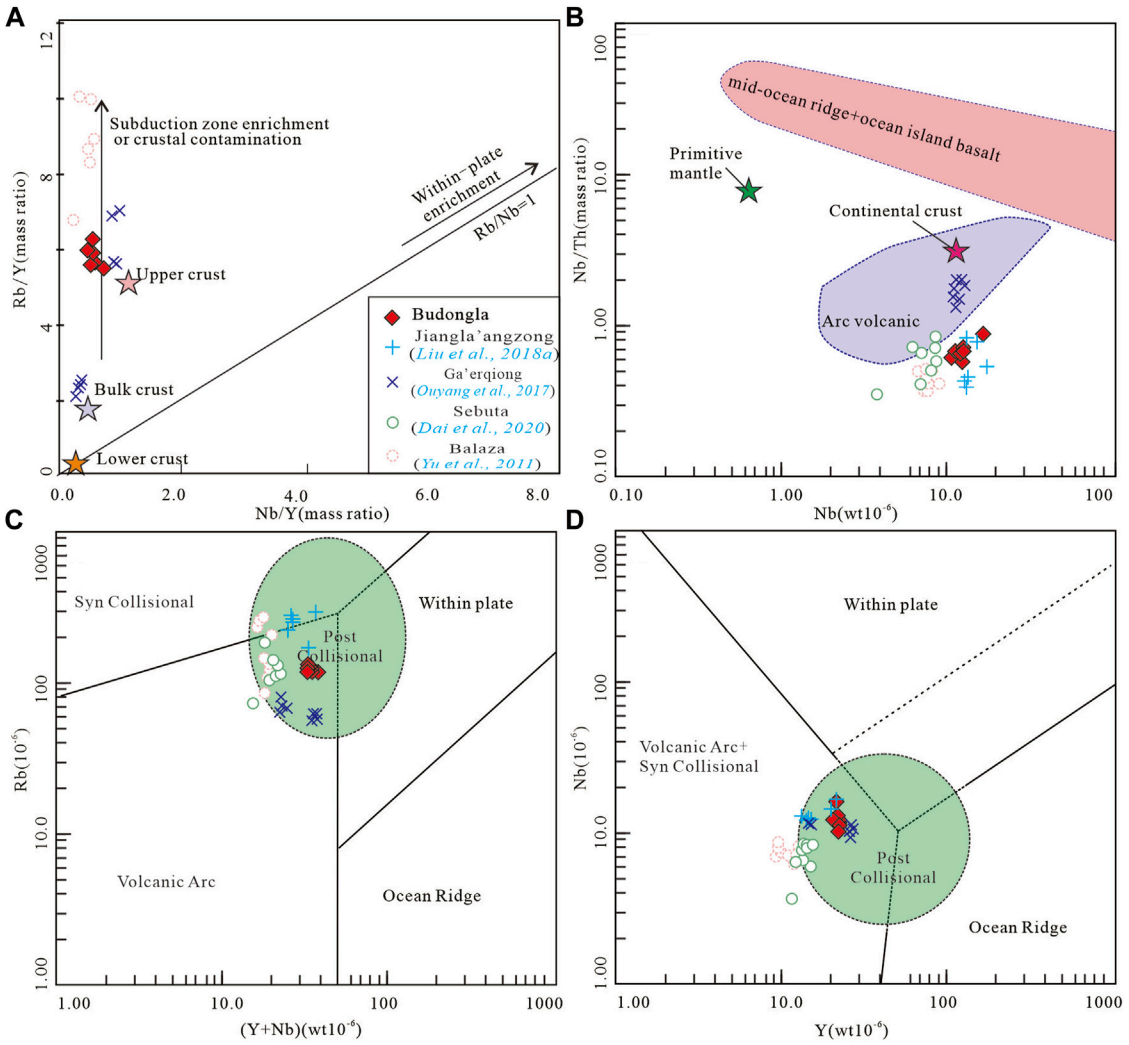

FIGURE 8
Tectonic discrimination diagrams. [**(A,B)**, Basemap after Pearce et al., 1984; **(C,D)**, Basemap after Boztuğ et al., 2007].

contribution of less radiogenic material was involved in the origin of monzodiorites or old crust (Scherer et al., 2000; Griffin et al., 2002). This could be crustal contamination during emplacement, or partial melting of the crust, which is consistent with the results of trace element analysis (Nb, Rb, Sr, Th, and U, etc.) But the arc volcanic rock characteristics of Ce/Pb, Ce, Nb/Th, and Nb (Figures 8A,B) show that the Budongla pluton is unlikely to have formed from pure crustal sources. In the Central Lhasa subterrane, from the early Cretaceous (~125 Ma) to the late Cretaceous (~90 Ma), the continuous increase of zircon $_{\varepsilon Hf}(t)$ values also suggest that the continuous increasing mantle contribution to Cretaceous magmatic rock (Figure 6). In addition, the high Mg# and MgO also indicate that the Budongla Mg-rich monzodiorite has some mantle-derived derived components.

In summary, we infer that the Budongla Mg-rich monzodiorite pluton was generated by increasing the contribution of mantle sources during crustal remelting.

Tectonic environment

The development of the northern and middle parts of the Lhasa terrane is controversial. Some scholars have proposed that this Late Cretaceous magmatic activity was related to the collision of the Qiangtang-Lhasa terranes (Gao et al., 2011; Wang et al., 2013; Li et al., 2020; Wang et al., 2021b); other scholars have also suggested that the northward subduction of the Yarlung Zangbo Neotethys Ocean involved low-angle subduction and an increase in subduction angle combined with slab rollback events, which

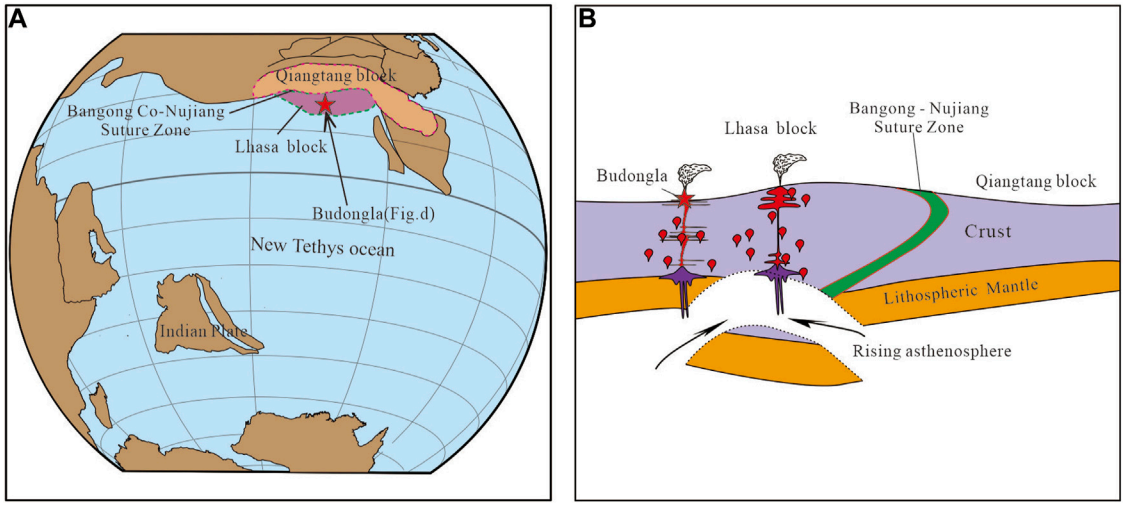

FIGURE 9
Schematic illustrations of the Late Cretaceous tectono-magmatic evolution of the Qiangtang-Lhasa terrane. [**(A)**, Basemap after Ma et al., 2014 **(B)**, Basemap after Zhu et al., 2016].

triggered the Late Cretaceous magmatism (Zhang et al., 2012; Zhang et al., 2015); and still other scholars believed that the northward subduction of the Yarlung Zangbo Neotethys Ocean was normal deep subduction and that slab breakoff events triggered the Late Cretaceous magmatic episodes (Dai et al., 2020). In the low-angle subduction model, the early subduction angle was small, and the corresponding magmatism was slight. However, in recent years, extensive Jurassic-Cretaceous magmatism has been found in the southern Lhasa terrane (Zhu et al., 2011; Liu et al., 2019c), which is contrary to the low-angle subduction model of the oceanic plate. Considering that the Lhasa terrane experienced significant crustal shortening after Cretaceous time, the distance between the northern magmatic arc and the southern Neotethyan subduction zone was more than 600 km (Ding and Lai, 2003; Kapp et al., 2007), which cannot be explained by the normal subduction model. Therefore, we believe that the 90 Ma magmatism in the Central Lhasa terrane was unlikely to have been related to the subduction of the Yarlung Zangbo oceanic lithosphere.

The magmatism of the Lhasa terrane was mainly influenced by the evolution of the Yarlung Zangbo Ocean and Bangong-Nujiang Ocean (Chen et al., 2014; Zheng et al., 2014). Currently, no consensus has been reached on the timing of tectonic evolution and subduction polarity of the Bangong-Nujiang suture zone (Kapp et al., 2005; Volkmer et al., 2007; Li G. M. et al., 2011; Gao et al., 2011; Geng et al., 2011; Li H. L. et al., 2014; Wang et al., 2016; Zhu et al., 2016): some scholars have proposed that the Bangong-Nujiang ocean basin subducted northward beneath the Qiangtang block in the Early Jurassic, while the arc-arc "soft" collision between the Lhasa and Qiangtang blocks is most likely to have occurred between 140 Ma and 130 Ma (Song et al., 2019); at the same time, the Nyima area in the Northern Lhasa terrane records a 125–118 Ma transition from marine facies to nonmarine facies (Kapp et al., 2007), and it was an intracontinental environment at approximately 110 Ma, which means that the Lhasa and Qiangtang blocks underwent a "soft" collision before 110 Ma (Zhu et al., 2009). Other scholars have proposed that the large-scale magmatic activity at approximately 113 Ma around Xainza in the middle of the Central Lhasa terrane was the product of the southward subduction of the Bangong-Nujiang ocean slab breakoff (Chen et al., 2014). In addition, the appearance of the large-scale Jingzhushan formation (K_{2j}) molasse in the BNSZ also suggests that the Lhasa terrane in the later part of the Early Cretaceous had entered the continental collision stage (Pan et al., 2006). Thus, the above lines of evidence fully show that the Bangong-Nujiang Ocean in the Nyima-Bange area had closed and entered a state of collisional orogeny by the middle-late part of the Early Cretaceous.

Similar to Balaza, Sebuta, Ga'erqiong, Jianglaangzong, and many other ca. 90 Ma intermediate-felsic intrusions in the Central Lhasa subterrane (Ouyang et al., 2017; Dai et al., 2020), the intermediate-felsic pluton in Budongla was formed in a post-collisional environment (Figures 8C,D). Based on the results of the above discussion, we believe that the ~90 Ma magmatism and mineralization in the Central Lhasa subterrane are not the products of melting of subducted seafloor or ocean ridge subduction of the Yarlung-Zangbo Ocean or southward subduction of the Bangong-Nujiang Ocean.

According to the analysis above, by the later part of the Early Cretaceous, the Bangong-Nujiang ocean basin had closed, and the central and northern parts of the Lhasa terrane had entered the stage of continental collision. During the disappearance of the Bangong-Nujiang oceanic crust, mantle material upwelling

caused mantle-derived magma underplating to occur at an unequal scale on either side of the Bangong-Nujiang junction zone (Zhu, et al., 2016). Subsequently, the lower crust of the Central Lhasa subterrane was continuously thickened due to the compression of north-south stress. And its thickness was greater than 50 km (Dai et al., 2020). At this time, the ultrahigh-pressure metamorphism occurred at the bottom of the crust, reaching eclogite facies (Li J. X. et al., 2011; Sun et al., 2015; Ding et al., 2016). During the Late Cretaceous period, this thickened crust underwent delamination (Yu et al., 2011; Liu et al., 2018c), which led to a series of ~90 Ma magmatic episodes, such as the event that produced the Budongla pluton (Figures 9A,B).

Conclusion

(i) The formation age of the monzodiorite pluton of the Budongla gold district in the western part of the Central Lhasa subterrane is 92.7 ± 1.1 Ma, and this pluton is the product of Late Cretaceous magmatism in the Central Lhasa subterrane.

(ii) The monzodiorite of the Budongla gold district in the western part of the Central Lhasa subterrane belongs to the metaluminous, high-K calc-alkaline Mg-rich intermediate-felsic magmatic series, and the Budongla monzodiorite was emplaced during the post-collisional period of the Lhasa terrane and the Qiangtang terrane.

Data availability statement

The original contributions presented in the study are included in the article/supplementary material, further inquiries can be directed to the corresponding authors.

Author contributions

Conceptualization, HL; software, J-YW; investigation, HL, D-FM, YO, H-XH, Z-LZ, and TL; data curation, HL; writing—original draft preparation, HL; writing—review and editing, HL and Y-GL; visualization, HL; supervision, H-XH; project admin-istration, W-CL and G-ML; funding acquisition, W-CL and G-ML. All authors have read and agreed to the published version of the manuscript.

Funding

Key Programme, National Natural Science Foundation of China (No. 92055314 and 91955208); the National Key R and D Program of China (Grant Numbers: 2021YFC2901803; 2019YFC0605201, and 2021YFC2901903), China Geological Survey Project (Grant Numbers: DD20221776; DD20190542, and DD20190147); Tianfu ten thousand talents program outstanding scientists project (No. 023).

Acknowledgments

The authors of this paper are very grateful to Associate Professor He Xiaohu from Yunnan University, Associate Professor Gao Sunbao, China University of Geosciences (Wuhan); Senior Engineer Liu Han, Senior Engineer Zhang Zhi, senior engineer Wang Yiyun, Professor Zhu Xiangping, Chengdu Center, China Geological Survey; Senior Engineer Liu Chaoqiang, Senior Engineer Li Yanbo, Engineer Yao Bo, Engineer Liu Huadong, the fifth Geological Team of Xizang Geological Exploration Bureau.

Conflict of interest

The authors declare that the research was conducted in the absence of any commercial or financial relationships that could be construed as a potential conflict of interest.

The reviewer JZ declared a shared affiliation with the author JW to the handling editor at the time of review.

Publisher's note

All claims expressed in this article are solely those of the authors and do not necessarily represent those of their affiliated organizations, or those of the publisher, the editors and the reviewers. Any product that may be evaluated in this article, or claim that may be made by its manufacturer, is not guaranteed or endorsed by the publisher.

References

Blichert-Toft, J., and Albarède, F. (1997). The Lu-Hf isotope geochemistry of chondrites and the evolution of the mantle-crust system. *Earth Planet. Sci. Lett.* 148 (1–2), 243–258. doi:10.1016/S0012-821X(97)00040-X

Boztuğ, D., Harlavan, Y., Arehart, G., Satir, M., and Avci, N. (2007). K-Ar age, whole-rock and isotope geochemistry of A-type granitoids in the Divriği-Sivas region, Eastern-Central Anatolia, Turkey. *Lithos* 97, 193–218. doi:10.1016/j.lithos.2006.12.014

Cao, H. W., Zhang, Y. H., Santosh, M., Li, G. M., Hollis, S. P., Zhang, L. K., et al. (2019). Petrogenesis and metallogenic implications of cretaceous magmatism in central Lhasa, Tibetan plateau: A case study from the lunggar Fe skarn deposit and perspective review. *Geol. J.* 54 (4), 2323–2346. doi:10.1002/gj.3299

Cai, Q. L., Zheng, Z. W., and He, J., (2015). Age of zircon U-Pb and its geological significance of granite from western Gangdese in Tibet. *J. East China Inst. of*

Technol. 38 (1), 49–57. (in Chinese with English abstract). doi:10.3969/j.issn.1674-3504.2015.01.007

Chen, Y., Zhu, D. C., Zhao, Z. D., Meng, F. Y., Wang, Q., Santosh, M., et al. (2014). Slab breakoff triggered ca.113Ma, magmatism around Xainza area of the Lhasa terrane, Tibet. *Gondwana Res.* 26 (2), 449–463. doi:10.1016/j.gr.2013.06.005

Dai, Z. W., Huang, H. X., Li, G. M., Huizenga, J. M., Santosh, M., Cao, H. W., et al. (2020). Formation of Late Cretaceous high-Mg granitoid porphyry in central Lhasa, Tibet: Implications for crustal thickening prior to India–Asia collision. *Geol. J.* 55, 6696–6717. doi:10.1002/gj.3834

Ding, H. X., Hou, Q. Y., and Zhang, Z. M. (2016). Petrogenesis and tectonic significance of the eocene adakite-like rocks in Western Yunnan, southeastern Tibetan plateau. *Lithos* 245, 161–173. doi:10.1016/j.lithos.2015.09.024

Ding, L., and Lai, Q. Z. (2003). New geological evidence of crustal thickening in the Gangdese block prior to the Indo-Asian collision. *Chin. Sci.*, 1610–1616. doi:10.1360/02wd0586

Gao, S. B. (2016). *Copper-iron polymetal metallogenic regularity and election of Targeet areas in the western of Gangdise metallogenic belt, Tibet*. Ph. D thesis. Wuhan: China University of Geosciences, 16. (in Chinese with English abstract).

Gao, S. B., Zheng, Y. Y., Wang, J. S., Zhang, Z., and Yang, C. (2011). The geochronology and geochemistry of intrusive rocks in Bange area: Constraints on the evolution time of the Bangong Lake - nujiang ocean basin. *Acta Petrol. Sin.* 27 (7), 1973–1982. (in Chinese with English abstract).

Geng, Q. R., Li, W. C., Wang, L. Q., Zeng, X. T., Peng, Z. M., Zhang, X. F., et al. (2021). Paleozoic tectonic framework and evolution of the central and western Tethys. *Sediment. Geol. Tethyan Geol.* 41 (2), 297–315. (in Chinese with English abstract). doi:10.19826/j.cnki.1009-3850.2021.02012

Geng, Q. R., Pan, G. T., Wang, L. Q., Peng, Z. M., and Zhang, Z. (2011). Tethyan evolution and metallogenic geological background of the Bangong Co–Nujiang belt and the Qiangtang massif in Tibet. *Geol. Bull. China* 30 (8), 1261–1274. (in Chinese with English abstract).

Griffin, W. L., Pearson, N. J., Belousova, E., Jackson, S. E., Achterbergh, E. V., O'Reilly, S. Y., et al. (2000). The Hf isotope composition of cratonic mantle: LAM-MC-ICPMS analysis of zircon megacrysts in kimberlites. *Geochim. Cosmochim. Acta* 64, 133–147. doi:10.1016/s0016-7037(99)00343-9

Griffin, W. L., Wang, X., Jackson, S. E., Pearson, N. J., O'Reilly, S. Y., Xu, X. S., et al. (2002). Zircon chemistry and magma mixing, SE China: In–situ analysis of Hf isotopes, tonglu and pingtan igneous complexes. *Lithos* 61, 237–269. doi:10.1016/s0024-4937(02)00082-8

Grimes, C. B., John, B. E., Kelemen, P. B., Mazdab, F. K., Wooden, J. L., Cheadle, M. J., et al. (2007). Trace element chemistry of zircons from oceanic crust: A method for distinguishing detrital zircon provenance. *Geol.* 35 (7), 643–646. doi:10.1130/g23603a.1

Hoskin, P., and Black, L. P. (2000). Metamorphic zircon formation by solid-state recrystallization of protolith igneous zircon. *J. Metamorph. Geol.* 18 (4), 423–439. doi:10.1046/j.1525-1314.2000.00266.x

Hoskin, P. W. O. (2005). Trace-element composition of hydrothermal zircon and the alteration of Hadean zircon from the Jack Hills, Australia. *Geochim. Cosmochim. Acta* 69, 637–648. doi:10.1016/j.gca.2004.07.006

Hou, Z. Q., Yang, Z. M., Lu, Y. J., Kemp, A., Zheng, Y. C., Li, Q. Y., et al. (2015). A genetic linkage between subduction- and collision-related porphyry Cu deposits in continental collision zones. *Geology* 43, 247–250. doi:10.1130/g36362.1

Huang, H. X., Dai, Z. W., Liu, H., Chen, M. H., Li, G. M., Cao, H. W., et al. (2021b). Hydrothermal zircon dating of Shangxu gold deposit in Tibet and restriction on the Early Cretaceous orogenic gold mineralization in the middle Bangonghu–Nujiang suture zone. *Acta Geol. Sin. Engl. Ed.* 95 (4), 1249–1259. doi:10.1111/1755-6724.14679

Huang, H. X., Dai, Z. W., Liu, H., Li, G. M., Huizenga, J. M., Zhang, L. K., et al. (2021a). Zircon U–Pb ages, geochemistry, and Sr–Nd–Pb–Hf isotopes of the mugagangri monzogranite in the southern Qiangtang of Tibet, Western China: Implications for the evolution of the bangong Co-nujiang meso-Tethyan Ocean. *Geol. J.* 56, 3170–3186. doi:10.1002/gj.4094

Huang, H. X., Li, G. M., Dong, S. L., Liu, B., Zhang, H., Zhang, L., et al. (2012b). SHRIMP zircon U-Pb age and geochemical characteristics of Qinglung, granodiorite in Baingoin area, Tibet. *Geol. Bull. China* 31 (6), 852–859. (in Chinese with English abstract).

Huang, H. X., Li, G. M., Liu, H., Cao, H. W., and Zhang, Z. L. (2018a). Zircon U-Pb age of the shangxu gold deposit from bangong - nujiang Co, northern Tibet, and restriction on the early cretaceous orogenic gold mineralisation. *Acta Geol. Sin. - Engl. Ed.* 92 (4), 1664–1666. doi:10.1111/1755-6724.13657

Huang, H. X., Li, G. M., Zeng, Q. G., Liu, B., Duan, Z. M., Dong, S. L., et al. (2012a). Geochronology of the Chagele Pb-Zn deposit in Tibet and its significance. *Geol. China* 39 (3), 750–759. (in Chinese with English abstract).

Huang, Y., Cao, H. W., Li, G. M., Brueckner, S. M., Zhang, Z., Dong, L., et al. (2018b). Middle-late triassic bimodal intrusive rocks from the Tethyan Himalaya in south Tibet: Geochronology, petrogenesis, and tectonic implications. *Lithos* 318–319, 78–90. doi:10.1016/j.lithos.2018.08.002

Huang, Y., Li, G. M., Ding, J., Dai, J., Yan, G. Q., Dong, S. L., et al. (2017). Origin of the newly discovered Zhunuo porphyry Cu-Mo-Au deposit in the Western part of the Gangdese porphyry copper belt in the southern Tibetan plateau, SW China. *Acta Geol. Sin. - Engl. Ed.* 91 (1), 109–134. doi:10.1111/1755-6724.13066

Huang, Y., Ren, M. H., Jowitt, S. M., Li, G. M., Fu, J. G., Lang, X. H., et al. (2021c). Middle triassic arc magmatism in the southern Lhasa terrane: Geochronology, petrogenesis, and tectonic setting. *Lithos* 380-381, 105857. doi:10.1016/j.lithos.2020.105857

Huang, Y., Ren, M. H., Liang, W., Li, G. M., Heilbronn, K., Dai, Z. W., et al. (2020). Origin of the oligocene Tuolangla porphyry-skarn Cu-W-Mo, deposit in Lhasa terrane, southern Tibet. *China Geol.* 3, 369–384. doi:10.31035/cg2020047

Kapp, P., DeCelles, P. G., Gehrels, G. E., Heizler, T. M., and Ding, L. (2007). Geological records of the Lhasa-Qiangtang and Indo-Asian collisions in the Nima area of central Tibet. *Geol. Soc. Am. Bull.* 119 (7–8), 917–933. doi:10.1130/b26033.1

Kapp, P., Yin, A., Harrison, T. M., and Ding, L. (2005). Cretaceous-Tertiary shortening, basin development, and volcanism in Central Tibet. *Geol. Soc. Am. Bull.* 117 (7–8), 865–878. doi:10.1130/b25595.1

LeMaitre, R. W. (2002). *Igneous rocks: A classification and glossary of terms*. Cambridge: Cambridge University Press, 3–42.

Li, G. M., Duan, Z. M., Liu, B., Zhang, H., Dong, S. L., and Zhang, L. (2011). The discovery of Jurassic accretionary complexes in Duolong area, northern Bangong Co - Nujiang suture zone, Tibet, and its geologic significance. *Geol. Bull. China* 30 (8), 1256–1260. (in Chinese with English abstract).

Li, H. L., Gao, C., Li, Z. H., Zhang, Z., Peng, Z. M., and Guan, J. L. (2016). Age and tectonic significance of Jingzhushan formation in bangong lake area, Tibet. *Geotect. Metallogenia* 40 (3), 535–542. (in Chinese with English abstract).

Li, H. L., Yang, S., Li, D. W., Zhang, S., Lü, Z. W., and Chen, G. F. (2014). Geochronology, geochemistry, tectonic setting, and metallogenetic significance of the Late Cretaceous quartz monzonite in the northwestern, Gangdise terrane. *Geotect. Metallogenia* 38 (3), 694–705. (in Chinese with English abstract).

Li, J. X., Qin, K. Z., Li, G. M., Richards, J. P., Zhao, J. X., and Cao, M. J. (2014). Geochronology, geochemistry, and zircon Hf isotopic compositions of Mesozoic intermediate–felsic intrusions in central Tibet: Petrogenetic and tectonic implications. *Lithos* 198, 77–91. doi:10.1016/j.lithos.2014.03.025

Li, J. X., Qin, K. Z., Li, G. M., Xiao, B., Chen, L., and Zhao, J. X. (2011). Post-collisional ore-bearing adakitic porphyries from gangdese porphyry copper belt, southern Tibet: Melting of thickened juvenile arc lower crust. *Lithos* 126 (3–4), 265–277. doi:10.1016/j.lithos.2011.07.018

Li, Y. C., Huang, H. X., Liu, H., and Lan, S. S. (2017). Gold mineralization in the Bangong lake-Nujiang metallogenic zone, Xizang. *Sediment. Geol. Tethyan Geol.* 37 (2), 1–13. (in Chinese with English abstract).

Liu, H., Huang, H. X., Li, G. M., Li, W. C., Li, Y. G., Ma, D. F., et al. (2022a). Petrogenesis of an Early Cretaceous Xiabie Co I-type granite in southern Qiangtang, Tibet: Evidence from geochemistry, geochronology, Rb-Sr, Sm-Nd, Lu-Hf and Pb isotopes. *Acta Geol. Sin. Engl. Ed.* 96 (3), 919–937. doi:10.1111/1755-6724.14777

Liu, H., Huang, H. X., Li, G. M., Xiao, W. F., Zhang, Z. L., Liu, B., et al. (2015). Factor analysis in geochemical survey of the Shangxu gold deposit, northern Tibet. *Geol. China* 42 (4), 1126–1136. (in Chinese with English abstract).

Liu, H., Huang, H. X., Zhang, L. K., Li, G. M., Lü, M. H., Yan, G. Q., et al. (2019a). Origin and evolution of Ore–Forming fluids in Luerma porphyry copper deposit from the Western Gangdise. *Earth Sci.* 44 (6), 1935–1956. (in Chinese with English abstract). doi:10.3799/dqkx.2018.370

Liu, H., Huang, H. X., Zhang, L. K., Li, G. M., Ouyang, Y., Huang, Y., et al. (2021a). Luerma, a newly discovered Late Triassic porphyry copper-gold ore-spot in the Western Gangdise metallogenic belt, Tibet. *Sediment. Geol. Tethyan Geol.* 41 (4), 599–611. (in Chinese with English abstract). doi:10.19826/j.cnki.1009-3850.2020.06001

Liu, H., Li, F. Q., Zhou, F., Li, J., Gou, Z. B., Yang, Y., et al. (2018c). Late paleozoic earthquake events in the Nixiong area and its geological significance, western Lhasa block. *Earth Sci.* 43 (8), 2767–2779. doi:10.3799/dqkx.2018.167

Liu, H., Li, G. M., Huang, H. X., Cao, H. W., Yuan, Q., Li, Y. X., et al. (2018a). Petrogenesis of late cretaceous jiangla'angzong I-type granite in central Lhasa terrane, Tibet, China: Constraints from whole-rock geochemistry, zircon U-Pb geochronology, and Sr-Nd-Pb-Hf isotopes. *Acta Geol. Sin. - Engl. Ed.* 92 (4), 1396–1414. doi:10.1111/1755-6724.13634

Liu, H., Li, G. M., Huang, H. X., Xiao, W. F., Yan, G. Q., Ma, D. F., et al. (2018b). Sources of ore-forming materials in the Shangxu orogenic gold deposit, northern Xizang (Tibet), constraints form C., S., and Pb isotopes. *Geol. Rev.* 64 (5), 1285–1301. (in Chinese with English abstract).

Liu, H., Li, G. M., Huang, H. X., Zhang, L. K., Lan, S. S., Fu, J. G., et al. (2019b). Sources of ore–forming materials of Luerma porphyry copper (gold) deposit, Western Gangdise. *Mineral. Deposits* 38 (4), 631–643. (in Chinese with English abstract). doi:10.16111/j.0258-7106.2019.03.012

Liu, H., Li, G. M., Huang, H. X., Zhang, L. K., Lü, M. H., Lan, S. S., et al. (2019c). The discovery of the Late Triassic porphyry type Cu deposit from Gangdise metallogenic belt, Tibet. *Geol. China* 46 (5), 1238–1240. (in Chinese with English abstract). doi:10.12029/gc20190524

Liu, H., Li, G. M., Huang, H. X., Zhang, Z. L., Xiao, W. F., Jiao, Y. J., et al. (2017). Prospecting potential analysis of deep No. III ore section in the Shangxu orogenic Gold deposit, bangong Co–Nujiang metallogenic belt, Tibet. *Acta Geol. Sin.* 91 (6), 1245–1258. (in Chinese with English abstract).

Liu, H., Li, G. M., Li, W. C., Huang, H. X., Li, Y. G., Ouyang, Y., et al. (2022b). Petrogenesis and tectonic setting of the late Early Cretaceous Kong Co A-type granite in the northern margin of Central Lhasa subterrane, Tibet. *Acta Petrol. Sin.* 38 (1), 230–252. (in Chinese with English abstract). doi:10.18654/1000-0569/2022.01.15

Liu, H., Li, G. M., Li, W. C., Zhang, J. H., Li, Y. G., Zhang, Z. L., et al. (2021b). Epithermal mineralization at Budongla gold deposit in Zhongba County of Tibet: Evidence from fluid inclusions and H–O isotopes. *Mineral. Deposits* 40 (2), 311–328. (in Chinese with English abstract). doi:10.16111/j.0258-7106.2021.02.008

Liu, H., Zhang, H., Li, G. M., Huang, H. X., Xiao, W. F., You, Q., et al. (2016). Petrogenesis of the early cretaceous Qingcaoshan strongly peraluminous S–type granitic pluton, southern Qiangtang, northern Tibet: Constraints from whole–rock geochemistry and zircon U–Pb geochronology. *Acta Sci. Nat. Univ. Pekin.* 52 (5), 848–860. (in Chinese with English abstract). doi:10.13209/j.0479-8023.2016.045

Liu, H., Zhang, L. K., Huang, H. X., Li, G. M., Ouyang, Y., Yu, H., et al. (2020). Evolution of ore–forming fluids in the Luobuzhen epithermal gold–silver deposit in Western gangdisi: Fluid inclusion and H–O isotope evidence. *Earth Sci. Front.* 27 (4), 49–65. (in Chinese with English abstract). doi:10.13745/j.esf.sf.2020.4.23

Ma, Y. M., Yang, T. S., Yang, Z. Y., Zhang, S. H., Wu, H. C., Li, H. Y., et al. (2014). Paleomagnetism and U-Pb zircon geochronology of lower cretaceous lava flows from the Western Lhasa terrane: New constraints on the India-Asia collision process and intracontinental deformation within Asia. *J. Geophys. Res. Solid Earth* 119, 7404–7424. doi:10.1002/2014jb011362

Maniar, P. D., and Piccoli, P. M. (1989). Tectonic discrimination of granitoids. *Geol. Soc. Am. Bull.* 101, 635–643. doi:10.1130/0016-7606(1989)101<0635:tdog>2.3.co;2

McDonough, W. F., and Sun, S. S. (1995). The composition of the Earth. *Chem. Geol.* 120, 223–253. doi:10.1016/0009-2541(94)00140-4

McKenzie, D., and Bickle, M. (1988). The volume and composition of melt generated by extension of the lithosphere. *J. Petrology* 29, 625–679. doi:10.1093/petrology/29.3.625

Meng, F. Y., Zhao, Z. D., Zhu, D. C., Mo, X. X., Guan, Q., Huang, Y., et al. (2014). Late cretaceous magmatism in mamba area, central Lhasa subterrane: Products of back-arc extension of Neo-Tethyan Ocean? *Gondwana Res.* 26 (2), 505–520. doi:10.1016/j.gr.2013.07.017

Middlemost, E. A. K. (1994). Naming materials in the magma/igneous rock system. *Earth Sci. Rev.* 37, 215–224. doi:10.1016/0012-8252(94)90029-9

Ouyang, Y., Yang, W. N., Huang, H. X., Liu, H., Zhang, J. L., and Zhang, J. H. (2017). Metallogenic dynamics background of Ga'erqiong Cu-Au deposit in Tibet, China. *Earth Sci. Res. J.* 21 (2), 59–65. doi:10.15446/esrj.v21n2.65192

Ouyang, Y., Zhao, Y. B., Ni, Z. Y., Zhang, J. H., and Gao, H. (2016). Alteration remote sensing anomaly extraction in Jiangla'angzong area of Tibet. *Remote Sens. Inf.* 31 (5), 90–95. (in Chinese with English abstract).

Pan, G. T., Mo, X. X., Hou, Z. Q., Zhu, D. C., Wang, L. Q., Li, G. M., et al. (2006). Spatial–temporal framework of the Gangdese orogenic belt and its evolution. *Acta Petrol. Sin.* 22 (3), 521–533. (in Chinese with English abstract). doi:10.3321/j.issn:1000-0569.2006.03.001

Pan, G. T., Wang, L. Q., Li, X. Z., Wang, J. M., and Xu, Q. (2001). The tectonic framework and spatial allocation of the archipelagic arc–basin systems on the Qinghai-Xizang Plateau. *Sediment. Geol. Tethyan Geol.* 21 (3), 1–26. (in Chinese with English abstract).

Pan, G. T., Xiao, Q. H., Lu, S. N., Deng, J. F., Feng, Y. M., Zhang, K. X., et al. (2009). Subdivision of tectonic units in China. *Geol. China* 36 (1), 1–28. (in Chinese with English abstract).

Pan, G. T., Wang, L. Q., Yin, F. G., Geng, Q. R., Li, G. M., and Zhu, D. C. (2022). Researches on geological-tectonic evolution of Tibetan Plateau: A review, recent advances, and directions in the future. *Sediment. Geol. Tethyan Geol.* 42 (2), 151–175. (in Chinese with English abstract). doi:10.19826/j.cnki.1009-3850.2022.05004

Pearce, J. A., Harris, N. B. W., and Tindle, A. G. (1984). Trace element discrimination diagrams for the tectonic interpretation of granitic rocks. *J. Petrology* 25, 956–983. doi:10.1093/petrology/25.4.956

Peng, J. H., Zhao, L. X., He, J., Huang, S. C., and Gong, C., (2013). Discovery of Indosinian magmatic rocks and its significance in western Gangdise, Tibet. J. East China Inst. *Technol.* 36 (6), 21–26. (in Chinese with English abstract). doi:10.3969/j.issn.1674-3504.2013.s2.004

Qin, Z., Yang, Z. J., Tang, L., Wang, M. Z., Yu, P. T., Han, K., et al. (2019). Geochemical characteristics, zircon U-Pb age and metallogenic significance of Chalong granites in the Gangdise Belt of Tibet. *Geol. Bull. China* 38 (2–3), 231–241. (in Chinese with English abstract).

Scherer, E. E., Cameron, K. L., and Blichert, J. (2000). Lu–hf garnet geochronology: Closure temperature relative to the Sm–Nd system and the effects of trace mineral inclusions. *Geochimica Cosmochimica Acta* 64, 3413–3432. doi:10.1016/s0016-7037(00)00440-3

Song, Y., Zeng, Q. G., Liu, H. Y., Liu, Z. B., Li, H. F., and De, Y. Z. (2019). An innovative perspective for the evolution of bangong–Nujiang Ocean: Also discussing the paleo- and neo-tethys conversion. *Acta Petrol. Sin.* 35 (3), 625–641. (in Chinese with English abstract). doi:10.18654/1000-0569/2019.03.02

Sun, G. Y., Hu, X. M., Zhu, D. C., Hong, M. T., Wang, J. G., and Wang, Q. (2015). Thickened juvenile lower crust–derived ~90 Ma, adakitic rocks in the Central Lhasa terrane, Tibet. *Lithos* 224–225, 225–239. doi:10.1016/j.lithos.2015.03.010

Sun, S. S., and MchDonough, W. F. (1989). Chemical and isotopic systematics of oceanic basalts: Implication for mantle composition and processes. *Geol. Soc. Spec. Pulication* 42, 303–345. doi:10.1144/GSL.SP.1989.042.01.19

Tang, J. X., Sun, X. G., Din, G. S., Wang, Q., Wang, Y. Y., Yang, C., et al. (2014). Discovery of the epithermal deposit of Cu (Au-Ag) in the Duolong ore concentrating area, Tibet. *Adv. Earth Sci.* 35 (1), 6–10. (in Chinese with English abstract). doi:10.3975/cagsb.2014.01.02

Taylor, S. R., and McLennan, S. M. (1985). *The continental crust: Its composition and evolution*. Oxford: Blackwell Scientific Publications, 0–312.

Volkmer, J. E., Kapp, P., Guyn, N. J. H., and Lai, Q. (2007). Cretaceous–tertiary structural evolution of the North central Lhasa terrane, Tibet. *Tectonics* 26, 6007. doi:10.1029/2005tc001832

Wang, B. D., Guo, L., Wang, L. Q., Li, B., Huang, H. X., Chen, F. Q., et al. (2012). Geochronology and petrogenesis of the ore–bearing pluton in Chagele deposit in middle of the Gangdese metallogenic belt. *Acta Petrol. Sin.* 28 (5), 1647–1662. (in Chinese with English abstract).

Wang, B. D., Wang, L. Q., Chung, S. L., Chen, J. L., Yin, F. G., Liu, H., et al. (2016). Evolution of the Bangong–Nujiang Tethyan ocean: Insights from the geochronology and geochemistry of mafic rocks within ophiolites. *Lithos* 245, 18–33. doi:10.1016/j.lithos.2015.07.016

Wang, B. D., Xu, J. F., Liu, B. M., Chen, J. L., Wang, L. Q., Guo, L., et al. (2013). Geochronology and ore-forming geological background of 90 Ma, porphyry copper deposit in the Lhasa terrane, Tibet plateau. *Acta Geol. Sin.* 87 (1), 71–80. (in Chinese with English abstract).

Wang, X. X., Yan, G. Q., Liu, H., Huang, H. X., Lai, Y., Tian, S. Y., et al. (2021b). The genesis of the late cretaceous qusang'gele granitie in central Lhasa terrane, Tibet: Constraints by geochemistry, zircon U-Pb geochronology, and Sr-Nd-Pb-Hf isotopes. *Earth Sci.* 46 (8), 2832–2849. (in Chinese with English abstract). doi:10.3799/dqkx.2020.278

Wang, L. Q., Wang, B. D., Li, G. M., Wang, D. B., and Peng, Z. M. (2021a). Major progresses of geological survey and research in East Tethys: An overview. *Sediment. Geol. Tethyan Geol.* 41 (2), 283–296. (in Chinese with English abstract). doi:10.19826/j.cnki.1009-3850.2021.01008

Wang, Q., Pan, G. T., Tang, F. W., Yang, J., Xia, S. B., Zhang, W., et al. (2022). Basic features of crust-mantle structure of the Tibet Plateau. *Sediment. Geol. Tethyan Geol.* 42 (2), 319–329. (in Chinese with English abstract). doi:10.19826/j.cnki.1009-3850.2022.04016

Wu, H. H., Zhang, G. Q., and Wang, W., (2017). U-Pb dating of Chromite from Shannan Jinluxi in Tibet and its Geological Significance. J. East China Inst. *Technol.* 40 (3), 246–252. (in Chinese with English abstract). doi:10.3969/j.issn.16743504.2017.03.005

Xu, Z. Q., Yang, J. S., Li, W. C., Li, H. Q., Cao, Z. H., Yan, Z., et al. (2013). Paleo–Tethys system and accretionary orogen in the Tibet plateau. Acta Petrol. Sin. 29 (6), 1847–1860. (in Chinese with English abstract).

Yan, L. L., and Zhang, K. J. (2020). Infant intra-oceanic arc magmatism due to initial subduction induced by oceanic plateau accretion: A case study of the bangong meso-tethys, central Tibet, Western China. *Gondwana Res.* 79, 110–124. doi:10.1016/j.gr.2019.08.008

Yang, J. S., Xu, Z. Q., Li, T. F., Li, H. Q., Li, Z. L., Ren, Y. F., et al. (2007). Oceanic subduction–type eclogite in the Lhasa terrane, Tibet, China: Remains of the

paleo–tethys Ocean basin? *Geol. Bull. China* 26 (10), 1277–1287. (in Chinese with English abstract).

Yu, H. X., Chen, J. L., Xu, J. F., Wang, B. D., Wu, J. B., and Liang, H. Y. (2011). Geochemistry and origin of late cretaceous (-90Ma) ore-bearing porphyry of balazha in mid-northern Lhasa terrane, Tibet. *Acta Petrol. Sin.* 27 (7), 2011–2022. (in Chinese with English abstract).

Zhang, K. J., Li, Q. H., Yan, L. L., Lu, L. Z., Zhang, Y. X., Hui, J., et al. (2017). Geochemistry of limestones deposited in various plate tectonic settings. *Earth-Science Rev.* 167, 27–46. doi:10.1016/j.earscirev.2017.02.003

Zhang, K. J., Zhang, Y. X., Tang, X. C., and Xia, B. (2012). Late Mesozoic tectonic evolution and growth of the Tibetan plateau prior to the Indo-Asian collision. *Earth-Science Rev.* 114 (3–4), 236–249. doi:10.1016/j.earscirev.2012.06.001

Zhang, Z., Yao, X., Tang, J., Li, Z. J., Wang, L. Q., Yang, Y., et al. (2015). Litho geochemical, Re-Os and U-Pb geochronological, Hf-Lu and S-Pb isotope data of the Ga'erqiong-galale Cu-Au ore-concentrated area: Evidence for the late cretaceous magmatism and metallogenic event in the bangong–nujiang suture zone, northwestern Tibet. *Resour. Geol.* 65 (2), 76–102. doi:10.1111/rge.12064

Zhao, Y. Y., Cui, Y. B., Lü, L. L., and Shi, D. H. (2011). Chronology, geochemical characteristics and the significance of Shesuo copper polymetallic deposit, Tibet. *Acta Petrol. Sin.* 27 (7), 2132–2142. (in Chinese with English abstract).

Zhao, L. X., Gong, C., He, J., Peng, J. H., Huang, S. C., and Yang, Z. L., (2013). Discovery of porphyry copper deposit and its significance of Dajiacuo in Cuoqin County, Tibet. *J. East China Inst. Technol.* 36 (6), 13–20. (in Chinese with English abstract). doi:10.3969/j.issn.16743504.2013.s2.003

Zheng, Y. C., Hou, Z. Q., Gong, Y. L., Liang, W., Sun, Q. Z., Zhang, S., et al. (2014). Petrogenesis of cretaceous adakite–like intrusions of the gangdese plutonic belt, southern Tibet: Implications for mid-ocean ridge subduction and crustal growth. *Lithos* 190–191, 240–263. doi:10.1016/j.lithos.2013.12.013

Zhu, D. C., Li, S. M., Cawood, P. A., Wang, Q., Zhang, Z. D., Liu, S., et al. (2016). Assembly of the Lhasa and Qiangtang terranes in central Tibet by divergent double subduction. *Lithos* 245, 7–17. doi:10.1016/j.lithos.2015.06.023

Zhu, D. C., Mo, X. X., Niu, Y. L., Zhao, Z. D., Wang, L. Q., Liu, Y. S., et al. (2009). Geochemical investigation of Early Cretaceous igneous rocks along an east-west traverse throughout the Central Lhasa terrane, Tibet. *Chem. Geol.* 268, 298–312. doi:10.1016/j.chemgeo.2009.09.008

Zhu, D. C., Zhao, Z. D., Niu, Y. L., Mo, X. X., Chung, S. L., Hou, Z. Q., et al. (2011). The Lhasa terrane: Record of a microcontinent and its histories of drift and growth. *Earth Planet. Sci. Lett.* 301 (1), 241–255. doi:10.1016/j.epsl.2010.11.005

frontiers | Frontiers in Earth Science

TYPE Original Research
PUBLISHED 30 August 2022
DOI 10.3389/feart.2022.930880

OPEN ACCESS

EDITED BY
Gillian Foulger,
Durham University, United Kingdom

REVIEWED BY
Weimin LI,
Jilin University, China
Liming Dai,
OUC, China

*CORRESPONDENCE
Guozhi Wang,
wangguozhi66@163.com
Yuzhen Fu,
fuyuzhen15@cdut.edu.cn

SPECIALTY SECTION
This article was submitted to Petrology, a section of the journal Frontiers in Earth Science

RECEIVED 28 April 2022
ACCEPTED 28 July 2022
PUBLISHED 30 August 2022

CITATION
Lu N, Wang G, Fu Y and Peng Z (2022), Implication of garnet zoning in high pressure- ultrahighpressure eclogite from Changning-Menglian suture zone, Bangbing area, Southeast Tibetan Plateau.
Front. Earth Sci. 10:930880.
doi: 10.3389/feart.2022.930880

Implication of garnet zoning in high pressure- ultrahighpressure eclogite from Changning-Menglian suture zone, Bangbing area, Southeast Tibetan Plateau

Nannan Lu[1], Guozhi Wang[2]*, Yuzhen Fu[1]* and Zhimin Peng[3]

[1]College of Earth Science, Chengdu University of Technology, Chengdu, China, [2]Institute of Sedimentary Geology, Chengdu University of Technology, Chengdu, China, [3]Chengdu Center of China Geological Survey, Chengdu, China

Major and trace element zonation patterns were determined in ultrahigh-pressure eclogite garnets from the Changning-Menglian suture, Bangbing area. Several stages of eclogite metamorphism are recorded by garnet zonation. Cores of garnets are generally darker and inclusion-rich, while rims are brighter and inclusion-poor. Garnets were analyzed for the major element by EPMA and trace element by LA-ICP-MS. The results show that both major elements and rare earth elements in garnet have typical compositional bands. The major element zonation recorded the process of increasing temperature and pressure and the metamorphism of the eclogite from the core to rim, and the rare earth element zonation recorded different mineral chemical reactions during the formation of the garnet and its three stages of growth. Eclogites completely imply the process of rapid exhumation, cooling, and depressurization after short-term peak metamorphism. The contents of some trace elements (such as Y and Sr) in garnet are controlled by major elements and mineral combinations. The formation of new minerals in the process of retrograde metamorphism affects the distribution of trace elements.

KEYWORDS

garnet, eclogite, zoning, HP/UHP metamorphism, Changning-Menglian suture

Introduction

Eclogite is generally considered a typical product of the high-pressure metamorphism of modern plate tectonics (Carswell, 1990; Condie and Kröner, 2008). Eclogite-facies rocks including garnet + omphacite + SiO_2 phase (quartz/coesite) assemblages are common components of the deeper part of subducted slabs and record information to constrain geochemical and geodynamic processes occurring at plate-convergent margins (Bebout, 2007; Hacker & Gerya, 2013; Taguchi et al., 2019). The Changning-Menglian suture zone is the southern extension of the Longmucuo-Shuanghu suture zone in the northern Qinghai–Tibetan Plateau. Many studies have been performed on these eclogites in the Longmucuo-Shuanghu suture zone. The eclogites are produced in the

form of lenses that occur in garnet-phegite schist. Apart from Baqing eclogites, most eclogites from the Qiangtang block are characterized by low peak temperatures and the presence of lawsonite or its pseudomorphs. The peak stage of metamorphism takes place in the lawsonite-eclogite facies, which is the main metamorphic age occurring during the Late Triassic. Four stages of metamorphic evolution in eclogites represent the process of subduction of the Paleo-Tethys Ocean and collision orogeny between Gondwana and the continent in the Paleo-Tethys Ocean (Zhai, 2008; Dong et al., 2010; Zhai, 2013; Zhang et al., 2018). The lithology of the Changning-Menglian suture zone is similar to that of the Longmucuo-Shuanghu suction zone, and they likely represent a united residual of the Paleozoic Tethys Ocean (Wang et al., 2018). Eclogite was discovered in recent years in the Mengku, Qianmai, and Bangbing areas in the Changning-Menglian suture zone. The eclogites in the Mengku area feature strong retrograde metamorphism that is mainly in the form of garnet-amphibolite, while the eclogites from the Qianmai and Bangbing areas are fresh with weak retrogression (Li et al., 2015; Li et al., 2017; Sun et al., 2019; Peng et al., 2019). The Bangbing eclogite retains complete petrological information and has become an important research object to investigate the metamorphic evolution of the Changning-Menglian suction zone and to further explore the subduction-orogeny process of the Paleo-Tethys Ocean on the southeastern Tibetan Plateau.

Garnet is highly refractory and has low solubility in metamorphic fluids and anatectic melts, meaning that it is stable over a wide range of temperatures and pressures (Baxter et al., 2013; Xia et al., 2013). It may preserve geochemical zonation and mineral/fluid/melt inclusions in many conditions and has become an important mineral for the study of metamorphism. It has been demonstrated that the geochemical zonation of garnet is related to metamorphic pressure, temperature, and associated mineral assemblages (Xia and Zheng, 2011; Xia, 2019; Kohn, 2003). The change in the chemical composition reveals the environmental change and metamorphic processes during the growth of garnet, so it could play a vital role in the study of metamorphic rocks and metamorphic evolution. Major element zonation in garnet is susceptible to metamorphic modification *via* thermal diffusion or even be flattened at high temperatures in excess of 650°C. Trace elements in garnet are less susceptible to diffusion modification at high temperatures because of their larger cation radii (Chernoff C B and Carlson W D, 1999; Zhou et al., 2011). Trace element zonation in garnet is stronger than major element zoning and allows a much clearer identification of phases contributing to garnet-forming reactions and is thus a better-defined metamorphic evolution. The composition of trace elements is more sensitive to changes in petrochemical kinetics and mineral assemblage than that of major elements, which can well indicate the crystallization and growth process of garnet and related mineral chemical reactions.

As a major mineral in eclogite, garnet can grow at almost every stage during continental subduction and exhumation, which presents a lot of information about the metamorphic properties of the host rock. Zonation patterns were determined in garnet from the Bangbing area. Based on the analysis of the main and trace elements of garnet zonation, this study identifies the multistage growth of garnet, attempts to reveal the metamorphic evolution process of host eclogite, and explores the migration behavior of trace elements.

Geological setting

The Changning-Menglian suture zone at the southeastern Tibetan Plateau has widespread ophiolitic complexes, and the zone is connected to the Longmucuo-Shuanghu suture zone to the north and the Qingmai suture zone in Thailand to the south (Figure 1). It is adjacent to the Baoshan block in the west and the Lincang-Menghai magmatic arc to the east. The eclogite that we studied occurs in the Lancang Group. The Lancang Group is distributed along an elongated belt from Fengqing County in the north via Yun County, Lincang (Peng et al., 2018a; Wang et al., 2018). The group is mainly dominated by mica–quartz schist and biotite–muscovite schist, greenschist, albite schist, and amphibole schist. Meta-basic rocks, meta-acidic rocks, and high-pressure metamorphic rocks discretely occur as blocks and lenses. The eclogites occur in grayish-white garnet–mica schist and are produced in the form of varied sizes of lenses. This group of mica schists has light color and is coarse-grained, which is different from other non-host muscovite schists. Glaucophane with different contents is common in the schist around the eclogite belt, which forms a nearly north–south blueschist belt, referred to as the Suyi blueschist belt in the literature. In summary, the eclogites in this study occur in the Suyi blueschist belt, and they are produced in the form of lenses of varied sizes. The Lancang Group has experienced three stages of metamorphic deformation, and all lithologic layers are connected by tectonic foliation (Fu et al., 2021).

Sample description

The samples are from the Bangbing area, including glaucophane eclogite and actinolite-bearing eclogite. Two kinds of eclogites all occur in the Lancang Group and Suyi blueschist belt. The eclogites are fresh and well preserved. According to the mineral composition of garnet, they are all type-C eclogites, typical of oceanic eclogites (Coleman et al., 1965).

Glaucophane eclogites are grayish-green with a porphyroblastic texture and a blocky structure. Porphyroblasts include garnet (25%), glaucophane (10%), and clinozoisite (5%–10%). The metamorphosed matrix with granular crystalloblastic

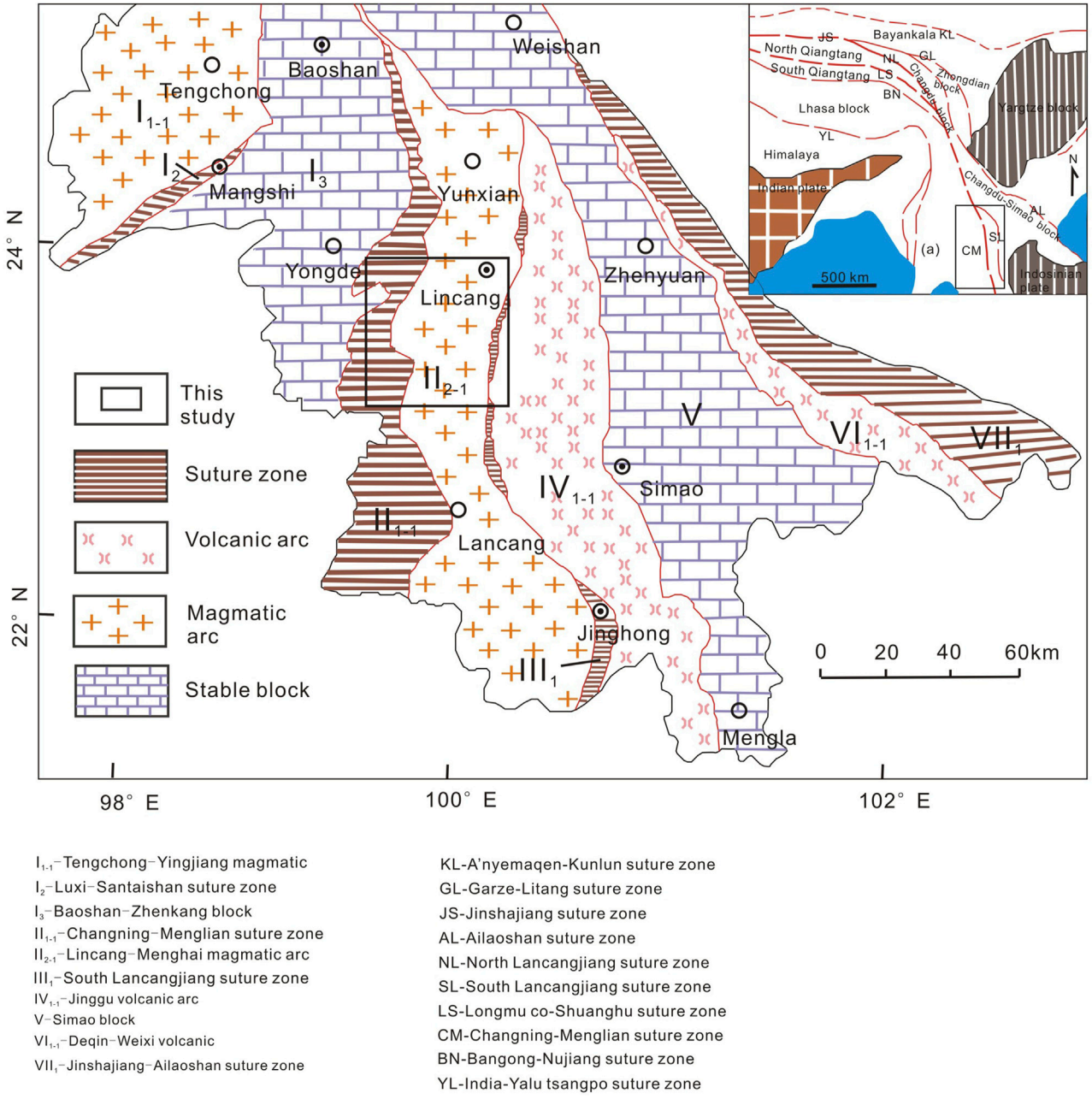

FIGURE 1
Geological map of the Changning-Menglian suture zone (after Fu et al., 2021)

texture consists of omphacite (40%), glaucophane (5%), quartz (5%), chlorite (5%), phengite (3%), and rutile (3%) (Figure 2A). Garnets from glaucophane eclogite in the selected samples are euhedral to subhedral granular, between 0.2 and 5 mm diameter, and rhombic dodecahedrons in shape and show visible growth zones. The boundary between omphacite and garnet in the metamorphosed matrix of glaucophane eclogite is clear and straight. The garnet is mostly dispersed in eclogite and occurs in the form of porphyroblasts. Small particle clusters and massive distribution can also be seen. Most of these garnets develop obvious zonation, which is mainly manifested in color zoning and inclusion zoning. The cores of garnet are dark red, and the rims are lighter. The cores of the garnets from glaucophane eclogites are generally inclusion-rich, while the rims are inclusion-poor. There are glaucophane, omphacite, chlorite, rutile, and minor amounts of quartz as inclusions in garnet.

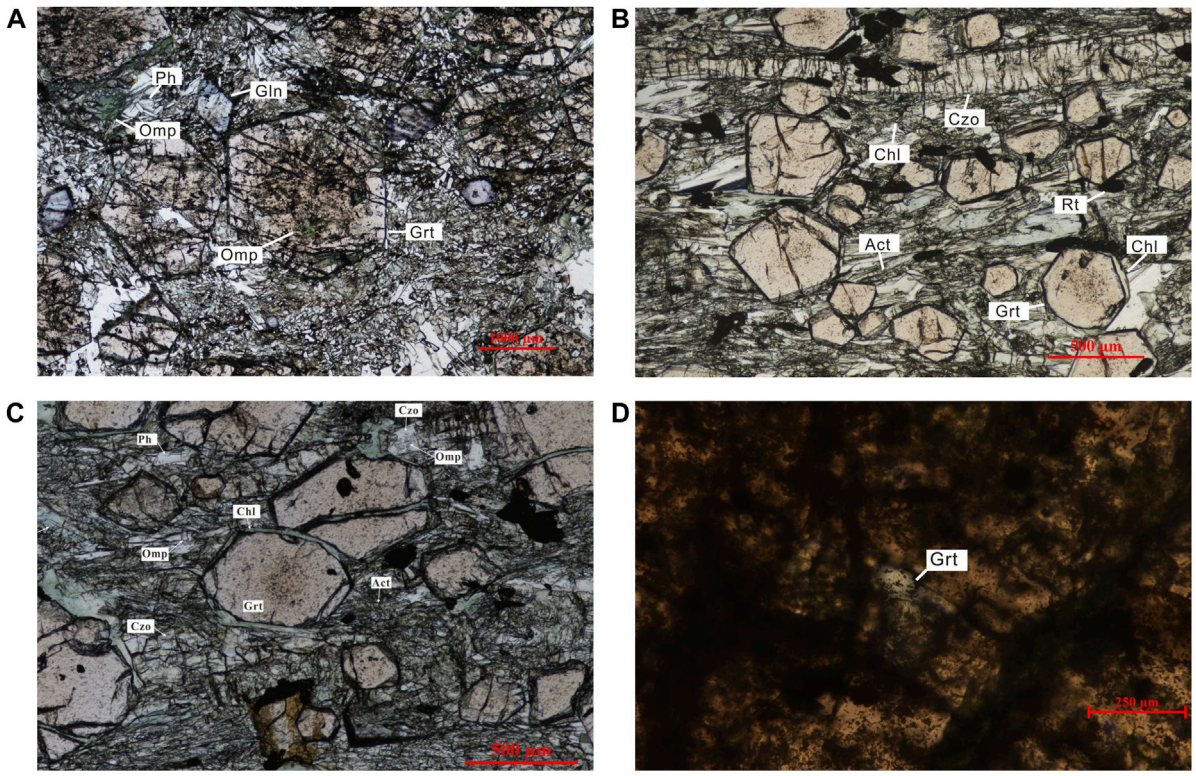

FIGURE 2
Photomicrograph images of eclogite. **(A)** Glaucophane eclogite with mineral assemblage of garnet + omphacite + glaucophane + phengite. **(B)** Actinolite-bearing eclogite with mineral assemblage of garnet + omphacite + actinolite + clinozoisite. **(C)** Chlorite surrounds garnet. **(D)** Radial cracks around quartz inclusion. Ph, phengite; Act, actinolite; Rt, rutile; Chl, chlorite; Czo, clinozoisite.

Subhedral glaucophane inclusions also show compositional zonation. The Na content from the core to the rim of the inclusion glaucophane increases, and the mineral composition is reflected in the change from winchite to riebeckite. This feature reflects the process of progressive metamorphism and temperature rise and shows that the host garnet experienced the process of progressive metamorphism during this period. Radial cracks around quartz inclusions may retrograde by coesite and indicate ultrahigh-pressure metamorphism (Figure 2C).

Actinolite-bearing eclogite features a porphyroblastic texture and a massive structure. Porphyroblasts include garnet (35%) and clinozoisite (5%). The metamorphosed matrix shows granular crystalloblastic texture, mainly including omphacite (40%), actinolite (10%), chlorite (5%), quartz (5%), and minor amounts of phengite and rutile (Figure 2B). Garnet from actinolite-bearing eclogite is mainly manifested in color zoning but is inclusion-poor. The actinolite-bearing eclogites may be retrograded by the glaucophane eclogites. The particle size of garnet from actinolite-bearing eclogite is less than that of garnet from glaucophane eclogite, while compositional and color zoning also developed. They are inclusion-poor and surrounded by chlorite. Chlorite surrounds garnet and is either circular or distributed along fractures of garnet grains (Figure 2D).

Analytical techniques

Mineral analyses were performed using a JEOL JXA-8230 electron probe microanalyzer with four wavelength-dispersive spectrometers (WDSs) at the Center for Global Tectonics, School of Earth Sciences, China University of Geosciences (Wuhan). First, the samples were observed under a light microscope. A 15 kV accelerating voltage, 20 nA probe current, and 1- or 5-micron beam diameter were used based on different minerals. The precision and accuracy of the analyses were better than 2%, and most elements were within ~1% of the relative error. The operating conditions were described in Wang J et al. (2019) and Ning et al. (2019) in detail.

Garnet was analyzed for REEs and trace elements in polished thin sections using laser ablation–inductively coupled plasma–mass spectrometry (LA-ICP-MS) using an Agilent 7900 ICP-MS system attached to a GeoLas HD laser ablation at Wuhan Sample Solution Analytical Technology Co., Ltd.,

Wuhan, China. The beam size was 44 μm with a 5 Hz repetition rate. The operating conditions followed those described in Liu et al. (2008) in detail.

Results

Major elements

The results of major element analysis of garnet in eclogite from the Bangbing area are listed in Table 1. Compositional zonation in the garnet from the glaucophane eclogites shows an increase in pyrope and grossular and a decrease in spessartine and almandine from the cores to rims, with the composition of the cores being $Alm_{65-70}Sps_{1.0-1.4}Grs_{20-23}Prp_{6-11}$ and that of the rims being $Alm_{53-62}Sps_{0.4-0.9}Grs_{22-28}Prp_{14-18}$ (Table 1; Figures 3A,B). The garnet has the highest almandine content and the lowest spessartine content. The composition of all garnets is in the field of C-type high-pressure and low-temperature eclogite, which is a typical marine eclogite.

Garnet from the actinolite-bearing eclogites also developed compositional zoning. Garnet has the following chemical composition: cores of $Alm_{66-68}Sps_{0.9-3.5}Grs_{21-22}Prp_{8-10}$ to the rims of $Alm_{44-50}Prp_{24-30}Grs_{24}Sps_{0.3-0.5}$ (Table 2; Figure 3C). The garnet in the actinolite-bearing eclogites and the garnet in the glaucophane eclogites have similar variation tendencies: from the cores to rims, an increase in pyrope and grossular and a decrease in spessartine and almandine. The compositions of garnet grains are within the type C field except for one data point, which is typical of oceanic eclogites. However, the almandine in the cores of garnets in the actinolite-bearing eclogites is lower than that in the glaucophane eclogites, while the pyrope is significantly higher.

Rare earth elements

The results of trace elements in the simple ΣREE concentrations vary from 21.65 to 900.68 ppm (Table 3). The enrichment by HREEs is relative to LREEs, as well as the generally high concentrations of REEs. Evident fractionation among REEs indicate LREE/HREE 0.007–0.13, δEu (Eu/Eu* =0.29–1.16), and δCe (Ce/Ce* =0.12–3.84). Rare earth element zonation in the garnets is stronger than major element zoning. REEs are predicted to have a maximum in the core followed by a continuous decrease toward the rim, especially HREEs. HREEs positively correlate with grossular contents. REE can be divided into three models from the core to rim (Figures 3D–F): 1) the core is characterized by steeply increasing normalized REE patterns from LREEs to HREEs. The HREE decreases toward the outer core MREE content, which remains constant in mode 1. 2) The second model is a moderately convex upward normalized REE pattern in which the HREE concentration decreases suddenly and the MREE concentration decreases slightly. 3) The REE pattern is characterized by a drastic increase in MREEs, whereas the increase in the HREE concentrations is limited. Types 1) and 2) grow in the glaucophane eclogite garnet samples, and types 1) and 3) grow in the actinolite-bearing eclogite garnet samples. Type 1) appears in the cores of the samples, and types 2) and 3) appear in the rims of the samples. The chondrite-normalized REE patterns are similar in the cores of the two kinds of garnet, while there are differences in the rims.

Discussion

Major element zonation

Major zonation patterns in the garnets are a promising way to interpret the change in pressure and temperature evolution during the metamorphic evolution of eclogite. The content of pyrope is positively correlated with temperature (Chen et al., 2005; Carswell et al., 2000). It can be observed that pyrope increased from the core to rim in all samples, which reflects the temperature rise process of glaucophane eclogites and actinolite-bearing eclogites during metamorphism. In most cases, grossular contents in prograde garnet reach a maximum in the rim, suggesting that the highest grossular content in the garnet may represent the highest pressure during subduction. It can be observed that grossular increased from the core to rim in all samples as well. This increase in grossular reflects the pressure rise (Carswell et al., 2000; Hermann and Green, 2001; Hermann, 2002). The pyrope content in the garnet rim of the actinolite-bearing eclogites is significantly higher than that of the glaucophane eclogites, which indicates that the formation temperature of actinolite-bearing eclogites is higher than that of glaucophane eclogites. Pyrope and grossular are all predicted to have a maximum temperature in the rim. This result indicates that the peak metamorphic temperature and pressure of garnet should have been achieved at the same time. The prograde zoning of the garnet reserve records the rapid exhumation of the eclogite.

Rare earth element zonation

Three types of normalized REE patterns correspond to different mineral chemical reactions in the formation of garnet. Garnet growth along the considered P-T path (Fu et al., 2021) is predicted to occur in three stages. According to petrographic observations and thermodynamic simulations (Konrad-Schmolke et al., 2008) carried out by predecessors, three mineral chemical reactions correspond to three types of normalized REE patterns. 1) Chl + Ep + Qz→ (almandine—rich) Grt + (sodic—calcic) Amp + H_2O. The almandine-rich garnet cores are formed mainly by the consumption of chlorite and grow

TABLE 1 Representative major element composition of minerals in glaucophane eclogites (wt%).

Mineral	Grt	Grt	Grt	Grt	Grt	Grt	Grt	Grt	Grt	Grt	Grt	Grt	Grt	Grt	Grt	Grt	Grt	Grt		Amp	Amp	Amp
Location	Grt-r	Grt-r	Grt-r	Grt-r	Grt-r	Grt-c	Grt-c	Grt-r	Grt-r	Grt-r	Grt-r	Grt-r	Grt-r	Grt-r	Grt-c	Grt-c	Grt-r	Grt-r		Win in Grt	Win in Grt	Gln in Grt
SiO_2	39.30	38.51	37.91	38.08	37.96	37.95	38.12	37.83	38.27	38.50	38.69	39.13	39.50	38.63	37.79	38.27	38.29	40.25		54.91	54.37	55.36
TiO_2	0.11	0.06	0.06	0.18	0.18	0.22	0.10	0.29	0.13	0.12	0.09	0.04	0.00	0.10	0.18	0.12	0.10	0.00		0.04	0.08	0.00
Al_2O_3	21.57	21.14	20.47	20.87	20.75	20.40	20.56	20.69	20.70	20.92	21.12	21.54	21.71	20.91	20.65	20.86	20.99	22.19		3.32	3.14	6.58
FeO	25.34	28.16	30.62	30.42	31.33	31.01	31.23	30.84	30.29	29.33	27.28	24.48	23.44	30.49	30.41	29.80	29.74	20.60		13.55	13.79	18.67
MnO	0.17	0.42	0.59	0.59	0.54	0.45	0.48	0.58	0.61	0.47	0.35	0.19	0.21	0.43	1.06	1.58	0.54	0.15		0.04	0.03	0.15
MgO	4.68	3.52	2.30	2.02	1.89	1.52	1.47	1.81	2.40	2.83	3.89	4.57	6.30	2.65	1.97	1.98	2.49	8.10		14.44	14.43	7.92
CaO	8.83	7.92	6.88	7.29	7.29	7.88	7.90	7.68	7.31	7.50	8.14	9.90	8.84	7.26	7.43	7.69	7.51	8.78		9.28	9.40	2.00
Na_2O	0.03	0.00	0.01	0.03	0.03	0.03	0.03	0.01	0.04	0.06	0.00	0.03	0.00	0.02	0.01	0.03	0.03	0.01		2.31	2.28	5.70
K_2O	0.02	0.00	0.00	0.01	0.00	0.00	0.00	0.00	0.00	0.00	0.00	0.00	0.00	0.00	0.00	0.00	0.00	0.00		0.09	0.09	0.02
Total	100.04	99.72	98.83	99.50	99.96	99.46	99.90	99.72	99.75	99.73	99.56	99.88	100.00	100.47	99.50	100.32	99.68	100.09		97.98	97.60	96.40
Alm	54.79	61.93	68.74	67.77	69.80	69.46	69.67	68.83	67.28	64.80	59.85	53.01	50.26	67.13	68.00	65.99	65.90	43.46	Na_B	0.59	0.56	1.69
Grs	24.46	22.30	19.80	20.82	20.80	22.60	22.57	21.96	20.80	21.22	22.87	27.47	24.27	20.46	21.30	21.82	21.33	23.74				
Prp	18.04	13.79	9.19	8.03	7.49	6.08	5.86	7.19	9.51	11.15	15.20	17.62	24.08	10.41	7.85	7.80	9.83	30.44				
Sps	0.37	0.94	1.33	1.33	1.21	1.03	1.09	1.31	1.37	1.06	0.78	0.42	0.45	0.95	2.39	3.54	1.21	0.33				

Note: Alm, almandine; Grs, grossular; Prp, pyrope; Sps, spessartine; Amp, amphibole; Win, winchite; Gln, glaucophane; c, core region of the mineral; r, rim region of the mineral.

10.3389/feart.2022.930880

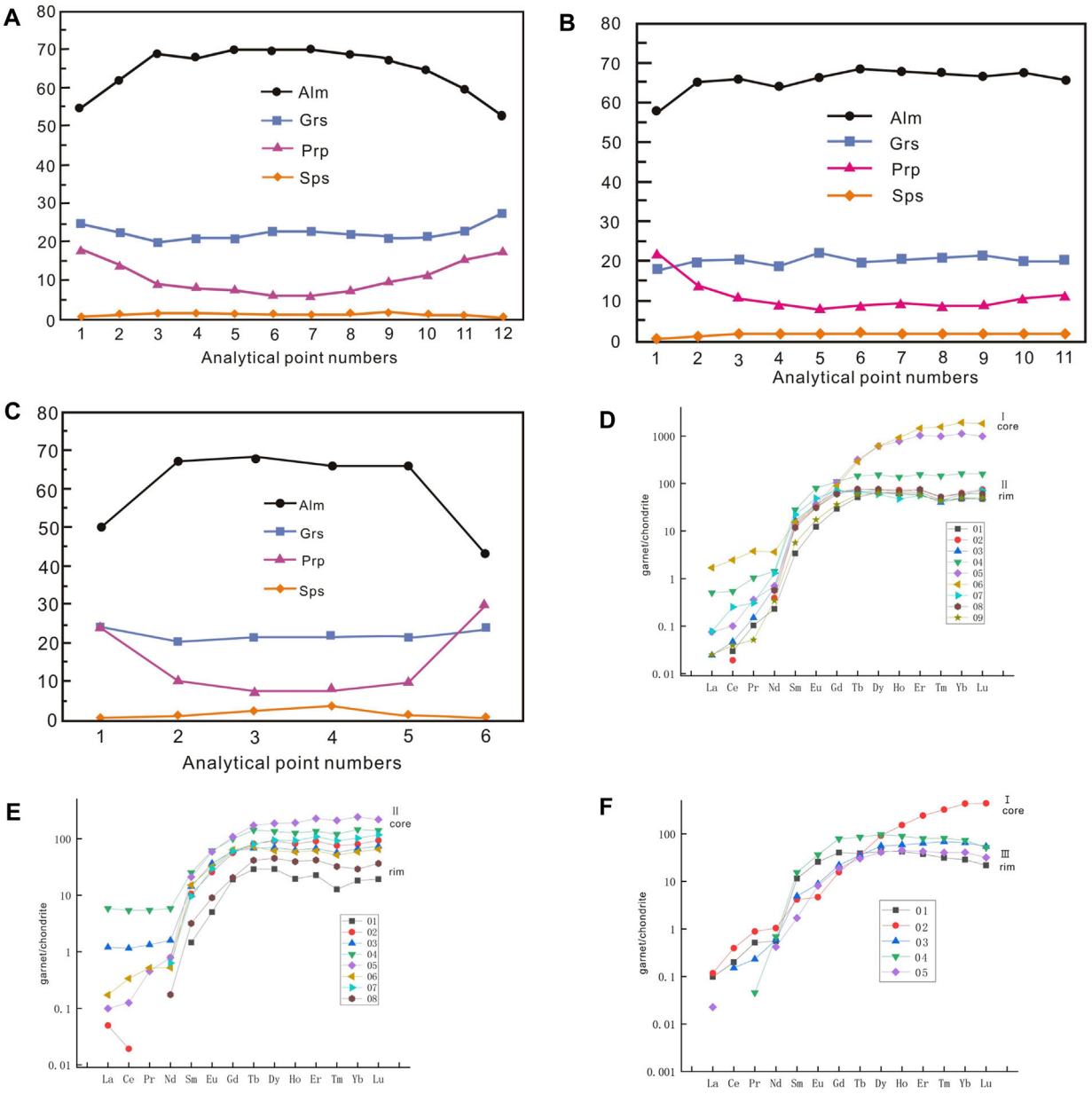

FIGURE 3
Compositional profile zonation of the garnet and chondrite-normalized REE patterns of garnet. **(A,B)** Major element compositional of garnet in glaucophane eclogite; **(C)** major element compositional of garnet in actinolite-bearing eclogite; **(D,E)** chondrite-normalized REE patterns of garnet in glaucophane eclogite; and **(F)** chondrite-normalized REE patterns of garnet in actinolite-bearing eclogite (Sun and Mcdough, 1989).

during the early stage of prograde metamorphism. After chlorite is completely consumed, the growth of garnet in the first stage is interrupted, and the garnet formed in the second stage begins to grow. In the second stage, epidote became the main garnet-forming mineral. Epidote is an important mineral for the occurrence of REEs. Epidote is an important hydrous mineral that can remain stable during peak ultrahigh-pressure (UHP) metamorphism. The dissolution of hydrous minerals is closely related to the activity of metamorphic fluid or metamorphic anatexis. The continuous decrease in the REE content from the core to the rim indicates that garnet is decreasing in the REE reservoir. This process is known as the reservoir effect. 2) (sodic—calcic) Amp + Ep→ Grt (2) (with increasing grs content) + Czo (1) + Ky + Qz + H_2O. 3) The rim of sample 3 (actinolite-bearing eclogites) is the third normalized REE pattern. Garnet is formed mainly by the consumption of

TABLE 2 Representative major element composition of minerals in actinolite eclogites (wt%).

Mineral	Grt	Grt	Grt	Grt	Grt	Grt	Grt	Grt	Grt	Grt	Grt
Location	Grt-r	Grt-r	Grt-r	Grt-r	Grt-c	Grt-c	Grt-c	Grt-r	Grt-r	Grt-r	Grt-r
SiO_2	39.61	38.59	38.49	35.64	38.31	38.36	38.29	38.27	38.34	37.82	38.35
TiO_2	0.02	0.06	0.14	6.02	0.16	0.13	0.11	0.16	0.13	0.09	0.06
Al_2O_3	22.03	21.01	20.73	19.76	20.63	21.05	20.92	20.87	20.74	20.86	20.98
FeO	27.09	29.58	29.74	28.68	29.72	31.02	30.66	30.53	30.11	30.15	29.69
MnO	0.19	0.42	0.61	0.61	0.78	0.80	0.87	0.80	0.79	0.59	0.56
MgO	5.77	3.53	2.76	2.28	2.03	2.26	2.38	2.22	2.17	2.69	2.91
CaO	6.59	6.99	7.20	6.62	7.75	6.99	7.23	7.33	7.58	6.98	7.17
Na_2O	0.01	0.02	0.01	0.02	0.02	0.03	0.03	0.02	0.05	0.03	0.00
K_2O	0.00	0.00	0.01	0.00	0.00	0.00	0.00	0.00	0.00	0.01	0.00
Total	101.32	100.19	99.69	99.62	99.39	100.63	100.49	100.19	99.91	99.21	99.70
Alm	57.84	65.00	65.85	63.85	66.19	68.44	67.74	67.60	66.80	67.29	65.69
Grs	18.01	19.68	20.41	18.87	22.11	19.75	20.47	20.80	21.53	19.95	20.32
Prp	21.96	13.82	10.91	9.03	8.07	8.90	9.36	8.78	8.60	10.70	11.46
Sps	0.42	0.93	1.37	1.37	1.76	1.78	1.95	1.79	1.77	1.33	1.24

amphibole in the third stage. Amp + Czo (1)→ Grt (3) + Czo (2) + Qz + H_2O. Type 3 appears only in garnet in actinolite-bearing eclogites. The occurrence of type 3 garnet may be related to the formation of actinolite.

According to the changes in major elements and rare earth elements from the core to the rim of the garnets, there are two growth modes of garnet. One is the continuous growth mode. During metamorphism, the main and trace elements change uniformly with changes in temperature and pressure, indicating that the geological environment changes slowly. The other is the episodic growth mode. After a metamorphic event, the geological environment of garnet suddenly changed rapidly, resulting in a sudden change in composition (Chen et al., 2003). According to the composition change characteristics from the core to the rim of the sample, sample 1 and sample 3 reflect episodic growth, that is, the core and rim have significant concentration differentiation and different types of rare earth element-normalized patterns. The main elements in sample 2 change uniformly and slowly, and there is only one rare earth distribution mode, which reflects continuous growth.

It can be seen that the growth from the core to the rim of the garnet in the glaucophane eclogites is a process of increasing temperature and pressure, and the growth ends before the peak of metamorphism. The rim of garnet in actinolite-bearing eclogites continues to grow under increasing pressure. It can be divided into three stages of garnet growth. The three growth stages of garnet can correspond to three metamorphic evolution stages. Each metamorphic stage is described as follows: the prograde stage of metamorphism (M1), the peak stage of metamorphism (M2), and the post-peak stage of metamorphism. Pressures of 20.0–23.1 Kbar (average 21.5 Kbr) and temperatures of 407–480°C (average 452°C) were obtained for eclogites at the prograde stage of metamorphism. The P-T conditions of the peak metamorphism of the eclogites were 30.0–32.7 Kbar (average 30.6 Kbr) and 617°C–658°C (average 630°C) (Fu et al., 2021).

The zoning of large ion lithophile elements, transition metal elements, and high field strength elements is non-obvious. The ion radii of different trace elements are distinct. The diffusion rate in garnet is also different, and the degree of homogenization is distinct at high temperatures.

Behavior of trace elements in garnet

At most points, a strong positive correlation exists between the contents of Ti and Ca (Figure 4A); the content of Ca increased from the core to the rim, and the content of Ti increased accordingly. Some samples have the highest Ca content at the rim, but the Ti content decreases greatly at this time. Ti in garnets is controlled by pressure and positively correlated with pressure. Combined with the analysis of petrographic characteristics and other element distributions, the content of Ti decreases when the edge reaches the peak pressure, which may be caused by the enrichment of Ti and the formation of rutile at this stage. The contents of Sr and Y elements are closely related to CaO (Figures 4B,C). Previous studies believe that the Y content in garnet is determined by CaO (Li TF et al., 2012), which is not affected by temperature and pressure. Because the ionic radius of Sr is similar to that of Ca, the lattice occupation is restricted by it (Harte and Kirkley, 1997). The CaO-Y and CaO-Sr projection maps of garnet from the Bangbing eclogite show that there is an obvious law of

TABLE 3 Representative rare earth element composition of garnets (ppm).

Mineral	Grt	Grt	Grt	Grt	Grt	Grt	Grt	Grt	Grt	Grt	Grt	Grt	Grt	Grt	Grt	Grt	Grt	Grt	Grt	Grt	Grt	Grt
Location	Grt-r	Grt-r	Grt-r	Grt-r	Grt-c	Grt-r	Grt-r	Grt-r	Grt-r	Grt-r	Grt-r	Grt-r	Grt-r	Grt-r	Grt-c	Grt-c	Grt-r	Grt-r	Grt-r	Grt-c	Grt-r	Grt-r
La	—	—	0.01	0.12	0.02	0.40	0.02	—	0.01	—	0.01	0.29	1.38	0.02	0.04	—	—	0.02	0.03	—	—	0.01
Ce	0.02	0.01	0.03	0.33	0.06	1.50	0.15	—	0.02	—	0.01	0.71	3.30	0.08	0.21	—	—	0.12	0.24	0.09	—	—
Pr	0.01	-	0.01	0.10	0.03	0.36	0.03	—	—	—	-	0.13	0.52	0.04	0.05	—	—	0.05	0.08	0.02	—	—
Nd	0.11	0.18	0.31	0.67	0.33	1.70	0.61	0.27	0.16	—	0.37	0.75	2.73	0.37	0.24	0.30	0.08	0.26	0.49	0.28	0.32	0.20
Sm	0.52	2.03	2.55	4.30	2.09	2.37	3.39	1.81	0.87	0.22	1.61	2.19	3.84	3.22	2.32	1.47	0.49	1.76	0.63	0.75	2.37	0.26
Eu	0.71	1.84	2.09	4.63	2.12	1.88	2.84	1.80	1.00	0.29	1.49	2.12	3.55	3.41	1.87	1.70	0.52	1.51	0.27	0.51	2.11	0.47
Gd	6.05	13.62	14.02	22.50	21.50	18.48	14.67	12.34	7.40	3.92	11.47	12.50	20.55	22.29	13.04	12.41	4.22	8.32	3.23	4.50	16.19	3.90
Tb	1.92	2.88	2.52	5.43	11.94	10.83	2.55	2.81	2.18	1.08	3.04	2.54	5.30	6.46	2.70	3.01	1.55	1.44	1.35	1.33	3.20	1.14
Dy	16.79	18.63	17.05	38.75	155.84	156.64	15.09	19.28	16.18	7.39	23.21	17.67	34.28	47.38	15.56	23.98	11.45	10.82	23.33	14.12	24.60	10.53
Ho	3.62	4.14	3.45	7.71	44.02	52.42	2.70	3.83	3.37	1.11	4.61	3.55	7.14	10.82	3.29	5.25	2.23	2.42	8.66	3.31	5.07	2.52
Er	10.89	12.04	9.94	25.61	170.23	241.17	9.25	12.44	9.48	3.73	15.01	11.20	22.43	37.66	10.13	17.95	6.94	6.21	40.13	10.48	13.24	7.06
Tm	1.15	1.33	1.02	3.70	25.17	39.72	1.13	1.34	1.10	0.32	1.93	1.44	3.07	5.36	1.31	2.34	0.83	0.80	8.27	1.74	2.08	1.03
Yb	8.12	10.74	8.34	27.60	191.36	326.56	9.86	10.33	8.45	3.09	13.56	11.37	24.67	41.28	9.96	17.35	4.95	4.89	73.53	11.06	12.47	6.90
Lu	1.21	1.90	1.27	4.06	25.14	46.64	1.81	1.54	1.27	0.49	2.38	1.87	3.55	5.55	1.65	2.97	0.93	0.55	11.16	1.38	1.31	0.81
LREE	1.36	4.06	5.00	10.15	4.66	8.22	7.04	3.88	2.07	0.52	3.49	6.17	15.32	7.15	4.73	3.47	1.09	3.72	1.74	1.66	4.82	0.93
HREE	49.74	65.28	57.62	135.36	645.19	892.47	57.05	63.92	49.43	21.13	75.21	62.15	120.98	176.80	57.63	85.26	33.10	35.46	169.67	47.93	78.14	33.89
∑REE	51.11	69.34	62.62	145.50	649.85	900.68	64.10	67.80	51.50	21.65	78.70	68.32	136.31	183.95	62.36	88.73	34.19	39.18	171.41	49.58	82.96	34.82

10.3389/feart.2022.930880

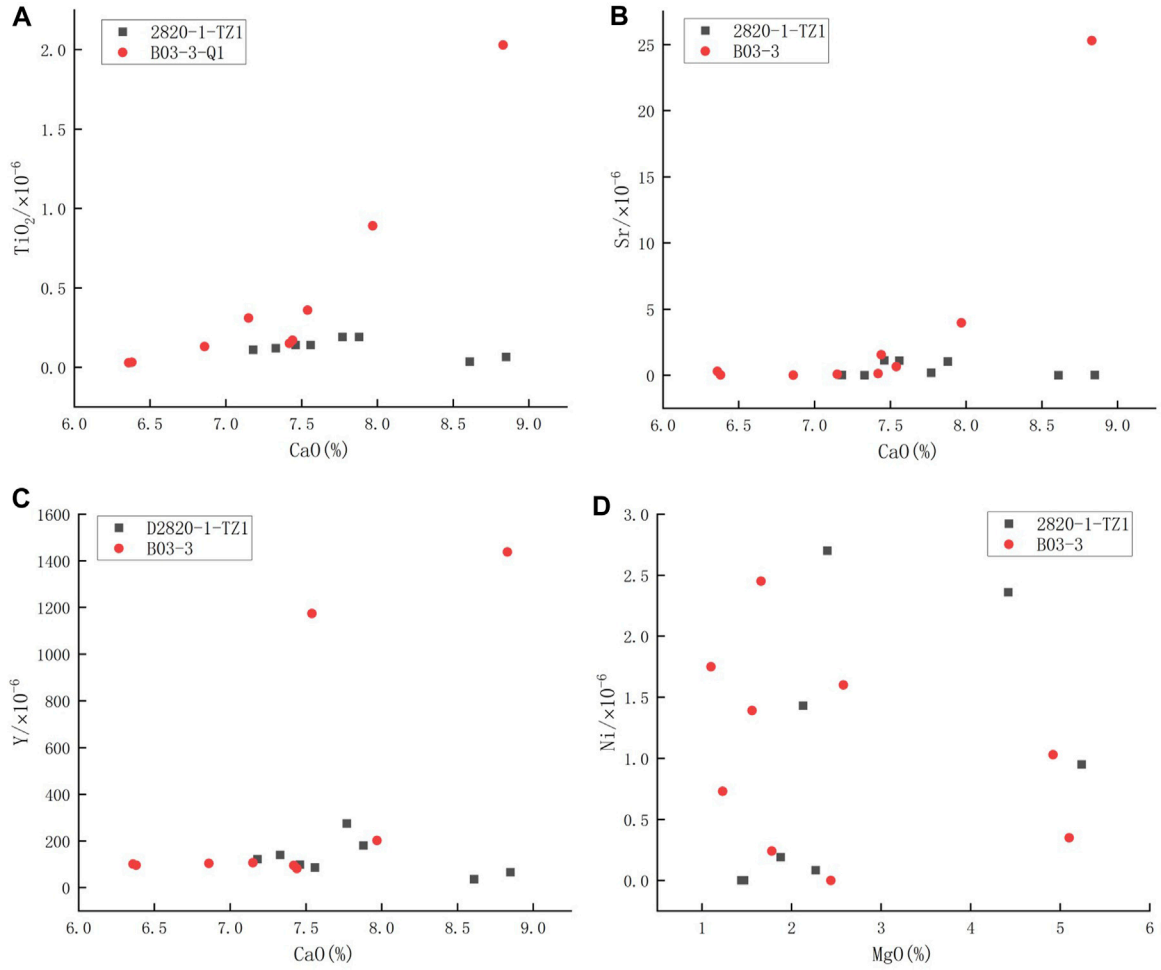

FIGURE 4
Variations between CaO and MgO and some trace elements of garnet. **(A)** variation of CaO-Ti; **(B)** variation of CaO-Sr; **(C)** variation of CaO-Y; and **(D)** variation of MgO-Ni.

positive correlation between the contents. The samples with the highest Ca content at the rim and a decrease in Ti content are affected when Ti decreases. Therefore, the content of these two elements is not only controlled by CaO content but also affected by other factors, such as the formation of new minerals, which may migrate and enrich Y, Sr, and Ti from garnet to rutile together. The Si content in the composition of rutile inclusions can reflect the pressure at the time of formation. This feature is reflected from the garnet core to the mantle in the eclogite in the Bangbing area. The rim with the highest Mg content decreases, which is similar to the Ca–Ti relationship. The Si content in the composition of rutile inclusions can reflect the pressure at the time of formation. It is generally considered that more than 500 ppm is a sign of ultrahigh pressure (Zhu et al., 2017). The Si content of rutile inclusions in the sample is 291–1,480 ppm, so the eclogite in the sample may have experienced high pressure–ultrahigh pressure. It is generally believed that Ni and Mg have similar ionic radii. In garnet, the Ni content is controlled by the MgO content and affected by temperature (O' Reilly and Griffin, 1995), which is positively correlated with temperature. This feature is reflected from the garnet core to the mantle in the eclogite in the Bangbing area. The rim with the highest Mg content decreases, which is similar to the Ca–Ti relationship (Figure 4D). The content of Zr gradually decreases from the core to the rim of garnet. Zr is mainly controlled by temperature and is positively correlated with the formation temperature of garnet (O' Reilly S. M. and Griffin W. L. 1995), which is contrary to the heating process reflected by the main elements. The possible reason is similar to that for the change in Ti content, which is the formation of rutile, and the content of Zr in rutile is high.

Conclusion

1) The garnet from the Bangbing area is generally euhedral, with color, inclusion, and composition zoning. Major element growth zonation exhibits pyrope and grossular increasing from the core to rim, showing the prograde growth of the garnet. Three types of normalized REE patterns in garnet correspond to different mineral chemical reactions in the formation of garnet and three stages of growth.
2) The contents of pyrope and grossular reached their highest values at the same time, indicating that the eclogite in the Bangbing area peaks in temperature and pressure at the same time after subduction. The garnet is surrounded by chlorite, suggesting a depressurization process after peak metamorphism. The zonation of garnet is well preserved, suggesting a relatively short peak metamorphic time and relatively rapid exhumation process.
3) The controlling factors of the chemical behavior of trace elements in garnet are the result of many aspects. Trace elements are not only controlled by the main elements but also affected by temperature, pressure, fluid, mineral combination, and other factors.

Data availability statement

The raw data supporting the conclusion of this article will be made available by the authors, without undue reservation.

Author contributions

NL: conceptualization, formal analysis, investigation, writing—original draft, and writing—review and editing. GW: formal analysis, resources, writing—review and editing, supervision, and funding acquisition. ZP: conceptualization, resources, and funding acquisition. YF: conceptualization, formal analysis, and investigation.

Funding

This study was supported by the National Natural Science Foundation of China (92055314) and the China Geological Survey (DD 20221635).

Acknowledgments

The authors thank the Center for Global Tectonics, School of Earth Sciences, China University of Geosciences (Wuhan) for their contribution to the EMPA work and Wuhan Sample Solution Analytical Technology Co., Ltd., Wuhan, China, for their contribution to the LA-ICP-MS work.

Conflict of interest

The authors declare that the research was conducted in the absence of any commercial or financial relationships that could be construed as a potential conflict of interest.

Publisher's note

References

Baxter, E. F., Caddick, M. J., and Dragovic, B. (2013). Garnet: A rock-forming mineral petrochronometer. *Rev. Mineral. Geochem.* 83, 469–533. doi:10.2138/rmg.2017.83.15

Bebout, G. E. (2007). Metamorphic chemical geodynamics of subduction zones. *Earth Planet. Sci. Lett.* 260, 373–393. doi:10.1016/j.epsl.2007.05.050

Carswell, D. A. (1990). "Eclogites and the eclogite facies rocks:Definitions and classification," in *Eclogite facies rocks*. Editor D. A. Carswell (Glasgow, London: Blackie & Son), 1 13.

Carswell, D. A., Wilson, R. N., and Zhai, M. (2000). Metamorphic evolution, mineral chemistry and thermobarometry of schists and orthogneisses hosting ultra-high pressure eclogites in the Dabieshan of central China. *LITHOS* 52 (1), 121–155. doi:10.1016/S0024-4937(99)00088-2

Chen, D. L., Sun, Y., Liu, L., Zhang, A. D., Luo, J. H., and Wang, Y. (2005). Metamorphic evolution of the yuka eclogite in the north qaidam, NW China: evidences from the compositional zonation of the garnet and reaction texture in the rock. *Acta Petrol. Sin.* 21 (4), 1039–1048. (in Chinese with English abstract). doi:10.3321/j.issn:1000-0569.2005.04.002

Chen, N. S., Sun, M., Yang, Y., Liu, R., and Wang, Q. Y. (2003). Major- and trace-element zoning in metamorphic gatnets and their THEIR metamorphic process implications. *Earth Sci. Front.* 10 (03), 315–320. (in Chinese with English abstract). doi:10.1016/S0955-2219(02)00073-0

Coleman, R., Lee, D., Beatty, L. B., and Brannock, W. W. (1965). Eclogites and eclogites: their differences and similarities. *Geol. Soc. Am. Bull.* 76 (5), 483–508. doi:10.1130/0016-7606(1965)76[483:EAETDA]2.0.CO

Condie, K. C., and Kröner, A. (2008). When did plate tectonics begin? Evidence from the geologic record, in *Geol. Soc. Am.* Editor K. C. Condie and V. Pease 440, 281–294.

Dong, Y. S., Li, C., Shi, J. R., Zhang, X. Z., and Wang, S. Y. (2010). Forming process of the high pressure metamorphic belt in central Qiangtang Tibet. *Acta Petrol. Sin.* 26 (7), 2099–2105. (in Chinese with English abstract).

Fu, Y. Z., Peng, Z. M., Wang, B. D., Wang, G. Z., Hu, J. F., Guan, J. L., et al. (2021). Petrology and metamorphism of glaucophane eclogites in changning-menglian suture zone, bangbing area, southeast Tibetan plateau: A evidence for paleo-tethyan subduction. *China Geol.* 4 (01), 111–116. doi:10.31035/cg2021017

Hacker, B., and Gerya, T. V. (2013). Paradigms, new and old, for ultrahigh-pressure tectonism. *Tectonophysics* 603, 79–88. doi:10.1016/j.tecto.2013.05.026

Harte, B., and Kirkley, M. B. (1997). Partitioning of trace elements between clinopyroxene and garnet:data from mantle eclogites. *Chem. Geol.* 136, 1–24. doi:10.1016/S0009-2541(96)00127-1

Hermann, J., and Green, D. H. (2001). Experimentalconstraints on high pressure meltingin subducted crust. *Earth Planet. Sci. Lett.* 188, 149–168. doi:10.1016/s0012-821x(01)00321-1

Hermann, J. (2002). Allanite:Thorium andlight rare Earth element carrier insubducted crust. *Chem. Geol.* 192, 289–306. doi:10.1016/s0009-2541(02)00222-x

Kohn, M. J. (2003). Geochemical zoning in metamorphic minerals. *Treatise Geochem.* 3, 229–261. doi:10.1016/B0-08-043751-6/03176-5

Konrad-Schmolke, M., Zack T, P. J., O'Brien, P. J., and Jacob, D. E. (2008). Combined thermodynamic and rare Earth element modelling of garnet growth during subduction: Examples from ultrahigh-pressure eclogite of the Western Gneiss Region, Norway. *Earth Planet. Sci. Lett.* 272, 488–498. doi:10.1016/j.epsl.2008.05.018

Li, J., Sun, Z. B., Huang, L., Xu, G. X., Tian, S. M., Deng, R. H., et al. (2017). P-T-t path and geological significance ofretrograded eclogites from Mengku area in Western Yunnnan Province, China. *Acta Petrol. Sin.* 33 (7), 2285–2301. (in Chinese with English abstract).

Li, J., Sun, Z. B., Xu, G. X., Zhou, K., Zeng, W. T., Huang, L., et al. (2015). Firstly discovered garnet-amphibolite from Mengku area, shuangjiang county, western yunnan province, China. *Acta Mineral. Sin.* 35 (04), 421–424. (in Chinese with English abstract). doi:10.16461/j.cnki.1000-4734.2015.04.001

Liu, Y. S., Hu, Z. C., Gao, S., Günther, D., Xu, J., Gao, C. G., et al. (2008). *In situ* analysis of major and trace elements of anhydrous minerals by LA-ICP-MS without applying an internalstandard. *Chem. Geol.* 257, 34–43. doi:10.1016/j.chemgeo.2008.08.004

Ning, W. B., Fu, D., Wang, J. P., Xiao, D., Li, F. F., and Huang, B. (2019). Electron probe microanalysis of monazite and its applications to U-th-Pb dating of geological samples. *J. Earth Sci.* 30 (5), 952–963. doi:10.1007/s12583-019-1020-8

O' Reilly, S. M., and Griffin, W. L. (1995). Trace-element partitioning between garnet and clinopyroxene in mantle-derived pyroxenites and eclogites: P-T-X controls. *Chem. Geol.* 121, 105. doi:10.1016/0009-2541(94)00147-Z

Peng, Z. M., Hu, J. F., Fu, Y. Z., Zhang, J., Guan, J. L., Han, W. W., et al. (2018a). Geological map of wendong sheet (F47e005016)(1:50000), the people's republic of China. In Press.

Peng, Z. M., Wang, G. Z., Wang, B. D., Wang, L. Q., Fu, Y. Z., Guan, J. L., et al. (2019). Discovery of glaucophane eclogites within the Lancang group in bangbing area, Western yunnan. *J. Chengdu Univ. Technol. Sci. Technol. Ed.* 46 (5), 639–640. (in Chinese with English abstract).

Spear, F. S., Selverstone, J., Hickmott, D., Crowley, P., and Hodges, K. V. (1984). P-T paths from garnet zoning: A new technique for deciphering tectonic processes in crystalline terranes. *Geology* 12 (2), 87–90. doi:10.1130/0091-7613(1984)12<87:PPFGZA>2.0.CO;2

Sun, S. S., and McDonough, W. F. (1989). "Chemical and isotopic systematic of oceanic basalt: Implications for mantle composition and processes," in *Magmatism in the ocean basins.* Editors A. D. Sanders and M. J. Norry (London, United Kingdom: Geol Soc Spec Publ), 42, 313–345.

Sun, Z. B., Hu, S. B., Zhou, K., Zhou, T. Q., Zhao, J. T., Wang, Y. X., et al. (2019). Petrology, mineralogy and metamorphic p-T path of eclogites from the Qianmai area, Lancang County, western Yunnan Province. *Geol. Bull. China* 38 (7), 1105–1115.

Taguchi, Tomoki, Enami, Masaki, and Kouketsu, Yui (2019). Metamorphic record of the Asemi-gawa eclogite unit in the Sanbagawa belt, Southwest Japan: Constraints from Inclusions study in garnet porphyroblasts. *J. Metamorph. Geol.* 37 (2), 181–201. doi:10.1111/jmg.12456

Wang, B. D., Wang, L. Q., Wang, D. B., Yin, F. G., He, J., Peng, Z. M., et al. (2018). Tectonic evolution of the changning-menglian proto-paleo Tethys Ocean in the sanjiang area, south Western China. *Earth Sci.* 43 (8), 2527–2550. doi:10.3799/dqkx.2018.160

Xia, Q. X. (2019). Different origins of garnet in high pressure to ultralpressure metamorphic rocks. *Earth Sci.* 44 (12), 4042–4049. (in Chinese with English abstract).

Xia, Q. X., and Zheng, Y. F. (2011). The composition and chemical zoning in garnet from high to ultrapressure metamorphic rocks. *Acta Petrol. Sin.* 27 (2), 433–450. (in Chinese with English abstract).

Xia, Q. X., Zhou, L. G., and Zheng, Y. F. (2013). Zonation and multiphase growth of garnet in UHP metamorphic rocks of continental subduciton zone. *Chin. Sci. Bull.* 58, 2138–2144. (in Chinese with English abstract). doi:10.1360/972013-599

Zhai, Q. G. (2008). "Petrology, Geochemistry and tectonic evolution of the eclogite from central Qiangtang area,North Tibet," (China, Beijing: Chinese Academy of Geological Sciences). dissertation's thesis.

Zhai, Q. G. (2013). Triassic metamorphic belt in central Qiangtang area, North Tibet. *Acta Geol. Sin.* 87 (S1), 19.

Zhang, X. Z., Dong, Y. S., Wang, Q., and Dan, W. (2018). High pressure metamorphic belt in central Qiangtang, Tibetan Plateau: Progressand unsolved problems. *Geol. Bull. China* 37 (8), 1406–1416. (in Chinese with English abstract).

Zhou, L. G., Xia, Q. X., Zheng, Y. F., and Chen, R. X. (2011). Multistage growth of garnet in ultrahigh-pressure eclogite during continental collision in the dabie orogen: constrained by trace elements and U-Pb ages. *Lithos* 127, 101–127. doi:10.1016/j.lithos.2011.08.010

Zhu, K., Liang, J. L., ShenJand Sun, W. D. (2017). Geochemical significance of silicon-bearing rutile in eclogites from Dabie - sulu ultra-high pressure metamorphic terrane. *Earth Sci. Front.* 24 (3), 288–300. doi:10.13745/j.esf.yx.2016-12-39

frontiers | Frontiers in Earth Science

TYPE Original Research
PUBLISHED 02 September 2022
DOI 10.3389/feart.2022.982354

OPEN ACCESS

EDITED BY
Shengyao Yu,
Ocean University of China, China

REVIEWED BY
Licheng Wang,
Institute of Tibetan Plateau Research (CAS), China
Yushuai Wei,
China University of Geosciences, China

*CORRESPONDENCE
Bo Ran,
ranbo08@cdut.cn

SPECIALTY SECTION
This article was submitted to Petrology, a section of the journal Frontiers in Earth Science

RECEIVED 30 June 2022
ACCEPTED 25 July 2022
PUBLISHED 02 September 2022

CITATION
Lv F, Ran B, Liu S, Wang Z, Sun T, Li X, Han Y and Liang K (2022), Provenance of the lower jurassic quartz-rich conglomerate in northwestern sichuan basin and its link with the pre-collisional unroofing history of the north longmen shan thrust belt, NE tibetan plateau margin.
Front. Earth Sci. 10:982354.
doi: 10.3389/feart.2022.982354

Provenance of the lower jurassic quartz-rich conglomerate in northwestern sichuan basin and its link with the pre-collisional unroofing history of the north longmen shan thrust belt, NE tibetan plateau margin

Fan Lv[1], Bo Ran[1]*, Shugen Liu[1,2], Zijian Wang[1], Tong Sun[1], Xianghui Li[3], Yuyue Han[1] and Ke Liang[1]

[1]State Key Laboratory of Oil and Gas Reservoir Geology and Exploitation, Chengdu University of Technology, Chengdu, China, [2]Xihua University, Chengdu, China, [3]Key Laboratory for Mineral Deposits Research, School of Earth Sciences and Engineering, Nanjing University, Nanjing, China

The research on the pre-collisional tectonic evolution of basin-mountain system at the margin of Tibetan plateau provides insights into the upward and outward growth mechanism of the plateau in the Cenozoic. Lower Jurassic Baitianba Formation quartz-rich conglomerate exposed along the edge of the northwest Sichuan Basin whereas these deposits were incompatible with peripheral carbonatite-dominated orogenic belts, which aroused our great interest. To better understand the origin of quartz-rich conglomerate and early erosional unroofing history of northeastern Tibetan Plateau margin, this study focuses on sandstone petrography analysis along with U-Pb age dating of the detrital zircons of Baitianba Formation gravel and sandstone sample from northwestern Sichuan Basin, which is located to north Longmen Shan thrust belt. In the distinctive Lower Jurassic quartz gravel samples, there are at least two distinct provenance sources. One is characterized by a unimodal age population at ca. 400–1,000 Ma but the absence of younger detrital zircons (<395 Ma), resembling the Early Paleozoic marine quartz sandstone due to the uplift and erosion of the Paleozoic basement of the Longmen Shan thrust belt. The other yield age clusters of ca. 1.8 Ga, 950–750 Ma, 450–420 Ma, 280–240 Ma, which is identical to the detrital zircons from the Upper Triassic strata. Furtherly, detrital zircon dating of our sandstone samples also exhibit strong similarity to the Upper Triassic strata detrital record. Detrital zircons linked with the sedimentological data show these quartz-rich conglomerate mainly recycled from the underlying Upper Triassic through long-term weathering.

KEYWORDS

early jurassic, quartz-rich conglomerate, detrital zircon, Longmen Shan thrust belt, tectonic evolution

1 Introduction

The early uplift of the boundary faults and orogenic belts of the Tibetan Plateau did not typically form during the Cenozoic. In reality, the strong collisions of terranes afforded the early uplift of the boundaries of the Tibetan Plateau starting mostly during the Mesozoic. This is attributed to the Qiangtang and Lhasa terranes constituting the middle part of the Tibetan Plateau collapsed sequentially to the southern margin of paleo-Asia during the Mesozoic (Ritts and Biffi, 2000; Tian et al., 2013; Zhu et al., 2013; Qi et al., 2016; Cheng et al., 2019).

Notably, the tectonic evolution of the Sichuan Basin, China's largest natural gas producer located on the eastern margin of the Tibetan Plateau, was mainly controlled by the tectonic evolution of

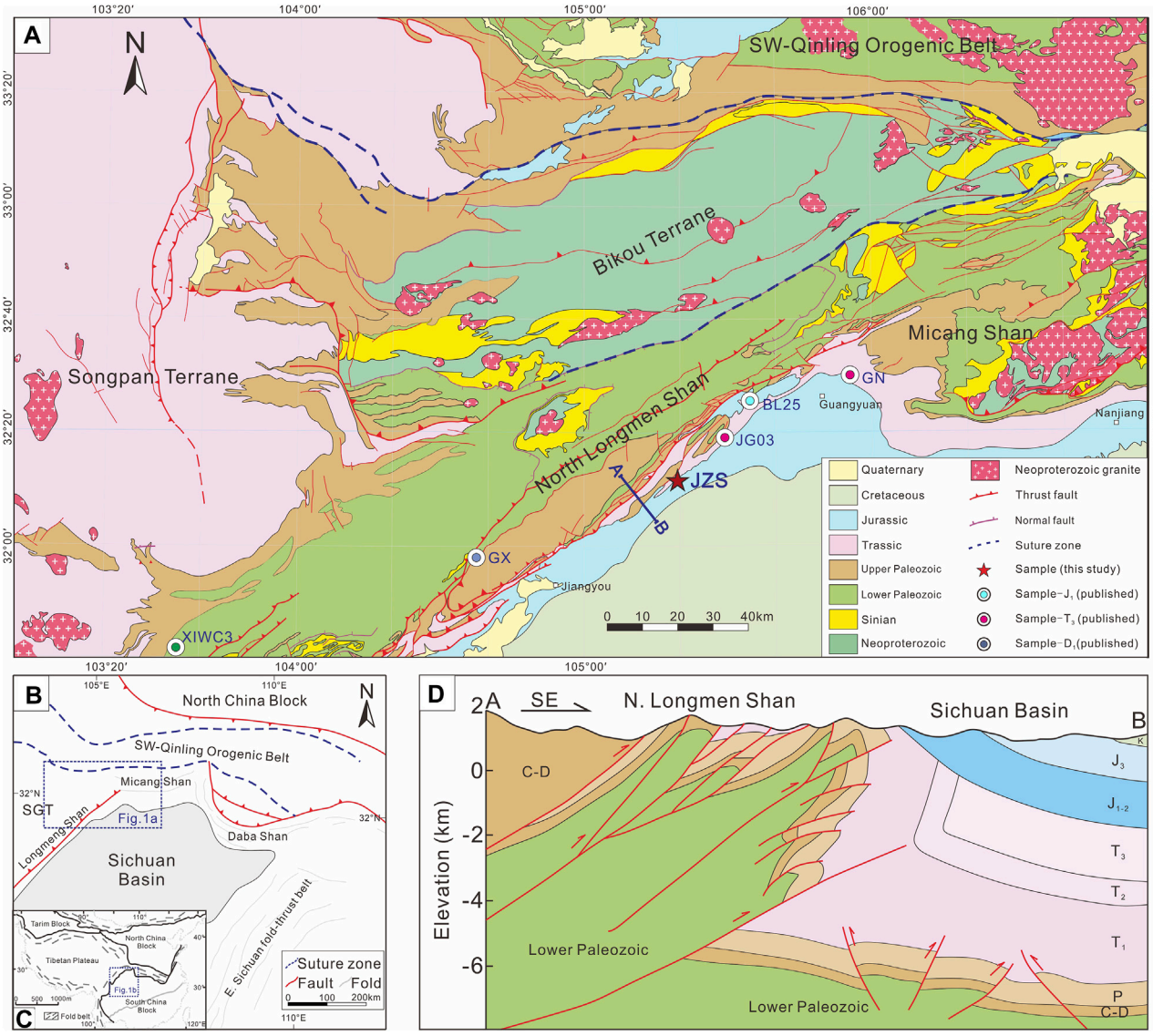

FIGURE 1
(A) Geological map of the northwestern Sichuan Basin and north Longmen Shan orogenic belt (adapted from Yan et al., 2018). The red star indicates the Jinzishan outcrop (JZS) analysed herein. **(B)** Tectonic setting of Sichuan basin and adjoining regions (adapted from Ma et al., 2019). **(C)** Simplified tectonic framework map (adapted from Yan et al., 2018). **(D)** Cross shows tectonic features and stratigraphic distribution in the study area, modified from Wang et al., 2014.

10.3389/feart.2022.982354

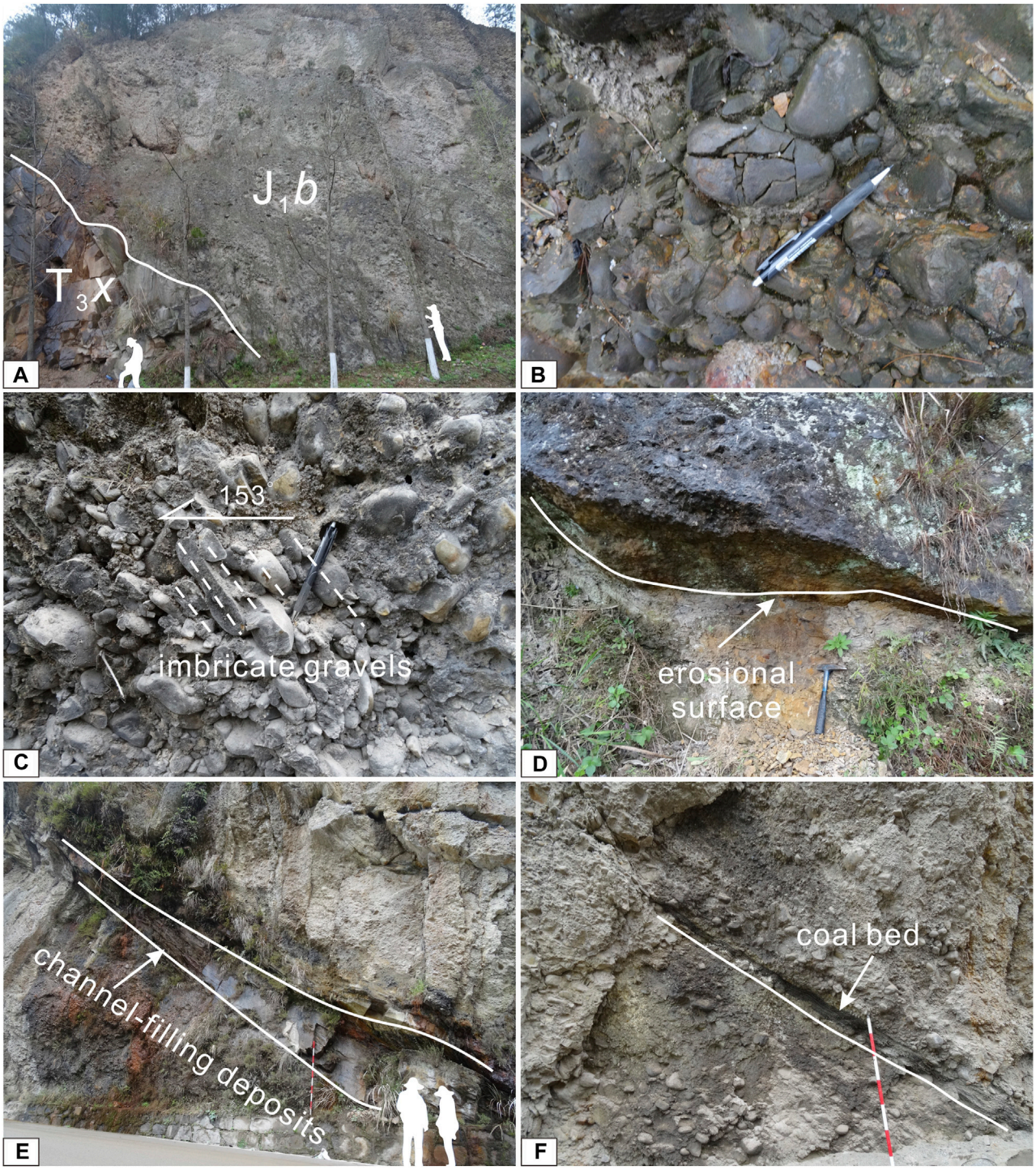

FIGURE 2
Photographs of the Lower Jurassic strata in the Jinzishan outcrop, northwestern Sichuan Basin. **(A)** The unconformity between Upper Triassic Xujiahe Fm and the overlying Baitianba Fm. **(B)** The well-rounded nature of the quartz clasts forming the Baitianba conglomerate. **(C)** Gravel imbrication indicates southeastward paleoflows. **(D)** Represents an erosional basal surface. **(E)** Channel-filling deposits. **(F)** Shows an interbedded coal bed.

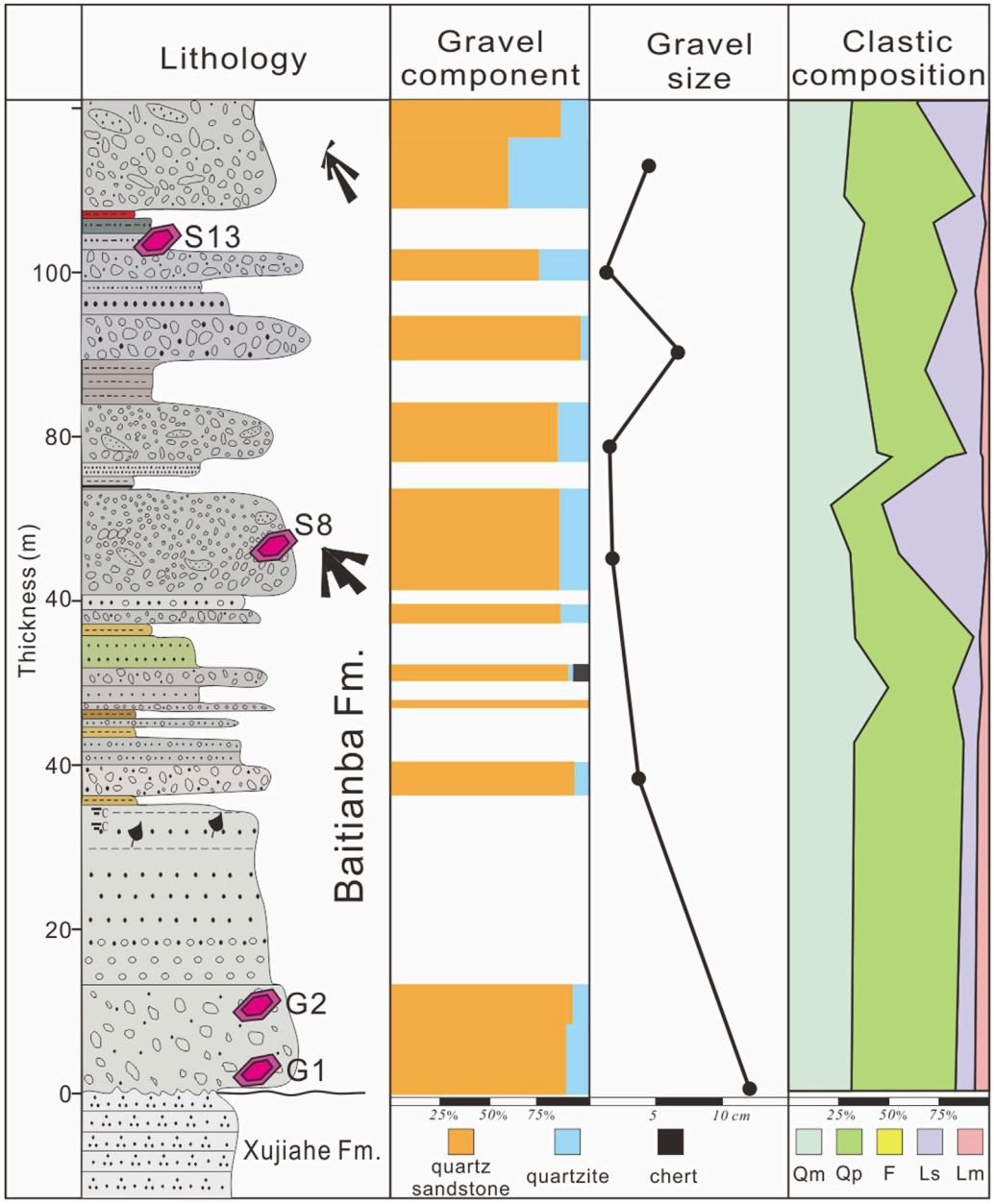

FIGURE 3
Lithostratigraphy, gravel component and sandstone composition of the Jinzishan outcrop. Qm: monocrystalline quartz; Qp: polycrystalline quartz; F: feldspar; Ls: sedimentary rock fragments; Lm: metamorphic rock fragments.

the Longmen Shan thrust belt (Liu et al., 2021). Therefore, the study of the early uplift history of the Longmen Shan thrust belt provides an insight into the formation and preservation of natural gas in the deep Sichuan Basin. Unfortunately, whether the early uplift of the Longmen Shan thrust belt formed the eastern margin of the Tibetan Plateau since the Mesozoic or not remains controversial. First, during the Late Triassic, the Longmen Shan thrust belt was uplifted due to the collision between the Qiangtang and Kunlun terranes during the closure of the paleo-Tethys ocean (Weislogel et al., 2006; Li et al., 2007; Zhan et al., 2018). Second, since the Early Jurassic, the continued northward extrusion of the Qiangtang terrane after the Qiangtang–Kunlun collision led to the early uplift of the Longmen Shan thrust belt (Meng et al., 2005; Deng et al., 2012; Yan et al., 2018).

The crux of this controversy is the question of which Early Mesozoic conglomerate (Upper Triassic or Lower Jurassic) most

closely represents the early uplift and unroofing of the Longmen Shan thrust belt. The lack of research on the quartz-rich conglomerate of the Lower Jurassic contributes to the uncertainty. Thus, herein, the Jinzishan ancient alluvial fan preserved on the northwestern margin of the Sichuan Basin was selected for the detailed analyses of sedimentology, detrital components and geochronology to trace the early uplift and unroofing history of the Longmen Shan thrust belt.

2 Geological background

The Sichuan Basin is located at the northwestern margin of the South China Block, separated from the Songpan-Ganze and Bikou terranes to the northwest by the Longmen Shan thrust belt and from the North China Block to the north by the Qinling Orogen (Figure 1C). Due to the oblique collision between North China and South China Block at the end of Triassic, the basin evolved from Sinian (Ediacaran)-Middle Triassic passive margin into a Late Triassic-Cenozoic foreland basin (Mu et al., 2019; Yan et al., 2019; Liu et al., 2021 and references therein). The Qinling Orogenic belt was also the result of this collision overprinted by the Late Jurassic to Cenozoic deformation. Micang-Daba Shan, as well as North Longmen Shan, was shaped as the foreland belts of the SW Qinling orogenic belt (Yan et al., 2018), and the main tectonic style subsequently transformed into extensional collapse during the Early Jurassic (Meng et al., 2005; Dong et al., 2011; Yan et al., 2011; Dong and Santosh, 2016).

In the study area, the Lower Jurassic rest unconformably on deformed Upper Triassic and older rocks along the front zone of the North Longmen Shan thrust belt (Figure 2A). It consists of the thickly bedded conglomerate (Figures 2B,C), cross-bedded sandstone (Figure 2E) and interbed coal (Figure 2F) deposited in alluvial fan whereas changes to clastic rocks and limestone dominate in the basin interior (Meng et al., 2005). Samples were collected from the Jinzishan (N32°11′17″, E105°19′24″) Jurassic paleo-alluvial fan for conglomerate compositions, sandstone detritals and geochronology (Figure 3). Paleocurrent measurements indicate southeastward paleoflows.

3 Methods and results

3.1 Gravel and sandstone petrography

The field investigation observed that Baitianba Formation conglomerate is composed of the well-rounded nature of the quartz clasts in Jinzishan outcrop, especially quartz-sandstone (Figure 3), and differ from the Baitianba formation dominated by quartzite and chert gravels in the Micang-Daba Shan (Qian et al., 2015). In order to determine trustier component of the gravels, twenty-two quartz gravel samples were collected from the lower

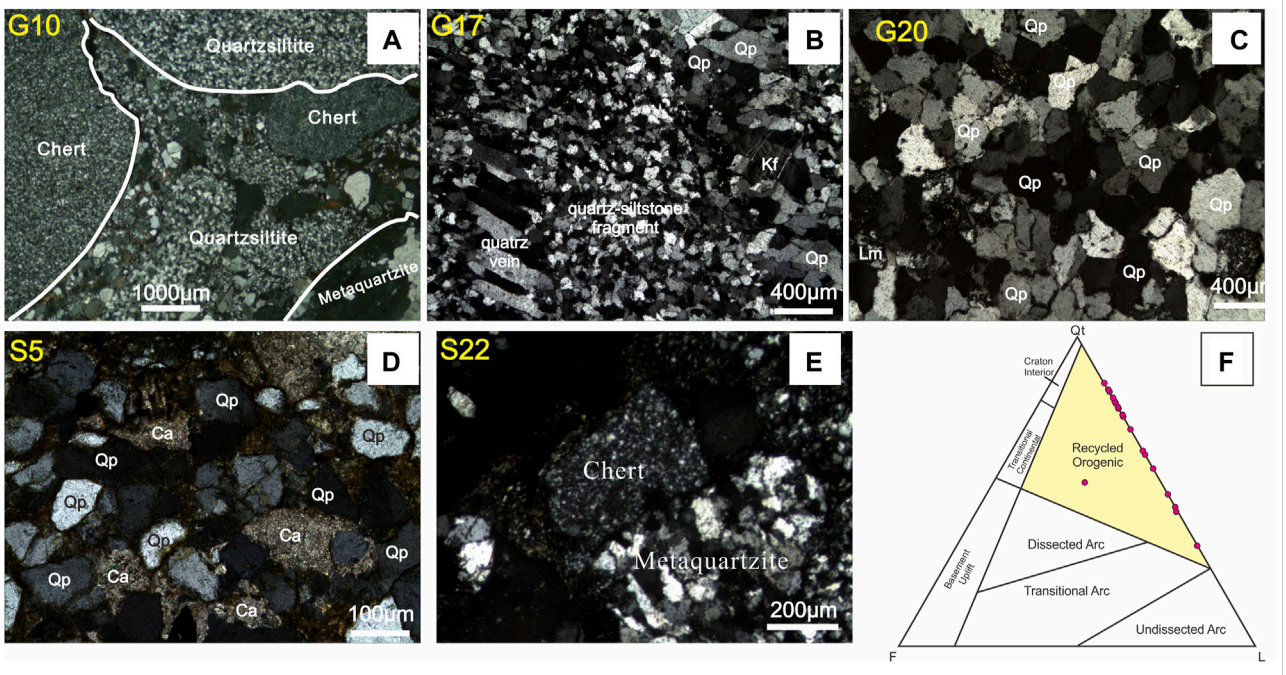

FIGURE 4
(A–C) Representative cross-polarized light photomicrograph of gravel samples. **(D,E)** Representative cross-polarized light photomicrograph of sandstone samples. **(F)** Qt-F-L ternary diagram displays the relative abundance of framework grains in sandstone, Qt: total quartz, F, feldspar, L: lithic rock fragments, Ca: carbonate fragment.

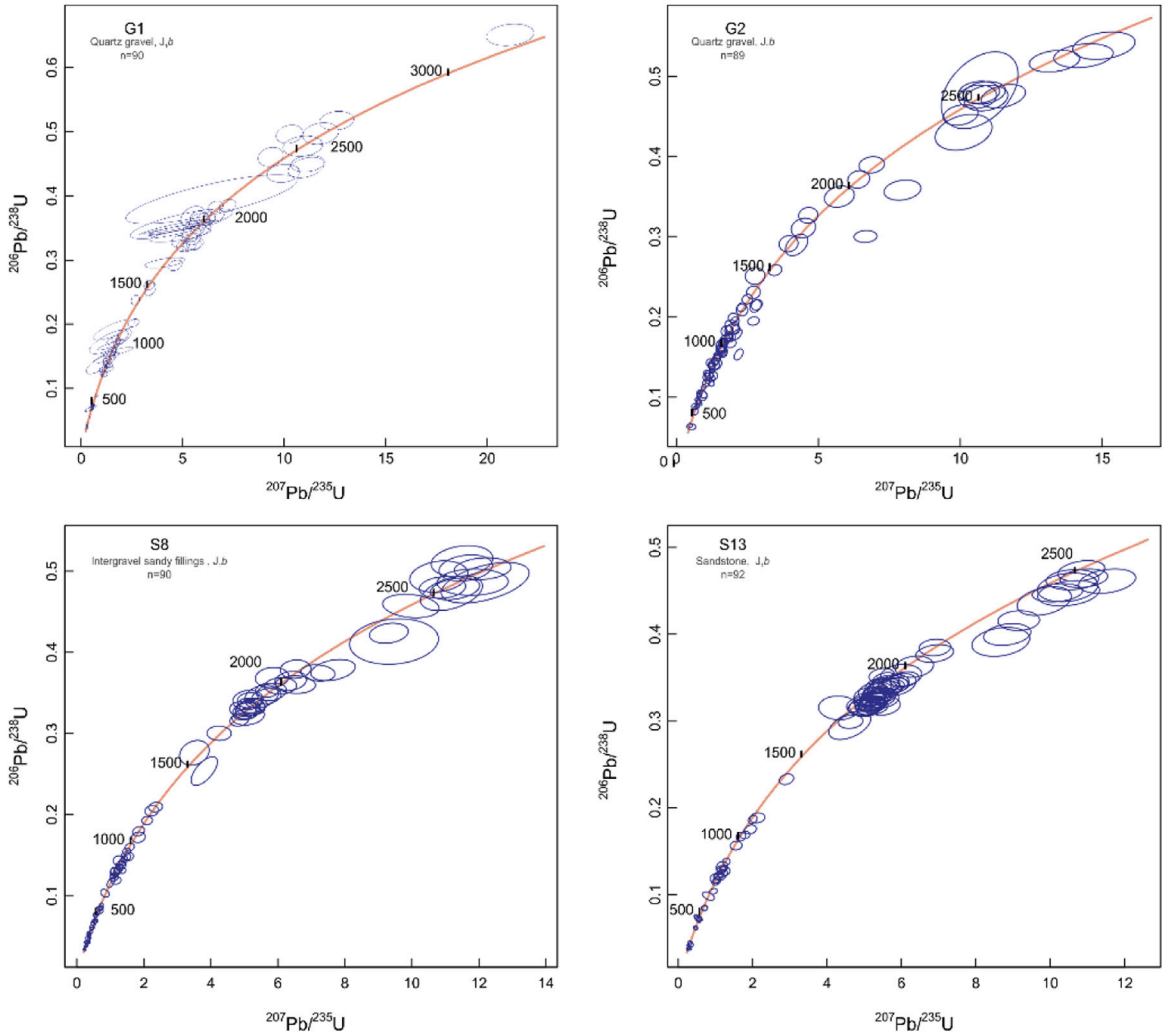

FIGURE 5
U-Pb concordia diagrams for zircon grains of each sample.

part of the Jinzishan outcrop from which polished thin sections were composed to analyse microscopic features. First, the detrital composition of 19 gravel samples was coarse–fine quartz sandstones, dominated by siliceous cemented dense quartz sandstones with durability similar to vein quartz, chert and quartzite (Figure 3, Figures 4A–C), consistent with quartz-pebble conglomerates (QPC) (Cox et al., 2002; Youngson et al., 2006). Second, another two gravel samples are fine conglomerates. Finally, only one gravel is lithic sandstone.

Twenty-nine sandstone samples were collected from the lithic sandstone layer in the Jinzishan. The microscopic characteristics and debris components divided the sandstone into 3 types, including rock-fragment sandstone, lithic quartz sandstone and lithic feldspathic sandstone. We used cross-polarization microscope to observe the petrographic features, including mineral composition, grain size, sorting and roundness. In general, the detrital components of Baitianba Formation sandstone are quartz rich with a percentage composition range 33–85, whereas the feldspar content is extremely low, the lithics observed in the samples are mostly the sandstone, siltstone, argillite, chert and mica. Significantly, carbonate fragment is only found in the top of the Jinzishan outcrops (Figure 4D). The modal compositions of sandstone samples plot near the boundary of "recycled orogenic" field in the QtFL diagram (Figure 4F).

3.2 Detrital zircon geochronology

Quart-rich conglomerates can be attributed to potential source in the thrust belt on the basis of their detrital zircon age population (Lawton et al., 2010). In this study, two gravel and two sandstone samples (about 5 kg each) were collected from Lower Jurassic Jinzishan outcrops, and zircon grains were extracted following the

standard procedures outlined in Li et al. (2007). Chengxin Geology Service Co. Ltd., Langfang, China performed this work. To avoid sampling bias, zircon crystals (N200 grains) were mounted in epoxy resin without handpicking and polished to obtain a smooth internal surface. Zircon U–Pb dating was performed using laser ablation-inductively coupled plasma mass spectrometry (LA-ICPMS) at the CUGB LaserChron Center. All four samples were ablated using a 30-μm diameter laser beam. The U–Pb fractionation results were corrected using the zircon standard 91500 reference, affording 324 concordant data points for the four samples. The U-Pb concordia diagrams for zircon grains of each sample are shown in Figure 5 and U–Pb age data set is provided as supplementary files in excel format (Supplementary File S1).

3.2.1 gravel sample G1

Gravel sample G1 was taken from the bottom of the Lower Jurassic outcrop. 87 valid DZ age data points ranging from 231 to 3,069 Ma, with peaks in five major age intervals: 230–290 Ma; 425–460 Ma; 740–1,100 Ma; 1,650–1,700 Ma; and 1,860–2,000 Ma were obtained, with minimum zircon ages constraining the age of deposition of its parent rock not earlier than the Late Triassic.

3.2.2 gravel sample G2

Gravel sample G2 was also derived from the bottom of this outcrop with 85 valid DZ age data points ranging from 395 to 2,829 Ma, with peaks at 540–640 Ma; 760–1,200 Ma; 1,500–1,690 Ma; 2,430–2,500 Ma, and about 53% of clastic zircons of Neoproterozoic age.

3.2.3 Sandstone sample S8

Sample S8 was taken from the lenticular sandstone formation within the conglomeratic strata, identified as lithic sandstone. Ninety valid DZ ages ranged from 211 to 2,647 Ma, with peaks in five main age intervals of 211–350 Ma; 410–490 Ma; 600–900 Ma; 1,700–2,000 Ma; and 2,400–2,600 Ma, with weaker peaks in 1,000–1,150 Ma.

3.2.3 Sandstone sample S13

Sample S13 was collected from the sandstone layer with 92 valid DZ ages ranging from 232 to 2,647 Ma, of which detrital zircons from 1,800 to 2,000 Ma account for 43% of the total quartz grains, showing a obvious age peak. The remaining zircon ages are distributed within the 200–300 Ma, 350–500 Ma and 2,300–2,400 Ma sub-age intervals.

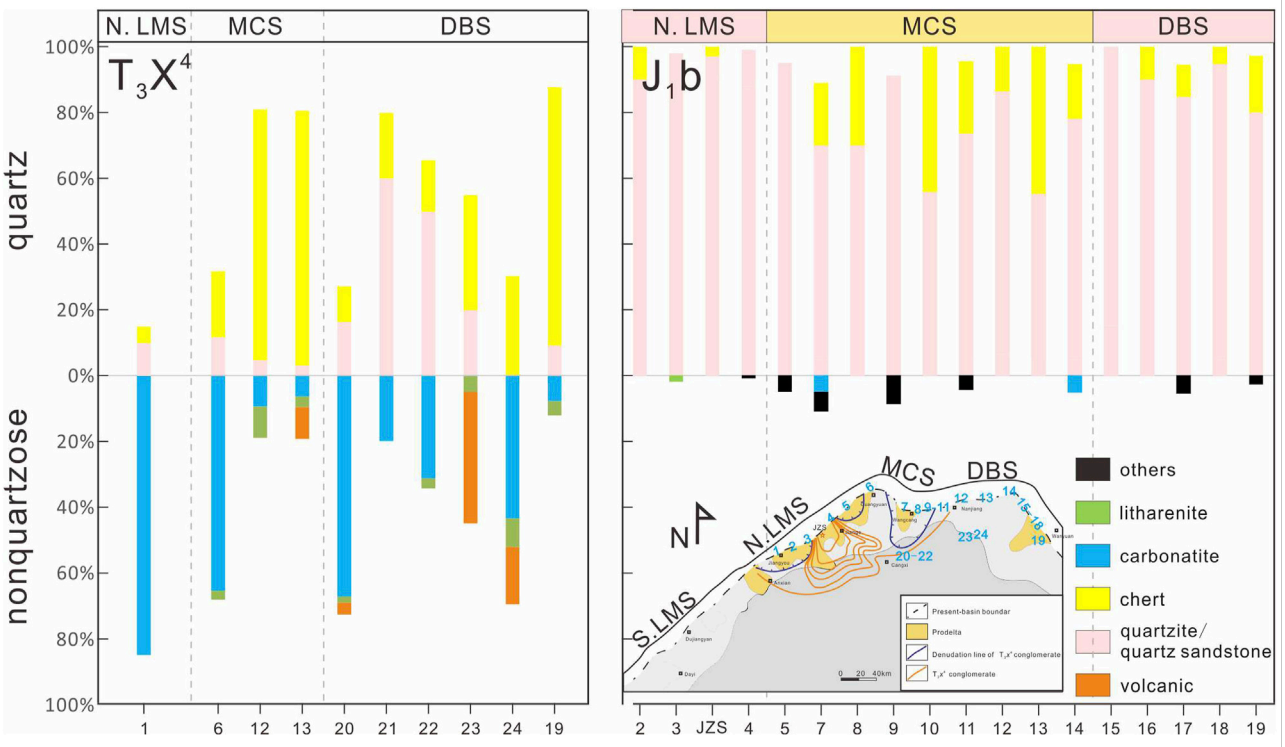

FIGURE 6
Comparison of conglomerate compositions between the Upper Triassic Xujiahe Formation and the Lower Jurassic Baitianba Formation in the NW Sichuan Basin. JZS-Jinzishan, 1-Jiangyou Qinglingkou, 2- Jiangyou Daliangshang, 3- Jiangyou Erlangmiao, 4- Baitianba, 5- Guangyuan Baolun, 6- Gongnong, 7- Guangyuan Baishui, 8-Wangcang, 9-Cangxi Puji, 10- Wangcang Sangjiang, 11- Wangcang Jinxi, 12-Nanjiang; 13- Tongjiang Pingxi; 14- Tongjiang Lianghekou; 15- Tongjiang Tiexi, 16- Wanyuan Zhuyu, 17- Wanyuan Huangzhong; 18- Wanyuan Jiuyuan, 19- Wanyuan Gujun, 20- Well YB6, 21- Well YB123, 22- Well YB203, 23- Well YB204, 24- Well M201.

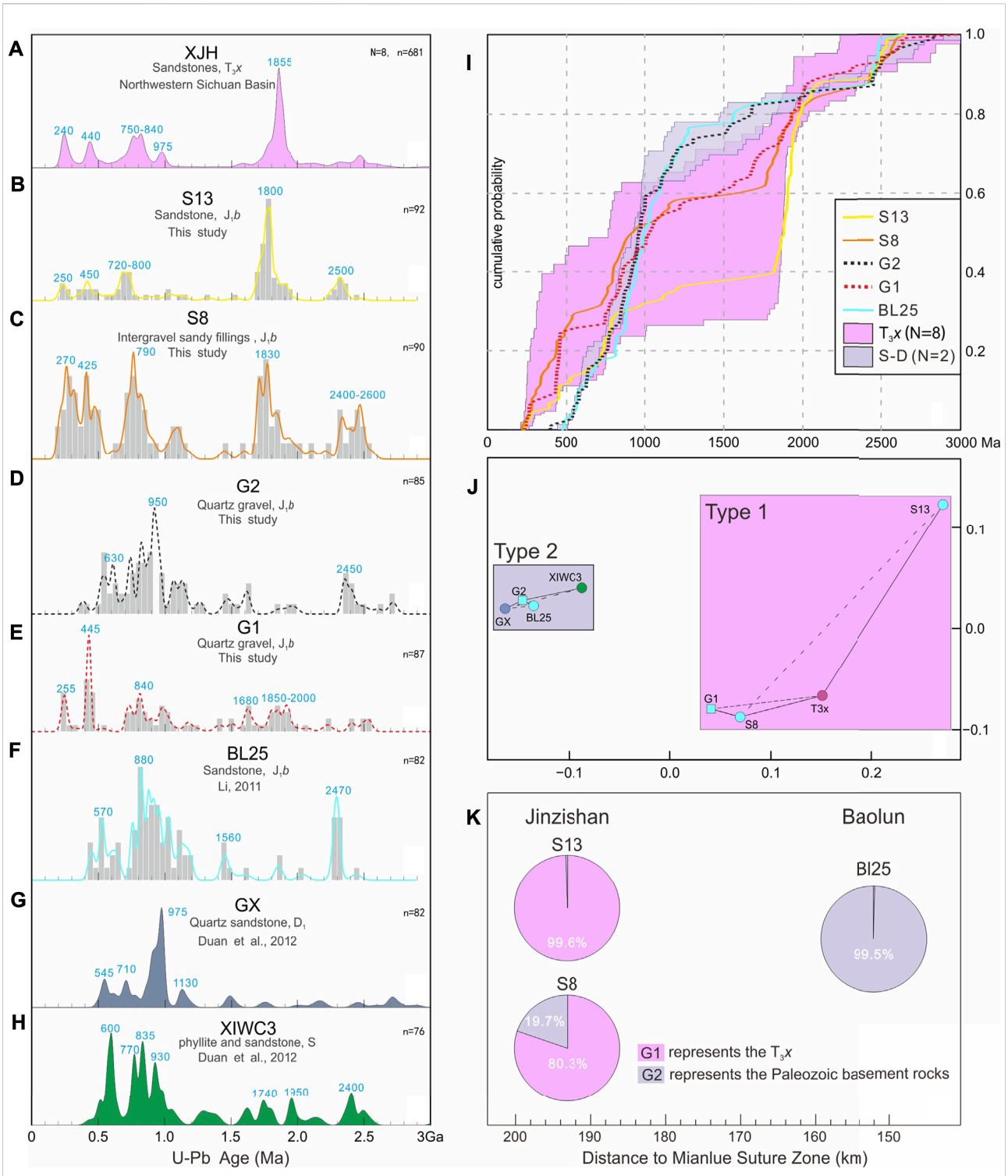

FIGURE 7
(A–H) Zircon U–Pb age cumulative probability distribution for each sample. XJH: Spectra of Upper Triassic Xujiahe Formation sediments in northwestern Sichuan Basin are taken from previous studies (Chen et al., 2011; Luo et al., 2014; Shao et al., 2016; Mu et al., 2019); G1, G2, S8 and S13 are new samples collected from the Lower Jurassic strata in the Jinzishan section; BLI25 is a Lower Jurassic sandstone sample from Li. (2013); Lower Devonian sample GX and Silurian sample XIWC3 are thrust belt source units in Longmen Shan, from Vermeesch, 2018 and Duan et al. (2012), respectively. **(I)** Cumulative distribution plot (CDF) of all samples; **(J)** Multidimensional scaling map (Vermeesch, 2018), showing the distinct signature of Baitianba Formation, Type 1 is similar to Upper Triassic continental deposits, and Type 2 is a population distribution similar to that of Lower Paleozoic Marine quartz-rich sandstones of the Longmen Shan thrust belt. The multi-dimensional scaling (MDS) map uses the Kolmogorov–Smirnov (KS) statistic for detrital zircon U–Pb datasets (Stevens et al., 2013; Vermeesch, 2018). **(K)** Unmixing detrital geochronology age distribution.

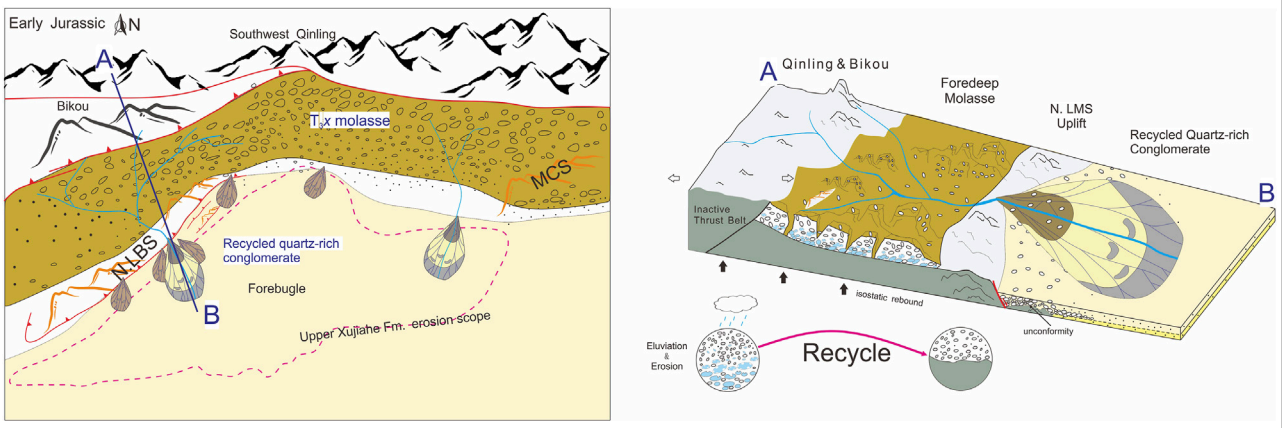

FIGURE 8
Depositional model of the QPC of the Lower Jurassic Baitianba Formation in the northern part of the Longmen Shan orogenic belt.

4 Discussion

In previous studies, based on the siliceous characteristics of the Lower Jurassic Baitianba Formation in the northwestern part of the Sichuan Basin, these QPC were arbitrarily considered to be mainly derived from Paleozoic Devonian quartz-sandstones deposited at the western margin of the Sichuan Basin (Cui et al., 1991) and combined with the underlying carbonate-rich conglomerates of the Upper Triassic Xujiahe Formation (Figure 6). Previous studies have proposed that these two sets of lithologically distinct conglomerates should represent the uplift erosion of the Longmen Shan thrust belt (Meng et al., 2005; Deng et al., 2012). However, this explanation for the detrital provenance of the Lower Jurassic QPC could not resolve the presence of carbonate strata over a 4-km distance from Triassic to Devonian (Liu et al., 2021), implying that Lower Devonian quartz sandstones from a 1.0–1.5 km range could not be the sole provenance of the Baitianba QPC. To further explore this paradox, the detrital zircon U–Pb ages from the gravel and sandstone samples were used to trace true provenance matching published detrital zircon data from possible provenance areas.

We performed multiple comparisons between the kernel density estimate (KDE, Figures 7A–H), cumulative age distribution (CAD, Figure 7I), and multidimensional scaling analysis (MDS, Figure 7J) of detrital zircons to demonstrate a similarity between the Lower Jurassic Baitianba Formation and probable provenance strata (Vermeesch, 2018). On the MDS diagram, the data points are distinctly divided into two different parts: 1) samples G1, S8 and S13 are highly correlated with the Upper Triassic Xujiahe Formation with notable peaks within 1,800–2,000 Ma; 2) sample G2 shows a typical "Paleozoic basement-type" feature of Lower Paleozoic quartz sandstone similar with sample BL25 from the northern Sichuan Basin (Li et al., 2012). However, the MDS interpretation reflects that the age spectra of the detrital zircons from the gravel samples were significantly different, indicating derivation from the underlying Upper Triassic Xujiahe Formation and the deeper Paleozoic basement of the Longmen Shan thrust belt, respectively. In addition, it is necessary to evaluate the topographic relief and denudation degree of the Longmen Shan thrust belt to quantify the mixing ratio of the two different provenances to the detrital material of the Lower Jurassic Baitianba Formation based on recycled features of the QPC. The DZ ages of gravel G1 and G2 represent the age spectra of the Upper Triassic Xujiahe sandstone and the Lower Paleozoic basement, respectively, which could be defined as a provenance zircon feature. The sandstone samples (S8 and S13) derived from the sandstone lenticular in the lower part of the alluvial fan and the sandstone layer in the upper part of the Jinzishan outcrop as well as the other sample (BL25, Figure 7F) from the Baolun outcrop are regarded as mixed sediments and statistically simulated based on the DZmix program of MATLAB (Sundell and Saylor, 2017). All of S13 was from the Upper Triassic Xujiahe Formation; all of Bl25 was derived from the Lower Paleozoic basement and S8 was collected from the above two provenances: 80.3% from eroded Xujiahe Formation strata and 19.7% from the Lower Paleozoic basement (Figure 7K).

The above spatial features of detrital zircons have indicated the following. First, the northern Guangyuan area was eroded to the Paleozoic basement in the Early Jurassic and second, the detritus of the Lower Jurassic in the southern Jinzishan area should be doubly supplied from the Upper Triassic and Lower Paleozoic quartz sandstones. However, the Upper Triassic Xujiahe sandstone mainly comprises lithic sandstone with <5% of quartz sandstone resembling the detritus of the Lower Jurassic QPC. At the same time, marine carbonates over a 4-km distance between the Lower Devonian and Upper Triassic only appear in the detrital grains of the upper sandstone member and not be found in the Jinzishan conglomerates. Thus, neither the Upper Triassic nor the Lower Devonian could directly supply the Lower Jurassic QPC. Therefore, the lithologic features of the Lower Jurassic QPC imply that only those quartz-rich conglomerates with high resistance to

weathering and abrasion that are among the composite conglomerates in periphery provenance areas could have been retained to form the Lower Jurassic QPC (Cui et al., 1991; Qian et al., 2015).

Herein, a new depositional model of the Lower Jurassic QPC was reconstructed. First, during the depositional process of the provenance area, the southwardly thrusting South Qinling orogenic belt formed a foreland basin in the northern Longmen Shan thrust belt as well as provided a large amount of detrital sediment during the Late Triassic (Qian et al., 2015; Mu et al., 2019). Meanwhile, the southward expansion of the thrust front afforded the absence of the upper part of the Xujiahe Formation (V and VI members) in the northwestern Sichuan Basin (Li Y et al., 2003; Deng et al., 2012). Second, during the weathering and leaching process of the provenance area, the Upper Triassic composite conglomerates were exposed to the surface and subjected to weathering and leaching, dissolving unstable carbonate and sandstone gravels in rainwater, except for hard quartz conglomerates (Cox et al., 2002; Youngson et al., 2006). Finally, as QPC were deposited, a southeast-tilting gently oblique zone formed in the northern Longmen Shan thrust belt. This occurred because the Bikou terrane was uplifted during regional extension in the Early Jurassic (Yan et al., 2018), allowing the weathering conglomerates to be transported into the Sichuan Basin. In the transporting process, the unstable components of the former composite conglomerates continued to be diluted, directly increasing the percentage of stable quartz-rich conglomerates and eventually forming a QPC alluvial fan in the study area underlying the gently sloping topography (Figure 8).

5 Conclusion

1) Detrital zircon U–Pb geochronology and petrography of tow Lower Jurassic gravel samples from Jinzishan outcrop reveal at least two source of quartz-rich conglomerate. One sample is characterized by the absence of younger detrital zircons (<395 Ma), resembling the Early Paleozoic marine quartz sandstone due to the uplift and erosion of the Paleozoic basement in the North Longmen Shan thrust belt. The other yield age clusters of ca. 1.8 Ga, 950–750 Ma, 450–420 Ma, and 280–240 Ma, which is identical to the detrital zircons from the Upper Triassic strata. Our results indicated Upper Triassic to Early Paleozoic strata had uplifted and suffered from erosion in adjacent Longmen Shan thrust belt before the Early Jurassic.
2) U–Pb dating of Baitianba Formation sandstone also exhibit strong similarity to the Upper Triassic strata detrital record.
3) The feature of Baitianba conglomerate fits the definition of QPCnew depositional model of the Lower Jurassic conglomerates mainly recycled from the uplifted Upper Triassic strata in the north Longmen Shan thrust belt through long-term weathering.

Data availability statement

The original contributions presented in the study are included in the article/Supplementary Material, further inquiries can be directed to the corresponding author.

Author contributions

BR and SL conceived and designed the study. ZW measured Chronological data. FL and BR wrote the first draft of the manuscript. XL provided constructive suggestions to improve the work. YH, KL, TS, and FL edited and reviewed the manuscript.

Funding

This study was financially supported by the National Natural Science Foundation of China (No. 42072129).

Acknowledgments

We thank Liangliang Zhang for contribution to the laboratory work. And we thank the reviewers for review suggestions of this work.

Conflict of interest

The authors declare that the research was conducted in the absence of any commercial or financial relationships that could be construed as a potential conflict of interest.

Publisher's note

Supplementary material

The Supplementary Material for this article can be found online at: https://www.frontiersin.org/articles/10.3389/feart.2022.982354/full#supplementary-material

References

Chen, Q., Sun, M., Long, X. P., Zhao, G. C., and Yuan, C. (2016). U–Pb ages and Hf isotopic record of zircons from the late neoproterozoic and silurian–devonian sedimentary rocks of the western yangtze block: Implications for its tectonic evolution and continental affinity. *Gondwana Res.* 31, 184–199. doi:10.1016/j.gr.2015.01.009

Chen, Y., Liu, S. G., Li, Z. W., Deng, B., Zeng, X. L., and Lin, J. (2011). LA-ICP-MS detrital zircon U-Pb geochronology approaches to the sediment provenance of the Western Sichuan foreland Basin and limited uplift of the longmen mountains during the early stage of Late Triassic. *Geotecton. Metallog.* 35 (2), 315–323. in Chinese with English abstract. doi:10.3969/j.issn.1001-1552.2011.02.017

Cheng, F., Garzione, C., Jolivet, M., Wang, W., Dong, J., Richter, F., et al. (2019). Provenance analysis of the Yumen Basin and northern Qilian Shan: Implications for the pre-collisional paleogeography in the NE Tibetan plateau and eastern termination of Altyn Tagh fault. *Gondwana Res.* 65, 156–171. doi:10.1016/j.gr.2018.08.009

Cox, R., Gutmann, E. D., and Hines, P. G. (2002). Diagenetic origin for quartz-pebble conglomerates. *Geology* 30 (4), 323–326. doi:10.1130/0091-7613(2002)030<0323:DOFQPC>2.0.CO;2

Cui, B. Q., Long, X, M., and Li, Y. (1991). The subsidence of western sichuan depression and the rise of longmenshan mountains. *Jour. Chengdu Coll. Geol.* 18, 39–45.

Deng, B., Liu, S., Jansa, L., Cao, J., Cheng, Y., Li, Z., et al. (2012). Sedimentary record of Late Triassic transpressional tectonics of the Longmenshan thrust belt, SW China. *J. Asian Earth Sci.* 48, 43–55. doi:10.1016/j.jseaes.2011.12.019

Dong, Y., and Santosh, M. (2016). Tectonic architecture and multiple orogeny of the qinling orogenic belt, Central China. *Gondwana Res.* 29 (1), 1–40. doi:10.1016/j.gr.2015.06.009

Dong, Y., Zhang, G., Neubauer, F., Liu, X., Genser, J., and Hauzenberger, C. (2011). Tectonic evolution of the qinling orogen, China: Review and synthesis. *J. Asian Earth Sci.* 41 (3), 213–237. doi:10.1016/j.jseaes.2011.03.002

Duan, L., Meng, Q. R., Wu, G. L., Ma, S. X., and Li, L. I. N. (2012). Detrital zircon evidence for the linkage of the South China block with Gondwanaland in early palaeozoic time. *Geol. Magaz.* 149 (6), 1124–1131. doi:10.1017/S0016756812000404

Lawton, T. F., Hunt, G. J., and Gehrels, G. E. (2010). Detrital zircon record of thrust belt unroofing in Lower Cretaceous synorogenic conglomerates, central Utah. *Geology* 38 (5), 463–466. doi:10.1130/G30684.1

Li, X. H., Chen, F., Guo, J. H., Li, Q. L., Xie, L. W., and Siebel, W. (2007). South China provenance of the lower-grade Penglai Group north of the Sulu UHP orogenic belt, eastern China: Evidence from detrital zircon ages and Nd-Hf isotopic composition. *Geochem. J.* 41 (1), 29–45. doi:10.2343/geochemj.41.29

Li, Z. W., Liu, S., Chen, H., Deng, B., Hou, M., Wu, W., et al. (2012). Spatial variation in Meso-Cenozoic exhumation history of the Longmen Shan thrust belt (eastern Tibetan Plateau) and the adjacent western Sichuan basin: Constraints from fission track thermochronology. *J. Asian Earth Sci.* 47, 185–203. doi:10.1016/j.jseaes.2011.10.016

Liu, S., Yang, Y., Deng, B., Zhong, Y., Wen, L., Sun, W., et al. (2021). Tectonic evolution of the sichuan basin, southwest China. *Earth. Sci. Rev.* 213, 103470. doi:10.1016/j.earscirev.2020.103470

Luo, L., Qi, J. F., Zhang, M. Z., Wang, K., and Han, Y. Z. (2014). Detrital zircon U–Pb ages of Late Triassic–Late Jurassic deposits in the western and northern Sichuan Basin margin: constraints on the foreland basin provenance and tectonic implications. *Int. J. of Earth Sci.* 103 (6), 1553–1568. doi:10.1007/s00531-014-1032-7

Ma, H. M., Wang, Y., Huang, Y. J., and Xie, Y. T. (2019). Three-stage Mesozoic intracontinental tectonic evolution of South China recorded in an overprinted basin: evidence from stratigraphy and detrital zircon U–Pb dating. *Geol. Magaz.* 156 (12), 2085–2103. doi:10.1017/S0016756819000451

Meng, Q. R., Wang, E., and Hu, J. M. (2005). Mesozoic sedimentary evolution of the northwest Sichuan basin: Implication for continued clockwise rotation of the South China block. *Geol. Soc. Am. Bull.* 117 (3-4), 396–410. doi:10.1130/B25407.1

Mu, H., Yan, D. P., Qiu, L., Yang, W. X., Kong, R. Y., Gong, L. X., et al. (2019). Formation of the late triassic western sichuan foreland basin of the qinling orogenic belt, SW China: Sedimentary and geochronological constraints from the Xujiahe Formation. *J. Asian Earth Sci.* 183, 103938. doi:10.1016/j.jseaes.2019.103938

Qi, B., Hu, D., Yang, X., Zhang, Y., Tan, C., Zhang, P., et al. (2016). Apatite fission track evidence for the Cretaceous–Cenozoic cooling history of the Qilian Shan (NW China) and for stepwise northeastward growth of the northeastern Tibetan Plateau since early Eocene. *J. Asian Earth Sci.* 124, 28–41. doi:10.1016/j.jseaes.2016.04.009

Qian, T., Liu, S., Li, W., Gao, T., and Chen, X. (2015). Early–middle jurassic evolution of the northern yangtze foreland basin: A record of uplift following triassic continent–continent collision to form the qinling–dabieshan orogenic belt. *Int. Geol. Rev.* 57 (3), 327–341. doi:10.1080/00206814.2015.1006270

Ritts, B. D., and Biffi, U. (2000). Magnitude of post–Middle Jurassic (Bajocian) displacement on the central Altyn Tagh fault system, northwest China. *Geol. Soc. Am. Bull.* 112 (1), 61–74. doi:10.1130/0016-7606(2000)112<61:MOPJBD>2.0.CO;2

Shao, T. B., Cheng, N. F., and Song, M. S. (2016). Provenance and tectonic-paleogeographic evolution: Constraints from detrital zircon U–Pb ages of Late Triassic-Early Jurassic deposits in the northern Sichuan basin, central China. *J. Asian Earth Sci.* 127, 12–31. doi:10.1016/j.jseaes.2016.05.027

Sundell, K. E., and Saylor, J. E. (2017). Unmixing detrital geochronology age distributions. *Geochem. Geophys. Geosyst.* 18 (8), 2872–2886. doi:10.1002/2016GC006774

Stevens, T., Carter, A., Watson, T. P., Vermeesch, P., Andò, S., and Bird, A. F. (2013). Genetic linkage between the Yellow River, the Mu Us desert and the Chinese loess plateau. *Quat. Sci. Rev.* 78, 355–368. doi:10.1016/j.quascirev.2012.11.032

Tian, Y., Kohn, B. P., Gleadow, A. J., and Hu, S. (2013). Constructing the Longmen Shan eastern Tibetan Plateau margin: Insights from low-temperature thermochronology. *Tectonics* 32 (3), 576–592. doi:10.1002/tect.20043

Vermeesch, P. (2018). IsoplotR: A free and open toolbox for geochronology. *Geosci. Front.* 9 (5), 1479–1493. doi:10.1016/j.gsf.2018.04.001

Wang, L., Chen, Z., Li, B., Lei, Y., and Yan, S. (2014). Structural characteristics of the northern Longmenshan fold-thrust belt and the favorable exploration areas, Sichuan Basin, Southwest China. *Petroleum Explor. Dev.* 41 (5), 591–597. doi:10.1016/S1876-3804(14)60070-7

Weislogel, A. L., Graham, S. A., Chang, E. Z., Wooden, J. L., Gehrels, G. E., and Yang, H. (2006). Detrital zircon provenance of the late triassic songpan-ganzi complex: Sedimentary record of collision of the north and South China blocks. *Geol.* 34 (2), 97–100. doi:10.1130/G21929.1

Yan, D. P., Zhou, M. F., Li, S. B., and Wei, G. Q. (2011). Structural and geochronological constraints on the Mesozoic-Cenozoic tectonic evolution of the Longmen Shan thrust belt, eastern Tibetan Plateau. *Tectonics* 30 (6). doi:10.1029/2011TC002867

Yan, D. P., Zhou, Y., Qiu, L., Wells, M. L., Mu, H., and Xu, C. G. (2018). The longmenshan tectonic complex and adjacent tectonic units in the eastern margin of the Tibetan plateau: A review. *J. Asian Earth Sci.* 164, 33–57. doi:10.1016/j.jseaes.2018.06.017

Yan, Z., Tian, Y., Li, R., Vermeesch, P., Sun, X., Li, Y., et al. (2019). Late Triassic tectonic inversion in the upper Yangtze Block: Insights from detrital zircon U–Pb geochronology from south-western Sichuan Basin. *Basin Res.* 31 (1), 92–113. doi:10.1111/bre.12310

Youngson, J. H., Craw, D., and Falconer, D. M. (2006). Evolution of Cretaceous–Cenozoic quartz pebble conglomerate gold placers during basin formation and inversion, southern New Zealand. *Ore Geol. Rev.* 28 (4), 451–474. doi:10.1016/j.oregeorev.2005.02.004

Zhan, Q. Y., Zhu, D. C., Wang, Q., Cawood, P. A., Xie, J. C., Li, S. M., et al. (2018). Constructing the eastern margin of the Tibetan plateau during the late triassic. *J. Geophys. Res. Solid Earth* 123 (12), 10–449. doi:10.1029/2018JB016353

Zhu, D. C., Zhao, Z. D., Niu, Y., Dilek, Y., Hou, Z. Q., and Mo, X. X. (2013). The origin and pre-Cenozoic evolution of the Tibetan Plateau. *Gondwana Res.* 23 (4), 1429–1454. doi:10.1016/j.gr.2012.02.002

frontiers | Frontiers in Earth Science

TYPE Original Research
PUBLISHED 05 September 2022
DOI 10.3389/feart.2022.982037

OPEN ACCESS

EDITED BY
Shengyao Yu,
Ocean University of China, China

REVIEWED BY
Hao Cheng,
Tongji University, China
Zaibo Sun,
Yunnan Institute of Ggieolocal Survey, China

*CORRESPONDENCE
Zhimin Peng,
pzm20022002@163.com

SPECIALTY SECTION
This article was submitted to Petrology, a section of the journal Frontiers in Earth Science

RECEIVED 30 June 2022
ACCEPTED 27 July 2022
PUBLISHED 05 September 2022

CITATION
Fu Y, Peng Z, Wang G, Hu J, Zhang Z, Guan J and Ren F (2022), Paleo-Tethys subduction and arc-continent collision: Evidence from zircon U-Pb chronology, geochemistry and Sr-Nd-Hf isotopes of eclogites in western Yunnan, bangbing area, southeastern Tibetan Plateau. *Front. Earth Sci.* 10:982037. doi: 10.3389/feart.2022.982037

Paleo-Tethys subduction and arc-continent collision: Evidence from zircon U-Pb chronology, geochemistry and Sr-Nd-Hf isotopes of eclogites in western Yunnan, bangbing area, southeastern Tibetan Plateau

Yuzhen Fu[1,2], Zhimin Peng[1,3]*, Guozhi Wang[1,2], Jingfeng Hu[4], Zhang Zhang[3], Junlei Guan[3] and Fei Ren[3]

[1]College of Earth Sciences, Chengdu University of Technology, Chengdu, China, [2]Key Laboratory of Tectonic Controls on Mineralization and Hydrocarbon Accumulation of Ministry of Natural Resources, Chengdu University of Technology, Chengdu, China, [3]Chengdu Center of China Geological Survey, Chengdu, China, [4]Institute No 280 of CNNC, Guanghan, China

The Changning-Menglian suture zone (CMSZ) in the southeastern Tibetan Plateau is a newly discovered HP-UHP metamorphic zone. The eclogites therein are the key evidence constraining the main suture of the Proto- and Paleo-Tethys Ocean in western Yunnan. Targeting the weakly studied Bangbing eclogites, we developed a comprehensive study on the whole-rock compositions, Sr-Nd isotope and zircon U-Pb ages, zircon trace elements and Lu-Hf isotope to reveal the subduction and arc-land collision. The eclogites occur as massive blocks or lenses and embedded in garnet phengite quartz schists of Lancang Group, Early Paleozoic accretionary complex. Their geochemistry is similar to E-MORB, and exhibit isotopic $\varepsilon_{Nd}(t)$ values of 3.14–4.49 and $\varepsilon_{Hf}(t)$ of 14.64–16.41, respectively. The Nb-enriched mafic protoliths suggested they were probably generated by partial melting of the enriched oceanic mantle within the spinel stability field and emplaced or erupted as mid-ocean ridge in the Paleo-Tethys Ocean. By LA-ICP-MS zircon U-Pb age testing, the magmatic zircon grains separated from the eclogites yield a wide range of ages, which may be capture zircon ages rather than protolith crystallization. We infer the age of eclogite-facies metamorphism to be 238 ± 2 Ma based on CL images, zircon trace element analysis, and that this metamorphism marks the collision between the Eastern Lincang magmatic arc, the Simao block and the Western Baoshan block. Thus, exhumation of the eclogites occurred only 7 to 23 Ma later, according to age 231–215 Ma for post-collisional volcanic and granitic rocks east of the CMSZ. Conclusively, the continued subduction of the Paleo-Tethys oceanic crust occurred during the Early-Middle Triassic, and rapid exhumation in the Late Triassic. The Changning-Menglian suture zone is a typical oceanic subduction-accretionary orogeny belt.

KEYWORDS

eclogite, zircon U-Pb, Sr-Nd-Hf isotope, Paleo-Tethys, Changning-Meglian suture zone

Introduction

The Changning-Menglian suture zone (CMSZ) locates in the southeastern Tibetan Plateau and represents the eastern part of the global Tethys tectonic domain. As an important "window" for investigating the evolution of Proto- and Paleo-Tethys in the Sanjiang region, it has been attracting great attention from geologists. Recently, it has been increasingly recognised that this suture zone shared similar geological evolution with the Longmucuo-Shuanghu suture zone (LSSZ) in the central Tibetan Plateau (Pan et al., 1997; Zhong 1998; Metcalfe, 2013; Deng et al., 2014). The two together represent the remains of the eventual disappearance of the Proto- and Paleo-Tethys Ocean, and record the magnificent geological history of subduction and arc-continent collisional orogenesis (Pan et al., 2004; Wang D.B. et al., 2016; Wang B.D. et al., 2013, 2018; Peng et al., 2020a). Understanding the evolutionary history of the Eastern Paleo-Tethys is essential for reconstructing the Asian tectonics and geodynamics.

As significant signatures of convergent slab boundary, high-pressure/ultra-high-pressure (HP/UHP) metamorphic rocks (e.g., eclogite, blueschist) record the dynamics of subduction and exhumation in oceanic and/or continental crust (Maruyama et al., 1996; Ernst, 2006; Zhang et al., 2008; Wei and Clarke, 2011). A number of typical eclogites and blueschists related to the evolution of the oceanic crust have been identified in the LSSZ, and rich research results have been published (e.g., Bao et al., 1999; Li et al., 2006, 2008, 2009; Dong and Li, 2009, 2010; Zhai et al., 2009, 2011, 2017; Zhang et al., 2010, 2014; Liu et al., 2011; Liang et al., 2017). In contrast, previous studies in the CMSZ have focused on the blueschists discovered in the Lancang Group in the early 1980s, concentrating on their spatial distribution, chronology, petrography and P-T conditions (e.g., Peng and Luo, 1982; Zhang et al., 1990; Zhao, 1993, 1994; Zhang et al., 2004; Fan et al., 2015; Wang DB. et al., 2016). Subsequently, Li Jing et al. (2015; 2017) first identified garnet-amphibolites in the Wanhe ophiolite mélange, and further studies by Wang et al. (2019) suggest that those rocks should be lawsonite-bearing retrograded eclogites. Recently, with the 1:50,000 regional geological survey in western Yunnan, a large number of eclogites and blueschists have been continuously identified along Changning, Shuangjiang and Lancang areas (Peng et al., 2019; Sun et al., 2019; Wang et al., 2020a, 2020b; Fu et al., 2021). These HP/UHP metamorphic rocks extend intermittently for about 600 km, structuring a giant HP/UHP metamorphic belt (Figure 1A). It makes the CMSZ a hotspot for the tectonic evolution studies of Paleo-Tethys.

In the CMSZ, the eclogites are mainly outcropped from north to south in the Mengku, Bangbing, Qianmai and Jinghong areas. Currently, some research has been conducted on the petrogenesis, chronology and P-T metamorphic evolution of the eclogites rocks from Mengku, Qianmai and Jinghong areas (Sun et al., 2019; Wang et al., 2020b; Zhao et al., 2021). Meanwhile, studies on the petrology and metamorphism of the eclogites in Bangbing area have been limited (Peng et al., 2019, 2020b; Fu et al., 2021). For this area, we are still not clear about such questions as the origin of the protoliths, the ages of the protoliths and metamorphism, and whether these features correspond to the evolution of regional metamorphic zones. Therefore, in this paper, further chronological, geochemical studies and isotopic analyses of the Bangbing eclogites are presented to investigate the evolution and accretionary orogeny of the Tethys Ocean in western Yunnan.

Geological background and samples

Geological background

The Changning-Menglian suture zone is located in southeastern Tibetan Plateau, and extends north-south for 600km, bordering the Lingcang-Menghai magmatic arc to the east, separating the Baoshan Block to the west from the Simao Block to the east (Figure 1B; Metcalfe, 2013; Wang et al., 2018). The study area falls along the Bangbing area of Shuangjiang County in the suture zone. The area is characterised by the Early Paleozoic-Late Triassic oceanic crust formations. The formations are mainly composed of Early Ordovician-Middle Triassic Niujinshan ophiolitic mélange, Carboniferous-Permian oceanic island-seamount strata, i.e., oceanic island basalt and its siliciclastic and carbonate cover, Devonian -Permian deep-sea or bathyal silica-mud assemblages, and Early Paleozoic accretionary complex (Wang et al., 2018; Peng et al., 2020b). The Upper Triassic Sanjiahe Group (T_3sc) and the Middle Jurassic Huakaizuo Group (J_2h), which are continental sedimentary clastic rocks, unconformably overlie these different oceanic formations, with the T_3sc representing the earliest sedimentary cover after the disappearance of the Changning-Menglian Ocean (Wang et al., 2018).

The widely outcropped accretionary complex in the CMSZ is mainly composed of the Lancang Group. The rocks are complex in composition and can be divided into "matrix" and "block" (Peng et al., 2020b). The matrix is mainly metasedimentary rocks, represented by mica quartz schist, garnet mica schist and carbonaceous mica schist. The blocks are composed of various rocks, including metavolcanic rocks (greenschist, albite schist, amphibole schist, etc.), metamorphic intermediate acid intrusive

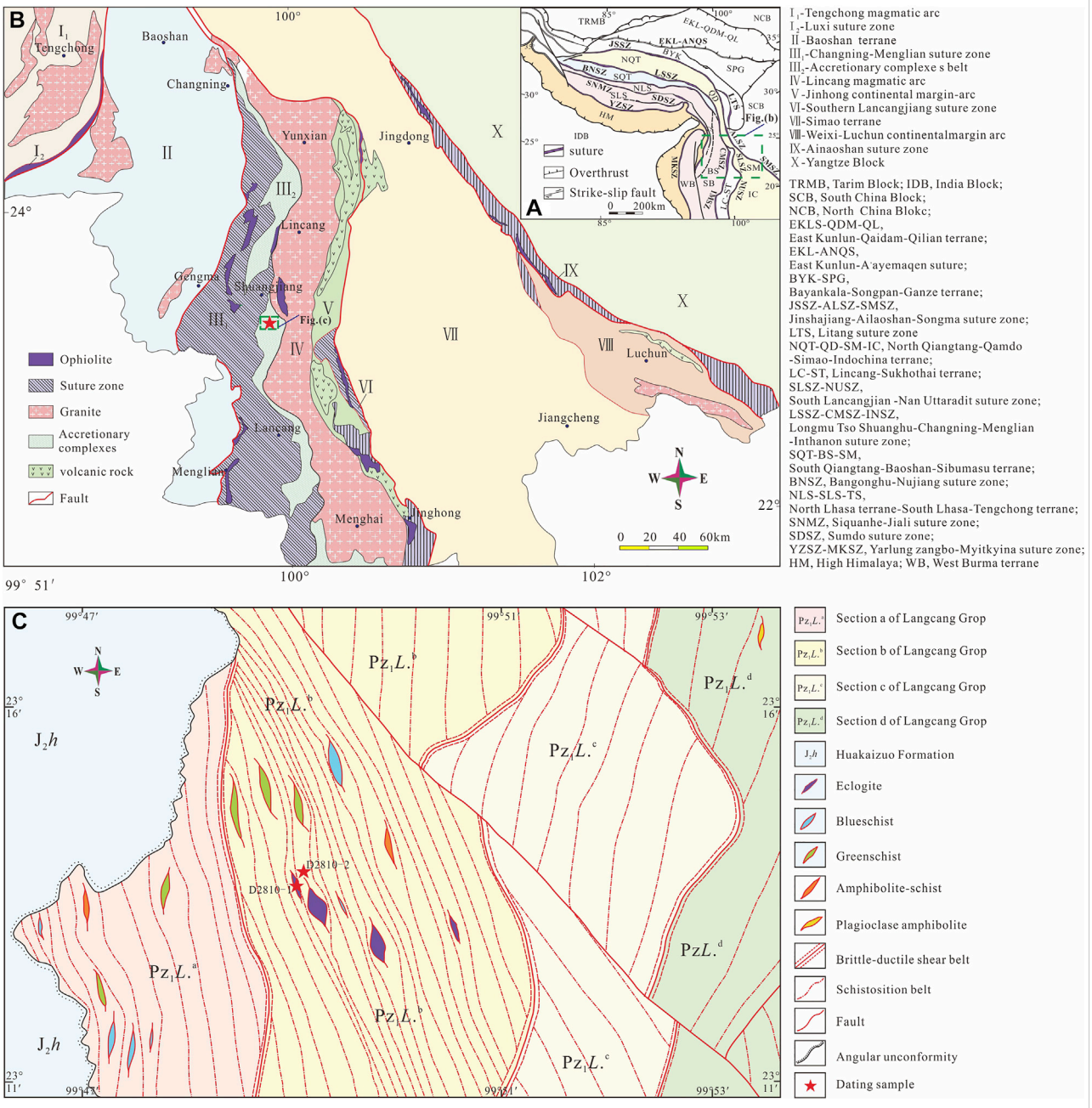

FIGURE 1
Tectonic framework of the East Tethys tectonic domain (**A**, after Xu et al., 2015), geotectonic view of the Changning-menglian orogenic system **(B)** and geological sketch of the Bangbing area **(C)**. (Fig.a after Xu et al., 2020).

rocks (granitic gneisses, albite leptynite) and HP metamorphic rocks (blueschist, eclogites, etc.). Based on whole-rock Rb-Sr and Sm-Nd isotope data and the fossil records, the Lancang Group was previously considered to be the Precambrian basement (Zhai et al., 1990; Zhong, 1998). However, zircon U-Pb age data from the metavolcanic and metaclastic rocks (462–454 Ma, 450–428 Ma, respectively) suggest that the depositional age was Late Ordovician-Silurian rather than Neoproterozoic (Nie et al., 2015; Xing et al., 2017; Wang F. et al., 2017; Wang B.D. et al., 2018). The Lancang Group is divided into several formations and rock sections (Figure 1C), all of which are in tectonic contact with each other, and the original stratigraphy has been completely replaced and the original sedimentary structure has been destroyed (Peng et al., 2020b).

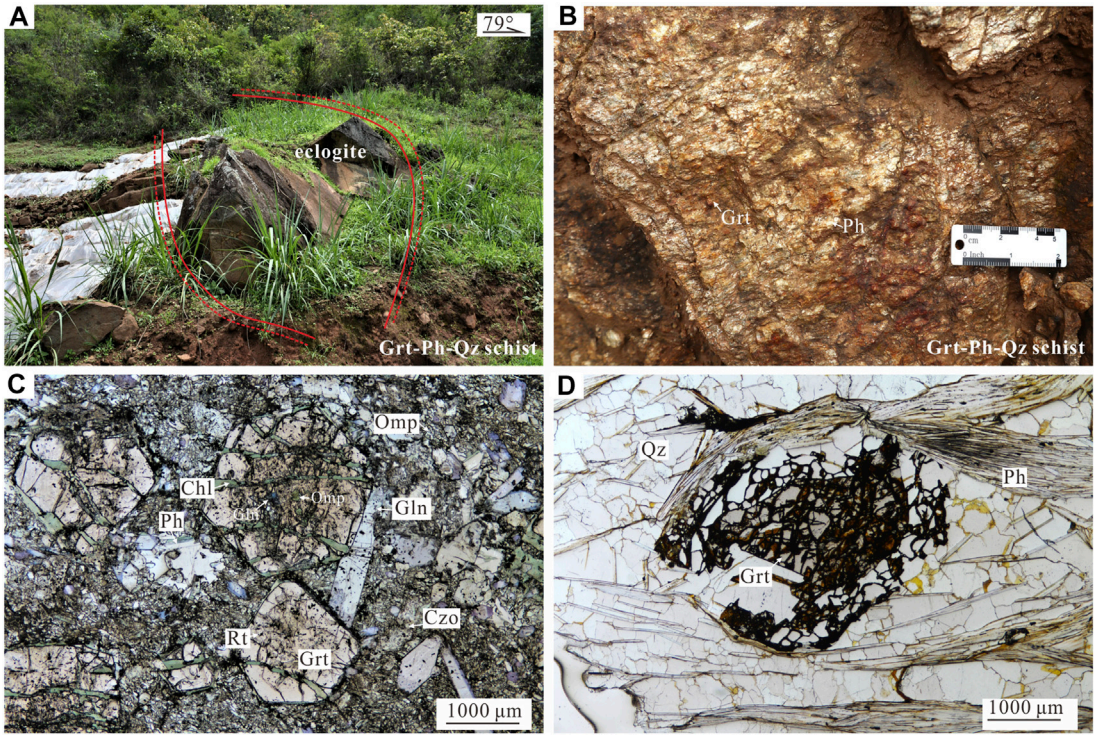

FIGURE 2
Field characteristics and microphotographs of the eclogites and their surrounding schists in Bangbing area. **(A)**, The eclogites (sample D2810-1) are lens-shaped, with strong foliations at the contact boundary to the surrounding rocks. **(B)**, The eclogites are surrounded by coarse-grained garnet phengite schists (sample D2810-2). **(C)**, The eclogite mainly consists of garnet, omphacite and glaucophane, with minor phengite, quartz, clinozoisite and rutile. **(D)**, Grt-Ph-Qz schist show well-developed foliation, and defined by fine layers of phengite, with garnet enclosed by the layers.

Samples description

The eclogites occur as massive blocks or lenses and embedded in schist (Figure 2A). The eclogites appear as tectonic sheets and the contact boundary with the schist is strongly foliated. The field characteristics and petrographic studies of Bangbing eclogite and its enclosing rocks have been discussed in detail previously (Peng et al., 2019; Fu et al., 2021). The Bangbing eclogite mainly consists of garnet, omphacite and glaucophane, with minor phengite, quartz, clinozoisite and rutile (Figure 2C). The clinozoisite is likely to have been transformed from lawonsite by dehydration (Clarke et al., 2006; Wei and Clarke, 2011). Several HP metamorphic rock samples in the CMSZ have identified lawonsite inclusions preserved in garnet or glaucophane (Wang et al., 2019; 2020a). The coexistence of lawonsite and glaucophane in the eclogite strongly points to a cold oceanic crust subduction. The peak P-T conditions of Bangbing eclogites were estimated at 3.0–3.2 GPa and 617–658°C by the Grt-Omp-Phn geothermobarometer (Fu et al., 2021). Correspondingly, researchers combined with phase equilibrium simulations to obtain peak P-T conditions for HP rocks in different locations in the CMSZ, such as 2.4–2.6 GPa, 520–530°C for lawsonite-bearing retrograded eclogite in the Mengku area (Wang et al., 2019); 2.3–2.6 GPa, 570–610°C for phengite/talc-glaucophane eclogites in the Heihe area; and 2.9 GPa, 600°C for glaucophane eclogites, 2.85–2.96 GPa, 580–594°C for dolomite–kyanite eclogites, and 675–754°C, 2.9–3.2 GPa for magnesite–kyanite eclogites, respectively, in the Qianmai area (Sun et al., 2019; Wang et al., 2020b; Wang W. et al., 2021).

The garnet phengite quartz (Grt-Ph-Qz) schists are the direct country rocks of the Bangbing eclogite body (Figure 2B). Grt-Ph-Qz schists are coarse grained and consist mainly of quartz (50%), phengite (35%), garnet (10%) and minor accessory mineral (5%) such as apatite and sphene. Quartz schists show well-developed foliation, and defined by fine layers of phengite, with garnet enclosed by the layers (Figure 2D). The mineral assemblages and microstructure suggest that quartz schists have suffered high pressure metamorphism. The peak P-T conditions of 1.88–2.16 GPa and 392–553°C were obtained by previous phase equilibrium simulations. The metamorphic zircon U-Pb and phengite $^{40}Ar/^{39}Ar$ isotopic analyses in the schist yielded consistent peak HP ages of 238–235 and 237–231 Ma, respectivel. A significant volume of sediments from the Lancang Group may

have been subducted to a depth of ~60–80 km in the Middle Triassic during the closure of the Paleotesti Ocean (Wang et al., 2020a).

The eclogite samples investigated in this work were collected from the Bangbin area, about 150 km south of Lincang (Figure 1B). The fresh eclogite samples (Sample D2810-1) from section b of the Lancang Group (Figure 1C) were selected for whole-rock major and trace element, and whole-rock Sr-Nd isotope analyses. The zircons separated from them were measured for U-Pb dating, trace element and Lu-Hf isotopic analyses. Comparatively, zircons separated from one surrounding rock sample (Sample D2810-2), a Grt-Ph-Qz schist, were also analysed for U-Pb dating. The two sampling sites were less than 50 m apart. Mineral abbreviations in this study are after Whitney and Evans (2010).

Analytical methods

Whole-rock major and trace elements

Major and trace element analyses of whole-rock geochemistry were conducted on X-ray fluorescence spectrometry (XRF, Primus II, Rigaku, Japan), inductively coupled plasma-mass spectrometry (ICP-MS, Agilent, 7,700 e, United States) at the Wuhan Sample Solution Analytical Technology Company Co., Ltd. Before analyses, samples were crushed and powdered to 200-mesh in an agate mill; then the sample powders were dried at 105°C in an oven. Four standards (AGV-2, BHVO-2, BCR-2 and RGM-2) were used to monitor the analytical quality. The relative standard deviations for the trace elements are within ±5%.

Zircon U-Pb dating, trace element and Lu-Hf isotopic

Zircons were separated by conventional heavy liquid and magnetic techniques at the Langfang Chengxin Geological Service Company (Hebei, China). Then they were handpicked under a binocular microscope, mounted in epoxy and polished to about half section. Cathodoluminescence (CL) images of zircon grains were taken on a Gatan Mono CL4 Cathode-Luminescence detector attached to a Zeiss Sigma 300 field emission SEM at the Wuhan Sample Solution Analytical Technology Company Co., Ltd., to observe the internal structure and to target potential sites for zircon U-Pb-Hf isotopic analyses.

In situ zircon U-Pb dating and trace element compositions were simultaneously analyzed by LA-ICP-MS at the Wuhan SampleSolution Analytical Technology Co., Ltd. China. Detailed operating conditions for the laser ablation system and the ICP-MS instrument and data reduction are the same as those described by Liu YS. et al. (2008). Laser sampling was performed using a GeolasPro laser ablation system that consists of a COMPexPro 102 ArF excimer laser (wavelength of 193 nm and maximum energy of 200 mJ) and a MicroLas optical system. An Agilent 7,700 e ICP-MS instrument was applied to acquire ion-signal intensities. Helium was applied as a carrier gas, which is mixed with Argon, the make-up gas, *via* a T-connector before entering the ICP. In this study, the spot size and frequency of the laser were set to 32 μm and 5 Hz, respectively. For every five analyses, zircon 91500, GJ-1 and glass NIST610 were used as external standards for U-Pb dating and trace element calibration. Each analysis incorporated a background acquisition of ~20–30 s followed by 50 s of data acquisition from the sample. Raw data were processed using an Excel-based software ICPMSDataCal (Liu et al., 2010). Concordia diagrams and age calculations were made using the program Isoplot/Ex_ver3 (Ludwig, 2003).

In situ zircon Lu-Hf isotopic analysis was conducted using a Neptune Plus MC-ICP-MS (Thermo Fisher Scientific, Germany) in combination with a Geolas HD excimer ArF laser ablation system (Coherent, Göttingen, Germany) at the Wuhan Sample Solution Analytical Technology Co., Ltd. China. In this study, all data were acquired on zircon in single spot ablation mode at a spot size of 44 μm, and the energy density of laser ablation was ~7.0 J cm^{-2}. Each measurement consisted of 20 s of acquisition of the background signal followed by 50 s of ablation signal acquisition. Detailed operating conditions for the laser ablation system and the MC-ICP-MS instrument and analytical method can be found in Hu et al. (2012). The calculated parameters used in this study are ^{176}Lu decay constants of 1.867×10^{-11} a^{-1} (Söderlund et al., 2004), $^{176}Hf/^{177}Hf$ and $^{176}Lu/^{177}Hf$ ratios of 0.2827720 and 0.0332 for Spherulitic meteorites, respectively (Blichert-Toft and Albarede., 1997), and present deficit mantle values of $^{176}Hf/^{177}Hf = 0.28325$ and $^{176}Lu/^{177}Hf = 0.0384$ (Griffin et al., 2000).

Whole-rock Sr-Nd isotopic

Whole-rock Sr-Nd-Pb isotopic analyses were carried out on a Neptune Plus MC-ICP-MS (Thermo Fisher Scientific, Dreieich, Germany) at the Wuhan Sample Solution Analytical Technology Co., Ltd., China. All chemical preparations were made on class 100 work benches within a class 1,000 over-pressured clean laboratory. The detailed methods and instrumentation for Sr-Nd isotopic analyses have been described by Li et al. (2012). During the Sr-Nd isotopic analyses, the NIST SRM 987 standard solution yielded $^{87}Sr/^{86}Sr$ ratio of 0.710,244 ± 0.000022 (2SD, n = 32) and the JNdi-1 106 standard gave $^{143}Nd/^{144}Nd$ ratio of 0.512118 ± 0.000015 (2SD, n = 31). In addition, the USGS107 reference materials BCR-2 (basalt) and RGM-2 (rhyolite) yielded results of 0.705034 ± 0.000014 (2SD, n = 4) and 0.704192 ± 0.000010 (2SD, n = 4) for $^{87}Sr/^{86}Sr$, 0.512644 ± 0.000015 (2SD, n= 6) and 0.512810 ± 0.000015 (2SD, n = 4) for $^{143}Nd/^{144}Nd$, respectively, both of which are identical within error to their published values (Li et al., 2012).

TABLE 1 Major, trace elements and Sr-Nd isotopes for the Bangbing eclogites.

Sample	D2810-1H1	D2810-1H2	D2810-1H3	D2810-1H4	D2810-1H5	D2810-1H6	D2810-1H7
Major element (%)							
SiO_2	47.77	46.49	47.00	45.92	47.02	50.95	49.65
TiO_2	2.01	2.00	1.98	2.01	2.07	1.44	1.46
Al_2O_3	14.74	14.58	14.53	14.78	15.00	15.23	15.60
TFeO	14.03	14.36	14.63	14.95	14.41	9.26	9.97
MnO	0.19	0.26	0.25	0.27	0.21	0.18	0.18
MgO	5.25	5.45	5.87	5.97	5.52	6.50	6.76
CaO	12.01	12.14	11.35	11.71	11.78	11.74	11.45
Na_2O	2.67	2.49	2.88	2.61	2.64	2.81	2.60
K_2O	0.16	0.24	0.39	0.32	0.39	0.18	0.49
P_2O_5	0.22	0.25	0.24	0.22	0.22	0.15	0.16
LOI	0.39	1.06	0.01	0.51	0.10	0.93	1.33
Trace element (ppm)							
Sc	37.66	37.68	37.10	38.44	39.59	36.17	37.24
V	305.27	310.12	301.04	307.49	311.88	317.23	319.78
Cr	148.33	156.04	155.58	163.34	144.29	123.51	130.67
Co	39.11	42.22	42.24	43.22	42.93	38.88	43.28
Ni	58.76	62.62	62.87	63.88	60.72	61.86	66.28
Cu	48.47	48.61	48.90	55.64	50.04	68.95	75.61
Zn	106.03	109.10	109.41	112.39	113.88	81.96	88.89
Ga	20.00	20.13	19.37	19.34	20.17	18.93	19.50
Rb	4.28	6.47	8.23	8.06	8.25	3.98	12.01
Sr	196.30	184.27	131.38	145.64	198.45	104.02	124.07
Y	50.28	47.38	49.32	50.80	52.05	27.46	27.52
Zr	175.28	175.65	164.53	170.40	177.46	97.19	98.34
Nb	14.35	14.55	14.62	15.26	15.68	9.02	9.23
Cs	0.88	1.38	0.94	1.40	0.77	0.37	1.19
Ba	19.73	29.75	51.38	40.73	50.93	21.32	50.06
La	14.03	14.08	13.01	12.75	15.91	9.56	8.01
Ce	31.02	31.80	29.43	29.45	34.78	21.54	19.72
Pr	4.18	4.20	3.95	4.04	4.66	2.87	2.80
Nd	19.22	19.15	17.92	18.12	21.52	13.51	13.17
Sm	5.23	5.37	5.15	5.28	6.01	3.93	3.90
Eu	1.76	1.66	1.63	1.70	1.86	1.32	1.30
Gd	6.77	6.73	6.77	6.66	7.24	4.89	4.65
Tb	1.25	1.20	1.26	1.24	1.28	0.78	0.75
Dy	8.03	7.75	8.28	8.45	8.44	4.73	4.67
Ho	1.72	1.76	1.77	1.83	1.84	0.94	0.99
Er	4.62	4.39	4.46	4.72	4.80	2.66	2.73
Tm	0.71	0.69	0.69	0.73	0.74	0.38	0.38
Yb	4.94	4.84	4.87	5.05	5.21	2.54	2.35
Lu	0.68	0.66	0.65	0.73	0.72	0.40	0.39
Hf	4.69	4.74	4.56	4.65	4.79	2.50	2.66
Ta	0.97	1.01	0.99	1.02	1.02	0.53	0.54
Pb	1.46	1.31	0.98	1.12	2.97	6.87	4.24
Th	1.69	1.69	1.67	1.57	1.80	1.05	1.08
U	0.53	0.51	0.43	0.48	0.97	0.28	0.24
∑REE	104	104	100	101	115	70	66

(Continued on following page)

TABLE 1 (*Continued*) Major, trace elements and Sr-Nd isotopes for the Bangbing eclogites.

Sample	D2810-1H1	D2810-1H2	D2810-1H3	D2810-1H4	D2810-1H5	D2810-1H6	D2810-1H7
δEu	0.90	0.84	0.85	0.88	0.86	0.92	0.93
$(La/Yb)_N$	2.04	2.08	1.92	1.81	2.19	2.70	2.45
$(La/Sm)_N$	1.73	1.69	1.63	1.56	1.71	1.57	1.32
Sr-Nd-Pb isotopes							
$^{87}Sr/^{86}Sr$	0.705,797	0.711922	0.707300			0.712837	0.708815
$^{143}Nd/^{144}Nd$	0.512773	0.512764	0.512731			0.512746	0.512750
$(^{87}Sr/^{86}Sr)t$	0.705392	0.711269	0.706136			0.712126	0.707016
$(^{143}Nd/^{144}Nd)t$	0.512287	0.512263	0.512218			0.512227	0.512221
εNd(*t*)	4.49	4.02	3.14			3.32	3.20

$(^{143}Nd/^{144}Nd)_t$ $(^{206}Pb/^{204}Pb)_t$, $\varepsilon_{Nd}(t)$ Values are calculated from t = 451 Ma. Parameters used for samples calibration $(^{143}Nd/^{144}Nd)_t=(^{143}Nd/^{144}Nd)_{sample}(^{147}Sm/^{144}Nd)_m\times(e^{\lambda t}-1)$, $\varepsilon_{Nd}(t)=[(^{143}Nd/^{144}Nd)_t/(^{143}Nd/^{144}Nd)_{CHUR(t)}-1]\times10^4$ $(^{143}Nd/^{144}Nd)_{CHUR(t)}=0.512,638-0.1967\times(e^{\lambda t}-1)$, $\lambda_{Sm-Nd}=6.54\times10^{-12}a^{-1}$.

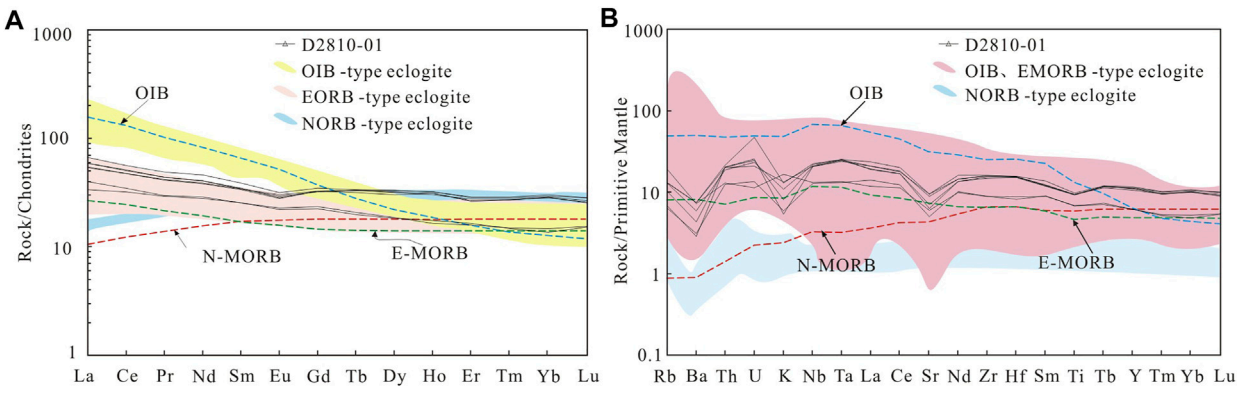

FIGURE 3
Chondrite-normalized rare earth element patterns **(A)** and primitive mantle-normalized trace element patterns **(B)** for Bangbing eclogites.

Results

Whole-rock major and trace elements

The major and trace elements in the Bangbing eclogites are listed in Table 1. The eclogites show losses of volatiles on ignition (LOI) ranging from 0.01 to 1.33 wt% with an average value of 0.62 wt%, indicating variable alteration of the rocks. All the eclogites samples have SiO_2 contents ranging from 45.92 to 50.59 wt%, averaging 47.83 wt%, with characteristics of basaltic. These samples are characterized by low MgO (5.25–6.76 wt%) contents, relatively high Al_2O_3 (14.53–15.60 wt%) and CaO (11.35–112.14 wt%) contents. K_2O/Na_2O ratios of 0.06–0.19 <1 and low all-alkaline (Na_2O+K_2O) contents (2.82–3.09 wt%) in the eclogites show compositional features corresponding to tholeiite basalt.

The total rare earth contents (∑REE) in the samples ranged from 66.00 to 115 ppm with an average of 94 ppm, which is higher than the typical E-MORB total REE (49.09×10^{-6}) and lower than the OIB total REE (Sun and McDonough, 1989). The chondrite normalized REE diagrams show that all the eclogites samples exhibit REE patterns characterized by light REE (LREE) enrichment, heavy REE (HREE) depletion and low degrees of LREE and HREE fractionation ($(La/Yb)_N$=1.81–2.70, averaging 2.17 $(La/Sm)_N$ = 1.32–1.73, averaging 1.60), and no significant negative Eu anomalies (δEu=0.84–0.93, averaging 0.88) (Figure 3A).

Normalized to primitive mantle, all the eclogites are characterized by a wide range of large ion lithophile elements (LILEs, e.g., Rb, Ba, K, U and Sr), a narrow range of high field-strength elements (HFSEs, e.g., Nb, Ta, Zr and Hf). The Ti in the samples has a slight negative anomaly, possibly affected by subduction fluids (Zheng, 2012). The trace elements are not

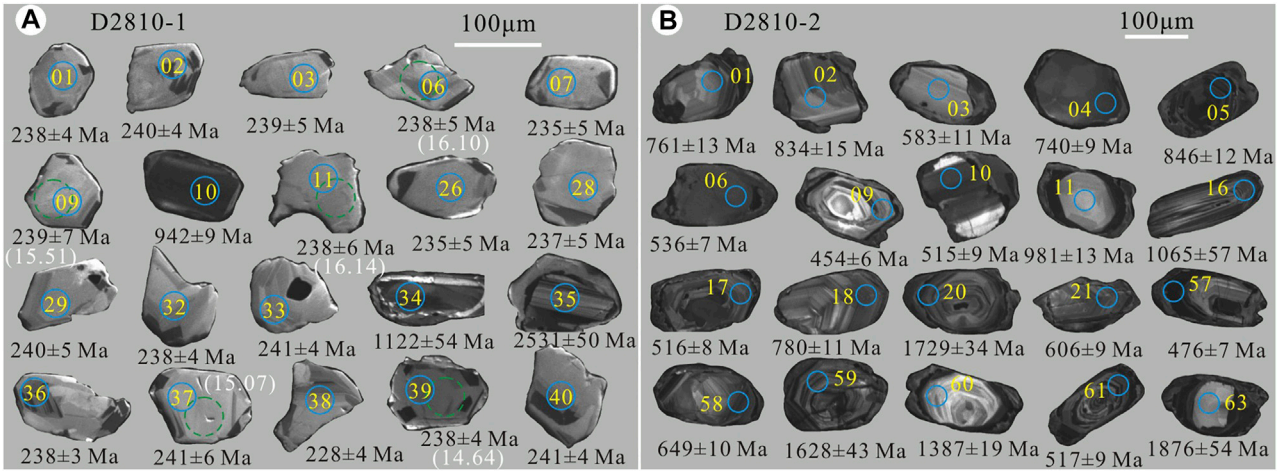

FIGURE 4
Zircon cathodoluminescence images and U-Pb ages, Hf isotope test spots for eclogites **(A)** and Grt-Ph schists **(B)**. Blue circles represent zircon analysis spots and green circles represent Hf isotope analysis spots. Data greater than 1,000 Ma follow $^{207}Pb/^{206}U$ ages, the rest follow $^{206}Pb/^{238}U$ ages.

obviously depleted or enriched and show nearly flat distribution patterns. These characteristics fall between E-MORB and OIB, and tend to be more in line with the former (Figure 3B).

Zircon U-Pb geochronology

Zircon grains were analysed from eclogite D2810-1 and its surrounding Grt-Ph-Qz schist D2810-2, separately. The CL images are presented in Figure 4. The U–Pb age data are listed in Table 2 and present in Figure 4.

In sample D2810-1, zircon grains are subhedral to euhedral crystal of plate. The lengths range from 60 to 150 μm with the aspect ratios of 1:1 to 1.5:1. (Figure 4). Some of them exhibit clear core–rim structures in cathodoluminescence (CL) images. The cores are zoned with dark or light grey oscillatory bands. The other part of the zircons show no core–rim structure or oscillating bands. The grains are more homogeneous internally and surrounded by narrow and bright overgrowths, indicative of a metamorphic origin. Forty spot analyses show $^{206}Pb/^{238}U$ ages ranging from 220 to 2,470 Ma and can be divided into three groups. Group I, $^{206}Pb/^{238}U$ ages, vary over a wide range from 256 to 2,470 Ma. The zircons obtained from this data group majority have core-rim structures with wide ranges of variation in Th and U content and high Th/U ratios (Th/U=0.12–6.91, Figure 5B), indicating magmatic zircon characteristics and may be captured. The second and third data groups are from zircons that show no rims, no cores and no oscillating rings. Group II $^{206}Pb/^{238}U$ ages range from 235 to 241 Ma, with U and Th contents of 43×10^{-6}–304 and 0.15–2.83 ppm, having low Th/U ratios of 0.004–0.01, much less than 0.1 (Figure 5B), indicative of a metamorphic origin. All twenty-five data spots in this group cluster on or near the harmonic line (Figure 5A), with a weighted mean of 238 ± 2 Ma (MSWD = 1.6). Discussion of this group of age data will be continued later. Group III of age data contains three spots. The zircon $^{206}Pb/^{238}U$ ages range from 220 to 229 Ma and, similar to the second group, have low Th/U ratios of 0.004–0.009, much less than 0.1 (Figure 5B), likely to represent much later ages of metamorphism.

In sample D2810-2, the morphology of the zircon grains appears to be more various than in the eclogites. The zircon grains are in long and short columns, 100–200 μm long. In the CL images, some grains show clear core-rim structure with an irregular, weakly luminescent, broad band in the core; some grains show homogeneous, undivided structure; while the other grains have distinct oscillatory bands of magmatic origin (Figure 4B). A total of 89 analyses on these zircons show high Th/U ratios ranging from 0.06 to 1.63 (only 4 spots less than 0.1), which generally correspond to the ranges of Th/U ratios of Group I capture- origin zircons from sample D2810-1 (Figure 5B). The ages range from 454 to 3,591 Ma (>1,000 Ma follow the $^{207}Pb/^{206}U$ age, the rest follow the $^{206}Pb/^{238}U$ age), and they have excellent harmonics (all >90% and most above 95%), all falling on or near the harmonic line (Figure 5C). In the zircon U-Pb age frequency histograms there are three dominant groups of age peaks, the youngest of which is around 450–600 Ma, with the rest at 700–1,200 Ma and 1,250–1800 Ma (Figure 5D).

Zircon trace elements

The zircon trace element content of the eclogite (sample D2810-1) is shown in Table 3. In the chondrite normalized REE

TABLE 2 Zircon LA-ICP-MS U-Pb age analysis results for Bangbing eclogites and their surrounding Grt-Ph schists.

Sample spot	Content ($\times10^{-6}$)		Th/U	Isotope ratio						Age/Ma					
	Th	U		$^{207}Pb/^{206}Pb$	1sigma	$^{207}Pb/^{235}U$	1sigma	$^{206}Pb/^{238}U$	1sigma	$^{207}Pb/^{206}Pb$	1sigma	$^{207}Pb/^{235}U$	1sigma	$^{206}Pb/^{238}U$	1sigma
D2810-1 Eclogites															
D2810-1-01	0.82	162	0.005	0.0551	0.0045	0.2779	0.0194	0.0377	0.0007	417	179	249	15	238	4
D2810-1-02	2.05	206	0.010	0.0506	0.0029	0.2654	0.0150	0.0380	0.0006	220	131	239	12	240	4
D2810-1-03	0.46	110	0.004	0.0563	0.0048	0.2826	0.0205	0.0377	0.0008	465	191	253	16	239	5
D2810-1-04	2.83	304	0.009	0.0524	0.0028	0.2692	0.0133	0.0371	0.0005	306	122	242	11	235	3
D2810-1-05	158	240	0.659	0.0527	0.0024	0.5426	0.0238	0.0744	0.0010	317	104	440	16	463	6
D2810-1-06	0.65	127	0.005	0.0531	0.0044	0.2736	0.0209	0.0375	0.0008	332	155	246	17	238	5
D2810-1-07	0.34	70	0.005	0.0532	0.0060	0.2606	0.0252	0.0371	0.0008	339	257	235	20	235	5
D2810-1-08	2.44	260	0.009	0.0498	0.0028	0.2415	0.0126	0.0348	0.0006	187	130	220	10	220	4
D2810-1-09	0.22	43	0.005	0.0496	0.0055	0.2512	0.0222	0.0378	0.0011	176	241	228	18	239	7
D2810-1-10	77	663	0.116	0.0669	0.0020	1.4614	0.0427	0.1574	0.0016	835	63	915	18	942	9
D2810-1-11	0.22	54	0.004	0.0535	0.0054	0.2585	0.0198	0.0377	0.0009	350	228	233	16	238	6
D2810-1-12	1	171	0.006	0.0499	0.0034	0.2546	0.0163	0.0374	0.0006	187	159	230	13	237	4
D2810-1-13	0.25	70	0.004	0.0485	0.0046	0.2536	0.0208	0.0382	0.0008	124	207	229	17	241	5
D2810-1-14	0.73	76	0.010	0.0486	0.0046	0.2464	0.0202	0.0379	0.0009	128	211	224	16	240	6
D2810-1-15	244	677	0.360	0.0690	0.0016	1.4340	0.0333	0.1494	0.0015	899	48	903	14	898	9
D2810-1-16	106	394	0.270	0.0686	0.0022	1.3945	0.0471	0.1461	0.0017	887	66	887	20	879	10
D2810-1-17	0.37	57	0.006	0.0549	0.0059	0.2698	0.0235	0.0380	0.0010	406	241	243	19	240	6
D2810-1-18	1.02	78	0.013	0.0529	0.0049	0.2645	0.0223	0.0380	0.0009	328	211	238	18	240	5
D2810-1-19	1.18	180	0.007	0.0509	0.0036	0.2519	0.0162	0.0361	0.0007	239	165	228	13	229	4
D2810-1-20	2.34	240	0.010	0.0476	0.0024	0.2458	0.0115	0.0379	0.0005	80	115	223	9	240	3
D2810-1-21	0.51	85	0.006	0.0494	0.0048	0.2444	0.0210	0.0376	0.0007	165	211	222	17	238	5
D2810-1-22	1,517	220	6.909	0.0603	0.0027	0.6598	0.0300	0.0788	0.0011	617	96	514	18	489	7
D2810-1-23	213	157	1.357	0.0566	0.0026	0.6338	0.0281	0.0812	0.0010	476	102	498	17	503	6
D2810-1-24	171	564	0.302	0.0693	0.0021	1.3974	0.0423	0.1451	0.0015	909	56	888	18	873	8
D2810-1-25	0.30	82	0.004	0.0526	0.0053	0.2648	0.0258	0.0373	0.0007	309	230	239	21	236	4
D2810-1-26	0.33	76	0.004	0.0504	0.0057	0.2520	0.0250	0.0370	0.0007	213	244	228	20	235	5
D2810-1-27	62	103	0.603	0.1069	0.0041	4.4798	0.1601	0.3009	0.0036	1747	70	1727	30	1,696	18
D2810-1-28	0.42	89	0.005	0.0520	0.0046	0.2522	0.0192	0.0374	0.0008	287	199	228	16	237	5
D2810-1-29	0.41	74	0.006	0.0543	0.0044	0.2763	0.0191	0.0379	0.0008	383	181	248	15	240	5
D2810-1-30	616	305	2.018	0.0544	0.0026	0.3063	0.0139	0.0406	0.0005	387	112	271	11	256	3
D2810-1-31	134	167	0.805	0.0575	0.0036	0.5664	0.0304	0.0722	0.0010	522	144	456	20	449	6

(Continued on following page)

TABLE 2 (*Continued*) Zircon LA-ICP-MS U-Pb age analysis results for Bangbing eclogites and their surrounding Grt-Ph schists.

Sample spot	Content ($\times10^{-6}$)		Th/U	Isotope ratio						Age/Ma					
	Th	U		$^{207}Pb/^{206}Pb$	1sigma	$^{207}Pb/^{235}U$	1sigma	$^{206}Pb/^{238}U$	1sigma	$^{207}Pb/^{206}Pb$	1sigma	$^{207}Pb/^{235}U$	1sigma	$^{206}Pb/^{238}U$	1sigma
D2810-1-32	0.79	146	0.005	0.0499	0.0036	0.2566	0.0177	0.0376	0.0007	191	167	232	14	238	4
D2810-1-33	1.12	153	0.007	0.0468	0.0034	0.2422	0.0157	0.0380	0.0006	43	163	220	13	241	4
D2810-1-34	238	358	0.664	0.0766	0.0021	1.8410	0.0524	0.1731	0.0018	1,122	54	1,060	19	1,029	10
D2810-1-35	82	245	0.333	0.1673	0.0051	10.8362	0.3519	0.4669	0.0070	2531	50	2509	30	2470	31
D2810-1-36	2.65	265	0.010	0.0517	0.0027	0.2668	0.0134	0.0377	0.0005	272	119	240	11	238	3
D2810-1-37	0.15	44.2	0.003	0.0570	0.0059	0.2857	0.0240	0.0381	0.0010	500	231	255	19	241	6
D2810-1-38	0.40	110	0.004	0.0485	0.0036	0.2388	0.0165	0.0360	0.0006	120	180	217	14	228	4
D2810-1-39	1.11	171	0.006	0.0510	0.0029	0.2629	0.0135	0.0376	0.0006	243	131	237	11	238	4
D2810-1-40	0.49	103	0.005	0.0544	0.0037	0.2811	0.0172	0.0380	0.0007	387	152	252	14	241	4
D2810-2 Grt-Ph schist															
D2810-2-01	187	448	0.42	0.0704	0.0021	1.2245	0.0401	0.1253	0.0022	940	66	812	18	761	13
D2810-2-02	216	319	0.67	0.0735	0.0022	1.4090	0.0484	0.1381	0.0026	1,028	62	893	20	834	15
D2810-2-03	60	191	0.32	0.0638	0.0028	0.8387	0.0381	0.0947	0.0019	744	93	618	21	583	11
D2810-2-04	314	416	0.75	0.0636	0.0019	1.0692	0.0323	0.1216	0.0015	728	64	738	16	740	9
D2810-2-05	616	1,119	0.55	0.0723	0.0015	1.4092	0.0347	0.1402	0.0022	994	42	893	15	846	12
D2810-2-06	235	561	0.42	0.0599	0.0017	0.7163	0.0204	0.0866	0.0011	611	31	548	12	536	7
D2810-2-07	184	541	0.34	0.0656	0.0016	1.1324	0.0293	0.1242	0.0014	794	58	769	14	754	8
D2810-2-08	221	311	0.71	0.0625	0.0019	0.8808	0.0276	0.1017	0.0013	692	71	641	15	624	8
D2810-2-09	333	430	0.78	0.0577	0.0018	0.5809	0.0180	0.0730	0.0010	517	66	465	12	454	6
D2810-2-10	72	594	0.12	0.0586	0.0018	0.6826	0.0245	0.0832	0.0015	554	69	528	15	515	9
D2810-2-11	346	316	1.10	0.0698	0.0021	1.5852	0.0460	0.1645	0.0023	920	61	964	18	981	13
D2810-2-12	311	633	0.49	0.0691	0.0019	1.1746	0.0366	0.1224	0.0023	902	61	789	17	745	13
D2810-2-13	680	1,163	0.58	0.0767	0.0018	1.8710	0.0452	0.1752	0.0026	1,115	14	1,071	16	1,041	14
D2810-2-14	349	282	1.24	0.0723	0.0027	1.2518	0.0469	0.1245	0.0019	994	108	824	21	756	11
D2810-2-15	231	375	0.62	0.0713	0.0020	1.6784	0.0513	0.1688	0.0027	965	64	1,000	19	1,006	15
D2810-2-16	129	481	0.27	0.0748	0.0021	1.8317	0.0505	0.1768	0.0025	1,065	57	1,057	18	1,049	14
D2810-2-17	563	383	1.47	0.0609	0.0020	0.7019	0.0232	0.0833	0.0014	635	72	540	14	516	8
D2810-2-18	117	545	0.22	0.0754	0.0021	1.3526	0.0402	0.1286	0.0019	1,080	57	869	17	780	11
D2810-2-19	221	508	0.43	0.0727	0.0022	1.3126	0.0449	0.1290	0.0023	1,006	62	851	20	782	13
D2810-2-20	295	367	0.80	0.1059	0.0023	4.1912	0.0939	0.2839	0.0032	1729	34	1,672	18	1,611	16
D2810-2-21	191	565	0.34	0.0665	0.0018	0.9087	0.0247	0.0987	0.0015	833	54	656	13	606	9
D2810-2-22	170	650	0.26	0.0777	0.0018	1.8882	0.0447	0.1748	0.0022	1,140	45	1,077	16	1,039	12
D2810-2-23	102	291	0.35	0.0796	0.0023	2.0262	0.0553	0.1847	0.0025	1,187	57	1,124	19	1,093	14

(Continued on following page)

TABLE 2 (*Continued*) Zircon LA-ICP-MS U-Pb age analysis results for Bangbing eclogites and their surrounding Grt-Ph schists.

Sample spot	Content ($\times10^{-6}$)		Th/U	Isotope ratio						Age/Ma					
	Th	U		$^{207}Pb/^{206}Pb$	1sigma	$^{207}Pb/^{235}U$	1sigma	$^{206}Pb/^{238}U$	1sigma	$^{207}Pb/^{206}Pb$	1sigma	$^{207}Pb/^{235}U$	1sigma	$^{206}Pb/^{238}U$	1sigma
D2810-2-24	92	323	0.28	0.1021	0.0025	3.5831	0.0904	0.2527	0.0032	1,665	46	1,546	20	1,452	16
D2810-2-25	150	232	0.65	0.0684	0.0027	1.1885	0.0475	0.1260	0.0020	880	84	795	22	765	11
D2810-2-26	523	1,075	0.49	0.0613	0.0019	0.6698	0.0205	0.0791	0.0011	650	69	521	12	491	7
D2810-2-27	339	664	0.51	0.0750	0.0022	1.5477	0.0458	0.1488	0.0020	1,133	58	950	18	894	11
D2810-2-28	397	386	1.03	0.0831	0.0025	1.9986	0.0693	0.1720	0.0028	1,272	59	1,115	23	1,023	15
D2810-2-29	77	1,378	0.06	0.0732	0.0019	1.2824	0.0358	0.1263	0.0017	1,020	54	838	16	767	10
D2810-2-30	577	1701	0.34	0.0687	0.0016	1.1302	0.0265	0.1188	0.0015	889	81	768	13	724	9
D2810-2-31	468	668	0.70	0.1041	0.0022	3.7809	0.0808	0.2630	0.0037	1,698	40	1,589	17	1,505	19
D2810-2-32	524	412	1.27	0.1638	0.0034	8.7129	0.1962	0.3831	0.0052	2495	35	2308	21	2091	24
D2810-2-33	224	931	0.24	0.0863	0.0017	2.7471	0.0597	0.2289	0.0028	1,346	39	1,341	16	1,329	15
D2810-2-34	89	918	0.10	0.0913	0.0019	2.5343	0.0573	0.2002	0.0030	1,454	39	1,282	16	1,176	16
D2810-2-35	487	508	0.96	0.0588	0.0019	0.7151	0.0227	0.0879	0.0012	561	70	548	13	543	7
D2810-2-36	486	1,051	0.46	0.0680	0.0016	1.1623	0.0289	0.1231	0.0016	878	50	783	14	748	9
D2810-2-37	211	302	0.70	0.0674	0.0022	1.3508	0.0442	0.1455	0.0023	850	64	868	19	875	13
D2810-2-38	151	258	0.58	0.0707	0.0019	1.7297	0.0504	0.1759	0.0026	950	56	1,020	19	1,045	14
D2810-2-39	329	535	0.61	0.1024	0.0023	4.1094	0.0945	0.2887	0.0037	1,678	42	1,656	19	1,635	18
D2810-2-40	947	746	1.27	0.0823	0.0021	2.0991	0.0565	0.1832	0.0026	1,254	18	1,149	19	1,084	14
D2810-2-41	226	287	0.79	0.0978	0.0027	3.7252	0.1074	0.2740	0.0043	1,583	51	1,577	23	1,561	22
D2810-2-42	444	400	1.11	0.0807	0.0022	2.1071	0.0590	0.1893	0.0033	1,215	59	1,151	19	1,118	18
D2810-2-43	230	284	0.81	0.0706	0.0021	1.6494	0.0481	0.1695	0.0026	946	61	989	18	1,009	14
D2810-2-44	186	394	0.47	0.0689	0.0023	1.1767	0.0405	0.1236	0.0021	895	67	790	19	751	12
D2810-2-45	351	622	0.56	0.0740	0.0019	1.7915	0.0552	0.1742	0.0037	1,043	55	1,042	20	1,035	20
D2810-2-46	387	782	0.50	0.0728	0.0017	1.5746	0.0376	0.1558	0.0022	1,009	46	960	15	933	12
D2810-2-47	419	1,109	0.38	0.0985	0.0019	3.2800	0.0664	0.2398	0.0030	1,596	36	1,476	16	1,386	15
D2810-2-48	873	775	1.13	0.0700	0.0017	1.3251	0.0340	0.1363	0.0019	929	49	857	15	824	11
D2810-2-49	430	552	0.78	0.0722	0.0017	1.4216	0.0346	0.1425	0.0020	991	49	898	15	859	11
D2810-2-50	453	560	0.81	0.0823	0.0022	2.1536	0.0630	0.1884	0.0028	1,254	19	1,166	20	1,113	15
D2810-2-51	212	605	0.35	0.0711	0.0017	1.4084	0.0332	0.1432	0.0017	961	49	892	14	863	10
D2810-2-52	98	1,218	0.08	0.0659	0.0016	1.1829	0.0271	0.1301	0.0017	1,200	51	793	13	789	10
D2810-2-53	176	635	0.28	0.0716	0.0018	1.6708	0.0476	0.1686	0.0031	976	55	998	18	1,004	17
D2810-2-54	176	222	0.79	0.0675	0.0024	1.4834	0.0506	0.1605	0.0025	854	68	924	21	960	14
D2810-2-55	199	463	0.43	0.0773	0.0020	1.6585	0.0450	0.1552	0.0022	1,128	58	993	17	930	12
	673	909	0.74	0.3240	0.0068	31.1132	0.7165	0.6936	0.0102	3,591	32	3,523	23	3,396	39

(Continued on following page)

TABLE 2 (*Continued*) Zircon LA-ICP-MS U-Pb age analysis results for Bangbing eclogites and their surrounding Grt-Ph schists.

Sample spot	Content ($\times10^{-6}$)		Th/U	Isotope ratio						Age/Ma					
	Th	U		$^{207}Pb/^{206}Pb$	1sigma	$^{207}Pb/^{235}U$	1sigma	$^{206}Pb/^{238}U$	1sigma	$^{207}Pb/^{206}Pb$	1sigma	$^{207}Pb/^{235}U$	1sigma	$^{206}Pb/^{238}U$	1sigma
D2810-2-56															
D2810-2-57	97	1,553	0.06	0.0591	0.0016	0.6282	0.0182	0.0767	0.0012	569	62	495	11	476	7
D2810-2-58	442	479	0.92	0.0639	0.0020	0.9305	0.0289	0.1059	0.0017	739	264	668	15	649	10
D2810-2-59	623	682	0.91	0.1002	0.0023	3.9074	0.0982	0.2820	0.0043	1,628	43	1,615	20	1,601	22
D2810-2-60	119	209	0.57	0.0882	0.0024	2.7151	0.0733	0.2234	0.0031	1,387	19	1,333	20	1,300	17
D2810-2-61	701	815	0.86	0.0606	0.0019	0.6961	0.0230	0.0835	0.0015	633	73	536	14	517	9
D2810-2-62	185	278	0.66	0.0711	0.0021	1.5028	0.0474	0.1539	0.0023	961	61	932	19	923	13
D2810-2-63	75	124	0.61	0.1147	0.0034	4.5940	0.1365	0.2911	0.0041	1876	54	1748	25	1,647	21
D2810-2-64	131	359	0.37	0.0681	0.0019	1.4591	0.0410	0.1553	0.0020	872	57	914	17	930	11
D2810-2-65	904	1,018	0.89	0.0806	0.0017	2.1972	0.0482	0.1967	0.0023	1,213	41	1,180	15	1,158	13
D2810-2-66	847	853	0.99	0.0730	0.0018	1.4341	0.0336	0.1430	0.0019	1,013	48	903	14	862	10
D2810-2-67	326	395	0.83	0.0932	0.0024	2.3825	0.0702	0.1849	0.0033	1,492	49	1,237	21	1,094	18
D2810-2-68	212	626	0.34	0.0695	0.0018	1.1808	0.0312	0.1234	0.0019	922	53	792	15	750	11
D2810-2-69	187	190	0.98	0.0630	0.0025	1.0185	0.0451	0.1158	0.0019	709	84	713	23	706	11
D2810-2-70	145	376	0.38	0.0876	0.0023	2.1524	0.0576	0.1781	0.0024	1,373	56	1,166	19	1,057	13
D2810-2-71	43	436	0.10	0.2729	0.0053	24.1833	0.5147	0.6403	0.0083	3,323	30	3,276	21	3,190	33
D2810-2-72	93	1,171	0.08	0.0673	0.0018	1.1045	0.0318	0.1182	0.0016	856	54	756	15	720	9
D2810-2-73	186	690	0.27	0.1643	0.0037	9.3819	0.2442	0.4134	0.0072	2502	38	2376	24	2230	33
D2810-2-74	301	582	0.52	0.1043	0.0026	3.7635	0.0947	0.2618	0.0036	1702	45	1,585	20	1,499	18
D2810-2-75	126	374	0.34	0.0648	0.0021	1.1655	0.0436	0.1300	0.0024	769	69	785	20	788	14
D2810-2-76	140	219	0.64	0.0747	0.0027	1.5589	0.0567	0.1521	0.0023	1,061	79	954	23	913	13
D2810-2-77	375	573	0.66	0.1007	0.0022	3.7950	0.0861	0.2723	0.0033	1,639	41	1,592	18	1,553	17
D2810-2-78	252	255	0.99	0.0618	0.0025	0.7277	0.0292	0.0863	0.0014	733	82	555	17	534	9
D2810-2-79	90	153	0.58	0.0757	0.0028	1.7338	0.0645	0.1670	0.0027	1,087	74	1,021	24	995	15
D2810-2-80	796	866	0.92	0.0857	0.0018	2.6439	0.0608	0.2226	0.0030	1,331	36	1,313	17	1,296	16
D2810-2-81	113	168	0.67	0.0820	0.0024	2.3465	0.0722	0.2073	0.0030	1,256	58	1,226	22	1,215	16
D2810-2-82	171	355	0.48	0.0732	0.0020	1.8535	0.0537	0.1843	0.0031	1,020	56	1,065	19	1,090	17
D2810-2-83	555	1,114	0.50	0.0769	0.0018	1.9594	0.0510	0.1839	0.0027	1,120	46	1,102	18	1,088	15
D2810-2-84	126	249	0.50	0.0736	0.0021	1.6877	0.0463	0.1672	0.0025	1,031	58	1,004	18	997	14
D2810-2-85	822	514	1.60	0.0759	0.0020	1.7696	0.0472	0.1689	0.0023	1,094	54	1,034	17	1,006	13
D2810-2-86	244	149	1.63	0.0754	0.0028	1.9517	0.0705	0.1899	0.0033	1,080	73	1,099	24	1,121	18
D2810-2-87	234	176	1.33	0.0665	0.0032	0.7933	0.0370	0.0870	0.0015	833	100	593	21	538	9
	93	227	0.41	0.0717	0.0028	1.3924	0.0583	0.1404	0.0026	989	81	886	25	847	15

(Continued on following page)

TABLE 2 (*Continued*) Zircon LA-ICP-MS U-Pb age analysis results for Bangbing eclogites and their surrounding Grt-Ph schists.

Sample spot	Content ($\times10^{-6}$)		Th/U	Isotope ratio						Age/Ma					
	Th	U		$^{207}Pb/^{206}Pb$	1sigma	$^{207}Pb/^{235}U$	1sigma	$^{206}Pb/^{238}U$	1sigma	$^{207}Pb/^{206}Pb$	1sigma	$^{207}Pb/^{235}U$	1sigma	$^{206}Pb/^{238}U$	1sigma
D2810-2-88															
D2810-2-89	311	491	0.63	0.0763	0.0022	1.7947	0.0518	0.1702	0.0025	1,102	51	1,044	19	1,013	14

TABLE 3 Zircon LA-ICP-MS trace element (ppm) analyses for Bangbing eclogites.

Sample spot	Y	Nb	Ta	La	Ce	Pr	Nd	Sm	Eu	Gd	Tb	Dy	Ho	Er	Tm	Yb	Lu	Ti	*T*°C	δEu
D2810-1-01	63	0.11	0.01	dd	0.13	dd	0.02	0.45	0.48	4.77	1.50	9.80	2.04	5.18	0.84	5.73	1.13	4.15	670	1.01
D2810-1-02	54	0.22	0.05	dd	0.17	dd	dd	0.06	0.16	2.51	0.86	7.34	1.77	4.64	0.70	4.78	0.82	1.26	582	1.19
D2810-1-03	47	0.16	0.03	dd	0.09	dd	dd	0.14	0.45	3.72	1.01	7.52	1.52	3.92	0.58	4.45	0.97	3.29	651	1.88
D2810-1-04	69	0.23	0.03	dd	0.26	dd	dd	0.06	0.28	3.18	1.11	10.08	2.18	6.06	0.81	5.42	0.98	2.55	632	1.98
D2810-1-05	1,187	2.64	0.92	0.01	12.51	0.05	1.05	2.73	1.01	17.47	6.58	92.52	40.07	192.52	44.45	436.93	99.06	11.73	761	0.45
D2810-1-06	85	0.19	0.03	dd	0.18	dd	0.08	0.12	0.35	3.49	1.23	11.42	2.93	9.01	1.36	10.52	1.99	4.08	668	1.68
D2810-1-07	52	0.09	0.02	0.01	0.08	dd	dd	0.18	0.43	5.18	1.26	8.96	1.65	4.22	0.60	5.10	0.87	1.14	576	1.39
D2810-1-08	50	0.13	0.01	0.15	dd	0.03	0.12	0.28	3.53	0.96	7.57	1.75	4.51	0.67	5.39	0.99	0.03	2.49	630	1.33
D2810-1-09	33	0.09	dd	0.07	dd	dd	0.24	0.20	2.62	0.85	5.19	1.01	2.72	0.39	3.42	0.72	0.04	1.15	576	0.79
D2810-1-10	826	1.90	1.23	dd	2.37	0.03	0.88	3.20	0.11	17.38	6.99	80.47	28.43	118.49	24.72	220.97	45.09	15.24	787	0.04
D2810-1-11	60	0.10	0.03	dd	0.14	dd	dd	0.33	0.32	4.04	1.16	8.32	1.94	5.58	0.84	6.25	1.26			0.84
D2810-1-12	56	0.16	0.04	dd	0.16	dd	dd	0.40	0.32	3.52	1.15	7.82	1.68	4.81	0.69	4.02	0.99	3.92	665	0.83
D2810-1-13	49	0.17	0.02	dd	0.11	dd	0.02	0.26	0.27	3.20	1.01	6.83	1.44	4.29	0.79	6.14	1.19	5.68	695	0.93
D2810-1-14	92	0.12	0.01	dd	0.09	dd	dd	0.15	0.34	2.67	1.16	11.06	2.85	8.65	1.40	9.48	2.08	2.90	642	1.65
D2810-1-15	1,327	9.90	4.75	dd	15.95	0.05	1.43	3.91	0.09	24.84	9.30	117.87	47.57	218.91	44.78	395.07	76.69	5.07	686	0.03
D2810-1-16	124	1.23	0.67	0.01	1.07	0.02	0.86	2.25	0.05	11.08	2.81	20.08	4.22	11.84	1.97	14.16	2.68	9.24	739	0.03
D2810-1-17	47	0.12	0.02	dd	0.08	dd	dd	0.08	0.09	1.96	0.56	5.22	1.49	4.42	0.61	4.59	0.83	1.31	585	0.70
D2810-1-18	83	0.18	0.02	dd	0.14	dd	0.05	0.20	0.20	2.96	1.21	9.78	2.46	7.98	1.19	7.72	1.67	3.51	656	0.78
D2810-1-19	54	0.20	0.04	dd	0.13	dd	0.06	0.20	0.37	2.82	1.05	7.57	1.80	5.15	0.79	5.58	1.16	2.24	622	1.50
D2810-1-20	66	0.14	0.04	dd	0.25	dd	0.03	0.26	0.36	3.31	1.11	9.00	2.00	5.82	0.78	4.62	0.82	4.10	669	1.19
D2810-1-21	100	0.12	0.02	dd	0.13	dd	0.05	0.24	0.32	3.62	1.38	12.34	3.36	9.18	1.32	9.45	1.88	0.63	539	1.04
D2810-1-22	1773	3.58	0.71	0.51	254.02	3.04	43.30	47.69	20.37	130.58	28.29	231.55	64.65	226.15	39.67	317.48	57.89	19.15	811	0.79
D2810-1-23	699	1.97	0.97	0.01	36.25	0.16	3.26	5.87	1.05	24.10	6.71	73.64	24.10	101.67	20.24	170.90	33.55	3.14	647	0.27
D2810-1-24	771	0.78	0.63	0.04	2.28	0.19	3.07	6.73	0.20	38.93	10.63	93.69	26.46	95.00	16.47	129.91	24.27	6.44	706	0.04
D2810-1-25	120	0.16	0.04	dd	0.12	dd	dd	0.18	0.40	3.86	1.59	14.26	3.77	11.59	1.67	11.89	2.38	1.57	597	1.47
D2810-1-26	84	0.13	0.03	dd	0.07	dd	0.02	0.26	0.28	3.12	1.19	10.25	2.48	8.21	1.21	8.50	1.83	3.02	645	0.94
D2810-1-27	469	1.12	0.68	dd	12.83	0.02	0.91	2.21	0.61	8.65	3.20	40.36	15.25	72.07	16.01	158.15	36.29	6.42	706	0.42
D2810-1-28	65	0.17	0.05	dd	0.10	dd	0.05	0.27	0.26	2.91	0.96	8.28	2.11	5.97	0.85	6.87	1.37	1.64	601	0.90
D2810-1-29	71	0.13	0.04	dd	0.11	dd	0.02	0.22	0.27	3.25	1.09	8.56	2.14	6.49	0.89	6.89	1.44	3.34	652	0.97
D2810-1-30	1,460	3.69	0.81	0.01	119.81	0.21	4.22	7.49	3.32	42.78	12.71	140.35	50.56	220.25	43.95	398.08	81.64	3.98	666	0.57
D2810-1-31	677	1.10	0.68	dd	14.94	0.06	0.95	2.15	0.46	12.98	4.83	56.58	22.54	104.40	21.69	197.62	41.57	10.52	751	0.27
D2810-1-32	70	0.11	0.05	0.01	0.11	dd	0.02	0.22	0.30	3.85	1.10	9.23	2.27	6.78	0.95	5.62	1.24	1.96	613	0.98
D2810-1-33	58	0.20	0.03	dd	0.13	dd	dd	0.22	0.23	3.00	0.85	7.93	1.91	5.17	0.68	4.96	0.91	1.73	604	0.85
D2810-1-34	596	2.66	1.84	0.02	15.38	0.11	1.27	3.00	0.11	14.39	4.62	54.40	21.21	91.76	18.81	17dd	32.86	3.78	662	0.05
D2810-1-35	374	0.83	0.47	0.02	7.51	0.07	1.06	1.41	0.39	8.49	2.86	31.20	12.43	57.22	12.42	119.74	28.06	4.48	676	0.35
D2810-1-36	62	0.27	0.05	0.01	0.21	dd	0.02	0.13	0.30	2.60	0.94	8.74	1.97	5.90	0.70	4.33	0.80	3.87	664	1.53
D2810-1-37	27	0.10	0.03	dd	0.06	dd	dd	0.23	0.29	2.45	0.71	3.87	0.84	1.82	0.33	2.52	0.57	2.53	631	1.19
D2810-1-38	56	0.19	0.03	0.01	0.14	dd	dd	0.41	0.31	3.46	1.12	7.40	1.72	4.60	0.68	5.15	1.06	1.75	605	0.79
D2810-1-39	74	0.12	0.03	dd	0.12	dd	0.06	0.35	0.37	4.78	1.41	12.13	2.44	6.69	0.96	7.20	1.54	4.23	671	0.88
D2810-1-40	113	0.09	0.03	dd	0.08	dd	0.02	0.31	0.27	4.18	1.44	13.19	3.58	10.62	1.48	11.42	2.19	0.19	474	0.73

dd indicates below detection limits. T°C according to Ferry and Watson, 2007, by assuming that $\alpha_{TiO2}=\alpha_{SiO2}$.

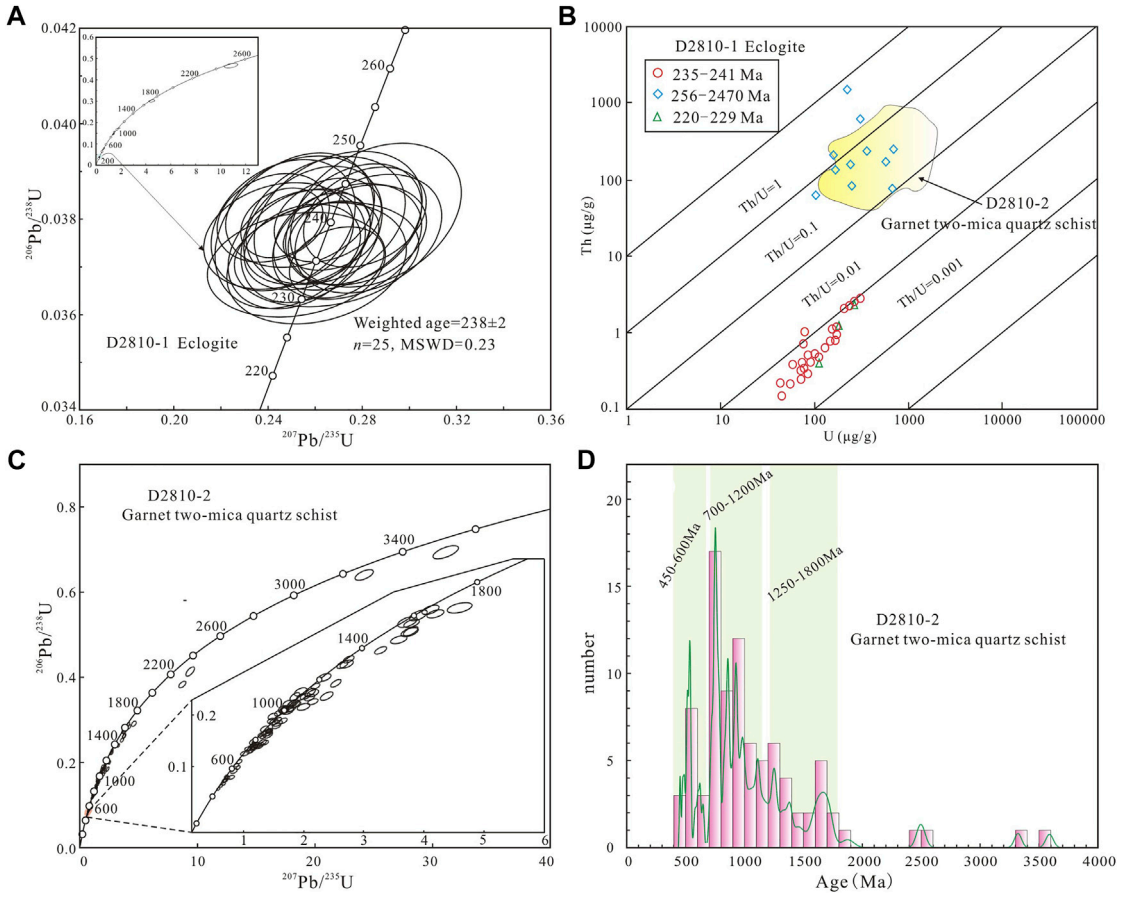

FIGURE 5
Zircon U-Pb ages **(A,C,D)** and Th/U ratios **(B)** for eclogites and Grt-Ph schists.

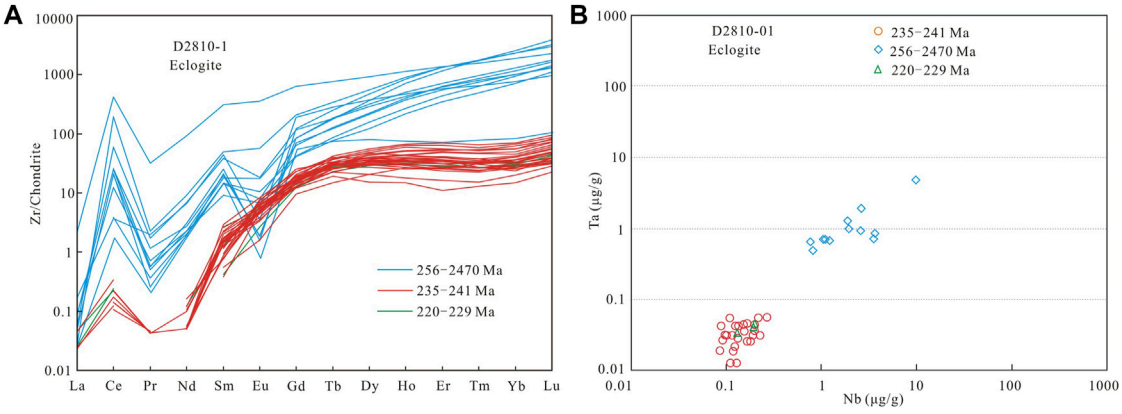

FIGURE 6
REE patterns **(A)** and Nb-Ta contents **(B)** of zircons from Bangbing eclogites.

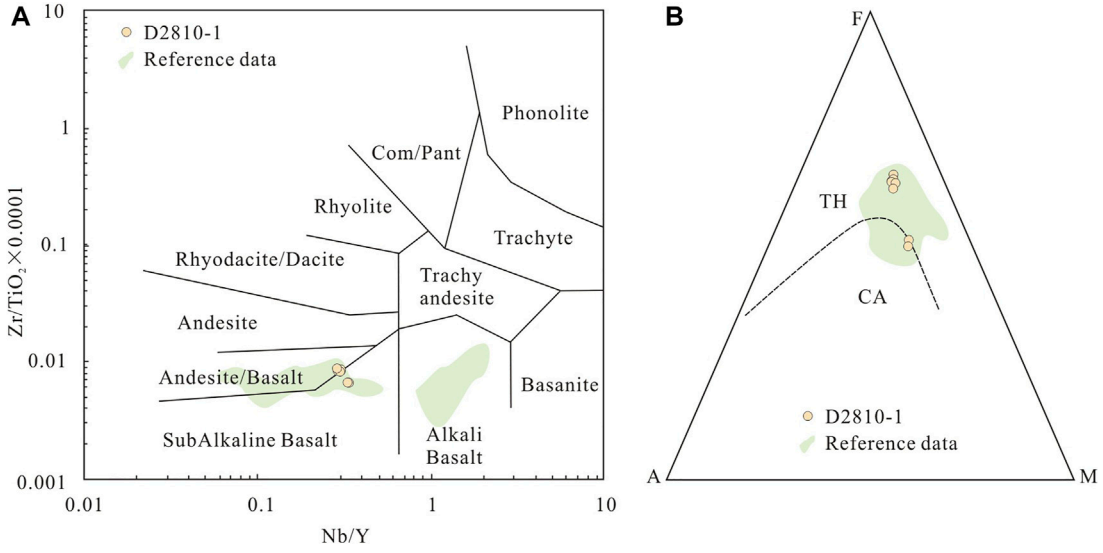

FIGURE 7
Zr/TiO_2-Nb/Y **(A)** and AFM **(B)** illustration for Bangbing eclogites.

TABLE 4 Zircon Lu-Hf isotope analysis results for Bangbing eclogites.

Sample spot	Age (Ma)	$^{176}Yb/^{177}Hf$	1σ	$^{176}Lu/^{177}Hf$	1σ	$^{176}Hf/^{177}Hf$	1σ	$\varepsilon_{Hf}(0)$	$\varepsilon_{Hf}(t)$	t_{DM1} (Ma)	t_{DM2} (Ma)	$f_{Lu/Hf}$
D2810-1												
06	451	0.000539	0.000021	0.000017	0.000001	0.282946	0.000012	6.16	16.10	422	404	−1.00
09	451	0.000420	0.000008	0.000014	0.000001	0.282929	0.000012	5.57	15.51	443	442	−1.00
11	451	0.000426	0.000015	0.000013	0.000001	0.282947	0.000014	6.20	16.14	421	402	−1.00
37	451	0.000407	0.000007	0.000012	0.000001	0.282917	0.000011	5.13	15.07	463	470	−1.00
39	451	0.000521	0.000012	0.000017	0.000001	0.282,905	0.000014	4.70	14.64	480	498	−1.00

diagrams, the sample shows a general pattern of LREE depletion and HREE enrichment gradually (Figure 6A). However, there are obvious differences in REE patterns between the core-rim and non-core-rim structures test spots. (1) ∑REE: high and variable for those with core-rim structures (73–1,465 ppm) and low for those without core-rim structures (14–52 ppm). (2) Enrichment of HREE: HREEs are significantly more abundant in core-rim structures (69–1,096 ppm), with high degrees of fractionation (1.28–25.01). Comparatively, HREEs in non-core-rim structures range from 13 to 51 ppm, with low degrees of fractionation of 0.85–3.55. (3) Eu and Ce anomalies: Eu negative anomalies are more strongly apparent in the non-core-rim than in the core-rim structures (0.03–0.79, mean 0.27; 0.70–1.98, mean 1.14). Conversely, Ce positive anomalies are more obvious in the core-rim structures.

The Y, Nb and Ta contents vary considerably in the zircons with different structures. The Nb and Ta contents and ratios of the test spots in the core-rim structures are much higher than those in the non-core-rim structures. Ti contents range 3.14–19.15 ppm and 0.19–5.68 ppm, respectively, corresponding to formed temperatures of 647–811°C (mean 716°C) and 447–695°C (mean 629°C, excluding 447°C) (calculated after Ferry and Watson, 2007).

Whole-rock Sr-Nd isotope

The results of whole-rock Sr-Nd isotope analysis are shown in Table 1. The eclogite samples have $^{87}Sr/^{86}Sr$ ranging from 0.705797 to 0.712837, mean=0.709334.$^{143}Nd/^{144}Nd$ range from 0.512731 to 0.512773, mean=0.512753 $(^{87}Sr/^{86}Sr)t$ range from 0.705392 to 0.712126, mean=0.708387 $(^{143}Nd/^{144}Nd)t$ range from 0.512218 to 0.512287, mean=0.5122432. $\varepsilon_{Nd}(t)$ values range from 3.14 to 4.49, mean=3.63 (t=451 Ma, Wang et al., 2019).

Zircon Lu-Hf isotope

The locations of the analyzed spots for the single grain zircon Lu-Hf isotope are shown in Figure 4 and their results are

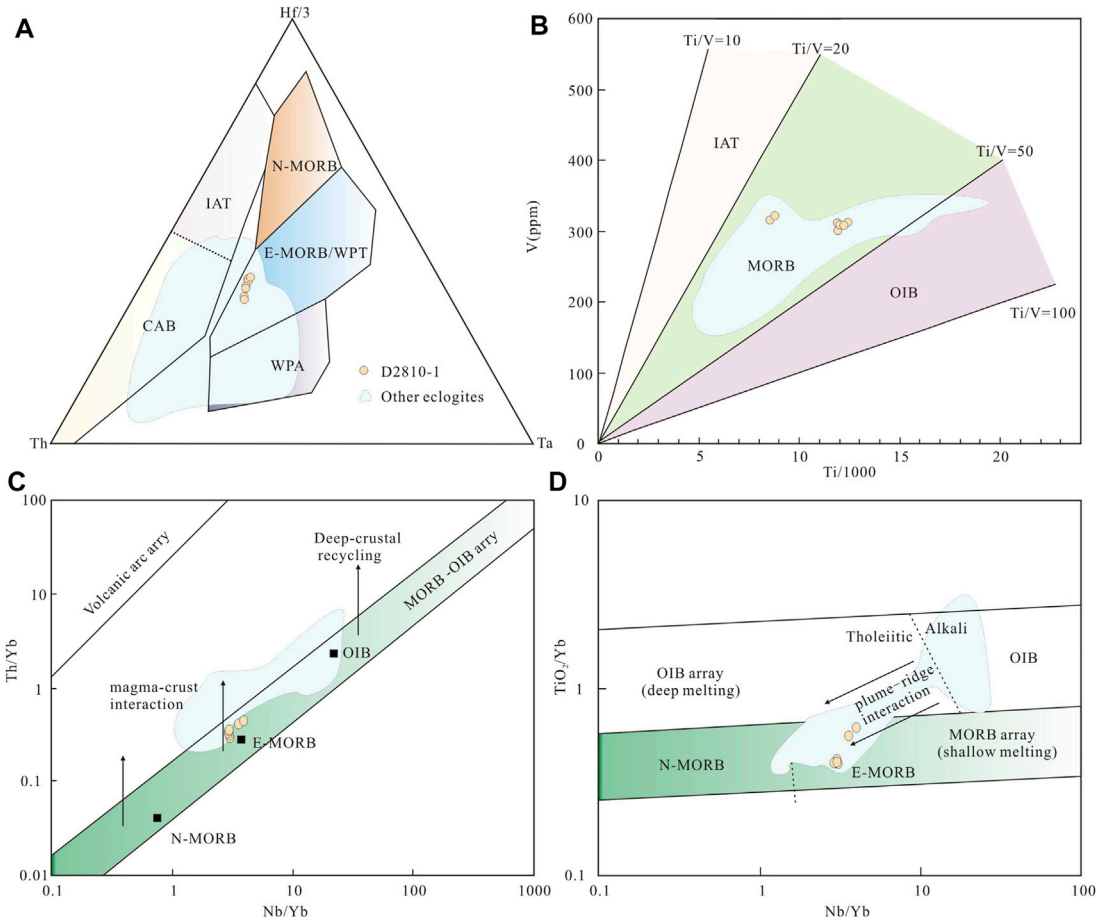

FIGURE 8
Discrimination diagrams of tectonic settings for Bangbing eclogites. **(A)** Hf/3-Th-Ta (after Wood, 1980). **(B)** V-Ti/1,000 (after Shervais, 1982) **(C,D)** Th/Yb-Nb/Yb, and TiO_2/Yb-Nb/Yb (after Pearce, 2008). Other eclogites (after Sun et al., 2017; Wang HN. et al., 2021). N-MORB, normal ocean ridge basalts; E-MORB, enriched mid ocean ridge basalts; OIB, oceanic island basalts; WPA, within-palte alkali basalts; WPT, within-plate tholeiites; WPA, within-plate basalts; IAT, island arc tholeiites; CAB, calc alkaline basalts.

presented in Table 4. Five analyses show low $^{176}Hf/^{177}Hf$ and $^{176}Lu/^{177}Hf$ values of 0.282905–0.282947 and 0.000012 to 0.000017, respectively. $\varepsilon_{Hf}(t)$ values range from 14.64 to 16.14, mean 15.49 (t = 451 Ma, Wang et al., 2019), and their stage II model ages range from 402 to 498 Ma, mean 443 Ma, which is older than zircon U-Pb metamorphic ages.

Discussion

Timing of HP metamorphism

Currently, the eclogites geochronology research in western Yunnan is mainly concentrated in Mengku and Qianmai areas. Sun et al. (2018) concluded from zircon U-Pb chronology of the retrograde eclogites from Daizhai, Kongjiao and Dijie in the Mengku area that 801 Ma is its protolithic age, which is consistent with Rodinia supercontinent initial breakup, and 447 Ma, 291 Ma and 229–227 Ma, respectively, represent the ages at different stages of metamorphism the eclogites have undergone. Wang et al. (2019) proposed 451 Ma as the protolithic age in this area, and 245–246 Ma as the peak metamorphic age. Wang et al. (2021) published the peak metamorphic age of 234–233 Ma for the eclogites in Qianmai area, which represents the timing of continental subduction (Zhao et al., 2021). Previous studies on zircon U-Pb geochronology from the Suyi blueschists yielded protolith ages of 279–260 Ma, and peak metamorphic ages of 214 Ma–242 Ma (Zhao et al., 1994; Fan et al., 2015). The eclogite-facies metamorphism in the LLSZ, which underwent a similar tectonic evolution as CMSZ, occurred at 237, 230 Ma, while continental collision and exhumation occurred at ~220 Ma (Li et al., 2006; Zhang et al., 2010; Zhai et al., 2011, 2017). In the Pianshishan area of central Qiangtang, the eclogites have a

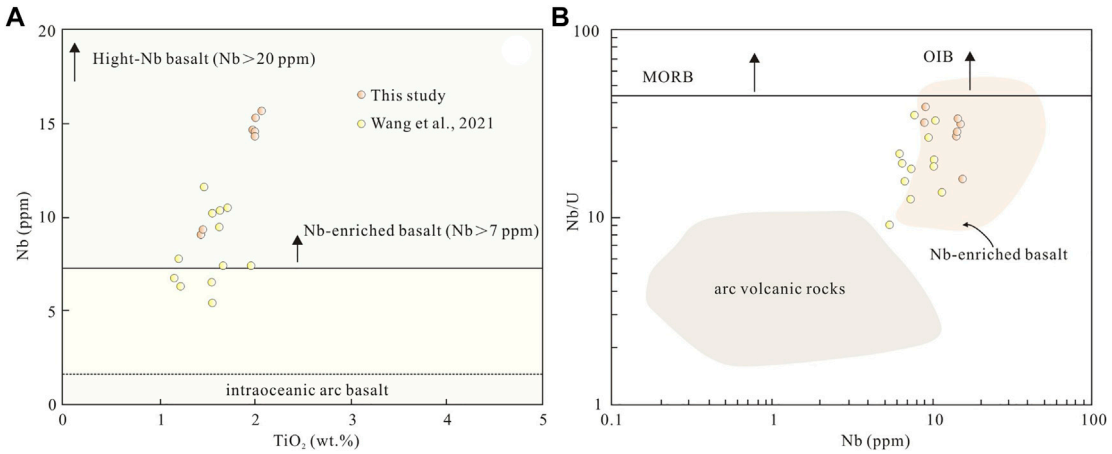

FIGURE 9
TiO_2 vs Nb **(A)** and Nb vs Nb/U **(B)** diagrams for Bangbing eclogites. **(A)**, High-Nb basalt and Nb-enriched data form Sajona et al., 1993, 1996; intra-oceanic arc basalts after Martin et al., 2005; **(B)**, arc volcanic rocks data and Nb-enriched basalts (NEB) data form Kepezhinaskas et al., 1996.

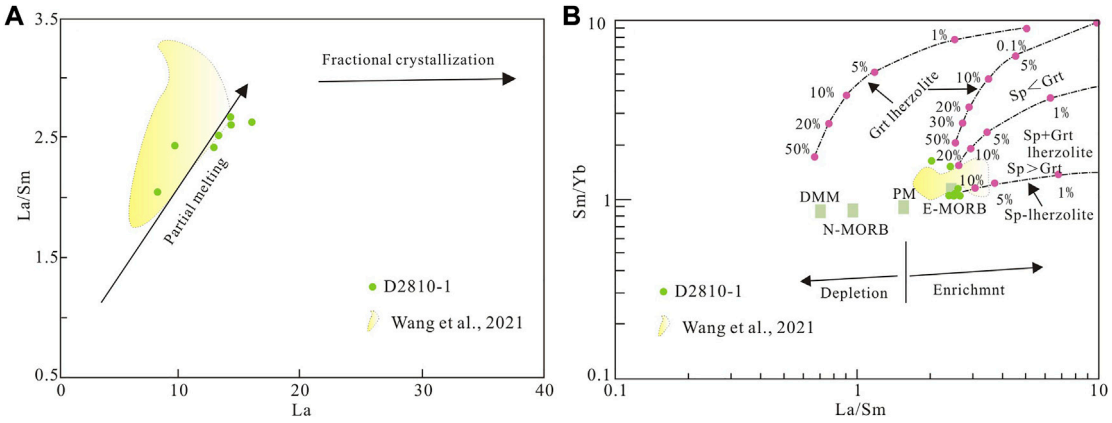

FIGURE 10
La/Sm-La **(A)** and Sm/Yb-La/Sm **(B)** diagrams for Bangbing eclogites. Numbers refer to percentages of melts. DMM, depleted MORB mantle; N-MORB, normal MORB; E-MORB, ecriched MORB; PM, primitive mantle.

protolithic age of 238 Ma, a peak metamorphic age of ~233 Ma and an outcrop age of ~220 Ma, which is considered to be a rare rapid subduction and exhumation evolution.

As shown above, the morphology and cathodoluminescence of the zircons in the Bangbing eclogites are consistent with a metamorphic origin (Figure 4A, Wu and Zheng, 2004). Twenty-five analyses (Group Ⅱ) in the zircon yield concentrated ages from 235 to 241 Ma, with $^{206}Pb/^{238}U$ weighted mean ages of 238 ± 2 Ma (MSWD=0.23). U and Th in zircons show low values of 0.15–2.83 and 43 × 10^{-6}–304 ppm, respectively, with Th/U ratios of 0.004–0.01, much less than 0.1. Zircons REE distribution patterns exhibit excellent agreement (Figure 6A). The above characteristics all suggest that these zircons were grown in the same environment. Enrichment of HREE relative to LREE, slight positive Ce anomaly, and weak Eu anomaly suggest the absence of feldspar, and support that these zircons was not produced from magmatic conditions (Rubatto, 2002; Sun et al., 2002). The high enrichment of HREE in the garnets causes a reduction in the zircons formed simultaneously with these garnets. Accordingly, metamorphic zircons grown in equilibrium with garnets are characterized by low ∑REE, with their HREE contents showing depletion compared to zircons of other origins (Wu et al., 2002; Hofmnn, 1988). Rutile, a widespread UHP-HP metamorphic mineral in eclogites, is highly enriched in HFSEs, especially Nb and Ta, and has high Nb/Ta ratios (Rudnicketal., 2000). Thus, low Nb and Ta content characteristics in metamorphic zircons are the

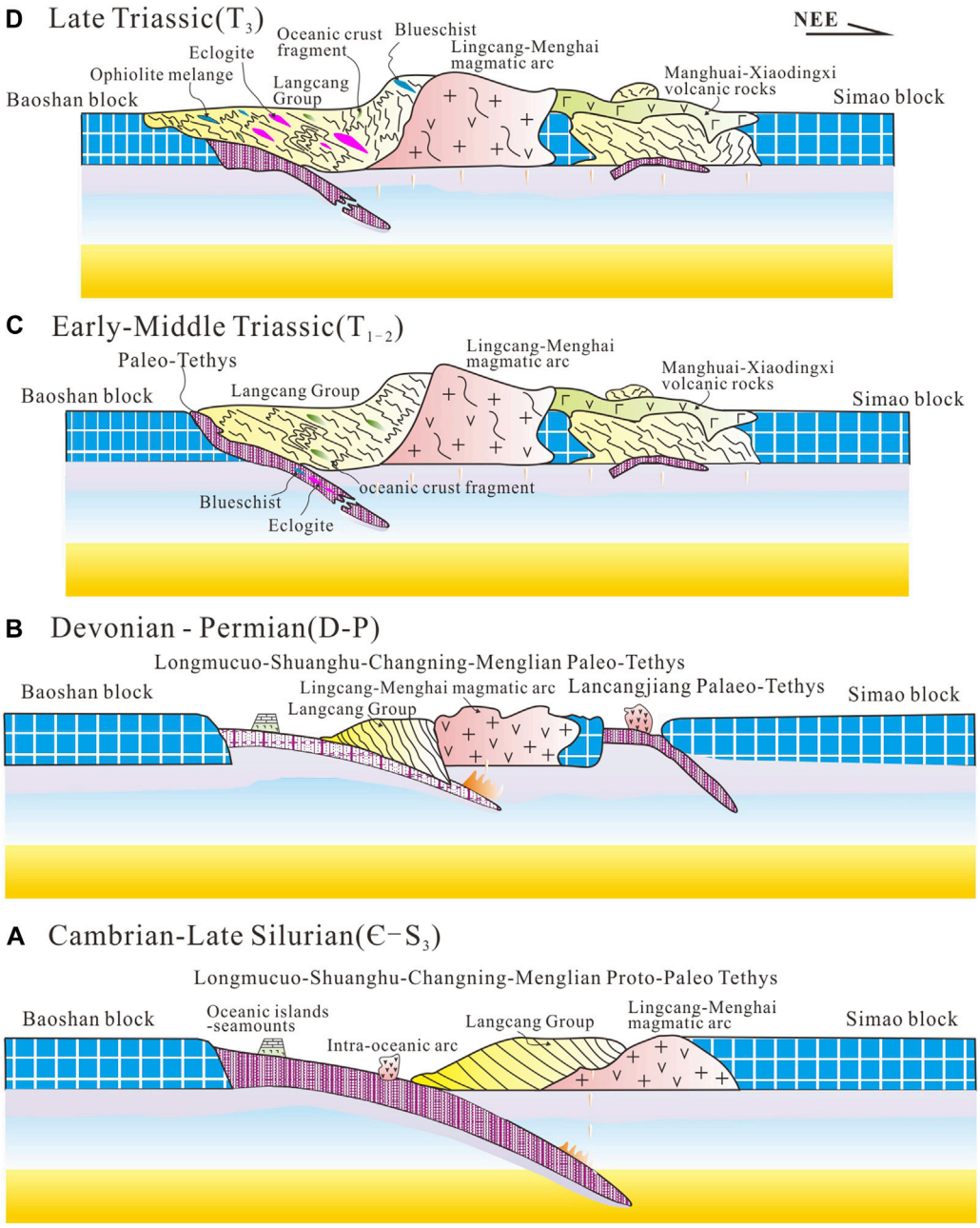

FIGURE 11
Model for the tectonic evolution of the Proto-Paleo Tethys in Changning-Menglian suture zone. **(A)**, Eastward subduction of the Proto-Tethys Ocean during the Late Paleozoic. **(B)**, Extended and subducted of the Paleo-Tethys Ocean during the Devonian and Early Carboniferous-Late Permian periods. **(C)**, Large-scale subduction of the Paleo-Tethys Ocean during the Early-Middle Triassic. **(D)**, the Changning-Menglian Ocean closed and the arc-continent and continent-continent collision orogeny in the Late Triassic. And final uplift of HP/UHP rocks.

result of equilibrium crystallization with rutile (Li et al., 2004). In this study the zircons show this typical REE distribution patterns (Figure 6A), while zircons in the samples have low Nb and Ta contents (0.089–0.27 ppm, 0.012–0.053 ppm) and significantly lower Nb/Ta ratios than magmatic zircons (Figure 6B). It is indicated that these zircons all crystallised in equilibrium with garnets and rutiles and formed during the eclogite-facies metamorphism, with weighted average ages most closely matching the peak metamorphic ages. The zircon Ti thermometer calculations of 539–695°C (mean 629°C, Table 3) are in general agreement with the regional peak metamorphic temperature of the eclogites (Sun et al., 2019; Wang et al., 2020b; Wang HN. et al., 2021; Fu et al., 2021). It further supports that 238 Ma should be the peak

metamorphic age. 220–229 Ma are probably the ages of exhumation. Other older values are captured ages.

The general characteristics of zircons in the surrounding Grt-Ph-Qz schists differ from those in the eclogites, with the youngest group of ages peaking around 450–600 Ma, suggesting that the metasedimentary rocks may have been deposited as recently as Early Paleozoic (Wang et al., 2018; Peng et al., 2020b).

Origin of protolith

The eclogite protoliths have undergone multi-phase complex metamorphic alteration, subject to fluids, recrystallization and accountings, resulting in large variations in the LILEs such as Sr and Pb (Becker et al., 1999). The HFSEs (e.g., Na, Ta, Ti, Hf, etc.) and some major elements (e.g., TiO_2, P_2O_5, Al_2O_3) remain less mobile during metamorphism and are believed to reflect their protolith compositions (Hou et al., 1996). SiO_2 contents of the Bangbing eclogites range from 45.92 to 50.59%, showing basaltic characteristics. TiO_2 values of 1.28%–2.01% (mean 1.61%) are higher than those of intraplate basalts (1.00%, Condie, 1989) and ocean island basalts (OIBs, 0.64%, Condie, 1989), and similar to normal mid-ocean ridge basalts (N-MORBs) and mid-ocean ridge tholeiitic basalts (E-MORB, 1.61%, Hofmann, 1988). As the samples were altered to some extent, analysis using anti-alteration elemental diagram (Zr/TiO_2-Nb/Y) showed that the data spots fell in the basaltic-andesite zone and in the subalkaline basaltic zone (Figure 7A). In the AFM diagram, except for two spots that fall within the boundary zone between calc-alkaline and tholeiitic basalts, all data are mainly classified as tholeiite series (Figure 7B), which is in agreement with the characteristics of the Qiangtang, and Mengku eclogites. Earlier studies have suggested that the protoliths of eclogites in the CMSZ are characterised by E-MORB and also by OIB (Sun et al., 2017; Wang et al., 2021). The results presented here show that the samples are similar to the E-MORB geochemistry in either the total REE and trace element patterns (Figure 3), the Hf/3-Th-Ta, V/Ti/1,000 diagrams (Figures 8A,B) or the Th/Yb-Nb/Yb, TiO_2/Yb-Nb/Yb diagrams (Figures 8C,D).

The chemical compositions of the samples are consistent with Nb-enriched basalts in the TiO_2-Nb and Nb-Nb/U diagrams (Figure 9), with high Nb contents (9.02–15.68 ppm, mean 13.25 ppm), high Nb/U ratios (16.16–39.23) and mantle-standardised La/Nb ratios <2 (0.84–1.06). In general, Nb-enriched basalts are the direct product of oceanic plate subduction, formed by partial melting of mantle wedge peridotites accounted for by adakite melts (Sajona et al., 1993, 1996). La/Sm-La can be effectively used to differentiate between partial melting and fractional crystallization of magma (Allegre and Minster, 1978). La and Sm are not affected by mineral alteration from the magma sources, and Yb is compatible with garnet but not with spinel. Sm/Yb ratios are therefore effective in tracing source minerals, and La/Sm ratios can be valuable in limiting the composition of the sources (Aldanmaz, 2002; Green, 2006; Sun et al., 2017). In the La/Sm-La diagram, the data from this study are concentrated along the partial melting line (Figure 10A). In the Sm/Yb-La/Sm diagram, most of the points lie on the spinel lherzolite melting curve, except for two which fall on the garnet lherzolite zone (Figure 10A). This leads us to believe that the eclogites originated from the partial melting of lherzolite containing spinel and minor garnet, which may have been undergone metasomatism by subduction fluids or melt. It is comparable to the source of Nb-enriched eclogites in the Heihe area, western Yunnan (Wang W. et al., 2021).

Sr-Nd isotopes are well traced for the source region, but Sr is easily affected by seawater or hydrothermal fluids, relatively $^{143}Nd/^{144}Nd$ is less sensitive to metamorphism (Zindler and Hart., 1986). In this study, $\varepsilon_{Nd}(t)$ values are positive (mean 3.63, Table 1) and the $^{143}Nd/^{144}Nd$ ratios is similar to that of the enriched mantle, implicating it is the magma source of the protolith.

In high grade metamorphic rocks, metamorphism results in lower Lu/Hf ratios for metamorphic zircons due to a process in which the Lu content decreases and the Hf content increases (Chen et al., 2007). Such ratios are not available to source tracing of protoliths (Wu et al., 2007). For the study of protolith chemistry, the only suitable zircon Lu-Hf isotopic data are those with magmatic crystallization, and the magmatic crystallization ages are required for the calculation of initial Hf isotopic values (Zheng et al., 2007). For the Bangbing eclogites, there are no magma crystallized cores or mantles retained in the metamorphic zircons. Consequently, it is not possible to discuss their protolithic origin in terms of Hf isotopes. Thus, the initial Hf isotope ratios were calculated based on the magmatic protolith age obtained from the retrograde eclogites from the Mengku area in the CMSZ (Wang et al., 2019). The resulting $\varepsilon_{Hf}(t)$ values (mean 15.49) are more than three times larger than $\varepsilon_{Nd}(t)$, with a positive correlation between Nd and Hf isotopes. It is inferred that these values cannot characterize the Hf isotopic content of the source region.

As discussed above, based on the whole-rock geochemical signatures generally characteristic of tholeiites, rare earth and trace element patterns, and positive $\varepsilon_{Nd}(t)$, $\varepsilon_{Hf}(t)$ values, we infer that the original Nb-enriched basalts were produced by partial melting of the oceanic asthenospheric mantle similar to the E-MORB sources.

Implication for the tectonic evolution of the Paleo-Tethys

In the previous studies, the Changning-Menglian Ocean has begun to subduct at 473–471 Ma (Wang et al., 2013; Liu et al., 2017). The Middle Ordovician O-type adakitic high-magnesium tonalite in the Niujingshan area (Wang F. et al., 2016), the

451–456 Ma volcanism in the Huimin area (Nie et al., 2015; Xing et al., 2017), and the Early-Middle Ordovician magmatic arc occurring in the Lincang granitic batholith in the Bangbin area (Peng et al., 2018; Han et al., 2020) are all products of the eastward subduction of the Proto-Tethys Ocean. The Late Silurian (421–419 Ma) island-arc volcanic rocks in the Dazhonghe area (Mao et al., 2012) represent a continental margin magmatic arc formed by eastward subduction of the Proto-Tethys Ocean during the Late Paleozoic (Figure 11A).

With the end of the subduction of the Proto-Tethys Ocean, the development of the Paleo-Tethys Ocean has initiated. The latter succeeded and evolved on the basis of the same ocean basin of the former (Wang et al., 2018). The Paleo-Tethys Ocean extended and subducted concurrently during the Devonian and Early Carboniferous-Late Permian periods. Basic-ultrabasic magmatism associated with the extension of the ocean basin developed in the Tongchangjie and Niujingshan area (Wang et al., 2017). The extension of the ocean basin was coupled with the formation of deep-sea sedimentary rocks (oceanic islands-seamounts) during the Carboniferous to Permian (Pan et al., 2020). The Lincang-Menghai magmatic arc includes a series of magmatic events associated with subduction (Peng, et al., 2006; Kong, et al., 2012; Nie et al., 2016). All the above lithological records indicate the occurrence of eastward subduction of the Paleo-Tethys Ocean during this period (Figure 11B).

Large-scale subduction of the Paleo-Tethys Ocean occurred in the Early-Middle Triassic and lasted until the beginning of Late Triassic. The identified high-pressure metamorphic protoliths ages in the CMSZ range from 451 to 260 Ma (Zhao et al., 1994; Fan et al., 2015; Wang et al., 2019), with peak metamorphic ages of 246–233 Ma (Wang et al., 2019, 2021). In this study, we obtained a peak metamorphic age of 238 Ma for the eclogites in Bangbing area. The 13 Ma range in peak metamorphic ages suggests that continuous subduction was occurring in the Changning-Menglian Ocean during this period. With continuous subduction, part of OIB and MORB oceanic crusts were involved in subduction channels due to tectonic effects such as shovelling and scraping to depths of more than 100 km (Lisun et al., 2017). Concurrently, arc magmatism associated with subduction occurred in the Lincang-Menghai area to the east (254–239 Ma; Yu et al., 2003; Peng et al., 2006; Liu DL. et al., 2008; Hennig et al., 2009). Oceanic crust from various sources and different epochs migrated and accreted towards active continental margins (trenches) in response to the subduction (Figure 11C).

After the cessation of Late Triassic subduction, the Changning-Menglian Ocean closed and proceeded to the arc-continent and continent-continent collision orogeny. As a result of mantle upwelling leading to partial melting of crustal material, a massive Lincang granitic batholith and associated post-collisional volcanic rocks occurred on the eastern side of the suture zone (231–215 Ma; Nie et al., 2012; Kong et al., 2012; Zhao et al., 2018). The 220–229 Ma metamorphic ages obtained in our study may correspond to such magmatic events. The time between the peak metamorphism and exhumation of the UHP/HP metamorphic rocks was thus <31 Ma. This range indicates a rapid rate of uplift, possibly 3–6 mm/a (Li, et al., 2015), during a relatively short exhumation. The few eclogites and blueschist exhumed to the surface occurred as variable-sized lenses within Grt-Ph-Qz schists in accretionary complex (Figure 11D).

Conclusion

1. The geochemical composition of Bangbing eclogites is similar to tholeiitic basalts. The samples show E-MORB-like geochemical affinities, and exhibit isotopic $\varepsilon_{Nd}(t)$ values of 3.14–4.49 and $\varepsilon_{Hf}(t)$ of 14.64–16.41, respectively. The Nb-enriched mafic protoliths of these samples suggested to be derived from oceanic crust which were produced by partial melting of the enriched mantle sources.
2. The youngest group of detrital zircon ages peaking at 450–600 Ma in the metasedimentary rocks, in which the eclogites were hosted, constrain the maximum depositional age for the Lancang Group to the Early Paleozoic.
3. The magmatic zircon grains separated from the eclogites samples yield a wide range of U-Pb ages, which may be capture zircon ages rather than protolith crystallization. The metamorphic zircon grains yield a weighted mean age of 238 ± 2 Ma. This data represents the time when eclogite-facies metamorphism occurred according to CL images, zircon trace element analysis. Combined with previous age results in the CMSZ, we propose that continued subduction of the Paleo-Tethys oceanic crust occurred during the Early-Middle Triassic (246–233 Ma), and rapid exhumation in the Late Triassic (231–215 Ma).
4. The Bangbeng Nb-enriched eclogites are products of oceanic crustal subduction and occurred as lenses in Grt-Ph-Qz schists after a rapid evolution. Their presence indicates that the Changning-Menglian suture zone is a typical oceanic subduction-accretionary orogeny belt.

Data availability statement

The original contributions presented in the study are included in the article/supplementary material, further inquiries can be directed to the corresponding author.

Author contributions

YF: Conceptualization, Formal analysis, Investigation, Writing-Original Draft, Writing-Review and Editing. ZP: Formal analysis, Resources, Writing-Review and Editing, Supervision, Funding acquisition. GW: Conceptualization, Resources, Funding acquisition. JH: Conceptualization, Formal

analysis, Investigation. ZZ: Conceptualization, Investigation. JG: Conceptualization, Investigation. FR: Conceptualization, Investigation.

Funding

This study was supported by the National Natural Science Foundation of China (No. 92055314, Tethyan tectonic maps compilation and regional comparative researches and No. 41602091), the China Geological Survey (No. DD20221635, Regional Basic Geological Survey of the Southwest China), and the China Scholarship Council (CSC, grant No. 202008515090).

Acknowledgments

We would like to express our sincere gratitude to Pan Guitang, Li Wenchang, Wang Liquan and Wang Baodi for their help in the field work, and to Chen Hongfang of the Wuhan Sample Solution Analytical Technology Company Co., Ltd. For her help in Zircon U-Pb dating. We would also appreciate the valuable comments from the reviewers.

Conflict of interest

The authors declare that the research was conducted in the absence of any commercial or financial relationships that could be construed as a potential conflict of interest.

Publisher's note

All claims expressed in this article are solely those of the authors and do not necessarily represent those of their affiliated organizations, or those of the publisher, the editors and the reviewers. Any product that may be evaluated in this article, or claim that may be made by its manufacturer, is not guaranteed or endorsed by the publisher.

References

Adanmaz, E. (2002). Mantle source characteristics of alkali basalts and basanites in an extensional intracontinental plate setting Western anatolia, Turkey: Implications for multi-stage melting. *Int. Geol. Rev.* 5 (44), 440–457. doi:10.2747/0020-6814.44.5.440

Allegre, C. J., and Minster, J. F. (1978). Quantitative models of trace element behavior in magmatic processes. *Earth Planet. Sci. Lett.* 38 (1), 1–25. doi:10.1016/0012-821x(78)90123-1

Bao, P. S., Xiao, X., Wang, J., Li, C., and Hu, K. (1999). Studies on the blueschist belt in the Shuanghu region, central northern Tibet and its tectonic implications. *Cont. Dyn.* 73 (4), 302–314. (in Chinese with English abstract). https://kns.cnki.net/kcms/detail/detail.aspx?FileName=DZXE199904001&DbName=CJFQ1999

Becker, H., Jochum, K. P., and Carlson, R. W. (1999). Constraints from High-Pressure veins in eclogites on the composition of hydrous fluids in subduction zones. *Chem. Geol.* 160 (4), 291–308. doi:10.1016/s0009-2541(99)00104-7

Blichert-Toft, J., and Albarède, F. (1997). The Lu-Hf isotope geochemistry of chondrites and the evolution of the mantle-crust system. *Earth Planet. Sci. Lett.* 148, 243–258. doi:10.1016/S0012-821X(97)00040-X

Chen, D. G., Ni, T., and Xie, L. W. (2007). Zircon Lu-Hf isotopic compositions of ultra-high pressure metamorphic rocks from Dabie Terrain, China. *Acta Petrol. Sin.* 23 (2), 331–342. doi:10.3969/j.issn.1000-0569.2007.02.013

Clarke, G. L., Powell, R., and Fitzherbert, J. A. (2006). The lawsonite paradox: A comparison of field evidence and mineral equilibria modelling. *J. Metamorph. Geol.* 24, 715–725. doi:10.1111/j.1525-1314.2006.00664.x

Condie, K. C. (1989). Geochemical changes in baslts and andesites across the Archean-Proterozoic boundary: Identification and significance. *Lithos* 23 (1-2), 1–18. doi:10.1016/0024-4937(89)90020-0

Deng, J., Wang, Q. F., Li, G. J., Li, C., and Wang, C. (2014). Tethys tectonic evolution and its bearing on the distribution of important mineral deposits in the Sanjiang region, SW China. *Gondwana Res.* 26 (2), 419–437. doi:10.1016/j.gr.2013.08.002

Dong, Y. S., and Li, C. (2009). Discovery of eclogite in the guoganjianian mountain, central Qiangtang area, northern tibet, China. *Geo-logical Bull. China* 28 (9), 1197–1200. (in Chinese with English abstract). doi:10.3969/j.issn.1671-2552.2009.09.006

Dong, Y. S., Li, C., Shi, J. R., Zhang, X. Z., and Wang, S. Y. (2010). Forming process of the high-pressure metamorphic belt in central Qiangtang, Tibet. *Acta Petrol. Sin.* 26 (7), 2099–2105. (in Chinese with English abstract).https://kns.cnki.net/kcms/detail/detail.aspx?FileName=YSXB201007012&DbName=CJFQ2010

Ernst, W. G. (2006). Preservation/exhumation of ultrahigh-pressure subduction complexes. *Lithos* 92, 321–335. doi:10.1016/j.lithos.2006.03.049

Fan, W. M., Wang, Y. J., Zhang, Y. H., Zhang, Y. Z., Jourdan, F., Zi, J. W., et al. (2015). Paleotethyan subduction process revealed fromTriassic blueschists in the Lancang tectonic belt of Southwest China. *Tectonophysics* 662, 95–108. doi:10.1016/j.tecto.2014.12.021

Ferry, J. M., and Watson, E. B. (2007). New thermodynamic models and revised calibrations for the Ti-in-zircon and Zr-in-rutile thermometers. *Contrib. Mineral. Pet.* 154, 429–437. doi:10.1007/s00410-007-0201-0)

Fu, Y. Z., Peng, Z. M., Wang, B. D., Wang, G. Z., Hu, J. F., Guan, J. L., et al. (2021). Petrology and metamorphism of glaucophane eclogites in changning-menglian suture zone, bangbing area, southeast Tibetan plateau: A evidence for paleo-tethyan subduction. *China Geol.* 4 (1), 111–116. doi:10.31035/cg2021017

Green, N. L. (2006). Influence of slab thermal structure on basalt source regions and melting conditions: REE and HFSE constraints from the garibaldi volcanic belt, northern cascadia subduction system. *Lithos* 87, 23–49. doi:10.1016/j.lithos.2005.05.003

Griffin, W. L., Pearson, N. J., Belousova, E., Jackson, S. E., Van, A. E., O'Reilly, S. R., et al. (2000). The Hf isotope composition of cratonic mantle: LAM-MC-ICP MS analysis of zircon megacrysts in kimberlites. *Geochimica Cosmochimica Acta* 64 (1), 133–147. doi:10.1016/S0016-7037(99)00343-9

Han, W. W., Peng, Z. M., Zhang, J., Guan, J. L., Hu, J. F., and Liu, Y. H. (2020). U-Pb dating of zircon, Hf isotope composition and tectonic significance of the albite-leptite of the Lancang Group in the Shuangjiang area of Western Yunnan, China. *Acta Geol. Sin.* 94 (4), 1282–1294. doi:10.19762/j.cnki.dizhixuebao.2020038

Hennig, D., Lehmann, B., Frei, D., Belyatsky, B., Zhao, X. F., Cabral, A. R., et al. (2009). Early permian sea floor to continental arc magmatism in the eastern paleo-tethys: U–Pb age and Nd–Sr isotope data from the southern lancangjiang zone, yunnan, China. *Lithos* 113 (3-4), 408–422. doi:10.1016/j.lithos.2009.04.031

Hofmnn, A. W. (1988). Chemical differentiation of the Earth: The relationship between mantle, continental crust, and Oceanic crust. *Earth Planet. Sci. Lett.* 90 (3), 297–314. doi:10.1016/0012-821x(88)90132-x

Hou, Z. Q., Mo, X. X., Zhu, Q. W., and Shen, S. Y. (1996). Mantle plume in the Sanjiang paleo-tethyan lithosphere: Evidence from mid-ocean ridge basalts. *Acta Geosci. Sin.* 17 (4), 362–375. https://kns.cnki.net/kcms/detail/detail.aspx?FileName=DQXB604.002&DbName=CJFQ1996.

Hu, Z. C., Liu, Y. S., Gao, S., Liu, W. G., Yang, L., Zhang, W., et al. (2012). Improved *in situ* Hf isotope ratio analysis of zircon using newly designed X skimmer cone and jet sample cone in combination with the addition of

nitrogen by laser ablation multiple collector ICP-MS. *J. Anal. At. Spectrom.* 27, 1391–1399. doi:10.1039/c2ja30078h

Kepezhinskas, P., Defant, M. J., and Drummond, M. S. (1996). Progressive enrichment of island arc mantle by melt-peridotite interaction inferred from Kamchatka xenoliths. *Geochim. Cosmochim. Acta* 60 (7), 1217–1229. doi:10.1016/0016-7037(96)00001-4

Kong, H. L., Dong, G. C., Mo, X. X., Zhao, Z. D., Zhu, D. C., Wang, S., et al. (2012). Petrogenesis of Lincang granites in Sanjiang area of Western Yunnan Province: Constraints from geochemistry, zircon U-Pb geochronology and Hf isotope. *Acta Petrol. Sin.* 28, 1438–1452. https://kns.cnki.net/kcms/detail/detail.aspx?FileName=YSXB201205010&DbName=CJFQ2012

Li, C., Dong, Y. S., Zhai, Q. G., Yu, J. J., and Huang, X. P. (2008). High-pressure metamorphic belt in Qiangtang, Qinghai-Tibet Plateau, and its tectonic significance. *Geol. Bull. China* 27 (1), 27–35. (in Chinese with English abstract). doi:10.3969/j.issn.1671-2552.2008.01.003

Li, C., Zhai, Q. G., Chen, W., Yu, J. J., Huang, X. P., and Zhang, Y. (2006). Ar-Ar chronometry of the eclogite from central Qiangtang area, Qinghai-Tibet Plateau. *Acta Petrol. Sin.* 22 (12), 2843–2849. doi:10.3969/j.issn.1000-0569.2006.12.003

Li, C., Zhai, Q. G., Dong, Y. S., Liu, S., Xie, C. M., and Wu, Y. W. (2009). High-pressureeclogite-blueschist metamorphic belt and closure of Paleo-Tethys ocean in central Qiangtang, qinghai-tibet plateau. *J. Earth Sci.* 20, 209–218. doi:10.1007/s12583-009-0021-4

Li, C. F., Li, X. H., Li, Q. L., Guo, J. H., and Yang, Y. H. (2012). Rapid and precise determination of Sr and Nd isotopic ratios in geological samples from the same filament loading by thermal ionization mass spectrometry employing a single-step separation scheme. *Anal. Chim. Acta* 727, 54–60. doi:10.1016/j.aca.2012.03.040

Li, J., Sun, Z. B., Xu, G. X., Zhou, K., Huang, L., Tian, S. M., et al. (2015). Firstly discovered garnet-amphibolite from Mengku area, Shuangjiang county, western yunnan province, China. *Acta Mineral. Sin.* 35, 421–424. doi:10.16461/j.cnki.1000-4734.2015.04.001

Li, J., Sun, Z. B., Huang, L., Xu, G. X., Tian, S. M., Deng, R. H., et al. (2017). P-T-t path and geological significance of retrograded eclogites from Mengku area in Western Yunnnan Province, China. *Acta Petrol. Sin.* 33, 2285–2301. https://kns.cnki.net/kcms/detail/detail.aspx?FileName=YSXB201707022&DbName=CJFQ2017

Li, Q. L., Li, S. G., Hou, Z. H., Hong, J. A., and Yang, W. (2004). High-pressure metamorphic neozoic zircon SHRIMP-U-Pb dating, trace elements and mineral inclusions in the Qinglongshan eclogites. *Sci. Bull.* 49 (22), 2329–2334. https://kns.cnki.net/kcms/detail/detail.aspx?FileName=KXTB20042200D&DbName=CJFQ2004.

Liang, X., Wang, G. H., Yang, B., Ran, H., Zheng, Y., Du, J., et al. (2017). Stepwise exhumation of the Triassic Lanling high-pressure metamorphic belt in Central Qiangtang, Tibet: Insights from a coupled study of metamorphism, deformation, and geochronology. *Tectonics* 36, 652–670. doi:10.1002/2016tc004455

Liu, D. L., Liu, J. S., Zhang, C. H., and Zhou, Y. G. (2008a). Geological characteristics and tectonic setting of Yunxian granite in the northern part of South Lancangjiang convergent margin, Western Yunnan Province. *Acta Petrologica Mineralogica* 27 (1), 23–31. doi:10.3969/j.issn.1000-6524.2008.01.003

Liu, G. C., Sun, Z. B., Zeng, W. T., Feng, Q. L., Huang, L., and Zhang, H. (2017). The age of Wanhe ophiolitic mélange from Mengku area, Shuangjiang County, Western Yunnan Province, and its geological significance. *Acta Petrologica Mineralogica* 36, 163–174. doi:10.3969/j.issn.1000-6524.2017.02.003

Liu, Y., Santosh, M., Zhao, Z. B., Niu, W. C., and Wang, G. H. (2011). Evidence for palaeo-Tethyan oceanic subduction within central Qiangtang, northern Tibet. *Lithos* 127, 39–53. doi:10.1016/j.lithos.2011.07.023

Liu, Y. S., Gao, S., Hu, Z. C., Gao, C. G., Zong, K. Q., and Wang, D. B. (2010). Continental and oceanic crust recycling-induced melt-peridotite interactions in the trans-north China orogen: U-Pb dating, Hf isotopes and trace elements in zircons from mantle xenoliths. *J. Petrology* 51 (1-2), 537–571. doi:10.1093/petrology/egp082

Liu, Y. S., Hu, Z. C., Gao, S., Gunther, D., Xu, J., Gao, C. G., et al. (2008b). *In situ* analysis of major and trace elements of anhydrous minerals by LA-ICP-MS without applying an internal standard. *Chem. Geol.* 257 (1-2), 34–43. doi:10.1016/j.chemgeo.2008.08.004

Ludwig, K. R. (2003). *User's manual for Isoplot 3.0: A geochronological tool kit for microsoft Excel*. California. Berkeley Geochronology Center Special Publication, 41–70.

Mao, X. C., Wang, L. Q., Li, B., Wang, B. D., Wang, D. B., Yin, F. G., et al. (2012). Discovery of the Late Silurian volcanic rocks in the Dazhonghe area, Yunxian-Jinggu volcanic arc belt, Western Yunnan, China and its geological significance. *Acta Petrol. Sin.* 28 (5), 1517–1528. (in Chinese with English abstract). https://kns.cnki.net/kcms/detail/detail.aspx?FileName=YSXB201205016&DbName=CJFQ2012

Martin, H., Smithies, R. H., Rapp, R., Moyen, J. F., and Champion, D. (2005). An overview of adakite, tonalite–trondhjemite–granodiorite (TTG), and sanukitoid: Relationships and some implications for crustal evolution. *Lithos* 79 (1-2), 1–24. doi:10.1016/j.lithos.2004.04.048

Maruyama, S., Lou, J. G., and Tarabayashi, M. (1996). Blueschists and eclogites of the world and their exhumation. *Int. Geol. Rev.* 38, 485–594. doi:10.1080/00206819709465347

Metcalfe, I. (2013). Gondwana dispersion and Asian accretion: Tectonic and palaeogeographic evolution of eastern Tethys. *J. Asian Earth Sci.* 66, 1–33. doi:10.1016/j.jseaes.2012.12.020

Nie, F., Dong, G. C., Mo, X. X., Zhu, D. C., Dong, M. L., and Wang, X. (2012). Geochemistry, zircon U-Pb chronology of the Triassic granites in the Changning-Menglian suture zone and their implications. *Acta Petrol. Sin.* 28 (5), 1465–1476. (in Chinese with English abstract). https://kns.cnki.net/kcms/detail/detail.aspx?FileName=YSXB201205012&DbName=CJFQ2012"

Nie, X. M., Feng, Q. L., Metcalfe, I., Baxter, A. T., and Liu, G. C. (2016). Discovery of a late devonian magmatic arc in the southern lancangjiang zone, western yunnan: Geochemical and ZirconU-Pb geochronological constraints on the evolution of tethyan ocean basins in SW China. *J. Asian Earth Sci.* 118, 32–50. doi:10.1016/j.jseaes.2015.12.026

Nie, X. M., Feng, Q. L., Qian, X., and Wang, Y. J. (2015). Magmatic record of Prototethyan evolution in SW Yunnan, China: Geochemical, zircon U–Pb geochronological and Lu–Hf isotopic evidence from the Huimin metavolcanic rocks in the southern Lancangjiang zone. *Gondwana Res.* 28, 757–768. doi:10.1016/j.gr.2014.05.011

Pan, G. T., Chen, Z. L., Li, X. Z., and Yan, Y. J. (1997). *Geological tectonic formation and evolution of the Eastern Tethys*. Beijing: Geological Press, 1–128. (in Chinese).

Pan, G. T., Wang, L. Q., Geng, Q. R., Yin, F. G., Wang, B. D., Wang, D. B., et al. (2020). Space-time structure of the bangonghu-shuanghu-nujiang-changning-menglian mega-suture zone: A discussion on geology and evolution of the Tethys ocean. *Sediment. Geol. Tethyan Geol.* 40 (3), 1–19. doi:10.19826/j.cnki.1009-3850.2020.07001

Pan, G. T., Wang, L. Q., and Zhu, D. C. (2004). Thoughts on some important scientific problems in regional geological survey of the Qinghai-Tibet Plateau. *Geol. Bull. China* 23 (1), 12–19. doi:10.3969/j.issn.1671-2552.2004.01.007

Pearce, J. A. (2008). Geochemical fingerprinting of oceanic basalts with applications to ophiolite classification and the search for Archean oceanic crust. *Lithos* 100 (1-4), 14–48. doi:10.1016/j.lithos.2007.06.016

Peng, T. P., Wang, Y. J., Fan, W. M., Liu, D., and Miao, L. (2006). SHRIMP zircon U-Pb geochronology of early Mesozoic felsic igneous rocks from the southern Lancangjiang and its tectonic implications. *Sci. China (Series D)* 36, 123–132. doi:10.3969/j.issn.1674-7240.2006.02.002

Peng, X. J., and Luo, W. L. (1982). The discovery and earth tectonic significance of the blueschist belt in lancangjiang south segment of west yunnan. *Regional Geol. China* 2, 69–75. https://kns.cnki.net/kcms/detail/detail.aspx?FileName=ZQYD198202007&DbName=CJFQ1982

Peng, Z. M., Fu, Y. Z., Wang, G. Z., Guan, J. L., Geng, Q. R., Hu, J. F., et al. (2020a). The results of geoehronological, geochemical and Sr-Nd-Hf isotopic investigations on amphibolites in the Qingping Region, Changning-Menglian Suture Zone. *Acta Geol. Sin.* 94 (2), 511–526. doi:10.19762/j.cnki.dizhixuebao.2019113

Peng, Z. M., Wang, B. D., Hu, J. F., Fu, Y. Z., Wang, G. Z., and Zhang, J. (2020b). Determination and significance of Early Palacozoic accretionary complexes in the Western Yunnnan Province—New cognition based on the geological survey of Wendong Sheet (1:50000). *Geol. China* 0, 1–21. https://kns.cnki.net/kcms/detail/detail.aspx?FileName=DIZI20200407001&DbName=CAPJ2020

Peng, Z. M., Wang, G. Z., Wang, B. D., Wang, L. Q., Fu, Y. Z., Guan, J. L., et al. (2019). Discovery of glaucophane eclogites within the Lancang group in bangbing area, Western yunnan. *J. Chengdu Univ. Technol. (Science& Technol. Ed.* 46 (5), 639–640. (in Chinese with English abstract). doi:10.3969/j.issn.1671-9727.2019.05.14

Peng, Z. M., Zhang, J., Guan, J. L., Zhang, Z., Han, W. W., and Fu, Y. Z. (2018). The discovery of early-middle Ordovician granitic gneiss from the giant Lincang batholith in Sanjiang area of Western Yunnan and its geological implications. *Earth Sci.* 43, 2571–2585. (in Chinese with English abstract). doi:10.3799/dqkx.2018.102

Rubatto, D. (2002). Zircon trace element geochemistry: Partitioning with garnet and the link between U-Pb ages and metamorphism. *Chem. Geol.* 184, 123–138. doi:10.1016/s0009-2541(01)00355-2

Rudnick, R., Barth, M., Horn, I., and McDonough, W. F. (2000). Rutile-bearing refractory eclogites: Missing link between continents and depleted mantle. *Science* 287, 278–281. doi:10.1126/science.287.5451.278

Sajona, F. G., Maury, R. C., Bellon, H., Cotton, J., and Defant, M. J. (1996). High field strength element enrichment of pliocene—pleistocene island arc basalts, zamboanga peninsula, western mindanao (Philippines). *J. Petrol.* 3 (37), 693–726. doi:10.1093/petrology/37.3.693

Sajona, F. G., Maury, R. C., Bellon, H., Cotton, J., Defant, M. J., and Pubellier, M. (1993). Initiation of subduction and the generation of slab melts in Western and eastern Mindanao, Philippines. *Geology* 21 (11), 1007–1010. doi:10.1130/0091-7613(1993)021<1007:IOSATG>2.3.CO;2

Shervais, J. W. (1982). Ti-V plots and the petrogenesis of modern and ophiolitic lavas. *Earth Planet. Sci. Lett.* 59, 101–118. doi:10.1016/0012-821x(82)90120-0

Söderlund, U., Patchett, P. J., Vervoot, J. D., and Isachsen, C. E. (2004). The^{176}Lu decay constant determined by Lu-Hf and U-Pb isotope systematics of Precambrian mafic intrusions. *Earth Planet. Sci. Lett.* 219, 311–324. doi:10.1016/S0012-821X(04)00012-3

Sun, S. S., and McDonough, W. F. (1989). Chemical and isotopic systematics of oceanic basalts: Implications for mantle composition and processes. *Geol. Soc. Lond. Spec. Publ.* 42, 313–345. doi:10.1144/gsl.sp.1989.042.01.19

Sun, W. D., Williams, I., and Li, S. G. (2002). Carboniferous and triassic eclogites in the Western dabie mountains, east-central China: Evidence for protracted convergence of the north and south China blocks. *J. Metamorph. Geol.* 20, 873–886. doi:10.1046/j.1525-1314.2002.00418.x

Sun, Z. B., Hu, S. B., Zhou, K., Zhou, T. Q., Zhao, J. T., Wang, Y. X., et al. (2019). Petrology, mineralogy and metamorphic P-T path of eclogites from the Qianmai area, Lancang County, Western Yunnan Province. *Geol. Bull. China* 38 (7), 1105–1115. (in Chinese with English abstract). https://kns.cnki.net/kcms/detail/detail.aspx?FileName=ZQYD201907004&DbName=CJFQ2019

Sun, Z. B., Li, J., Zhou, K., Zeng, W. T., Duan, X. D., Zhao, J. T., et al. (2017). Lithogeochemistry characteristics and geological significance of retrograde eclogite in Mengku area, Shuangjiang County, Western Yunnan Province, China. *Geoscience* 31, 746–756. (in Chinese with English abstract). doi:10.3969/j.issn.1000-8527.2017.04.009

Sun, Z. B., Li, J., Zhou, K., Zeng, W. T., Wu, J. L., Hu, S. B., et al. (2018). Zircon U-Pb age and geological significance of retro-graded eclogites from Mengku area in Western Yunnan Province. *Geol. Bull. China* 37 (11), 2032–2043. (in Chinese with English abstract). doi:10.12097/j.issn.1671-2552.2018.11.009

Wang, B. D., Wang, L. Q., Pan, G. T., Yin, F. G., Wang, D. B., and Tang, Y. (2013). U-Pb zircon dating of Early Paleozoic gabbro from the Nantinghe ophiolite in the Changning-Menglian suture zone and its geological implication. *Chin. Sci. Bull.* 58, 920–930. doi:10.1007/s11434-012-5481-8

Wang, B. D., Wang, L. Q., Wang, D. B., Yin, F. G., He, J., Peng, Z. M., et al. (2018). Tectonic evolution of the changning-menglian proto-paleo Tethys ocean in the Sanjiang area, southwestern China. *Earth Sci.* 43 (8), 2527–2550. (in Chinese with English abstract). https://kns.cnki.net/kcms/detail/detail.aspx?FileName=DQKX201808001&DbName=CJFQ2018

Wang, D. B., Luo, L., Tang, Y., Yin, F. G., Wang, B. D., and Wang, L. Q. (2016a). Zircon U-Pb dating and petrogenesis of Early Paleozoic adakites from the Niujingshan ophiolitic mélange in the Changning-Menglian suture zone and its geological implications. *Acta Petrol. Sin.* 32, 2317–2329. (in Chinese with English abstract). https://kns.cnki.net/kcms/detail/detail.aspx?FileName=YSXB201608006&DbName=CJFQ2016

Wang, F., Liu, F. L., Ji, L., and Liu, L. S. (2017). LA-ICP-MS U-Pb dating of detrital zircon from low-grade metamorphic rocks of the Lancang Group in the Lancangjiang Complex and its tectonic implications. *Acta Petrol. Sin.* 33, 2975–2985. (in Chinese with English abstract). https://kns.cnki.net/kcms/detail/detail.aspx?FileName=YSXB201709020&DbName=CJFQ2017

Wang, F., Liu, F. L., Ji, L., Liu, P. H., Cai, J., Tian, Z. H., et al. (2016b). Petrogenesis and metamorphic evolution of blueschist from Xiaoheijiang-Shangyun area in Lancangjiang metamorphic complex. *Acta Petrologica Mineralogica* 35, 804–820. (in Chinese with English abstract). doi:10.3969/j.issn.1000-6524.2016.05.005

Wang, H. N., Liu, F. L., Li, J., Sun, Z. B., Ji, L., Tian, Z. H., et al. (2019). Petrology, geochemistry and P-T-t path of lawsonite-bearing retrograded eclogites in the Changning-Menglian orogenic belt, southeast Tibetan Plateau. *J. Metamorph. Geol.* 39, 439–478. doi:10.1111/jmg.12462

Wang, H. N., Liu, F. L., Santosh, M., Cai, J., Wang, F., and Ji, L. (2020a). Rapid cold slab subduction of the Paleo-Tethys: Insights from lawsonite-bearing blueschist in the Changning-Menglian orogenic belt, southeastern Tibetan Plateau. *Gondwana Res.* 85, 189–223. doi:10.1016/j.gy.2020.01.001

Wang, H. N., Liu, F. L., Sun, Z. B., Ji, L., Cai, J., and Zhu, J. J. (2021a). Identification of continental-type eclogites in the Paleo-Tethyan Changning–Menglian orogenic belt, southeastern Tibetan Plateau: Implications for the transition from oceanic to continental subduction. *Lithos* 396-397, 106215–215. doi:10.1016/j.lithos.2021.106215

Wang, H. N., Liu, F. L., Sun, Z. B., Ji, L., Zh, J. J., Cai, J., et al. (2020b). A new HP–UHP eclogite belt identified in the southeastern Tibetan plateau: Tracing the extension of the main palaeo-tethys suture zone. *J. Petrology* 61, 1–45. doi:10.1093/petrology/egaa073

Wang, W., Zhang, X. P., Sun, Z. B., Tian, Y. G., Zhou, K., Li, X. J., et al. (2021b). Petrology and geochemistry of the eclogite in Heihe area of Lancang county, Western yunnan: The magmatism of the initial subduction of the oceanic crust. *Geol. Bull. China* 40 (7), 1057–1067. (in Chinese with English abstract). https://kns.cnki.net/kcms/detail/detail.aspx?FileName=ZQYD202107005&DbName=CJFQ2021

Wei, C. J., and Clarke, G. L. (2011). Calculated phase equilibria for MORB compositions: A reappraisal of the metamorphic evolution of lawsonite eclogite. *J. Metamorph. Geol.* 29, 939–952. doi:10.1111/j.1525-1314.2011.00948.x

Whitney, D. L., and Evans, B. W. (2010). Abbreviations for names of rock-forming minerals. *Am. Mineral.* 95, 185–187. doi:10.2138/am.2010.3371

Wood, D. A. (1980). The application of a ThHfTa diagram to problems of tectonomagmatic classification and to establishing the nature of crustal contamination of basaltic lavas of the British Tertiary Volcanic Province. *Earth Planet. Sci. Lett.* 1 (50), 11–30. doi:10.1016/0012-821X(80)90116-8

Wu, F. Y., Li, X. H., Zheng, Y. F., and Gao, S. (2007). Lu-Hf isotopic systematics and their applications in petrology. *Acta Petrol. Sin.* 23 (2), 185–220. (in Chinese with English abstract). doi:10.3321/j.issn:1000-0569.2007.02.001

Wu, Y. B., and Zheng, Y. F. (2004). Mineralogical studies on the Genesis of zircon and its constraints on the interpretation of U-Pb ages. *Sci. Bull.* 49 (16), 1589–1604. (in Chinese with English abstract). doi:10.3321/j.issn:0023-074X.2004.16.002

Xing, X., Wang, Y., Cawood, P. A., and Zhang, Y. (2017). Early paleozoic accretionary orogenesis along northern margin of gondwana constrained by high-Mg metaigneous rocks, SW Yunnan. *Int. J. Earth Sci.* 106, 1469–1486. doi:10.1007/s00531-015-1282-z

Xu, Y., wang, Q., Tang, G., Wang, J., Li, H., Zhou, J., et al. (2020). The origin of arc basalts: New advances and remaining questions. *Sci. China Earth Sci.* 50 (12), 1969–1991. doi:10.1007/s11430-020-9675-y

Yu, S. Y., Li, K. Q., Shi, Y. P., and Zhang, H. H. (2003). A study on the granodiorite in the middle part of lincang granite batholith. *Yunnan Geol.* 22 (4), 426–442. (in Chinese with English abstract). doi:10.3969/j.issn.1004-1885.2003.04.009

Zhai, M. G., Cong, B. L., and Zhang, R. Y. (1990). Distinguishing of two volcanic rock series in the Lancang Group, Yunnan Province, SW China and its geological implication. *Sci. China* 33, 968–979. (in Chinese with English abstract). https://kns.cnki.net/kcms/detail/detail.aspx?FileName=JBXG199008009&DbName=CJFQ1990

Zhai, Q. G., Jahn, B. M., Li, X. H., Zhang, R. Y., Li, Q. L., et al. (2017). Zircon U–Pb dating of eclogite from the Qiangtang terrane, north-central tibet: A case of metamorphic zircon with magmatic geochemical features. *Int. J. Earth Sci.* 106, 1239–1255. doi:10.1007/s00531-016-1418-9

Zhai, Q. G., Wang, J., and Wang, Y. (2009). Discovery of eclogite at gangmacuo area from gerze county, tibet, China. *Geol. Bull. China* 28 (12), 1720–1724. (in Chinese with English abstract). doi:10.3969/j.issn.1671-2552.2009.12.005

Zhai, Q. G., Zhang, R. Y., Jahn, B. M., Cai, L., Song, S. G., and Wang, J. (2011). Triassic eclogites from central Qiangtang, northern Tibet, China: Petrology, geochronology and metamorphic P–T path. *Lithos* 125, 173–189. doi:10.1016/j.lithos.2011.02.004

Zhang, L. F., Lü, Z., Zhang, G. B., and Song, S. G. (2008). The geological characteristics of oceanic-type UHP metamorphic belts and their tectonic implications: Case studies from Southwest Tianshan and North Qaidam in NW China. *Sci. Bull. (Beijing).* 53, 3120–3130. doi:10.1007/s11434-008-0386-2

Zhang, R. Y., Cong, B. L., and Han, X. L. (1990). Amphiboles of blueschist in west Yunnan region. *Sci. Geol. Sin.* 1, 43–53. (in Chinese with English abstract). https://kns.cnki.net/kcms/detail/detail.aspx?FileName=DZKX199001004&DbName=CJFQ1990

Zhang, X. Z., Dong, Y. S., Li, C., Shi, J. R., and Wang, S. Y. (2010). Geochemistry and tectonic significance of eclogites in central Qiangtang, Tibetan Plateau. *Geol. Bull. China* 29 (12), 1804–1814. (in Chinese with English abstract). doi:10.3969/j.issn.1671-2552.2010.12.008

Zhang, X. Z., Dong, Y. S., Li, C., Xie, C. M., Wang, M., Deng, M. R., et al. (2014). A record of complex histories from oceanic lithosphere subduction to continental subduction and collision: Constraints on geochemistry of eclogite and blueschist in Central Qiangtang, Tibetan Plateau. *Acta Petrol. Sin.* 30 (10), 2821–2834. (in Chinese with English abstract). https://kns.cnki.net/kcms/detail/detail.aspx?FileName=YSXB201410003&DbName=CJFQ2014

Zhang, Z. B., Li, J., Lü, G. X., Yu, H., and Wang, F. Z. (2004). Characteristics of blueschist in Shuangjiang tectonic mélange zone, West Yunnan province. *J. China Univ. Geosciences* 15 (2), 224–231. https://kns.cnki.net/kcms/detail/detail.aspx?FileName=ZDDY200402014&DbName=CJFQ2004

Zhao, F., Li, G. J., Zhang, P. F., Wang, C. B., Sun, Z. B., and Tang, X. (2018). Petrogenesis and tectonic implications of the Lincang batholith in the Sanjiang, Southwest China: Constraints by geochemistry, zircon U-Pb chronology and Hf isotope. *Acla Petrol. Sin.* 34 (5), 1397–1412. (in Chinese with English abstract). https://kns.cnki.net/kcms/detail/detail.aspx?FileName=YSXB201805013&DbName=CJFQ2018

Zhao, F., Xue, S. C., Li, G. J., Sun, Z. B., Tang, X., Hu, X. W., et al. (2021). Petrology and geochemistry of retrograde eclogites in the Changning-Menglian suture zone, southwest China: Insights into the Palaeo-Tethyan subduction and rutile mineralization. *Ore Geol. Rev.* 139, 104493. doi:10.1016/j.oregeorev.2021.104493

Zhao, J. (1993). A study of muscovites from the Lancang metamorphic belt in Western Yunnan and its geological significance. *Acta Petrologica Mineralogica* 12, 251–260. (in Chinese with English abstract). https://kns.cnki.net/kcms/detail/detail.aspx?FileName=YSKW199303006&DbName=CJFQ1993

Zhao, J., Zhong, D. L., and Wang, Y. (1994). Metamorphism of Lancang metamorphic belt, the Western Yunnan and its relation to deformation. *Acta Petrol. Sin.* 10, 27–40. (in Chinese with English abstract). doi:10.3321/j.issn:1000-0569.1994.01.003

Zheng, Y. F., Chen, R. X., Zhang, S. B., Tang, J., Zhao, Z. F., and Wu, Y. B. (2007). Zircon Lu-Hf isotope study of ultrahigh-pressure eclogite and granitic gneiss in the Dabie orogen. *Acta Petrol. Sin.* 23 (2), 317–330. (in Chinese with English abstract). doi:10.3321/j.issn:1000-0569.2007.02.012

Zheng, Y. F. (2012). Metamorphic chemical geodynamics in continental subduction zones. *Chem. Geol.* 328, 5–48. doi:10.1016/j.chemgeo.2012.02.005

Zhong, D. L. (1998). *The paleotethys orogenic belt in west of sichuan and yunnan*. Beijing: Science Publishing House China, 1–216. (in Chinese).

Zindler, A., and Hart, S. R. (1986). Chemical geodynamics. *Annu. Rev. Earth Planet. Sci.* 14, 493–571. doi:10.1146/annurev.ea.14.050186.002425

frontiers | Frontiers in Earth Science

TYPE Original Research
PUBLISHED 14 September 2022
DOI 10.3389/feart.2022.957337

OPEN ACCESS

EDITED BY
Fuhao Xiong,
Chengdu University of Technology, China

REVIEWED BY
Hu Huang,
Chengdu University of Technology, China
Qi Deng,
Chengdu Geological Survey Center, China

*CORRESPONDENCE
Tiannan Yang,
yangtn@cags.ac.cn

SPECIALTY SECTION
This article was submitted to Structural Geology and Tectonics, a section of the journal Frontiers in Earth Science

RECEIVED 31 May 2022
ACCEPTED 22 August 2022
PUBLISHED 14 September 2022

CITATION
Liang M, Yang T, Yan Z, Xue C, Xin D, Qi S, Dong M, Wang W, Shi P, Xiang K, Han X and Bao J (2022), Early Late Triassic retro-foreland basin in response to flat subduction of the Paleo-Tethyan oceanic plate, SE Tibet.
Front. Earth Sci. 10:957337.
doi: 10.3389/feart.2022.957337

Early Late Triassic retro-foreland basin in response to flat subduction of the Paleo-Tethyan oceanic plate, SE Tibet

Mingjuan Liang[1,2], Tiannan Yang[2]*, Zhen Yan[2], Chuandong Xue[3], Di Xin[2], Shaofeng Qi[1], Mengmeng Dong[2], Wei Wang[3], Pengliang Shi[4], Kun Xiang[5], Xue Han[6] and Jingkun Bao[3]

[1]Geological Museum of Guizhou, Guiyang, China, [2]Institute of Geology, Chinese Academy of Geological Sciences, Beijing, China, [3]Department of Earth-Sciences, Kunming University of Sciences and Technology, Kunming, China, [4]Beijing Jinyou Geological Exploration Co. Ltd., Beijing, China, [5]School of Resources and Environmental Engineering, Guizhou Institute of Technology, Guiyang, China, [6]Guizhou Geological Survey, Guiyang, China

Syn-subduction basins bear significant implications to understand tectonic evolution of any fossil subduction zone. The late Paleozoic to early Mesozoic (Paleo-Tethyan) tectonics of the eastern and southeastern Tibetan Plateau (i.e., the Sanjiang Orogenic Belt) is featured by ocean-continent subduction systems. A huge pile of volcanic-absent sedimentary succession developed in the middle segment of the Sanjiang orogenic belt, its age and tectonic nature remain unclear. Detailed geological mapping and zircon U-Pb dating results demonstrate that the early Late Triassic volcanic-absent succession comprises the nonmarine Maichuqing Formation in the lower part and the shallow marine Sanhedong Formation in the upper part. The Maichuqing Formation consists of coarse to fine-grained sandstone, siltstone and mudstone with abundant basal erosional surfaces, trough and planar cross-beddings, ripples, mudcracks, and plant fragments. The Sanhedong Formation comprises predominantly bioclastic limestones interlayered with marl, calcareous-muddy siltstone, and calcareous sandstone with abundant bivalve fossils. Syn-sedimentation deformation structures, such as slump folds and associated normal faults are common, suggesting intense tectonism during deposition. Synthesizing sedimentary data, paleocurrent and provenance results, combined with other available data, demonstrate that the volcanic-absent succession deposited within a retro-foreland basin along the rear part of the Permian-Triassic Jomda-Weixi-Yunxian arc in response to flat-subduction of the Paleo-Tethyan Ocean during the early Late Triassic time.

KEYWORDS

sedimentary environment, early Late Triassic, retro-foreland basin, flat subduction, SE Tibet

1 Introduction

Subduction of oceanic plate between two continents commonly ended by collision of these two continents. Sedimentary basins of different types may develop during each stage of the process from subduction to collision, whereas the natures of these basins well reflect tectonic regimes of each individual stage of the related orogenic belt (Allen and Allen, 2005; Hu et al., 2016). For example, retro (arc)-foreland basin commonly develops at leading edge of the folded part of an arc as a flexural response to crustal shortening in a compressional setting (Jordan, 1995). As such, identification of a retro foreland basin (Decelles and Giles, 1996; García-Castellanos, 2002; Decelles et al., 2011), combined with geochemistry and structure of arc-volcanic rocks, may much better constrain subduction dynamics of the related subduction zone than by evidence from any single principle.

Tectonic facies analysis (e.g., Burchfiel and Chen, 2012; Yang et al., 2012, 2014; Xin et al., 2018) shows that the late Paleozoic to Early Mesozoic (Paleo-Tethyan) tectonics of the northern, eastern, and southeastern Tibetan Plateau (Figure 1A) are featured by subduction of oceanic plates and subsequent continental collisions. At present time, less attention has been paid to any subduction- or collision-related sedimentary basin (Burchfiel and Chen, 2012). As the result, the Paleo-Tethyan tectonics of these regions is still hotly debated, on which, our understanding was derived mainly from geochemical and geochronological studies of igneous rocks (e.g., Wang et al., 2011, 2014).

Geological mapping results with scale 1/200,000 (Edit Committee of the Sanjiang Geological Map, 1986) have revealed an Upper Triassic volcanic-absent succession in the eastern Tibetan Plateau, which was termed as the transitional unit by Burchfiel and Chen (2012). This unit gradually changes northwestward into the Late Triassic Yushu-Yidun arc belt (Yang et al., 2012) and southward into the Late Triassic Yunxian arc belt (Figure 1B). Given most Triassic rocks in the eastern and southeastern Tibetan Plateau are volcanic-bearing, the forming of such a volcanic-absent sedimentary unit is still a puzzle.

In this study, we try to document the stratigraphic architecture of the transitional unit and discuss its sedimentary environments according to the sedimentary textures and syn-sedimentation deformation structures. Its depositional time was determined based on zircon U-Pb age data. These new data and other available data were used to discuss the forming process and tectonic nature of the transitional unit.

2 Tectonic background

The Paleo-Tethyan tectonics of the eastern and southeastern Tibetan Plateau (i.e., the Sanjiang orogenic belt; Figures 1A,B) is featured by two ocean-continent subduction systems. The major ocean-continent subduction system consists of the huge early Permian to late Triassic Jomda-Weixi-Yunxian arc (Yang et al., 2014) to the northeast or to the east and the Longmu co-Shuanghu-Changning-Menglian suture (Mo et al., 2001; Li et al., 2006) to the south or to the west. This system is commonly interpreted as the results of the northeastward or eastward subduction of the Paleo-Tethyan Ocean beneath the Eastern Qiangtang Continent (northern segment) and the Lanping-Simao Continent (southern segment; Xin et al., 2018). Another ocean-continent subduction system comprises the Upper Triassic Yushu-Yidun arc to the south and the western Jinshajiang–Garzê–Litang suture to the north. This system was formed by southward subduction of the Garzê-Litang Ocean beneath the Qiantang Continent during the middle to late Triassic (Yang et al., 2012).

The Jomda–Weixi–Yunxian arc consists of three segments with different magmatism history (Xin et al., 2018). The northern segment contains a long-lasting magmatic evolution from the early Permian to middle Triassic (Yang et al., 2011). The subduction-related magmatism of the middle segment is short-lived and exhibits an early to middle Triassic magmatic flare-up (Xin et al., 2018). The southern segment contains a long-lasting magmatic evolution as well, consisting of several pulses of magmatism from middle Permian to late Triassic (Yang et al., 2014). The Triassic volcanic-absent transitional unit is spatially coinciding with the middle segment of the Jomda–Weixi–Yunxian arc. Its northern and southern boundaries with the Late Triassic Yushu–Yidun arc volcanoclastic rocks and the Late Triassic volcanoclastic rocks of the southern segment of the Jomda–Weixi–Yunxian arc, respectively, are both gradual. The eastern boundary of the transitional unit is not very clear, where Late Triassic sedimentary rocks are conformable with the underlain shallow marine platform sedimentary rocks of the Yangtze Block (Burchfiel and Chen, 2012). On contrary, its western boundary is an unconformity, along which the volcanic-absent rocks overlie the middle segment of the Jomda–Weixi–Yunxian arc, where the subduction-related volcanoclastic rocks are tightly folded (Yang et al., 2012; Liang et al., 2015; Tang et al., 2016; Xin et al., 2018). This spatiotemporal relationship between these tectonic units (Figure 1B) makes it hard to understand tectonic nature of the basin represented by volcanic-absent sedimentary rocks of the transitional unit (Burchfiel and Chen, 2012). Widespread Mesozoic and Cenozoic basins, such as the Cretaceous Lanping basin (Liang, 2017 and references therein) and the Eocene Jianchuan basin (Liao et al., 2020) as well as the crustal deformation induced by the India–Eurasia collision (Yang et al., 2021; Liang et al., 2022) worse the situation.

This paper focuses on the tectonic nature of the transitional unit. On basis of geological mapping with scale 1/50,000 in the Lanping and Madeng areas (Figure 2A; Liang et al., 2022), we conducted detail sedimentary studies along the Misha–Xiangtu profile and in the open mining pits of the supergiant Jinding Zn–Pb deposit (Song et al., 2020). The locations of the study areas are marked in Figure 2A.

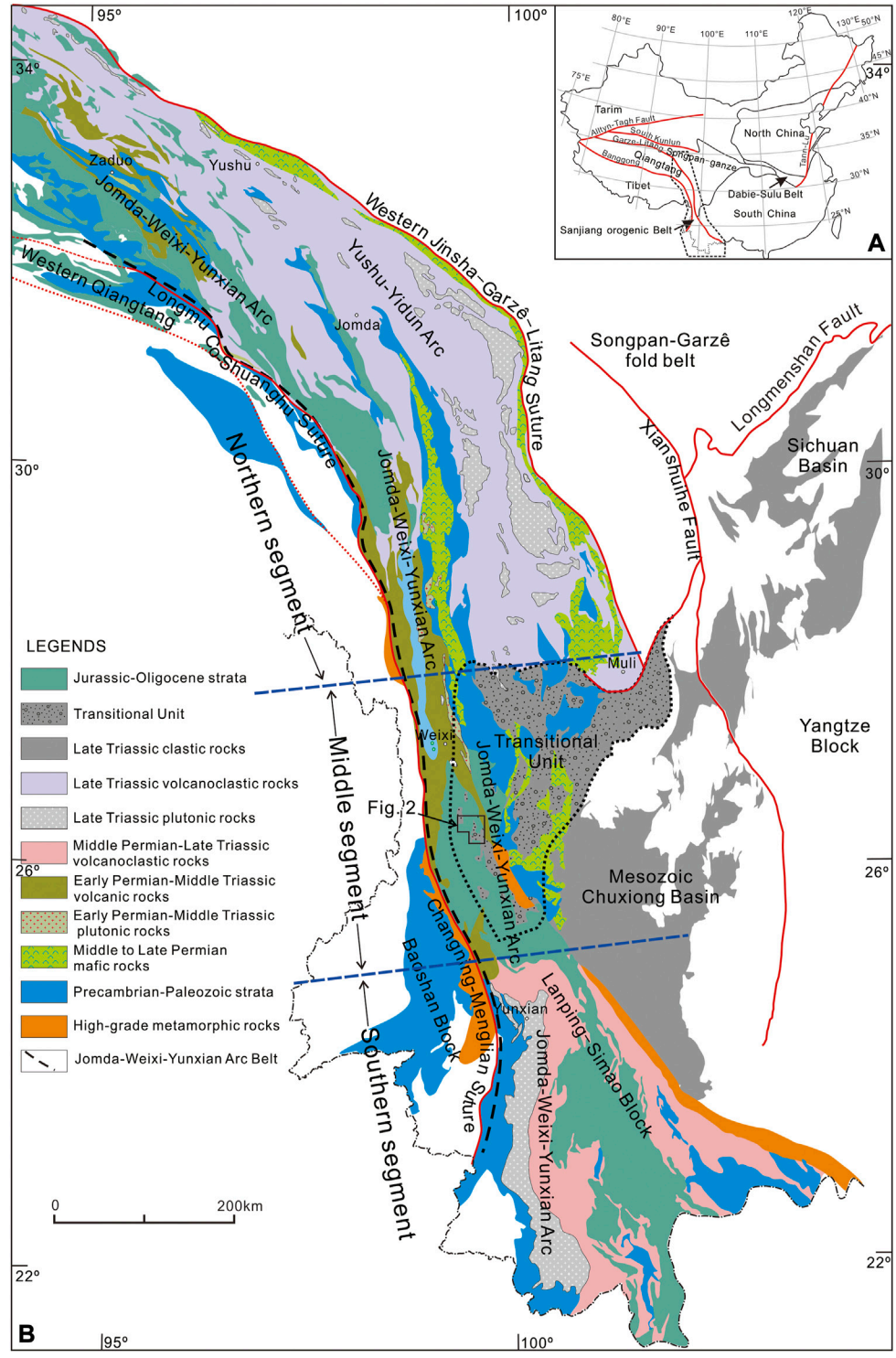

FIGURE 1
(A) Tectonic framework of China mainland showing the location of the Sanjiang orogenic belt. **(B)** Simplified geological map of the Sanjiang orogenic belt showing the tectonic framework and the locations of the Transitional Unit (thick dash-line) and the study area (the solid polygon) (modified after ECSGM, 1986; Burchfiel and Chen, 2012; Yang et al., 2014, 2021). The two blue dashed lines are the approximate boundaries separating the northern, middle, and southern segments of the Jomda–Weixi–Yunxian arc belt, respectively.

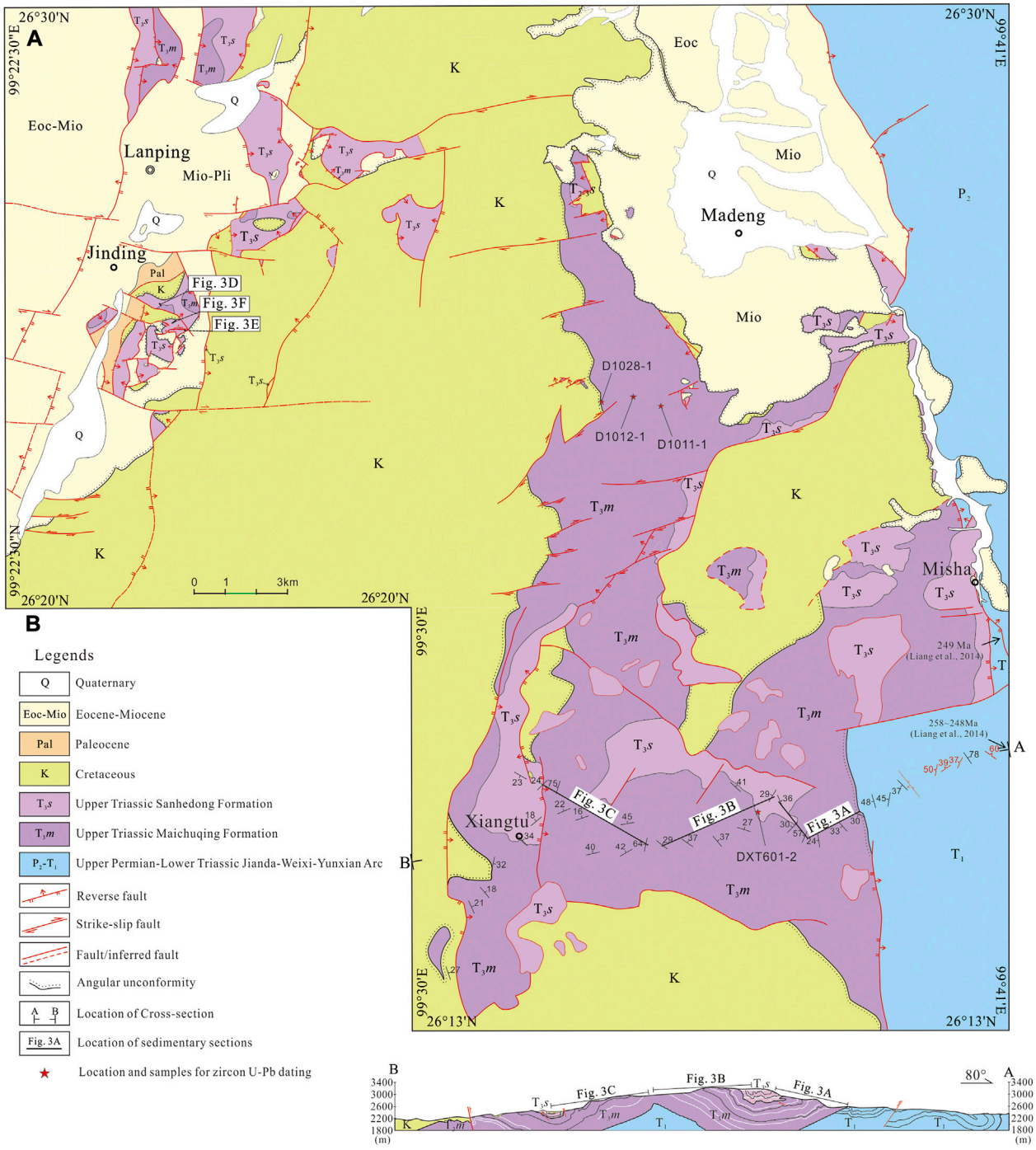

FIGURE 2
(A) Geologic map of Jinding–Madeng–Misha–Xiangtu area in the northwest Yunnan Province, China. Its location was marked in Figure 1B. **(B)** Cross-section showing the structures and contact relationships between the Upper Triassic and underlain strata along the Misha to Xiangtu profile.

3 Sedimentary facies and depositional environments

The Late Triassic sedimentary rocks of the Lanping and Madeng areas are exposed as numerous isolated patches of irregular outlines setting in a groundmass of Cretaceous red-beds. These Triassic sedimentary rocks were initially defined as the Maichuqing Formation (T_3m) in the lower part and the Sanhedong Formation (T_3s) in the upper part based on their rock assemblages and associated fossils by YBGMR (1974). Both

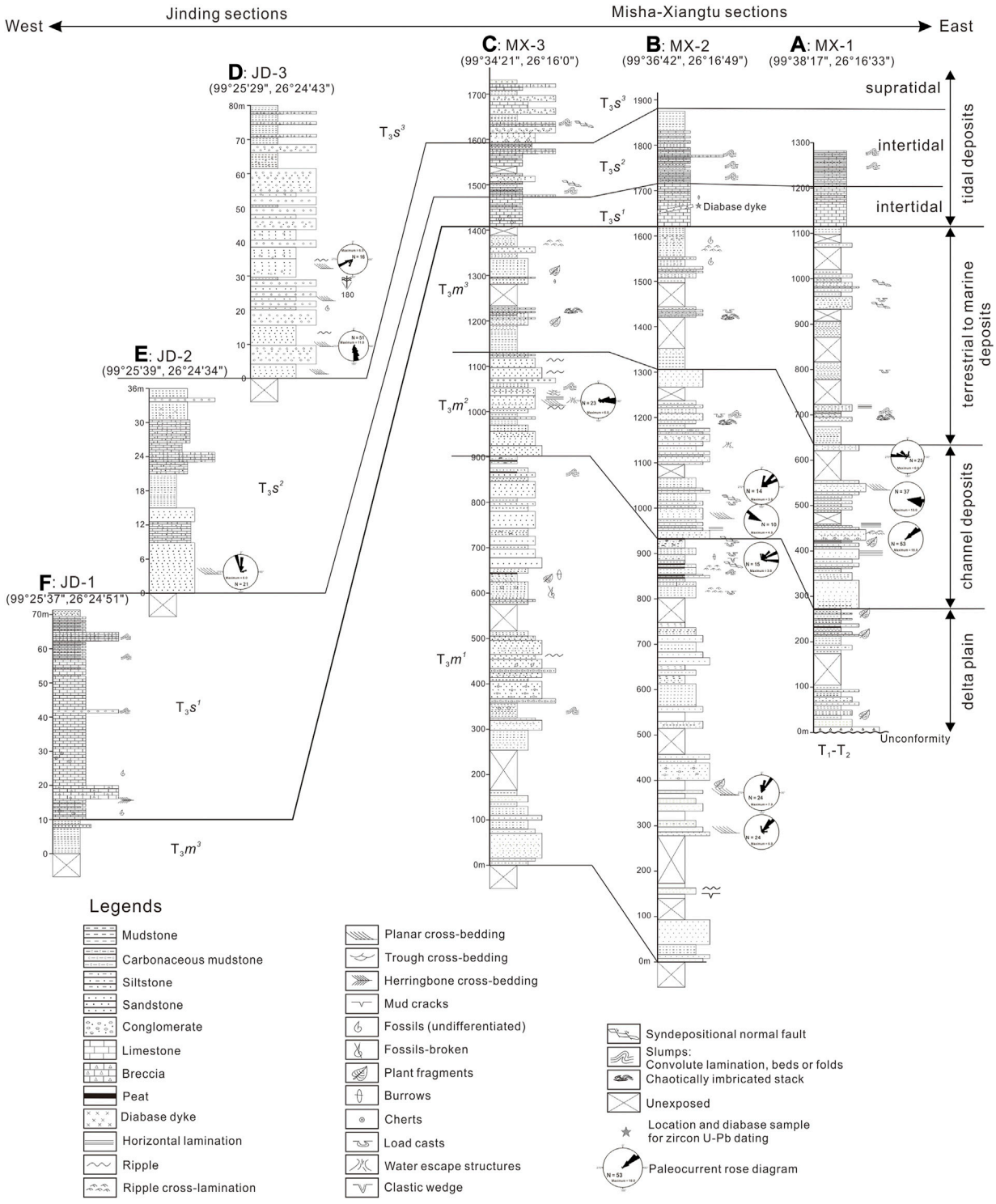

FIGURE 3
Measured sedimentary logs of the Maichuqing and Sanhedong formations. See Figure 2A for the locations of each section. From east to west, the three sections **(A–C)** along the Misha–Xiantu profile show successive variation in sedimentary features of the Maichuqing and Sanhedong formations, whereas the Jinding sections **(D–F)** show the lower, middle and upper part of the Sanhedong Formation. Note that the paleocurrent data of the Jinding section are not used to discuss because of the uncertainty in rotation of the related small fragments (see Figure 2A).

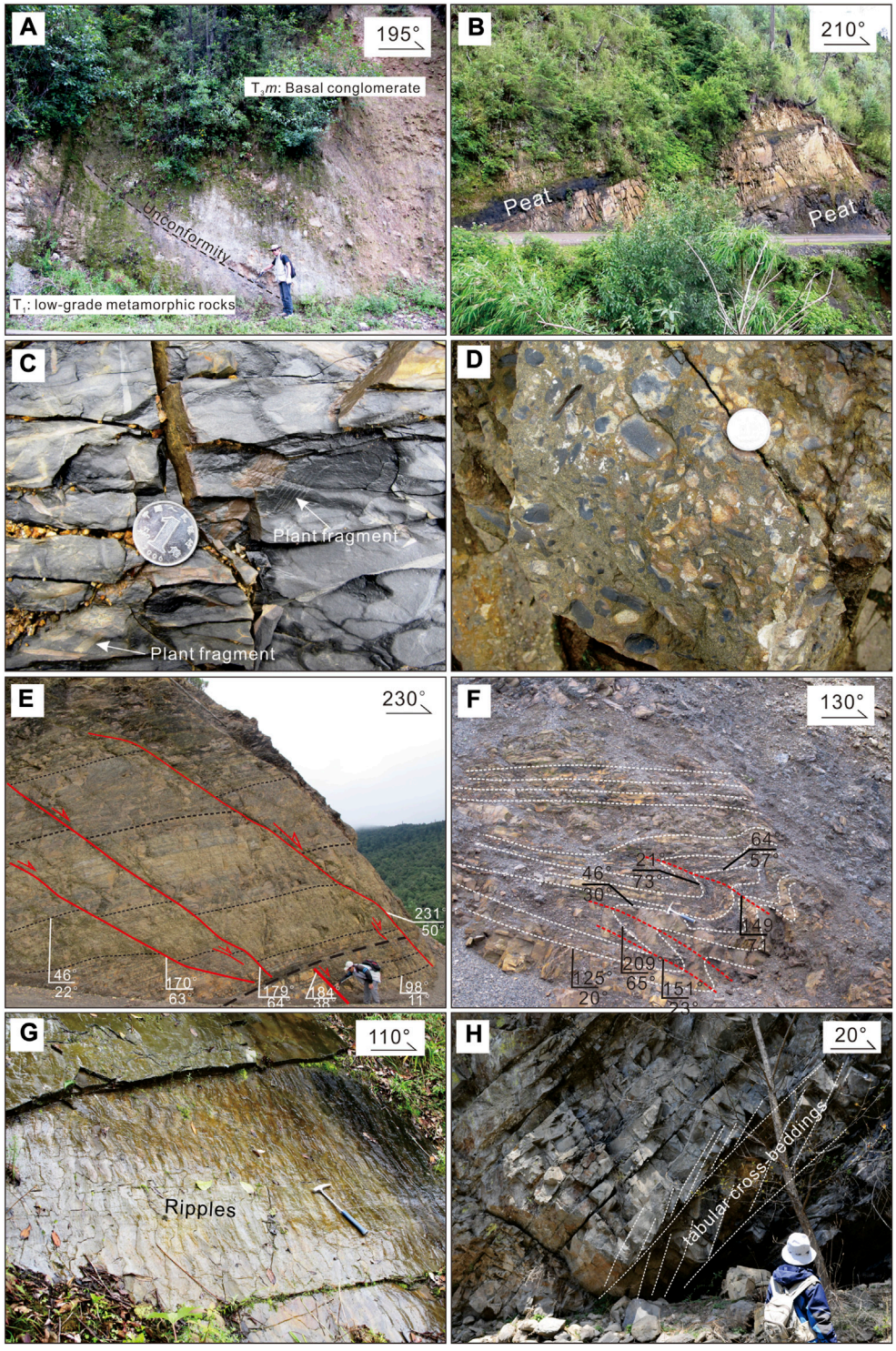

FIGURE 4
Field photographs showing typical sedimentary features of the Maichuqing Formation. **(A)** The Maichuqing Formation nonconformably overlies the early Triassic low-grade metamorphic rocks (GPS: 99.38′17″, 26.16′33″); **(B)** Peats in the high level of the lower segment of the Maichuqing Formation; **(C)** Plant fragments in siltstone; **(D)** Conglomerate; **(E)** and **(F)** Syn-sedimentation faults and folds in siltstone and mudstone; **(G)** Ripples in siltstone; **(H)** Planar cross-beddings of sandstone.

formations are well exposed in the Madeng–Misha area and the open pits of the supergiant Jinding Pb–Zn deposit. In the Misha–Xiangtu profile (Figure 2B), they folded and exhibited two open synclines and an open anticline. As such, the repeating of any stratigraphic units (see the sections MX-1 to 3 of Figure 3) shows the changes in thickness, sedimentary textures, and rock assemblage of the related units.

3.1 The Maichuqing formation

The ca. 1,100~1,650-m-thick Maichuqing Formation noncomfortably overlies the volcanoclastic rocks of the Jomda–Weixi–Yunxian arc (Figure 2A). This formation contains three segments according to the rock assemblages and associated sedimentary structures. In addition, the thickness, rock assemblage, and sedimentary texture of these three segments are variable from east to west, showing a westward thickening sequence (Figures 3A–C).

3.1.1 Lower segment

The lower part of the Maichuqing Formation consists of conglomerate, sandstone, siltstone, mudstone and lenticular peats. In the MX-1 section, it is ca. 270 m thick and nonconformably overlies the volcanoclastic rocks of the Jomda–Weixi–Yunxian arc (Figure 3A). Ca. 12-m-thick conglomerates exist at the bottom. They are matrix-to clast-supported and dominated by slate, phyllite, mudstone and sandstone clasts. These clasts originated from the underlain rocks of the Jomda–Weixi–Yunxian arc (Figure 4A) based on their same lithology. The conglomerate graded upward into an assemblage of siltstone, mudstone and sandstone with coalbeds or peats on the topmost (Figure 4B). Both sandstone and siltstone contain abundant plant fragments (Figure 4C).

To the west, the lower part of the Maichuqing Formation has a thickness of >900 m, where the underlain rocks and associated unconformity are not exposed (Figures 3B,C). In the MX-2 section, the equivalent consists of coarse-grain sandstone, siltstone, and mudstone; mud clasts common occur within siltstone and sandstone. Mud-cracks and ripple cross-laminations as well as normal grading and ripples are common, whereas slumped folds and syn-sedimentary normal faults were widely developed (Figures 4E,F).

To the west further in the MX-3 section, a suite of conglomerate (Figure 4D), pebbly coarse-grained sandstone, sandstone and siltstone with a thickness of ca. 150 m develops in the middle part of the lower segment. Other rocks both below and above the suite are the assemblages of sandstone and mudstone. Thinner siltstone, mudstone, and lenticular sandstone with several interbedded peats occur in the high level of the lower segment. These rocks are characterized by abundant burrows, plant fragments, ripple laminations. These characters demonstrate that they should deposit in a swamp environment. In addition, mud-cracks also occur in the mudstones, indicating that these fine-grained sediments experienced subaerial exposure. Conspicuous irregular basal erosional surface and imbricated clasts are easily observed in the outcrops of the conglomerate-bearing suite, indicating a channel environment (Miall, 1985). These observations demonstrate that the lower portion of the Maichuqing Formation deposited in channel, levee, and swamp environments of a delta plain (Miall, 1985).

3.1.2 Middle segment

The middle segment of the Maichuqing Formation consists of dark-gray sandstone, dark siltstone, and dark-gray calcareous mudstone with minor lenticular pebbly sandstone, showing a decreasing total thickness from 350 m in the east to 200 m in the west. Sandstones are massive, thin-to medium-bedded, and fine-to medium-grained, showing normal grading with distinct erosional base. Reverse grading also occurs locally. Siltstone is thinner and has parallel laminations, showing rhythmic sequence with mudstone. Conglomerate lenses occur in the high level with a thickness of <5 m, which extends laterally into the sandstone with distinct basal erosion surface. They are characterized by imbricated clasts comprising carbonaceous mudstone and mica-bearing medium-grained sandstone. Symmetrical ripples and trough cross-beddings widely occur in the thick, fine-grained sandstone (Figure 4G). Planar and trough cross-beddings are common within the sandstones in the upper level (Figure 4H); load casts are also observed locally. Slump folds occur near top of this part. We interpreted these sedimentary rocks as channel deposits of the delta plain (Miall, 1985).

3.1.3 Upper segment

The upper segment of the Maichuqing Formation has a variable thickness of ca. 260–450 m, which is dominated by interlayers of grey mudstone and siltstone. Lenticular sandstones and minor peats also occur locally in different sections. Abundant plant leaves fossils exist within the siltstone and mudstone at the lower level, and some lamellibranch fossils, including *Burmesia lirata* Healey, *Cuspidaria* sp., *Prolaria sollasii* Healey, and *Nuculanna* cf. *perlonga* (Mansuy), also exist at the upper level (YBGMR, 1974). Spatially, abundance and thickness of siltstone and sandstone increase vertically and to the west. Lenticular, ripple and parallel laminations are common in the sandstone and siltstone, and slump folds and normal faults also occur within mudstone. These characters demonstrate that the upper part of the Machuqing Formation deposited in a transitional environment from terrestrial to marine setting (Reading, 1996).

3.2 The Sanhedong Formation

The exposed thickness of the Sanhedong Formation is >300 m (Figure 3). This formation conformably overlies the

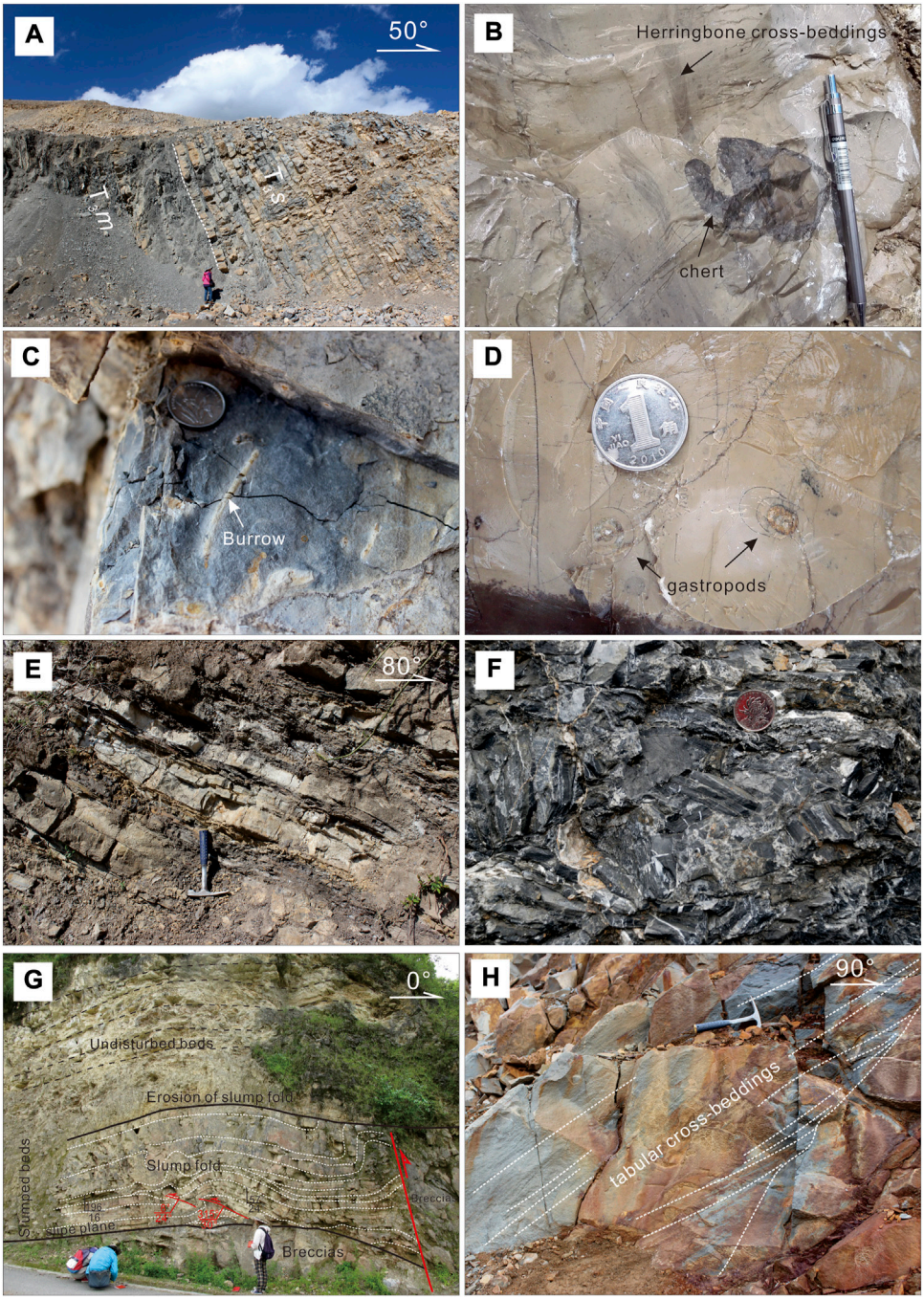

FIGURE 5
Field photographs showing the typical sedimentary features of the Sanhedong Formation. **(A)** Conformable contact between the Sanhedong Formation and the Maichuqing Formation (GPS: 99°25′37″, 26°24′51″); **(B)** Herringbone cross-beddings and chert nodules within micrite; **(C)** Burrows within thick limestone; **(D)** Gastropod fossil in micrite; **(E)** Thinly bedded micrite and marl with minor calcareous mudstone; **(F)** Brecciated limestone; **(G)** Slumped folds of thinner calcareous mudstone and micrite and associated brecciated limestone; **(H)** Tabular cross-beddings of sandstones.

Maichuqing Formation (Figure 5A) and can be subdivided into three segments based on its rock assemblages. *Halobia pluriradiata* Reed and *H.* cf. *yunnanensis* Reed in the upper part and some ammonoid, brachiopoda, lamellibranchiate in the lower part of this formation (YBGMR, 1974) indicate a shallow marine environment of depositional setting.

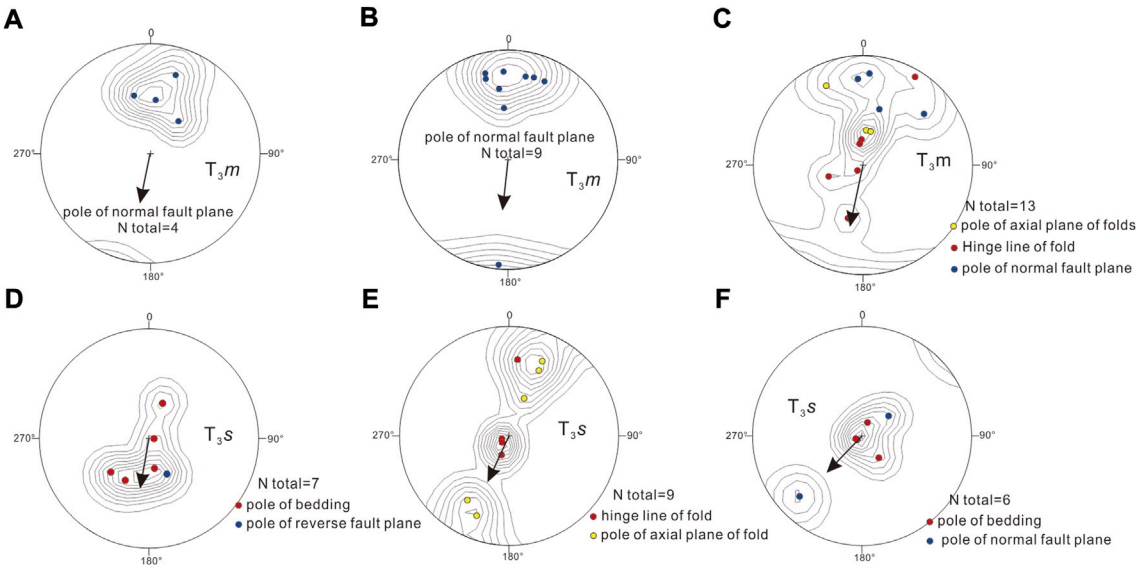

FIGURE 6
Equal angle stereonet projections of planes of syn-sedimentation normal fault and axial planes of slump folds. See text for detailed discussions. "N" means total number of measured altitudes of related structural elements.

The lower segment of the Sanhedong Formation consists of chert nodules-bearing micrite (Figure 5B) and bioclastic limestone with interbedded calcareous mudstone. It was crosscut by 220.0 ± 7.7 Ma diabase sheet (see the following) in the outcrops. The micrite and bioclastic limestone are thinly bedded with abundant euhedral pyrites. Locally, some brecciated limestones are associated with slump folded limestone. Burrows occasionally exist in thick limestone and thinner mudstone (Figure 5C). Bivalves, gastropods (Figure 5D), and crinoids within limestone have a good shape. Herringbone cross-beddings (Figure 5B) and ripples can be easily observed in the outcrops of micrite. These observations demonstrate they deposited in an intertidal environment (Reading, 1996).

The middle segment comprises thinly bedded micrite and marl with minor calcareous mudstone and siltstone interlayers. The thickness of any single bed of micrite varies from 10 cm in the lower part to 3 cm in the upper part in association with an upward increasing of the abundance of mudstone and siltstone (Figure 5E). Micrites are similar to those in the lower segment, both have been heterogeneously brecciated. Laterally, abundance and thickness of brecciated limestone increases dramatically from Xiangtu in the east to Jinding in the west (Figure 2). The brecciated limestone is characterized by numerous angular fragments of micrite with a variable length of 1.5–10 cm (Figure 5F). These fragments are cemented by calcic sands or muds. Alternatively, slumped folds developed in the interlayers of thinner calcareous mudstone (Figure 5G). Irregular bituminous veins occur within the micrite. Conspicuous basal erosion surfaces are common at the bottom of the micrite and brecciated limestone. In addition, wavy and flaser beddings (Figure 5E) exist locally in the marl. Planar cross-beddings occur in the lower level and lenticular conglomerates occur in the high level. These characters demonstrate that these rock assemblages belong to channel deposits of the intertidal setting (Reading, 1996).

The upper segment of the Sanhedong Formation was mainly exposed in the Xiangtu (Figure 3C) and Jinding lead-zinc mining areas (Figures 3D–F). It consists of calcareous conglomerate, coarse-grained calcareous sandstone, calcarenite, brecciated limestone and minor micrite and mudstone. The conglomerates consist of angular-subrounded limestone pebbles with distinct large-scale-scoured basal surface. Size of clasts and thickness of the conglomerates increase upward. The sandstone is thick and made of subrounded quartz, chert fragments, and minor feldspar. Slumped folds and associated normal faults are common in the Xiangtu area. Ripples, wave and flaser laminations are common in calcarenite, while mudcracks occur in mudstone. These observations indicate that these rocks deposited in a supratidal environment and experienced subaerial exposure (Reading, 1996), where the sandstones with tabular cross-beddings (Figure 5H) and associated lenticular conglomerates represent channel deposition.

4 Paleocurrent data

We measured 522 planar cross-beddings, ripple laminations, ripples, and imbricated clasts at suitable outcrops so as to provide information for source location and basin paleogeography of the

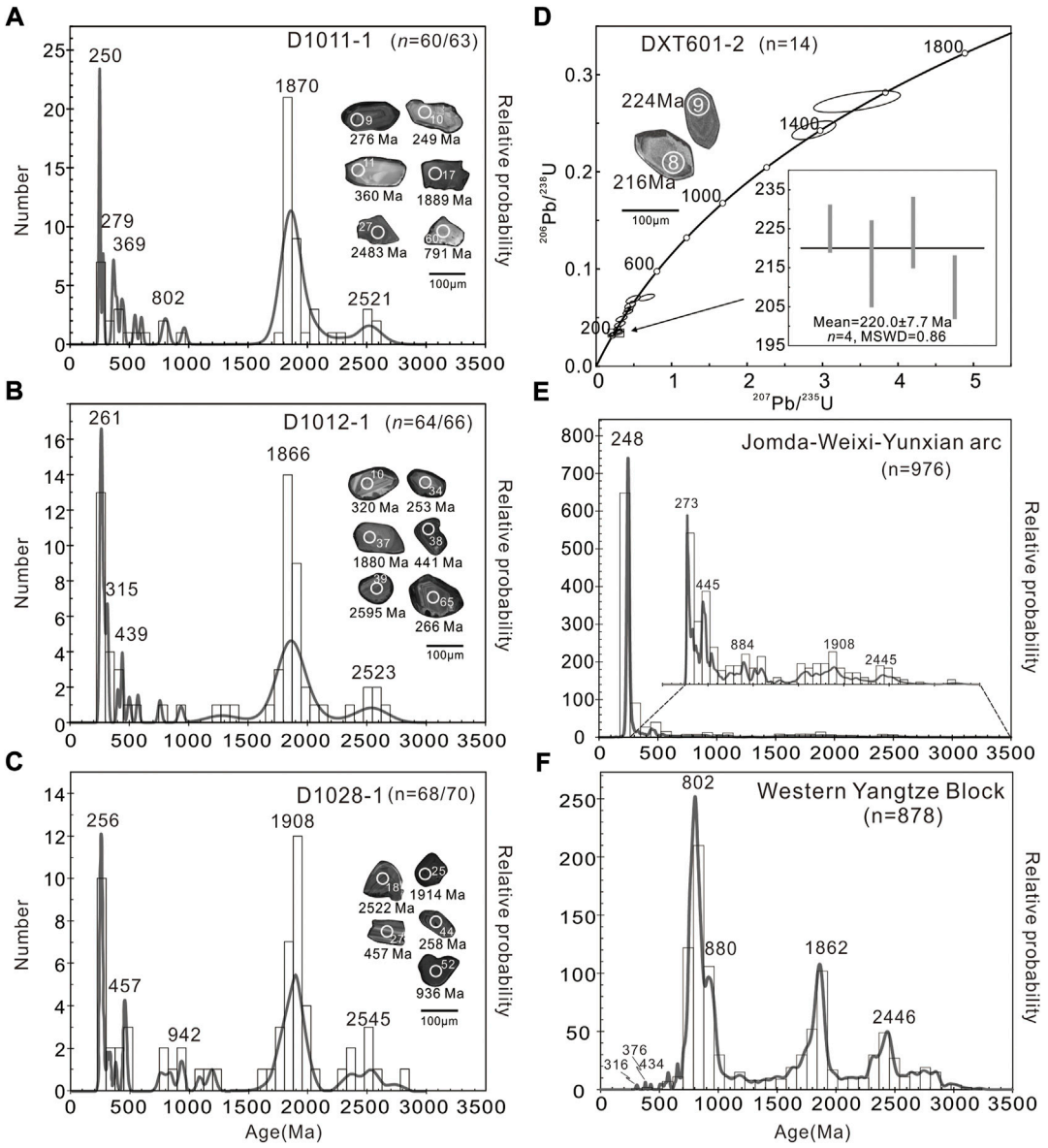

FIGURE 7
(A–C) Probability histograms of detrital zircon U-Pb ages of sandstone samples of the Maichuqing Formation. **(D)** Zircon U-Pb concordia diagram for the diabase dyke that intrudes the Sanhedong Formation. Relative probability of zircon U-Pb ages for igneous rocks of the middle Jomda–Weixi–Yuanxian arc **(E)** and for the western Yangtze Block **(F)** data sources: Sun et al., 2009 and Wang et al., 2012).

Maichuqing and Sanhedong formations (Figure 3). All data were corrected for local dip but not for possible later rotation because of lack of any regional rotation data to use as reference. However, geological mapping results demonstrate that 90 of the 522 measurements were located in some small blocks where available structural analysis results (Liang et al., 2022) show that these small blocks experienced heterogeneously rotation by thrust-and-tear fault associations. The remnant 432 measurements were conducted in the Misha–Xiangtu profile, along which the Late Triassic sedimentary rocks expose as a relatively complete block. Their results display that lower part of the Maichuqing Formation has a paleocurrent azimuth from 35° to 65°, but the lower and high levels of the middle part have two paleocurrent azimuths of 55°–100° and 275°–310°, respectively.

Syn-sedimentation deformation refers to sedimentary instabilities when the sediments in a slope were not solidified (Allen, 1982; Postma, 1983; Steen and Andresen, 1997; Moretti and Sabato, 2007). Abundant syn-sedimentation deformation structures in the Late Triassic rocks of the Misha-Xiangtu profile can also help us to infer basin paleogeography (Ortner,

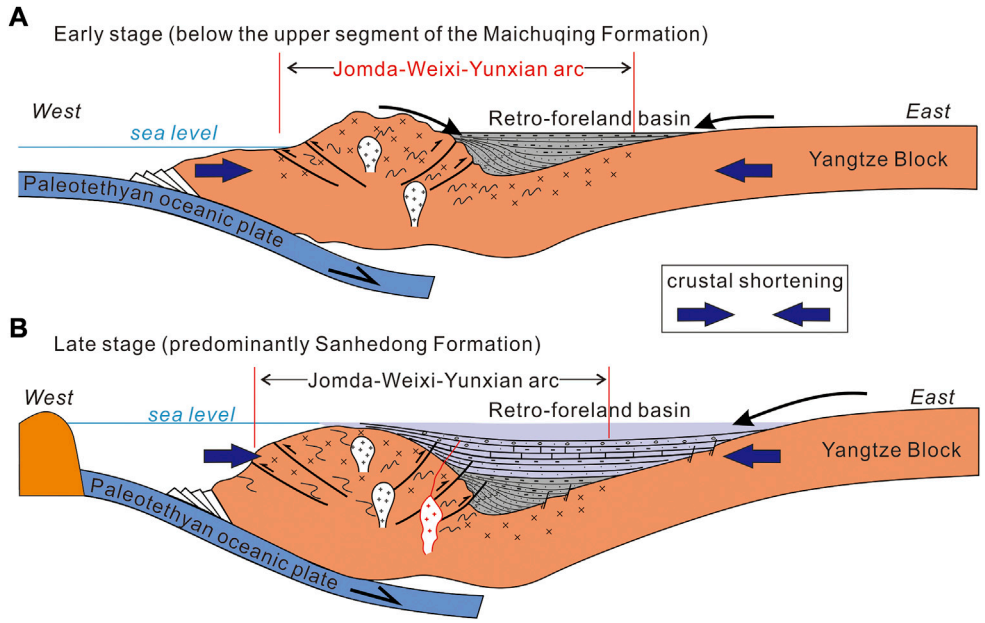

FIGURE 8
Cartoons show the development of the early Late Triassic retro-foreland basin, SE Tibet. See text for detail discussion.

2007; Lee and Phillips, 2008; Alsop and Marco, 2011; Lunina et al., 2012). Normal fault in high levels of the lower part of the Maichuqing Formation indicate 190°~200°-directed sliding of sediments (Figures 6A,B), Geometry of the recumbent slump folds supports this suggestion (Figure 6C). Intraformational reverse faults and overturned fold in the middle part of the Sanhedong Formation suggests 170°~190°-directed movement along the slipping plane (Figure 6D). Intraformational reverse faults and associated overturned folds in the middle part of the Sanhedong Formation suggest SSW-directed movement along the slipping plane (Figures 6D–F).

5 Zircon U-Pb ages of sandstones and diabase

In order to determine the timing of sedimentation and to reveal the provenance of the Triassic sedimentary rocks, three sandstone samples (D1011-1, D1012-1, and D1028-1) were collected from the middle portion of the Maichuqing Formation for detrital zircon U-Pb dating and one diabase dyke sample (DXT601-2) was collected to separate zircons for U–Pb dating, which intruded into the Sanhedong Formation. The locations of these samples are marked on Figure 2.

Zircons were separated using standard crushing, heavy liquid, and magnetic techniques. Exception for sample DXT601-2 that only 40 zircon grains were obtained, 150 to 200 zircon grains were hand-picked from the >25 μm non-magnetic fraction of each sandstone sample. Zircon grains were then mounted and cast in epoxy resin discs for photographing under reflected and transmitted light, obtaining cathodoluminescence (CL) images, and performing laser ablation LA-ICP-MS U-Pb dating. The U-Pb analyses of zircon were undertaken at the University of Science and Technology of China in Hefei, China, using an ArF excimer laser system (GeoLas Pro, 193 nm wavelength) and a quadrupole ICP-MS (PerkinElmer Elan DRCII). Analyses involved an ablation pulse rate of 10 Hz, beam energy of 10 J/cm^2, and a spot diameter of 32 μm. Procedures were described by Yuan et al. (2004). Standard zircon 91,500 (Wiedenbeck et al., 1995) was used for mass discrimination and elemental fractionation corrections, and U-Pb ratios were determined using the Excel program LaDating@Zrn. Common Pb was corrected by ComPb corr#3-18 (Anderson, 2002). Final statistics and age calculations were processed using Isoplot/EX ver. 4.15. We used $^{206}Pb/^{238}U$ and $^{207}Pb/^{206}Pb$ ages for zircons younger and older than 1.0 Ga, respectively (Griffin et al., 2004). Grains with >10% age discordance were discarded. Detailed procedures of zircon age determinations and trace-element analyses are followed Liu et al. (2007). Zircon U-Pb results are shown in Supplementary Table 1 with 1σ uncertainties.

5.1 Sample D1011-1

Sixty-three zircon grains with well-developed growth zonings yielded sixty concordant U–Pb ages of 2604–246 Ma. These spots can be grouped into two age populations of 246-963 Ma and

1,794–2,604 with a main peak at ca. 250 Ma, a secondary peak at ca. 1,870 Ma, and several minor peaks at ca. 369, ca. 802 and ca. 2,521 Ma (Figure 7A). They have a variable U content of 8–401 ppm and Th/U ratio of 0.06–4.09.

5.2 Sample D1012-1

Sixty-six zircon grains with well-developed growth zonings were analyzed and 64 of which yielded a concordant U–Pb age, ranging from 2,686 Ma to 246 Ma. They have a variable U content of 5–393 ppm and 0.02–3.15. These ages can be grouped into two age populations of 246–573 Ma and 1,248–2,686 Ma with a main peak at ca. 261 Ma, a secondary peak at ca. 1,866 Ma, and two minor peaks at ca. 439 and 2,523 Ma (Figure 7B).

5.3 Sample D1028-1

Sixty-eight spots of 70 analyzed zircon grains yielded a concordant age of 2,785–243 Ma, with a variable U content of 12–1,244 ppm and Th/U ratio of 0.05–2.44. These spots can be grouped into three age populations of 243–469 Ma, 606–941 Ma, and 1,020–2,785 Ma. They have a main peak at ca. 254 Ma, two secondary peaks at ca. 1,908 Ma and 457 Ma, and two minor peaks at 942 Ma and 2,545 Ma (Figure 7C). These data are similar to the sample D1011-1 and D1012-1.

5.4 Sample DXT601-2

Fourteen relatively large zircons from the diabase sample DXT601-2 were analyzed, yielding concordant ages ranging from 1,470 to 210 Ma. They have a variable U content of 65–3,105 ppm and high Th/U ratio of 0.22–0.87. Four long prismatic grains of which with broad oscillatory zoning in CL images yielded Late Triassic ages between 210 and 225 Ma, with a weighted mean age of 220.0 ± 7.7 Ma (MSWD = 0.86) (Figure 7D). This age probably represents the crystalline age of the diabase.

6 Discussion

6.1 depositional age of the Maichuqing and Sanhedong Formations

Fossil data, for example *Burmesia lirata* Healey, *Cuspidaria* sp., *Prolaria sollasii* Healey, and *Nuculanna* cf. *perlonga* (Mansuy) derived from the Maichuqing Formation and *Halobia pluriradiata* Reed and *H.* cf. *yunnanensis* Reed and ammonoid, brachiopoda, and lamellibranchiate fossils in the Sanhedong Formation indicate these formations deposited during the Late Triassic (YBGMR, 1974). This is consistent with our new detrital zircon U–Pb dating results, in which the 32 youngest zircons yielded $^{206}Pb/^{238}U$ age of 243–312 Ma with the peak at ca. 254 Ma (Supplementary Table 1).

Our zircon U–Pb dating results show that the Sanhedong Formation was intruded by diabase dyke at 220.0 ± 7.7 Ma. This value provides an upper limitation for deposition time of these two formations. Accordingly, the Maichuqing and Sanhedong Formation deposited during the earliest stage (Carnian) of the Late Triassic.

6.2 possible sources of the Maichuqing and Sanhedong formations

The Maichuqing and Sanhedong formations distribute in an area that astride the Jomda–Weixi–Yuanxian arc in the west and western margin of the Yangtze Block in the east (Figure 1B). Our paleocurrent data demonstrate that the detritus of the Maichuqing Formation is mainly derived from the SW or W (215°–280°) (Figure 3). In addition, some detritus of the upper level of middle portion of this formation originated from NE-SE-ward (85°–130°) sources.

We do not consider paleocurrent data derived from the Jinding deposit (Figures 3D,E) because uncertainty in local block rotation. As such, no sedimentary data are available to constrain paleocurrent of the Sanhedong Formation. As mentioned earlier, syn-sedimentation structures (Figures 6D–F) indicates an SSW-ward slope for the related basin when the Sanhedong Formation deposited. Thus, we suggest that detritus of the Sanhedong Formation was mainly sourced from an area of NNE, where platform limestones of the Yangtze Block are common. These limestones likely have provided calcareous materials for the Sanhedong Formation.

In summary, the detritus of the Maichuqing Formation was mainly derived from the Jomda–Weixi–Yunxian arc in SSW with minor from the Yangtze Block. Detrital zircon U–Pb dating results support this suggestion. The Jomda–Weixi–Yunxian arc rocks contain many 273–248 Ma magmatic zircons as well as numerous Early Paleozoic, Late and Middle Proterozoic zircons (Figure 7E; Yang et al., 2014; Liang et al., 2015; Tang et al., 2016; Xin et al., 2018), whereas the western Yangtze Block contain voluminous Neoproterozoic and Paleoproterozic magmatic rocks (Figure 7F, e.g., Sun et al., 2009; Wang et al., 2012). On contrary, the detritus of the Sanhedong Formation probably come predominantly from the Yangtze Block in the NNE.

6.3 Tectonic evolution of Late Triassic retro-foreland basin

As mentioned earlier, the volcanic-absent Upper Triassic strata (Burchfiel and Chen, 2012) including the Maichuqing and

Sanhedong formations developed exclusively in the middle segment of the Jomda–Weixi–Yunxian arc. Structural analyses (Yang et al., 2014; Tang et al., 2016; Xin et al., 2018) have shown that Permian to Middle Triassic volcanoclastic rocks of the middle Jomda–Weixi–Yunxian arc are tightly folded. This, combined with geochemistry of volcanic rocks and granites (Xin et al., 2018) suggests that the middle segment of the Jomda–Weixi–Yunxian arc formed in responding to eastward flat subduction of Paleo-Tethys. The intensely shortened Permian to Middle Triassic volcanoclastic rocks were covered by early Late Triassic sedimentary rocks; the latter are only slightly shortened evidenced by open folds (Figure 2B). This tectonic scenario is highly comparable to the Miocene Andean retro-foreland basin in the NW Argentina (del Papa et al., 2021), where the Nazca plate flatly subducted beneath the southern American continent (e.g., Gutscher et al., 2000; Farias et al., 2008). Therefore, we infer that the basin represented by the lower Upper Triassic Maichuqing and Sanhedong Formations is a retro (arc) foreland basin corresponding the flat subduction of Paleo-Tethyan Ocean, during which the upper plate was successively shortened (Espurt et al., 2008). Meanwhile, some rocks of the basement of the upper plate were tectonically eroded as evidenced by the extremely enriched isotopic geochemistry (including zircon Lu-Hf isotopic, i.e., Yang et al., 2014; Xin et al., 2018) and the widespread inherited Yangtze-affinity zircons of the subduction-related volcanic rocks (Tang et al., 2016; Liang, 2017; Xin et al., 2018). The 220 Ma diabase dyke intruded the Sanhedong Formation probably represents the last pulse of arc-volcanism.

Available geochronological data show that, from northwest to southeast, the cessation of magmatism in the Jomda–Weixi–Yunxian arc varies from the Middle Triassic (ca. 235 Ma) to the Late Triassic (ca. 210 Ma), whereas the onset of magmatism appears to have been in the Early Permian throughout the arc (Yang et al., 2014). Different segments of the diachronous Jomda–Weixi–Yunxian arc seem to have formed due to subduction of different tectonic regimes indicated by the different type of subduction-related basins: back-arc basins developed in both the northern and southern segments (Yang et al., 2014 and references therein), whereas retro-foreland basin is solely identified in the middle segment (this study).

Paleocurrent data and syn-sedimentation structures can help to reconstruct the palaeography of the retro-foreland basins (Allen and Allen, 2005). Our paleocurrent data (Figure 3) demonstrate that a major NEE-facing slope should have been existed during deposition of the Maichuqing Formation (Figure 8A), which then shifted into a southwestward-facing one during deposition of the Sanhedong Formation (Figure 8B). We infer that, at the end of deposition of the Maichuqing Formation, the northern segment of the Paleotethyan Ocean was closed (Yang et al., 2014) and subduction along the middle segment became weak (Figure 8B). The subsequent continent-continent collision in the northern segment would have inevitably led to a higher landscape than its middle and southern equivalents whereas the oceanic subduction continued. This well explains the S- or SW-wards sliding of unsolidified sediments indicated by the syn-sedimentation structures in the upper segment of the Maichuqing Formation and in the Sanhedong Formation.

Rock assemblages and associated sedimentary structures demonstrate that the Maichuqing Formation deposited predominantly in a delta plain setting and transitional setting of the marine and terrestrial environments (Figure 8A), which evolved upward into a tide environment of costal setting for deposition of the Sanhedong Formation (Figure 8B). In addition, the thickness of the lowest part of the Maichuqing Formation rapidly increases westward (Figures 3A–C), indicating that depocenter of the retro-foreland basin should be adjacent to the west at its earliest stage (Figure 8A). On contrary, the largest accumulation of the upper segment of the Maichuqing Formation occurred in the east (Figures 3A–C). This suggest the depocenter shifted to the east immediately before the transition from the terrestrial to marine environments (Figure 8B). For other stages, the shifts of depocenter are not very clear. The depocenter shift as well as the transition in sedimentary setting probably corresponds to a significant tectonic event. The Late Triassic continental collision in the northern segment of the Jomda–Weixi–Yunxian arc (Yang et al., 2014) is an appreciate candidate.

7 Conclusion

(1) The volcanics-absent transitional unit in the SE Tibetan Plateau developed solely on the middle segment of the Jomda–Weixi–Yunxian arc owing to flat-subduction of the Paleo-Tethyan oceanic plate.
(2) The volcanics-absent transitional unit in SE Tibetan Plateau deposited within a retro-foreland basin in responds to the flat subduction during the early Late Triassic (Carnian Stage).
(3) This retro-foreland basin was filled initially by coarse-grain sediments of a delta environment, which was then gradually changed to a tidal environment of shallow marine.
(4) Syn-sedimentation structures widely developed in the retro-foreland basin, suggesting intense tectonism during sedimentation of the retro-foreland basin.

Data availability statement

The original contributions presented in the study are included in the article/Supplementary Material, further inquiries can be directed to the corresponding author.

Author contributions

TY contributed to field observations, geological-maps compiling, structural analyses, conceptualization, writing and revising, and funding acquisition. ML contributed to field observations, structural analyses, formal analyses, data processing, and draft-writing and revising. ZY contributed to field observations, draft-writing and revising. CX contributed to field observations, structural analysis, and draft-writing. DX contributed to field observations, formal analyses, and structural analysis. SQ contributed to data processing and draft-revising. PS contributed to field observations, data processing, and draft-revising. MD, WW, KX, XH and JB carried out field observations. All authors contributed to manuscript revision, read, and approved the submitted version.

Funding

This work was financially supported by the Natural Sciences Foundation of China (No. 92055206) and Ministry of Sciences and Technology of People's Republic of China (grant numbers 2016YFC0600306-4 and 2015CB452601).

Acknowledgments

This study benefited a lot from our geological mappings in SE Tibet. Numerous students have taken part in these geological mappings although the direct contribution to this study is rare. They include but not limited Cheng Liao, Lei Wang, Yunlu Yangtian, Jingkun Liu, Yuantao Yao, Lili Jiang, Liangchun Wan, Wenbin Zhu, Jing Tang, Xiaotian Li, Ruijuan Lai, and Xinpeng Yang. Dr. Zhenhui Hou helped zircon U-Pb analyses. Comments and suggestions from journal's editor and Reviewers greatly improved this manuscript.

Conflict of interest

Author PS is employed by the Beijing Jinyou Geological Exploration Co., Ltd.

The remaining authors declare that the research was conducted in the absence of any commercial or financial relationships that could be construed as a potential conflict of interest.

Publisher's note

Supplementary material

The Supplementary Material for this article can be found online at: https://www.frontiersin.org/articles/10.3389/feart.2022.957337/full#supplementary-material

References

Allen, J. R. (1982). *Sedimentary structures: Their character and physical basis, II*. Amsterdam: Elsevier.

Allen, P. A., and Allen, J. R. (2005). *Basin analysis: Principles and applications*. Oxford, UK: Wiley-Blackwell.

Alsop, G. I., and Marco, S. (2011). Soft-sediment deformation within seismogenic slumps of the dead sea basin. *J. Struct. Geol.* 33 (4), 433–457. doi:10.1016/j.jsg.2011.02.003

Anderson, T. (2002). Correction of common lead in U–Pb analyses that do not report 204Pb. *Chem. Geol.* 29, 59–79. doi:10.1016/S0009-2541(02)00195-X

Burchfiel, B. C., and Chen, Z. (2012). *Tectonics of the southeastern Tibetan plateau and its adjacent foreland*. Boulder, Colorado, USA: The Geological Society of America.

Decelles, P. G., Carrapa, B., Horton, B. K., and Gehrels, G. E. (2011). Cenozoic foreland basin system in the central Andes of northwestern Argentina: Implications for Andean geodynamics and modes of deformation. *Tectonics* 30 (TC6013). 1–30. doi:10.1029/2011TC002948

Decelles, P. G., and Giles, K. A. (1996). Foreland basin systems. *Basin Res.* 8, 105–123. doi:10.1046/j.1365-2117.1996.01491.x

del Papa, C., Payrola, P., Pingel, H., Hongn, F., Do Campo, M., Sobel, E. R., et al. (2021). Stratigraphic response to fragmentation of the Miocene Andean foreland basin, NW Argentina. *Basin Res.* 33, 2914–2937. doi:10.1111/bre.12589

Edit Committee of the Sanjiang Geological Map (1986). *1:1,000,000 geological map of the Jinshajiang, langcangjiang, nujiang regions*. Beijing: Geological Publishing House.

Espurt, N., Funiciello, F., Martinod, J., Guillaume, B., Regard, V., Faccenna, C., et al. (2008). Flat subduction dynamics and deformation of the South American plate: Insights from analog modeling. *Tectonics* 27 (TC3011). 1–19. doi:10.1029/2007TC002175

Farias, M., Charrier, R., Carretier, S., Martinod, J., Fock, A., Campbell, D., et al. (2008). Late Miocene high and rapid surface uplift and its erosional response in the Andes of central Chile (33°– 35°S). *Tectonics* 27 (TC1005). 1–22. doi:10.1029/2006TC002046

García-Castellanos, D. (2002). Interplay between lithospheric flexure and river transport in foreland basins. *Basin Res.* 14, 89–104. doi:10.1046/j.1365-2117.2002.00174.x

Griffin, W.L., Belousova, E. A., Shee, S. R., Pearson, N. J., and O'Reilly, S. Y. (2004). Archean crustal evolution in the northern Yilgarn Craton: U-Pb and Hf-isotope evidence from detrital zircons. *Precambrian Res.* 131 (3, 4), 231–282. doi:10.1016/j.precamres.2003.12.011

Gutscher, M. A., Spakman, W., Bijwaard, H., and Engdalh, E. R. (2000). Geodynamics of flat subduction: Seismicity and tomographic constraints from the Andean margin. *Tectonics* 19, 814–833. doi:10.1029/1999TC001152

Hu, X. M., Wang, J. G., BouDagher-Fadel, M., Garzanti, E., An, W., and Webb, A. (2016). The timing of India-Asia collision onset – facts, theories, controversies. *Earth-Science Rev.* 32, 264–299. doi:10.1016/j.earscirev.2016.07.014

Jordan, T. E. (1995). "Retroarc foreland and related basins," in *Tectonics of sedimentary basins*. Editors D. J. Busby and R. V. Ingersoll (Hoboken, New Jersey, United States: Blackwell Science), 331–362.

Lee, J. R., and Phillips, E. R. (2008). Progressive soft sediment deformation within a subglacial shear zone—A hybrid mosaic–pervasive deformation model for middle pleistocene glaciotectonised sediments from eastern England. *Quat. Sci. Rev.* 27 (13-14), 1350–1362. doi:10.1016/j.quascirev.2008.03.009

Li, C., Zhai, Q., Dong, Y., and Huang, X. (2006). Discovery of eclogite and its geological significance in Qiangtang area, central Tibet. *Chin. Sci. Bull.* 51, 1095–1100. doi:10.1007/s11434-006-1095-3

Liang, M. J. (2017). "Filling the Lanping basin: Response to the neotethyan tectonics in the Sanjiang orogenic belt," (Beijing, China: China University of Geosciences). Ph.D. Thesis.

Liang, M. J., Yang, T. N., Shi, P. L., Xue, C. D., Xiang, K., and Liao, C. (2015). U-Pb geochronology, Hf isotopes of zircons from the volcanic rocks along the eastern margin of Lanping basin, Sanjiang orogenic belt. *Acta Petrol. Sin.* 31 (11), 3247–3248.

Liang, M. J., Yang, T. N., Xue, C. D., Xin, D., Yan, Z., Liao, C., et al. (2022). Complete deformation history of the transition zone between oblique and orthogonal collision belts of the SE Tibetan Plateau: Crustal shortening and rotation caused by the indentation of India into Eurasia. *J. Struct. Geol.* 156, 1–18. doi:10.1016/j.jsg.2022.104545

Liao, C., Yang, T. N., Xue, C. D., Liang, M. J., Xin, D., Xiang, K., et al. (2020). Eocene basins on the SE Tibetan plateau: Markers of minor offset along the xuelongshan-diancangshan-ailaoshan structural system. *Acta Geol. Sin.* 94, 1020–1041. doi:10.1111/1755-6724.14557

Liu, X. M., Gao, S., Diwu, C. R., Yuan, H. L., and Hu, Z. C. (2007). Simultaneous *in-situ* determination of U-Pb age and trace elements in zircon by LA-ICP-MS in 20 μm spot size. *Chin. Sci. Bull.* 52, 1257–1264. doi:10.1007/s11434-007-0160-x

Lunina, O. V., Andreev, A. V., and Gladkov, A. S. (2012). The tsagan earthquake of 1862 on lake baikal revisited: A study of secondary coseismic soft-sediment deformation. *Russ. Geol. Geophys.* 53 (6), 594–610. doi:10.1016/j.rgg.2012.04.007

Miall, A. D. (1985). Architectural-element analysis: A new method of facies analysis applied to fluvial deposits. *Earth-Science Rev.* 22, 261–308. doi:10.1016/0012-8252(85)90001-7

Mo, X. X., Deng, J. F., Dong, F. L., Yu, X. H., Wang, Y., Zhou, S., et al. (2001). Volcanic petro-tectonic assemblages in the Sangjiang orogenic belt, SW China and implication for tectonics. *Geol. J. China Univ.* 7 (2), 121–138.

Moretti, M., and Sabato, L. (2007). Recognition of trigger mechanisms for soft-sediment deformation in the pleistocene lacustrine deposits of the Sant'Arcangelo basin (southern Italy): Seismic shock vs. overloading. *Sediment. Geol.* 196, 31–45. doi:10.1016/j.sedgeo.2006.05.012

Ortner, H. (2007). Styles of soft-sediment deformation on top of a growing fold system in the Gosau Group at Muttekopf, Northern Calcareous Alps, Austria: Slumping versus tectonic deformation. *Sediment. Geol.* 196 (1-4), 99–118. doi:10.1016/j.sedgeo.2006.05.028

Postma, G. (1983). Water escape structures in the context of a depositional model of a mass flow dominated conglomeratic fan-delta (Abrioja Formation, Pliocene, Almeria Basin, SE Spain). *Sedimentology* 30, 91–103. doi:10.1111/j.1365-3091.1983.tb00652.x

Reading, H. G. (1996). *Sedimentary environment: Processes, facies and stratigraphy*. 3rd Edition. Oxford: Blackwell Science.

Song, Y. C., Hou, Z. Q., Xue, C. D., and Huang, S. Q. (2020). New mapping of the world-class jinding Zn-Pb deposit, Lanping basin, southwest China: Genesis of ore host rocks and records of hydrocarbon-rock interaction. *Econ. Geol.* 115 (5), 981–1002. doi:10.5382/econgeo.4721

Steen, O., and Andresen, A. (1997). Deformational structures associated with gravitational block gliding: Examples from sedimentary olistoliths in the kalvag melange, Western Norway. *Am. J. Sci.* 297, 56–97. doi:10.2475/ajs.297.1.56

Sun, W. H., Zhou, M. F., Gao, J. F., Yang, Y. H., Zhao, X. F., and Zhao, J. H. (2009). Detrital zircon U-Pb geochronological and Lu-Hf isotopic constraints on the precambrian magmatic and crustal evolution of the Western Yangtze Block, SW China. *Precambrian Res.* 172 (1-2), 99–126. doi:10.1016/j.precamres.2009.03.010

Tang, J., Xue, C. D., Yang, T. N., Liang, M. J., Xiang, K., Liao, C., et al. (2016). Late permian to early triassic tectonostratigraphy of Madeng area, northwestern yunnan, S.W. China: Bolcanics zircon U-Pb dating. *Acta Petrol. Sin.* 32 (8), 2535–2554.

Wang, B. D., Wang, L. Q., Chen, J. L., Yin, F. G., Wang, D. B., Zhang, W. P., et al. (2014). Triassic three-stage collision in the Paleo-Tethys: Constraints from magmatism in the Jiangda–Deqen–Weixi continental margin arc, SW China. *Gondwana Res.* 26 (2), 475–491. doi:10.1016/j.gr.2013.07.023

Wang, B. D., Wang, L. Q., Qiangba, Z. X., Zeng, Q. G., Zhang, W. P., Wang, D. B., et al. (2011). Early Triassic collision of Northern Lancangjiang suture: Geochronological, geochemical and Hf isotope evidence from the granitic gneiss in Leiwuqi area, eastern Tibet. *Acta Petrol. Sin.* 27, 2752–2762.

Wang, L. J., Yu, J. H., Griffin, W. L., and O'Reilly, S. Y. (2012). Early crustal evolution in the Western Yangtze Block: Evidence from U–Pb and Lu–Hf isotopes on detrital zircons from sedimentary rocks. *Precambrian Res.* 222-223, 368–385. doi:10.1016/j.precamres.2011.08.001

Wiedenbeck, M., Allé, P., Corfu, F., Griffin, W. L., Meier, M., Oberli, F., et al. (1995). Three natural zircon standards for U-Th-Pb, Lu-Hf, trace element and REE analyses. *Geostand. Geoanal. Res.* 19, 1–23. doi:10.1111/j.1751-908X.1995.tb00147.x

Xin, D., Yang, T. N., Liang, M. J., Xue, C. D., Han, X., Liao, C., et al. (2018). Synsubduction crustal shortening produced a magmatic flare-up in middle Sanjiang orogenic belt, southeastern Tibet plateau: Evidence from geochronology, geochemistry, and structural geology. *Gondwana Res.* 62, 93–111. doi:10.1016/j.gr.2018.03.009

Yang, T. N., Ding, Y., Zhang, H. R., Fan, J. W., Liang, M. J., and Wang, X. H. (2014). Two-phase subduction and subsequent collision defines the paleotethyan tectonics of the southeastern Tibetan plateau: Evidence from zircon U-Pb dating, geochemistry, and structural geology of the Sanjiang orogenic belt, southwest China. *Geol. Soc. Am. Bull.* 126, 1654–1682. doi:10.1130/B30921.1

Yang, T. N., Hou, Z. Q., Wang, Y., Zhang, H. R., and Wang, Z. L. (2012). Late paleozoic to early mesozoic tectonic evolution of northeast Tibet: Evidence from the triassic composite Western jinsha-garze-litang suture. *Tectonics* 31 (TC4004). 1–20. doi:10.1029/2011TC003044

Yang, T. N., Yan, Z., Xue, C. D., Xin, D., and Dong, M. M. (2021). India indenting eurasia: A brief review and new data from the yongping basin on the SE Tibetan plateau. *Geosciences* 11, 1–29. doi:10.3390/geosciences11120518

Yang, T. N., Zhang, H. R., Liu, Y. X., Wang, Z. L., Song, Y. C., Yang, Z. S., et al. (2011). Permo-Triassic arc magmatism in central Tibet: Evidence from zircon U–Pb geochronology, Hf isotopes, rare Earth elements, and bulk geochemistry. *Chem. Geol.* 284, 270–282. doi:10.1016/j.chemgeo.2011.03.006

YBGMR (Yunnan Bureau of Geology and Mineral Resource) (1974). *Geological map (scale 1/200,000) with geological report of Lanping (block G-47-X VI)*. Kunming, Yunnan: Yunnan Bureau of Geology and Mineral Resource.

Yuan, H. L., Gao, S., Liu, X. M., Li, H. M., Gunther, D., and Wu, F. Y. (2004). Accurate U–Pb age and trace element determinations of zircon by laser ablation-inductively coupled plasma-mass spectrometry. *Geostand. Geoanal. Res.* 28, 353–370. doi:10.1111/j.1751-908x.2004.tb00755.x

Frontiers in Earth Science

Investigates the processes operating within the major spheres of our planet

Advances our understanding across the earth sciences, providing a theoretical background for better use of our planet's resources and equipping us to face major environmental challenges.

Discover the latest Research Topics

See more →

Frontiers

Avenue du Tribunal-Fédéral 34
1005 Lausanne, Switzerland
frontiersin.org

Contact us

+41 (0)21 510 17 00
frontiersin.org/about/contact